Mechanical Properties of STRUCTURAL FILMS

CHRISTOPHER L. MUHLSTEIN
STUART B. BROWN
EDITORS

ASTM STP 1413

STP 1413

Mechanical Properties of Structural Films

Christopher L. Muhlstein and Stuart B. Brown, editors

ASTM Stock Number: STP1413

ASTM
100 Barr Harbor Drive
PO Box C700
West Conshohocken, PA 19428-2959

Printed in the U.S.A.

Library of Congress Cataloging-in-Publication Data

Mechanical properties of structural films / Christopher L. Muhlstein and Stuart B. Brown, editors.
p. cm. -- (STP ; 1413)
"ASTM Stock Number: STP1413."
Includes bibliographical references and index.
ISBN 0-8031-2889-4
1. Thin films--Mechanical properties--Congresses. I. Muhlstein, Christopher L., 1971- II. Brown, Stuart B. III. American Society for Testing and Materials. IV. ASTM special technical publication ; 1413.

TA418.9.T45 M43 2001
621.3815'2--dc21

2001053566

Peer Review Policy

Each paper published in this volume was evaluated by two peer reviewers and at least one editor. The authors addressed all of the reviewers' comments to the satisfaction of both the technical editor(s) and the ASTM Committee on Publications.

The quality of the papers in this publication reflects not only the obvious efforts of the authors and the technical editor(s), but also the work of the peer reviewers. In keeping with long-standing publication practices, ASTM maintains the anonymity of the peer reviewers. The ASTM Committee on Publications acknowledges with appreciation their dedication and contribution of time and effort on behalf of ASTM.

Printed in Bridgeport, NJ
November 2001

Foreword

This publication, *Mechanical Properties of Structural Films*, contains papers presented at the symposium of the same name held in Orlando, Florida, on 15–16 November 2000. The symposium was sponsored by ASTM Committee E08 on Fatigue and Fracture and by its Subcommittees E08.01 on Research and Education and E08.05 on Cyclic Deformation and Fatigue Crack Formation. The symposium chairman was Chris Muhlstein, University of California at Berkeley, and the symposium co-chairman was Stuart Brown, Exponent Failure Analysis Associates, Natick Massachusetts.

Contents

TENSILE TESTING OF STRUCTURAL FILMS

THERMOMECHANICAL, WEAR, AND RADIATION DAMAGE OF STRUCTURAL FILMS

Overview

Films or layers that are applied to substrates are frequently used for electronic, decorative, barrier, and wear applications. In addition, photolithography used by the microelectronics industry has led to the development of micron-scale mechanical components made from thin films. The class of structural materials that are manufactured as films is referred to as "structural films." The mechanical properties of thin films have been recognized as an important part of the performance of materials for over a century. However, the advent of microelectromechanical systems and other applications of structural films has led to a renewed interest in both the measurement and understanding of the mechanical behavior of thin films.

The papers from this symposium are distributed among four major areas of structural films characterization. Presented by an international group of experts from six countries, this symposium is one of the most complete assemblies of papers on the characterization of the mechanical properties of structural films available to date. The symposium begins with sessions on elastic behavior, residual stress, and fracture and fatigue. The remaining sessions are dedicated to tensile testing and thermomechanical, wear, and radiation damage. In the rapidly developing field of structural films, this event is a milestone in the engineering of these materials systems and their characterization.

Chris Muhlstein
University of California
at Berkeley
Berkeley, CA

Fracture and Fatigue of Structural Films

S. M. Allameh,[1] *B. Gally,*[2] *S. Brown,*[3] *and W. O. Soboyejo*[4]

Surface Topology and Fatigue in Si MEMS Structures

REFERENCE: Allameh, S. M., Gally, B., Brown, S., and Soboyejo, W.O., "**Surface Topology and Fatigue in Si MEMS Structures**," *Mechanical Properties of Structural Films, STP 1413,* C. Muhlstein and S. Brown, Eds., American Society for Testing and Materials, West Conshohocken, PA, Online, Available: www.astm.org/STP/1413/1413_11, 15 June 2001.

ABSTRACT: This paper presents the results of an experimental study of surface topology evolution that leads to crack nucleation and propagation in silicon MEMS structures. Following an initial description of the unactuated surface topology and nanoscale microstructure of polysilicon, the micromechanisms of crack nucleation and propagation are elucidated via in situ atomic force microscopy examination of cyclically actuated comb-drive structures fabricated from polysilicon. It is found that the surface of the polycrystalline silicon MEMS undergoes topological changes that lead to elongation of surface features at the highest tensile point on the surface. A smoothing trend is also observed after a critical stress level is reached.

KEYWORDS: surface, topology, fatigue, Si MEMS, AFM, morphology

Introduction

In recent years, there has been an explosion in the application of Micro Electro Mechanical Systems (MEMS) [1-3]. These include applications in gears, steam engines, accelerometers, hydrostats, linear racks, optical encoders/shutters, and biological sensors in the human body [1-3]. The projected market for MEMS products is estimated to be about $8 billion by the year 2002, and the prognosis for future growth appears to be very strong [3]. Most of the MEMS structures in service have been fabricated from polycrystalline silicon (polysilicon) or single crystal silicon. The reliability of these devices is a strong function of type of loading and environment. Due to the small size of the devices, most of the useful life of MEMS devices corresponds with the crack initiation stage. Once a crack is initiated, it rapidly propagates through the device, causing failure.

Our current understanding of the micromechanisms of fatigue crack initiation and propagation in silicon MEMS structures is still limited, in spite of the recent rush to apply MEMS structures in a wide range of applications [1-3]. This has stimulated some research activity, especially on single crystal silicon and polycrystalline (polysilicon) [4-13]. The early work on the fatigue of MEMS structures was done by Brown and co-workers [4-7], who developed microtesters [5,7] for conducting static/fatigue tests on MEMS structures. Their work demonstrated that stable crack growth can occur in MEMS structures fabricated from polysilicon and single crystal silicon, even though reversed plasticity [16] would not normally be expected to occur in such materials at room temperature. Subsequent work by Brown et al. [17,18] showed that crack growth is

[1]Research staff scientist, Princeton University, Olden St., Princeton, NJ 08544.
[2]Engineer, Exponent, 21 Strathmore Rd., Natick, MA 01760.
[3]Director, Exponent, 21 Strathmore Rd., Natick, MA 01760.
[4]Professor, Princeton University, Olden St., Princeton, NJ 08544.

enhanced in the presence of water/water vapor and stress.

Studies of fatigue in MEMS structures have also been performed by Heuer and Ballarini and their co-workers [8], Sharpe et al. [9,10], Marxer et al. [11], and Douglas [12]. However, there have been only limited studies of the micromechanisms of fatigue crack initiation that are likely to dominate the fatigue lives of MEMS structures [7]. The current level of understanding is, therefore, insufficient for the development of mechanics models. There is a need for detailed studies of environmentally assisted fatigue crack initiation and growth in MEMS structures.

Many of the applications of polysilicon are in MEMS systems in which cyclic actuation is an inherent part of the device function. For example, in the case of microswitches operating at a few kHz, millions or billions of cycles may be applied to the devices during their service lives [2,3]. Since such cycles may result ultimately in the nucleation and propagation of fatigue cracks, it is important to understand the mechanisms of fatigue in silicon MEMS structures that are subjected to cyclic actuation.

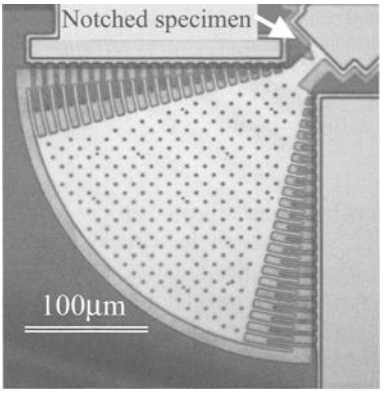

FIG. 1—*Photograph of a notched comb drive structure.*

The current paper presents the results of an initial study of the evolution of surface topology during the cyclic actuation of polysilicon MEMS structures. Following a brief description of the initial surface topology and microstructure, the evolution of surface topology is examined over a range of cyclic actuation voltages. Quantitative atomic force microscopy (AFM) techniques are used to reveal local changes in grain morphology and orientation and the evolution of surface morphology due to cyclic actuation. The AFM techniques analyses are also used to reveal the formation of grain boundary phases after cyclic actuation at intermediate actuation conditions.

Material

The polysilicon MEMS structures that were used in this study were supplied by Cronos Integrated Microsystems (formerly MCNC) of Raleigh-Durham, NC. The MEMS structures were fabricated in batch runs at Cronos. Details of the micromachining processing schemes are given in Ref 2. After releasing in a solution of 49.6% hydrofluoric acid, the surface topology of the silica (SiO_2) surface layer was studied with

an atomic force microscope operated in tapping mode with a silicon tip. The microstructure of the released polysilicon structure was also examined under a scanning electron microscope instrumented with a field emission gun.

The initial scanning electron microscope (SEM) image of the released polysilicon structures is shown in Fig. 2. This shows a nanocrystalline structure consisting of near-equiaxed grains with an average diameter of ~200 nm. Porosity was also observed in the polysilicon structure, especially at grain boundary triple points. Such distributed porosity may contribute to crack nucleation in polysilicon. However, crack nucleation may also occur as a result of stress-assisted dissolution of silica glass films, as proposed by Suo in Ref 19. The stress-assisted dissolution of silica can give rise to the evolution of grooves that lead ultimately to the nucleation of sharp cracks, as shown in Fig. 3.

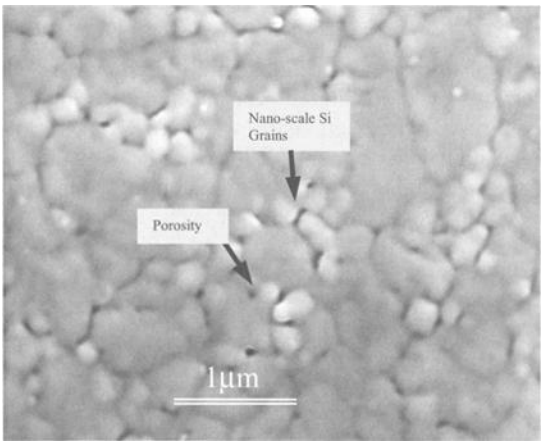

FIG. 2—*Scanning electron micrograph of polysilicon MEMS. structure before actuation.*

Experimental Procedures

The polysilicon comb drives used in this study (Fig. 1) were based on original designs by Van Arsdell [20] in which capacitive forces are induced between interdigitating comb drives. These forces are then applied to notched or unnotched constrained specimens within an area of ~ 10 μm by 20 μm. Due to the complex geometries of the comb drive devices, finite element analyses are needed to compute the stress/strain distributions and crack-driving forces [20]. Microvision methods [11,12] are also needed for the calibration of displacements during the electrical actuation of polysilicon MEMS structures.

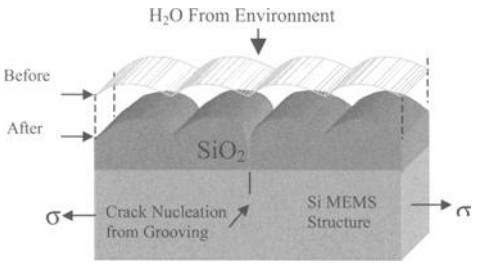

FIG. 3—*Schematic illustration of crack nucleation arising from possible stress-assisted dissolution.*

Since the displacements of the specimens must be known as functions of applied voltage, a special effort was made to calibrate each specimen as a function of the applied voltage, V. This was done using the microvision system (Fig. 4) developed by Freeman et al. [21-23]. We used National Instrument Vision Builder software to analyze optical images obtained under strobe light. In this way, the applied voltage could be related to the local displacements during static, monotonic, or cyclic actuation. Using this method, a calibration curve relating the applied voltage to angular displacement was obtained (Fig. 5).

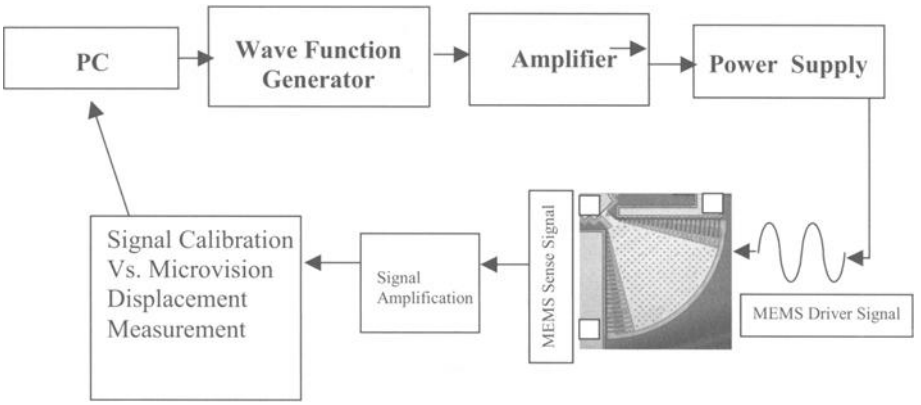

FIG. 4—*Schematic of microelectronic circuits for the control of the MEMS structure.*

Following the calibration, cyclic deformation experiments were performed on the specimens. The initial specimens were actuated continuously to failure in an effort to determine the number of cycles to failure, N_f. However, subsequent specimens were actuated incrementally to fractions of N_f. These include actuating at voltages of 100, 110, 120, 130, 135, 140, 142.5, and 145 V, each for 1 h except for the last actuation voltage that led to the failure of the sample after about 30 min.

The fracture of the sample occurred after a total of ~1.1 x 10^{10} cycles. After each incremental loading step (associated with an actuation voltage), the surface topologies of the specimens were examined using AFM techniques. For each loading step, AFM observations were made before actuation, after 5 min into the actuation, and at the end of the actuation (1 h total time for each loading step). SEM images of the specimens were also obtained in an effort to study possible changes in microstructure associated with cyclic actuation. The incremental loading was continued until failure occurred. The fracture surfaces of the failed specimens were then studied in a scanning electron microscope.

Results and Discussion

The results of this study show that the surface of the silicon MEMS sample undergoes discernable changes under fatigue loading conditions. SEM images of the surface before and after actuation show the microstructure of the surface and also some details of the fracture surface. Polysilicon MEMS structure used in this study has a nano-scale structure with an average grain size of ~ 200 nm.

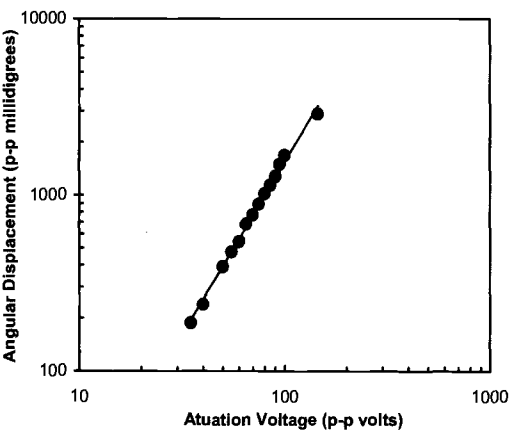

FIG. 5—*Calibration of the angular displacement of the polysilicon structure on the actuation voltage using microvision .system.*

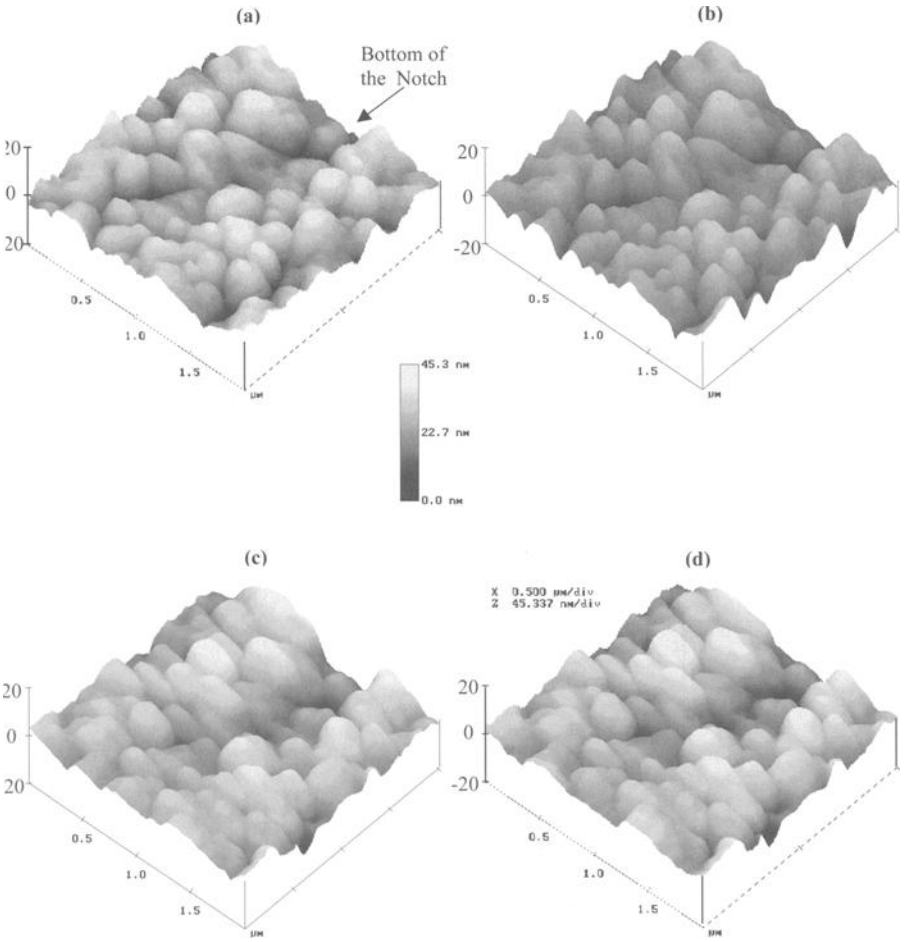

FIG. 6—*AFM images showing surface evolution of the silicon MEMS sample under cyclic loading conditions:* (a) *before actuation and after actuation at voltages up to* (b) *135V,* (c) *142.5V and* (d) *145 V.*

The AFM analyses of numerous specimens also show that the mean root square surface roughness of the SiO_2 layer on surfaces of the polysilicon is between 5 to 10 nm. The depth of the naturally occurring oxide layer is known to be ~ 20 Å [24]. However, the thickness of the oxide layer formed during the processing of MEMS depends on the fabrication process and is in the range of 10 to 100 nm.

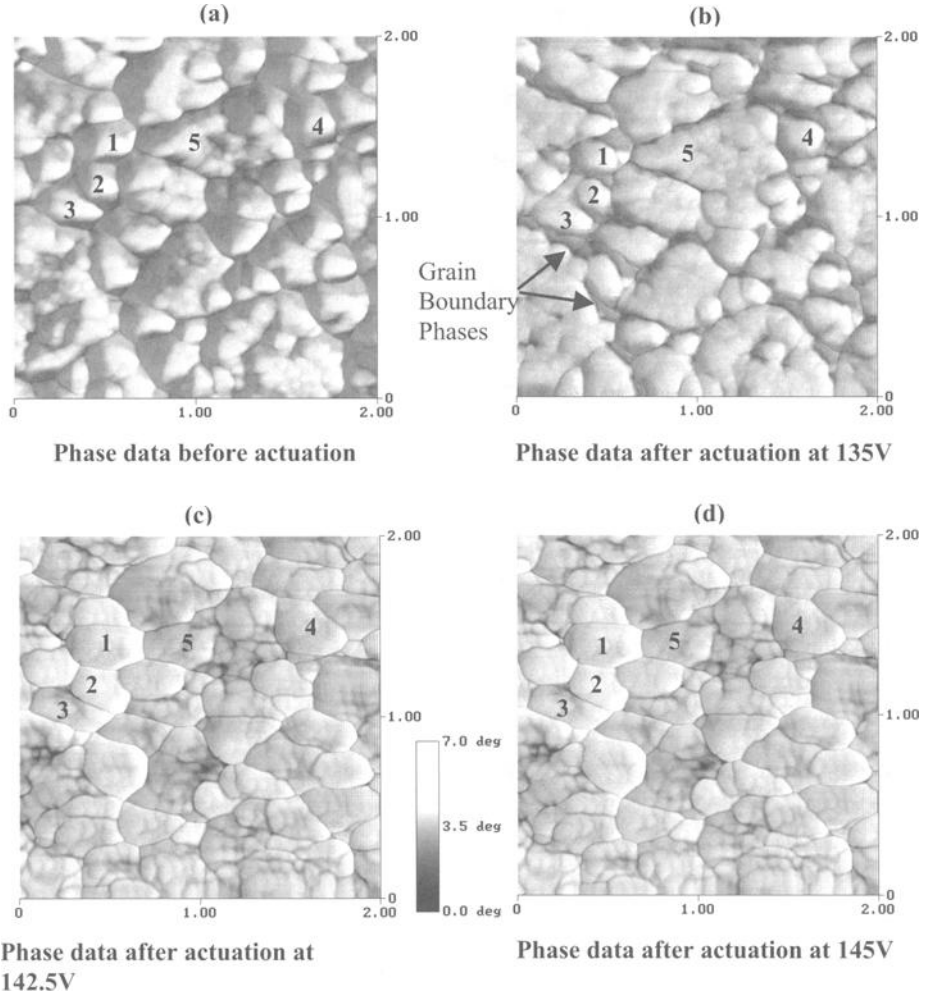

FIG. 7—*Phase-data-based AFM images showing surface evolution of the silicon MEMS sample under cyclic loading conditions:* (a) *before actuation and after actuation at voltages up to* (b) *135 V,* (c) *142.5 V, and* (d) *145 V.*

It is particularly important to note here that during the course of this study, a surface smoothing effect was observed which was activated at higher actuation voltages. This effect is evident in Figs. 8 and 9. Consistent with this effect, the RMS roughness values obtained from the surface roughness analyses (Fig. 9) drop at voltages close to 140 V.

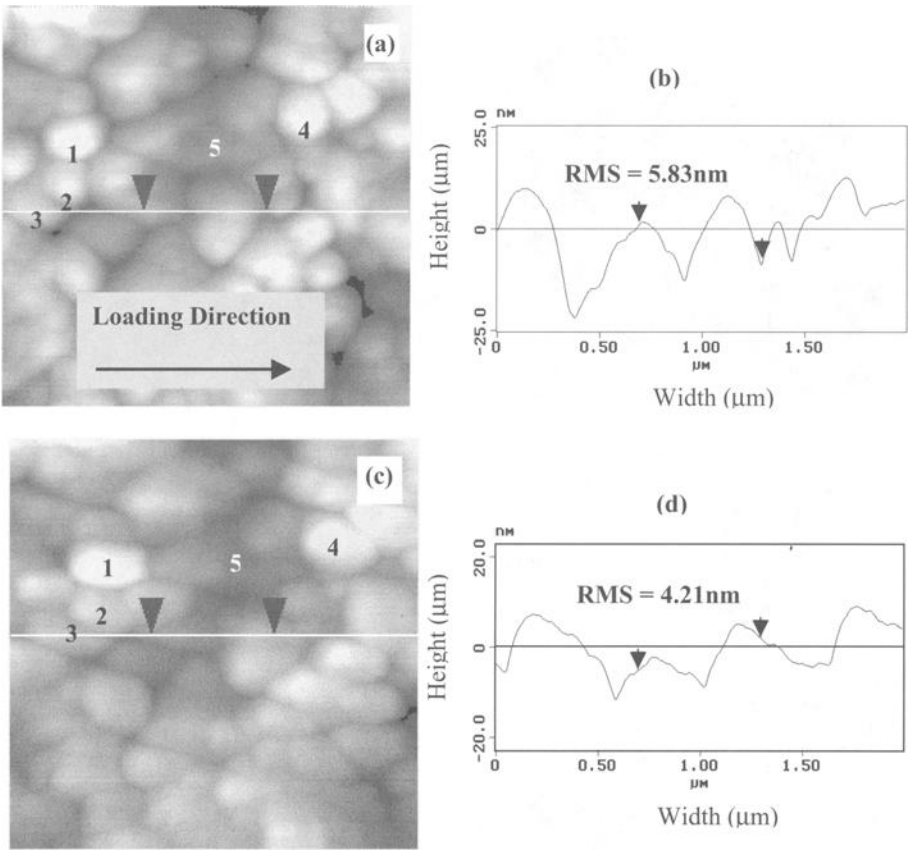

FIG. 8—*Height-data-based AFM images showing surface evolution of the silicon MEMS sample under cyclic loading conditions:* (a) *size, shape, and distribution of the grains located at the bottom of the notch before actuation;* (b) *a scan line close to the middle of the sample showing surface roughness;* (c) *size, shape, and distribution of grains in same region as in (a) after actuation at 145 V for 1.03 x* 10^{10} *cycles, and* (d) *corresponding scan line showing a lower RMS roughness.*

This effect is seen for two scan area sizes of 2 by 2 and 5 by 5 μm. Figure 9 shows that this effect can be as high as 30% of the initial RMS value. The smoothing effect is more clearly shown in Fig. 8 with the aid of two line scans from similar regions of the sample before and after actuation. The first line scan (Fig. 8*b*) shows an RMS roughness of 5.83 nm for the sample before actuation. However, a similar scan line (Fig. 8*d*) obtained from the same sample after cyclic actuation reveals an RMS roughness of 4.21 nm.

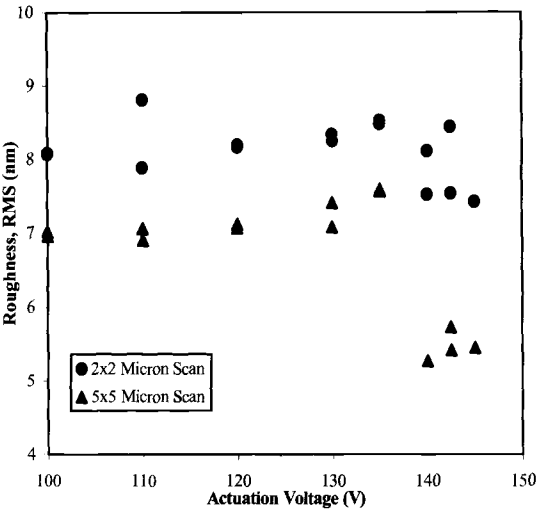

FIG. 9—*Surface roughness data for two sizes of scan areas show a surface smoothing effect at higher voltages.*

From the AFM images, surface roughness analyses, and image subtraction results, there appears to be a critical voltage at which the surface evolution process is accelerated. In our experiments, this critical voltage is estimated to be between 135 V and 142.5 V. The evidence for the presence of such a voltage can be seen from Figs. 6 to 9. The morphology of the surface does not change noticeably for actuation voltages up to the 135 V step. This is shown in Figs. 6*a* and 6*b*. On the other hand, a noticeable change is observed in the surface topology between the 135 V and 142.5 V steps (Figs. 6*c* and 6*d*). The data obtained from the surface roughness analyses are also consistent with the presence of such a critical voltage (Fig. 9). Furthermore, the RMS value of the roughness does not change appreciably until the voltage is increased to 140 V, at which the RMS roughness drops and continues to drop until the sample fails.

Careful examination of the AFM profiles and images reveals that the surface features on the Si MEMS sample elongate in the direction of the applied load. This is shown clearly in Figs. 7 and 8. Some of the grains are numbered to examine their shapes before and after actuation. Figure 7*a* shows grains labeled 1 to 5 before actuation. The orientations and morphologies of these grains can be followed during the actuation process through Figs. 7*b* to 7*d*. The phase-data images obtained from these grains (1-4 in Figs. 7*a*-7*d*) appear to be

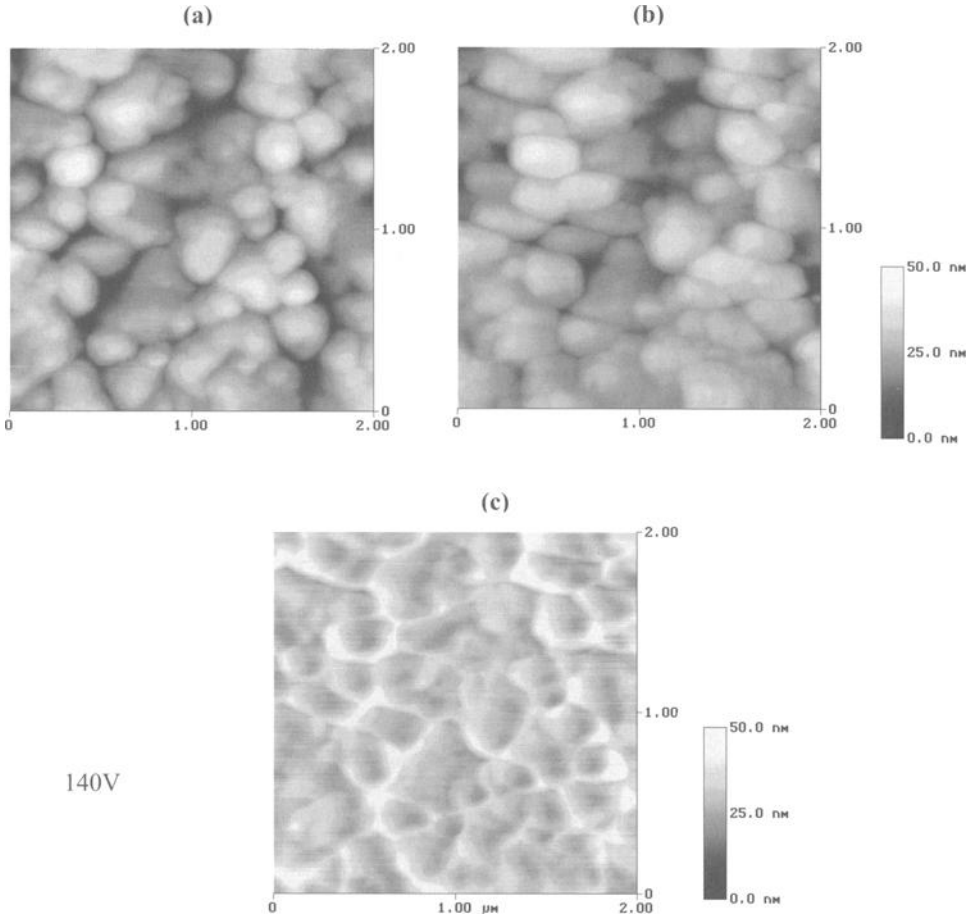

FIG. 10—*AFM images from the Si MEMS sample:* (a) *before actuation;* (b) *after actuation and* (c) *subtracted image, i.e., image (a)-image (b). White areas have highest height difference while the darker areas have the smallest difference in height.*

elongated in the direction of applied stress which coincides with the scanning direction of the AFM tip. While the size of the scanned areas in Figs. 7*a*-7*d* remains the same, the grains appear to increase in length as the actuation voltage is increased. Since the elongation occurs in the direction of scanning, it may not be attributed to a shift in the position of sample (any drift of the sample during imaging affects the width of the grains, perpendicular to the scanning, orders of magnitude greater than that of the length of the grains which lie in the direction of scanning). However, because the elongation is in the direction of applied tensile load, it is more likely due to surface phenomena that are enhanced in the loading direction.

The same effect can be seen in images obtained from the height-base images of Figs. 8*a* and 8*c*, which show the same grains labeled 1 to 5 before and after actuation. To examine the possible elongation effect, the two images in Figs. 8*a* and 8*c* were subtracted to reveal the differences more clearly in Fig. 10. Brighter areas represent larger differences, while darker areas correspond to smallest differences in the surface topologies. It is easy to see the alignment of such differences perpendicular to the loading direction. If surface features elongate, the boundaries between them, oriented in the elongation direction, will not change as much as the ones perpendicular to the loading direction. When the latter boundaries move, they create areas of difference behind in the subtracted image of Fig. 10. It is also interesting to note that some surface features like that of Grain 5 have shrunk in length after actuation (Figs. 7 and 8).

The AFM examination also revealed the presence of some grain boundary phases at the intermediate stages. Figures 7*c* and 7*d* show boundaries, which are clean after high voltage actuation. However, at intermediate actuation voltages, the phase-data image of Fig. 7*b* shows the presence of grain boundary phases. These phases cannot be easily identified due to their relatively small width (<0.1 nm). They are approximately 10 to 100 nm in length, and their area fraction varies with the extent of actuation. The phase-data image of the non-actuated sample contains some darker regions. However, they are due largely to grain boundary porosity and are not attributed to the presence of grain boundary phases.

Summary and Concluding Remarks

This paper examines surface evolution in Si MEMS structures deformed under cyclic loading conditions. The results of AFM and SEM analyses of the surface are presented. The major findings are as follows:

1. Polysilicon MEMS structures used in this study have a nano-scale structure with an average grain size of ~ 200 nm. The root mean square surface roughness of the SiO_2 layer on surface of the polysilicon is ~ 5 to 10 nm. The SiO_2 layer has an average thickness of ~ 20 nm.
2. The preliminary studies show that cyclic actuation of the comb drives results in sub-critical damage evolution that is attributed to fatigue mechanisms. However, the mechanisms of crack nucleation and propagation are yet to be fully established. Nevertheless, it is hypothesized that crack nucleation occurs as a result of surface topology evolution in the SiO_2 surface layer, although distributed porosity within the SiO_2 layer and the formation of grain boundary phases may lead to other mechanisms of crack nucleation.

3. The surface topology only evolves significantly during cyclic actuation at applied voltages (stress ranges) above a critical level (~140 V). Above the critical actuation voltage, surface features elongate in the direction of loading. The RMS roughness also drops significantly (~30%) beyond the critical voltage, indicating a smoothing effect due to cyclic actuation. At intermediate stages (activation voltages between 135 and 140 V, grain boundary phases are observed which disappear at higher voltages. The possible role of these phases is yet to be established.

Acknowledgments

The research was supported by the Division of Mechanics and Materials of The National Science Foundation (NSF) and The Defense Arms Research Projects Agency (DARPA). SMA and WOS are grateful to Dr. J. Larsen-Basse, the project manager at NSF, for his encouragement and support. SB and BG would also like to thank Dr. William Tang, the DARPA program manager, for financial support. Uniphase, (formerly CORONOS) Raleigh-Durham, NC is acknowledged for manufacturing the polysilicon comb drives used in this study.

References

[1] Wise, K. D. and Najafi, K., "Microfabrication Techniques for Integrated Sensors and Microsystems," *Science*, Nov. 1991, Vol. 254, No. 5036, pp. 1335–1342.

[2] Madou, M., *Fundamentals of Microfabrication*, CRC Press, New York, 1997.

[3] Togawa, T., *Biomedical Transducers and Instruments*, CRC Press, 1997.

[4] Connally, J. A. and Brown, S. B., "Slow Crack Growth in Single-Crystal Silicon," *Science*, 1992, Vol. 256, pp. 1537–39.

[5] Connally, J. A., and Brown, S. B., "Micromechanical Fatigue Testing," *Experimental Mechanics*, June 1993, Vol. 33, pp. 81–90.

[6] Brown, S., Povuk, G., and Connally, J., "Measurement of Slow Crack Growth in Silicon and Nickel Micromechanical Devices," *Proceedings of MEMS-93*, Fort Lauderdale, FL, 7-10 Feb. 1993, pp. 99–104.

[7] Brown, S. B., Van Arsdell, W., and Muhlstein, C. L., "Materials Reliability in MEMS Devices," *Proceedings, Transducers 97, International Conference on Solid-State Sensors and Actuators, Digest of Technical Papers*, Vol. 1, 1997, pp. 591–593.

[8] Kahn, H., Ballarini, R. L., Mullen, R., and Heuer, A. H., "Electrostatically Actuated Failure of Microfabricated Polysilicon Fracture Mechanics Specimens," *Proceedings of the Royal Society, Series A* (Mathematical, Physical and Engineering Sciences) Vol. 455, No. 1990, 1999, pp. 3807–3823.

[9] Sharpe, Jr., W. N. and Turner, K. T., "Fatigue Testing of Materials Used in Microelectromechanical Systems," *Proceedings, Fatigue 99*, 1999, pp. 1837–1844.

[10] Sharpe, W. N., Jr., Yuan, B., and Edwards, R. L., "Fracture Tests of Polysilicon Films," *Journal of Microelectromechanical Systems*, 1997, Vol. 6, pp. 193–199.

[11] Marxer, C., Gretillat, M. A., de Rooij, N. J., Battig, R., Anthametten, O., Valk, B., and Vogel, P., "Reliability Considerations for Electrostatic Polysilicon Actuators Using as an Example the REMO Component," *Sensors and Actuators*, 1997, Vol. 61, pp. 449–454.

[12] Douglass, M. R., "Lifetime Estimates and Unique Failure Mechanisms of the Digital Micromirror Device (DMD)," *Proceedings, IEEE International Reliability Symposium*, Reno, IEEE, Piscataway, NJ, 1998, pp. 9–16.

[13] Minoshima, K., Inoue, S., Terada, T., and Komai, K., "Influence of Specimen Size and Sub-Micron Notch on the Fracture Behavior of Single Crystal Silicon Microelements and Nanoscopic AFM Damage Evaluation," *Materials Science of Microelectromechanical Systems (MEMS) Devices Symposium*, MRS, 1999, pp. 15–20.

[14] Mohr, J. and Strohrmann, M., "Examination of Long-Term Stability of Metallic LIGA Microstructures by Electromagnetic Activation," *Journal of Micromechanics and Microengineering*, 1992, Vol. 2, pp. 193–195.

[15] Cornella, G., Vinci, R. P., Suryanarayanan Iyer, R., Dauskardt, R. H., and Bravman, J. C., "Observations of Low Cycle Fatigue of Al Thin Films for MEMS Applications," *Materials Research Society Symposium Proceedings*, 1998, Vol. 518, pp. 81–88.

[16] Suresh, S., *Fatigue of Materials*, 2nd ed., Cambridge University Press, 1998.

[17] Van Arsdell, W. and Brown, S. B., *Proceedings of the ASME Symposium on Micro-Electro-Mechanical Systems (MEMS) Structures*, ASME, New York, NY, 1998, pp. 267–272.

[18] Brown, S. B., Van Arsdell, W., and Muhlstein, C. L., "Materials Reliability in MEMS Devices," *Proceedings of the IEEE Conference on Solid-State Sensors and Actuators*, IEEE, Piscataway, NJ, 1997, Vol. 1, pp. 591–593.

[19] Provost, J. H., Baker, T.-J., Liang, J., and Suo, Z., "A Finite Element Model of Stress-Assisted Surface Reaction and Delayed Fracture," *International Journal of Solids and Structures*, submitted.

[20] Van Arsdell, W., "Sub-Critical Crack Growth in Polysilicon MEMS," Ph.D. thesis, Massachusetts Institute of Technology, 1997.

[21] Freeman, D. M., Aranyosi, A. J., Gordon, M. J., and Hong, S. S., "Multidimensional Motion Analysis of MEMS Using Computer Microvision," *Proceedings of the. Solid-State Sensor and Actuator Workshop*, Hilton Head Island, SC, June 1998, pp. 150–155.

[22] Quentin Davis, C. and Freeman, D.M., "Using a Light Microscope to Measure Motions with Nanometer Accuracy," *Optical Engineering*, Vol. 37, 1998, pp. 1299-1304.

[23] Ritchie, R. O., "Mechanisms of Fatigue Crack Propagation in Metals, Ceramics and Composites: Role of Crack Tip Shielding," *Materials Science Engineering A*, Vol. A103, 1988, pp. 15–28.

[24] Ghandhi, S. K., "Native Oxide Films," in *VLSI Fabrication Principles*, Wiley, New York, 1983.

David A. LaVan,[1] *Toshiyuki Tsuchiya,*[2] *George Coles,*[3] *Wolfgang G. Knauss,*[4] *Ioannis Chasiotis,*[4] *and David Read*[5]

Cross Comparison of Direct Strength Testing Techniques on Polysilicon Films

REFERENCE: LaVan, D. A., Tsuchiya, T., Coles, G., Knauss, W. G., Chasiotis, I., and Read, D., **"Cross Comparison of Direct Strength Testing Techniques on Polysilicon Films,"** *Mechanical Properties of Structural Films, ASTM STP 1413*, C. Muhlstein and S. B. Brown, Eds., American Society for Testing and Materials, West Conshohocken, PA, Online, Available: www.astm.org/STP/1413/1413_06, 10 April 2001.

ABSTRACT: Several direct and indirect testing techniques to characterize the strength and distribution in strength of structural thin films have been developed with widely varying results appearing in the literature (roughly 1 to 4 GPa for polysilicon). Much of the variation between authors has been explained in terms of microstructural differences, sample size effects, and release techniques. Five laboratories participated in a cross comparison of direct tensile testing techniques in an effort to study these variations; all samples were fabricated and released simultaneously at Sandia National Labs to eliminate material variations. Sample lengths ranged from 15 to 1000 μm long. All the samples were fabricated with a thickness of 2.5 μm. The distributions in strength are reported along with a tabulation of mean, standard deviation, and Weibull modulus of fracture strength for each lab.

KEYWORDS: polysilicon, MEMS, thin film, tensile, fracture, strength, testing, distribution

Introduction

The development of microelectromechanical systems (MEMS) and their subsequent utilization in critical applications has led to an interest in characterizing the strength and distribution in strength of structural thin films to assess system reliability. Several direct and indirect testing techniques have been developed with widely varying results appearing in the literature (roughly 1 to 4 GPa) [1-6]. Much of the variation between authors has been explained in terms of microstructural differences due to deposition conditions, sample size effects, and release processing. A previous cross comparison exercise involving direct and indirect testing techniques using the same material found significant disagreement between techniques [7]. In the current study, five laboratories participated in a cross comparison of direct tensile testing techniques in an effort to study the variation within the direct techniques, which should be less sensitive to experimental uncertainties. To address the sample size effect, each investigator received samples of at least four sizes; the range of specimen sizes overlapped. Two different approaches were applied, and this provided the opportunity to make a direct comparison between techniques as well as laboratories. Further, all the samples were produced and

[1]Formerly of Sandia National Laboratories; Massachusetts Institute of Technology, Cambridge, MA; and Children's Hospital, Boston, MA; lavan@mit.edu.

[2]Toyota Central Research and Development Laboratories, Nagakute, Japan.

[3]Department of Mechanical Engineering, The Johns Hopkins University, Baltimore, MD.

[4]Graduate, Aeronautical Laboratories, California Institute of Technology, Pasadena, CA.

[5]Materials Reliability Division, National Institute of Standards and Technology, Boulder, CO.

released at the same time and in the same way to eliminate influences of processing or release.

Two essentially different types of samples were distributed (with variations in size within each group). The first samples were designed to be gripped with an electrostatic force applied to the enlarged end of a sample, and the tensile force application and measurement were performed with a macro scale system; slightly different versions of this system were used by Tsuchiya [4,8], and Coles [5,9]. Knauss and Chasiotis also tested this sample, but used the electrostatic force only to assist in the adhesive bonding of the sample to the grip [10]. Samples of four sizes were tested by these three labs, with widths of 6 and 20 μm and lengths of 250 and 1000 μm, which resulted in nominal gage surface areas of 4250 to 45 000 μm^2. The second sample type, tested by Read [11] and LaVan [12], is 1.8 μm wide and 15 to 1000 μm long. These samples have nominal gage surface areas of 135 to 9000 μm^2. The distributions in strength are shown. The mean, standard deviation, Weibull characteristic strength, and Weibull Modulus are tabulated. The testing and data reduction techniques used by each lab are described in detail in the references attributed to each investigator.

Sample Preparation

All of the samples were produced using Sandia National Labs SUMMiT IV polysilicon process—they were patterned in the poly1-2 composite layer that is 2.5 μm thick. Samples of each size were produced side by side on the same die, and five or more die were sent to each participant. The films were deposited as n-type, fine-grained polysilicon from silane in a low-pressure chemical vapor deposition (LPCVD) furnace at ~580°C. The intervening sacrificial oxide layers were also deposited in an LPCVD furnace from tetraethylorthosilicate (TEOS) at ~720°C. This process usually uses 6-in., (100) n-type silicon wafers of 2 to 20 ohm/cm resistivity covered by 6000 Å of thermal oxide followed by 8000 Å of LPCVD silicon nitride for electrical isolation. Thickness was accurately controlled during the deposition process and was measured, along with width, in a calibrated SEM after release (accuracy 0.1 μm). The samples were released, coated with a self-assembling monolayer (SAM) such as octadecyltrichlorosilane (ODTS) or perfluorodecyltrichloro-silane (FDTS) as an anti-stiction coating, and then dried with super-critical CO_2. The microstructure and crystallographic texture of this polysilicon have been well characterized. The texture is random. The grain morphology is columnar, with a mean column diameter of 300 to 400 nm. Most of the grains bridge from the top to bottom surface of the film. More details of the process may be found in Ref 13.

Tensile Testing Techniques

The tensile testing technique employed by Tsuchiya and Coles is characterized by its electrostatic grip system. Figure 1 shows a schematic of this system. The thin film specimen is a cantilever beam with a large free end. The free end of the specimen is gripped to a probe by electrostatic force. Because the electrostatic force is weak compared with the mechanical forces necessary to break the sample, the grip cannot withstand bulk specimens, but works for samples with thin, narrow gage sections.

First, the probe is moved close to the free end of a specimen. By applying voltage between the specimen and the probe, electrostatic force is generated and the specimen is

fixed to the grip (probe). Then, tensile force is applied to the specimen until it fractures. During the test, the friction force between the two surfaces in contact holds the specimen in place. After the specimen fractures, the fractured free end can easily be recovered.

Knauss and Chasiotis have modified this technique with a new gripping method that makes use of an Ultraviolet (UV) light curable adhesive. This avoids side effects due to accumulated charges. The process for gluing the sample to the grip in shown in Fig. 2. They also use Digital Image Correlation (DIC) [14,15] with AFM data to determine the strain field.

The sample and testing technique employed by LaVan is shown schematically in Figs. 3 and 4. The samples are much smaller in overall size; the gage section width is 1.8 μm and the gage lengths ranged from 15 to 1000 μm. The specimens are attached to the substrate by a freely rotating pivot, which allows for proper alignment during the test. On each side of the free end are bumpers attached to the substrate to keep the specimens in place. Corrections for errors due to frictional losses from the tip sliding on the substrate and due to lateral compliance can be found in the references.

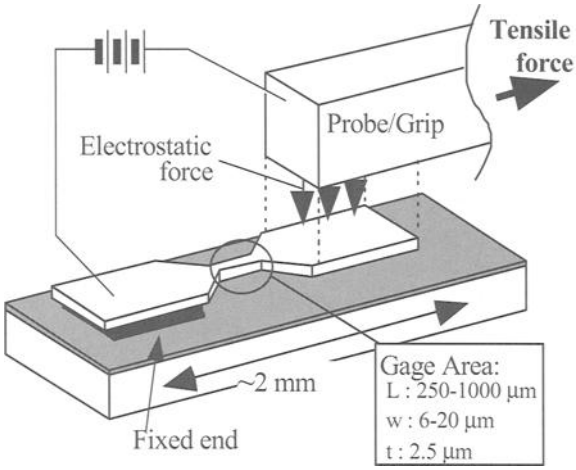

FIG. 1—*Technique of Tsuchiya and Coles. Tensile testing using electrostatic force grip.*

Read also tested the sample shown in Fig. 3. However, these tests were conducted under an optical microscope, and observed through its video camera. The specimens were loaded with a newly developed force probe. This device, shown schematically in Fig. 5, consists of a computer-controlled three-axis micro-manipulator, a pair of flex strips supporting a standard wafer-probe tip holder, and a non-contacting eddy current displacement sensor to indicate the displacement of the probe. A standard tungsten probe tip is bent slightly to form a loading pin, which resembles an open hook, as shown. The force probe had been previously calibrated, using a force pendulum; its displacement, as indicated by the eddy-current sensor, is a linear function of the tensile force applied at the tip. Corrections were made for the probe sliding on the substrate by observing the measured force after fracture.

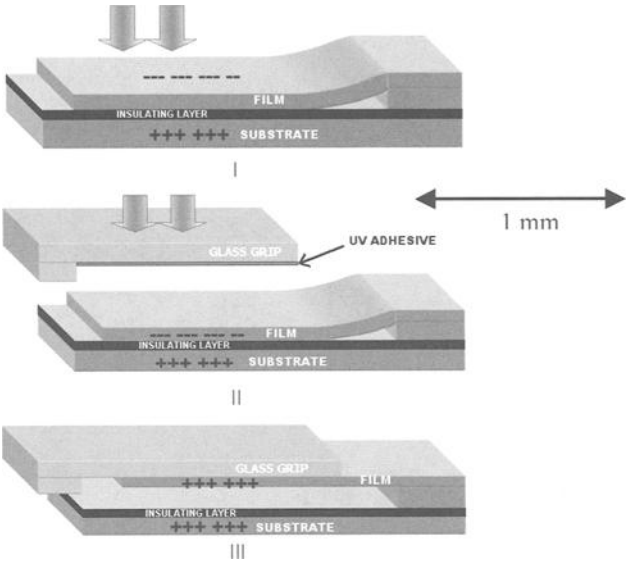

FIG. 2—*Technique of Knauss and Chasiotis. Successive steps of film gripping: I. The film is forced electrostatically to lie flat on the substrate, II. The glass grip with a UV curable adhesive layer is approached to the surface of the film; III. The film adheres to the UV adhesive under the grip.*

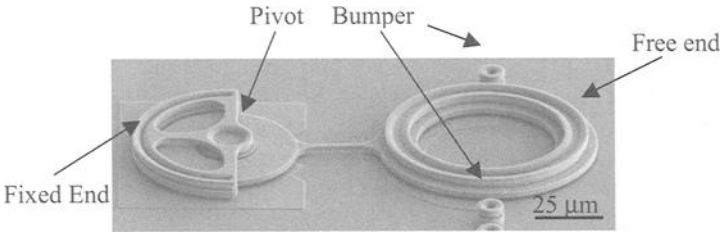

FIG. 3--*Sample tested by LaVan and Read.*

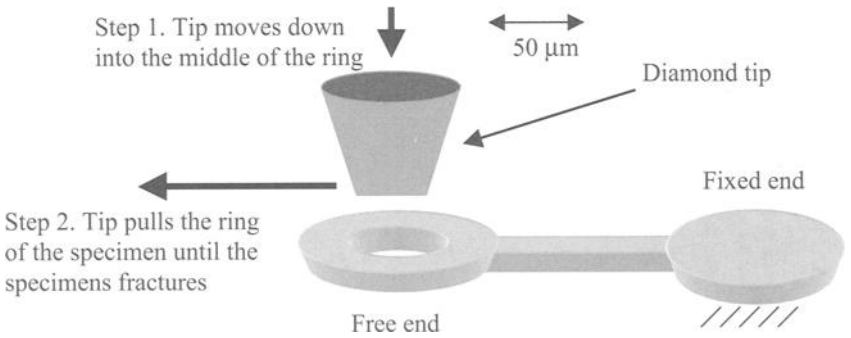

FIG. 4—*Lateral force testing procedure.*

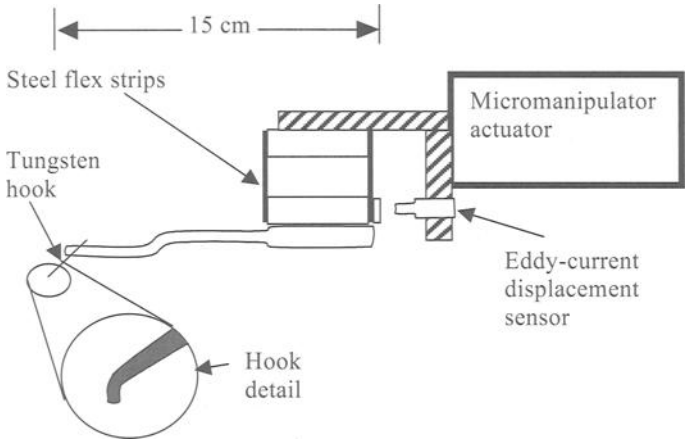

FIG. 5—*Force probe used for tensile testing.*

Results

The data for the comparison are presented using both normal and Weibull distributions. Not all of the labs tested enough samples to present the results solely as a Weibull distribution, and most existing polysilicon tensile data have been reported in terms of mean and standard deviation. Where sufficient data were collected, Weibull parameters are provided as failure of brittle materials and is best represented in this manner. A summary of the strength for all samples from each lab and statistical analysis is given in Table 1, and the properties are reported as a function of sample size in Tables 2 and 3. The Weibull modulus and characteristic strength are reported in Table 4. A graph of strength versus probability of failure is shown in Fig. 6. The Weibull distribution [16] is plotted in Fig. 7. The following probability estimator was used for the limited number of samples, where n is the number of samples in the population [17]:

$$P_f = (j\text{-}0.5)/n \tag{1}$$

The data from each lab were plotted as a function of gage surface area, gage volume, and gage sidewall area, shown in Figs. 8-10.

TABLE 1—*Summary of strength data (all sizes combined).*

Lab	Number of Samples	Mean Strength (GPa)	Std. Dev. Strength (GPa)	Coeff. of Variation (CV)	Minimum Strength (GPa)	Maximum Strength (GPa)
Coles	28	2.85	0.40	14%	1.76	3.31
Knauss & Chasiotis	19	3.13	0.46	15%	2.25	3.81
LaVan	98	4.27	0.61	14%	2.90	5.54
Read	5	2.87	0.41	14%	2.42	3.53
Tsuchiya	41	3.16	0.27	8.5%	2.49	3.59

TABLE 2—*Strength data for small samples, all 1.8 μm wide and 2.5 μm thick (GPa).*

Length	LaVan			Read	
(μm)	*N*	mean	SD	*n*	mean
15	13	4.35	0.67		
30	15	4.44	0.53		
60	13	4.44	0.52	1	3.53
90	15	4.27	0.49	1	2.92
150	12	4.24	0.65	1	2.84
300	15	4.19	0.80	1	2.42
500	13	4.03	0.62		
1000	2	4.07	*	1	2.65

TABLE 3—*Strength data for large samples, all 2.5 μm thick, (strength and standard deviation in GPa).*

Length	Width	Coles			Knauss & Chasiotis			Tsuchiya		
(μm)	(μm)	*n*	mean	SD	*N*	mean	SD	*n*	mean	SD
250	5.8	7	3.12	0.13	4	3.25	0.67	9	3.27	0.24
250	19.8	7	2.74	0.53	5	3.47	0.20	10	3.37	0.17
1000	5.8	7	2.93	0.16	5	2.88	0.40	14	2.97	0.24
1000	19.8	7	2.62	0.48	5	2.94	0.35	8	3.10	0.22

TABLE 4—*Summary of Weibull analysis.*

Lab	Number Of Samples	Weibull Modulus	Characteristic Strength (GPa)
Coles	28	7.7	3.1
Knauss & Chasiotis	19	7.9	3.3
LaVan	98	8.4	4.5
Read	5	Insufficient data	Insufficient data
Tsuchiya	41	14.4	3.3

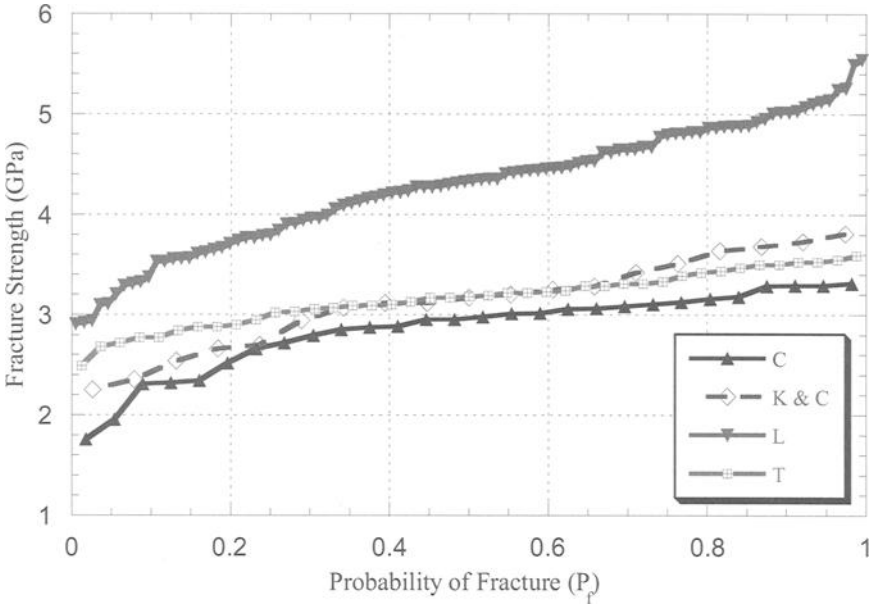

FIG. 6--*Strength versus probability of fracture.*

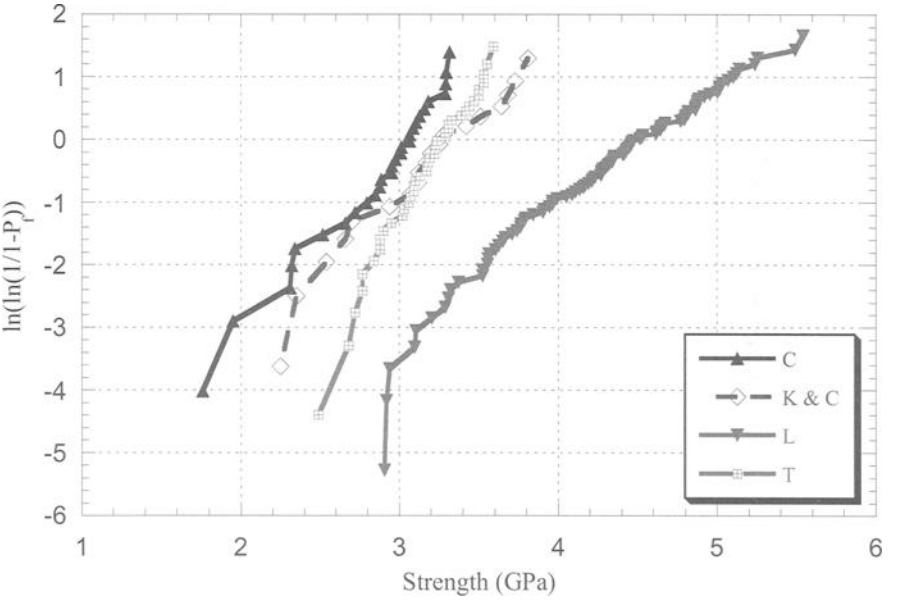

FIG. 7--*Weibull plot of strength.*

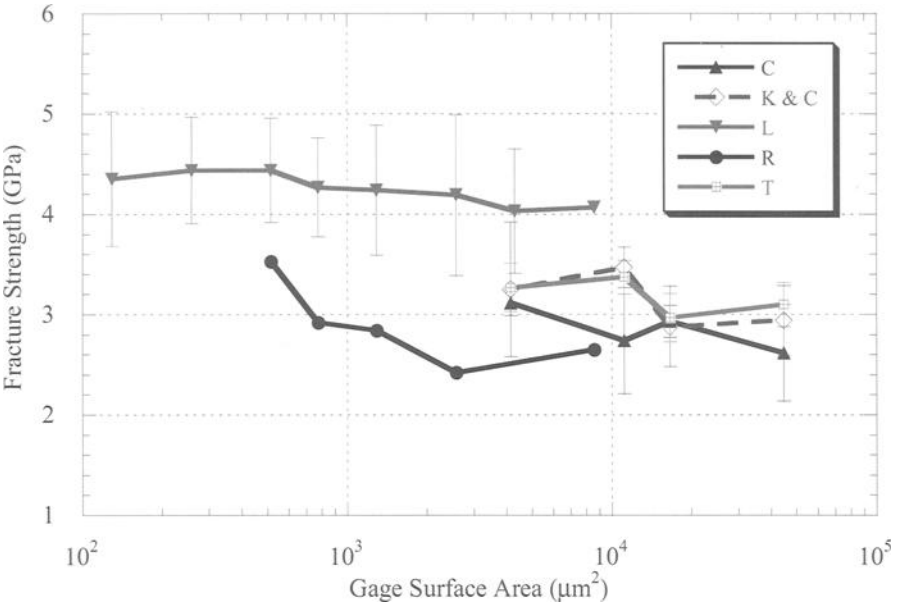

FIG. 8—*Strength as a function of gage surface area.*

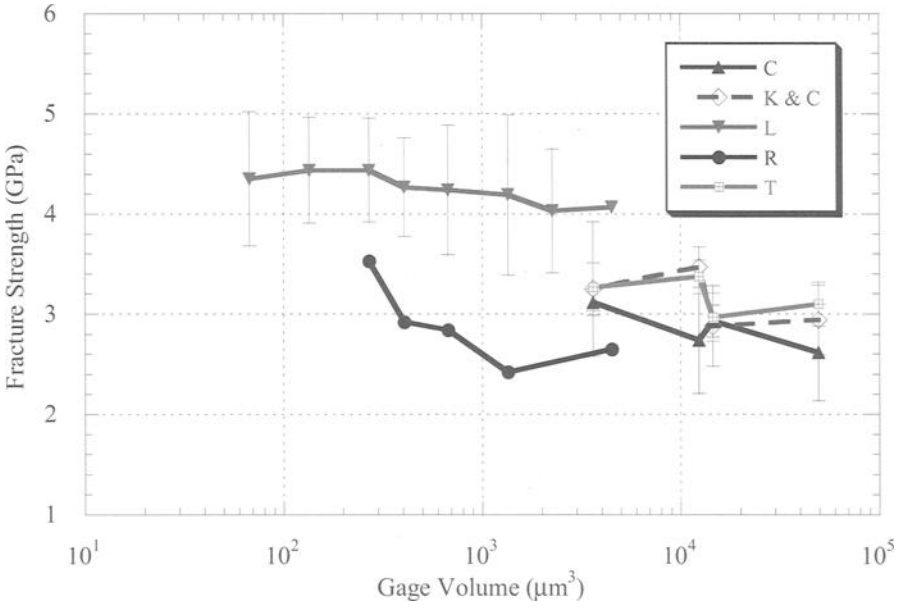

FIG. 9—*Strength as a function of gage volume.*

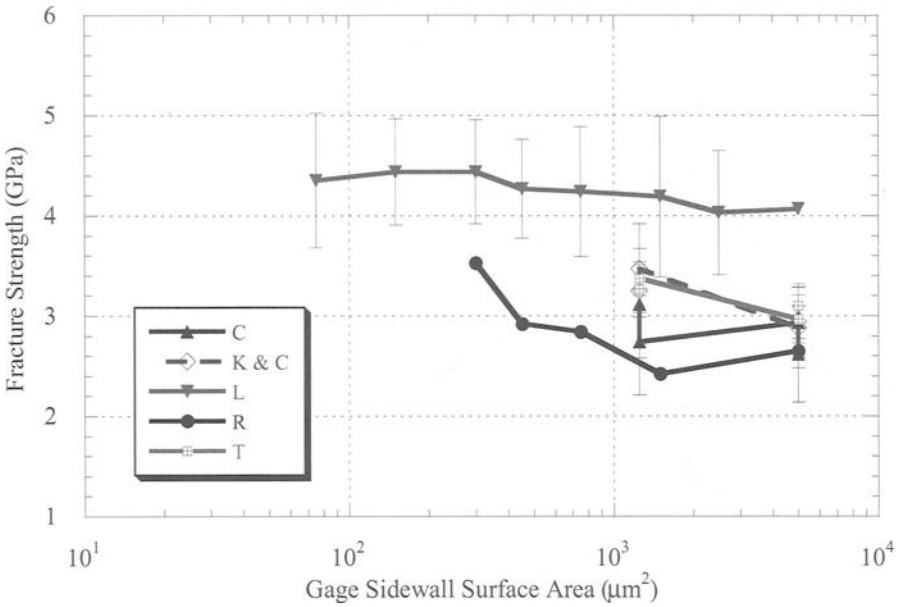

FIG. 10—*Strength as a function of gage sidewall surface area.*

Discussion

This cross comparison of direct tensile techniques has generated interesting (and mixed) results. In every statistic tabulated, there appeared to be consistent results with one lab falling outside the others. In terms of precision of the measurements, Tsuchiya was able to achieve a coefficient of variation of strength of 8.5%, roughly half that which was reported by the other labs, 14 to 15%. These C.V. are higher than that generally expected for bulk tensile testing. For probably related reasons, the Weibull modulus reported by Tsuchiya was 14.4, almost twice that reported by the other labs (7.7 to 8.4). The mean strength value reported by LaVan et al. is 1 to 1.4 GPa higher than that of the other labs.

In searching for explanations of the differences, the variety of techniques applied permits some broad interpretation. There was no systematic error that could be attributed to electrostatic gripping, catching the pull ring, or gluing of the samples. Each technique has its strong point, especially when generalized to unknown materials. The techniques employed by Coles, Knauss and Chasiotis, and Tsuchiya permit simple calibration of the commercial load cell. Read's technique uses a load transducer integrated into the probe, much like the Nanoindenter® used by LaVan, but designed in a manner to permit simple calibration checks. Checking the lateral force calibration of the nanomechanical test system is more difficult. The calibration for this machine was checked by a factory technician before the series of tests reported here. Standards should be adopted for user verification of lateral force instrumentation as has been done with the use of indentation

standards for conventional indentation testing.

In the SUMMiT IV process, the poly1-2 layer is not deposited on planarized oxide, so poly0 surface topography that was transferred into the poly1-2 layer may have affected the results for both the small and large samples. Several investigators reported grip breaks that coincided with the location of the edge of an underlying poly0 layer. No samples that were identified as a grip break were included in the results; this may have eliminated some of the stronger samples from the distributions. Every effort should be made to avoid these types of artifacts, even in the grip areas of the samples. The labs reported successful tests on 75 to 95% of samples attempted.

Consistent processing and release procedures also contributed to decreased variability between the labs—there were no problems reported shipping the released samples to the participating laboratories. Future MEMS testing cross-comparisons should ensure that sample release is not a variable.

Several figures in the Results section are dedicated to the analysis of the sample scale effect, in terms of gage surface area, volume, and sidewall surface area. This behavior is addressed here since there has been much discussion in the literature to evaluate this effect on MEMS. While the data appear to weakly follow the expected trend, a fit to Weibull's size dependency for fracture of brittle materials (Eq 2) gives a poor correlation, as indicated by the square of the correlation coefficient, R^2 less than 0.2 for each group.

$$\frac{\sigma_1}{\sigma_2} = \left(\frac{V_2}{V_1} \right)^{\frac{1}{m}} \tag{2}$$

where V = volume,
σ = fracture strength, and
m = Weibull modulus.

Acknowledgments

This work was sponsored by ASTM Working Group E08.05.03 on Structural Films for MEMS and Electronic Applications. D.L. was supported by Sandia National Laboratories, Albuquerque, NM; Sandia is a multiprogram laboratory operated by Sandia Corporation, a Lockheed Martin Company, for the United States Department of Energy under Contract DE-AC04-94AL85000. George Coles was supported by the Defense Advanced Research Projects Agency (DARPA) and Air Force Research Laboratory, Air Force Materiel Command, USAF, under agreement number F30602-99-2-0553. Wolfgang G. Knauss and Ioannis Chasiotis were supported by the Airforce Office of Scientific Research through grant F49629-97-1-0324 (Round Robin Program), and under grant F49620-99-1-0091, with Major Brian Sanders, Drs. O. Ochoa, D. Segalman, and T. Hahn as the monitors. The U.S. Government is authorized to reproduce and distribute reprints for Governmental purposes notwithstanding any copyright annotation thereon.

References

[1] Connally J. A. and Brown, S., "Slow Crack Growth in Single-Crystal Silicon," *Science*, Vol. 256, No. 5063, 12 June 1992, pp. 1537–1539.

[2] Koskinen J., Steinwall, J. E., Soave, R., and Johnson, H. H., "Microtensile Testing of Free-Standing Polysilicon Fibers of Various Grain Sizes," *Journal of Micromechanics & Microengineering*, Vol. 3, No. 1, March 1993, pp. 13–17.

[3] Read, D. T. and Marshall, J. C., "Measurements of Fracture Strength and Young's Modulus of Surface-Micromachined Polysilicon," *SPIE Proceedings*, Vol. 2880, 1996, pp. 56–63.

[4] Tsuchiya T., Tabata, O., Sakata, J., and Taga, Y., "Tensile Testing of Polycrystalline Silicon Thin Films Using Electrostatic Force Grip," *Transactions of the Institute of Electrical Engineers of Japan, Part A*, Vol. 116-E, No. 10, December 1996, pp. 441–446.

[5] Sharpe, W. N. Jr., Yuan, B., and Edwards, R. L., "Fracture Tests of Polysilicon Film," *Thin-Films—Stresses and Mechanical Properties VII., MRS Proceeding*, Warrendale, PA, 1998, pp. 51–56.

[6] Greek, S. and Ericson, F., "Young's Modulus, Yield Strength and Fracture Strength of Microelements Determined by Tensile Testing," *Microelectromechanical Structures for Materials Research, MRS Proceedings*, Vol. 518, Warrendale, PA, 1998, pp. 51–56.

[7] Sharpe, W. N. Jr., Brown, S., Johnson, G. C., and Knauss, W., "Round-Robin Tests of Modulus and Strength of Polysilicon," *Microelectromechanical Structures for Materials Research, MRS Proceedings*, Vol. 518, Warrendale, PA, 1998, pp. 57–65.

[8] Tsuchiya T. and Sakata, J., "Tensile Testing of Thin Films Using Electrostatic Force Grip," *Mechanical Properties of Structural Films, ASTM STP 1413*, C. Muhlstein and S. B. Brown, Eds., American Society for Testing and Materials, West Conshohocken, PA, 2001.

[9] Sharpe W. N., Jr., Coles, G., Jackson, K., and Edwards, R., "Tensile Tests of Various Thin Films," *Mechanical Properties of Structural Films, ASTM STP 1413*, C. Muhlstein and S. B. Brown, Eds., American Society for Testing and Materials, West Conshohocken, PA, 2001.

[10] Chasiotis, I. and Knauss, W. G., "Microtensile Tests with the Aid of Probe Microscopy for the Study of MEMS Materials," *Proceedings of the International for Optical Engineering (SPIE)*, Santa Clara, CA, Vol. 4175, 2000, pp. 92–99.

[11] Read, D. T., McColskey, J. D., and Cheng, Y.-W., "New Microscale Test Technique for Thin Films," *SEM Annual Conference Proceedings*, to be published in June 2001.

[12] LaVan D. A., Jackson, K., Glass, S. J., Friedmann, T. A., Sullivan, J. P., and Buchheit, T., "Direct Tension and Fracture Toughness Testing Using the Lateral Force Capabilities of a Nanomechanical Test System," *Mechanical Properties of Structural Films, ASTM STP 1413*, C. Muhlstein and S. B. Brown, Eds., American Society for Testing and Materials, West Conshohocken, PA, 2001.

[13] Sniegowski, J. J. and de Boer, M. P., "IC-Compatible Polysilicon Surface Micromachining" *Annual Review Materials Science*, Vol. 30, 2000, pp. 299–333.

[14] Sutton, M. A., Cheng, M., Peters, W. H., Chao, Y. J., and McNeil, S. R., "Application of an Optimized Digital Image Correlation Method to Planar Deformation Analysis," *Image Vision Computing*, Vol. 4, No. 3, 1986, pp. 143–150.

[15] Vendroux, G. and Knauss, W. G., "Submicron Deformation Field Measurements II: Improved Digital Image Correlation," *Experimental Mechanics*, Vol. 38, No. 2, 1998, pp. 86–92.

[16] Weibull W., "A Statistical Theory of the Strength of Materials," *Proceedings of the Royal Swedish Institute Engineering Research*, No. 151, 1939, pp. 1–45.

[17] Sullivan J. D. and Lauzon, P. H., "Experimental Probability Estimators for Weibull Plots," *J. Mater. Sci. Lett.*, Vol. 5, 1986, pp. 1245–1247.

D. F. Bahr,[1] *B. T. Crozier,*[1] *C. D. Richards,*[1] *and R. F. Richards*[1]

Fatigue and Fracture in Membranes for MEMS Power Generation

REFERENCE: Bahr, D. F., Crozier, B. T., Richards, C. D., and Richards, R. F., "**Fatigue and Fracture in Membranes for MEMS Power Generation**," *Mechanical Properties of Structural Films, STP No. 1413*, C. L. Muhlstein and S. B. Brown, Eds., American Society for Testing and Materials, West Conshohocken, PA, Online, Available: www.astm.org/STP/1413/1413_03, 16 March 2001.

ABSTRACT: Bulk micromachined membranes containing PZT thin films deposited via sol-gel processing have been tested for fatigue and fracture using a dynamic bulge testing apparatus. These membranes, consisting of silicon, titanium, platinum, PZT, and gold, were pressurized monotonically until failure to determine an average failure pressure and then cyclically pressurized to examine fatigue behavior. Membranes containing PZT show significant degradation of strength as compared to membranes of just silicon or the metallic layers. This is discussed in terms of the residual stresses and defects present in the PZT thin film due to thermal processing. Fractography of the failed membranes shows that delamination does occur at the metal-silicon interface during both types of loading, suggesting both through- thickness and interfacial cracking are possible failure mechanisms in this system.

KEYWORDS: fatigue, fracture, MEMS devices, bulge testing, PZT Introduction

With the advent of microelectromechanical systems (MEMS), it has become increasingly important to understand the mechanical properties of the materials used in devices that are exposed to significant stresses and harsh environments. A device currently under development for MEMS power generation consists of a ceramic piezoelectric membrane, $PbZr_xTi_{1-x}O_3$ (PZT), which caps a cavity filled with a two-phase fluid. This cavity acts as a Carnot cycle engine when heated, resulting in cyclic flexing of the PZT membrane when heat is applied and removed from the cavity. Since the proposed device will cycle at rates approaching 1 kHz at strains that may approach 1%, the mechanical strength and reliability of this membrane generator becomes a key design parameter.

Many researchers using silicon-based technology for MEMS have examined the strength and fracture of both single crystal and polycrystalline silicon structures. At the current time there is no standard test morphology for these structures, which is likely due to the wide variety of loading conditions these devices are subjected to. Some studies have focused on applying external loading mechanisms to thin films, while others have centered on creating on-chip loading structures to electrostatically test the strength of a component. It has been noted that there is a wide range of data reported for both the tensile fracture strength as well as the elastic modulus of polycrystalline thin films [1]. These properties can vary by a factor of 4 for different films tested in methods ranging from tensile tests to beam bending tests. Fatigue data for polycrystalline silicon thin films

[1]Mechanical and Materials Engineering, Washington State University, Pullman, WA 99164.

[2] shows that when some MEMS structures are cycled at stresses greater than about three quarters of the stress required for failure, failure can occur around 10 billion cycles.

In addition to test geometry, the surrounding environment has been shown to impact the fracture strength of silicon as well as the number of cycles required for failure at a given stress during a fatigue test [3]. It is not surprising that silicon and oxides in MEMS behave differently in wet and dry environments, as this has been observed on a bulk test of these materials. However, the variation between tests performed in ambient conditions, in vacuum, and in humid environments suggests that any testing of devices should be carried out in conditions similar to those expected during service.

While there exists mechanical test data on silicon for MEMS [1-4], the device currently being considered for this power generation application utilizes PZT. There exist some data on hardness and adhesion measured via nanoindentation [5,6], but these measurements do not probe the properties of the material in a manner similar to the service environment. In service the films will flex in tension, whereas during nanoindentation testing the primary mode of deformation is compression and shear. Additionally, the early tests did not account for any environmental effects that may occur when the membranes are loaded in the presence of water. As it has been shown by studies of metal ceramic interfaces that cyclic stresses can substantially differ than those measured in either bulk material [7], it would be appropriate to expect differences between monotonic loading and cyclic loading in the current device.

Therefore, the goal of this study was to examine the fracture and fatigue of membranes based on silicon and PZT for a power generation application. A test fixture was developed to simulate the loading situation as well as the environmental effects that may occur in the device. Materials properties were evaluated based on processing treatments that are required for device fabrication.

Experimental Procedures

An SiO_2 layer ≈500 nm thick is thermally grown on a silicon (100) wafer surface and is then patterned and etched to generate a silicon membrane fabricated using wet chemical anisotropic etching [8] to form pits in the silicon wafer that were 1.45 mm square, leaving a silicon membrane 2.2 μm thick, and the SiO_2 layer is then removed. This wafer is then platinized using 20 nm of Ti and 200 nm of Pt deposited via electron beam evaporation to act as a bottom electrode. The films in this study were deposited using organometallic sol-gel methods onto the platinized wafers [6]. Some of these platinized wafers were annealed in ambient atmosphere at 400°C for 5 h in an attempt to improve the Pt-Ti-Si adhesion. Films of PZT approximately 65 nm thick per layer were spun onto wafers at 4000 rpm; four or six layers were deposited after sequential heat treatments of 150°C and 300°C prior to a crystallization heat treatment at 700°C for 10 min. Gold was then sputter deposited onto the PZT to create an easily patterned top electrode to a thickness of 40 nm.

The testing apparatus is a closed system bulge tester. A sealed chamber of fluid is capped by a pressurizing membrane on one side and the micromachined membrane to be tested on the other. This chamber is pressurized using either a piezoelectric actuator or a mechanical cam. The piezoelectric actuator is capable of cycling at frequencies

approaching 1 kHz and produces chamber pressures on the membrane on the order of 20 kPa (similar to the conditions expected for the device operation). Larger pressures are generated using a mechanical cam system, which can reach frequencies of 50 Hz at chamber pressures of 675 kPa. The mechanical system is not cycled in a sinusoidal manner, but instead is a parabolic pressure step from a pressure of 0 to the maximum pressure followed by a small delay until the cycle repeats. Cycling is carried out at frequencies that do not cause excessive resonance in the sealed chamber. A Michelson interferometer using a long working distance (≈10 cm) microscope and He-Ne laser is attached to a vibration isolation table containing the bulge tester. The deflection of the pressurized membrane is monitored via a charge coupled device (CCD) camera, and by counting fringes generated during pressurization it is possible to determine both the shape and total deflection of the membrane. A pressure transducer is coupled to the chamber, and a data collection routine was developed to count the number of cycles as well as recording the applied pressure wave during fatigue testing. It should be noted that unlike a similar air piston driven bulge tester [9] this test provides for testing in a variety of fluids that are being considered for use in the device and could lead to stress corrosion cracking in the device.

Wafers are loaded into a wafer carrier that allows each membrane to be tested individually. After a given mechanical test the carrier can be moved with respect to the sealed chamber to access another membrane on a given wafer. Given this geometry, approximately 20 membranes can be tested on a 75 mm diameter silicon wafer. Membranes were tested first under monotonic loading, and the pressure-membrane deflection relationship was determined. After identifying the pressure at which the membranes fracture during monotonic loading, cyclic testing was carried out on different membranes fabricated on the same wafer using pressures less than the average pressure that generated fracture.

Results

Monotonic Fracture of PZT Membrane Structures

A pressure-deflection curve is shown in Fig. 1 for a platinized membrane, which corresponds to the interferogram shown in Fig. 2. This pressure-deflection curve was fitted using a model developed by Bonnotte et al. [10].

$$P = \frac{t^3 d}{a^4}\left(66.14\frac{E}{1-\nu^2} + 29.17\frac{E}{1-\nu^2}\frac{d^2}{t^2}\right) + 13.64\frac{\sigma_r t d}{a^2} \qquad (1)$$

where P is the pressure in the membrane, E and ν are the composite elastic modulus and Poisson's ratio, respectively, t is the membrane thickness, d is the maximum deflection of the membrane, a is the side length of a square membrane, and σ_r is the residual stress in the membrane. Thicknesses of various layers were measured using contact profilometry, and those values and elastic modulii were used to determine a composite film modulus, as described by Kriese [11]. The data [5] used for determining the composite modulus are shown in Table 1; a simple rule of mixtures for the membrane containing four layers of

PZT produces a biaxial modulus of 158 GPa. The pressure-deflection relationship was then fit to determine the effective residual stress in the membrane, σ_r. Wafers with annealed Ti-Pt layers exhibited a reduction in the residual stress in the layer from 110 MPa to 90 MPa.

For determining the pressure at failure during monotonic loading, the pressure in the chamber was slowly increased until the film fractured and the pressure in the chamber rapidly dropped to zero. Due to the large deflections at these pressures (up to 50 μm) it was not possible to resolve individual fringes in the interferogram. Therefore, to determine the strain at failure, the pressure at failure was recorded and the deflection extrapolated from the curve fit of the pressure-deflection curve as a first order approximation. In Table 2, the pressure and deflection at failure are documented. Note that the failure in the membrane containing PZT occurs at significantly lower pressures and deflections than that of the bare silicon or platinized silicon membranes.

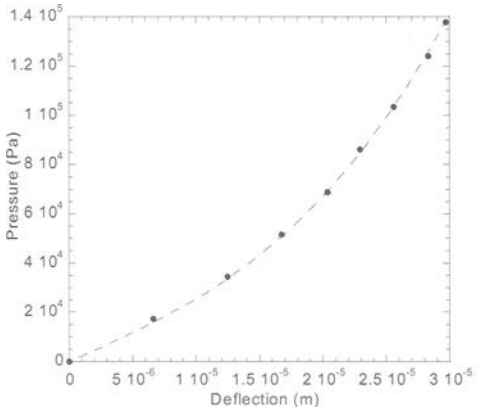

FIG. 1—*Pressure-deflection relationship of Ti-Pt coated membrane.*

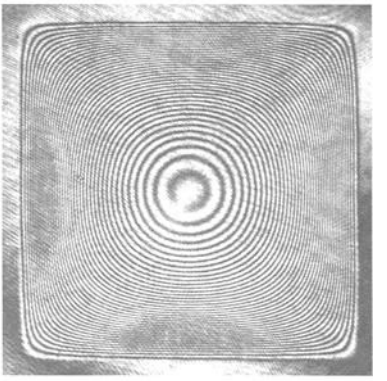

FIG. 2—*Interference pattern of bulging membrane 1.45 mm on a side.*

TABLE 1—*Materials properties used for composite modulus calculation.*

	Si	Ti	Pt	PZT	Au
t (nm)	2200	20	200	65/layer	40
E (GPa)	155	110	171	60	75
ν	0.27	0.41	0.39	0.25	0.42

TABLE 2—*Failure pressures under monotonic loading for various membranes.*

	Failure Pressure, kPa	Composite Biaxial Modulus, GPa	d at Failure, μm
Bare Si	407.5 ± 7.8	167	52 ± 0.8
TiPt, as deposited	306.8 ± 43	169	43 ± 2.6
TiPt, annealed	333.7 ± 71.7	169	48.5 ± 8
4-layer PZT	229.6 ± 4.8	158	37 ± 0.5
6-layer PZT	209.6 ± 27.6	154	35 ± 2

Cyclic Failures in Membranes with PZT Layers

Cycling loading was carried out using the mechanically driven bulge tester at a rate of approximately 30 Hz. The applied pressure amplitude during cycling is related to the number of cycles to failure as shown in Fig. 3 for both a 4-layer and 6-layer PZT film on similar membrane structures. These materials appear to show some fatigue cracking behavior; lower stress amplitudes require longer cycles to failure in a semi-logarithmic manner. No clear evidence of a fatigue limit has been observed in these materials, but it should be noted that testing beyond 10^7 cycles should be carried out to explore the possible existence of a fatigue limit. It is suspected the increased scatter in the 6-layer films is due to additional cracking due to a larger thermal strain upon decomposing the organic PZT precursor. The scatter shown by error bars was determined by sampling the range over which static failure occurs. The scatter is likely caused by defects in the films, leading to uncertainty in the actual pressure ratio applied as there is no way of knowing a priori if a given membrane will fail at the average value.

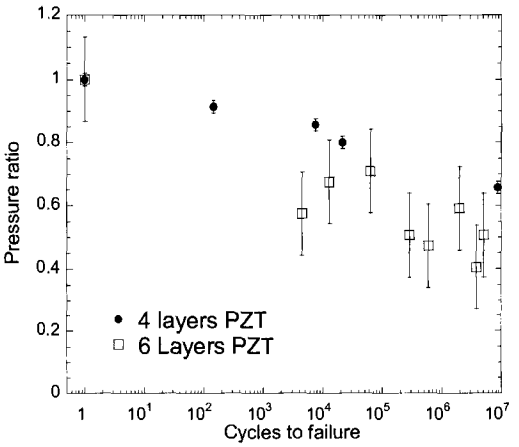

FIG. 3—*Normalized pressure (pressure to failure during cycling)/(pressure to failure under monotonic loading) as a function of cycles required for failure in membrane structures with four and six layers of PZT. The error bars represent the standard deviation in fracture strain for monotonic tests.*

Crack growth was monitored by determining the compliance of the membrane periodically during the cyclic testing. As shown in Fig. 4, there was a slight change in the calculated side length for a sample that failed at 8×10^6 cycles. This was determined by applying the curve fit in Eq 1 to the pressure-deflection data, allowing the side length to vary while holding the residual stresses constant as would be expected during testing.

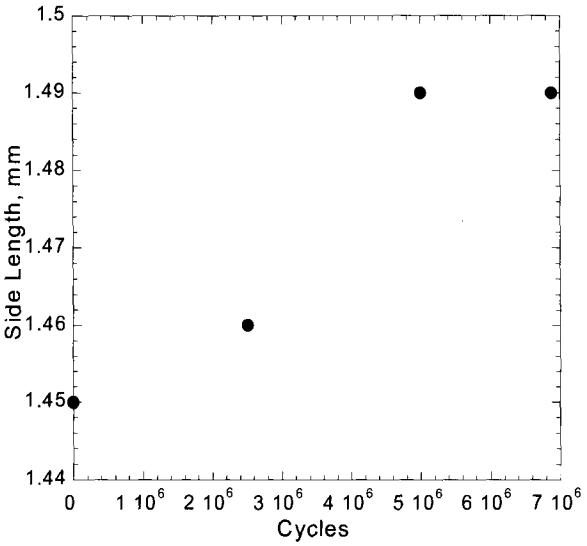

FIG. 4—*Side length of membrane as a function of cycling for a four-layer PZT membrane. An increase in side length likely corresponds to crack propagation during testing.*

Fractography

Delaminations at the metal-silicon interface have been observed in monotonically loaded membranes, as shown in Fig. 5. Note that in this case the bare silicon membrane has fractured, and the fracture appears to have begun at the metal-silicon interface based on river patterns in the silicon. Membranes cyclically loaded show more extensive film delamination, as shown in Fig. 6. In Fig. 6 there appears to have been regions of delamination extending at least 10 μm away from the membrane edge, whereas the largest delaminations in the monotonically loaded membranes are approximately 5 μm.

Discussion

There are small areas of delamination around the membranes failed monotonically and during cyclic loading. While the interface failing appears to be the Ti-Si interface, a crack in that interface would lead to compliance changes that would manifest themselves as apparent increases in the size of the membrane. Therefore, the small increases in crack length observed in Fig. 4 appear to be reasonable. The deflection of the membrane has been modeled by other researchers [10], and in this case the

maximum tensile strain at failure is approximately 0.85%. The strains applied during the cyclic testing that cause failure in the 1 to 10 million cycle range are lower, on the order of 0.4%, but still are on the same order of those that caused failure in 1 to 10 billion cycles in polycrystalline silicon [2]; this could well be due to the significant residual stresses that develop during thermal processing of the PZT thin films.

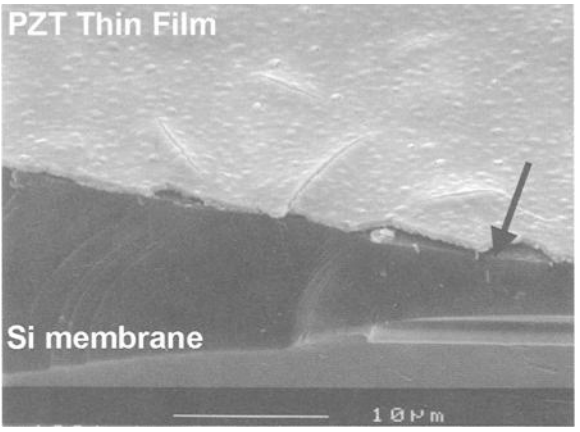

FIG. 5—*Fracture surface of membrane at 45° tilt, showing some delamination at the silicon-metal interface. The fracture in the silicon membrane propagated into the bulk silicon; the membrane is still only 2.2 μm thick in this sample. Arrow notes delamination. Cracks in the film are clearly observed.*

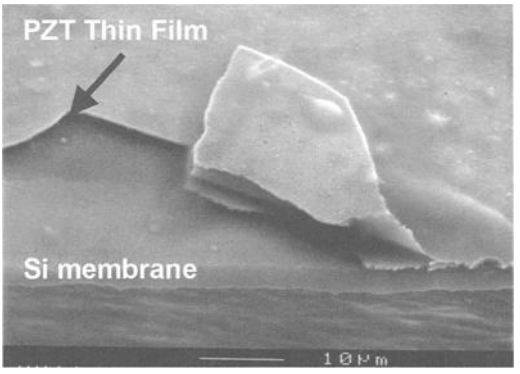

FIG. 6—*Fracture surface after cyclic loading of four-layer PZT membrane for 8.9 million cycles. Delamination at the interface is significantly larger than in the monotonically loaded samples. Arrow notes delamination.*

The largest change in film strength occurs with the deposition of PZT onto the platinized membranes. There are two possible explanations for this behavior: tensile

stresses develop during thermal processing that alters the residual stress in the film, or cracks in the PZT film itself due to the deposition method act as crack nucleation sites for through-film-thickness cracking. Cracks in the PZT membranes (Fig. 5) are caused from the tensile stresses that develop during processing, so it is difficult to separate these two mechanisms at the current time.

Conclusions

Experiments have been performed using a newly developed bulge testing apparatus that allows both large pressures and high (≈30 Hz) cycling rates on multilayer membranes containing a PZT film. These films appear to degrade with cyclic loading, failing after approximately 10 million cycles at strains of 75% of the monotonic failure strain and pressure. Annealing the Ti-Pt bottom electrode to improve adhesion during further processing appears to reduce the residual stress in the membrane by approximately 20% (from 110 MPa to 90 MPa) without significantly weakening the film. However, deposition of PZT thin films using sol gel processing decreases the strength of the membrane under monotonic loading by approximately 33%. Cyclic loading does appear to enhance the amount of interfacial failure at the metal-silicon interface.

Acknowledgments

This work was supported by the National Science Foundation under Grant Number 9980837. The authors wish to thank J. D. Hall, K. R. Bruce, B. W. Olson, and L. M. Randall for assistance with fabrication of the bulge tester, PZT thin film deposition, and fractography.

References

[1] Ballarini, R., "Recent Developments in Experimental and Theoretical Studies of the Mechanical Behavior of Polycrystalline Silicon for Microelectromechanical Systems," *Materials Research Society Symposium Proceedings, Materials Science of MEMS Devices*, A. H. Heuer and S. J. Jacobs, Eds., Vol. 546, 1999, pp. 3–14.

[2] Brown, S. B., Van Arsdell, W. V., and Muhlstein, C. L., "Materials Reliability in MEMS Devices," *Transducers 97, 1997 International Conference on Solid-State Sensors and Actuators*, 1997, pp. 591–593.

[3] Minoshima, K., Inoue, S., Terada, T., and Komai, K., "Influence of Specimen Size and Sub-Micron Notch on the Fracture Behavior of Single Crystal Silicon Microelements and Anoscopic AFM Damage Evaluation," *Materials Research Society Symposium Proceedings, Materials Science of MEMS Devices*, A. H. Heuer and S. J. Jacobs, Eds.,Vol. 546, 1999, pp.15–20.

[4] Ding, X., Ko, W. H., and Mansour, J. H., "Residual Stress and Mechanical Properties of Boron Doped p^+ Silicon Films," *Sensors and Actuators*, Vol. A21-23, 1990, pp. 866–871.

[5] Bahr, D. F., Robach, J. S.,Wright, J. S., Francis, L. F., and Gerberich, W. W., "Mechanical Deformation of PZT Thin Films for MEMS Applications," *Materials Science and Engineering A*, Vol. 259, 1999, p. 126.

[6] Bahr, D. F., Merlino, J. C., Banerjee, P., Yip, C. M., and Bandyopadhyay, A., "Reliability and Properties of PZT Thin Films for MEMS Applications,"

Materials Research Society Symposium Proceedings, Materials Science of MEMS Devices, A. H. Heuer and S. J. Jacobs, Eds., Vol. 546, 1999, pp. 153–158.

[7] Cannon, R. M., Dalgleish, B. J., Dauskardt, R. H., Oh, T. S., and Ritchie, R. O., "Cyclic Fatigue Crack Propagation Along Ceramic Metal Interfaces," *Acta Metallurgical et Materiallia*, Vol. 39, 1991, pp. 2145–2156.

[8] Kovacs, G. T. A., *Micromachined Transducers*, McGraw Hill, New York, 1998, pp. 29–61.

[9] Keiner, H., von Preissig, F. J., Zeng, H., Nejhad, M. N. G., and Kim, E. S., "Advanced Bulge Testing System," *Materials Research Society Symposium Proceedings, Thin-Films: Stresses and Mechanical Properties VII*, R. C. Cammarata, E. P. Busso, M. Nastasi, and W. C. Oliver, Eds., Vol. 505, 1998, pp. 229–234.

[10] Bonnotte, E., Delobelle, P., Bornier, L., Trolard, B., and Tribillon, G., "Interferometric Methods for the Mechanical Characterization of Thin Films by Bulging Tests. Application to Single Crystal of Silicon," *Journal of Materials Research*, Vol. 12, 1997, pp. 2234–2248.

[11] Kriese, M. D., Moody, N. R., and Gerberich, W. W., "Quantitative Adhesion Measures of Multilayer Films: Part I. Indentation Mechanics," *Journal of Materials Research,* Vol. 14, 1999, pp. 3007–3022.

R. Ballarini,[1] *H. Kahn,*[2] *N. Tayebi,*[3] *and A. H. Heuer*[4]

Effects of Microstructure on the Strength and Fracture Toughness of Polysilicon: A Wafer Level Testing Approach

REFERENCE: Ballarini, R., Kahn, H., Tayebi, N., and Heuer, A. H., **"Effects of Microstructure on the Strength and Fracture Toughness of Polysilicon: A Wafer Level Testing Approach,"** *Mechanical Properties of Structural Films, ASTM STP 1413*, C. L. Muhlstein and S. B. Brown, Eds., ASTM, West Conshohocken, PA, Online, Available: www.astm.org/STP/1413/1413_13, 15 June 2001.

ABSTRACT: Specimens have been developed to measure the strength and fracture toughness, of polycrystalline silicon and silicon carbide at the micron scale. The specimens have been fabricated using standard microelectromechanical systems (MEMS) processing techniques, and so have characteristic dimensions comparable to typical MEMS devices (notches, cracks and uncracked ligaments of several microns). They are fully integrated with simultaneously fabricated electrostatic actuators that are capable of providing sufficient force to ensure failure under monotonic loading. Thus the entire experiment takes place on-chip, eliminating the difficulties associated with attaching the specimen to an external loading source. Polycrystalline specimens containing cracks formed by indentation were associated with a microstructure-independent average fracture toughness of 1.0 MPa$\sqrt{m}$. The strength of specimens containing micromachined blunt notches demonstrated a strong dependence on processing procedures and resulting surface roughness. Fractographic investigation suggests that this dependence is related to the size of processing-related flaws on the side surfaces of the films.

KEYWORDS: polysilicon, fracture toughness, strength, microstructure, actuator, fractography, amorphous, polycrystalline

[1] Professor of Civil Engineering, Case Western Reserve University, Cleveland, Ohio 44106
[2] Researcher, Department of Materials Science and Engineering
[3] Graduate student, Department of Mechanical and Aerospace Engineering
[4] Kyocera Professor of Materials Science and Engineering

Introduction

At present, polycrystalline silicon (polysilicon) is the most commonly used material for fabricating microelectromechanical systems (MEMS) devices that operate at ambient temperatures. Long-term durability predictions for such devices require a fundamental understanding of the strength, stiffness, fatigue, fracture, and wear behavior of polysilicon at *relevant length scales*, and of how this behavior is affected by *operating environments* and by *variations in MEMS processing procedures*. While significant progress has been made during the past few years on measurements of tensile strengths and elastic moduli of micron-size specimens, the material properties data required for fracture mechanics-based reliability analyses of engineered devices is extremely limited and not well understood [1].

Consider, for example, the fracture toughness, K_{Ic}, of polysilicon, defined as the critical stress intensity factor that is required to extend the tip of an *atomically sharp* crack. Our recent measurements of this fundamental parameter are the only available data derived from atomically sharp cracks in micron-size polysilicon specimens [2]. The reported average value of 1.1 MPa$\sqrt{m}$ for fine-grained polysilicon is close to that of single crystal silicon (whose toughness is anisotropic and lies in the range 0.7 to 1.2 MPa$\sqrt{m}$ [3]) and clearly demonstrates that previously published average "nominal" values for K_{Ic} (1.4 MPa$\sqrt{m}$ for tension specimens containing center crack-mimicking notches with length to root radius ratio of 100 [4], 1.9 to 4.5 MPa$\sqrt{m}$ for tension specimens containing edge notches with radii of the same order of magnitude as the uncracked ligament [5], and 1.7 to 4.0 MPa$\sqrt{m}$ for bend specimens containing edge notches with a tip radius of 1 μm [3,6] do not represent fracture toughness but rather strength in the vicinity of a notch. We note that the discrepancy between fracture toughness and nominal toughness measured on notched specimens has been demonstrated for single crystal silicon by Myers et al. [7], who reported nominal values of 1.24 to 2.85 MPa$\sqrt{m}$ for notch radii of 80 to 580 μm.

Another phenomenon that is not sufficiently understood and that is expected to be intimately connected with processing procedures and material microstructure is time-delayed failure of polysilicon. Connally and Brown [8–10] demonstrated that the natural frequency of their precracked (using indentation) single crystal silicon specimens, when placed in a humid environment, decreased with time. They attributed this phenomenon to environmentally assisted crack growth. As noted recently by Van Arsdell and Brown [11] however, Connally and Brown "...were unable to confirm their hypothesis that this subcritical crack growth was occurring due to a stress corrosion attacking mechanism." Van Arsdell and Brown [11] also reported evidence that polysilicon is susceptible to stress corrosion cracking under cyclic tension-compression loading. However, their data (obtained from indentation induced precracks) does not appear to show a close correlation between crack velocity and applied stress intensity factor, or crack velocity and relative humidity. While they observed no time delayed failure in the absence of humidity, they attribute crack velocities as low as $2x10^{-14}$ m/s to environmentally assisted cracking of the native oxide layer that forms along the crack front in humid air.

We have also observed time delayed failure in polysilicon under cyclic tension-compression loading, both in humid environments and in near vacuum (8 Pa) [6,12]. Our results suggest that polysilicon may be susceptible to subcritical crack propagation or crack initiation in the absence of humidity. We are currently investigating the possibility of compression-induced cracking near notches and crack tips, a phenomena observed in ceramic composites [13]. It is worth noting that nanoscopic damage evolution has been observed in single crystal silicon by Komai et al. [14]. They performed cyclic 3-point loading on MEMS-size single crystal silicon samples and observed failure from cracks that initiated in the vicinity of the indenter (on the compressive face). They also reported that multiple cracking occurred when the tests were performed underwater, suggesting effects of stress corrosion.

Bhaduri and Wang [15] are the only researchers to report slow crack growth in statically loaded single crystal silicon and measured velocities as high as 10^{-4} m/s; however, several other researchers studying static fatigue in silicon have not observed crack growth [9,10].

All these observations suggest that time-delayed failure in these relatively small polysilicon devices may not be a result of (moisture-controlled) static fatigue of the bulk material, as occurs in inorganic glasses [16]. Instead, it may be associated with other types of mechanisms, including static fatigue of the native oxide, or stress-induced damage evolution in the vicinity of stress concentrators.

These two examples clearly illustrate the need for a sound fracture mechanics base for MEMS devices. That a sound materials science base relating processing parameters to (material) microstructures and (material) microstructures to mechanical behavior is equally necessary will be demonstrated in this paper. We present results of a study of the effects of microstructure (we use microstructure in the materials science sense rather than in reference to small structures, as is common in MEMS literature) on the fracture toughness and strength of polysilicon. We present what we believe to be the first convincing (MEMS) polysilicon fracture toughness data. We also present recently measured bend strength data for amorphous silicon, and compare it with our previously reported values for polysilicon. The independence of fracture toughness on microstructure, together with a fracture mechanics analysis of the data, illustrates that differences in strength are intimately connected to the size of processing-related flaws on the free surfaces of the films. This point is underscored by a comparison of the bend strengths of our amorphous silicon with those of Tsuchiya et al. [5].

The Microstructure of LPCVD Polysilicon Films

As with all deposition processes, the microstructure of LPCVD (low pressure chemical vapor deposition) polysilicon films is dependent on the deposition conditions. In general, the films are amorphous at the lowest growth temperatures (lower than ~570°C), display fine (~0.1 μm diameter) ellipsoidal grains at intermediate temperatures (~570°C to ~610°C), and contain columnar (110)-textured grains with a thin fine-grained nucleation layer at the substrate interface at higher temperatures (~610°C to ~700°C) [17]. The fine-grained microstructures seen at intermediate deposition temperatures are essentially randomly oriented, although modest (and poorly understood) (311) and (111) textures (compared to the randomly oriented powder diffraction pattern) are present. The

fine-grained microstructure results from the homogeneous nucleation and growth of silicon crystallites within an as-deposited amorphous silicon film. In other words, in this regime, the deposition rate is just slightly faster than the crystallization rate. This is confirmed by cross-sectional transmission electron microscopy (XTEM), which shows mostly crystalline films that are still amorphous at the free (growth) surface [18]. The columnar and crystallographically textured microstructure, seen at the higher growth temperatures, results from the deposition of crystalline silicon, with growth being fastest in the <110> directions. The differences in these growth mechanisms also affect the relative surface roughness of the films. The amorphous films, and the fine-grained films which were amorphous as-deposited, both display very smooth surfaces, while the columnar films are significantly rougher, the scale of the roughness reflecting the columnar microstructure. As discussed subsequently, the morphology, i.e., the detailed nature of the roughness of free surfaces, governs the tensile and bending strength of polysilicon microdevices.

The residual stresses of polysilicon films depend sensitively on the microstructure. The amorphous and the columnar films are under compressive stresses, while the fine-grained films are tensile [18–23]. The origin of the tensile stress in the fine-grained polysilicon is easily understood; it arises from the volume decrease that accompanies the crystallization of the as-deposited amorphous material. The origins of the compressive stresses, on the other hand, are not well understood. Impurity incorporation has been suggested, either of oxygen [24] or hydrogen, particularly for amorphous films [22], and hydrogen evolution has been detected during high temperature annealing of columnar polysilicon films [21]. For the columnar films, it has been suggested that excess (interstitial) atoms depositing in the developing grain boundaries could contribute compressive stresses [25]. For the fully crystalline films, irrespective of the sign of the residual stress, the effects of high temperature annealing in inert atmospheres are similar. The stresses are essentially unchanged at annealing temperatures below ~1000°C, but reduction of the residual stresses occurs dramatically (to a near-zero condition) for higher annealing temperatures [21,23,25]. In addition to the possible evolution of hydrogen discussed above, the reduction in residual stress is attributed to dislocation rearrangement during annealing [21].

Electrostatically Loaded Specimens Containing Sharp Cracks and Notches

Polysilicon films with varying microstructures have been used to fabricate fracture mechanics test specimens, which are fully integrated with simultaneously microfabricated actuators. This allows on-chip testing of the micromachined specimens, without the need of an external loading device. Specimens were designed to measure fracture toughness (using indentation-induced precracks) as well as bend strength (using micromachined single-edge notches with a 1-μm-tip radius).

The different polysilicon microstructures used in this investigation were all produced by standard LPCVD and are shown in the cross-sectional transmission electron micrographs in Fig. 1. Figure 1*a* shows an amorphous silicon (a-Si) film deposited at 550°C; Fig. 1*b* is of a fine-grained film deposited at 580°C with an average grain diameter

of 0.1 μm; Fig. 1*c* shows a columnar film deposited at 615°C with an average column diameter of 1 μm; and Fig. 1*d* shows a multilayer film deposited alternately at 570°C and 615°C. (The motivation behind the development of the multilayer polysilicon specimen was to exploit the inherent tensile and compressive residual stresses in an alternating design, in order to achieve as-deposited near-zero overall film stresses and near-zero residual stress gradients, and in turn, flat surfaces [23]. In addition to these four films, all of which are undoped, fine-grained films were also processed which were heavily P-doped and then annealed at 1150°C for two h. This led to an increase in average grain diameter to 0.7 μm. Fine-grained films were also B-doped at 1100°C; this doping did not increase the grain size.

The test specimens were fabricated using standard surface micromachining techniques. We have previously reported [2] the fracture toughness of polysilicon measured on a sharp-cracked specimen whose fabrication involved a two-mask process. This data exhibited large scatter, which we tentatively attributed to a high temperature anneal performed before the second mask step. Therefore, we have developed an improved procedure for introducing sharp cracks that involves a one-mask process, illustrated in Fig. 2 and summarized as follows.

A 3.0-μm-thick sacrificial oxide was thermally grown on 100-mm-diameter {100} silicon wafers. Polysilicon films were deposited by LPCVD at temperatures between 550°C and 615°C. The fine-grained and columnar films were then annealed at 1000°C for one h in nitrogen to relieve some of the residual stresses. The columnar films deposited at 615°C were chemo-mechanically polished in order to achieve the mirror finish displayed by the fine-grained and amorphous films. The external masking oxide was then deposited by LPCVD at 450°C (Fig. 2*a*). The masking oxide was photolithographically masked and (dry) plasma etched using CHF_3/C_2F_6, and the polysilicon was plasma etched using Cl_2 (Fig. 2*b*). For the doped films, the remaining masking oxide was chemically removed using aqueous hydrofluoric acid (HF). The P-doped films were exposed to POCl for 13 h at 875°C, followed by a two-hour anneal at 1150°C. The B-doped films were exposed to B_2O_5 for 30 min at 1100°C. At this stage, a Vickers indent (with a 1-kg load) was placed on the sacrificial oxide near the specimen, causing radial cracks to form in the oxide and propagate into the overlying polysilicon (Fig. 2*c*). The devices were then time-release etched in aqueous HF, followed by supercritical CO_2 drying (Fig. 2*d*). For the undoped films, the devices were sputter-coated with ~10 nm of palladium following release to provide sufficient conductivity for electrostatic actuation; this very thin metal layer is not expected to affect the mechanical behavior of the polysilicon specimens. The specimens used for bend strength determination were processed identically, except that no indentation was performed.

The specimens used for fracture toughness and bend strength measurements are shown in Fig. 3*a* and *b*, respectively. All of the specimens are integrated with simultaneously fabricated electrostatic actuators containing from 1400 to 2200 pairs of interdigitated comb fingers, an example of which is shown in Fig. 4. The outer frame of the actuator is fully

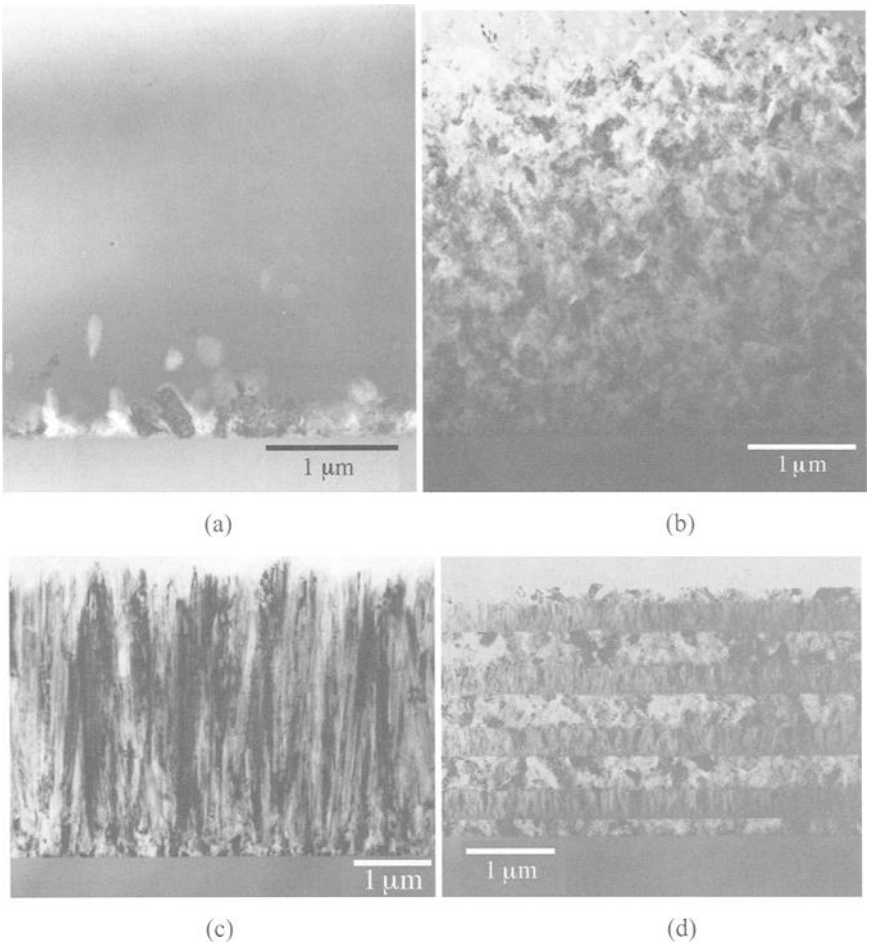

FIG. 1—*Cross-sectional transmission electron micrographs of* (a) *an amorphous silicon film deposited at 550°C,* (b) *a fine-grained polysilicon film deposited at 580°C,* (c) *a columnar polysilicon film deposited at 615°C, and* (d) *a multilayer polysilicon film deposited alternately at 570°C and 615°C. The amorphous film in* (a) *contains heterogeneously nucleated crystallites of Si at the amorphous Si/SiO_2 interface, which formed in the later stages of film deposition; a few homogeneously nucleated crystallites are also present. Crack extension in the fracture toughness tests occurred from cracks which only penetrated the amorphous Si (see text below). The tensile surface in the bend tests to be discussed below were also confined to the purely amorphous material.*

released from the substrate and is free to move when subjected to the electrostatic attraction of the comb drives. The frame is anchored to the substrate at the ends of eight

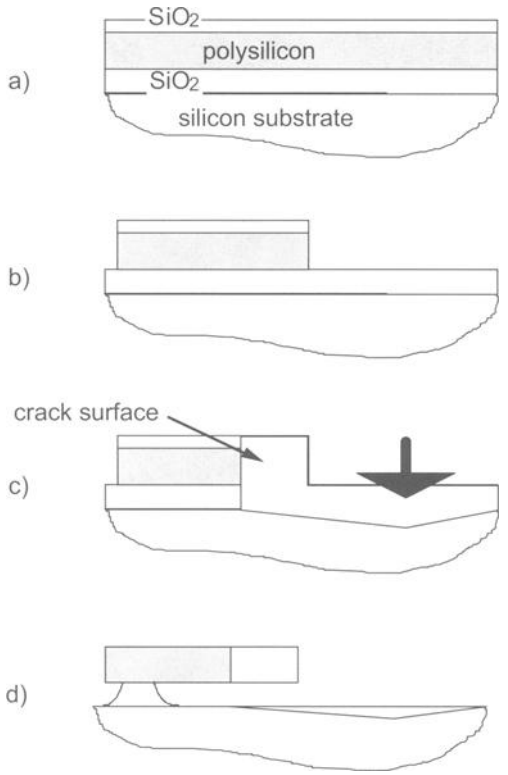

FIG. 2—*Schematic drawings of the fabrication sequence for the surface-micromachined polysilicon devices containing sharp cracks. See text for further details.*

long, thin beams, which constrain movement in the side-to-side direction, but allow in-plane vertical movement. The interdigitated comb fingers pull the actuator down (in the orientation of Fig. 4) when a voltage is applied, achieving forces of up to 700 μN. This, in turn, pulls on the connecting beam and the left side of the fracture mechanics specimens (as viewed in Fig. 3), which are anchored to the substrate on the opposite side. A stress intensity factor at the crack tip, or a stress concentration at the notch of the specimen, is thus achieved (in all calculations the radius of the notch was assumed to be the design value 2 μm). When the displacement reaches a critical value, the mechanical stresses become sufficiently high to initiate fracture. The critical displacement for the notched and cracked specimens is measured optically from two scales fabricated as part of the testing device; one of these is shown at the top left in Fig. 3*a*.

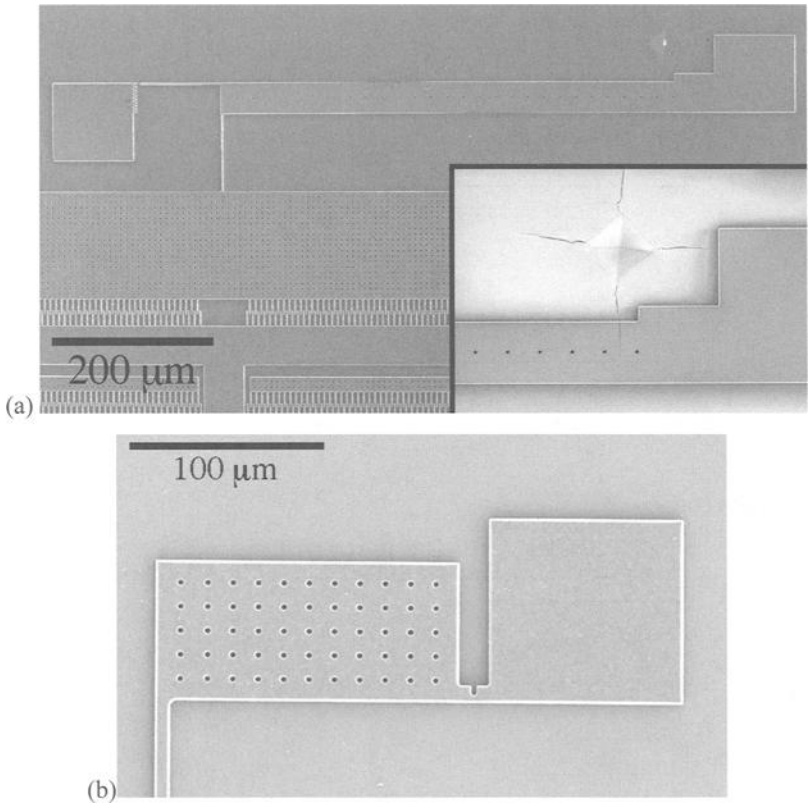

FIG. 3—*Scanning electron micrographs of surface-micromachined fracture mechanics specimens used for measuring* (a) *fracture toughness and* (b) *bend strength. The inset in* (a) *shows a higher magnification view of the precracked region.*

Figure 5 shows a typical finite element mesh for a sharp cracked specimen, as well as a close-up view of the crack position and length. It is noted that a finite element analysis was performed for all crack configurations, where the crack's length was within the range 10.6 to 34 μm, and its position from the fixed edge varied. The critical stress intensity factor is calculated to within a few percent error by prescribing the experimentally measured critical displacement together with a Young's modulus equal to 160 GPa (A similar procedure is used for the notched specimens to infer the maximum tensile stress at the root of the notch). For the polysilicon specimens, this Young's modulus represents the average value measured from electrostatically driven resonant frequency test structures that were fabricated on the same chip as the strength and fracture specimens (for all material microstructures we measured a modulus equal to 160 ± 9.0 GPa). For the a-Si specimens, we assumed the same value of Young's modulus, because we were not able to actuate electrostatically the resonant frequency test structures, as explained next (we are in the process of fabricating test structures to

measure the Young's modulus of a-Si).

As discussed above, the a-Si films contained high residual compressive stresses. As a result, the actuators were severely buckled as-released, the interdigitated comb fingers did not overlap, and electrostatic actuation could not be performed. These devices were mechanically pushed with a probe ("mechanically" as opposed to "electrostatically" tested), while the actuator displacement was monitored optically, as in the electrostatic experiments. (To verify the legitimacy of this technique, some polysilicon devices were also mechanically tested. The strengths were equivalent to those obtained by electrostatic testing.)

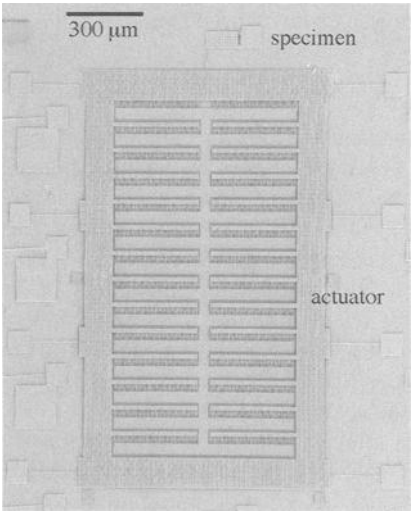

FIG. 4—*Scanning electron micrograph of a fracture mechanics specimen integrated with an electrostatic comb-drive actuator.*

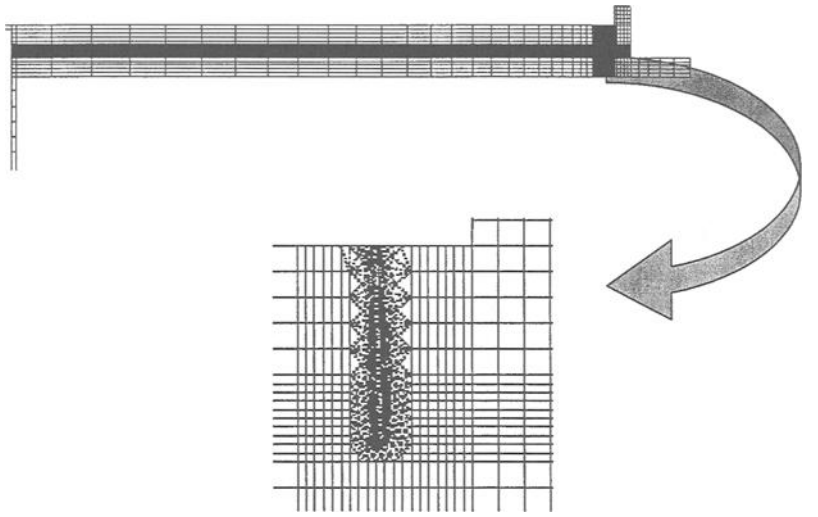

FIG. 5—*Finite element mesh used to calculate the stress intensity factor of a sharp crack specimen.*

Results and Discussion

The fracture toughness results for the improved specimen design fabricated with a variety of microstructures are shown in the histograms in Fig. 6. This data exhibits significantly less scatter than that obtained using the previously discussed two-mask process. The average values and standard deviations are included on the figures. As mentioned previously, the toughness values were inferred using the average value of the measured Young's modulus; the values corresponding to the upper and lower bound values can be recovered readily because in the calculations toughness scales linearly with modulus. It is noteworthy that K_{Ic} is independent of microstructure. This suggests that only the region of the material immediately in front of the precrack controls the toughness; it is only the strength and characteristics of the Si-Si chemical bonds that are involved in initiating fracture. This most satisfying result is expected in truly brittle materials such as silicon. To the authors' knowledge, a microstructure-independent fracture toughness has not been demonstrated in any other brittle materials, most likely because of the difficulty of generating atomically sharp precracks in fracture specimens subjected to different processing histories.

The bend strength results for a-Si and for B-doped and undoped fine-grained polysilicon are shown in Fig. 7. We could not generate sufficient force in the undoped specimens (due to the residual tensile stress within these specimens) to initiate fracture; therefore, these specimens were mechanically tested. To confirm again the validity of this procedure, B-doped specimens were tested both mechanically and electrostatically, with no difference in the measured strengths. The undoped polysilicon displays a slight increase in bend strength compared to the B-doped polysilicon, while the a-Si demonstrates a significant increase in bend strength.

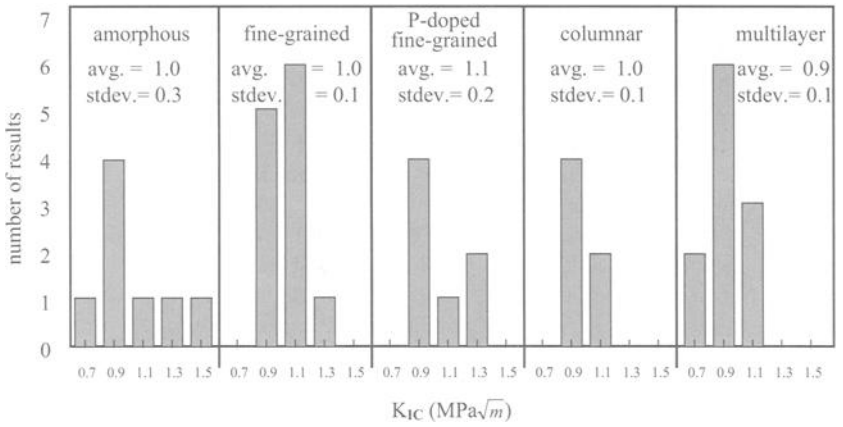

FIG. 6—*Histograms showing fracture toughness results using the one-mask process (various polysilicon microstructures).*

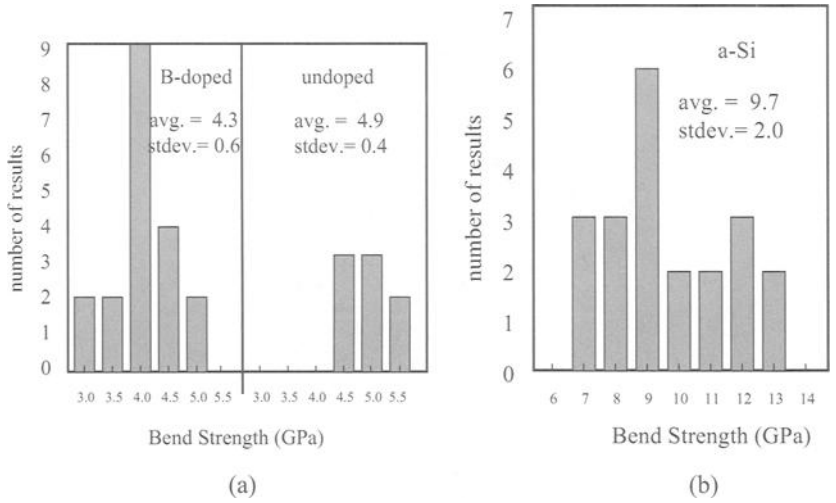

FIG. 7—*Histograms showing bend strength results for* (a) *B-doped and undoped polysilicon and* (b) *amorphous silicon.*

Bend strength is not a fundamental material property, but depends on both K_{Ic} and the flaw size at the fracture initiation site. For a semicircular flaw, the maximum stress intensity factor is given by

$$K = 1.25S\sqrt{a} \tag{1}$$

where S is the nominal stress, and a is the flaw radius [26]. Since the toughness is constant regardless of microstructure or doping level, the observed differences in bend strength must be due to variations in the flaw size. Equation 1 implies that the flaw size of a-Si samples is four times smaller than the flaw size of polysilicon samples (because the nominal strength of a-Si is roughly double that of polysilicon).

For the notched specimens, the flaw sizes are determined by the morphology of the surface of the specimen which is under tensile stress during the test, which corresponds to the inside surface of the notch. Fracture surfaces from all three types of material are shown in Fig. 8. (These are three of the best examples of "classical" features present on fracture surfaces that were observed.) In all three samples, a semicircular "mirror" is present, characteristic of brittle fracture, and surrounds the crack-initiating flaw. Beyond the relatively smooth mirror zone, branching cracks can be seen radiating from the crack initiation site. In brittle ceramics, the radius of the mirror is known to be 6 to 10 times the radius of the original flaw [26]. In this figure, it appears that the mirror of the a-Si sample is indeed roughly four times smaller than that of the polysilicon sample.

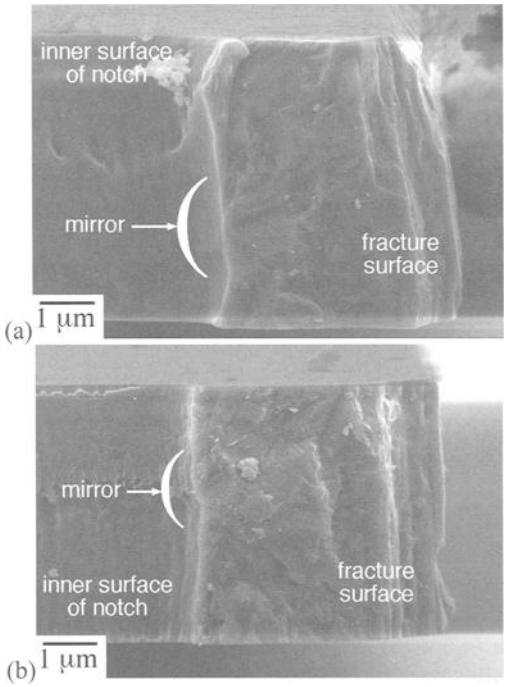

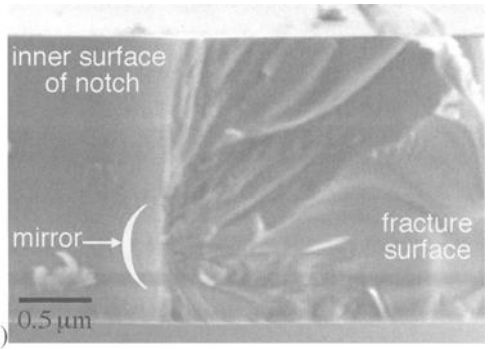

FIG. 8—*Scanning electron micrographs showing the fracture surfaces of notched specimens fabricated from* (a) *B-doped polysilicon,* (b) *undoped polysilicon, and* (c) *amorphous silicon. Note the magnification in* (c) *is more than twice that in* (a) *and* (b).

The inner surfaces of the notches, where fracture initiated, are also shown in Fig. 8. These surfaces were created during the Cl_2 plasma etching of the devices. The surface of the amorphous sample is visibly smoother, consistent with its smaller flaw sizes. The surface morphology of the B-doped specimen appears slightly smoother than the undoped specimen. This obtains because some modest oxidation occurs during doping; this oxide is removed during the release process, and so any sharp features will become rounded. While this could be expected to increase the bend strength, another byproduct of the doping process is also evident in Fig. 8*a*. During doping, thermal grooving occurs where grain boundaries intersect the free surface. (The undoped specimens are only annealed before polysilicon etching, i.e., before these surfaces are created.) These grain boundary grooves are likely acting as the flaws that control the bend strength and are more severe than the strength-controlling flaws in the undoped specimens.

A comparison of the average bend strength of our a-Si with those of Tsuchiya et al. [5] underscores the importance of processing-related flaws. While our a-Si is twice as strong as our polysilicon, their a-Si is half as strong as their polysilicon. They attribute the lower strength of their amorphous films to the presence of 0.4% hydrogen, as well as increased surface roughness.

Summary and Conclusions

We have developed a wafer-level testing approach for measuring the strength and fracture toughness of polysilicon in specimens containing length scales relevant to MEMS devices. The data suggest that the fracture toughness of polysilicon is microstructure-independent and equal to 1.0 MPa$\sqrt{m}$, while its strength is controlled by processing-related flaws on the side surfaces of the films. Average strengths up to 9.7 GPa have been achieved in amorphous silicon, while the strength of polysilicon is ~5.0 GPa (these strengths appear to be independent of the residual stresses that exist in the

films before release).

Acknowledgments

This work was supported by the National Science Foundation under Grant MSS94-16752, by DARPA under Grants DABT63-95-C0070, by ONR under N00014-00-1-0881, by ARO-MURI, and by the Glennan Microsystems Initiative.

References

[1] Ballarini, R., "Recent Developments in Experimental and Theoretical Studiesof the Mechanical Behavior of Polycrystalline Silicon for Microelectromechanical Systems," *Materials Research Society Symposium Proceedings*, Vol. 546, 1999, pp. 3–14.

[2] Kahn, H., Tayebi, N., Ballarini, R., Mullen, R. L., and Heuer, A. H., "Fracture Toughness of Polysilicon MEMS Devices," *Sensors and Actuators*, Vol. 82, 2000, pp. 274–280.

[3] Ballarini, R., Mullen, R. L., Kahn, H., and Heuer, A. H., "The Fracture Toughness of Polysilicon Microdevices: A First Report," *Journal of Materials Research*, Vol. 12, No. 4, 1997, pp. 915–922.

[4] Sharpe, W. N., Yuan, B., and Edwards, R. L., "Fracture Tests of Polysilicon Film," *Materials Research Society Symposium Proceedings*, Vol. 505, 1997, pp. 51–56.

[5] Tsuchiya, T., Sakata, J., and Taga, Y., "Tensile Strength and Fracture Toughness of Surface Micromachined Polycrystalline Silicon Thin Films Prepared Under Various Conditions," *Materials Research Society Symposium Proceedings*, Vol. 505, 1997, pp. 285–290.

[6] Ballarini, R., Mullen, R. L., Kahn, H., and Heuer, A. H., "The Fracture Toughness of Polysilicon Microdevices," *Materials Research Society Symposium Proceedings*, Vol. 518, 1998, pp. 137–142.

[7] Myers, R. J. and Hilbery, B. M., "Effect of Notch Root Radius on the Fracture Behavior of Monocrystalline Silicon," *Proceedings, 4th International Conference On Fracture*, Waterloo, Canada, June 19-24, 1977, pp. 1001–1005.

[8] Connally, J. A. and Brown, S. B., "Slow Crack Growth in Single-Crystal Silicon," *Science*, Vol. 256, 1992, pp. 1537–1539.

[9] Connally, J. A. and Brown, S. B., "Nanosystem Measures Ultraslow Crack Growth," *Materials Research Society Bulletin*, June 1993, p. 4.

[10] Connally, J. A. and Brown, S. B., "Micromechanical Fatigue Testing," *Experimental Mechanics*, June 1993, pp. 81–90.

[11] Van Arsdell, W. W. and Brown, S. B., "Subcritical Crack Growth in Silicon MEMS," *Institute of Electrical and Electronic Engineers Journal of Microelectromechanical Systems*, Vol. 8, No. 3, 1999, pp. 319–327.

[12] Kahn, H., Ballarini, R., Mullen, R. L., and Heuer, A. H., "Fracture Toughness of Polysilicon MEMS Devices," *Proceedings, Royal Society of London*, A 455, 1999, pp. 3807–3823.

[13] Suresh, S., *Fatigue of Materials*, Cambridge University Press, 1991.

[14] Komai, K., Minoshima, K., and Inoue, S., "Fracture and Fatigue Behavior of Single Crystal Silicon Microelements and Nanoscopic AFM Damage Evaluation," *Microsystem Technologies*, Vol. 5, 1998, pp. 30–37.

[15] Bhaduri, S. B. and Wang, F. F. Y., "Slow Crack Growth Studies in Silicon," in *Fracture Mechanics of Ceramics*, Vol. 5, Plenum Press, 1983, pp. 327–336.

[16] Wiederhorn, S. M., "Influence of Water Vapor on Crack Propagation in Soda-Lime Glass," *Journal of the American Ceramic Society*, Vol. 50, No. 8, 1967,

pp. 407–414.
[17] Joubert, P., Loisel, B., Chouan, Y., and Haji, L., "The Effect of Low Pressure on the Structure of LPCVD Polycrystalline Silicon Films," *Journal of the Electrochemical Society*, Vol. 134, 1987, pp. 2541–2544.
[18] Guckel, H., Sniegowski, J. J., Christenson, T. R., and Raissi, F., "The Application of Fine-Grained, Tensile Polysilicon to Mechanically Resonant Transducers," *Sensors and Actuators*, A21-A23, 1990, pp. 346–351.
[19] Krulevitch, P., Howe R. T., Johnson, G. C., and Huang, J., "Stress in Undoped LPCVD Polycrystalline Silicon," *Proceedings, International Conference on Solid-State Sensors and Actuators, Transducers 91*, Institute of Electrical and Electronic Engineers, New York, 1991, pp. 949–952.
[20] Oei, D. G. and McCarthy, S. L., "The Effect of Temperature and Pressure on Residual Stress in LPCVD Polysilicon Films," *Materials Research Society Symposium Proceedings*, Vol. 276, 1992, pp. 85–90.
[21] Yu, C. L., Flinn, P. A., Lee, S. H., and Bravman, J. C., "Stress and Microstructural Evolution of LPCVD Polysilicon Thin Films During High Temperature Annealing," *Materials Research Society Symposium Proceedings*, Vol. 441, 1997, pp. 403–408.
[22] Temple-Boyer, P., Inbernon, E., Rousset, B., and Scheid, E., "Residual Stress of Silicon Films Deposited by LPCVD From Silane," *Materials Research Society Symposium Proceedings*, Vol. 518, 1998, pp. 209–214.
[23] Yang, J., Kahn, H., He, A. Q., Phillips, S. M., and Heuer, A. H., "An Improved Technique for Producing Zero Stress LPCVD Polysilicon Films: the *MultiPoly*™ Process," *Journal of Microelectromechanical Systems*, Vol. 9, 2000, pp. 485–494.
[24] Kamins, T. I., "Design Properties of Polycrystalline Silicon," *Sensors and Actuators*, Vol. A21-A23, 1990, pp. 817–824.
[25] Maier-Schneider, D., Koprululu, A., Holm, S. B., and Obermeier, E., "Elastic Properties and Microstructure of LPCVD Polysilicon Films," *Journal of Micromechanics and Microengineering*, Vol. 6, 1996, pp. 436–446.
[26] Mecholsky, J. J., "Quantitative Fractographic Analysis of Fracture Origins in Glass," In *Fractography of Glass*, R. C. Bradt and R. E. Tressler, Eds., Plenum Press, 1994, pp. 37–73.

Kazuki Takashima,[1] *Masayuki Shimojo,*[1] *Yakichi Higo,*[1] *and Michael V. Swain*[2]

Fatigue Crack Growth of a Ni-P Amorphous Alloy Thin Film

REFERENCE: Takashima, K., Shimojo, M., Higo, Y. and Swain, M. V., **"Fatigue Crack Growth of a Ni-P Amorphous Alloy Thin Film,"** *Mechanical Properties of Structural Films, ASTM STP 1413*, C. Muhlstein and S. B. Brown, Eds., American Society for Testing and Materials, West Conshohocken, PA, Online, Available: www.astm.org/STP/1413/1413_17, 15 June 2001.

ABSTRACT: Fatigue crack growth behavior has been investigated for micro-sized Ni-P amorphous alloy specimens. Cantilever beam type specimens (10 μm by 12 μm by 50 μm) with notches were prepared from Ni-P amorphous thin film by focused ion beam machining. Fatigue crack growth tests were carried out in air at room temperature using a newly developed mechanical testing machine that can apply cyclic loading to micro-sized specimens. Striations were observed clearly on the fatigue surface, and fatigue crack growth resistance curves as a function of stress intensity range (ΔK) were obtained from careful measurements of the striation spacings. The fatigue crack growth rates at stress ratios of 0.3 and 0.5 were greater than that at 0.1 under a given value of ΔK. This suggests crack closure may occur even in such micro-sized specimens and may affect the fatigue crack growth behavior.

KEYWORDS: thin film, Ni-P, amorphous alloy, fatigue crack growth, bending test, R ratio

Introduction

Micro-sized machines and microelectromechanical systems (MEMS) are expected to be applied to bio-medical and micro-photonics devices such as micro-catheters for brain surgery and optical switches for electro-optical communications. These devices are usually prepared from a thin film deposited on a substrate using surface micromachining techniques. The size of the components used in such devices is thus considered to be in the order of microns, and the mechanical properties of such micro-sized materials are considered to be different from those of bulk (ordinary sized) materials, as surface effects on the deformation mechanisms are prominent. Therefore, the evaluation of mechanical properties, including elastic modulus, tensile strength, fracture toughness and fatigue properties, are essential for practical applications of such MEMS devices.

Several studies have investigated the mechanical properties of small-sized materials [1–5]. In particular, properties such as fatigue life and fatigue crack growth of micro-sized materials are extremely important to enable reliable design of actual MEMS devices, as the many micro-sized components are subjected to cyclic loading as they move. For example, the components used in micro-optical mirrors and switches are considered to experience an extremely high number of cyclic loads (over 10^8 cycles). Fatigue tests for thin films and fatigue life of such films have been evaluated [6–8]. However, to date there has been an absence of fatigue data available for designing reliable

[1] Associate professor, research associate, and professor, respectively, Precision and Intelligence Laboratory, Tokyo Institute of Technology, 4259 Nagatsuta, Midori-ku, Yokohama 226-8503, Japan.

[2] Professor, Faculty of Dentistry and Department of Mechanical & Mechatronic Engineering, The University of Sydney, Australian Technology Park, Everleigh NSW 1430, Australia.

and log-term durable MEMS devices. Particularly, there have been no data for fatigue crack growth properties which are important for damage tolerant design of actual devices. This is due to the lack of suitable fatigue testing equipment for micro-sized materials. In our previous investigation, we have designed a new fatigue testing machine for micro-sized specimens [9–10], and fatigue life curves have been obtained for micro-sized Ni-P amorphous alloys [11].

Amorphous alloy thin films deposited on substrates by sputtering or plating techniques are considered to be potential candidate materials for MEMS devices because of their isotropic mechanical properties and high corrosion resistance. Therefore, it is important to clarify the fatigue properties of these amorphous thin films. However, the fatigue properties of micro-sized amorphous specimens have not yet been studied apart from our previous investigation on the fatigue life of a micro-sized Ni-P amorphous alloy [11]. In the present study, fatigue crack growth tests have been performed for micro-sized specimens prepared from an electroless deposited Ni-P amorphous alloy thin film, and the size effects on the fatigue crack growth behavior of micro-sized specimens have been discussed.

Experimental Procedure

Preparation of Specimens

The material used in this investigation was a Ni-11.5 mass% P amorphous thin film electroless plated on an Al-4.5 mass% Mg alloy. The thickness of the amorphous layer was 12 μm and that of the Al-4.5 mass%Mg alloy substrate was 0.79 mm, respectively. A disk with a diameter of 3 mm was cut from the Ni-P/Al-Mg sheet by electro discharge machining. An amorphous layer was separated from the Al-Mg alloy substrate by dissolving the substrate with a NaOH aqueous solution. The amorphous thin film was fixed on a holder, and micro-cantilever beam specimens with dimensions of 10 (B) by 12 (W) by 50 (L) μm^3 were cut from the amorphous layer by focused ion beam machining. This specimen size is equivalent to approximately 1/1000 of ordinary-sized bending specimens. Figure 1 shows the specimen prepared by the above procedures. Notches with a depth of 3 μm were introduced into the specimens by focused ion beam machining. This notch depth is equivalent to $a/W = 0.25$, where a is notch length and W is specimen width. The width of the notch was 0.5 μm, and the notch radius is thus deduced to be 0.25 μm. The notch position was 10 μm away from the fixed end of the specimen. The loading position is set at 40 μm from the fixed end of the specimen.

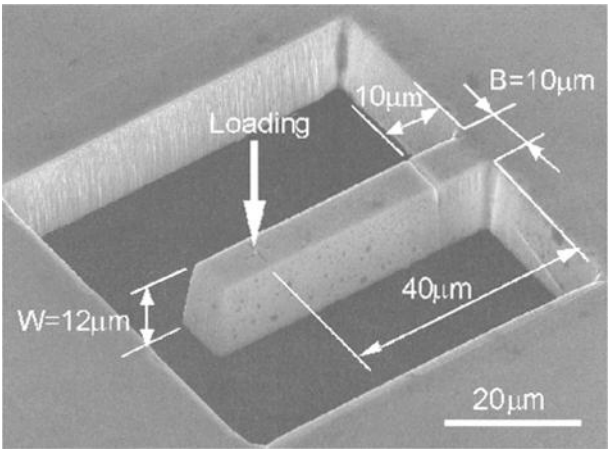

FIG. 1—*Scanning electron micrograph of the micro-sized cantilever type specimen.*

Fatigue Testing Machine

Fatigue crack growth tests were carried out using a newly developed fatigue testing machine for micro-sized specimens. Figures 2(a) and 2(b) show a photograph and a block diagram of the fatigue testing machine. The testing machine consists of an actuator, a specimen holder, a load cell, and a controller.

A magnetostrictive device is used as an actuator that imparts a small amount of displacement to a specimen. The magnetostrictive material used is TERFENOL-D (TbDyFe), which is able to produce displacements up to 10 μm with an accuracy of 5 nm, and the maximum response frequency of cyclic displacement is 100 Hz. So far, a nano-indentor type loading system has been applied for the measurement of mechanical properties in thin film specimens [1]. The stiffness of such system is very low and it is inadequate for applying cyclic loading. In this testing machine, the end of the actuator is connected to a metal shaft and a diamond tip of 5 μm in radius is attached to the other end of the shaft. This makes it possible to construct a high stiffness loading fixture. The displacement of the actuator is measured by a laser displacement meter with an accuracy of 5 nm, and the displacement signal is used as feed back control.

The micro-sized specimen is set in a specimen holder and the holder is placed on a load cell as shown in Fig. 2(b). This holder is interchangeable and is also used in the focused ion beam machine for machining the micro-sized specimens, in this fatigue testing machine and in a field emission-gun type scanning electron microscope. Therefore, machining, testing and observation processes are able to be performed without removing the specimen. This makes it easier to handle the micro-sized specimens. A CCD camera is set near the specimen holder to monitor the specimen appearance during fatigue testing. A small amount of displacement is applied to the specimen through the diamond tip. The amount of load applied to the specimen is measured by a strain gage type load cell with a load resolution of 10 μN, which is set under the specimen. Load control is also an available option on this instrument. The horizontal location of the

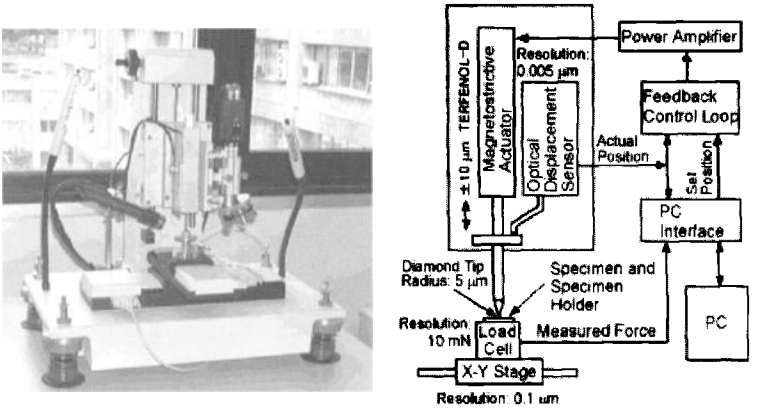

FIG. 2 — *Photograph (a) and block diagram (b) of the fatigue testing machine for micro-sized specimens used in this investigation.*

specimen stage and the load cell can be moved to adjust the loading position precisely by a stepping motor at a translation resolution of 0.1 μm.

This testing machine is set up in a clean room with constant temperature and humidity to eliminate dust and the effect of temperature change during the measurement. The testing machine is also placed in a windscreen box to shield from the slight wind stream in the room. Further details of the testing machine are described in our previous papers [9–10].

Fatigue Crack Growth Test

Fatigue crack growth tests were performed in air at room temperature. Fatigue tests were carried out at a frequency of 10 Hz and different stress ratios, R ($R = P_{min}/P_{max}$, where P_{min} is a minimum load and P_{max} is a maximum load applied over the fatigue cycle) of 0.1, 0.3, 0.5, and 0.7 under constant load amplitude ($\Delta P/2$, where $\Delta P = P_{max} - P_{min}$) of 2 mN. This fatigue test condition was determined from our preliminary experiments. Although the crack length was not able to be measured directly in this testing machine, the change in specimen compliance can be measured during fatigue tests. The initiation of crack growth was then determined by monitoring the specimen compliance. The fatigue surfaces after the tests were observed using a HITACHI S-4000 field emission-gun type scanning electron microscope operating at 30 kV.

Results and Discussion

Fatigue Crack Growth Behavior

Figures 3(a) and 3(b) show a scanning electron micrographs of the specimen appearance after a fatigue crack growth test at a stress ratio of 0.5. A fatigue crack initiates from the notch root. The crack did not begin to grow immediately after applying cyclic load but started to grow after approximately 20 000 cycles (this was confirmed by a

compliance change of the specimen during fatigue test, but the number of cycles to fatigue crack initiation varied between specimens). This also supports our previous result that even the notch with root radius of only 0.25 μm was not regarded as a natural crack for this specimen size [12]. The fracture surface consists of a flat region and a rough one which is featured by a vein pattern as shown in Fig. 3(b). The vein pattern is often observed on a monotonic fracture surface in this amorphous alloy [12]. The region between the notch and the final fractured region is thus a fatigue surface. Figure 4 shows a high magnification of fatigue surface in Fig. 3. Very fine equispaced markings are clearly observed on the fatigue surface. The spacing between these markings increased with the crack extension and are approximately 30 nm near the notch root and 80 nm near the final fractured region. It is not certain whether these markings correspond to striations, but these markings are aligned perpendicular to the crack growth direction and

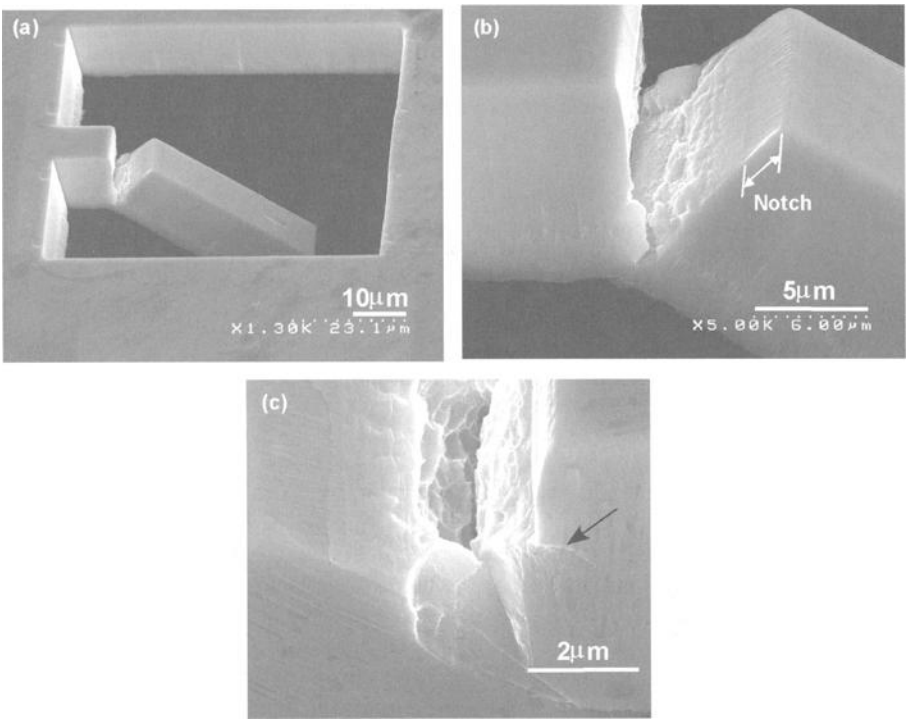

FIG. 3—*Scanning electron micrographs of specimen appearance after fatigue crack growth tests at a stress ratio of 0.3: (a) general view, (b) close view near notch and fracture surface and (c) shear bands (indicated by arrow) observed on the side surface of the specimen near fatigue surface.*

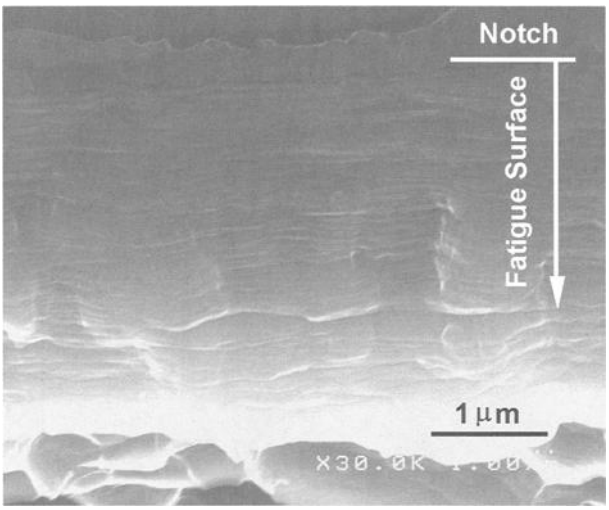

FIG. 4—*High magnification scanning electron micrograph of fatigue surface in Fig. 3. Fine equispaced markings considered to be striations are observed. Crack growth direction is from top to bottom.*

were not observed on the fracture surface by static bending tests [12], so these markings are deduced to be fatigue striations. Such striations have also been observed on fatigue surfaces of metallic glass bulk specimens [13]. The formation of striations suggests that the crack has propagated by cyclic plastic deformation at the crack tip (i.e., blunting and resharpening of the crack tip). Actually, shear bands which are considered to be formed by plastic deformation were observed on the side surface of the specimen near the crack tip as shown in Fig. 3(c). Consequently, the fatigue crack growth appears to be based on cyclic plastic deformation at the crack tip even in micro-sized amorphous alloys.

Effect of Stress Ratio on Fatigue Crack Growth

If the spacing between the striations on the fatigue surface is assumed to be equivalent to the fatigue crack growth rate for the specimens, a fatigue crack growth resistance curve can be obtained from the measurement of the striation spacings. Careful measurements of the striation spacings were made and fatigue crack growth rates (da/dN) as a function of applied stress intensity factor range (ΔK) (where $\Delta K = K_{max} - K_{min}$) were obtained. Stress intensity factor (K) is calculated from the equation for a single edge notched cantilever beam specimen [14]. The crack length, a, was measured from scanning electron micrographs of the fatigue surfaces.

Figure 5 shows the fatigue crack growth resistance curves at different stress ratios. As once a crack started to grow, the specimen failed after only several thousand cycles for the micro-sized specimens, so ΔK_{th} (a stress intensity range at which a crack starts to grow) was not able to be determined. Also, the number of data points is only two or three for one specimen, but this is due to the difficulty of the measurement of striation spacings

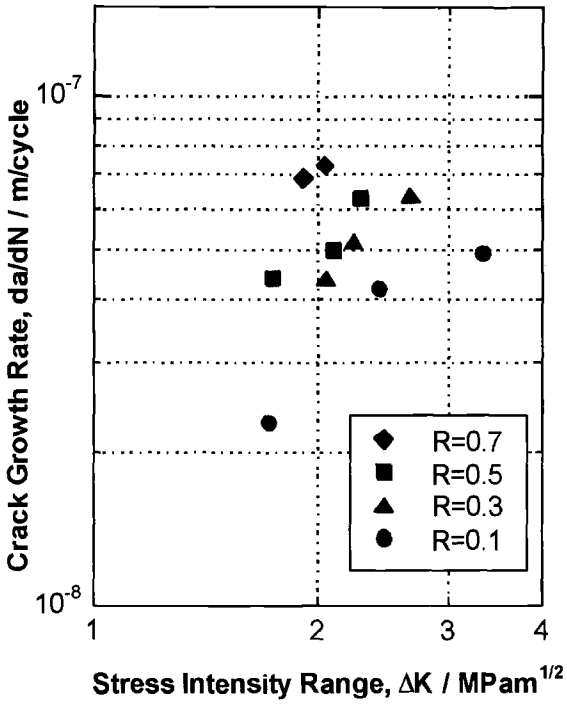

FIG. 5—*Fatigue crack growth resistance curves for micro-sized specimens at different stress ratios.*

since the spacing is only between 20 to 70 nm. It is not certain whether a Paris-Erdogan relationship ($da/dN = A\Delta K^m$, where A and m are material constants) is applicable for these data. The fatigue crack growth rates at a stress ratio of 0.3 and 0.5 are almost the same. In contrast, the fatigue crack growth rate at a stress ratio of 0.1 is lower than those at 0.3 and 0.5 at a given value of ΔK. Generally, a decrease in fatigue crack growth rate at a low stress ratio can be explained by crack closure effects for ordinary-sized specimens. This suggests crack closure effects may occur even in such micro-sized specimens and may affect the fatigue crack growth behavior. The fatigue surface is relatively flat as shown in Fig. 4, so this crack closure is deduced to be a plasticity-induced crack closure.

On the other hand, the fatigue crack growth rate at a stress ratio of 0.7 is higher than those of 0.3 and 0.5. Figure 6 shows a fatigue surface at a stress ratio of 0.7. The fatigue surface is very rough, and some vein patterned regions that were also observed on the static fracture surfaces of micro-sized specimens of the same material [12] are visible in addition to the striation pattern. At this stress ratio, K_{max} was 6.8 MPa $m^{1/2}$ and this value is close to K_Q value of the specimen [12]. Therefore, the crack is deduced to extend by both cyclic and static mode, and this resulted in higher crack growth rate at stress ratio of 0.7.

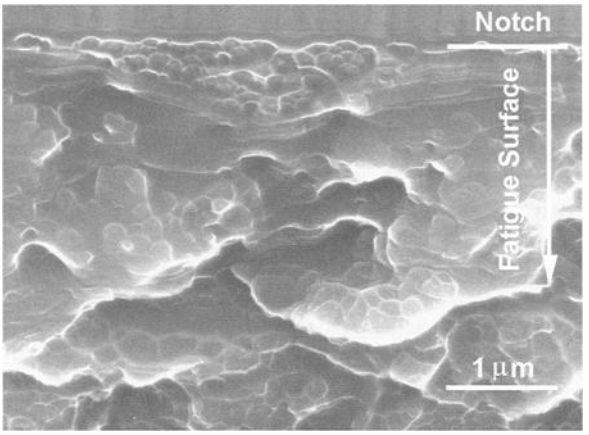

FIG. 6—*Scanning electron micrograph of fatigue surface tested at a stress ratio of 0.7. Crack growth direction is from top to bottom.*

Effect of Specimen Size on Fatigue Crack Growth

As shown in Fig. 5, the effect of stress ratio on fatigue crack growth, which is deduced to be associated with a crack closure effect, is observed even for micro-sized specimens. The length of crack extended by fatigue loading in the micro-sized specimens used in this investigation was only 2 to 3 μm as shown in Fig. 4. Generally, crack closure effects are less pronounced for short cracks with length of less than 100 μm, and almost no closure effects are observed for extremely short cracks with a length in the order of microns [15]. However, these observations have been obtained for short cracks in ordinary-sized specimens. In contrast, the size of the specimen used in this investigation is three dimensionally small, so the normalized crack length is sufficiently long compared to the specimen size (actually, a/W is approximately over 0.5 at final fracture). Therefore, the crack length of 2 to 3 μm should be regarded as a long crack for this size of specimen, so the closure effects are deduced to be pronounced even for micro-sized specimens.

The final fatigue fracture occurred at a crack growth rate of less than 10^{-7} m/cycles. This crack growth rate is much lower compared to that of ordinary-sized specimens. This means that once a fatigue crack starts to grow then the fatigue fracture occurs only after several thousands cycles (this was confirmed in the actual fatigue crack growth tests for the micro-sized specimens in this investigation). Therefore, the fatigue life of micro-sized specimens is dominated by crack initiation. This also suggests that even a micro-sized surface flaw may be an initiation site of fatigue crack growth and this will shorten the fatigue life of micro-sized specimens.

In this investigation, the fatigue crack growth properties for micro-sized specimen were able to be measured for the first time. However, the detail of size effects on fatigue crack growth behavior is still unclear. Further investigation is required to quantify the size effect on fatigue mechanisms in micro-sized specimens.

Conclusions

Fatigue crack growth tests have been performed for micro-sized cantilever beam type specimens prepared from an electroless plated Ni-P amorphous alloy thin film to investigate the size effects on fatigue crack growth behavior of such micro-sized specimens.

Striations were observed on the fatigue fracture surfaces, and fatigue crack propagation rates were estimated by a careful measurement of the striation spacing. The fatigue crack growth rates at stress ratios of 0.3 and 0.5 were almost identical, but the fatigue crack growth rate at a stress ratio of 0.1 were lower compared to that at 0.3 and 0.5 at a given value of ΔK. This suggests that crack closure may occur even in such micro-sized specimens. In contrast, the fatigue crack growth rate at a stress ratio of 0.7 was higher than those at 0.3 and 0.5. The fatigue crack extended by both cyclic and static loading and this causes higher fatigue crack growth rate at stress ratio of 0.7. The results obtained in this investigation are the first measurements of fatigue crack growth properties for micro-sized specimens and provide basic guidelines for design of actual micro-sized machine and MEMS devices.

Acknowledgments

This work was partly supported by the Grant-in-Aid for Scientific Research (B) (2) No. 12555186 from the Ministry of Education, Science, Sports and Culture, Japan. The authors would like to thank to Mr. S. Maekawa for his help in experiments.

References

[1] Weihs, T. P., Hong, S., Bravman J. C. and Nix, W. D., "Mechanical Deflection of Cantilever Microbeams: A New Technique for Testing Mechanical Properties of Thin Films," *J. Mater. Res.*, Vol. 3, No. 5, 1988, pp. 931–942.

[2] Sharpe, Jr., W. N., Yuan, B. and Edwards, R. L., "A New Technique for Measuring the Mechanical Properties of Thin Films," *Journal of Microelectromechanical Systems*, Vol. 6, No. 3, 1997, pp. 193–199.

[3] Ballarini, R., Mullen, R. L., Yin, Y., Kahn, H., Stemmer, S. and Heuer, A. H.: "The Fracture Toughness of Polysilicon Microdevices: A First Report," *J. Mater. Res.*, Vol. 12, No. 4, 1997, pp. 915–922.

[4] Tsuchiya, T., Tabata, O., Sakata, J. and Taga, Y., "Specimen Size Effect on Tensile Strength of Surface-Micromachined Polycrystalline Silicon Thin Films," *Journal of Microelectromechanical Systems*, Vol. 7, No. 1, 1998, 106–113.

[5] Sato, K., Yoshioka, T., Ando, T., Shikida, M. and Kawabata, T., "Tensile Testing of Silicon Film Having Different Crystallographic Orientations Carried Out on a Silicon Chip," *Sensors and Actuators A: Physical*, Vol. 70, No. 1-2, 1998, pp. 148-152.

[6] Read, D. T. and Dally, W., "Fatigue of Microlithographically-patterned Free-Standing Aluminium Thin Film Under Axial Stresses," *Journal of Electronic Packaging*, Vol. 117, No. 1, 1995, pp. 1-6.

[7] Muhlstein, C. L. and Brown, S., "Reliability and Fatigue Testing of MEMS," *Tribology Issues and Opportunities in MEMS*, B. Bhusan, Ed., Klewer Academic Publications, Dordrecht, 1998, pp. 529–538.

[8] Schwaiger, R. and Kraft, O., "High Cycle Fatigue of Thin Silver Films Investigated by Dynamic Microbeam Deflection," *Scripta Materialia*, Vol. 41, No. 8, 1999, pp. 823–829.

[9] Takashima, K., Kimura, T., Shimojo, M., Higo, Y., Sugiura, S. and Swain, M. V.,

"A New Fatigue Testing Machine for Micro-Sized Specimens," *Fatigiue '99 (Proceedings of the 7th Fatigue Congress)*, X.-R. Wu and Z.-G. Wang, Higher Education Press, Beijing, 1999, pp. 1871–1876.

[10] Higo, Y., Takashima, K., Shimojo, M., Sugiura, S., Pfister, B. and Swain, M. V., "Fatigue Testing Machine of Micro-Sized Specimens for MEMS Applications," *Materials Science of Microelectromechanical Systems (MEMS) Devices II, MRS Symp. Proceedings*, 605, M. P. deBoer, A. H. Heuer, S. J. Jacobs, and E. Peeters, E., The Materials Research Society, Warrendale, PA, in press.

[11] Maekawa, S., Takashima, K., Shimojo, M., Higo, Y., Sugiura, S., Pfister, B., and Swain, M. V., "Fatigue Tests of Ni-P Amorphous Alloy Microcantilever Beam," *Japanese Journal of Applied Physics*, Vol. 38, No. 12B, 1999, pp. 7194–7198.

[12] Ichikawa, Y., Maekawa, S., Takashima, K., Shimojo, M., Higo, Y., and Swain, M. V., "Fracture Behavior of Micro-Sized Ni-P Amorphous Alloy Specimens," *Materials Science of Microelectromechanical Systems (MEMS) Devices II, MRS Symp. Proceedings*, Vol. 605, M. P. deBoer, A. H. Heuer, S. J. Jacobs, and E. Peeters, The Materials Research Society, Warrendale, Pennsylvania, in press.

[13] Gilbert, C. J. and Ritchie, R. O., "Fracture Toughness and Fatigue-Crack Propagation in a Zr-Ti-Ni-Cu-Be Bulk Metallic Glass," *Appl. Phys. Lett.*, Vol. 71, No. 4, 1997, pp. 476–478.

[14] Okamura, H., *Introduction to Linear Fracture Mechanics*, Baifukan, Tokyo, 1976, p. 218 (in Japanese).

[15] Suresh, S., *Fatigue of Materials*, Cambridge University Press, Cambridge, 1991, p. 308.

David A. LaVan,[1] Kamili Jackson,[2] Bonnie McKenzie,[2] S. Jill Glass,[2] Thomas A. Friedmann,[2] John P. Sullivan,[2] and Thomas E. Buchheit[2]

Direct Tension and Fracture Toughness Testing Using the Lateral Force Capabilities of a Nanomechanical Test System

REFERENCE: LaVan, D. A., Jackson, K., McKenzie, B., Glass, S. J., Friedmann, T. A., Sullivan, J. P., and Buchheit, T. E. **"Direct Tension and Fracture Toughness Testing Using the Lateral Force Capabilities of a Nanomechanical Test System,"** *Mechanical Properties of Structural Films, ASTM STP 1413*, C. L. Muhlstein and S. B. Brown, Eds., American Society for Testing and Materials, West Conshohocken, PA, Online, Available: www.astm.org/STP/1413/1413_21, 1 September 2001.

ABSTRACT: The behavior of MEMS devices is limited by the strength of critical features such as thin ligaments, oxide cuts joining layers, pin joints, and hinges. Polysilicon devices fabricated at Sandia's Microelectronic Development Laboratory as well as single layer amorphous diamond MEMS structures have been successfully tested to investigate these features. A series of measurements was performed on 2.5 μm thick, 1.8 μm wide samples with gage lengths of 15 to 1000 μm. Conventional samples, notched samples, as well as samples that include the critical features of standard components in the test section were tested.

KEYWORDS: polysilicon, amorphous diamond, MEMS, thin film, tensile, fracture, strength, testing, distribution, lateral force, nano, nanomechanical, indenter

Introduction

Understanding and predicting the behavior and reliability of polysilicon micromachined MEMS devices requires a thorough knowledge of the distribution in mechanical properties and the effect of stress concentrating features in these devices. Previous work [1–6] has not addressed samples of the same scale as the critical features found in MEMS devices—beams 1 to 2 μm wide and as short as 15 μm long. Samples designed to directly measure, under uniform tensile loading, the fracture strength, fracture toughness, and Young's modulus of polysilicon have been fabricated using Sandia National Laboratories's Ultra-planar Multi-level MEMS Technology (SUMMiT) process [7–8]. The samples have one end fixed to the surface by a freely moving pivot. The free, pull-ring, end of the sample is engaged by a flat-tipped conical diamond using the lateral force capabilities of a nanomechanical test system. Single level samples have also been tested to characterize novel materials for MEMS such as amorphous diamond [9–10].

Test Technique

Typical single layer and multi-layer specimens are shown in Fig. 1. The samples are 1 to 2.5 μm thick (depending on material), 1.8 or 3.8 μm wide, with gage lengths of 15 to 1000 μm. Cross section dimensions were verified in a SEM by comparison against a 1 μm lithography standard. The indenter was a flat bottomed conical diamond that fits

[1] Children's Hospital, Boston, MA and Massachusetts Institute of Technology, Cambridge, MA. Formerly of Sandia National Laboratories, Albuquerque, NM, lavan@MIT.EDU.

[2] Sandia National Laboratories, Albuquerque, NM.

into a ring on the free end of a specimen; the tip diameter is 35 μm at the bottom with an included double angle of 59°. During a test, the tip engages the pull ring (free end) of the specimen and a normal force is applied to keep the tip from slipping out (moving upward). The samples are designed to load the gage section in uniform tension, mimicking a standard tension test. There are no out-of-plane displacements of the sample, and the pivot on the multi layer sample reduces in-plane bending. The stage (with the die attached) moves at a rate of 40 nm/s. The control software increases the normal force on the indenter tip as the lateral force increases, thus preventing the tip from rising up and disengaging the sample (this is necessary since the diamond tip is not cylindrical). A schematic of the test procedure is shown in Fig. 2. Normal force, lateral force and lateral displacement are recorded using a user defined algorithm programmed into the nanomechanical test system.

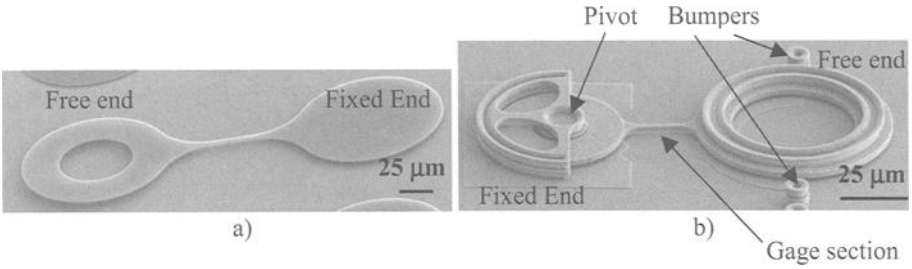

FIG. 1—a) *Single layer amorphous-Diamond sample;* b) *SUMMiT IV polysilicon tensile sample.*

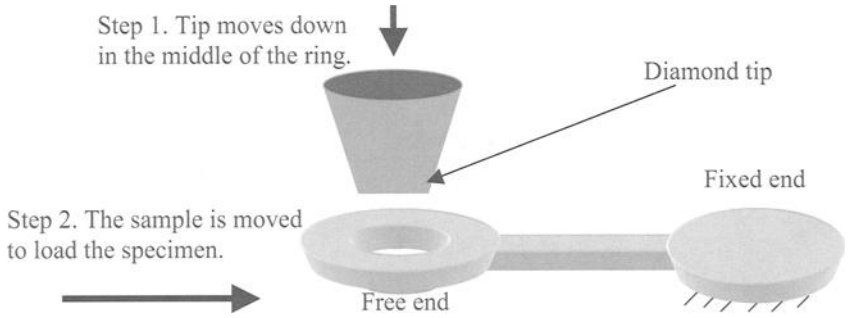

FIG. 2—*Schematic of the test procedure.*

Data Analysis

Correcting for Tip Angle and Contact on the Substrate.

To determine the tensile load applied to the gage section, T, the force recorded during the test is corrected for the reaction caused by the tip angle and the losses caused

by the tip contacting the substrate (the control software required the substrate contact). The method for doing this is given in Eqs 1–4, a diagram is shown in Fig. 3. The corrected normal force, N^*, applied to the tip creates a frictional force, L_f, that must be subtracted from the total recorded lateral force, L, to give T. To determine L_f, the coefficient of friction, μ, between the tip and the substrate is evaluated for each sample as the tip is sliding along the surface without lateral load. Eq 3 and 4 show the corrected normal force, N^*, found by subtracting the upward reaction of the tip, R_N, from T, due to the tip angle, θ:

$$L_f = \mu N^* \tag{1}$$

$$T = L - L_f \tag{2}$$

$$N^* = N - R_N \tag{3}$$

$$R_N = T \tan\theta \tag{4}$$

Equations 1–4 can be reduced to Eq 5, which describes the tensile force in the sample gage section as a function of the recorded data. The result of the correction is shown in Fig. 4. The shift of the tensile force to zero during the tip sliding section of the test is a graphical check of the correction. The difference, before and after the data correction, between the maximum force and the force recorded just after failure is very little, since the coefficient of friction, μ, between the diamond tip and the die is on the order of 0.05.

$$T = \frac{(L - \mu N)}{(1 - \mu \tan\theta)} \tag{5}$$

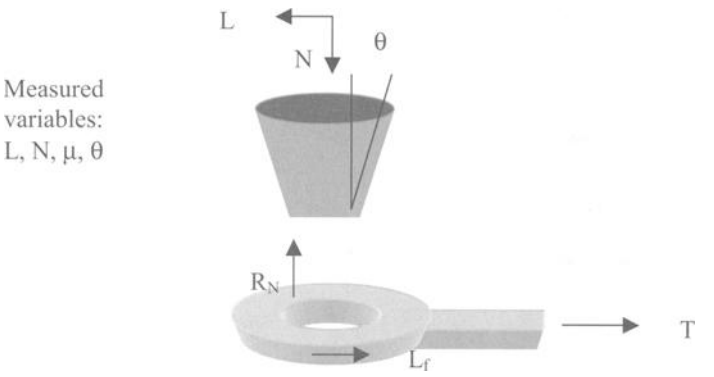

FIG. 3—*Force diagram illustrating how tensile force,* T, *is calculated.*

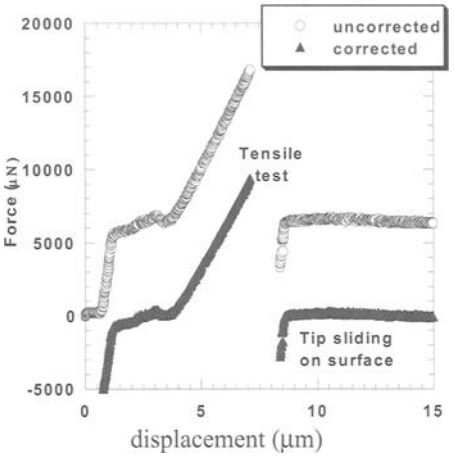

FIG. 4—*Corrections to the lateral force measurements to account for tip angle and contact of the tip on the substrate.*

Correcting for Machine Compliance in the Calculation of Modulus

If samples with several different gage lengths are tested, the lateral machine compliance can be determined by fitting a linear least squares line through a plot of the measured compliance, K_{exp}, versus the sample gage length, and evaluating the intercept at length equal to zero, as shown in Fig. 5. After the machine compliance, $K_{machine}$, is determined the measured compliance from each test is corrected by removing the contribution of machine compliance from the experimentally measured sample stiffness; providing a stiffness attributable to the sample gage section, K_{gage}. It is important to recognize that $K_{machine}$ includes all sources of extraneous compliance, such as the attachment of the sample to the die as well as the die to the stage, which is why this parameter is evaluated for each group of samples, and is not considered a fixed machine property:

$$\frac{1}{K_{\exp}} = \frac{1}{K_{machine}} + \frac{1}{K_{gage}} \tag{6}$$

Figure 6*a* is a plot of modulus for polysilicon samples based on uncorrected and corrected displacements as a function of gage length. The correction for machine compliance introduces a large scatter into the modulus data. In an effort to reduce the effect of this correction, the modulus is extracted from a plot of K_{gage} v 1/gage length, as shown in Fig. 6*b*. The modulus found in this manner is 170 GPa.

To illustrate the versatility of this test technique, a sample with the hinge assembly from a pop-up mirror is shown in Fig. 7. The ultimate load the hinge withstood was 1 mN.

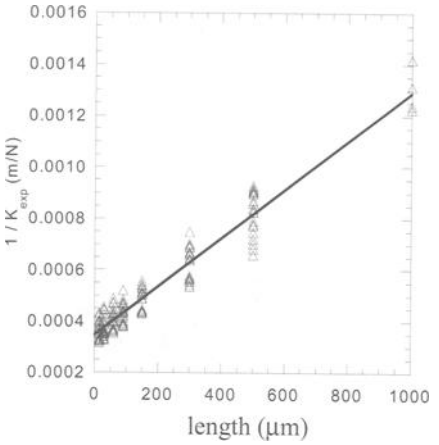

FIG. 5—*Curve fit to find extraneous compliance, $K_{machine}$, evaluated at length of zero.*

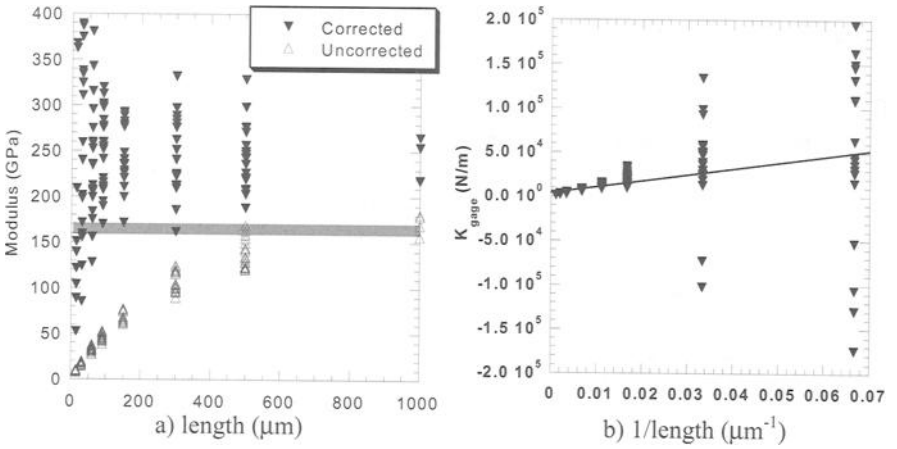

FIG. 6—a) *Modulus with and without the compliance correction;* b) *alternative method using a curve fit to evaluate modulus.*

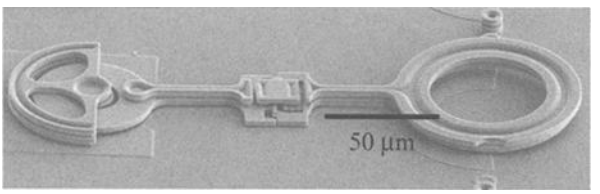

FIG 7—*A special sample designed to evaluate the maximum loading force for a pop-up mirror hinge.*

Results and Discussion

Strength

Figure 8 shows a plot of the strength of SUMMiT polysilicon and amorphous diamond samples in terms of probability of failure as well as the Weibull analysis [11–12] of this data. The data is summarized in Table 1.

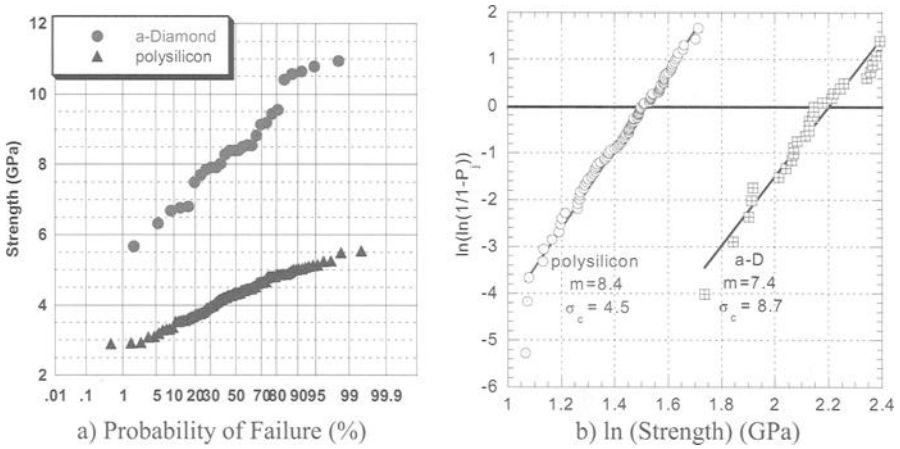

FIG 8—*Strength of MEMS materials* a*) probability of failure;* b*) plot to extract Weibull Modulus and characteristic strength.*

TABLE 1—*Summary of tensile properties.*

Material	Mean Strength (GPa)	Std. Dev. (GPa)	Min. Strength (GPa)	Max. Strength (GPa)	Weibull Modulus	Weibull Characteristic Strength (GPa)
SUMMiT polysilicon (n = 98)	4.27	0.61	2.90	5.54	8.4	4.5
Amorphous diamond (n = 28)	8.49	1.38	5.67	10.95	7.4	8.7

Fracture Toughness

The tensile technique describe above was modified to evaluate the notched tensile fracture toughness of MEMS materials (not standardized Plane Strain Fracture Toughness). A small corner notch with a width of 30 to 60 nm, and a length of 200 to 600 nm was introduced into samples using a focused ion beam (FIB). A typical notch viewed in the scanning electron microscope (SEM) is seen in Fig. 9. Fracture surfaces are shown in Fig. 10, showing classical glassy and hackle regions. This type of notch can

be approximated several different ways: as an elliptical corner crack, circular corner crack, or a modified elliptical surface crack. Since, for most of the samples, the length on the top and side of the sample was unequal, only the values calculated using the elliptical corner crack and modified elliptical surface crack analysis are reported. The elliptical corner crack analysis is taken from Anderson [13]. This analysis requires the angle of maximum stress that is assumed to be 45°:

$$K = (1.12)^2 \frac{2}{\pi} \sigma \sqrt{\pi a} \tag{7}$$

The modified surface crack formulation is from Hertzberg [14]. The elliptical surface crack analysis assumes a modified surface crack length of $b = \sqrt{(e^2 + f^2)}$ where $e = \sqrt{(a^2 + c^2)}$ and f is $c\sin[\tan^{-1}(a/c)]$:

$$K = 1.24 \sigma_f \sqrt{b} \tag{8}$$

A summary of fracture toughness results is included in Table 2. The mean value is 1.6 or 1.7 MPa $\sqrt{m}$, depending on the analysis used. The average is close to the range reported by Sharpe et. al [15] of 1.4 MPa $\sqrt{m}$ and Kahn et. al. [16] of 1.2 MPa$\sqrt{m}$.

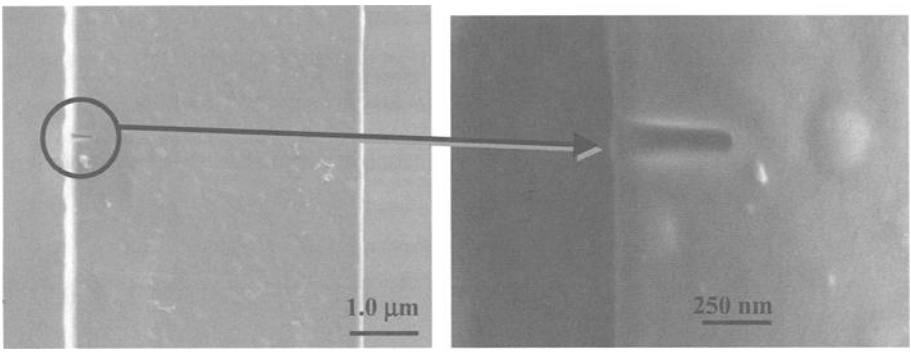

FIG. 9—*Corner notch cut into a 4 μm wide specimen.*

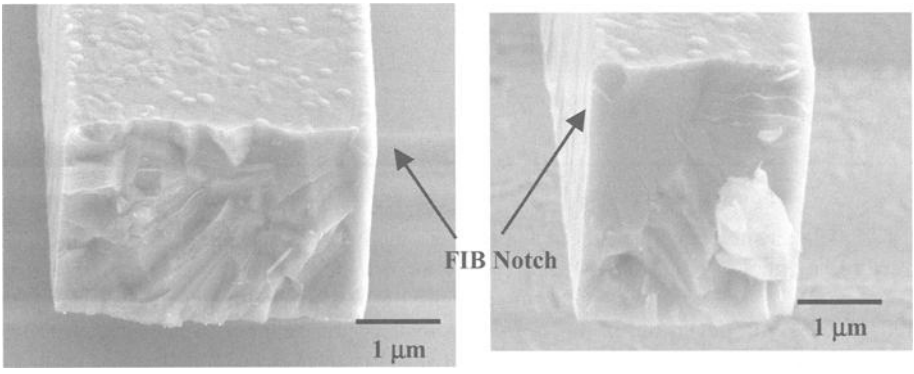

FIG 10—*Fractured* a) *3.8 μm and* b) *1.8 μm wide specimens.*

TABLE 2—*Results of Fracture Toughness Calculations (all values are in MPa$\sqrt{m}$).*

Specimen Number	Corner Elliptical Crack	Elliptical Surface Crack
DU17015-4	1.80	1.86
DU17030-2	1.36	1.41
DU17030-4	1.48	1.53
DU17060-4	1.61	1.67
DU170150-2	1.30	1.68
DU170150-4	1.55	1.61
DU17815-4	1.61	1.72
DU17830-4	1.51	1.59
DU17860-4	1.68	1.76
DU178150-4	1.31	1.37
DU178300-4	2.21	2.31
Average ± S.D.	1.58 ± 0.26	1.68 ± 0.25

Microstructural and Texture Analysis

It is important to consider possible microstructural influences in microsample testing, and to understand the relationship between the grain size and minimum sample features. For the smallest sample tested in this work, the gage section contains approximately 170 grains, enough to consider even these small samples to behave as continuum level polycrystals.

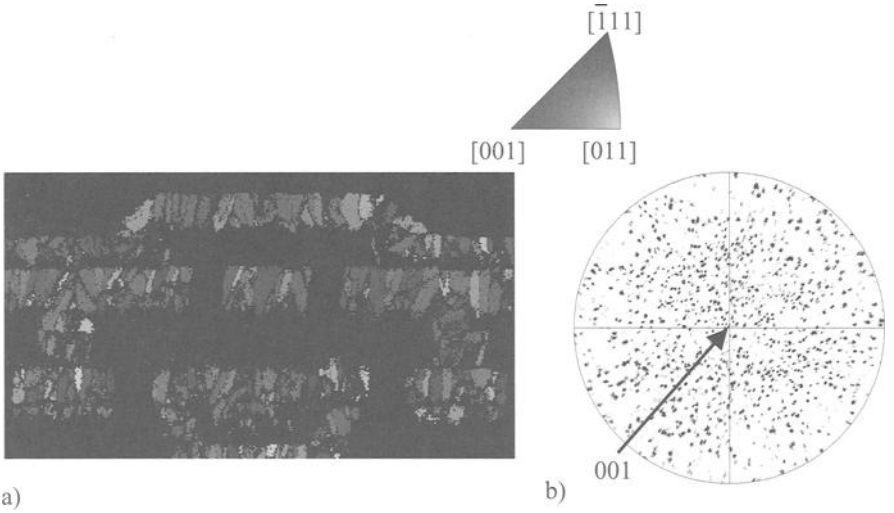

FIG. 11—a) *Microstructure of SUMMiT polysilicon as determined by EBKP illustrated using colorized inverse pole figure representation*; b) *(100) Micropole figure. of the same data indicating random crystallographic texture of the polysilicon relative to the deposition direction, indicated as 001 on the pole figure.*

Microstructural morphology and texture were documented using the Electron Backscatter Kikuchi Pattern (EBKP) technique [17]. This measurement was performed on SUMMiT polysilicon, fabricated using the same process as that used for the tensile and fracture samples, in an automated field emission scanning electron microscope (FE-SEM) with a grid spacing of 50 nm. A microstructure map delineating grain orientations relative to the deposition direction using a colorized inverse pole figure representation is illustrated in Fig. 11*a* and a corresponding (100) micro-pole figure is shown in Fig. 11*b*. The results show a columnar microstructural morphology with random crystallographic texture. Most grains bridged from top to bottom surface of the individual polysilicon layers. The average column diameter is 400 nm.

The amorphous diamond has also been examined with various electron and x-ray techniques with no crystalline domains found. A description of the synthesis and characterization of amorphous diamond can be found in Ref 9.

Conclusions

New techniques have been presented to measure the strength, distribution of strength, fracture toughness and modulus of MEMS materials using the lateral force capabilities of a nanomechanical test system. Two systematic problems were encountered; the low stiffness in the lateral direction that lead to erroneous modulus results for small samples, and the inability to check the lateral force calibration of the instrument against a standard as is customary for tensile and indentation tests. Both issues may be resolved with other machines. In the meantime, evaluating large numbers of samples and correcting for the machine compliance provides a reasonable remedy. The ability to test large numbers of samples without operator involvement is a very attractive feature of this technique, as is testing samples with feature sizes on the same scale as true MEMS devices. Further application of this technique to measure the force-displacement relationship for MEMS actuators is being undertaken.

Acknowledgments

This work was supported by Sandia National Laboratories, Albuquerque, New Mexico; Sandia is a multiprogram laboratory operated by Sandia Corporation, a Lockheed Martin Company, for the United States Department of Energy under Contract DE-AC04-94AL85000.

References

[1] Connally, J. A. and Brown, S. B., "Slow Crack Growth In Single-Crystal Silicon," *Science*, 12 June 1992, Vol. 256, No. 5063, pp.1537–1539.

[2] Koskinen J., Steinwall, J. E., Soave, R., and Johnson, H. H., "Microtensile Testing of Free-Standing Polysilicon Fibers of Various Grain Sizes," *Journal of Micromechanics & Microengineering*, March 1993, Vol. 3, No.1, pp.13–17.

[3] Read D. T. and Marshall, J. C., "Measurements of Fracture Strength and Young's Modulus of Surface-Micromachined Polysilicon," *SPIE Proceedings*, 1996, Vol. 2880, pp. 56–63.

[4] Tsuchiya T., Tabata, O., Sakata, J., and Taga, Y., "Tensile Testing of Polycrystalline Silicon Thin Films Using Electrostatic Force Grip," *Transactions of the Institute of Electrical Engineers of Japan*, Part A, Dec. 1996, Vol.116-E,

No.10, pp. 441–446.

[5] Sharpe, Jr., W. N., Yuan, B., and Edwards, R. L., "Fracture Tests of Polysilicon Film," *Thin-Films - Stresses and Mechanical Properties VII. MRS Proceedings*, Warrendale, PA, 1998, pp. 51–56.

[6] Greek, S. and Ericson, F., "Young's Modulus, Yield Strength and Fracture Strength of Microelements Determined By Tensile Testing," *Microelectromechanical Structures for Materials Research, MRS Proceedings,* Warrendale, PA, 1998, Vol. 518, pp. 51–56.

[7] Intelligent Micromachine Initiative, Sandia National Laboratories, available online, http://www.mdl.sandia.gov/Micromachine, 2000.

[8] Sniegowski, J. J. and de Boer, M. P., "IC-Compatible Polysilicon Surface Micromachining," *Annual Review of Material Science,* No. 30, 2000, pp. 299–333.

[9] Friedmann, T. A., Sullivan, J. P., Knapp, J. A., Tallant, D. R., Follstaedt, D. M., Medlin, D. L., and Mirkarimi, P. B., "Thick Stress-Free Amorphous-Tetrahedral Carbon Films With Hardness Near That of Diamond," *Applied Physics Letters*, Vol. 71, No. 26, Dec. 29 1997, pp. 3820–3822.

[10] LaVan, D. A., Hohlfelder, R., Sullivan, J. P., Friedmann, T. A., Mitchell, M. A., and Ashby, C. I. H., "Tensile Properties of Amorphous Diamond Films," *Symposium U Amorphous and Nanostructured Carbon, Proceedings of the 1999 MRS Fall Meeting,* 1-3 Dec. 1999, Boston, MA.

[11] Weibull, W., "A Statistical Theory of the Strength of Materials," *Proceedings, Royal Swedish Institute Engineering Research*, No. 151, 1939, pp. 1–45.

[12] Sullivan, J. D. and Lauzon, P. H., "Experimental Probability Estimators for Weibull Plots," *Journal of Material Science Letters*, Vol. 5, 1986, pp. 1245–1247.

[13] Anderson, T. L., *Fracture Mechanics Fundamentals and Applications,* 2nd ed., CRC Press: Ann Arbor, 1995.

[14] Hertzberg, R. W., *Deformation and Fracture Mechanics of Engineering Materials*, 2nd ed., John Wiley and Sons: New York, 1983.

[15] Sharpe, W. N., Yuan, B., and Edwards, R. L., "Fracture Tests of Polysilicon Film," *MRS Symposium, Proceedings*, Boston, MA, December 1997, Vol. 505, pp. 51–56.

[16] Kahn, H., Tayebi, N., Ballarini, R., Mullen, R. L., and Heuer, A. H., "Fracture Toughness of Polysilicon Mems Devices," *Sensors and Actuators*, 2000, Vol. 82, pp. 274–280.

[17] Adams, B. L., Wright, S. I., and Kunze, K., "Orientation Imaging: The Emergence of a New Microscopy," *Metallurgic Transactions, A,* 1993, Vol. 24A, No. 4, p. 819.

Kazuki Takashima,[1] *Masayuki Shimojo,*[1] *Yakichi Higo,*[1] *and Michael V. Swain*[2]

Fracture Behavior of Micro-Sized Specimens with Fatigue Pre-Crack Prepared from a Ni-P Amorphous Alloy Thin Film

REFERENCE: Takashima, K., Shimojo, M., Higo, Y., and Swain, M. V., **"Fracture Behavior of Micro-Sized Specimens with Fatigue Pre-Crack Prepared from a Ni-P Amorphous Alloy Thin Film,"** *Mechanical Properties of Structural Films, ASTM STP 1413,* C. L. Muhlstein and S. B. Brown, Eds., ASTM, West Conshohocken, PA, Online, Available: www.astm.org/STP/1413/1413_02, 16 March 2001.

ABSTRACT: Fracture toughness tests have been performed for an electroless deposited Ni-P amorphous alloy thin film with different crack growth directions, which are perpendicular and parallel to the deposition growth direction. Cantilever beam type specimens with dimensions of 10 by 10 by 50 μm^3 were prepared from a Ni-P amorphous thin film, and notches with different direction were introduced by focused ion beam machining. Fatigue pre-cracks were introduced ahead of the notches. Both introduction of fatigue pre-cracks and fracture tests were performed using a newly developed mechanical testing machine for micro-sized specimens. Fracture behavior is different between the two types of specimens. K_{IC} values were not obtained as the criteria of plane strain requirements were not satisfied for this size of the specimen, so that the provisional fracture toughness K_Q values were obtained. The K_Q value of the specimen with crack propagation direction being parallel to the deposition growth direction was 7.3 MPa $m^{1/2}$, while that with crack propagation direction being perpendicular to the deposition growth direction was 4.2 MPa $m^{1/2}$. These results suggest that the electroless deposited amorphous alloy thin film has anisotropic mechanical properties.

KEYWORDS: fracture toughness, thin film, Ni-P, amorphous alloy, anisotropy

Introduction

Microelectromechanical systems (MEMS) or micro-sized machines are under intensive development for utilization in many scientific and technological fields such as information and biomedical technologies. In particular, medical MEMS devices, including micro-catheters and drug delivery systems, are one of the most important and urgent applications of MEMS devices. These MEMS devices are usually fabricated from a thin film deposited on a substrate by a suitable surface machining technique, and the micro-sized elements prepared from a thin film layer are used as mechanical components. The fracture of the components used in such medical devices may cause serious medical accidents, so that the evaluation of fracture toughness of thin films is extremely important to ensure the reliability of medical MEMS devices.

The thickness of the thin film used in such MEMS devices is considered to be on

[1] Associate professor, research associate, and professor, respectively, Precision and Intelligence Laboratory, Tokyo Institute of Technology, 4259 Nagatsuta, Midori-ku, Yokohama 226-8503, Japan.

[2] Professor, Faculty of Dentistry and Department of Mechanical & Mechatronic Engineering, The University of Sydney, Australian Technology Park, Everleigh NSW 1430, Australia.

the order of microns. The fracture toughness measurements of such thin films have been attempted by a nanoindentation technique [1,2] and an on-chip type testing, which includes a specimen and a comb type electrostatic actuator on one Si chip [3,4]. In the nanoindentation technique, fracture toughness of a thin film on a substrate can be measured, but it is rather difficult to apply to measure fracture toughness of freestanding films. In the on-chip type testing, only fracture toughness for "in-plane" crack propagation of films can be determined, and it is impossible to measure fracture toughness for "out-of-plane" crack propagation of films. Therefore, anisotropic fracture behavior of thin film cannot be evaluated by these techniques. Micro-elements on MEMS devices are considered to be subjected to load in both the direction of "in-plane" and "out-of plane" of thin film. The fracture toughness values for both in-plane and out-of-plane are thus required to be evaluated for actual design of MEMS devices, as the fracture toughness of thin films prepared by sputtering or deposition has been considered to have anisotropy [5]. In addition, fracture toughness measurements have been carried out for the specimens with notch only (i.e., without fatigue precrack), as the introduction of fatigue precrack has been difficult for micro-sized specimens prepared from thin films.

In our previous investigations [6,7], we have demonstrated that the introduction of fatigue precrack is required to evaluate the fracture toughness even for micro-sized specimens. In this investigation, micro-sized cantilever beam type specimens were prepared from an electroless deposited Ni-P amorphous alloy thin film and fracture tests for two types of specimens with fatigue pre-cracks, of which directions are "in-plane" and "out-of-plane" of the thin film were carried out. Fracture behavior of the specimens is then discussed.

Experimental Procedure

Material

The material used in this investigation was a Ni-11.5 mass %P amorphous alloy thin film electroless deposited on an Al-4.5 mass %Mg alloy. The thickness of the amorphous layer was 12 μm and that of the Al-4.5 mass %Mg alloy substrate was 0.79 mm, respectively. A disk with a diameter of 3 mm was cut from the Ni-P/Al-Mg sheet by electro discharge machining. The amorphous layer was separated from the Al-Mg alloy substrate by dissolving the substrate with a NaOH aqueous solution.

Specimen Preparation

Two types of micro-sized cantilever beam specimens with different crack orientations were prepared to investigate the anisotropic fracture behavior and are referred to as "out-of-plane type specimen" and "in-plane type specimen" as schematically shown in Figs. 1*a* and 1*b*, respectively. The crack will propagate parallel to the deposition direction in the out-of-plane type specimen, while the crack will propagate perpendicular to the deposition direction in the out-of-plane type specimen.

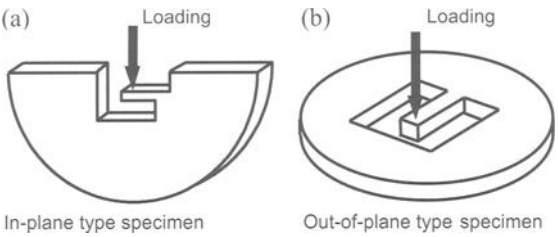

FIG. 1—*Two types of specimen orientation. The loading direction is perpendicular to the deposition growth direction for the in-plane type specimen, while the loading direction is parallel to the deposition growth direction.*

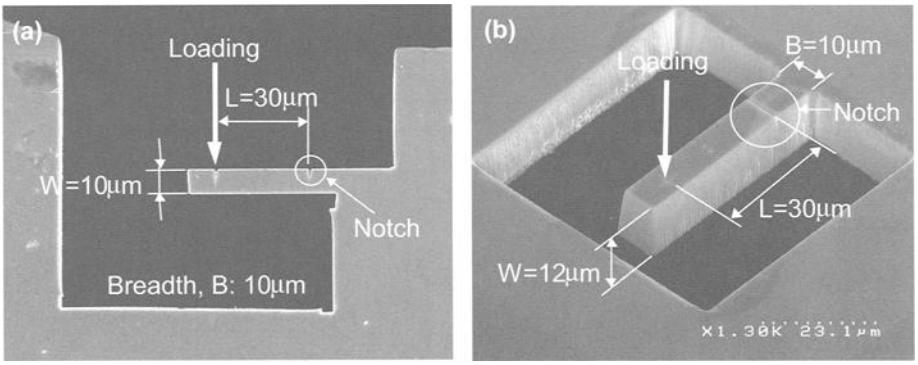

FIG. 2—*Scanning electron micrographs of micro-sized specimens by focused iron beam (FIB) machining: (a) in-plane type specimen and (b) out-of-plane type specimen. Notches were also introduced by FIB.*

Figures 2*a* and 2*b* show scanning electron micrographs of the specimens. The breadth of the out-of-plane type specimen, B, was 12 μm, the distance from the loading point to the notch position, L, was 30 μm, and the width of the specimen, W, was 10 μm. The size of the in-plane type specimen is approximately the same size; B was 10 μm, L was 30 μm, and W was 10 μm. All specimens were prepared by focused ion beam machining. Notches with depth equivalent to a/W = 0.25 (a = notch length) were introduced into the specimens as shown in Fig. 2. The width of the notch was 0.5 μm, and the notch radius is thus deduced to be 0.25 μm. The notch position was 10 μm from the fixed end of the specimen. The notches were introduced from the top surface side (the side at the end of deposition growth) for out-of-plane type specimens. A specimen with notch only (the total notch length was adjusted to be a/W = 0.5) was also prepared for in-plane type specimen to investigate the effect of introducing a fatigue pre-crack on fracture behavior for this type of specimen.

Fracture Toughness Test

A fatigue precrack was introduced ahead of the notch in air at room temperature

under constant load amplitude using the mechanical testing machine for micro-sized specimens, which was developed in our previous investigation [8,9]. This testing machine can apply both static and cyclic loading to micro-sized specimens with a load resolution of 10 μN and a displacement resolution of 5 nm. The specimen can be positioned with an accuracy of 0.1 μm using a precise X-Y stage. The details of the testing machine are described elsewhere [9]. The total crack length over specimen width (a/W) was adjusted to be approximately 0.5 for all specimens.

Fracture toughness tests were also carried out in air at room temperature using the same mechanical testing machine that was used for introducing fatigue pre-cracks. Fracture surfaces after the tests were observed using a HITACHI S-4000 field emission-gun type scanning electron microscope.

Results and Discussion

Fracture Behavior

Figure 3 shows typical load-displacement curves for in-plane type specimens with a notch only and with a fatigue precrack. The fracture behavior is different between these two specimens. The specimen with a notch only fractured in a brittle manner, while the specimen with a fatigue pre-crack fractured in a ductile manner. The maximum load of the specimen with a notch only is approximately twice that of the specimen with a fatigue precrack. This may be due to the difference in stress concentration at the crack tip. The stress concentration arising at a fatigue crack tip is larger than that of the notch tip. This indicates that even the notch with a root radius of 0.25 μm cannot be regarded as a crack for micro-sized specimens. In addition, the ion implantation caused by focused ion beam machining may change the mechanical properties around the notch tip. As the depth of ion implantation area is estimated to be less than 1 μm, the influence of ion implantation can be ignored by introducing a fatigue precrack of more than 1 μm in length. Therefore, it is essential for evaluating fracture toughness to introduce a fatigue pre-crack for the material used in this investigation.

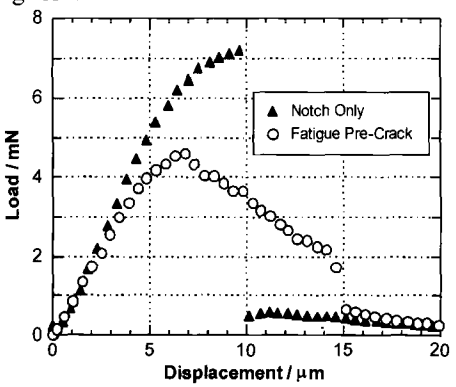

FIG. 3—*Load-displacement curves for micro-sized specimens with notch only and with fatigue pre-crack.*

Figure 4 shows typical load-displacement curves during fracture tests for the in-plane and the out-of-plane type specimens with fatigue precrack. The maximum load of

the out-of-plane type specimen is higher than that of the in-plane type specimen in spite of the size of specimen and the length of fatigue precrack being approximately the same. Fracture tests were carried out for five specimens to each type of specimen, and almost similar results were obtained. This suggests that the elecroless deposited Ni-P amorphous thin film exhibits anisotrpic fracture behavior.

Fracture Toughness Measurement

As crack opening displacement could not be measured for this specimen, the crack initiation load was not able to be determined. The maximum load was then assumed to be the crack initiation load, and this load was used to calculate fracture toughness value. Stress intensity factor, K, is calculated from the equation for a single edge notched cantilever beam specimen [10].

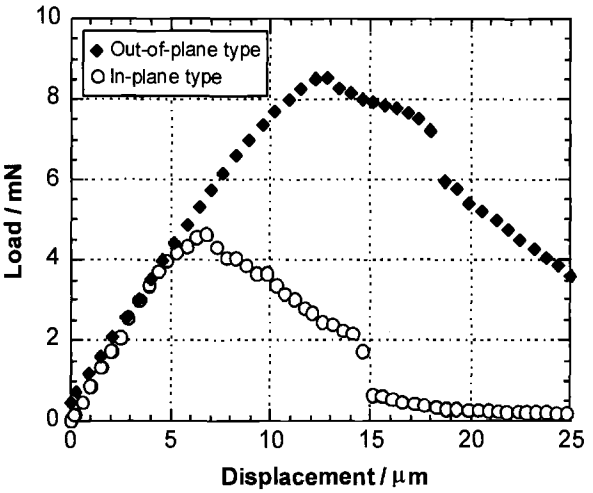

FIG. 4—*Load-displacement curves for micro-sized specimens with different fatigue pre-crack orientations.*

Figure 5 shows a scanning electron micrograph of a fracture surface for an out-of-plane type specimen. Fine equi-spaced markings aligned perpendicular to the crack propagation direction are observed ahead of the notch. These kinds of markings were also observed on the fatigue fracture surface of micro-sized Ni-P amorphous alloy specimens in our previous investigation [8] and are considered to be striations. This indicates that a fatigue pre-crack was introduced by cyclic loading successfully for micro-sized specimens. Vein patterns that have been observed on static fractured surface on Ni-P amorphous alloy are visible ahead of the fatigue precracked region. The total precrack length was then measured from scanning electron micrographs of the fracture surfaces for the calculation of the K value as shown in Fig. 5. The calculated provisional fracture toughness values (K_Q) for the out-of-plane and in-plane specimens are 7.3 and 4.2 MPa $m^{1/2}$, respectively.

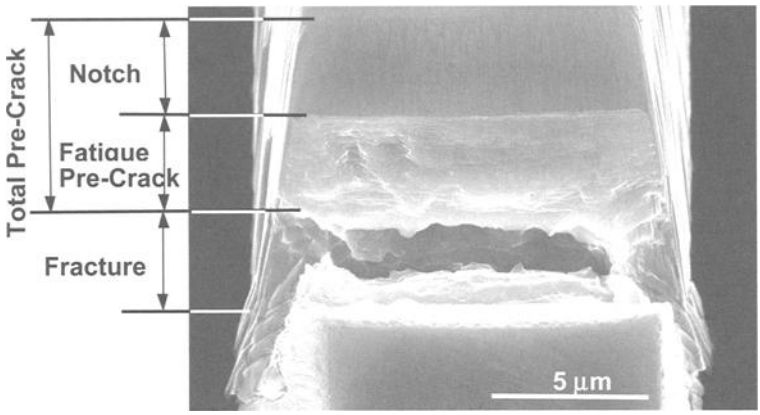

FIG. 5—*Scanning electron micrograph of fracture surface of out-of-plane type specimen.*

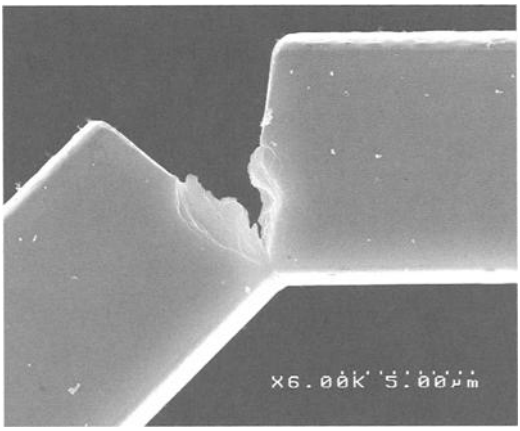

FIG. 6—*Scanning electron micrograph of specimen side surface of in-plane type specimen.*

However, these values are not valid plane strain fracture toughness values (K_{IC}), as the criteria of plane strain requirements (a, $W - a$, $B > 2.5\,(K_Q/\sigma_y)^2$) were not satisfied for this specimen size. Actually, a plastic zone was observed clearly at the crack tip as shown in Fig. 6. As the plane strain requirements are determined by K and σ_y, it is difficult for micro-sized specimens to satisfy these requirements. Consequently, other criterion such as J integral might be required to evaluate fracture toughness of such micro-sized specimens.

Fracture Surface Observation

Figures 7*a* and 7*b* show scanning electron micrographs of fracture surfaces of the specimens with different crack orientation. The fracture surface of an in-plane type specimen is relatively flat. In contrast, the fracture surface of an out-of-plane type specimen is rough, and the crack seems to propagate tortuously. The difference in K_Q values is considered to result from the difference in fracture surface morphologies.

Another feature of the fracture surface is the slant fractured regions observed near the side surfaces of cracks. The width of the region is approximately 1 μm for the in-plane type specimen and 3 μm for the out-of-plane type specimen. If these are shear lips, these areas should be plane stress dominated regions. The width of shear lip is expressed approximately as $2r_y/3$, where r_y is the size of the plane stress plastic zone ($r_y = (K/\sigma_y)^2/\pi$, where K is the stress intensity factor and σ_y is the yield stress of the specimen) [12]. The calculated value of shear lip width at K_Q is 1.2 μm for the in-plane type specimen and is 3.4 μm for the out-of-plane type specimen (the value of σ_y = 1.8 GPa in Ni-24 at %P amorphous alloy thin film was quoted [13] in this calculation). These sizes are very close to those of slant fractured regions in Figs. 7*a* and 7*b*. Therefore, these slant fractured zones are plane stress dominated regions and the flat region corresponds to a plane strain dominated one. It is very interesting that there exists a plane strain region even in such micro-sized specimens.

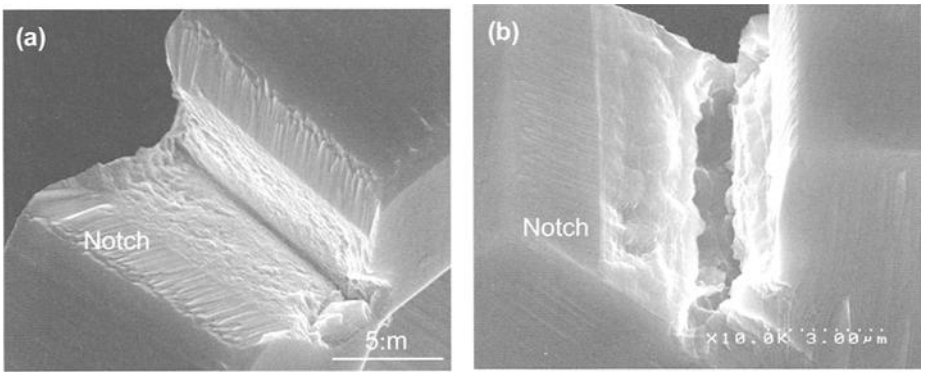

FIG. 7—*Scanning electron micrographs of fracture surfaces of (a) in-plane type specimen and (b) out-of-plane type specimen.*

Origin of Anisotropy in Fracture Behavior

The provisional fracture toughness, K_Q, of the out-of-phase specimen was much higher than that of the in-plane specimen. Figure 8 shows a transmission electron micrograph and its diffraction pattern of the Ni-P amorphous alloy thin film (the beam direction is parallel to the deposition growth direction), and a halo pattern that is characteristic of amorphous phase is observed. Therefore, there is no medium or long range ordering in the direction perpendicular to the deposition growth direction in this amorphous thin film. However, it has not been confirmed whether there is medium or

long range ordering in the direction parallel to the deposition growth direction. The difference in K_Q values and fracture surfaces between these two specimens suggests that there is some ordering towards the growth direction. Actually, anisotropical magnetic properties have been often observed for sputtered and deposited amorphous thin films [14]. Consequently, there may be some columnar type domain structures oriented towards the deposition growth direction as schematically shown in Fig. 9. Actually, such a columnar structure was observed for electrodeposited amorphous Fe-P alloys [15]. If there is such a columnar structure aligned towards the growth direction, the cantilever specimens have an anisotropy. This may be one reason that the K_Q of out-of-plane specimen is higher compared to that of the in-plane specimen.

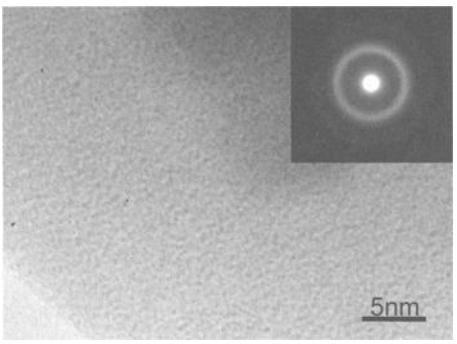

FIG. 8—*Transmission electron micrograph and diffraction pattern of the Ni-P amorphous thin film.*

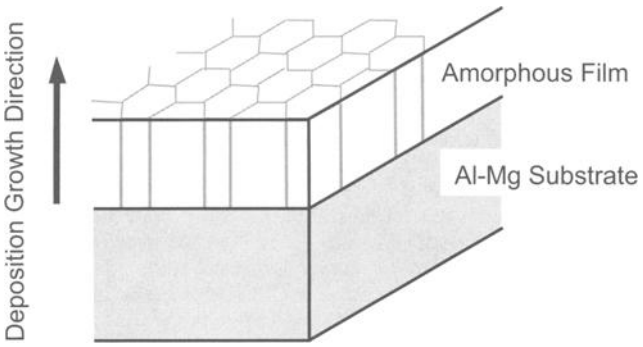

FIG. 9—*Schematic image of columnar structure in electroless deposited amorphous thin film on substrate.*

Conclusions

Fracture toughness tests have been performed for micro-sized cantilever beam specimens prepared from an electroless deposited Ni-P amorphous alloy thin film. Two

types of specimens with different crack propagation directions (in-plane type and out-of-plane type specimens) were prepared to investigate anisotropic fracture behavior of the thin film.

Fracture behavior is different between the two types of specimens. K_{IC} values were not obtained as the criteria of plane strain requirements were not satisfied for this size of the specimen, so that the provisional fracture toughness K_Q values were obtained. K_Q value of the specimen with crack propagation direction being parallel to the deposition growth direction was 7.3 MPa $m^{1/2}$, while that with crack propagation direction being perpendicular to the deposition growth direction was 4.2 MPa $m^{1/2}$. These results suggest the electroless deposited amorphous alloy thin film has anisotropic mechanical properties. It is required to consider the anisotropic fracture behavior when designing actual MEMS devices using electro deposited amorphous thin films.

Acknowledgments

This work was partly supported by the Grant-in-Aid for Scientific Research (B) (2) No. 12555186 from the Ministry of Education, Science, Sports, and Culture, Japan. The authors would like to thank to Messrs. A. Ogura and Y. Ichikawa for their help with experiments.

References

[1] Li, X. and Bhushan, B., "Measurement of Fracture Toughness of Ultra-Thin Amorphous Carbon Films," *Thin Solid Films*, Vol. 315, Nos.1–2, 1998, pp. 214–217.

[2] Ding, J., Meng, Y., and Wen, S., "Mechanical Properties and Fracture Toughness of Multilayer Hard Coatings Using Nanoindentation," *Thin Solid Films*, Vol. 371, No. 1–2, 2000, pp. 178–182.

[3] Ballarini, R., Mullen, R. L., Yin, Y., Kahn, H., Stemmer, S., and Heuer, A. H., "The Fracture Toughness of Polysilicon Microdevices: A First Report," *Journal of Material Resources*, Vol. 12, No. 4, 1997, pp. 915–922.

[4] Kahn, H., Tayebi, N., Ballarini, R., Mullen, R. L., and Heuer, A. H., "Fracture Toughness of Polysilicon MEMS Devices," *Sensor and Actuators A: Physical*, Vol. 82, Nos. 1-3, 2000, pp. 274–280.

[5] Lewis D. B. and Marshall, G. W., "Investigation into the Structure of Electrodeposited Nickel-Phosphorous Alloy Deposits," *Surface and Coating Technology*, Vol. 78, Nos. 1-3, 1996, pp.150–156.

[6] Ichikawa, Y., Maekawa, S., Takashima, K., Shimojo, M., Higo, Y., and Swain, M. V., "Fracture Behavior of Micro-Sized Ni-P Amorphous Alloy Specimens," *Materials Science of Microelectromechanical Systems (MEMS) Devices II, MRS Symposium Proceedings*, Vol. 605, M. P. deBoer, A. H. Heuer, S. J. Jacobs, and E. Peeters, Eds., The Materials Research Society, Warrendale, PA, 2000, in press.

[7] Takashima, K., Shimojo, M., Higo, Y., and Swain, M. V., "Fracture and Fatigue Behavior of Micro-Sized Amorphous Alloy Specimens," *Proceedings of Microscale Systems: Mechanics and Measurements Symposium, Society for Experimental Mechanics, Inc.*, Orlando, FL, 8 July 2000, pp. 32–35.

[8] Takashima, K., Kimura, T., Shimojo, M., Higo, Y., Sugiura, S., and Swain, M. V., "A New Fatigue Testing Machine for Micro-Sized Specimens," *Fatigiue '99 (Proceedings of 7th Fatigue Congress)*, X.-R. Wu and Z.-G. Wang, Eds., Higher Education Press, Beijing, 1999, pp. 1871–1876.

[9] Higo, Y., Takashima, K., Shimojo, M., Sugiura, S., Pfister, B., and Swain, M.

V., "Fatigue Testing Machine of Micro-Sized Specimens for MEMS Applications," *Materials Science of Microelectromechanical Systems (MEMS) Devices II, MRS Symposium Proceedings*, 605, M. P. deBoer, A. H. Heuer, J. S. Jacobs, and E. Peeters, Eds., The Materials Research Society, Warrendale, PA, 2000, in press.

[10] Okamura, H., *Introduction to Linear Fracture Mechanics*, Baifukan, Tokyo, 1976, p. 218 (in Japanese).

[11] Takashima, K., Shimojo, M., Higo, Y., and Swain, M. V., "Fatigue Crack Growth of a Ni-P Amorphous Alloy Thin Film," *Mechanical Properties of Structural Films, ASTM STP1413 (to be published)*, C. L. Muhlstein and S. B. Brown, Eds., ASTM, West Conshohocken, PA, Online, Available: *To be published.*

[12] Knott, J. F., *Fundamentals of Fracture Mechanics*, Butterworths, London, 1976, p. 124.

[13] Gilmann, J. J., "Mechanical Behavior of Metallic Glasses," *Journal of Applied Physics*, Vol. 46, No. 4, 1975, 1625–1633.

[14] Lanchava, B., Hoffmann, H., Bechert, A., Gegenfurtner, S., Amann, C., and Rohrmann, I., "Anisotropic Growth of Magnetic Domains in Amorphous Fe-Tb Thin Films," *Journal of Magnetism and Magnetic Materials*, Vol. 176, Nos. 2-3, 1997, pp. 139–144.

[15] Armyanov, S., Vitkowa, S., and Blajiev, O., "Internal Stress and Magnetic Properties of Elecrodeposited Amorphous Fe-P Alloys," *Journal of Applied Electrochemistry*, Vol. 27, No. 2, 1997, pp. 185–191.

Elastic Behavior and Residual Stress in Thin Films

Maarten P. de Boer,[1] *Norman F. Smith,*[1] *Nathan D. Masters,*[1] *Michael B. Sinclair,*[1] *and Emily J. Pryputniewicz*[2]

Integrated Platform for Testing MEMS Mechanical Properties at the Wafer Scale by the IMaP Methodology

REFERENCE: de Boer, M. P., Smith, N. F., Masters, N. D., Sinclair M. B., and Pryputniewicz, E. J., "**Integrated Platform for Testing MEMS Mechanical Properties at the Wafer Scale by the IMaP Methodology,**" *Mechanical Properties of Structural Films, STP 1413,* S. B. Brown and C. L. Muhlstein, Eds., American Society for Testing and Materials, West Conshohocken, PA, Online, Available: www/astm.org/STP/1413/1413_10, 1 June 2001.

ABSTRACT: A new instrument to accurately and verifiably measure mechanical properties across an entire MEMS wafer is under development. We have modified the optics on a conventional microelectronics probe station to enable three-dimensional imaging while maintaining the full working distance of a long working distance objective. This allows standard probes or probe cards to be used. We have proceeded to map out mechanical properties of polycrystalline silicon along a wafer column by the Interferometry for Material Property Measurement (IMaP) methodology. From interferograms of simple actuated cantilevers, out-of-plane deflection profiles at the nanometer scale are obtained. These are analyzed by integrated software routines that extract basic mechanical properties such as cantilever curvature and Young's modulus. Non-idealities such as support post compliance and beam take off angle are simultaneously quantified. Curvature and residual stress are found to depend on wafer position. Although deflections of cantilevers varied across the wafer, Young's modulus $E \sim 161$ GPa is independent of wafer position as expected. This result is achieved because the non-idealities have been taken into account.

KEYWORDS: MEMS metrology, long working distance interferometry, software integration, wafer scale, mechanical property characterization

Introduction

Fabrication of microelectromechanical systems (MEMS) devices for a variety of applications including optical switches and displays, microrelays and rf-switches, accelerometers, gyroscopes, image correctors, printheads, flow sensors, and medical devices is currently of great interest. MEMS are fabricated in a fashion similar to microelectronics in the integrated circuit (IC) industry. Free-standing structures are created at the end of the process flow by removing an oxide matrix that surrounds thin film structural members. Polycrystalline silicon (polysilicon) is to date perhaps the most successful MEMS material because many requirements can be satisfied simultaneously

[1] Sandia National Laboratories, PO Box 5800, Albuquerque, NM, 87185.
[2] Worcestor Polytechnic Institute, Worcester, MA, 01609.

[1]. Other structural materials such as aluminum [2], silicon carbide [3], and "amorphous diamond" [1] are in use or being explored.

Thin film techniques such as chemical vapor deposition, sputtering, or pulsed laser ablation are used to form such structural materials. For volume production, the same MEMS device will be fabricated repeatedly over the surface of a wafer, usually 15 cm or more in diameter. Typically there are 50 or more identical die sites. The microstructure of the resulting films from any of these deposition methods can exhibit cross-wafer non-uniformities resulting in variations of thickness, height, residual stress, stress gradient, and even modulus across the wafer. Mechanical properties must be sufficiently well controlled to guarantee that the intended design function of the MEMS device is met. For example, the resonant frequency of an accelerometer can be sensitive to small variations in residual stress. Also, highly curved comb drive fingers or suspensions (caused by stress gradient) will result in device malfunction. Furthermore, surface properties such as adhesion and friction are very sensitive to processing and may exhibit cross-wafer non-uniformity as well. Poor control of surface properties can result in failure of devices that allow contact or sliding. Multiple levels of structural material are now being fabricated. It is important to determine mechanical and surface properties at each of these levels. No MEMS metrology instrument exists today that (1) is highly sensitive to both mechanical and surface properties and (2) allows rapid property extraction across an entire wafer.

We have been investigating interferometry of simple electrostatically actuated beam test structures to accurately measure both mechanical and surface properties in MEMS [4-11]. We call this set of test structures, metrology, and analysis tools "Interferometry for Materials Property Measurement" (IMaP) [12]. Our experience is that mechanical properties in MEMS are best determined by integrating optically measured deflection data with materials property models that include the effects of non-idealities. We believe this is a necessary enhancement over the purely electrical methods [13] because given all the possible non-idealities of test structures, it is difficult to validate assumed models. With interferometry of actuated test structures as in IMaP, out-of-plane flexures can be measured to high resolution, and properties can be validated via independent measurements on the same test structure. In most cases, test structures are reusable. This is important for monitoring the effect of packaging on properties such as residual stress. The test structures occupy only a small area on a MEMS die site, important because more area is then available to build the intended devices. Electrostatic loading is used in IMaP because this is the primary actuation means in MEMS. Leakage currents that adversely affect test structures can then also serve as early diagnosis for failure of real MEMS devices.

The test structures we have been investigating are schematically represented in Fig. 1. Properties including thickness t, gap g, takeoff angle θ_o, curvature κ, support post compliance β, and Young's modulus E can be obtained from cantilevers [4-6], as seen in Figs. 1(a) and 4. Deflections of actuated fixed-fixed beams provide a sensitive measure of residual stress σ_R [4,5] (Fig. 1(b)). Cantilevers are also very sensitive to adhesion to the substrate due to capillary or van der Waals forces (Fig. 1(c)), and can be used to accurately measure adhesion Γ [7,8] as well as adhesion hysteresis $\Delta\Gamma$ [9]. Also, small area devices to monitor the coefficient of friction μ [10,14] (Fig. 1(d)) and

fracture strength σ_f [11] (Fig. 1(e) – top view) have been designed, measured by interferometry, and analyzed.

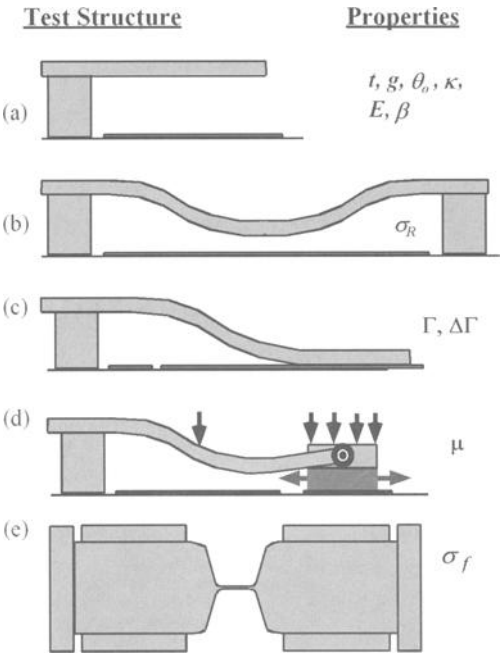

Fig. 1 Suite of test devices to measure mechanical and surface properties in MEMS. See text for discussion.

Although we have shown that all these properties can be well monitored by integrating nm-scale deflection data with computer-based finite difference models, two factors limit the ability to apply these techniques at the wafer scale. First, it is expedient to use conventional microelectronics probe stations that are manufactured to align wafers and move from one die site to the next. The electrical probes or probe cards for such systems usually require 1 to 2 cm of free space between the wafer surface and the microscope objective. However, the free working distance of commercially available interferometers is generally small (less than 1 cm) because an attachment enabling the interferometry is placed between the objective and the sample surface. The lack of free working distance requires that non-standard probes be built to fit under the interferometric attachment. That approach is awkward at best. Second, analysis procedures to rapidly extract material properties from deflection data of actuated beams do not exist.

We demonstrate in this paper that both of these problems can be surmounted. We have adapted the optics on a conventional microelectronics probe station microscope to allow interferometry with no loss of free working distance. This microscope has been mounted on the probe station manufactured to align wafers and move from one die site to the next, allowing wafer scale testing. Also, we have significantly enhanced the speed of material property determination code by writing three computer programs that are optimized for the task of acquiring and analyzing the data. These include an image analyzer program, a deflection calculator, and a materials property extraction program. We show testing results of actuated cantilevers and fixed-fixed beams from different die sites on a column of a wafer. While the results here are for polysilicon, the technique is also applicable to other MEMS materials. This work demonstrates a viable path towards full automation of accurate mechanical property testing in MEMS at the wafer scale.

Long Free Working Distance Interferometry

In most interferometric microscopes, an incoherent source with a coherence length of ~10 μm is used for illumination. The key requirement for incoherent source interferometry is that the optical path lengths from the beam splitter to the reference surface and to the sample must be the same to within a few microns. This is usually achieved by placing the beam splitter and reference surface under the microscope objective in either a Michelson or Mirau realization, and comes at the expense of free working distance. In work to show the feasibility of the IMaP approach [4-11], we used a Michelson attachment that had a 5 mm free working distance. Test structures were actuated on individual chips with 3 mm high electrical probes. As explained above, it is preferable to use commercially available electrical probes at the wafer scale. One method to gain the full free working distance of an objective is to use a second objective matched to the first, i.e., the Linnik interferometer. However, long working distance objectives required for wafer scale probing were not suitably matched for this approach to be effective.

If the illumination is replaced by a coherent source, the path length requirement is alleviated. In Fig. 2(a), a beam splitter *behind* the objective is used for the reference wave, and the optical path lengths to the sample and to the reference surface are quite different. The illumination source is a 532 nm (green light) diode pumped, frequency-doubled Nd:YAG laser, with a coherence length of greater than 100 m. Green light is chosen because polysilicon has low transmission at this wavelength, and because objective aberrations are minimized at the center of the visible spectrum. As seen in Fig. 2(b), the full free working distance of the original microscope objective (~2.5 cm) is maintained, and off-the-shelf probes fit underneath easily. A good quality inteferometric image of cantilever beam test structures as captured by a CCD camera is shown in Fig. 2(c). Vibration has been reduced by placing the unit on an isolation table. Because the reference surface is mounted on a voltage-controlled piezoelectric crystal, its z-height is finely controlled. Details of the implementation will be published elsewhere.

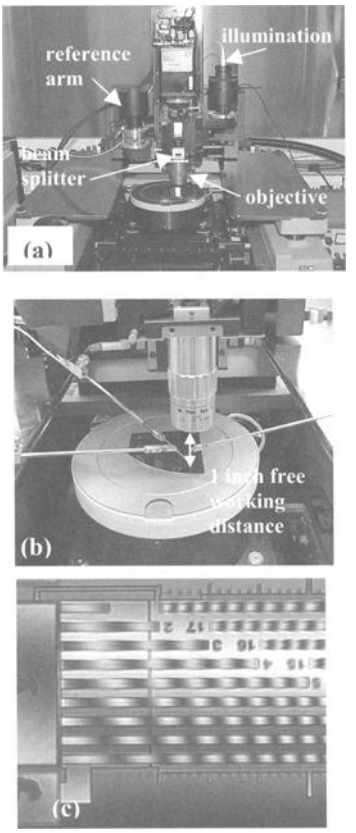

FIG. 2(a)—*Modified microscope on probe station,* (b) *closeup of objective with 2.5 cm free working distance,* (c) *interferogram of cantilever beam array.*

This design realization has numerous advantages over incoherent light interferometry. First, it is possible to obtain interferometry using different microscope objectives with only minor adjustment of the reference surface. Although 5X and 10X

objectives were used in this work, good quality images of small structures have been obtained with a 50X objective at 1.3 cm free working distance. Also, the microscope has an internal zoom, producing a continuously adjustable magnification range of greater than 20 without changing objectives. Second, it is possible to image through a glass window in this implementation, important for applications where the device is in vacuum or in a sealed package. Third, besides monitoring simple test structures as in this work, this capability will also be very useful for three-dimensional imaging of full-scale micromachined devices at the wafer level. Fourth, the illumination is very bright, which is advantageous in high frame rate or stroboscopic applications.

Algorithm and Software to Determine Cantilever Properties

To test the effectiveness of the new system, we measured cantilever and fixed-fixed beam properties along a column of a wafer. In Fig. 3, a step-by-step procedure to determine properties is shown, and in Fig. 4 the cantilever and its non-idealities are schematically represented. According to Step 1 of Fig. 3, thickness of the polysilicon layers was measured using a mechanical profilometer, and gap height g was measured by interferometry on cantilevers actuated into contact with the substrate (both to ~20 nm accuracy). The algorithm in Fig. 3 to determine cantilever properties has been detailed [6] and along with software enhancements is briefly described next.

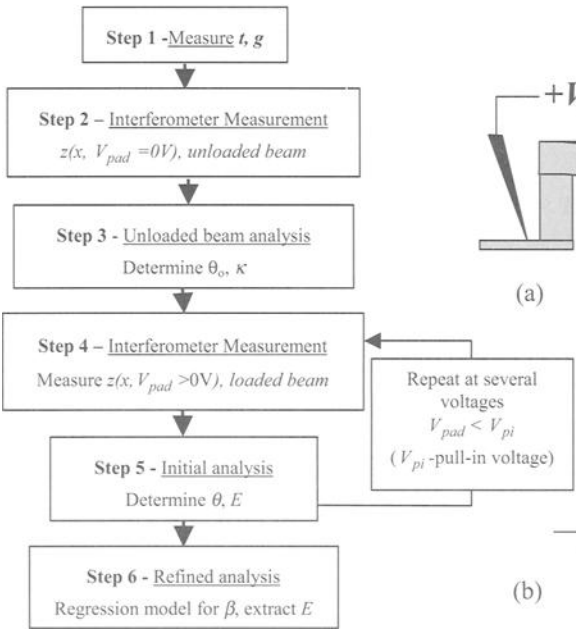

FIG. 3—*Step-by-step procedure to determine cantilever*

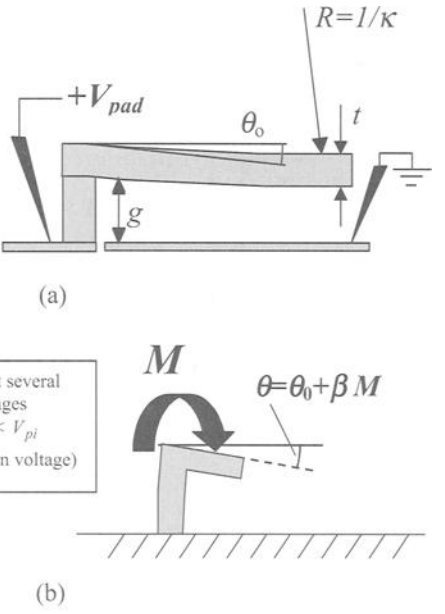

FIG. 4(a)—*Cantilever parameters t, g, θ_o and $R=1/\kappa$,* (b) *support post model.*

Three programs as portrayed in Fig. 5 were written to extract mechanical properties from deflection data (Steps 2-6 of Fig. 3). Interferograms of unloaded beams are recorded using an image analyzer program called "LineProfile Tool" per Steps 2 and 4 of Fig. 3. Within this program, reference points that indicate the beginning and end of the beam and where the linescan begins and ends are superposed on the image. The linescan (right side of Fig. 5), which contains fringe information as a function of pixel position, is stored in a file for further processing by a program called "Deflection Calculator." This program converts the linescan information into pixel by pixel z-deflection data with near nm resolution, and also converts pixel data into x-position data.

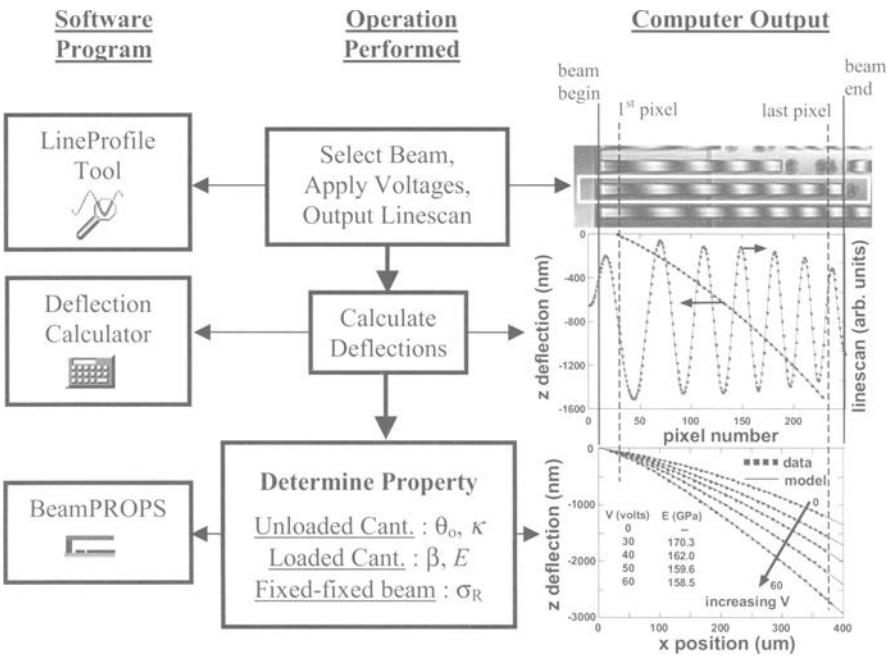

FIG. 5—*Overview of algorithms to determine properties of beams. See text for discussion.*

A program called "BeamPROPS" operates on the deflection data to extract properties in Steps 3, 5, and 6 of Fig. 3. BeamPROPS calculates model deflections by the finite difference method. For unloaded beams, it accounts for the non-idealities θ_o and κ, and for the small effect of gravity. It determines the properties using a quasi-Newton search algorithm by adjusting the model until the error between the data and the model deflections are minimized. Model fits to deflections of unloaded cantilevers along a wafer column are shown in Fig. 6. These deflections are well described by the equation

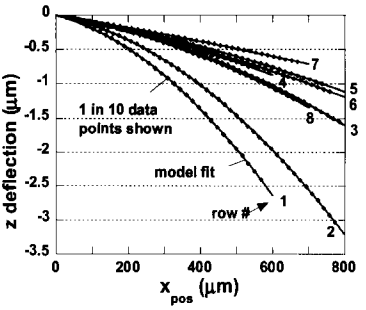

FIG. 6—*Deflection profiles of unloaded cantilevers along a wafer column.*

$$z(x) = \theta_o x + \kappa \frac{x^2}{2}, \tag{1}$$

where $z(x)$ is positive for deflections away from the substrate. Typical root mean square (rms) errors between the data and the model are ~2 nm/pixel. The resolution for θ_o is approximately 50 μrad, while for κ it is approximately 1 m^{-1}, corresponding to ~0.15 MPa/μm stress gradient resolution (note that stress gradient = $E\kappa$).

Once θ_o and κ are known for a given cantilever, a similar analysis procedure is performed by BeamPROPS on electrostatically loaded beams (Fig. 4(a)) to find loaded beam takeoff angle θ and E per step 5 of Fig. 3. Electrostatic loading with a fringing field correction is incorporated in the finite difference model calculations. The quasi-Newton search algorithm travels through (θ, E) space to rapidly find an optimum fit to the measured data, typically within five seconds. For a given cantilever, values of θ and E are found at each voltage loading. Non-systematic errors affect these values. Therefore, the slope in a regression model in which θ is plotted against the best fit calculated moment M is used to determine a value for support post compliance β, according to the equation

$$\theta = \theta_o + \beta M, \tag{2}$$

as shown in Fig 4(b). Using the value for β, the deflection data is re-analyzed by BeamPROPS to determine the best values for E per step 6 of Fig. 3. An example of the optimum fit to the measured data and the associated values for E are shown in the bottom right hand corner of Fig. 5. Note that at larger voltages, where E exerts its maximum effect on flexures, the values of E are repeatable. An actuation pad of 180 μm length near the support post was used to apply the voltages according to the principle of leveraged bending [15], and cantilevers analyzed were 300 to 700 μm in length. In the wafer column data below, values of E at each die site are averaged for several voltage loadings and several beams.

To determine residual stress (due to average residual stress through the thickness of the film), the deflection profiles of unloaded fixed-fixed beams of 1000 μm length were measured and found to be well represented by a sinusoidal shape, indicating that the beams were buckled in compression. Residual stress σ_R was calculated from the Euler buckling result

$$\sigma_R = -E \frac{\pi^2}{12} \left(\frac{3A^2 + 4t^2}{L^2} \right), \tag{3}$$

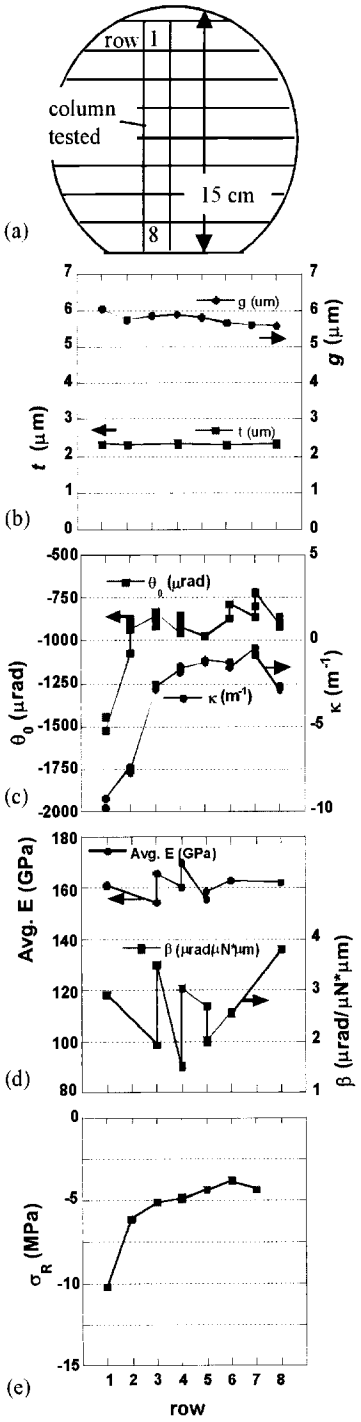

where L is the length of the fixed-fixed beam and A is the buckled beam amplitude, and the minus sign is for compression. Equation 3 assumes that the beam is well into the post-buckling regime, which is very reasonable for these long beams. The effect of stress gradient on the calculated result is small, and the resolution of the measurement with respect to σ_R is approximately 1 MPa. A value of E = 161 GPa was assumed in the calculations. Here, only unloaded beams were analyzed. However, we have demonstrated that by applying voltages to fixed-fixed beams, independent confirmation of σ_R can be obtained [16].

Results and Discussion

Diagnostic test structures were laid out and included on each die site along with MEMS devices. A lot was fabricated according to our standard MEMS process flow [1], in which four independent structural layers of polysilicon are produced. After processing, structures were freed by a standard "release" process. The wafer was then loaded onto the testbed described above. Wafer alignment was accomplished by manual operation of the chuck motor, voltages were manually programmed, and the three software tools listed above were run sequentially. Work is in progress to seamlessly integrate the three programs with automatic operation of the chuck.

Figure 7 shows testing results of mechanical properties along a column of die sites as represented in Fig. 7(a) for the third level of polysilicon, "Poly 3". Figure 7(b) shows tight control of thickness, with t = 2.34 +/- 0.02 μm. Poly 3 gap height g is not as well controlled as thickness, with values from 5.53 to 6.03 μm. This variation across the wafer is reasonable given the chemical mechanical polishing (CMP) process of the oxide layer underlying Poly 3. It is important to measure the geometrical properties t and g accurately (to ~20 nm) on each individual device, because the subsequent analysis to determine E depends strongly on these values.

FIG. 7—*Column map for materials properties (a) wafer, (b) t, g, (c) θ_o, κ, (d) E, β, (e) σ_R.*

The values of unloaded cantilever takeoff angle θ_o and curvature κ, reflecting the data of Fig. 6, are shown in Fig. 7(c). It is seen that θ_o is negative but relatively constant across the wafer, with values of –750 to –1000 μradians. We attribute the negative values of θ_o to oxide incorporation within the support post structure [6]. After release, the highly compressive deposited oxide is no longer constrained, and we believe this induces the support to pivot (we have subsequently reduced θ_o by an improved support post design). Typical values in Fig. 7(c) of κ from -1 to -2.5 m^{-1} (corresponding to stress gradient values of –0.16 to -0.4 MPa/μm) are quite low for MEMS devices. Note in Row 1 that θ_o drops sharply to –1500 μrad and also that κ decreases significantly to –10 m^{-1}. The change in κ may be due to a subtle microstructural feature [17] or trace contaminant such as the oxygen level [18] being different in the Poly 3 layer at this die location relative to the rest of the wafer (other sources are also possible, and this is a subject for future research). This in turn may be responsible for the sharp drop in θ_o. Clearly, both negative θ_o and negative κ are undesirable for MEMS devices, which often contain long structural elements assumed to be flat over the substrate.

In Fig. 7(d), the values of E are seen to be relatively constant across the substrate. This is expected because it is unlikely that the subtle changes in stress gradient at the sub MPa/μm level (or the changes in σ_R at <10 MPa, see below) will affect the bulk modulus of ~163 GPa expected for our isotropically textured films. However, it is important to note that given the highly non-linear mechanics of the electrostatically actuated beam, this result can only be achieved because t, g, θ_o, and κ were measured and modeled on the same individual cantilevers. The average value of β ~ 2.5 μrad/(μN*μm) compares well with finite element modeling of similar geometries, where β values of 2.47 to 2.73 μrad/(μN*μm) were determined [6]. However, it is seen in Fig. 7(d) that β varies significantly across the wafer without a trend. Because its value is dominated by the polysilicon thickness which was well controlled, we would not expect that β would vary to this degree. We investigated this issue and found that errors of 100% in β result if there is a 2 pixel error (~ 5 μm) in the starting location of the beam ("x-offset error"). This is a bookkeeping issue in that the location of the beginning of the beam is effectively being reassigned [6]. Fortunately, a 2 pixel x-offset error induces a change in E of less than 4%.

The values of residual stress σ_R, while typically low in magnitude at ~ -5 MPa, correlate well with curvature κ, as seen in Fig. 7(e). This has been observed previously [18] and is not necessary but perhaps not surprising because κ is caused by the gradient in σ_R through the thickness of the film. The high stress resolution inherently available from the interferometry enables correlation at the subtle levels of change in stress observed here (compare Fig. 7(c) to 7(e)). The correlation between κ and σ_R along the wafer column suggests that control of stress gradient and residual stress may be affected by the same processing non-uniformities.

Concluding Remarks

We have constructed a long working distance interferometer to enable three-dimensional visualization of MEMS devices and test structures on a standard microelectronics probing station. This innovation permits nm-scale deflection profiles of electrostatically actuated test structures to be conveniently acquired across a wafer. We have also written software routines that facilitate rapid comparison of deflection data with test structure models, allowing fundamental property extraction. In the course of obtaining test structure properties along a wafer column, the new instrument has been validated to work well. Young's modulus did not depend on wafer position, as expected, while curvature and residual stress did depend on wafer position. Although low in magnitude, these latter parameters correlated well with each other, suggesting that control of stress gradient and residual stress may be affected by the same processing non-uniformities. This property measurement capability will prove invaluable for process control and yield enhancement in MEMS and for understanding limitations of MEMS device design. Future work will include further integration of the software, extending this technique to measurement of other polysilicon layers in our MEMS process, and to surface properties such as adhesion and friction.

Acknowledgments

We would like to acknowledge the staff in the microelectronics development lab at Sandia National Laboratories for fabrication of the test structures. Sandia is a multiprogram laboratory operated by Sandia Corporation, a Lockheed Martin Company, for the United States Department of Energy under Contract DE-AC04-94AL85000.

References

[1] Sniegowski, J. J. and de Boer, M. P., "IC-Compatible Polysilicon Surface Micromachining," *Annual Review of Material Science*, Vol. 30, No. 297, 2000.

[2] Vankessel, P. F., Hornbeck, L. J., Meier, R. E., and Douglass, M. R., "MEMS Based Projection Display," *Proceedings of IEEE*, Vol. 86, No. 8, 1998, p.1687.

[3] Mehregany, M. and Zorman, C. A., "SiC MEMS: Opportunities and Challenges for Applications in Harsh Environments," *Thin Solid Films*, Vol. 356, 1999, p. 518.

[4] Jensen, B. D., de Boer, M. P., and Miller, S. L., *IMaP: Interferometry for Materials Property Evaluation in MEMS*, MSM '99, vol., San Juan, Puerto Rico, 1999, pp. 206-209.

[5] Jensen, B. D., de Boer, M. P., and Bitsie, F., *Interferometric Measurement for Improved Understanding of Boundary Effects in Micromachined Beams, Proceedings of the SPIE*, Vol. 3875, Santa Clara, CA, 1999, pp. 61-72.

[6] Jensen, B. D., de Boer, M. P., Masters, N. D., Bitsie, F., and LaVan, D. A., "Interferometry of Actuated Cantilevers to Determine Material Properties and Test Structure Non-Idealities in MEMS," *J. MEMS*, Vol. 10, No. 3, in press.

[7] de Boer, M. P. and Michalske, T. A., "Accurate Method for Determining Adhesion of Cantilever Beams," *Journal of Applied Physics*, Vol. 86, No. 2, 1999, p. 817.

[8] de Boer, M. P., Clews, P. J., Smith, B. K., and Michalske, T. A., "Adhesion of

Polysilicon Microbeams in Controlled Humidity Ambients," *Mater. Res. Soc. Proc.*, Vol. 518, San Francisco, CA, 1998, pp. 131-136.

[9] de Boer, M. P., Knapp, J. A., Michalske, T. A., Srinivasan, U., and Maboudian, R., "Adhesion Hysteresis of Silane Coated Microcantilevers," *Acta Mater.*, Vol. 48, Vol. 18-19, 2000, p. 4531.

[10] de Boer, M. P., Redmond, J. M., and Michalske, T. A., "A Hinged-Pad Test Structure for Sliding Friction Measurement in Micromachining," *Proceedings of the SPIE*, Vol. 3512, Santa Clara, CA, 1998, pp. 241-250.

[11] de Boer, M. P., Jensen, B. D., and Bitsie, F., "A Small Area In-Situ MEMS Test Structure to Measure Fracture Strength by Electrostatic Probing," *Proceedings of the SPIE*, vol. 3875, Santa Clara, CA, 1999, pp. 97-103.

[12] de Boer, M. P., Jensen, B. D., Miller, S. L., Smith, N. F., and Miller, S. L., "*Automated Test System to Accurately Measure and Verify Mechanical and Surface Properties in MEMS,*" patent pending, 2000.

[13] Osterberg, P. M. and Senturia, S. D., "M-TEST: A Test Chip for MEMS Material Property Measurement Using Electrostatically Actuated Test Structures," *J. MEMS*, Vol. 6, No. 2, 1997, p. 107.

[14] Crozier, B. T., de Boer, M. P., Redmond, J. M., Bahr, D. F., and Michalske, T. A., *Friction Measurement in MEMS Using a New Test Structure*, Mater. Res. Soc. Proc., vol. 605, Boston, MA, (2000), pp. 129-134.

[15] Hung, E. S. and Senturia, S. D., "Leveraged Bending for Full-Gap Positioning with Electrostatic Actuation," *Hilton Head '98*, Hilton Head Island, SC, 1998, pp. 83-86.

[16] Baker, M. S., de Boer, M. P., Smith, N. F., and Sinclair, M. B., "Measurement of Residual Stress in MEMS to Sub Megapascal Accuracy," Society for Experimental Mechanics Annual Conference and Exposition, Portland, OR, submitted.

[17] Krulevitch, P., Johnson, G. C., and Howe, R. T., "*Stress and Microstructure in Phosphorus Doped Polycrystalline Silicon*," *Mater. Res. Soc. Proc.*, Vol. 202, 1992, pp. 79-84.

[18] Fuertsch, M., Offenberg, M., Muenzel, H., and Morante, J. R., "*Influence of Anneals in Oxygen Ambient on Stress of Thick Polysilicon Layers*," *Sensors and Actuators*, Vol. A 76, 1999, p. 335.

Thomas Ganne,[1,2] *Guy Farges,*[1] *Jérôme Crépin,*[2] *Rachel-Marie Pradeilles-Duval,*[2] *André Zaoui*[2]

Influence of the Film Thickness on Texture, Residual Stresses and Cracking Behavior of PVD Tungsten Coatings Deposited on a Ductile Substrate

REFERENCE: Ganne, T., Farges, G., Crépin, J., Pradeilles Duval, R. M., and Zaoui, A., **"Influence of the Film Thickness on Texture, Residual Stresses and Cracking Behavior of PVD Tungsten Coatings Deposited on a Ductile Substrate,"** *Mechanical Properties of Structural Films, ASTM STP 1413*, C. Muhlstein and S. B. Brown, Eds., American Society of Testing and Materials, West Conshohocken, PA, Online, Available: www.astm.org/STP/1413/1413_14, 1 July 2001.

ABSTRACT: Tungsten coatings are deposited on a steel substrate by magnetron sputtering. For coatings deposited under identical processing conditions, a (111) texture develops with the increase of the coating thickness and the decrease of the residual stress. No gradient stress has been observed in the diffracted volume and the residual stress state is isotropic and plane. Tensile and four-point bending tests are performed in a SEM chamber in order to study the cracking kinetics. Taking account of the residual stresses, an intrinsic cracking stress can be determined. Cracking kinetics are found to depend on the coating thickness and the substrate yield stress. No debonding was observed at the interface despite the large plastic deformation of the substrate at the crack tips. This corresponding strain localization has a strong influence on the crack density and the cracking kinetics.

KEYWORDS: magnetron sputtering, residual stresses, crystallographic texture, cracking behavior, tungsten coating

Introduction

Coatings are used to improve the mechanical, thermal, and chemical properties of a substrate. The optimization of the coating-substrate system needs an identification of the damage mechanisms, the analysis of the damage kinetics and a good understanding of the correlation between microstructure and macroscopic behavior. Usually, the weak part in such systems is the coating cracking and the interface debonding. These damage mechanisms appear when the overall stress reaches a critical value. For physical vapor deposited (PVD) coatings, the residual stresses are generated during the deposition stage. They are generally composed by a thermal stress and an "intrinsic stress." The thermal stress is due to the temperature variation after deposition and to the difference between the thermal expansion coefficients of the coating and substrate materials. The "intrinsic stress" is due to the cumulative effect of crystallographic flaws developing in the coating during deposition [1].

In the present work, we first studied the dependence of the residual stress level and the crystallographic texture on the coating thickness. The mechanical behavior was then investigated using tensile and four-point bending tests. The cracking mechanisms and kinetics as well as a critical cracking stress were determined as a function of the coating thickness. Finally, a local study of the heterogeneity of the strain field and of the

[1] Centre Technique d'Arcueil, 16 Bis avenue Prieur de la Côte d'Or, F-94114 Arcueil Cedex.
[2] Laboratoire de Mécanique des Solides, CNRS, Ecole Polytechnique, F-91128 Palaiseau Cedex.

displacement field in the substrate near the interface was performed, giving access to a better understanding of the cracking kinetics.

Materials

Tungsten coatings were deposited on steel substrates by magnetron sputtering. The practical details of the used sputtering device are reported in a previous paper [2]. The processing conditions are the following: 3 kW target power, -25 V substrate bias, 3.5 Pa Ar pressure; the corresponding samples are labelled from A to I with a coating thickness ranging from 0.6 to 30 μm.

The experimental analysis of the mechanical characteristics of these coatings, such as the residual stresses or the critical cracking stress, requires knowledge of their elastic properties. We assumed that Young's modulus, Poisson's ratio and the coefficient of thermal expansion of the studied coatings, which are submitted to compressive residual stresses, are given by the bulk tungsten values (see Table 1).

TABLE 1 — *Mechanical properties and thermal expansion coefficients of PVD tungsten coatings and 35NCDV12 steel substrates.*

	Young's Modulus, E (GPa)	Poisson's Ratio, ν	Coefficient of Thermal Expansion, α ($10^{-6}K^{-1}$)	Yield Stress, σ_y (MPa)
PVD W	410	0.28	4.6	...
Substrate 1	200	0.29	12.3	1100
Substrate 2	200	0.29	12.3	800

The substrate is a 35NCDV12 steel. Some of the substrates were subjected to a specific thermal treatment in order to modify their yield stress and to make possible the study of the influence of this parameter on the cracking kinetics. The mechanical properties of the two kinds of substrates are also reported in Table 1. The different sample characteristics (coating thickness, processing conditions, and substrate) are reported in Table 2.

TABLE 2 — *Characteristics of the coating-substrate systems.*

Sample	Coating Thickness (μm)	Substrate
A	0.6	1
B	1.6	1
C	1.6	1
D	6	1
E	13.9	1
F	13.9	2
G	31.1	1
H	30.9	1
I	30.1	2

Crystallographic Texture, Residual Stresses

The initial state of the studied coatings was characterized through their crystallographic texture and residual stress state.

Crystallographic Texture

The crystallographic texture of f..c.c coatings with a <110> growth orientation [3] and of b.c.c coatings with a <111> growth orientation [4] have been shown to depend on thickness. So, the crystallographic texture of our samples has been determined by X-ray diffraction with use of a Cu K_α radiation; the analyzed volume is 1mm² × 1 μm (average depth) large. The texture has been characterized by the texture coefficient T_{hkl} [5]. The larger this coefficient with respect to 1, the stronger the texture along the considered direction. Fig. 1 shows that the coefficient T_{222} increases with the coating thickness, which characterizes the development of a <111> texture. This result is in agreement with Gergaud's [4] observations on Mo coatings that have the same crystallographic structure.

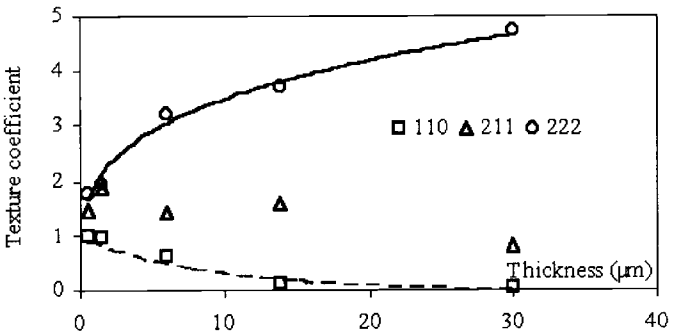

FIG. 1 — *Variation of the coatings texture coefficient versus their thickness.*

Residual Stresses

Residual stresses were determined by X-ray diffraction with a Cu K_α radiation (λ_{cu} = 0.1504 nm), according to the "$\sin^2\psi$" method [6]. Since tungsten single crystals are considered as elastically isotropic [7], the same property is true for textured polycrystalline coatings [8]. If we assume that the stress state is uniform in the diffracted volume and that the residual stress field in the coating is plane and isotropic (σ_{i3} [i = {1,2,3}] = σ_{12} = 0 and $\sigma_{11} = \sigma_{22} = \sigma$), then the stress-strain relation is given by:

$$\varepsilon_{\phi\psi} = \frac{1+\nu}{E} \cdot \sigma \cdot \sin^2\psi - \frac{\nu}{E} \cdot \sigma \qquad (1)$$

so that the stress σ directly derives from the slope of the ($\varepsilon_{\phi\psi}$, $\sin^2\psi$) curve, through the elastic constants of the material.

Figure 2 shows that the relation between $\varepsilon_{\phi\psi}$ and $\sin^2\psi$ is linear; this result

confirms the assumption of a negligible stress gradient in the diffracted volume. For the 0.6 and 1.6 μm thick coatings (A and C), the whole thickness of the coatings has been investigated.

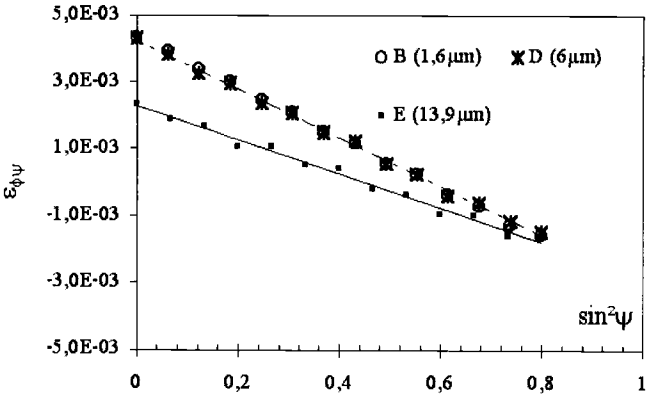

FIG. 2 — *($\varepsilon_{\phi\psi}$, $\sin^2\psi$) plots for different thickness values of PVD W coatings.*

The strain-free lattice parameter has been found to be equal to 0.3168 ± 0.0001 nm. This value is a little bit larger than the bulk tungsten parameter (0.3165 nm), which is in agreement with previous results on PVD tungsten coatings [9,10].

Discussion

There is a definite correlation between the texture evolution and the decrease of the residual stress level. Drobrev [3] has proposed to correlate this texture evolution with the channeling directions of ions in the crystal lattice. In the case of b.c.c lattice, these channeling directions are more and more favorable in the sequence <110>, <100>, <111>. During the impact between an energetic particle and the crystal lattice, the energy dissipation induces either a partial recrystallization due to the "thermal spike" effect or a creation of defects due to consecutive binary collisions. Therefore, under this bombardment, the coating grows in the more favorable channeling directions, that corresponds to a <111> growth direction for b.c.c lattice.

Moreover, according to Thornton and Hoffman [1], the creation of defects enhances the intrinsic residual stress level. As the size of the concerned region increases in the sequence <110>, <100>, <111>, a <111> growth direction induces a lower density of defects and subsequently a decrease of the intrinsic residual stress level. This is in agreement with our experimental observations: when the coating thickness increases, a <111> texture develops and the residual stress level decreases.

Cracking Behavior

The experimental devices and techniques used to characterize the cracking behavior of magnetron tungsten coatings are first described; we then report on the results of an investigation of the cracking mechanisms and kinetics.

Experimental Devices and Techniques

The substrate-coating samples are submitted to tensile tests, at a nominal $3.10^{-4}s^{-1}$

strain rate, in a *Raith*™ tension loading stage that is inserted inside the chamber of a scanning electronic microscope (SEM). Such a device allows a more precise and realistic investigation of the cracking mechanisms under loading, of the cracking kinetics and of the substrate-coating adhesion properties. The tests are instrumented with an extensometer device and coupled with an acoustic emission analysis, using a piezo-electric sensor with a 20kHz filter and a sampling period of 100 ns (Fig. 3), so as to be able to determine the critical strain (±0.01%) for crack initiation and to analyze the cracking kinetics.

The correlation between acoustic emission signals recorded during mechanical tests and crack initiation has first been investigated. Recorded acoustic emission signals during the tensile test give access to the characterization of cracks through the determination of the F ratio (shape factor) of the maximum amplitude (V_c) to the efficient value ($V_{R.M.S}$) [11]. The cracking kinetics analysis was then performed by use of in situ four-point bending tests (Fig. 4). This test was analyzed by use of a local microextensometry technique based on a correlation analysis of high-resolution images (4000 × 4000 pixels) of microgrids with a 2 μm path in the reference and deformed states [12–13]. This treatment gives access to local surface strain fields, as reported in the next.

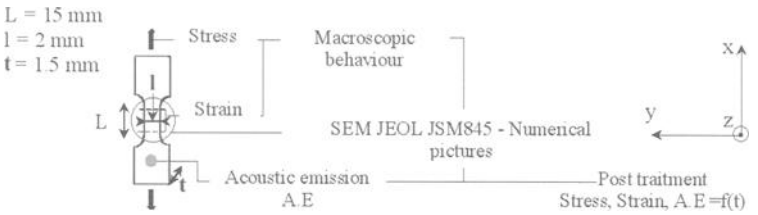

FIG. 3 — *Experimental tensile device used to study the cracking behavior of coatings.*

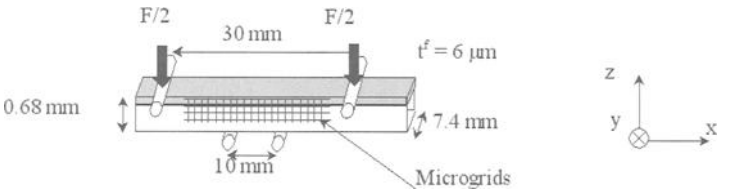

FIG. 4 — *Four-point bending sample and device.*

Damage Analysis

For 6 – 13.9 – 30 μm thick coatings, cracks are straight and perpendicular to the tensile axis (Fig. 5). This mode I cracking behavior of PVD coatings is frequently observed under bending and tensile loading [14-15]. No debonding effect has been observed at the interface but strain localization develops in the substrate at the crack tip (Fig. 6), as revealed during a four-point bending test by the deformation analysis of a microgrid deposited on the crack tip area of a 6 μm thick coating (Fig. 6*a*).

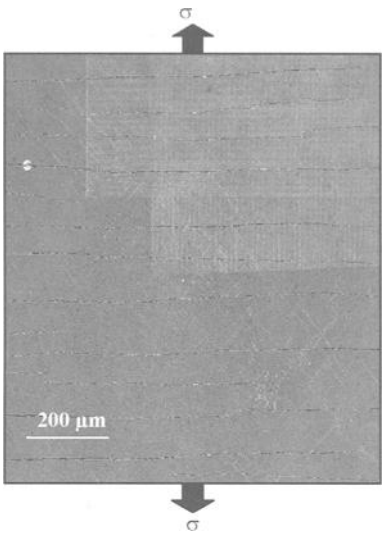

FIG. 5 — *Damage mechanisms observed on the coating surface (SEM images) - t_f = 13.9 µm ε = 5.3 % - Sample E - Mechanisms observed for a thickness larger than 6µm.*

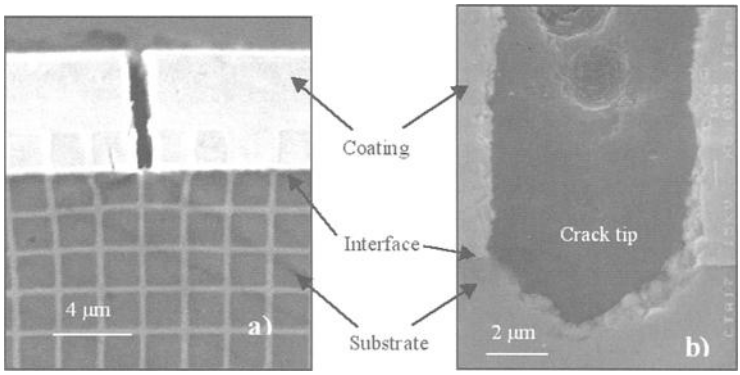

FIG. 6 — *Perpendicular cut of samples. Illustration of the strong adhesion between the coating and the substrate at the crack tip.*

a) t_f = 6 µm (four point bending test)

b) b) t_f =31.1 µm (tensile test) – Sample G

The influence of the substrate stiffness is illustrated in Fig. 7 by the responses of a similar 13.9 µm thick coating deposited either on Substrate 1 or on Substrate 2, where black square points correspond to (σ, ε) values associated with acoustic signals detected during the test. The acoustic signals are characterized by their F ratio, which serves as an acoustic signature of the cracks, which they originate from. As this ratio F is found to be

constant during the tensile test, it can be concluded that one cracking mechanism only is active throughout the test. So we can conclude that no interface debonding occurs. This conclusion is in agreement with direct SEM observations.

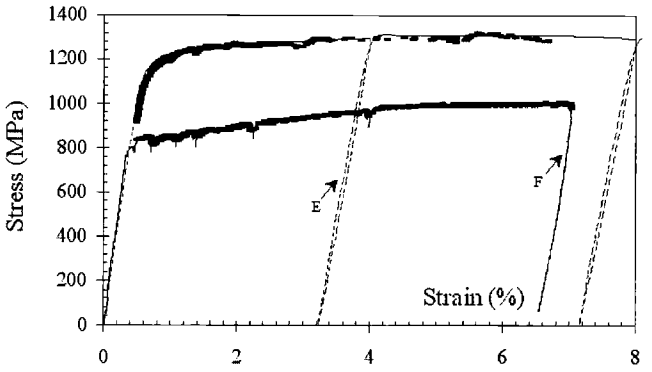

FIG 7 — *Global responses of a W PVD coating sample (E – F - t_f = 13.9 μm) deposited on substrates 1 and 2. Characteristic curve of the W coating/steel sample for a thickness larger than 6μm (--: E - W/Substrate 1, – : F - W/Substrate 2, ■ : (σ, ε) values associated with acoustic emission).*

Cracking Kinetics

Since the overall behavior of our samples is rate-independent, the cracking kinetics can be described by the variation of the crack density D with the prescribed strain $\varepsilon_{s,xx}$, that can be assimilated to the substrate overall strain [16, 17]. This crack density is defined as the ratio of the total number of observed Mode I cracks to the sample length. The crack density is known to be decreasing with the coating thickness [16], but no experimental information is available on the influence of the substrate yield stress σ_y.

The crack density is plotted in Fig. 8 as a function of $\varepsilon_{s,xx}$ for various values of the coating thickness and the two studied substrates. The crack density first rapidly increases with $\varepsilon_{s,xx}$ and then saturates slowly to a limit value D_{sat}. This limit value decreases with the coating thickness (Fig. 8*a*) and increases with the substrate yield stress (Fig. 8*b*) for a given coating (same thickness and residual stress level).

The obtained curves can be fitted with Weibull's law (2); for a given substrate, coefficients A (= 0.92 ± 0.1) and n (= 1.1 ± 0.10) do not depend on the coating thickness t_f. The limit crack density D_{sat} is given in (2) as a function of t_f, with B = 31.8 ± 1.0 and α = 0.35 ± 0.01. The values of $\varepsilon^s_{xx,c}$, the critical strain for cracking initiation, are reported in Table 3.

$$D = D_{sat} \cdot \left(1 - e^{\left(-A\cdot(\varepsilon^s_{xx} - \varepsilon^s_{xx,c})^n\right)}\right) \text{ for } \varepsilon^s_{xx} > \varepsilon^s_{xx,c} \text{ with } D_{sat} = \frac{B}{t_f^{\alpha}} \qquad (2)$$

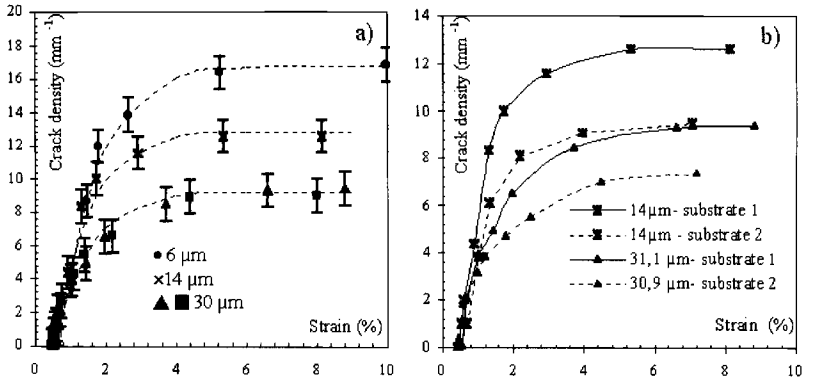

FIG. 8 — *Evolution of the crack density. a) Influence of the thickness (dotted line : fit with Weibull law) (Substrate 1). b) Influence of the substrate yield stress and the coating thickness.*

These effects can be analyzed according to Hu and Evans's approach [18], that assumes an elastic behavior of both the substrate and the coating but considers a plastic yielding zone at the crack tip on a distance *d* from the crack. They obtain the estimate:

$$\sqrt{3} < \frac{\lambda \cdot \sigma_y}{\sigma^f_{xx,c} \cdot t_f} < 2\sqrt{3} \tag{3}$$

where $\sigma^f_{xx,c}$ is the critical cracking stress of the coating, t_f is the coating thickness, σ_y is the substrate yield stress and λ is the minimum spacing between two cracks.

Since the maximum crack density D_{sat} is inversely proportional to λ, it increases with the substrate yield stress and decreases with the coating thickness, as observed experimentally. Moreover, this approach emphasizes the important role of local plasticity at the crack tip in the substrate, which will be stressed next.

Intrinsic Critical Cracking Stress

It can be noticed (Table 3) that the strain associated with cracking initiation $\varepsilon^s_{xx,c}$ depends on the coating thickness, so that it cannot be considered as an intrinsic damage parameter for tungsten coatings. Since it is likely to depend on the residual stress level, the associated stress parameter can be thought to lead to a more relevant cracking criterion.

For a coating-substrate perfectly bound system, subjected to uniaxial tension along the x axis (Fig. 3), with elastic, homogeneous and isotropic materials, an isotropic plane residual stress state and a very thin coating as compared with the substrate (so that stresses can be supposed uniform through the coating thickness with $\sigma_{iz} = 0$), the stress $\sigma^f_{xx,c}$ associated with the critical strain $\varepsilon^s_{xx,c}$ is given by [18]:

$$\sigma^f_{xx,c} \approx E^f \cdot \varepsilon^s_{xx,c} + \sigma^f_r \tag{3}$$

where indices *f* and *s* refer to the coating and the substrate respectively and *r* stands for "residual."

The resulting $\sigma^f_{xx,c}$ values are found to be remarkably close to each other ($\sigma^f_{xx,c}$ = 275 ± 50 MPa) whatever the coating thickness and the substrate yield stress (Table 3): it can be considered as an intrinsic critical cracking stress value, which is in good agreement with previous results derived from a 3-point bending test for PVD tungsten coatings deposited on a steel substrate [16]. Nevertheless, our experimental investigation, performed under homogeneous loading conditions, leads to a more accurate determination of this parameter and a more complete derivation of its intrinsic nature.

TABLE 3 — *Values of residual stresses (σ^f_r), $\varepsilon^s_{xx,c}$ and $\sigma^f_{xx,c}$ for different values of the coating thickness and the substrate yield stress.*

	Substrate σ_y MPa	Coating thickness, μm	Coating σ^f_r, MPa	$\varepsilon_{s,xx,c}$, % (±0.01%)	$\sigma^f_{xx,c}$, Mpa
D	1100	6	-2390	ε_c = 0.66%	310 ± 50
E	1100	13.9	-1670	ε_c = 0,47%	260 ± 50
G	1100	31.1	-1600	ε_c = 0.46%	280 ± 50
H	1100	30.9	-1500	ε_c = 0.43%	265 ± 50
F	800	13.9	-1680	ε_c = 0.47%	250 ± 50
I	800	30.4	-1550	ε_c = 0.44%	260 ± 50

Crack Opening and Strain Distribution

In view of a better understanding of the cracking kinetics that has been characterized experimentally above, the displacement field along the sample length was investigated with more details: the crack opening distribution has been analyzed during tensile and 4-point bending tests and, using the above mentioned microextensometry technique, the local strain field was measured in the substrate near the interface during 4-point bending tests. The main results are the following.

The crack opening, ΔL^f, was measured under tensile loading from numerical images (500 × 500 μm² sample surface) at several strain steps on the 6, 14, and 30 μm thick coatings, by counting the total number of pixels inside cracks on the coating surface. We define the ratio R (4) of crack opening ΔL^f to the total prescribed displacement ΔL:

$$R = \frac{\Delta L^f}{\Delta L} \tag{4}$$

The variation of R is plotted in Fig. 9 as a function of the prescribed axial strain for a 30 μm thick coating. The ratio R rapidly increases and the crack opening is prominent as soon as the overall strain is larger than 1%. Similar observations have been made for the 6 and 14 μm thick coatings. Note that the R variation with strain is analogous with that of the crack density (Fig. 8): this suggests crack opening, which induces some unloading of uncracked coating parts, governs most of the cracking kinetics.

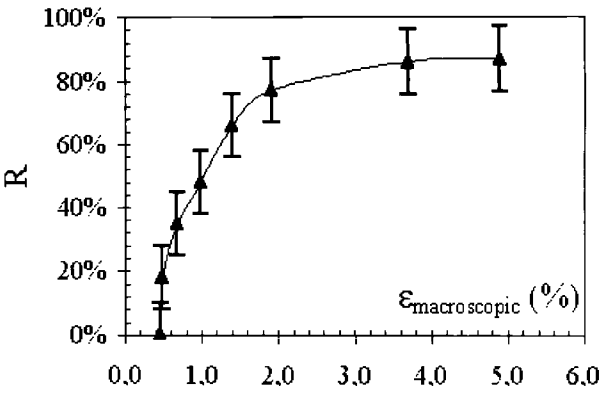

FIG. 9 — *Evolution of the ratio R versus macroscopic strain ($R = \Delta L^f/\Delta L$ - ▲) for a 30 μm thick coating.*

To validate this conclusion, crack opening was analyzed at the coating-substrate interface of a 6 μm thick coated sample during a 4-point bending test performed inside the SEM chamber; the mechanical response was investigated both at the macroscopic and the local scales on a 260 × 220 μm² sample area. At different strain steps, the strain heterogeneity of the substrate and the average strain on a 260 μm length were characterized close to the interface. Moreover, the crack density and the average crack opening were estimated at the interface. These values were compared with those obtained during a tensile test for an identical 6 μm thick coating (Table 4). It can be checked that the correlation between the average strain values and the average crack opening displacements for a given crack density is quite good for these two tests.

TABLE 4 — *Comparison, for a given crack density, of average strain and average crack opening between tensile test and bending test performed on a 6 μm thick coating.*

	Average Cracks Opening, μm		Average Strain, %	
Crack Density, mm^{-1} ($\pm$ 0.5 mm^{-1})	Tensile Test ($\pm$ 0.3 μm)	Four Points Bending Test ($\pm$ 0.2μm)	Tensile Test ($\pm$ 0.01 %)	Four Points Bending Test ($\pm$ 0.3 %)
4.6	0.7	0.5	1.0	/
9.4	0.8	0.6	1.3	1.3
11.2	0.9	1.0	1.7	1.9
12.6	1.2	1.1	2.4	2.2
15.6	2.0	1.9	3.7	3.7

For a crack density equal to 15.6 mm^{-1}, the ratio *R* is equal to 80%; actually, this ratio sizes to 97% if the cumulative crack opening displacement is referred to the total displacement as measured after the first crack formation, instead of the initial total displacement. This better stress emphasizes the rapidly increasing influence of crack

opening on the deceleration of the cracking kinetics. Moreover, we could infer from what precedes that the evolution of the crack density, associated with the stress redistribution in the uncracked coating blocks, is slower and harder when the block length L^f is shorter and their thickness t_f is larger (so that blocks are more difficult to be stressed enough for further cracking). As a matter of fact, this conclusion is corroborated and completed by Mezin's analysis [19] according to which, in a coating - substrate sample under tensile loading, the longitudinal stress σ^f_{xx} level in the coating uncracked parts is decreasing with the ratio L^f/t_f (Fig. 10).

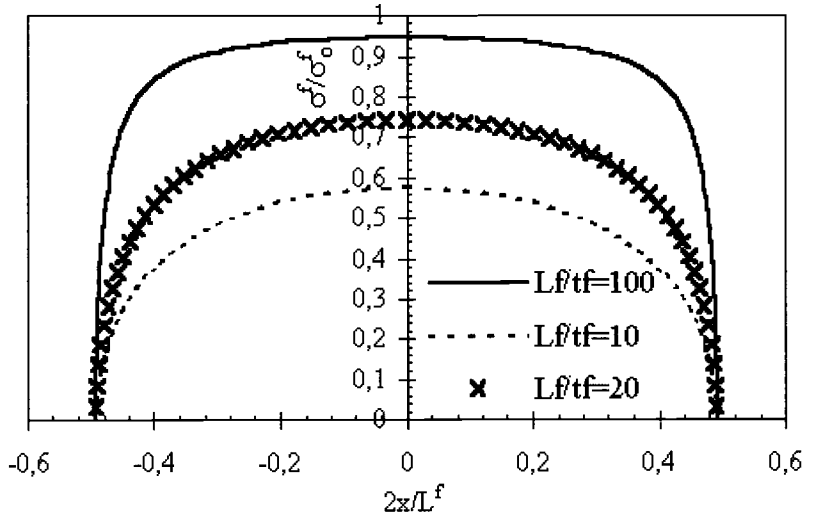

FIG. 10 — *Evolution of the normalized stress vs the ratio L^f / t_f - X is the distance from the uncracked coating portion center [19].*

Finally, the microextensometry technique [12–13] has been used to evaluate the surface distribution of the three strain components in the xy plane in order to obtain a qualitative information on the strain localization modes. The effect of a crack formation in the coating is illustrated in Fig. 11 that reports on the distribution of the longitudinal strain ε_{xx}. Thus, the development of cracks and the increase of the macroscopic strain induce a marked heterogeneity of the strain field in the substrate close to the interface where most of the strain is confined inside deformation bands.

The resultant strain maps give rich qualitative information on the strain localization modes. This development of strain concentration inside deformation bands is responsible for the decrease of the cracking kinetics. While the macroscopic strain increases, the strain level under the crack tips increases whereas the strain level under the uncracked coating parts is much lower, and that slows down the cracking kinetics. This is the reason why the minimum measured distance between cracks is larger than theoretical.

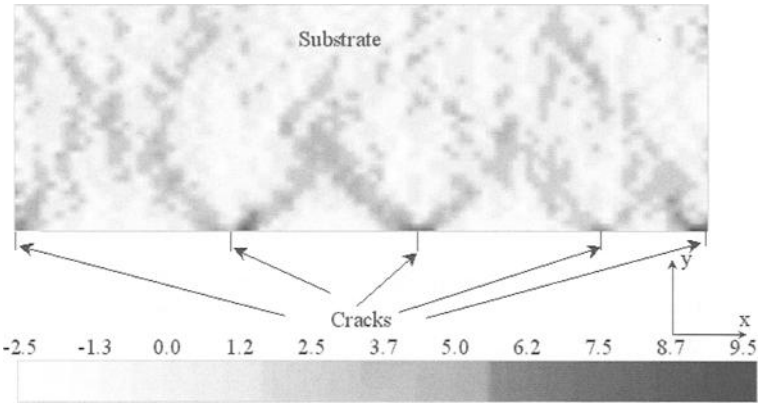

Fig. 11 — *Strain (ε_{xx}) distribution below the interface for a crack density equal to 12.6 cracks.mm^{-1}.*

Conclusion

Tensile tests coupled with an acoustic emission analysis and a microextensometry technique were used to investigate the cracking behavior of W PVD coatings deposited on steel substrates. Taking account of the residual stress field in the coating, as it results from the processing conditions, an intrinsic critical cracking stress of the order of 275 ± 50 MPa, can be defined. This value was shown to be independent of the coating thickness and the substrate yield stress.

Moreover, the study of the evolution of the crack density with the applied strain shows that the saturation level of the crack density is decreasing when the coating thickness increases and the substrate yield stress decreases. This effect was explained qualitatively through a shear lag-type analysis, including plastic yielding of the substrate at the crack tip, proposed by Hu and Evans [18]. The importance of strain localization phenomena at the crack tips was emphasized through the measurement of the crack opening displacements under loading during 4-point bending tests associated with the determination of local strain fields in the substrate close to the interface. Consequently, it is harder and harder to deform the uncracked coating parts and to provoke further cracking: the crack kinetics is slowing down, that is, as observed experimentally, more pronounced when the coating thickness increases and the substrate yield stress decreases.

Numerical simulations are now developing in order to obtain a quantitative agreement of the cracking kinetics with the above reported experimental measurements.

Acknowledgments

The authors wish to thank M. Le Cornec (DCE/CTA) for texture and residual stresses determination, M. Terrien (LMS) for his assistance to the acoustic emission analysis and D. Caldemaison (LMS), M. Bornert (LMS), and P. Doumalin (LMS) for microgrids deposition and microextensometry developments. DGA is gratefully acknowledged for financial support.

References

[1] Thornton, J. A. and Hoffman, D. W. "Stress Related Effects in Thin Films," *Thin Solid Films*, Vol. 171, 1989, pp. 5–31.
[2] Patureau, C., Farges, G., Sainte Catherine, M. C., and Machet, J., "Influence of Particle Energies on the Properties of Magnetron Sputtered Tungsten Films," *Surface & Coatings Technology*, Vol. 98, 1998, pp. 1257–1261.
[3] Dobrev, D., "Ion-Beam-Induced Texture Formation In Vacuum Condensed Thin Metal Films," *Thin Solid Films*, Vol. 92, 1982, pp. 41–53.
[4] Gergaud, P., Ph.D. Thesis, Ecole Nationale Supérieure des Arts et Métiers, France, 1992.
[5] Paturaud, C., Ph.D. Thesis, Université de Limoges, France, 1997.
[6] Maeder, G., "Mesure de Contraintes Résiduelles par Diffraction X. Applications," *Revue Françaize de Mécanique*, 1982, Vol. 82, pp. 57–70.
[7] Smithells Materials Reference Book, Sixth Edition, Eric A. Brandes, Ed., 1983.
[8] Zaouali, M., Ph.D. Thesis, Ecole Nationale Supérieure des Arts et Métiers, France, 1990.
[9] Vink, T. J., Walrave, W., Daams, J. L. C., Dirks, A.G., Somers, M. A. J., and Van der Aker, K. J. A., "Stress, Strain, And Microstructure in Thin Tungsten Films Deposited By DC Magnetron Sputtering," *Journal of Applied Physics*, Vol. 74, No. 2, 1993, pp. 988–995.
[10] Renault, P. O., Badawi, K. F., Bimbault, L., Goudeau, Ph., Elkhaïm, E., and Lauriat, J. P., "Residual Stresses And Microstructure In Tungsten Thin Films Analyzed By X-Ray Diffraction-Evolution Under Ion Irradiation," *Applied Physics Letters*, Vol. 73, No. 14, 1998, pp. 1952–1954.
[11] Crépin, J., Bretheau, T., Caldemaison, D., and Ferrer, F. "Plastic Deformation Mechanisms of β Treated Zirconium," *Acta Materials*, Vol. 48, 2000, pp. 505–516.
[12] Allais, L., Bornert, M., Bretheau, M. and Caldemaison, D., "Experimental Characterization of the Local Strain Field in a Heterogeneous Elastoplastic Material," *Acta Metallugica Materials*, Vol. 42, 1994, pp. 3865–3880.
[13] Doumalin, P., Ph.D. Thesis, Ecole Polytechnique, France, 2000.
[14] Su, Y. L., Yao, S. H., Wei, C. S., and Wu, C. T., "Tension and Fatigue Behavior of a PVD TiN-coated Material," *Thin Solid Film*s, Vol. 315, 1998, pp. 153–158.
[15] Scafidi, P. and Ignat, M., "Cracking and Loss of Adhesion of Si3N4 and SiO2:P Films Deposited on Al Substrates," *Journal of Adhesion Science and Technology*, Vol. 12, No.11, 1998, pp. 1219–1242.
[16] Harry, E., Rouzaud, A., Ignat, M., and Juliet, P., "Mechanical Properties of W and WC Thin Films: Young's Modulus, Fracture Toughness and Adhesion," *Thin Solid Films*, Vol. 332, 1998, pp. 195–201.
[17] Wiklund, U., Bromark, M., Larson, M., Hedenqvist, P., and Hogmark, S., "Cracking Resistance of Thin Hard Coatings Estimated by Four-Point Bending," *Surface and Coatings Technology*, Vol. 91, 1997, pp. 57–63.
[18] Hu, M. S. and Evans, A.G. "The Cracking and Decohesion of the Thin Films on Ductile Substrates," *Acta Metallurgica*, Vol. 37, No. 3, 1989, pp. 917–925.
[19] Mezin, A., Chambard, J.-P., Lepage, J., and Nivoit, M., "Relaxation de contrainte dans un dépôt fissuré," *Thin Solid Films*, Vol. 185, 1990, pp. 57–69.

M. G. Beghi,[1] *C. E. Bottani,*[1] *and R. Pastorelli*[1]

High Accuracy Measurement of Elastic Constants of Thin Films by Surface Brillouin Scattering

REFERENCE: Beghi, M. G., Bottani, C. E., and Pastorelli, R., **"High Accuracy Measurement of Elastic Constants of Thin Films by Surface Brillouin Scattering,"** *Mechanical Properties of Structural Films, ASTM STP 1413*, C. Muhlstein and S. B. Brown, Eds., American Society for Testing and Materials, West Conshohocken, PA, Online, Available: www.astm.org/STP/1413/1413_08, 15 May 2001.

ABSTRACT: Elastic properties of thin supported films can be derived from the dispersion relations of surface acoustic waves (SAWs) of layered structures. SAW velocities can be measured by surface Brillouin scattering (SBS), i.e., light scattering by thermally excited SAWs. Since SAW velocities can be computed as functions of the elastic properties of both the film and the substrate, if film thickness and density are independently measured the elastic constants can be obtained fitting the computed velocities to the measured ones. Our data analysis technique is discussed. Accuracy of the measured velocities is crucial: the SBS measurement technique is analyzed, giving quantitative estimates of errors and uncertainties, and discussing procedures to reduce them. Some examples are considered in detail, showing that SBS measurements allow the determination of film elastic constants on films of thickness down to tens of nanometers, with precision ranging from reasonable to very good.

KEYWORDS: Brillouin scattering, acoustic waves, surface waves, thin films, elastic constants

Introduction

When the measurement of the elastic properties of a material or a structure is of interest, the most appropriate experiments are those that involve only elastic deformations. Oscillations and acoustic waves fulfill this requirement well, meaning that the measurement of the acoustic properties provides a clean way to measure the elastic properties. Generally, in an acoustic excitation, the most easily measured quantity is frequency, or a frequency spectrum. The spectrum of the acoustic excitations of a structure is a function of its stiffness and its inertia, both depending also on the structure geometry. It is often not possible to derive both the stiffness and inertial properties from the measured spectra. However, if the inertial properties are well characterized by independent measurements, i.e., if the spatial distribution of masses is known, the measured spectrum of acoustic excitations can be exploited to derive the stiffness properties. Periodic oscillations and waves involve only reversible strains: knowledge of the acoustic behavior provides accurate information on the elastic behavior, but no

[1]INFM and Nuclear Engineering Department, Politecnico di Milano, Via Ponzio 34/3, I-20133 Milano, Italy, marco.beghi@polimi.it.

information on the structure behavior under high stresses.

These general considerations are well suited to the measurement of the elastic properties of layered structures. For a homogeneous layer, geometry is defined by the layer thickness, inertial properties are characterized by mass density, and stiffness properties are characterized by the tensor of the elastic constants. A layered structure is characterized by the ensemble of the properties of the individual layers and by the conditions at the interfaces. Throughout this work, perfect adhesion is assumed, meaning continuity of both stresses and strains across each interface. An external surface imposes instead a null stress condition on the surface itself.

Films support acoustic waves; sufficiently thick films support bulk waves, and both thick and thin films generally support surface acoustic waves (SAWs). Spectra of acoustic waves can be measured, either exciting the waves by piezoelectric excitation in quantitative acoustic microscopy [1-3] or by laser pulses in laser acoustic methods [4-6], or relying on the thermally excited waves, in Brillouin scattering experiments [7-10]. Interdigital transducers can also be exploited [11,12], but they require a piezoelectric layer and the transducer built on it. In acoustic microscopy a piezoelectric transducer is coupled, through an acoustic lens and a contact fluid, to the specimen surface: the transducer excites and detects the waves. In laser acoustic methods, waves are excited by laser pulses and the displacement of the specimen surface is sensed by optical means, typically by an interferometric setup. Brillouin scattering is the scattering of an electromagnetic wave by an acoustic wave. In a Brillouin scattering experiment a monochromatic laser beam is directed onto the specimen, and the scattered light is collected and analyzed: its spectrum reproduces the spectrum of the acoustic waves. Brillouin scattering by SAWs is called surface Brillouin scattering (SBS) [9].

Since spontaneous Brillouin scattering relies on thermally excited acoustic waves, the waves it detects have an amplitude much smaller than those waves excited in the other techniques, implying that: Brillouin scattering measurements are therefore more time consuming. However, the probed wavelengths can be significantly smaller than those probed by other techniques, giving Brillouin scattering a peculiar spatial resolution, particularly relevant in the case of thin films. In this work, the general features of SAWs and of Brillouin spectroscopy, which are valid for either single-layered or multi-layered and either free-standing or supported films, are recalled first. Attention is then focused on single-supported layers: the data analysis methods to derive the elastic constants are outlined, and some examples are finally presented.

Acoustic Waves and Brillouin Scattering

Solids support bulk acoustic waves; a plane wave in a homogeneous medium has velocity v, wave vector $\mathbf{q}$, and circular frequency ω: $\omega = vq$. Velocity is independent from wavelength, i.e., the waves are nondispersive. In isotropic media, waves are either purely longitudinal or purely transverse, the velocities being respectively $\sqrt{C_{11}/\rho}$ and $\sqrt{C_{44}/\rho}$, where ρ is mass density and the C_{ij} are (in matrix notation) the elements of the tensor of the elastic constants. In anisotropic media (crystals), waves are not necessarily purely longitudinal or purely transversal, and their velocity depends on the direction of $\mathbf{q}$ (the propagation direction), but still does not depend on the modulus q (the wavelength).

Bulk acoustic waves can interact with electromagnetic waves by the elasto-optic

(also called acousto-optic) effect: the variation of the electric polarizability of a medium, that is, of its dielectric constant (dielectric tensor), induced by a mechanical strain. The strain field of an acoustic wave induces a periodic modulation of the dielectric constant, analogous to a diffraction grating traveling at velocity v. An electromagnetic wave can interact with this grating when wavelengths are properly matched [10]. In the interaction, conservation of energy and momentum take the form

$$\Omega_s = \Omega_i \pm \omega \tag{1}$$

$$\mathbf{k}_s = \mathbf{k}_i \pm \mathbf{q} \tag{2}$$

where $\mathbf{k}_i$ and Ω_i are the wave vector and circular frequency of the incident electromagnetic wave, and $\mathbf{k}_s$ and Ω_s are those of the scattered wave. In Eqs 1 and 2, the + and – signs correspond respectively to anti-Stokes and Stokes events. Obviously, the electromagnetic wave can interact with the bulk acoustic wave only if the medium is sufficiently transparent and if the elasto-optic coupling coefficients are nonvanishing. Note, however, that a material-like silicon, in which the penetration depth of visible light is of the order of 1 μm, is transparent enough: Brillouin scattering from its bulk waves is well measurable, also because its elasto-optic coefficients are relatively high.

A surface can support SAWs, which travel along the surface and have a strain field confined in the neighborhood of the surface itself. A generic SAW has velocity v_{SAW} and is characterized by a wave vector parallel to the surface $\mathbf{q}_{\|}$, with $\omega = v_{SAW}\, q_{\|}$. The spectrum of SAWs is discussed elsewhere [8,13,14]. It is sufficient to recall here that at the external surface of a bare substrate the Rayleigh wave (RW) generally exists; it is the only SAW in this case, its velocity v_R being independent from wavelength and determined mainly, but not exclusively, by C_{44}. Its strain field decays with depth, penetration being of the order of $2\pi/q_{\|}$. The RW has a mixed longitudinal and transverse character, the relative weight of the two components varying with depth [14].

When a film of thickness h is deposited on the substrate, the spectrum of SAWs is modified. A characteristic length h is now present: SAW velocities are no longer independent from wavelength and are a function of $q_{\|}h$ [15]. In general, a modified Rayleigh wave (MRW), of velocity v_{MRW}, still exists. If the film is acoustically slower than the substrate, it tends to act as a wave guide and can support guided waves: such waves, called Sezawa waves (SW), are reminiscent of the Lamb modes of a free-standing slab. The number of SW modes that can be supported depends on the value of $q_{\|}h$ (if the film is too thin it does not support guided waves) and on the difference between the properties of the film and the substrate. The velocity of SWs is always higher than v_{MRW} and is a decreasing function of of $q_{\|}h$: when $q_{\|}$ increases the strain field is more confined within the acoustically slow film and the velocity decreases [15]. In isotropic or highly symmetric films, the above modes have a transversal component perpendicular to the surface. In layered media the Love waves also exist, polarized in the transversal direction parallel to the surface. It must also be remembered that when films are sufficiently thick ($q_{\|}h>>1$) they also support bulk waves, relatively unaffected by the finite thickness. In the case of multilayer structures the SAWs can have more complicated behaviors, the slowest layers always tending to act as wave guides, as in the case of a single buried slow film [16].

SAWs can interact with electromagnetic waves by the elasto-optic effect, if the

structure is transparent enough. They also interact by the ripple effect: the periodic corrugation of the external surface due to the displacement component normal to the surface [17]. Also by this mechanism the SAW creates a diffraction grating traveling at v_{SAW}. Due to the limited depth of the strain field, i.e., the limited scattering volume available for the elasto-optic effect, in the case of SAWs the ripple mechanism is typically dominant [18]. It is the only one in the case of opaque materials like most metals, and it is absent only for SAWs or pseudo SAWs which have, at the external surface, a prevailing longitudinal polarization. This happens for some of the Sezawa waves, which, then, in the case of metals, remain nondetectable [19]. It can be noted that in acoustic microscopy and in laser acoustic methods SAW detection relies exclusively on the ripple effect, meaning that such longitudinally polarized waves are never observable. Similarly, Love waves, polarized in the transverse direction parallel to the surface, can be detected only by SBS [16,20].

In the scattering of electromagnetic waves by SAWs, energy is always conserved (Eq 1), while, due to the lack of translational symmetry in the normal direction, only the parallel wave vector is conserved, and Eq 2 becomes [9]

$$\mathbf{q}_{\parallel} = \pm(\mathbf{k}_s - \mathbf{k}_i)_{\parallel} \tag{3}$$

Brillouin Scattering Measurements

A Brillouin scattering measurement is performed illuminating the specimen by a laser beam of given $\mathbf{k}_i$, collecting the scattered light at a given $\mathbf{k}_s$, and analyzing its spectrum. The most intense feature is light elastically scattered at $\Omega_i = \Omega_s$, and scattering by any acoustic wave introduces a doublet at frequencies given by Eq 1. These doublets have a small intensity, because the Brillouin scattering cross sections are typically small. The frequency shifts

$$\Omega_s - \Omega_i = \pm\omega \tag{4}$$

give the circular frequency of the acoustic wave; Eq 2 or Eq 3 give its wave vector: velocity is immediately obtained. In the scattering event, the wide difference between the acoustic velocity v and the electromagnetic wave velocity c/n ($v/(c/n) \approx 10^{-4} \div 10^{-5}$) must be taken into account ($v = \omega/q$, $c/n = \Omega_i/k_i = \Omega_s/k_s$, c is the velocity of light in vacuum, n is the refractive index). Equations 1 and 2 imply that $|k_s - k_i|/k_i \leq 2v/(c/n)$, the maximum difference being achieved by the backscattering configuration ($\mathbf{k}_s = -\mathbf{k}_i$). This means that the relative difference between k_s and k_i can be neglected: $k_s \approx k_i = (2\pi/\lambda_0)n$, where λ_0 is the laser wavelength in vacuum. The moduli k_s and k_i being determined by the laser source, the scattering configuration and the wave vector $\mathbf{q}$ are completely determined by the scattering geometry.

The laser beam is focused on the specimen surface at an incidence angle θ_i (the angle between $\mathbf{k}_i$ and the normal to the specimen surface) and light is collected at a scattering angle θ_s. The backscattering geometry ($|\theta_s| = |\theta_i|$) is typically adopted because it maximizes q. In backscattering, interaction with bulk waves occurs at

$$q = 2(2\pi/\lambda_0)n \tag{5}$$

(see Eq 2) while interaction with SAWs occurs at

$$q_{\parallel} = 2(2\pi/\lambda_0)\sin\theta_i \tag{6}$$

(see Eq 3 and Fig. 1). It is worth noting that since upon refraction at specimen surface the electromagnetic wave vector component $k_{\|}$ is preserved, SAWs are probed at a wave vector that is determined by the scattering geometry alone and is independent from the refractive index (Eq 6). This is a specific feature of SBS: the probed wave vector (and therefore the product $q_{\|}h$ and the spatial resolution) is completely predetermined by the experimental setup. In acoustic microscopy, the frequency is instead predetermined [2], and the value of $q_{\|}h$ depends on the specimen properties; similar considerations also apply to the laser acoustic techniques.

A typical experimental setup for a SBS measurement in backscattering is shown in Fig. 1. The laser beam is directed onto the specimen by a small mirror and focused onto the specimen surface by a lens, called here the front lens. In backscattering the same lens collects the scattered light, while in other configurations the collection optics are separate. Scattered light coming from the focus of the front lens is collected and emerges from the lens as a parallel beam. A slit can be inserted to limit the collection solid angle, as discussed below. The parallel beam is focused, for spatial filtering, on the entrance pinhole of the spectrometer and transformed back into a parallel beam to be analyzed by the Fabry-Perot interferometer (FP) [21], the heart of the spectrometer.

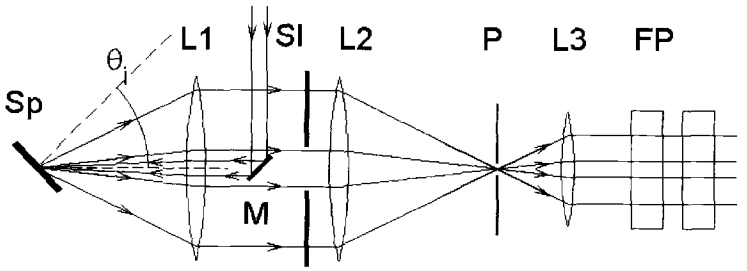

FIG. 1—*Experimental setup for SBS measurements in backscattering: M: mirror; L1: front lens; Sp: specimen; Sl: slit (when present); L2: focusing lens; P: entrance pinhole of the spectrometer; L3 lens to reconvert to a parallel beam; FP: Fabry-Perot interferometer. A single FP is shown, instead of the actual tandem multipass FP.*

Measurement of the frequency shifts (Eq 4) poses stringent requisites to the spectrometer. Equations 5 and 6 show that in backscattering $q_{\|} < q$, and both q and $q_{\|}$ are of the same order of $(2\pi/\lambda_0)$, meaning that $\omega/\Omega_i \sim v/c \sim 10^{-4} \div 10^{-5}$, the doublets to be observed have very small relative frequency shifts from the elastic peak at Ω_i, which is orders of magnitude more intense. Out of backscattering, $q_{\|}$, q, and the frequency shifts are even smaller. Diffraction gratings and conventional FP spectrometers can at most resolve the doublets scattered by bulk waves. Light scattered by SAWs became observable with the introduction of the tandem multipass FP interferometer [21,22]. The FP is operated varying its mirror distance: it thus acts as a bandpass filter of very narrow bandwidth which scans a given frequency shift interval [21]. Scan is performed by discrete steps: the spectrum is sampled and discretized. Light is detected by a photomultiplier, operated in the single photon counting mode due to the low intensity of light scattered by acoustic waves.

Figure 2 presents a spectrum measured in backscattering on a crystalline silicon

specimen, for $q\|$ directed along the [100] crystallographic direction on a (001) crystalline face. The spectrum is drawn on a logarithmic scale to appreciate all the features, including the intense elastic peak at null frequency shift (a small interval around $\omega = 0$ has been attenuated to avoid damaging the photomultiplier) and the two symmetric double peaks at the extremes of the spectral range: these are instrumental artifacts [21], useful for frequency calibration. The broad central feature, extending between approximately ±100 GHz, is due to two-phonons Raman scattering [7], and three doublets are noticeable due to scattering from the longitudinal bulk wave, the transverse bulk wave and the Rayleigh wave. Figure 3 shows the central part of the spectrum, measured, with a smaller frequency range and a better resolution, on an alloyed gold film deposited on silicon (see the section on experimental results). Gold being acoustically much slower than silicon, the film, beside the RW, confines 6 Sezawa waves; the third, fourth, and sixth are not detected because at the surface they are longitudinally polarized and do not induce a surface ripple [19].

A dispersion relation is measured repeating the SBS measurement at a set of incidence angles $\theta_i^{(j)}$, i.e., a set of wave vectors $q_\|^{(j)}$. The measured circular frequencies $\omega_m^{(j)}$ give the measured velocities $v_m^{(j)} = \omega_m^{(j)}/q_\|^{(j)}$. The dispersion relations for the waves of Fig. 3 are shown in Fig. 5.

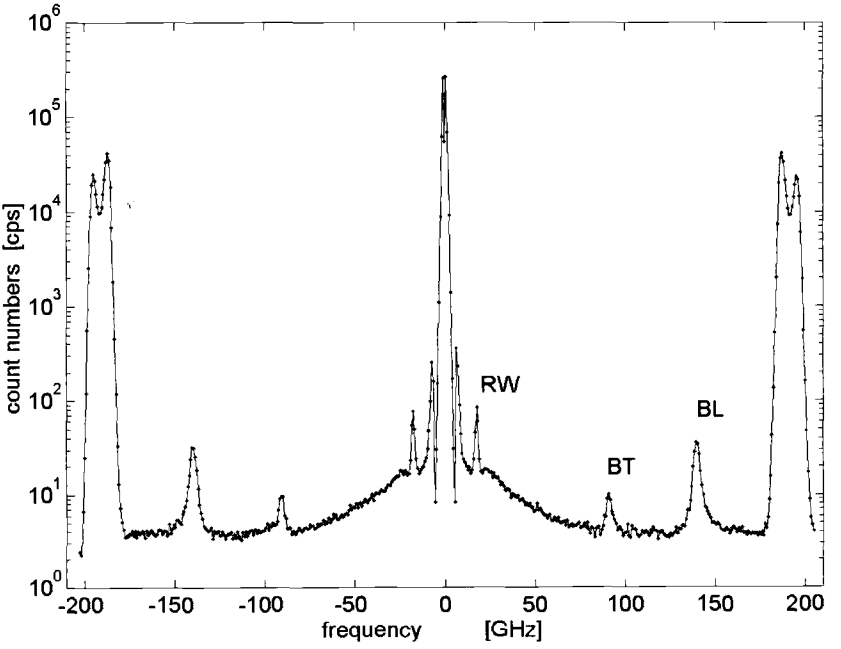

FIG. 2—*Brillouin spectrum for the (001) face of a crystalline silicon specimen, for propagation along [100]. Ar ion laser (λ_0 = 514.5 nm), 70° incidence angle. BL: bulk longitudinal wave; BT: bulk transverse wave; RW: Rayleigh wave.*

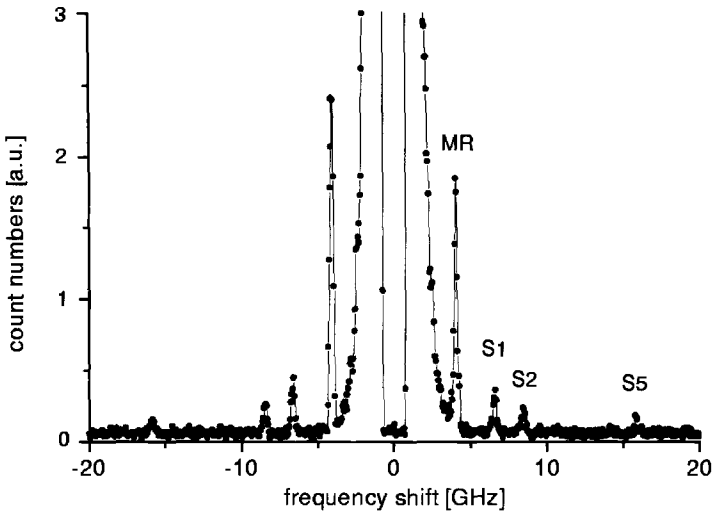

FIG. 3—*Surface Brillouin spectrum for an alloyed gold film on silicon (001) (see Fig. 5); propagation along [100]. Ar ion laser (λ_0 = 514.5 nm), 50° incidence angle. MR: modified Rayleigh wave, S1, S2, S5: Sezawa waves.*

Data Analysis

The velocities of bulk acoustic waves measured by Brillouin scattering experiments have been extensively exploited to measure the elastic constants of crystals [23-28]; this determination requires the value of the refractive index of the crystal. The case of films is conceptually analogous, but experimentally and computationally more involved. The value of $q_{\|}h$ discriminates among two main cases. When $q_{\|}h >> 1$, the film, either free standing or supported, behaves essentially as a semi-infinite solid: it is thick enough to support bulk waves, and the displacement field of its SAWs does not reach the back surface. The SAWs are thus not sensitive to the conditions (free surface or adhesion to a substrate) at the back surface, and the data analysis methods for bulk solids are fully applicable. When instead $q_{\|}h$ is not much greater than 1, free standing and supported films behave differently. In the case of free-standing films, the acoustic modes of a free-standing slab must be considered [29-31]; this case is not further analyzed here.

The rest of this work focuses instead on the case of a single supported layer. The substrate and film materials are characterized by their respective mass density and tensor of the elastic constants, $\rho^{(s)}$, $C_{ij}^{(s)}$ and $\rho^{(f)}$, $C_{ij}^{(f)}$; film thickness is h and perfect adhesion is assumed. Methods are available [15,18,32,33] to compute the velocity of any specified SAW, obtaining the computed velocities $v_c(\rho^{(s)}, C_{ij}^{(s)}, \rho^{(f)}, C_{ij}^{(f)}; hq_{\|})$ (direct problem). Velocities can be measured at a set of incidence angles $\theta_i^{(j)}$ (typically four to six angles), corresponding to a set of $q_{\|}^{(j)}$ values. Once the velocities $v_m^{(j)}$ are available with their uncertainties, it is possible to face the inverse problem: derivation of physical properties, by fitting the computed velocities to the measured ones. It is not possible to derive all the above quantities, but if some of them are independently known, the remaining ones can be obtained by the fitting procedure [19,34-40].

In particular the substrate properties are assumed to be known; film thickness can be measured by, e.g., X-ray reflectivity measurements or transmission electron microscopy, and film mass density can be measured by X-ray reflectivity and/or diffractometry. Only the film elastic constants $C_{ij}^{(f)}$ remain unknown and can be obtained from the measured acoustic velocities. If the film is elastically isotropic, as it is the case for nanocrystalline and amorphous films, all the elastic constants are determined by only two independent quantities, typically taken among C_{11}, C_{44}, Young's modulus E, shear modulus G, bulk modulus B, and Poisson's ratio ν. If the film is crystalline, further independent quantities are required to fully specify its elastic constants: a third quantity in the case of cubic symmetry films, and other ones in the case of lower symmetry films. The elastic constants must satisfy thermodynamic stability limits corresponding to the physical requirement that the elastic strain energy be definite positive.

The rest of this work focuses on the simplest case, the isotropic film. The extension to crystalline film only implies a higher number of independent variables. Two quantities must be selected, among those mentioned above, as the independent ones, which define all the tensor $C_{ij}^{(f)}$ and consequently the velocities v_c. To this purpose the above quantities are not completely equivalent, because the sensitivity of computed velocities to all of them, which can be evaluated by derivatives like $\partial v_c/\partial C_{11}^{(f)}$ or $\partial v_c/\partial \nu^{(f)}$, are not the same. It is obviously preferable to select the couple to which the v_c are more sensitive and, in the case of the MRW, this turns out to be (E,G) couple [41]. This reflects the fact that in the MRW the strains are closer to shear strains than to hydrostatic strains. The (E,G) couple is thus selected, and the velocities are accordingly computed as $v_c^{(j)}(E,G,q_{\parallel}^{(j)})$, the superscripts $^{(f)}$ being understood. All the other quantities are known, and the wavevectors $q_{\parallel}^{(j)}$ correspond to the incidence angles $\theta_i^{(j)}$ at which the measurements are taken. It must be remembered that not all the (E,G) plane is physically meaningful: since $\nu = E/(2G) - 1$, the conditions $\nu \leq 0.5$ (thermodynamic stability limit) and $\nu \geq 0$ (satisfied by practically all known materials) imply that $E/3 \leq G \leq E/2$. When approaching and crossing the stability limit $G = E/3$ the bulk modulus B diverges, while the velocities v_c remain continuous functions.

It can be shown [42] that, taking into account the statistical sources of uncertainty, the measured velocities $v_m^{(j)}$ can be seen as samplings from normal distributions, and that the variances $\sigma_m^{(j)}$ of these distributions can be evaluated. Consequently, the appropriate estimation of the most probable values of the (E,G) couple is obtained by the generalized least squares (GLS) estimator [37,38,42]

$$GLS(E,G) = \sum_j \left(\frac{v_c^{(j)}(E,G) - v_m^{(j)}}{\sigma_m^{(j)}} \right)^2 . \qquad (7)$$

The most probable value of the (E,G) couple is the couple $(\overline{E},\overline{G})$ that minimizes $GLS(E,G)$. An approximation to this value can be found computing the GLS function on a sufficiently fine mesh. This evaluation can be computationally expensive, because the computed velocities $v_c^{(j)}$ are not available in closed form, and are in turn the outcome of numerical computations. Once the $(\overline{E},\overline{G})$ couple is found, the normalized GLS estimator $GLS(E,G)/GLS(\overline{E},\overline{G})$ can be computed: its iso-level curves give, via the F distribution (the Fisher function), the confidence regions in the (E,G) plane, at any given confidence

level. The outcome of the derivation are thus a most probable value and confidence regions; in view of the experimental uncertainties in the measurements of the velocities, the film thickness and mass density, the confidence regions are more appropriately taken as the final result [42]. A few examples are discussed in the following.

Accuracy of SAW Velocity Measurements

The accuracy of the measured velocities is crucial for the accuracy of the obtained elastic constants and has to be assessed. Velocities are obtained as $v_m^{(j)} = \omega/q_{\|}^{(j)}$, and both ω and $q_{\|}^{(j)}$ are subjected to errors. The wave vector $q_{\|}$ is subjected to the deterministic consequences of geometrical imperfections of the experimental setup, and ω is affected by the uncertainties connected to the spectrum measurement. The scattering geometry is presented in Figs. 1 and 4. In Fig. 4 the x_3 direction is normal to the specimen surface, and the x_1 and x_2 directions are taken in such a way that $\mathbf{k}_i$ belongs to the (x_1, x_3) plane.

Firstly, the incidence angle θi is known with a finite precision. The specimen is positioned by a rotator, and rotators are available which have accuracies better than 0.1 mrad. However, this is only the accuracy of rotations from a given reference position. The most practical reference is normal incidence, at which the incident and reflected beams overlap. Perfect overlap is practically found to a precision of about $0.2° \approx 3.5$ mrad; the error of θi is essentially this error in the identification of the reference position. An error $\delta\theta i$ implies an error in $q\|$: $\delta q\| = (\partial q\|/\partial\theta i)\ \delta\theta i = \delta\theta i/\tan\theta i$ (see Eq 6), which is more severe at small incidence angles. This error can be reduced by a setup which includes a longer path for the incident laser beam, resulting in a better identification of the reference position [43].

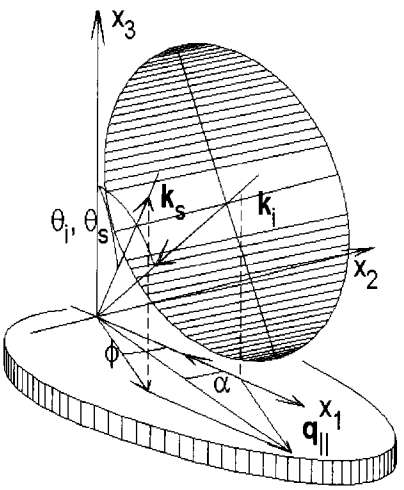

FIG. 4—*Scattering geometry: $\mathbf{k}_i$: incident wave vector at polar angles $(\theta_i, 0)$; $\mathbf{k}_s$: scattered wave vector, at polar angles (θ_s, ϕ); $\mathbf{q}_{\|}$: SAW wave vector, at angle α from x_1.*

Secondly, as it is evident from Figs. 1 and 4, $\mathbf{k}_i$ is defined with good precision by the incident laser beam, while the front lens collects scattered light with any direction lying within a cone. The collection solid angle Ω has a non-negligible aperture: the wave vector $\mathbf{k}_s$ is not precisely defined. The nominal $\mathbf{k}_s$ coincides with $-\mathbf{k}_i$, but a whole range of wave vectors $\mathbf{k}_s$ is collected [10,43,44], resulting from interactions with a whole range of wave vectors $q_{\|}$ (see Eq 3). It can also be noted that light scattered within a small solid angle around $-\mathbf{k}_i$ is in fact not collected, because it is intercepted by the mirror.

This has a twofold consequence. If alignment is perfect, all the collected wave vectors belong to a circular cone: its axis coincides with the nominal $\mathbf{k}_s$ and the average of the collected wave vectors therefore coincides with the nominal one. The cone semiangle is $\gamma^{lens} = \tan^{-1}(1/2A)$, where A is the numerical aperture of the lens; a lens of aperture f/2 has $\gamma^{lens} \cong 14°$. Alignment can however be not perfect: the laser beam can not be perfectly coincident with the optical axis of the front lens, and the lenses are aligned with a finite precision, especially when the alignment with the internal optics of the interferometer is considered. Consequently, the cone of the wave vectors collected and analyzed is not perfectly symmetric around the nominal one: the average of the collected wave vectors does not coincide with the nominal one, at $\theta_s = \theta_i$, but is at $\theta_s = \theta_i + \delta\theta_s$ [*43,44*]. Since backscattering is not perfectly achieved, Eq 6 becomes $q_{\|}=(2\pi/\lambda_0)(\sin\theta_i + \sin\theta_s)$ and the average of the collected wave vectors differs from the nominal one, given by Eq 6, by $\delta q_{\|} = \delta\theta_s/(2\tan\theta_i)$. The effects of uncertainties in θ_i and/or θ_s are both inversely proportional to $\tan\theta_i$, being thus more severe at low incidence angles.

Another consequence of the finite aperture of the collection solid angle Ω arises also in ideal alignment conditions. It is easily shown (see Fig. 4) that for a given $\mathbf{k}_i$ the wave vector $\mathbf{q}_{\|}$ is a nonlinear function of $\mathbf{k}_s$, since

$$q_{\|1} = (2\pi/\lambda_0)\,(\sin\theta_i + \sin\theta_s \cos\phi) \tag{7a}$$

$$q_{\|2} = (2\pi/\lambda_0)\,\sin\theta_s \sin\phi\,. \tag{7b}$$

Consequently, even when the average of the collected $\mathbf{k}_s$ coincides with the nominal one, the corresponding average of the exchanged wave vectors $\mathbf{q}_{\|}$ does not coincide with the nominal one, given by Eq 6. The average exchanged wave vector $\langle \mathbf{q}_{\|} \rangle$ is found integrating over the collection solid angle Ω [43,44]:

$$\langle \mathbf{q}_{\|} \rangle = \frac{1}{\Omega} \int_{\Omega} (\mathbf{k}_s - \mathbf{k}_i)_{\|}\, d\Omega \tag{8}$$

A more refined analysis can be performed by including includes weighting by the scattering cross section, which is not uniform throughout the angle Ω [43,44]. The cross section is known in closed form for ripple scattering, but for the elasto-optic scattering its computation is involved [18] and requires the elasto-optic coefficients of the material, which are seldom known. For a lens of aperture of the order of f/2 the average value $\langle q_{\|} \rangle$ turns out to differ from the nominal one by an amount which depends on θi and is of the order of 1%. More importantly, even $\langle q_{\|} \rangle$ still differs, by a fraction of a percent, from the more accurate value computed taking into account the cross section. This means that the error in the evaluation of $q\|$ becomes negligible only if the cumbersome computation of the cross section is performed [43,44].

A significant improvement comes from the adoption of a slit which reduces the collection solid angle (see Figs. 1 and 4). The spread of $q_{\parallel}$ is significantly reduced. Even more importantly, in this smaller solid angle the variation of the scattering cross section is much more limited. Consequently, its computation becomes unnecessary, and the value $\langle q_{\parallel} \rangle$ computed by Eq 8 gives a very accurate estimate of the actual average exchanged wave vector [43]. Quantitative assessments [43] show that with the slit the limiting factor for the accuracy of the value of the exchanged wave vector is the overall alignment, and namely the accuracy with which the slit itself is centered with the incidence direction of the laser beam. Inaccuracies in slit position of f/200 ÷ f/400 imply inaccuracies $\delta q_{\parallel} = \delta\theta_s/(2\tan\theta_i)$ which are negligible at high θ_i, but rise to 0.2 ÷ 0.4 % at $\theta_i = 30°$. Without the slit inaccuracies in alignment and the difference between the nominal and the average exchanged wave, vectors lead to inaccuracies $\delta q_{\parallel}$ which can exceed 1%.

Circular frequencies ω are obtained from the measured spectra (Figs. 2 and 3), typically by fitting the measured line shapes with analytical line shapes like gaussians. Due to the small intensity, light is detected by a photomultiplier operated in the single photon counting mode, and intensity is thus detected as a count number. Count numbers are intrinsically subject to statistical variations, and the measured line shapes are affected by these fluctuations. Accordingly, the central frequencies of the measured peaks can be determined with a finite precision, that can be evaluated from the fitting procedure [42]. This uncertainty can be reduced by increasing the incident laser power, if the focused laser does not damage the specimen, or increasing the measurement time. In both cases the count numbers are increased and the ratio of the fluctuation to the count number is decreased. A compromise between precision and measurement time has to be found: with specimens having low scattering cross section, a spectrum of good quality can require a measurement time of several hours.

Typical uncertainties found in the peak fitting procedure are of a fraction of a percent [42]. In the configuration with the slit they are the limiting factor for velocity accuracy, and their reduction can deserve a longer measurement time. Without the slit, the limiting factor for accuracy is instead given by the geometrical factors discussed above.

Experimental Results

Three cases are considered here to show the performance of the method in different conditions. In all the three cases, the substrate is the (001) face of a silicon wafer, of well-known properties: $\rho = 2.33\ 10^3$ kg m^{-3}, $C_{11} = 166$ GPa, $C_{12} = 63.9$ GPa, $C_{44} = 79.6$ GPa. The three films are elastically isotropic, being either nanocrystalline or amorphous, while the anisotropy of silicon is fully taken into account in the computation of the $v_c^{(j)}$. All the measurements were performed at room temperature in backscattering for propagation along the [100] direction of the substrate. The incident light, from an Argon ion laser operating in single frequency at the wavelength $\lambda_0 = 514.5$ nm, was p polarized, and scattered light was collected without polarization analysis. The power incident onto the sample was, for all the three cases, around 100 mW. Four to six spectra were taken in each case, the incidence angles being in the 20 ÷ 70° interval. Scattered light was analyzed by a tandem 3+3 pass high contrast interferometer of the Sandercock type [7,9] with a finesse above 100 (in Fabry-Perot interferometry the finesse is the ratio of the free spectral range to the transmission bandwidth). Light was detected by a

Hamamatsu bialkali photomultiplier tube, operated for single photon counting, with a dark current of 0.7 c.p.s.

The three films are an alloyed gold film 134.5 nm thick, a titanium silicide film of thickness around 75 nm, and a hydrogenated diamond like carbon film, 43 nm thick. Gold has acoustic properties markedly different from silicon, being acoustically much slower, and the mentioned scattering setup explored the interval $q_{\|}h = 1.1 \div 2.8$. Titanium silicide, although significantly heavier than silicon, has acoustic properties closer to those of silicon; the film had nonuniform thickness, an interval of $q_{\|}h \approx 0.6 \div 1.5$ being explored. The hydrogenated carbon film is a test of the sensitivity of the method to very thin films having acoustic properties not much different from those of the substrate; the interval of $q_{\|}h$ is $0.4 \div 0.9$.

Alloyed Gold Film

A film of nominal composition $Au_{90}Cu_5Ni_5$ was prepared by dc magnetron sputtering, in an Ar atmosphere at a pressure of 0.1 Pa, with a fixed energy of 300 eV. Film thickness and mass density were measured by X-ray diffraction and X-ray reflectivity. Diffraction showed that the structure of the film is fcc, with lattice parameter of 0.40376 nm ± 0.0009 nm; assuming equal Cu and Ni concentrations, this means that the CuNi concentration is 8 % (atomic) and that the mass density is $1.89\ 10^4$ kg m^{-3}. The good planarity of the interface and the external surface allowed a precise measurement of thickness by X-ray reflectivity: $h = 134.5$ nm ± 0.2 nm. Diffraction data also determined a grain size of about 10 nm, meaning that film isotropy can be assumed.

Figure 3 shows the Brillouin spectrum measured at incidence angle $\theta i = 50°$. The peaks correspond to the MRW and to three Sezawa waves. These are identified as the first, the second, and the fifth because, as already mentioned, computations of the displacement field indicate that the third, the fourth, and the sixth have, at the surface, a longitudinal polarization, and are thus not detectable on a metallic film. The measured velocities are presented in Fig. 5, with those computed by the most probable values $(\overline{E}, \overline{G})$ = (74 GPa, 26 GPa) found by the *GLS* estimator shown in Fig. 6. The isolevel curves of the normalized *GLS* estimator are drawn up to levels corresponding to confidences well above 99%; the regularity of the *GLS* and the identification of a well-defined minimum are thus shown. These results, obtained by the method outlined in this work, are a significant improvement over previously published results [*19*] obtained by an earlier development of this methodology. The values (E,G) within the 95% confidence region correspond for ν to the interval $0.4 \div 0.44$, and for B to the interval $120 \div 200$ GPa. The relatively wide interval of B is due to the fact that the $(\overline{E}, \overline{G})$ couple lies not far from the thermodynamic stability limit ($G = E/3$): approaching this limit B diverges, and, also in the small confidence region, has a strong gradient.

Titanium Silicide Film

Titanium silicide (TiSi2) films were produced by thermally activated direct Ti/Si interaction on p-type silicon (001). The C49 crystalline phase was obtained, having a mass density of $4.04\ 10^3$ kg m^{-3}, independently measured. Film thickness was measured by cross-section TEM: due to the specific preparation process, a variable thickness was found. Thickness varies in the 60 nm ÷ 85 nm range, the whole interval being found over

a few micrometres length. Since a Brillouin spectrum is measured by a laser beam focused into a spot of the order of tens of micrometers, inhomogeneities at a micrometer scale are averaged and data can be analyzed assuming an average thickness value. The average grain size and misorientation allow to assume elastic isotropy.

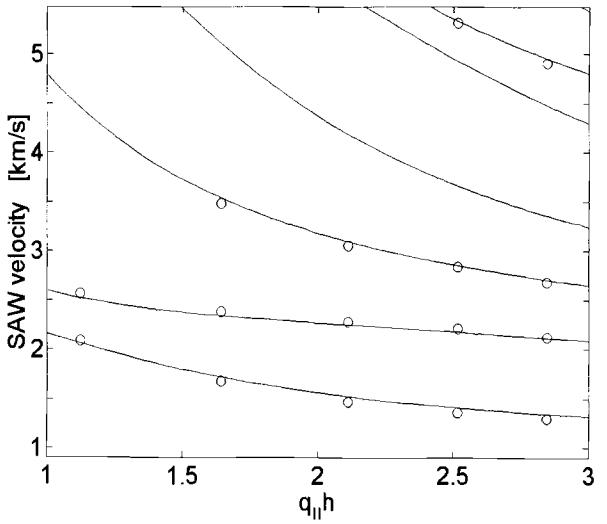

FIG. 5—*Measured (°) and computed dispersion relations for the Rayleigh and Sezawa waves in an alloyed gold film (4% Ni, 4% Cu), 134.5 nm thick, deposited on silicon, (001) face; propagation along [100].*

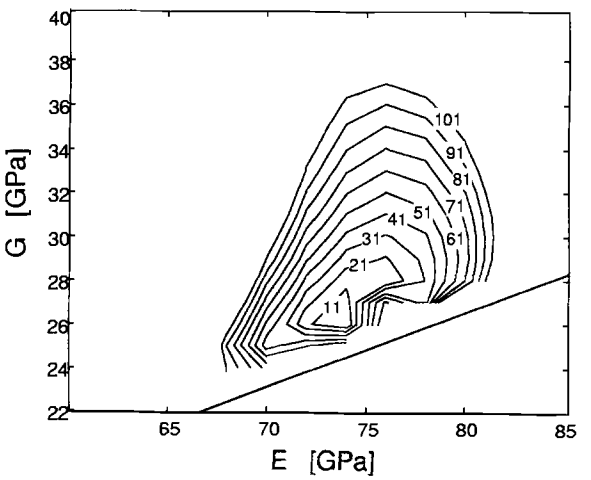

FIG. 6—*Isolevel curves of the normalized least squares estimator (Eq 7) computed from the measured velocities of Fig. 5. The 95% and 99% confidence regions correspond respectively to the values 7.4 and 21.5. The thermodynamic limit G = E/3 is shown.*

In order to assess the effects of thickness uncertainty, data analysis was repeated with three different values of thickness, obtaining different values for $(\overline{E},\overline{G})$ and for the minimum of the *GLS* estimator, as shown in Fig. 7. The values of *GLS* show, not surprisingly, a slightly better agreement for the intermediate value. More importantly, the confidence intervals for E and G found with the different thickness values are largely overlapped, meaning that the measurement of the elastic constants is not hampered by an uncertainty of this order in film thickness. The intervals $E = 175 \div 220$ GPa and $G = 63 \div 95$ GPa are conservatively identified. A sensitivity analysis assessment [13,41] confirmed that a very precise value of film thickness is not crucial for the determination of $(\overline{E},\overline{G})$. It can thus be concluded that, when comparing these results with the previous case, the lower precision found in the silicide case is not to be attributed to the much lower precision of the thickness value. The lower precision is mainly due to the fact the alloyed gold film is thicker, and its acoustic properties are more markedly different from those of silicon. The gold film modifies significantly the Rayleigh wave of the substrate, while in the silicide case the influence of the substrate remains more relevant.

It can be noted that the mentioned extremes of the intervals for E and G correspond to values of the bulk modulus B ranging from 75 GPa to extremely high values, and to values of ν ranging from 0.05 to 0.5: the values of B and ν remain thus essentially indeterminate. Also, this finding was confirmed by the sensitivity analysis assessment [13,41]: the sensitivity to E is high, meaning that E can generally be determined, while the sensitivity to ν is low, meaning that ν can be determined only when the results for E and G are particularly good, as in the previous case.

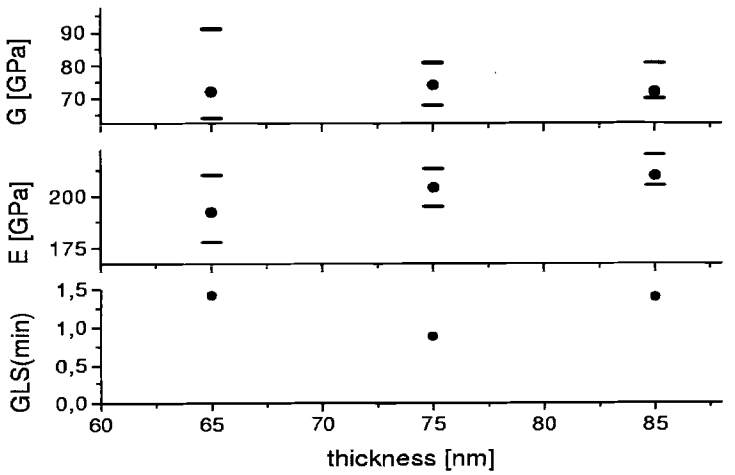

FIG. 7—*Most probable values (•) and 90% confidence intervals for E and G, obtained for a TiSi2 film in the C49 phase, on silicon (001). Computations repeated for three thickness values, obtaining the indicated values of the minimum of the least squares estimator GLS.*

Hydrogenated Carbon Film

In order to assess the sensitivity of the method to very thin films having acoustic properties not very different from those of the substrate, a tetrahedral amorphous hydrogenated carbon (ta-C:H) film, deposited on Si(001), was considered. The film was deposited from acetylene using an electron cyclotron wave resonance plasma source. The film underwent an extensive characterization by electron energy loss spectroscopy (EELS), X-ray reflectivity, ellipsometry, and profilometry, obtaining sp^3 content (70%), density (2.35 10^3 kg m^{-3}), thickness (43 nm), and internal stress (8.4 GPa). The film is amorphous, therefore elastically isotropic.

The results in the (E,G) plane are shown in Fig. 8. The most probable value falls at $(\overline{E},\overline{G})$ = (248 GPa, 96 GPa) but the confidence region has a curved and elongated shape, which would extend into the regions corresponding to $\nu < 0$ and to $\nu > 0.5$. This corresponds to the fact that the elastodynamic equations admit solutions in waveform also in the physically nonmeaningful regions. In this case, a meaningful result can be obtained supplementing the Brillouin results by physical plausibility considerations. In particular only a part of the confidence region was considered: the part that corresponds to a bulk modulus lower than that of diamond (445 GPa), and to a non-negative Poisson ratio. The part of the confidence region delimited this way corresponds to the intervals E = 215 ÷ 275 GPa, G = 75 ÷ 135 GPa, and B > 85 GPa, while ν is completely indeterminate. The precision is obviously not very high, but this procedure allows identification of meaningful results for the elastic properties of a film only 43 nm thick.

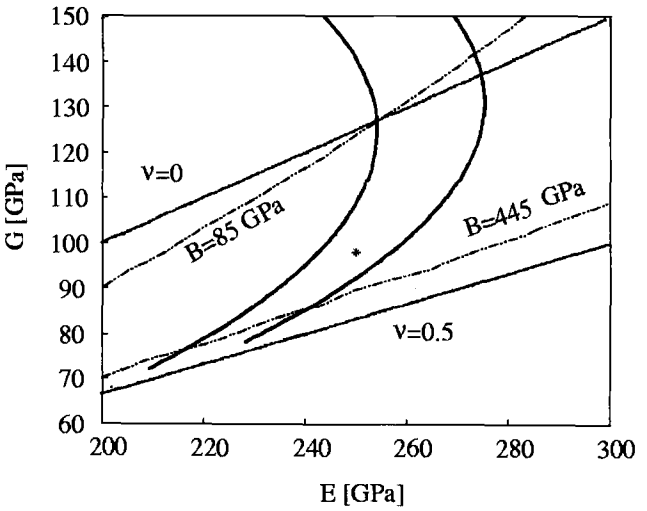

FIG. 8—*Most probable value (*) and 95% confidence region obtained for a ta-C:H film, 43 nm thick, on silicon (001). Only the part of the confidence region compatible with the physical plausibility limits* $\nu > 0$ *and* $B < B_{diamond}$ *is considered.*

Conclusions

It has been shown that the velocity of surface acoustic waves, measured by surface Brillouin scattering, can be exploited to measure the elastic constants of thin supported films of thickness down to few tens of nanometers. The derivation of the elastic constants requires independent measurements of film thickness and film mass density. Isotropic films on crystalline substrate have been considered in detail. It has been shown that the achievable precision depends on the thickness and the elastic properties of the film. In particular, due to the peculiar dependence of velocities on the various elastic moduli, Young modulus and shear modulus can generally be determined, while a complete characterization of the elastic properties, with also the determination of bulk modulus and Poisson's ratio, is achievable only in certain cases. In some cases the acoustic data have to be supplemented by the additional consideration of physical plausibility criteria, namely about the meaningful ranges of the elastic constants.

The method can be extended to nonisotropic films and/or to multilayers. In these cases more independent variables have to be determined by fitting of the experimental data, but more information can be available from the measurement of the direction dependence of velocity.

References

[1] Kim, J. O., Achenbach, J. D., Mirkarimi, P. B., Shinn M., and Barnett, S. A., "Elastic Constants of Single Crystal Transition-Metal Nitride Films Measured by Line-Focus Acoustic Microscopy," *Journal of Applied Physics,* Vol. 72, 1992, pp. 805–1811.

[2] Atalar, A., Koymen, H., Bozkurt, A., and Yaralioglu, G., "Lens Geometries for Quantitative Acoustic Microscopy," *Advances in Acoustic Microscopy*, A. Briggs, Ed., Plenum Press, New York, 1995, pp. 117–151.

[3] Sklar, Z., Mutti, P., Stoodley, N. C., and Briggs, G. A. D., "Measuring the Elastic Properties of Stressed Materials by Quantitative Acoustic Microscopy," *Advances in Acoustic Microscopy*, A. Briggs, Ed., Plenum Press, New York, 1995, pp. 209–247.

[4] Neubrand, A. and Hess, P., "Laser Generation and Detection of Surface Acoustic Waves: Elastic Properties of Surface Layers," *Journal of Applied Physics,* Vol. 71, 1992, pp. 227–238.

[5] Schneider, D., Schwarz, Th., Scheibe, H. J., and Panzner, M., "Nondestructive Evaluation of Diamond and Diamond-Like Carbon Films by Laser Induced Surface Acoustic Waves," *Thin Solid Films,* Vol. 295, 1997, pp. 107–116.

[6] Schneider, D., Witke, Th., Schwarz, Th., Schöneich B., and Schultrich B., "Testing Ultra-Thin Films by Laser Acoustics," *Surface and Coatings Technology,* Vol. 126, 2000, pp. 136–141.

[7] Sandercock, J. R., "Trends in Brillouin Scattering," *Light Scattering in Solids III*, M. Cardona and G. Güntherodt, Eds., G. Springer, Berlin, 1982, pp. 173–206.

[8] Stegeman, G. I. and Nizzoli, F., "Surface Vibrations," *Surface Excitations*, V. M. Agranovitch and R. Loudon, Eds., Elsevier Science Publishers, 1984, pp. 195–378.

[9] Nizzoli, F. and Sandercock, J. R., "Surface Brillouin Scattering from Phonons," *Dynamical Properties of Solids*, Vol. 6, G. K. Horton and A. A. Maradudin, Eds., Elsevier Science Publishers B.V., Amsterdam, 1990, pp. 281–335.

[10] Mutti, P., Bottani, C. E., Ghislotti, G., Beghi, M., Briggs, G. A. D., and Sandercock, J. R., "Surface Brillouin Scattering—Extending Surface Wave

Measurements to 20 GHz," *Advances in Acoustic Microscopy*, A. Briggs, Ed., Plenum Press, New York, 1995, pp. 249–300.

[11] Nakahata H., Hachigo A., Higaki K., Fujii S., Shikata S., and Fujimori, N., "Theoretical Study on SAW Characteristics of Layered Structures Including a Diamond Layer," *IEEE Transactions on Ultrasonics, Ferroelectrics and Frequency Control,* Vol. 42, 1995, pp. 362–375.

[12] Kim J. Y., Chung H. J., Kim H. J., Cho H. M., Yang H. K., and Park J. C., "Surface Acoustic Wave Propagation Properties of Nitrogenated Diamond-Like Carbon Films," *Journal of Vacuum Science and Technology,* Vol. A18, 2000, pp. 1993–1997.

[13] Pastorelli, R., Tarantola, S., Beghi, M. G., Bottani, C. E., and Saltelli, A., "Derivation of Elastic Properties of Thin Films from Measured Acoustic Velocities," *Mechanical Properties of Structural Films, ASTM STP 1413*, C. Muhlstein and S. B. Brown, Eds., American Society for Testing and Materials, West Conshohocken, PA, 2001.

[14] Farnell, G. W., "Properties of Elastic Surface Waves," *Physical Acoustics*, Vol. 6, W. P. Mason and R. N. Thurston eds.,Academic, New York, 1970, pp.109–166.

[15] Farnell G. W. and Adler E. L., "Elastic wave propagation in thin layers," in W. P. Mason and R. N. Thurston, Eds., *Physical Acoustics*, Vol. 9, Academic Press, New York, 1972, pp. 35–127.

[16] Ghislotti, G. and Bottani, C. E., "Brillouin Scattering from Shear Horizontal Surface Phonons in Silicon on Insulator Structures: Theory and Experiment," *Physical Review B*, Vol. 50, 1994, pp. 12131–12137.

[17] Loudon, R., "Theory of Surface Ripple Brillouin Scattering by Solids," *Physical Review Letters*, Vol. 40, 1978, p. 581.

[18] Amici, A., Beghi, M. G., and Bottani, C. E., "Computation of Brillouin Scattering Cross Sections for Multilayers," *Computational Materials Science,* Vol. 17, 2000, pp. 404–408.

[19] Beghi, M. G., Bottani, C. E., Ossi, P. M., Lafford, T., and Tanner, B. K., "Combined Surface Brillouin Scattering and X-Ray Reflectivity Characterization of Thin Metallic Films," *Journal of Applied Physics*, Vol. 81, 1997, pp. 672–678.

[20] Albuquerque, E. L., Loudon, R., and Tilley, D. R., "Theory of Brillouin Scattering by Love Waves," *Journal of Physics C,* Vol. 13, 1980, p. 1775.

[21] Vaughan, J. M., *The Fabry-Perot Interferometer*, Adam Hilger, Bristol, 1989.

[22] Sandercock, J. R., "Light Scattering from Surface Acoustic Phonons in Metals and Semiconductors," *Solid State Communications*, Vol. 26, 1978, pp. 547–551.

[23] Vacher, R. and Boyer, L., "Brillouin Scattering: A Tool for the Measurement of Elastic and Photoelastic Constants," *Physical Review B,* Vol. 6, 1972, pp. 639–673.

[24] Aleksandrov, V. V., Velichkina, T. S., Voronkova, V. I., Koltsova, L. V., Iakovlev I. A., and Yanovskii V. K., "Elastic Coefficients of $KTiOPO_4$, $RbTiOPO_4$, $TlTiOPO_4$ Crystals Determined from Mandelstamm-Brillouin Light Scattering Spectra," *Solid State Communications*, Vol. 69, 1989, pp. 877–881.

[25] Boekholt, M., Harzer, J. V., Hillebrands, B., and Güntherodt, G., "Determination of the Sound Velocities and the Complete Set of Elastic Constants for $Bi_2Sr_2CaCu_2O_{8+\delta}$ Single Crystals Using Brillouin Light Scattering," *Physica C*, Vol. 179, 1991, pp. 101–106.

[26] Grimsditch, M., Zouboulis, E. S., and Polian A., "Elastic Constants of Boron Nitride," *Journal of Applied Physics*, Vol. 76, 1994, pp. 832–834.

[27] Vogelgesang, R., Ramdas, A. K., Rodriguez, S., Grimsditch, M., and Anthony, T. R., "Brillouin and Raman Scattering in Natural and Isotopically Controlled Diamond," *Physical Review B,* Vol. 54, 1996, pp. 3989–3999.

[28] Grimsditch, M., "Brillouin Scattering," *Handbook of Elastic Properties of Solids, Liquids and Gases, Vol. 1,* M. Levy, H. Bass, R. Stern, and V. Keppens, Eds.,

Academic Press/Harcourt Publishers Ltd., Sidcup, UK, 2000.

[29] Albuquerque, E. L., Oliveros, M. C., and Tilley D. R., "Theory of Brillouin Scattering from an Isotropic Elastic Film," *Journal of Physics C*, Vol. 17, 1984, pp. 1451–1463.

[30] Grimsditch, M., Bhadra, R. and Schuller, I. K., "Lamb Waves in Unsupported Thin Films: a Brillouin Scattering Study," *Physical Review Letters,* Vol. 58, 1987, pp. 1216–1219.

[31] Carlotti, G., Fioretto, D., Giovannini L., and Socino, G., "Selective Determination of the C_{11} Elastic Constant in Unsupported Ag/Ni Superlattices by Brillouin Scattering," *Solid State Communications,* Vol. 81, 1992, pp. 487–490.

[32] Hardouin Duparc, O., Sanz-Velasco, E., and Velasco, V. R., "Elastic Surface Waves in Crystals with Overlayers: Cubic Symmetry," *Physical Review B*, Vol. 30, 1984, pp. 2042–2048.

[33] Bria, D., El Boudouti, E. H., Nougaoui, A., Djafari-Rouhani, B., and Velasco, V. R., "Localized and Resonant Guided Elastic Waves in an Adsorbed Layer on a Semi-Infinite Superlattice," *Physical Review B*, Vol. 61, 2000, pp. 15858–15865.

[34] Lee, S., Hillebrands, B., Stegeman, G. I., Cheng, H., Potts, J. E., and Nizzoli, F., "Elastic Properties of Epitaxial ZnSe(001) Films on GaAs Measured by Brillouin Spectroscopy," *Journal of Applied Physics,* Vol. 63, 1988, pp. 1914–1916.

[35] Karanikas, J. M., Sooryakumar, R., and Phillips, J. M., "Dispersion of Elastic Waves in Supported CaF_2 Films," *Journal of Applied Physics*, Vol. 65, 1989, pp. 3407–3410.

[36] Carlotti, G., Fioretto, D., Palmieri, L., Socino, G., Verdini, L., and Verona, E., "Brillouin Scattering by Surface Acoustic Modes for Elastic Characterization of ZnO Films," *IEEE Transactions on Ultrasonics, Ferroelectrics, and Frequency Control*, Vol. 38, 1991, pp. 56–60.

[37] Makarov, S., Chilla, E., and Frölich, H. J., "Determination of Elastic Constants of Thin Films from Phase Velocity Dispersion of Different Surface Acoustic Wave Modes," *Journal of Applied Physics,* Vol. 78, 1995, pp. 5028–5034.

[38] Ferrari, A. C., Robertson, J., Beghi, M. G., Bottani, C. E., Ferulano, R., and Pastorelli, R., "Elastic Constants of Tetrahedral Amorphous Carbon Thin Films," *Applied Physics Letters,* Vol. 75, 1999, pp. 1893–1895.

[39] Zinin, P., Manghnani, M. H., Tlechev, S., Askarpour, V., Lefeuvre, O., and Every, A., "Brillouin Spectroscopy of Surface Modes in Thin-Film Si_3N_4 on GaAs," *Physical Review B,* Vol. 60, 1999, p. 2844.

[40] Comins, J. D., "Surface Brillouin Scattering," *Handbook of Elastic Properties of Solids, Liquids and Gases, Vol. 1,* M. Levy, H. Bass, R. Stern,and V. Keppens, Eds., Academic Press/Harcourt Publishers Ltd., Sidcup, UK, 2000.

[41] Pastorelli, R., Tarantola, S., Beghi, M. G., Bottani, C. E., and Saltelli A., "Design of Surface Brillouin Scattering Experiments by Sensitivity Analysis," *Surface Science*, Vol. 468, 2000, pp. 37–50.

[42] Pastorelli, R., Ferulano R., Beghi M. G., and Bottani C. E., "About the Reliability of the Elastic Constants of Thin Supported Films Derived from Surface Brillouin Scattering Data," to be published.

[43] Beghi, M. G., Bottani C. E., and Pastorelli R., "Accuracy of Surface Acoustic Wave Velocity Measurements by Surface Brillouin Scattering," submitted for publication.

[44] Stoddart, P. R., Crowhurst, J. C., Every, A. G., and Comins, J. D, "Measurement Precision in Surface Brillouin scattering," *Journal of the Optical Society of America B,* Vol. 15, 1998, pp. 2481–2489.

S. A. Catledge[1] *and Y. K. Vohra*[2]

Effect of Nitrogen Feedgas Addition on the Mechanical Properties of Nano-Structured Carbon Coatings

REFERENCE: Catledge, S. A. and Vohra, Y. K., **"Effect of Nitrogen Feedgas Addition on the Mechanical Properties of Nano-Structured Carbon Coatings,"** *Mechanical Properties of Structural Films, ASTM STP 1413*, C. Muhlstein and S. B. Brown, Eds., American Society for Testing and Materials, West Conshohocken, PA, Online, Available: www.astm.org/STP/1413/1413_16, 15 June 2001.

ABSTRACT: Chemical vapor deposition was employed to grow nano-structured carbon films on a titanium alloy (Ti-6Al-4V) using different N_2/CH_4 feedgas ratios in a balance of H_2. Of particular interest is a determination of how the film hardness changes with N_2/CH_4 feedgas ratio and how this measurement correlates with the film structure as determined using micro-Raman spectroscopy, X-ray diffraction, and atomic force microscopy. We find that the broad Raman peak at 1550 cm^{-1} (attributed predominantly to tetrahedral amorphous carbon) becomes more intense and sharp with increasing N_2/CH_4 ratio and that the relative concentrations of CH_4 and N_2 are critically linked to the hardness of the film. The combination of high film hardness, low surface roughness, and good toughness is highly desirable (especially for deposition on metals) and these properties can be optimized by manipulation of the N_2 and CH_4 feedgas concentrations.

KEYWORDS: chemical vapor deposition, diamond, nano-structured carbon, nano-indentation, titanium, hardness, nitrogen

Introduction

Crystalline diamond films of high phase purity and faceted grain structure can be grown using chemical vapor deposition (CVD) employing CH_4 and H_2 feedgas. The most prevalent concentration of CH_4 used to grow such films ranges from 0.2% to 3% of the total gas flow, although our previous work has shown that similar high phase purity crystalline diamond films can be grown with CH_4 concentrations as high as 15% [1]. We found that higher CH_4 concentration has the benefit of higher growth rates and better adhesion to the substrate without a dramatic change in film structure. These highly crystalline diamond films are expected to be as hard as natural diamond. However, the high-surface roughness characteristic of these films (typically several hundred nano-meters) prevents their use for applications requiring low-friction surface contacts.

The effects of adding N_2 to the conventional low CH_4 concentration plasmas has previously been studied with respect to morphology [2-4], growth rate [5], and quality [2]. At very low N_2 concentrations in the range of 10 to 200 ppm the films exhibit pronounced <100> texture and improved diamond phase purity. Higher N_2 additions (up to 40% N_2/CH_4 ratio) result in a loss of faceting and a reduction of diamond phase purity.

[1]Research associate, Department of Physics, University of Alabama at Birmingham (UAB), 1300 University Blvd., 310 Campbell Hall, Birmingham, AL 35294-1170.

[2]Professor of Physics, Department of Physics, University of Alabama at Birmingham (UAB), 1300 University Blvd., 310 Campbell Hall, Birmingham, AL 35294-1170.

These films have been characterized as consisting of nano-crystalline diamond grains (typically 3 to 30 nm grain size) intermixed with amorphous sp^3- and sp^2-bonded carbon [6]. The doping efficiency of nitrogen in the films was shown to be below the detection limit of X-ray photo-electron spectroscopy, 0.5% (8.5×10^{20} cm^{-3}), even for films in which the ratio of N/C in the gas phase was 40% [*2*]. It has been suggested that the strong dependence of N_2 feedgas additions on morphology is not a result of nitrogen incorporation, but is instead directly caused by nitrogen-related surface processes such as micro-twinning brought on by changes in gas-phase chemistry and surface kinetics [*3*].

In this study we show the effects of adding N_2 to feedgas mixtures with high CH_4 concentrations (15% of H_2 flow rate) and compare this to the case of conventional mixtures using low methane (1.8% of H_2 flow rate). The corresponding N_2/CH_4 ratio is observed to be a critical parameter in determining film structure and properties. The film structure is characterized by Raman spectroscopy, X-ray diffraction (XRD), and atomic force microscopy (AFM). Measurements of film hardness have been lacking in previous studies of nano-structured carbon films produced from N_2 feedgas additions. Therefore, in this study we address this issue and use nano-indention techniques[3] to study the mechanical response of these films.

Experimental Details

Titanium alloy (Ti-6Al-4V) disks of 7 mm diameter and 1 mm thickness were prepared by polishing to a surface roughness of 15 nm (rms value) followed by seeding in a diamond powder/water solution via ultrasonic agitation for 50 min. All experiments were performed using microwave plasma CVD with an operating pressure of 125 Torr, microwave power of 675 ± 10 W, substrate temperature of 1113 ± 15 K, and H_2 flow rate of 500 sccm. Five of the experiments were performed using the high methane concentration (CH_4 flow rate of 88 sccm) with N_2 flow rates of 0, 4.4, 8.8, 17.6, and 26.4 sccm, respectively. For comparison, one more experiment was performed using the low methane concentration (CH_4 flow rate of 8.8 sccm) and N_2 flow rate of 8.8 sccm. Each film was grown to a thickness of approximately 7 μm.

Micro-Raman spectra were collected for each film using an argon-ion laser with 514.5 nm excitation. Glancing angle XRD (1 degree incident beam using Cu-Kα radiation) was used to determine crystalline structure of the film. Film hardness and AFM imaging of the film surface was obtained using a nano-indentation system[3] with AFM attachment.

Results

Figure 1 shows micro-Raman spectra (background substracted) for all six films produced in this study having N_2/CH_4 ratios ranging from 0.0 to 1.0. Note that five of the films were grown using the high methane concentration (CH_4 flow rate of 88 sccm) while

[3] MTS NANO INSTRUMENTS, Oak Ridge, TN.

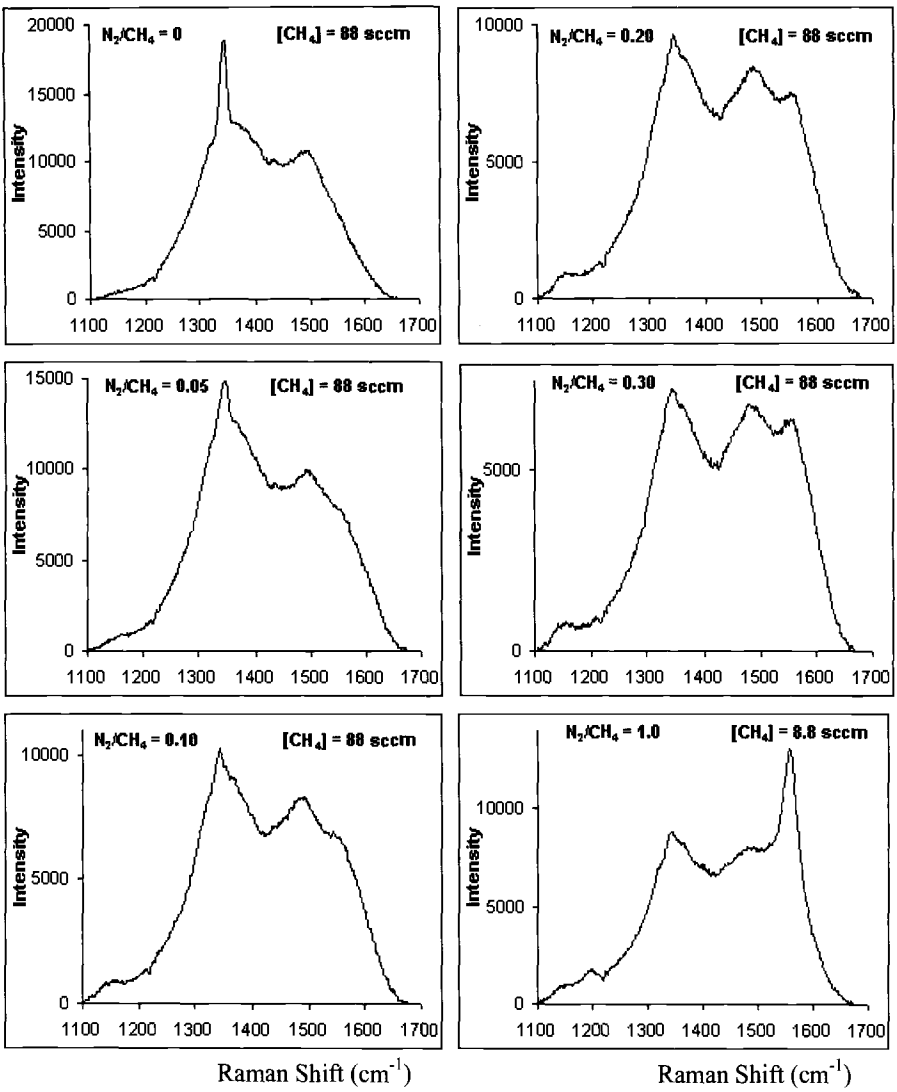

FIG. 1—*Raman spectra of carbon films grown using different N_2/CH_4 feedgas ratios. Note that the last inset on the right (corresponding to a N_2/CH_4 ratio of 1.0) was grown using the low methane concentration of 8.8 sccm.*

the final film corresponding to the lower right inset of Fig. 1 was grown using the low methane concentration (CH_4 flow rate of 8.8 sccm). Several trends are observed in the spectra as the N_2/CH_4 ratio is increased. First of all, it is clear that the crystalline diamond

component (sharp Raman peak ca. 1340 cm^{-1})[4] is decreasing with increasing N_2/CH_4 ratio. Concomitant with the decrease in crystalline diamond content is an increase in the intensity and sharpness of the Raman peak at 1555 cm^{-1}, and for the film grown using the highest N_2/CH_4 ratio of 1.0 the sharp 1555 cm^{-1} peak is the dominant Raman feature. Deposition techniques for growing carbon films at room temperature such as pulsed laser or ion-beam deposition exhibit a single, very broad Raman peak at 1555 cm^{-1} and have been attributed to tetrahedral amorphous carbon with an sp^3 carbon content as high as 85% and hardness near that of diamond [7]. However, the presence of a sharp 1555 cm^{-1} peak as observed for our films grown using a N_2/CH_4 ratio of 1.0 is not well understood. We observe this sharp peak to always be present along with another weaker peak at 1195 cm^{-1}, also of unknown origin. Similar Raman spectra have been obtained by Zhang et al. [8] when using low CH_4/high N_2 feedgas mixtures. The small broad peak at 1140 cm^{-1} is due to defective or nano-meter-size sp^3-bonded carbon crystals. All the films in this study also exhibit broad Raman bands at 1350 cm^{-1} and 1500 cm^{-1} attributed to amorphous carbon. The 1350 cm^{-1} band also indicates the presence of small sp^2-bonded carbon clusters of six-fold aromatic rings. The 1500 cm^{-1} band is associated with a mixture of sp^2 and sp^3 disordered carbon.

The Raman spectra, while complicated and somewhat ambiguous, can still be useful in forming a simple structural model of the films. The films grown with nitrogen feedgas additions can be thought of as consisting of small sp^3- and sp^2-bonded carbon nano-crystals imbedded in an amorphous carbon host which is itself predominantly sp^3-bonded. There are significant differences, however, in the Raman spectra for the films grown over an order of magnitude variation in N_2/CH_4 ratio. It is important to investigate these differences with respect to the mechanical response and surface morphology of these films.

Glancing angle XRD was also used to characterize the film structure. The films were found to be comprised of cubic diamond (a = 35.60 nm) along with an interfacial titanium carbide (a = 43.04 nm) layer. No graphitic carbon was observed in any of the XRD patterns. For each film the most intense peaks were indexed to cubic diamond. However, the intensity and full-width-at-half-max (FWHM) of these peaks varied with N_2/CH_4 ratio. These variations for the cubic diamond (111) reflection (at 44° 2-theta) are shown in Fig. 2 for the films grown with the high CH_4 concentration. Consistent with the Raman spectra, the XRD data show that the crystalline diamond component decreases with increasing N_2/CH_4 ratio. In addition, the FWHM increases with increasing N_2/CH_4 ratio, indicating a reduction in grain size and/or crystallinity. The Scherrer equation was used to calculate grain size based on the FWHM of the diamond (111) reflection for films grown using N_2/CH_4 ratios of 0.10, 0.20, and 0.30. The average grain size from this calculation was 12 ± 2 nm. This assumes that XRD broadening is due to crystallite size only, and therefore represents a lower limit estimate.

It is interesting to compare the XRD patterns for the films grown with N_2/CH_4 ratios of 0.10 and 1.0 as shown in Fig. 3. The only processing difference between these films is the concentration of CH_4 used (88 sccm vs. 8.8 sccm, respectively). The most

[4] This peak position is frequency shifted from the normal 1332 cm^{-1} value for stress-free diamond due to the presence of compressive stress in the film.

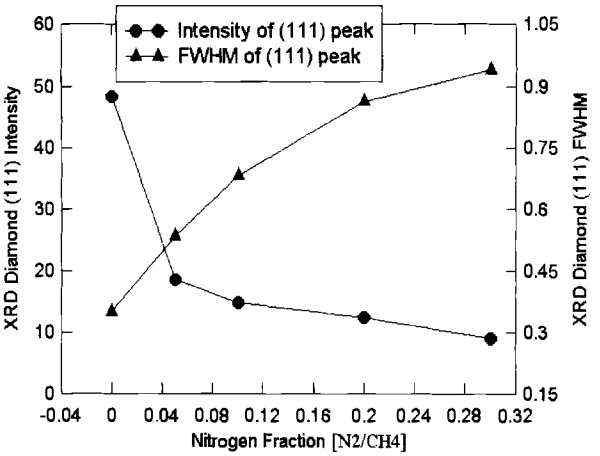

FIG. 2—*Effect of nitrogen feedgas addition on the x-ray diffraction diamond (111) intensity and full-width at half-max (FWHM) for experiments performed using the high methane concentration [CH_4 = 88 sccm]. The intensities were normalized to film thickness which varied only slightly from film to film.*

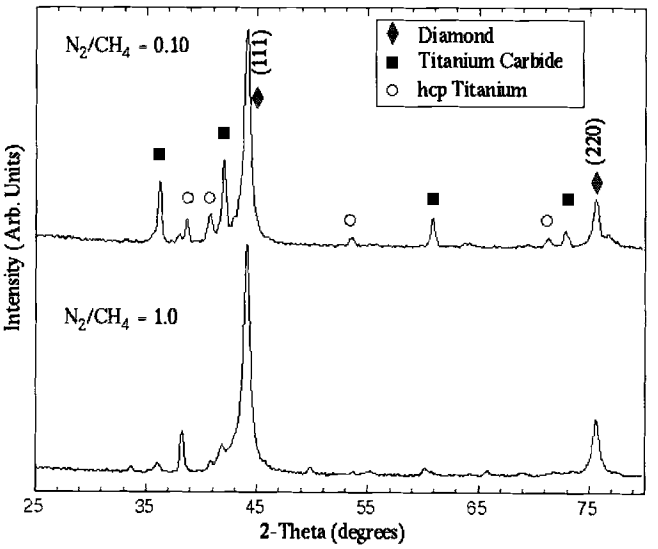

FIG. 3—*Glancing-angle XRD patterns for films grown with N_2/CH_4 ratios of 0.10 (high methane) and 1.0 (low methane). For each film the N_2 feedgas concentration used was 8.8 sccm.*

significant difference in XRD spectra between these two films is that the peaks indexed to the titanium carbide interfacial phase are much stronger for the film grown using the high CH_4 concentration. This is expected since higher CH_4 feedgas concentrations will

produce a higher flux of carbon species such as C_2 and CH radicals to the growth surface, as verified experimentally using optical emission spectroscopy [6]. Note also that the diamond peak intensities and FWHM values are similar for each film. The FWHM values for the films with N_2/CH_4 ratios of 0.10 and 1.0 are 0.67 and 0.65, respectively. Therefore, both films are expected to have nearly the same diamond crystallinity and grain size.

Figure 4 shows AFM images for the film grown with N_2/CH_4 ratios of 0.0, 0.10, 0.30, and 1.0 at two different scanning magnifications. The well-defined crystal faceting characteristic of the film grown without N_2 addition is completely lost for all other films grown with N_2 additions. High magnification reveals agglomeration of particles with nearly spherical shape resembling the so-called "cauliflower" morphology. These images reveal that the degree of agglomeration, at least for the films grown with the high CH_4 concentration, is lower for higher N_2/CH_4 ratios. This is consistent with the measured surface roughness values which are lowest for the film grown with the N_2/CH_4 ratio of 0.30. All the films grown with N_2 feedgas additions were very smooth in comparison to the film grown without N_2 feedgas addition. The average root-mean-squared (rms) surface roughness parameter as measured via surface profilometry [9] was 14 nm for films grown with the N_2/CH_4 ratio of 0.10.

In order to investigate the mechanical response of these films, nano-indentation testing was performed. Due to the extreme hardness of these films, blunting of the diamond indenter tip was a concern. A fused silica calibration standard was tested before and after each set of indents to determine the severity of tip blunting. Figure 5 shows the measured hardness vs. indentation depth for the film grown with the N_2/CH_4 ratio of 0.30, along with error bars designating standard deviation for 12 separate indentations. It was anticipated that this film would exhibit the lowest hardness of all those tested in this study. The calibration of the instrument using the fused silica standard remained unchanged after testing this film. The average measured hardness of the film with standard deviation was 64 ± 12 GPa. For comparison, the expected hardness of crystalline diamond is 100 GPa.

Indentation of the other films in this study resulted in significant blunting of the diamond tip. With the blunted tip, we performed a single indent on the films grown with N_2/CH_4 ratios of 0.10, 0.30, and 1.0, testing the fused silica standard between each indentation. Further blunting of the tip was not experienced for these measurements. Therefore, a direct comparison can be made of the measured load/displacement curves to investigate differences in the mechanical response of these films.

Figure 6 shows the load/displacement curves for the films grown with N_2/CH_4 ratios of 0.10, 0.30, and 1.0, as well as for the fused silica standard. It can be seen that for a given indentation depth, the load is highest for the film grown with N_2/CH_4 ratio of 1.0, followed second by the film grown with N_2/CH_4 ratio of 0.10, and finally by the film grown with N_2/CH_4 ratio of 0.30. In addition, the film with N_2/CH_4 ratio of 1.0 shows the largest elastic response as indicated by the decreased amount of hysteresis between the load and unloading cycle. Since the hardness of the film with N_2/CH_4 ratio of 0.30 was

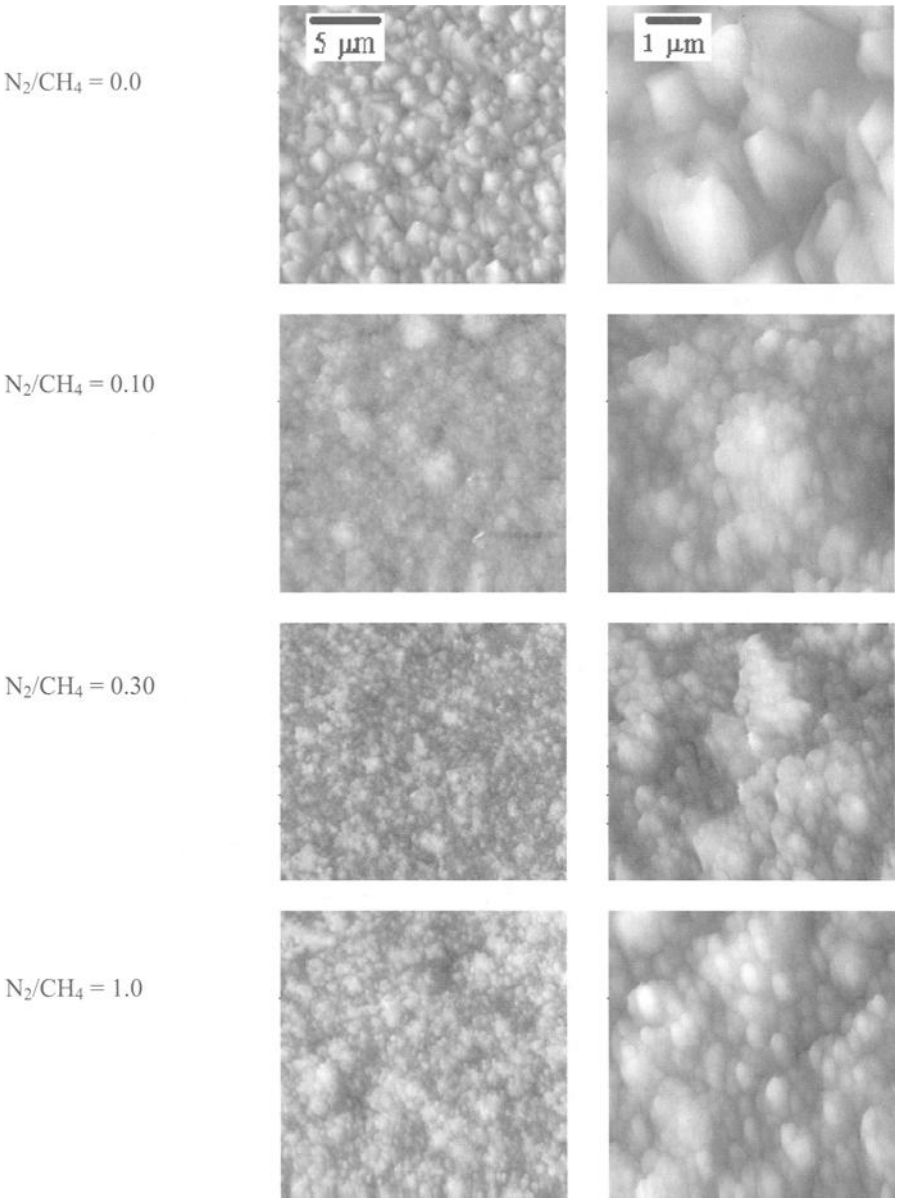

FIG. 4—*AFM images for films grown using the N_2/CH_4 ratios of 0.0, 0.10, 0.30, and 1.0. All images in the left column use the 5 μm scale and all images in the right column use the 1 μm scale.*

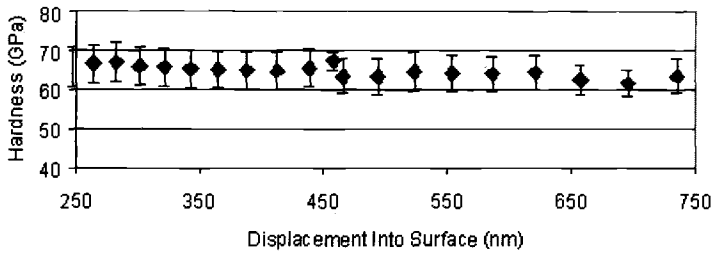

FIG. 5—*Nano-indentation hardness versus depth for the film grown with a N_2/CH_4 feedgas ratio of 0.30. Each error bar represents the standard deviation from 12 indentations.*

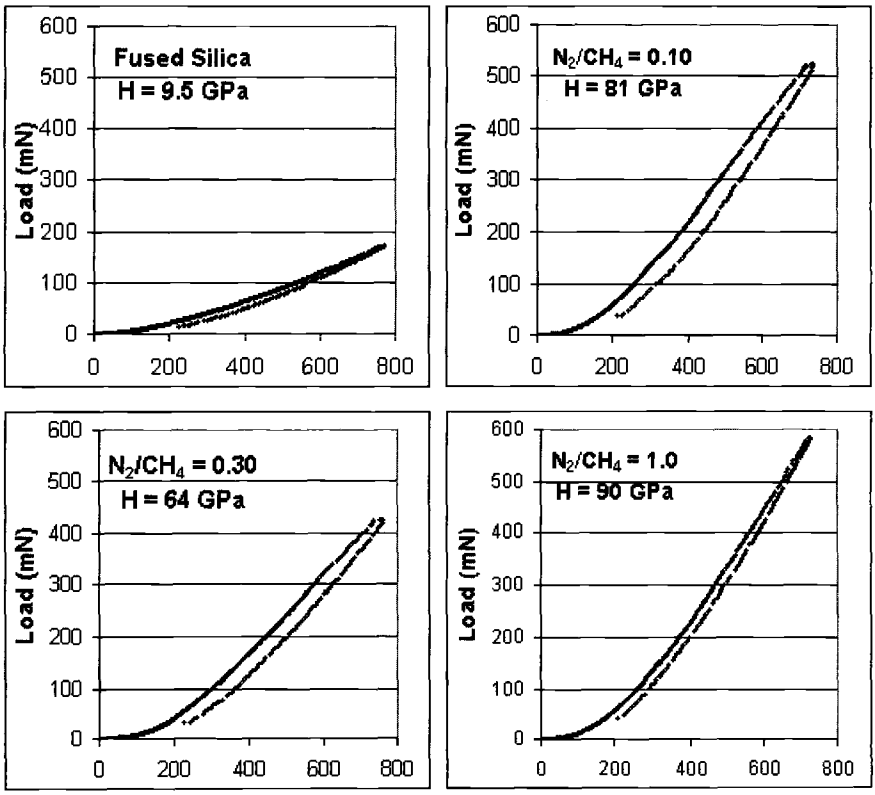

FIG. 6—*Nano-indentation load-displacement curves showing a comparison between fused quartz and nano-structured carbon films grown with different N_2/CH_4 feedgas ratios. Note that all curves are plotted on the same scale.*

initially measured using a sharp indenter tip, it is stated with high confidence. In order to estimate the hardness of the other films, we re-tested the known film with the blunt tip and changed the tip calibration to again reproduce the initial value of 64 GPa. Using this revised calibration, the measured hardness values for the films grown with N_2/CH_4 ratios of 0.10 and 1.0 were 81 GPa and 90 GPa, respectively. The trend in these hardness values is consistent with the load/displacement curves, which show that the film grown with the N_2/CH_4 ratio of 1.0 exhibits the highest load at a given depth, followed by the films grown with N_2/CH_4 ratios of 0.10 and 0.30, respectively.

The highly crystalline diamond film grown without nitrogen feedgas addition is expected to be about as hard as natural diamond. However, when compared with the other films grown with N_2 feedgas additions (at the high CH_4 concentration), the crystalline film suffers from a much lower fracture toughness. This was confirmed by indentation testing up to 1471 N load with a 3.2 mm diameter tungsten carbide ball. The crystalline diamond film fractured and completely delaminated at the lowest load of 294 N. Figure 7 shows an optical micrograph of four indentations made on the nano-structured carbon film grown with a N_2/CH_4 ratio of 0.10. The indentation loads (clockwise from upper left) are 294, 588, 981, and 1471 N. In contrast to the crystalline diamond film, no delamination of the nano-structured carbon film occurs even at the highest load of 1471 N. Figure 8 shows scanning electron micrographs (SEM) of the area around the indents, which reveal circumferential micro-cracking. These micro-cracks were seen only for indentation loads of 588 N or higher, and sometimes were not observed until the highest loads of 1471 N. Higher magnifications may be required to observe nano-cracks surrounding the lower load indents. The strain to cause micro-cracking was estimated from calculations of indentation surface areas to be as high as 1.9 ± 0.2% [9]. This represents a significant improvement in toughness over crystalline diamond and other ceramic coatings that undergo brittle fracture.

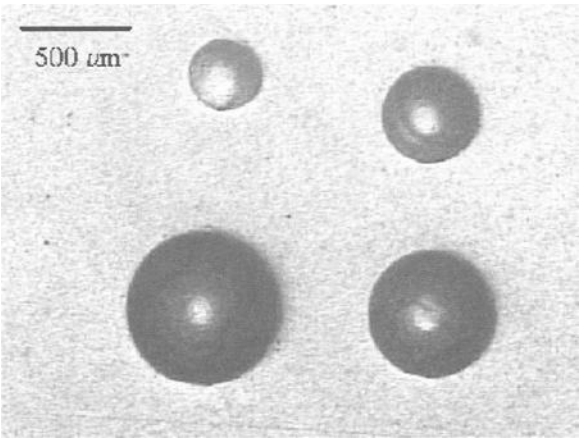

FIG. 7—*Optical micrograph showing a set of four indentations on a nano-structured carbon film grown using N_2/CH_4 feedgas ratio of 0.10. The indentation loads (clockwise from upper left) are 294, 588, 981, and 1471 N. No film delamination occurs.*

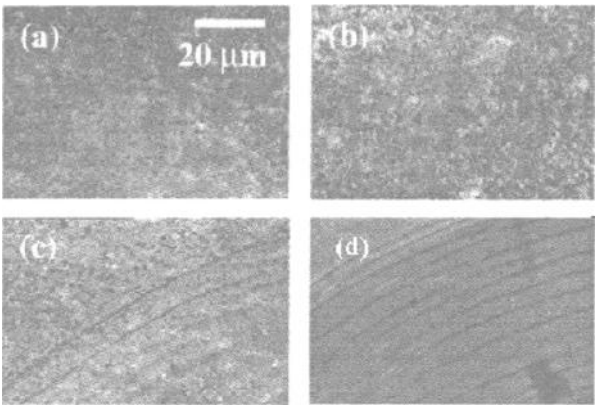

FIG. 8—*SEM micrographs showing circumferential micro-cracks surrounding the indents produced from (a) 294 N, (b) 588 N, (c) 981 N, and (d) 1471 N load.*

Discussion

Clearly, the nanostructured carbon films of this study can undergo significant plastic deformation without brittle fracture occurring. The observed ductility of our nano-structured carbon coatings is not expected to be a result of dislocation motion because the grain size (10-14 nm) is too small to act as a sufficient source of dislocation activity. Instead, nano- and micro-cracks appear to develop with a directionality according to the nature of the applied load. In this case, circumferential cracks are formed as material flows outward from the indent. These cracks are not catastrophic and do not result in delamination at the film/substrate interface, nor do they appear to lead to in-film crack propagation characteristic of a very brittle material. It is plausible that the durability of the coatings is attributable to the prevention of both of these failure modes by having a combination of high fracture toughness at the film/substrate interface as well as microcrack-induced toughness within the film itself. Similar behavior is observed in other hard/tough nano-composite systems such as those involving nano-crystalline TiC grains imbedded in amorphous carbon [10].

It is encouraging that the nano-structured carbon films in this study are tough as well as extremely hard. The film grown with the highest N_2/CH_4 ratio of 0.30 has a measured hardness that is 64% that of natural diamond. The film grown with a N_2/CH_4 ratio of 0.10 is even harder and is estimated to be 81% as hard as natural diamond. Such high hardness values imply that the majority of carbon bonds are tetrahedrally coordinated. The Raman spectra indicate a structure consisting of crystalline and amorphous carbon phases. Although homogeneous, the nano-structured film may be loosely defined as a "nano-composite" in which nano-crystalline diamond grains are surrounded in amorphous carbon which itself has a high fraction of sp^3 bonds. The majority of sp^2-bonded carbon is expected to reside in the grain boundaries. According to simulation studies by Keblinski et al. [11], the grain boundary (GB) structure of nano-crystalline diamond is more ordered than for the case of nano-crystalline silicon because

of the ability of the carbon to change to sp^2 hybridization. Therefore, the relatively high degree of structural disorder in the mostly fourfold-coordinated silicon GBs is replaced by bond-coordination disorder in the mostly threefold-coordinated, less structurally disordered diamond GBs. Most GBs in randomly oriented nano-crystalline diamond are generic high energy planes but exhibit a high work of adhesion due to the high bonding density across the GB. It has been suggested that this may result in the dominant fracture mode being intragranular rather than intergranular.

Based on the load/displacement curves in Fig. 6, the optimum choice for a combination high hardness/high toughness film corresponds to the N_2/CH_4 ratio of 0.10. The film with higher estimated hardness grown using the N_2/CH_4 ratio of 1.0 is expected to be less tough as observed from the decreased hysteresis between the load/unload curve. It also suffers from inferior film/substrate adhesion. This is likely due to the much lower CH_4 concentration used and the resulting decrease in TiC interfacial layer and diamond nucleation density.

Conclusion

The trends observed in the Raman, XRD, and nano-indentation data suggest that nitrogen plays a significant role in manipulating the structure and mechanical properties of carbon films grown by chemical vapor deposition. By adding appropriate amounts of N_2 to the feedgas mixture and by using the high CH_4 concentration (15% by volume), we can achieve well-adhered, highly fracture resistant films with near-diamond hardness and low surface roughness. The films are characteristic of load-adaptive nano-crystalline-amorphous composite materials that exhibit deformation from elastic to plastic at loads above the elastic limit, as opposed to brittle fracture. Such behavior can be attributed to the formation of stable micro- and nano-cracks as well as to the high fracture toughness of the film/substrate interface expected for this system. The mechanisms and reactions that take place involving nitrogen in the plasma as well as on the surface require further investigation.

Acknowledgments

The authors acknowledge support from the Bioengineering Research Grant (BRG) by the National Institutes of Health (NIH) under Grant No. 1 RO1DE13952-01.

References

[1] Catledge, S. A. and Vohra, Y. K., "Effect of Nitrogen Addition on the Microstructure and Mechanical Properties of Diamond Films Grown Using High-Methane Concentrations," *Journal of Applied Physics*, Vol. 86, July 1999, pp. 698–700.

[2] Jin S. and Moustakas, T. D., "Effect of Nitrogen on the Growth of Diamond Films," *Applied Physics Letters*, Vol. 65, July 1994, pp. 403–405.

[3] Cao, G. Z., Schermer, J. J., van Enckevort, W. J. P., Elst, W. A. L. M., and Giling, L. J., "Growth of {100} Textured Diamond Films by the Addition of Nitrogen," *Journal of Applied Physics*, Vol. 79, February 1996, pp. 1357–1364.

[4] Locher, R., Wild, C., Herres, D., Behr, D., and Koidl, P., "Nitrogen Stabilized <100> Texture in Chemical Vapor Deposited Diamond Films," *Applied Physics Letters*, Vol. 65, July 1994, pp. 34–36.

[5] Muller-Sebert, W., Worner, E., Fuchs, F., Wild, C., and Koidl, P., "Nitrogen Induced Increase of Growth Rate in Chemical Vapor Deposition of Diamond," *Applied Physics Letters*, Vol. 68, February 1996, pp. 759–760.

[6] Catledge, S. A. and Vohra, Y. K., "High Density Plasma Processing of Nanostructured Diamond Films on Metals," *Journal of Applied Physics*, Vol. 84, December 1998, pp. 6469–6471.

[7] Friedmann, T. A., Sullivan, J. P., Knapp, J. A., Tallant, D. R., Follstaedt, D. M., Medlin, D. L. and Mirkarimi, P. B., "Thick Stress-Free Amorphous-Tetrahedral Carbon Films with Hardness Near that of Diamond," *Applied Physics Letters*, Vol. 71, December 1997, pp. 3820–3822.

[8] Zhang, Q., Yoon, S. F., Ahn, J, Rusli, Guo, Y., "The Effects of Nitrogen Flow on the Raman Spectra of Polycrystalline Diamond Films," *Microelectronics Journal*, Vol. 29, 1998, pp. 875–879.

[9] Toprani, N., Catledge, S. A., Vohra, Y. K and Thompson, R., "Interfacial Adhesion and Toughness of Nanostructured Diamond Coatings," *Journal of Materials Research*, Vol. 15, May 2000, pp. 1052–1055.

[10] Voevodin, A. A. and Zabinski, J. S., "Load-Adaptive Crystalline-Amorphous Nanocomposites," *Journal of Materials Science*, Vol. 33, January 1998, pp. 319–327.

[11] Keblinski, P., Wolf, D., Cleri, F., Phillpot, S. R. and Gleiter, H., *MRS Bulletin*, Vol. 23, September 1998, pp. 36–41.

Naushad Hossain,[1] *J. W. Ju,*[1] *Brett Warneke,*[2] *Kristofer S. J. Pister*[2]

Characterization of the Young's Modulus of CMOS Thin Films

REFERENCE: Hossain, N., Ju, J. W., Warneke, B., and Pister, K., **"Characterization of the Young's Modulus of CMOS Thin Films,"** *Mechanical Properties of Structural Films, STP 1413,* C. Muhlstein and S. B. Brown, Eds., American Society for Testing and Materials, West Conshohocken, PA, Online, Available: www.astm.org/STP/1413/1413_15, 1 July 2001.

ABSTRACT: We have developed a technique to determine the local Young's moduli of the thin films within a composite stack of CMOS films, without accessing the individual layers during processing. By fabricating cantilevers of various combinations of field oxide, polysilicon 1, gate oxide, polysilicon 2, oxide 1, metal 1, oxide 2, metal 2, and overglass, measuring the thicknesses of each layer in a cross-section SEM, and deflecting the cantilevers with a Tencor Alpha Step profilometer, we were able to determine the Young's modulus for each film from elastic beam theory. The values we determined for the field oxide, polysilicon, and metal layers were in close agreement with published data on similar but isolated pure films. Values were also determined for the proprietary interlayer dielectrics and passivation overglass layers whose compositions are unknown and thus not available in the literature. These results are of use to MEMS designers utilizing CMOS processes since they do not have control over the mechanical properties of the films in the process nor are they able to directly measure them.

KEYWORDS: Young's modulus, beam, CMOS, MOSIS, deflection, residual stress, thin films, CMOS micromachining

Introduction

Many researchers are utilizing various foundry CMOS processes as the basis for micro electro-mechanical systems (MEMS), but since these processes are developed for their electrical properties, the mechanical properties are not optimized. In addition, MEMS designers have no direct control over the mechanical properties of the thin films available in the process. CMOS mechanical structures are made up of composite stacks of proprietary films, so the values available in the literature for single films are not applicable. In this work, methods were developed and test structures were fabricated to determine the Young's modulus of the composite thin films of the AMI 1.2 μm CMOS process available through MOSIS [1,2]. Foundry CMOS MEMS designers can better optimize their structures and predict device performance once they have reasonably accurate material properties in hand.

Young's modulus has been an extremely difficult parameter to measure in thin films due to the fragility of the samples and the concomitant problems in their handling and mounting as well as minutely deforming them and monitoring their motions [3]. Mechanical properties of materials can be investigated on a micron and submicron scale using submicron indentation testing, wafer curvature testing, bulge testing, and resonant frequency testing. However, all of these techniques have limitations that restrict their

[1]Department of Civil and Environmental Engineering, University of California, Los Angeles, CA.
[2]Department of Electrical Engineering and Computer Sciences, University of California, Berkley, CA.

utility in experimental studies. A quick and accurate measurement of hardness can be achieved by the submicron indentation of thin films on substrates, but the large pressure under the indenter may alter the thin film being tested. The average stress and strain in a film can be measured with the wafer curvature techniques, but the range of stresses is limited by the thermal expansion and/or growth mismatch of the substrate and film. Furthermore, the measured stress is an average value for a large part of the wafer, and this may mask significant, local fluctuations. The bulge test also fails to provide localized information even though a smaller test specimen is used for this test [4]. Resonant frequency measurements of elastic moduli of cantilever beams can be local, but the experimental error can be large [5]. To avoid some of these difficulties, several cantilever beams of various composite layers were fabricated and then were scanned with a Tencor Alpha Step profilometer to generate displacements as a function of force [6]. One advantage of using the profilometer is that residual stress gradients can be calculated from the profile of the beam. The other advantages of this technique include an experimental error low enough [4] to be useful for designers and localized measurements due to micron-scale beam dimensions.

Beam Fabrication

The AMI 1.2 μm proprietary CMOS process contains two polysilicon and two aluminum layers. Figure 1 shows the various thin films in this process along with cross sections of the typical integrated circuit devices made with them. A total of 105 beams were fabricated with various combinations of the following films: field oxide, polysilicon 1, gate oxide, polysilicon 2, oxide 1, metal 1, oxide 2, metal 2, and overglass (Fig. 2), but only nine beams were needed for study. Beam 1 was used to measure individual film thicknesses, and the rest of the beams were used to calculate Young's moduli of elasticity of individual films. Figure 3 shows some of these composite beams. The following are the compositions of some of these composite beams:

Beam 1: Field Oxide, Poly 1, Gate Oxide, Poly 2, Oxide 1, Metal 1, Oxide 2, Metal 2, Overglass
Beam 3: Gate Oxide, Metal 1, Oxide 2, Metal 2, Overglass
Beam 5: Gate Oxide, Poly 1, Oxide 1, Oxide 2, Metal 2
Beam 8: Gate Oxide, Poly 1, Metal 1, Metal 2, Overglass

In general, a typical beam consists of three to eight films.

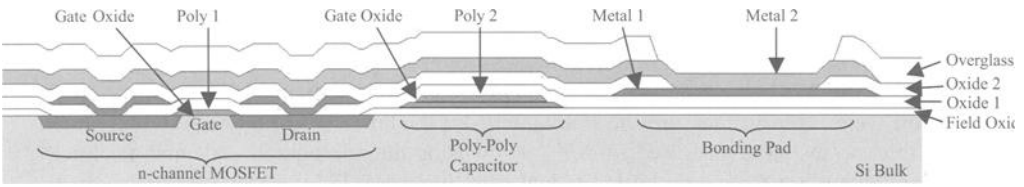

FIG. 1—*A typical integrated circuit device made with thin films.*

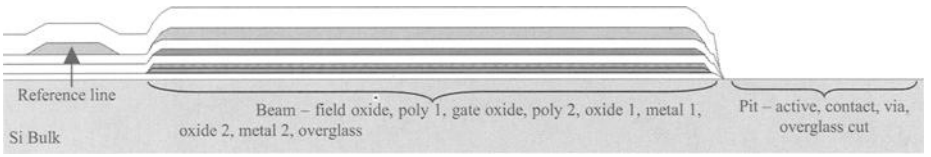

FIG. 2—*Beam with thin films before etching.*

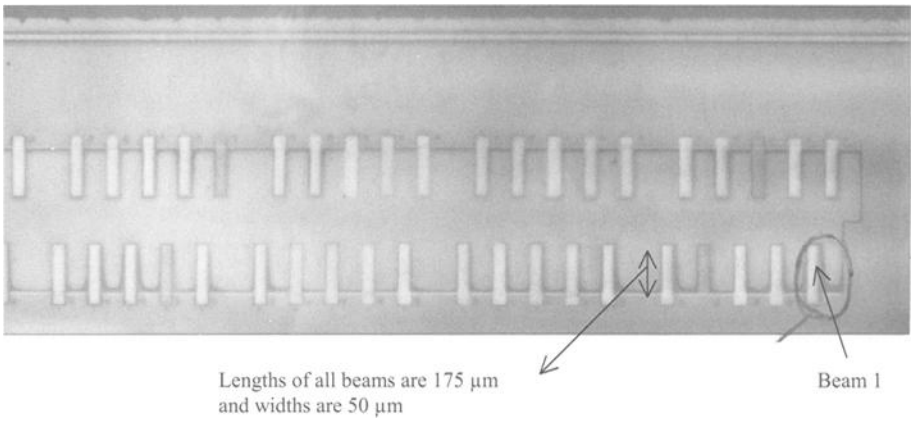

FIG. 3—*Photograph of an array of composite beams.*

The length and the width of the beams are 175 μm and 50 μm. The length and the width of the beams were measured by scanning the beams using the Alpha Step profilometer [11]. Individual film thicknesses were measured by cross sectioning Beam 1 at the section A-A' shown in Fig. 4. Scanning electron micrographs (SEMs) of the cross section were taken to measure the individual film thickness (Figs. 5 and 6). Individual film thicknesses were measured from Fig. 6 by using the micrograph scale and a caliper. The following are the measured individual film thickness: field oxide: 1.90 μm; poly 1: 0.30 μm; gate oxide: 0.08 μm; poly 2: 0.30 μm; oxide 1: 0.83 μm; metal 1: 0.60 μm; oxide 2: 0.95 μm; metal 2: 1.00 μm; and overglass: 1.30 μm. Based on these results and the as-designed beam compositions, the thickness of the beams varies from 2.85 μm to 7.26 μm. The beam thickness was calculated by adding the thickness of the individual films. For example, Beam 1 consists of field oxide, poly 1, gate oxide, poly 2, oxide 1, metal 1, oxide 2, metal 2, and overglass films. So, the beam thickness of Beam 1 is 7.26 μm.

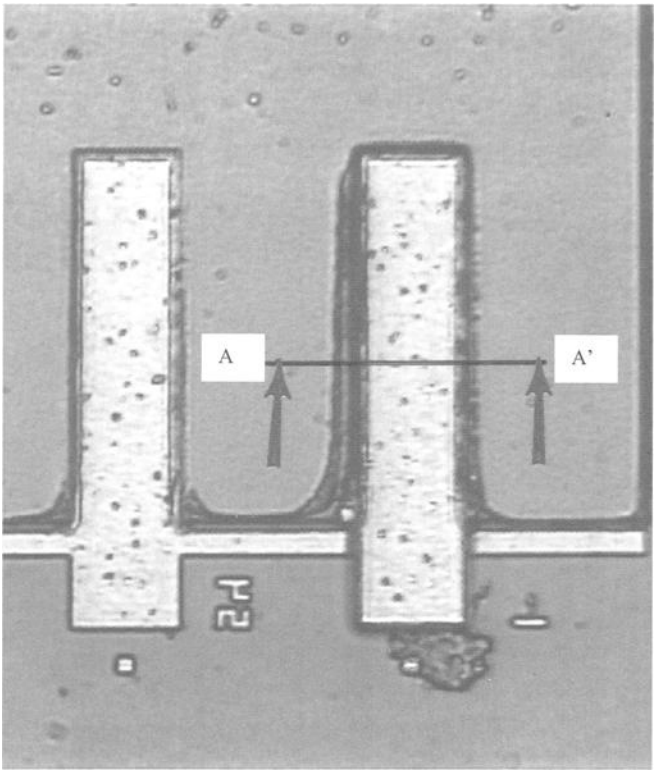

FIG. 4—*Section A-A' on Beam 1 used for the cross-section.*

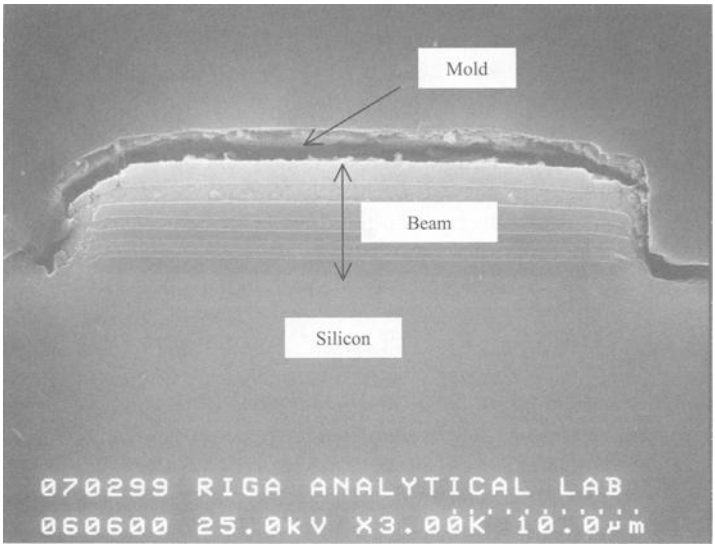

FIG. 5—*Cross section of Beam 1 at 3.0 k magnification.*

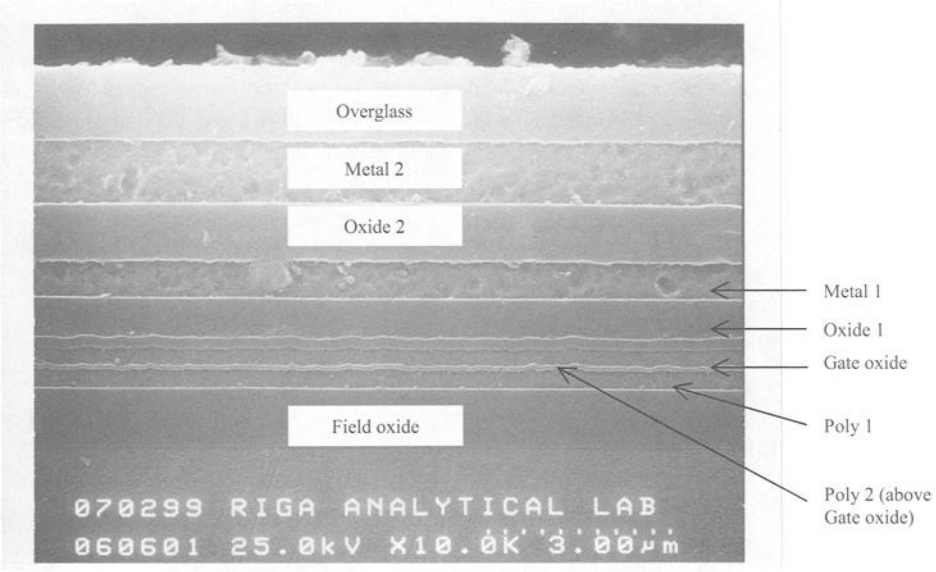

FIG. 6—*Cross section of beam 1 at 10.0 k magnification.*

During layout, the beams are surrounded on three sides by active areas (this mask results in thin gate oxide instead of the field oxide), contact cuts (this mask causes holes in oxide 1), via cuts (this mask causes holes in oxide 2), and overglass cuts (this mask causes holes in the overglass passivation layer) as shown in Fig. 2. When the chip returns from the foundry, these regions will have exposed silicon. The chip is then put in a silicon etchant that attacks these regions of bare silicon and eventually undercuts the cantilever (Fig. 7), resulting in a released mechanical structure composed of the CMOS thin films. For this work, we used xenon difluoride (XeF_2) [7,8], a gas-phase isotropic silicon etchant that is selective to silicon dioxide and aluminum, but tetramethylammonium hydroxide (TMAH) and ethylenediamine-pyrocatechol (EDP) [9] could also be used.

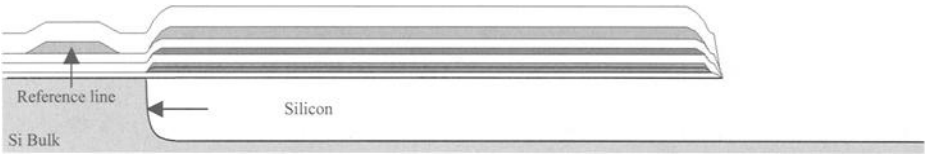

FIG. 7—*Cantilever beam after etching.*

After release, the beams bent upward or downward due to residual stress gradients caused both by stress gradients within each film and differences between the average residual stress of each film in the composite beam. Compositional or density gradients through a film thickness, which result in a gradient in the thermal coefficient of expansion, and other variations in deposition conditions with time can cause residual stress gradients within a film. These effects vary by material and deposition technique [3], so the magnitude and sign of the resulting stress gradient is different for each combination of films.

Analysis

The theory of linear elastic deflection of a cantilever beam with rectangular cross section has been well developed [10]. For the deflection of a cantilever beam, we have:

$$v = PL^3/3EI \tag{1}$$

From the above equation, the Young's modulus, E_{mi}, of an individual composite beam can be calculated:

$$E_{mi} = PL^3/3vI_{mi} \tag{2}$$

where

V = Composite beam deflection,
P = Force applied,
L = The effect of composite beam length,
I_{mi} = The moment of inertia of the composite beam.

The composite beam moment of inertia is calculated by adding the moment of inertia of the individual films. The moment of inertia of an individual film, I_j, is evaluated according to the parallel axis theorem:

$$I_j = bh_j^3/12 + A_j d_j^2 \tag{3}$$

where

b = the beam width,
h_j = the thickness of an individual film,
A_j = the cross-sectional area of an individual film ($A_j = bh_j$), and
d = the distance between the centroidal axis of the composite beam and the neutral axis of an individual film.

It is noted that $bh_j^3/12$ represents the moment of inertia of an individual film with respect to its own neutral axis. For all the beams, the length L was 175 μm, the width b was 50 μm, and the load P exerted by the Alpha Step profilometer was 4 mg.

If the ratio of length and width (L/b) is greater than 3, the calculations for a plate can be replaced by those for a beam without substantial error [17]. It is valid to use beam theory instead of plate theory for this study because the L/b ratio of the beams is 3.5. All the beams were deflected several times using a 4 mg force to verify the elasticity of the beams. The deflections were repeatable to within 0.1 μm. This shows that beams were elastic after the deflections and therefore Eq 1 was valid for this analysis.

Equation 1 applies to a cantilever beam under a point loading at its tip. However, the residual stress gradient in these thin film beams causes a distributed moment within the beam that linearly adds another component to the deflection. That is, the residual stress results in an additional deflection in the beam. Therefore, two loads of 4 mg and 1 mg were applied to the beams to allow the zero-load deflection (due to the residual stress gradient) to be extrapolated and then added to the 4 mg load deflection. This total tip-deflection could then be used in Eq 2.

To evaluate the composite flexural rigidity, $E_{mi}I_{mi}$, we employ the following summation formula:

$$E_{mi}I_{mi} = \sum_j E_j I_j \tag{4}$$

It is emphasized that the individual film I_j is calculated on the basis of the parallel axis theorem, Eq 3. Moreover, E_j is the individual Young's modulus of the jth film. Therefore, we can calculate the Young's modulus of each individual film by solving the following linear system of equations for eight selected beams:

Beam 2: $E_{m2}I_{m2} = E_1I_1 + E_6I_6 + E_7I_7 + E_8I_8$ (5)

Beam 3: $E_{m3}I_{m3} = E_6I_6 + E_7I_7 + E_8I_8 + E_9I_9$ (6)

Beam 4: $E_{m4}I_{m4} = E_6I_6 + E_7I_7 + E_9I_9$ (7)

Beam 5: $E_{m5}I_{m5} = E_2I_2 + E_5I_5 + E_7I_7 + E_8I_8$ (8)

Beam 6: $E_{m6}I_{m6} = E_2I_2 + E_5I_5 + E_7I_7 + E_9I_9$ (9)

Beam 7: $E_{m7}I_{m7} = E_2I_2 + E_5I_5 + E_6I_6 + E_7I_7 + E_8I_8$ (10)

Beam 8: $E_{m8}I_{m8} = E_2I_2 + E_6I_6 + E_8I_8 + E_9I_9$ (11)

Beam 9: $E_{m9}I_{m9} = E_4I_4 + E_5I_5 + E_7I_7 + E_8I_8$ (12)

where E_{mi} and I_{mi} are the composite beam Young's modulus and moment of inertia of beam i (i = 2, 3, 4, 5, 6, 7, 8, 9). There is a total of eight equations and eight unknowns in the above system of equations. The thickness of gate oxide film was very thin (only 0.08 μm) and therefore was neglected in the calculation.

Test Method

The test sample (0.5 × 0.5 cm^2 die) was mounted on a plastic block using double-sided cellophane tape and placed under the stylus of the Alpha Step profilometer. The Alpha Step is normally used to profile patterned thin films during microfabrication. However, in the technique described here, the Alpha Step is used to mechanically deflect beams with a given force. The Alpha Step is calibrated for step height with two calibration standards, one at 9084 Å and the other one at 452 Å. The calibration standards are measured five to ten times in the same area and a correction factor is programmed in as needed. The calibration is done every six months.

The stylus force was set at 4 mg, the optimum for the various thicknesses of beams. For the thicker beams, the force had to be high enough for the beams to deflect significantly, while for the thinner beams the force had to be below the buckling limit.

A schematic diagram of the stylus loading is shown in Fig. 8. Preceding the fixed end of the beam was a 10 μm wide metal 2 line to provide a reference point in the scan. The stylus scanned the beam from left to right, recording the deflection of the beam as it moved. The procedure was repeated for a 1mg stylus force.

Results

Figure 9 shows typical deflection data for the bending of a composite beam under a 4 mg force. The tip deflection of the beam is very clear. After reaching the tip of the beam, the stylus of the Alpha Step profilometer drops sharply as shown in Fig. 9. The films of this composite beam are gate oxide, metal 1, oxide 2, and overglass. Figure 10 shows the deflection data for the bending of the same composite beam under a 1 mg force. Even with a 1 mg force, the effect of the residual stress gradient is clear—the beam was still bent upward by 1.4 μm. In Fig. 9, the downward deflection of the beam due to a 4 mg force is 4.1 μm. Zero load deflection due to the residual stress gradient was extrapolated from the 1 mg and 4 mg deflection data. This zero load deflection was then added to the 4 mg deflection to get the effective tip deflection of 7.3 μm. Similar deflection data for all the beams are shown in Table 1. Negative deflection data in Table 1 indicate upwardly bent beams.

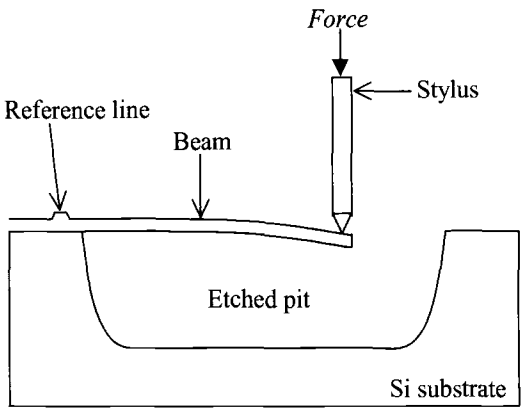

FIG. 8—*Schematic diagram of stylus loading.*

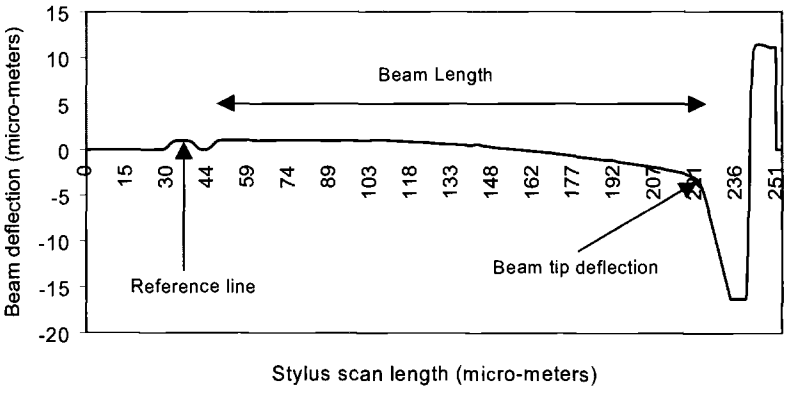

FIG. 9—*Deflection curve of a composite beam at 4 mg force.*

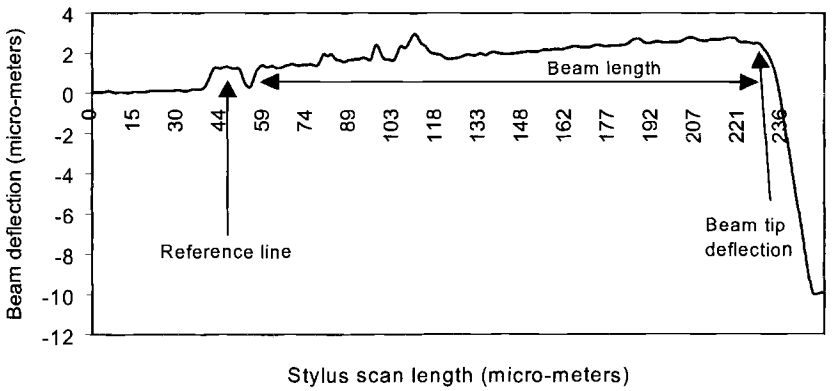

FIG. 10—*Deflection curve of the beam shown in Fig. 9 at 1 mg force.*

Using the force-deflection data from the experiment and the equations mentioned in the "Analysis" section, the Young's moduli of the individual films are calculated. Table 2 shows the values of Young's moduli with uncertainties for the individual films from this experiment along with published values for similar films.

TABLE 1—*Beam deflection data.*

Beam	Deflection 1 mg Load (μm)	Deflection 4 mg Load (μm)	Zero Load Deflection Due to Residual Stress (μm)	Beam Tip Deflection, v (μm)
2	0.3	2.2	-0.3	2.5
3	4.7	7.3	3.8	3.5
4	-1.4	4.1	-3.2	7.3
5	3.2	7.5	1.8	5.7
6	1.5	4.0	0.6	3.4
7	3.5	6.1	2.7	3.4
8	-1.4	1.7	-2.4	4.1
9	3.7	7.9	2.3	5.6

TABLE 2—*Values of Young's Moduli.*

Film	Young's Modulus, E (GPa)	E (Published Literature) (GPa)
Field Oxide	76.6 ± 7.5	73 (bulk) [12] 70 (film) [13]
Poly 1	164.8 ± 16.2	181 (bulk) [14] 160 (film) [15]
Poly 2	172.3 ± 16.9	181 (bulk) [14] 160 (film) [15]
Oxide 1	90.9 ± 8.9	
Metal 1	66.4 ± 6.3	70 (bulk) [16] 74 (film) [16]
Oxide 2	58.7 ± 5.8	
Metal 2	77.3 ± 7.9	70 (bulk) [16] 74 (film) [16]
Overglass	136.3 ± 13.8	

Discussion

The Young's moduli found in this experiment are in good agreement with the published data. In Table 2, agreement is found between the value determined for field oxide and with both bulk [12] data and thermally grown SiO_2 film [13] data. Field oxide is usually a high-quality wet-thermal oxide, and our measurements provide confirmation that AMI is using such a film. The experimental data for poly 1 and poly 2 are also in agreement with the bulk published data [14] and LPCVD polysilicon film data [15], which again confirms that AMI is using a standard film and that our experimental technique is valid. Both metal 1 and metal 2, which are aluminum, are in good agreement with both bulk [16] and sputtered film [16] published data. The interlayer dielectrics (oxide 1 and 2) and the passivation layer (overglass) are proprietary films or combinations of films that may include silicon dioxide, silicon nitride, and oxynitride deposited through a variety of techniques including LPCVD, PECVD, and spin-cast sol-gel. Therefore, it is not possible to compare the experimental data for them with published data for pure films. This proprietary mix is confirmed by the differences between our measurements for the three films and the differences with published values for pure SiO_2 films. However, this proprietary and composite nature was an additional motivation for this study, since without these measurements we could not predict the Young's moduli for these films. From the experiment it is also clear that AMI uses the same process for poly 1 and poly 2 because the difference in experimental data between these two films is only 4.6 %.

The difference between the above experimental data and the published data of Young's modulus could be due to the difference in the AMI process and the exact processes used in the published data, such as the percentage of water used in the wet-thermal oxide. Additional differences can be attributed to experimental errors. The

thicknesses of composite beams and individual films were measured from the SEM photograph of a beam cross-section. In addition to the above measurement, die-to-die thickness variations, thickness variations along the length of the beam, and differences due to overetches on beams with different layer compositions could lead to 0.04 μm or 5.4% error in the beam thickness measurement. During the experiment it was very hard to place the stylus at the center of the beam due to the limitations of the Alpha Step profilometer. There could be some torsional effects on the beam force deflection data if the stylus was not exactly at the centerline of the beam. At 1 mg force the stylus was noisy during the first 35% of its scan path (Fig. 10); this might have contributed some error to the beam deflection data at 1 mg force. The total error in measuring the deflection of each beam was 0.2 μm or 6.4%. In measuring the effective lengths of the beams with the Alpha Step profilometer, a maximum error of up to 1.0 μm or 0.6% was estimated. The error involved in the measurement of widths of beams with the Alpha Step profilometer could be as large as 1.0 μm or 2.0%. The error in the force exerted on the beams was 0.1 mg or 2.5%. Using the Propagation of Uncertainties technique [18], these errors result in uncertainties of 9.5% to 10.2% in the Young's moduli of elasticity of individual films as shown in Table 2.

Conclusion

We have developed a technique that allows us to determine the local Young's moduli of the thin films within a composite stack of CMOS films, without requiring access to the individual layers. The values we determined for the field oxide, polysilicon, and metal layers were in close agreement with published data on similar but isolated pure films. Values were also determined for the proprietary interlayer dielectrics and passivation layers whose compositions are unknown and thus not available in the literature. These results are of use to MEMS designers utilizing CMOS processes since they do not have control over the mechanical properties of the films in the process.

Acknowledgments

The authors would like to thank Professor Jack Judy of UCLA Electrical Engineering Department for providing his Nanolab support.

References

[1] Marshal, J. et al., "Realizing Suspended Structures on Chips Fabricated by CMOS Foundry Processes through The Mosis Service," NISTIR 5402, U.S. National Institute of Standards and Technology, Gaithersburg, MD, June 1994.

[2] Parameswaran, M., Baltes, H. P., Ristic, L., Dhaded, A. C., and Robinson, A. M., "A New Approach for The Fabrication of Micromechanical Structures," *Sensors and Actuators,* Vol. 19, 1989, pp. 289–307.

[3] Petersen, K. E., "Silicon as a Mechanical Material," *IEEE Proceedings*, Vol. 70, No. 5, 1982.

[4] Weihs, T., Hong, S., Bravman, J. C., and Nix, W. D., "Mechanical Deflection of Cantilever Microbeams: A New Technique for Testing the Mechanical Properties of Thin Films," *J. Mater. Res.*, Vol. 3, No. 5, September/October 1988.

[5] Petersen, K. E., Guarnieri, C. R., "Young's Modulus Measurements of Thin Films Using Micromechanics," *Journal of Applied Physics*, Vol. 50, No. 11,

November 1979.
[6] Tai, Y. C. and Muller, R. S., "Integrated Stylus-Force Gage," *Sensors and Actuators*, Vol. A21-A23, 1990, pp. 410–413.
[7] Chu, P. B., Chen, J. T., Yeh, R., Lin, G., Huang, J. C. P., Warneke, B. A., and Pister, K. S. J., "Controlled Pulse-Etching with Xenon Difluoride," *1997 International Conference on Solid State Sensors and Actuators – TRANSDUCERS '97,* Chicago, , 16-19 June 1997, pp. 665–668.
[8] Warneke, B. and Pister, K. S. J., "An Integrated Circuit for the *In Situ* Characterization of CMOS Post-Process Micromachining," *XIII Symposium on Integrated Circuits and System Design (SBCCI 2000),* Manaus, Amazonas, Brazil, 18-24 Sept. 2000.
[9] Tea, N., Milanovic, V., Zincke, C., Suehle, J., Gaitan, M., Zaghloul, M., and Geist, J., "Hybrid Postprocessing Etching for CMOS-Compatible MEMS," *IEEE Journal of Micro-Electromechanical Systems,* Vol. 6, 1997, pp. 363–372.
[10] Craig Jr., R. R., "Mechanics of Materials," 2nd ed. John Wiley & Sons, 2000.
[11] http://www.kla-tencor.com
[12] *Sensors & Actuators*, Vol. 20, No. 1&2, 1989, p. 124.
[13] *Thin Solid Films*, Vol. 283, 1996, p. 15.
[14] *J. Mater Res*, Vol. 12, No. 1, January 1997.
[15] *Sensors & Actuators*, Vol. 20, 1989, p. 138.
[16] *Thin Solid Films*, Vol. 270, 1995, p. 263.
[17] Timoshenko, S. and Woinowsky-Krieger, S., Theory of Plates and Shells, 2nd ed., McGraw-Hill Book Company, 1987.
[18] Taylor, J. R., "An Introduction to Error Analysis," University Science Book, Oxford University Press, 1982, p. 57.

R. Pastorelli,[1] *S. Tarantola,*[2] *M. G. Beghi,*[1] *C. E. Bottani,*[1] *and A. Saltelli*[2]

Derivation of Elastic Properties of Thin Films from Measured Acoustic Velocities

REFERENCE: Pastorelli, R., Tarantola, S., Beghi, M. G., Bottani, C. E., and Saltelli, A., **"Derivation of Elastic Properties of Thin Films from Measured Acoustic Velocities,"** *Mechanical Properties of Structural Films, ASTM STP 1413*, C. Muhlstein and S. B. Brown, Eds., American Society for Testing and Materials, West Conshohocken, PA, Online, Available: www.astm.org/STP/1413/1413_12, 15 June 2001.

ABSTRACT: The dispersion relations of surface acoustic waves (SAWs) of layered structures can be measured by quantitative acoustic microscopy, laser acoustic methods, and surface Brillouin scattering. Since methods are available to compute SAW dispersion relations as functions of material properties (direct problem), material properties can be derived fitting the computed velocities to the measured ones (inverse problem). The stability and robustness of the inverse problem solution for an isotropic supported thin film is studied with an appropriate sensitivity analysis. The elastic constants that mainly determine each branch of the dispersion relations are pinpointed: the constants that are more reliably determined in each range of film properties are thus identified. Simulations allow one to estimate the level of experimental errors, either in SAW velocities or in film density and thickness, which still allow a meaningful solution of the inverse problem.

KEYWORDS: acoustic waves, surface waves, thin films, elastic constants, inverse problem, sensitivity analysis

Introduction

Solids support bulk acoustic waves and surface acoustic waves (SAWs). They are solutions of the elastodynamic equations [1,2], and their velocities can be computed as functions of the elastic properties. Measurements of the velocities of acoustic waves can thus be exploited to derive material properties. In the case of bulk waves in homogeneous media velocities can be expressed in closed form as relatively simple functions of mass density and elastic constants [3]: derivation of the elastic constants from measured velocities and mass density can be rather direct [4]. In the case of SAWs the dependence of velocities on material properties can be non trivial [5]: closed form expressions are generally not available, and velocities are obtained as the outcome of numerical computations. In particular in the case of layered structures formed by homogeneous layers the velocities depends on the mass densities and the elastic constants of all the layers, on the thicknesses of the layers, on wavelength and on the boundary conditions at the interfaces among layers [6]. If the layers are not isotropic velocities further depend on propagation direction. Methods are available to numerically compute the velocities of SAWs in multilayers [7–10], at least in the case of perfect adhesion, well schematized by

[1]INFM and Nuclear Engineering Department, Politecnico di Milano, Via Ponzio 34/3, I-20133 Milano, Italy, marco.beghi@polimi.it

[2]Institute for Systems, Informatics and Safety, EC Joint Research Centre, TP361, I-21020 Ispra (VA), Italy.

continuity of both displacements and stresses across each interface.

SAW velocities can be measured by several methods, including quantitative acoustic microscopy [8,11–13], laser acoustic methods [14–17], interdigital transducers [18,19], and surface Brillouin scattering [20–25]. The methods are different and operate in different frequency ranges, but their outcome can anyhow be put in the form of SAW dispersion relations, i.e., velocity v as function of wavelength or wave vector $q_{\|}$. Measured dispersion relations of SAWs in layered structures can be exploited to derive material properties of the layers, namely their elastic constants, by fitting the computed velocities to the measured ones [8,13–17,19,25–32].

The reliability of results has to be assessed: which elastic constants can be obtained? Which level of measurement accuracy is required? This work addresses these questions. The spectrum of SAWs is recalled first, to better analyze the information contained in their dispersion relations. The data analysis procedure to derive the elastic constants is discussed next. A sensitivity analysis identifies the elastic constants, which are better determined, and simulations give indications on the level of accuracy of velocity measurements, which allows a meaningful derivation of the elastic constants.

The Spectrum of Surface Acoustic Waves

For simplicity, the spectrum is discussed with reference to isotropic materials; indications on the consequences of anisotropy are then given. Materials are characterized by mass density ρ and the elements of the tensor of the elastic constants: in matrix notation, C_{ij}. In isotropic solids all the elastic constants are determined by only two independent quantities, additional quantities being required by anisotropic materials [33]. In a homogeneous solid bulk waves, of wave vector $\mathbf{q}$ and circular frequency ω, are either longitudinal or transverse, their velocities being respectively v_l and v_t. Thermodynamic stability requires that $v_t < v_l$ [1]. In presence of a surface, if the longitudinal direction is parallel to the surface itself the two transverse directions, normal and parallel to the surface, can be distinguished. With a denomination borrowed from geophysics these directions are respectively called shear vertical and shear horizontal; the plane defined by the longitudinal and the shear vertical directions is called the sagittal plane.

At a surface, either an external surface or an interface, translational symmetry is broken in the direction normal to the surface, and SAWs can exist. Such waves travel along the surface, their strain field being confined in the neighborhood of the surface itself [5,6]. They are characterized by the wave vector component parallel to the surface $\mathbf{q}_{\|}$, which is a real quantity, while the component $\mathbf{q}_{\perp}$ orthogonal to the surface has an imaginary part, meaning that the displacement field decays with depth. The velocity parallel to the surface of an acoustic excitation is called here $v_{\|} = \omega/q_{\|}$. Velocities of SAWs are intrinsically parallel velocities, and are simply indicated by v.

The spectrum of acoustic excitations at a free surface is formed by a discrete part and a continuum part, separated by a threshold velocity v_{thr}, the lowest $v_{\|}$ achievable by bulk waves. In an isotropic medium v_{thr} simply coincides with the velocity v_t of a hypothetical transverse bulk wave having a wave vector parallel to the surface (although such a wave cannot exist because it does not satisfy the boundary conditions at the free surface); in an anisotropic medium, its determination can be more involved [34]. At $v_{\|} > v_{\text{thr}}$ the spectrum is a continuum because any such parallel velocity can be achieved by

bulk waves being reflected by the free surface at a proper angle, while at $v_{\|} < v_{thr}$ the elastodynamic equations admit wave solutions only at a discrete set of velocities [2]. These solutions are the proper SAWs. The continuous spectrum for $v_{\|} > v_{thr}$ can also have sharp maxima: they correspond to acoustic modes which are not properly SAWs, but still have a displacement field mainly localized in the neighborhood of the surface and a well defined velocity. Such modes are called pseudo surface waves. In isotropic media SAWs and pseudo surface waves polarized in the shear horizontal direction decouple [7] from those polarized in the sagittal plane, which generally have both longitudinal and shear vertical components.

At the external surface of a thick slab (a bare substrate) a single SAW generally exists, the Rayleigh wave (RW) [5], which has sagittal polarization. It has velocity v_R and a displacement field that penetrates into the medium up to a depth of the order of $2\pi/q_{\|}$. A single pseudo surface wave can also exist: the so-called High Frequency Pseudo Surface Wave (HFPSW), which is also polarized in the sagittal plane. It is also called Longitudinal Resonance (LR) because at the surface it is analogous to a longitudinal wave, of velocity v_l, travelling parallel to the surface. At the interface between two thick layers the Stoneley wave can instead exist, but only for restricted ranges of the elastic properties of the two layers. In thick media the elastodynamic equations and boundary conditions do not depend on any characteristic length: accordingly, velocities do not depend on wavelength or on $q_{\|}$.

When a homogeneous film of thickness h is deposited on the substrate, it modifies the spectrum of SAWs. A discontinuity of material properties is present at the characteristic depth h: accordingly, SAW velocities depend on the ratio of the wavelength to h, i.e., on the product $q_{\|}h$. This is evident in Fig. 1, which shows the dispersion relation for a silica layer on a silicon substrate, computed [6] by literature values of material properties [35,36]. The corresponding power spectra of the displacement components were also computed [7], and are shown in Fig. 2. The threshold velocity v_{thr} is determined by the substrate, in which the displacement field eventually decays. A modified Rayleigh wave (MRW) generally exists, of velocity v_{MRW}. For $q_{\|}h < 1$ the strain field of the MRW extends far beyond the film (see Fig. 2, left) and v_{MRW} approaches the Rayleigh velocity of the substrate $v_R^{(subs)}$, while for $q_{\|}h >> 1$ the strain field of the MRW is essentially confined within the film (see Fig. 2, right) and v_{MRW} approaches the Rayleigh velocity of the film $v_R^{(film)}$. Accordingly, among the supported film structures, a distinction can be made between the slow film cases ($v_R^{(film)} < v_R^{(subs)}$) in which the dispersion relation $v_{MRW}(q_{\|}h)$ is a decreasing function of $q_{\|}h$ (see Fig. 1), and the fast film cases ($v_R^{(film)} > v_R^{(subs)}$) in which the dispersion relation is instead an increasing function.

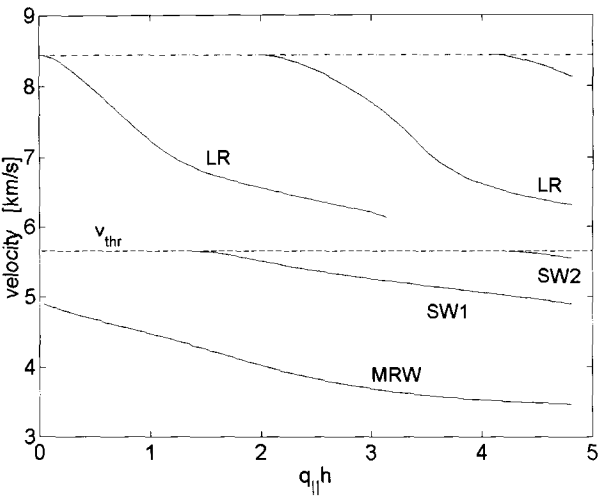

FIG. 1—*Dispersion relations for SAWs in a amorphous silica (SiO_2) layer of thickness h on a crystalline silicon (001) substrate. Propagation along [100] with wavevector $q_{||}$. v_{thr}: threshold velocity; MRW: modified Rayleigh wave; SW1, SW2: Sezawa waves; LR: longitudinal resonance.*

In the fast film case only a modified HFPSW can at most exist, beside the MRW. A slow film can instead act as a waveguide and support guided waves: those polarized in the sagittal plane are called Sezawa waves (SW) [6] and are reminiscent of the Lamb modes of a free standing slab (see Fig. 2). Their velocities v_{SW} are decreasing functions of $q_{||}h$ and lie between v_{MRW} and v_{thr}. As it can be seen from Fig. 1, any SW typically exists only for a finite range of $q_{||}h$. The number of supported SWs is an increasing function of $q_{||}h$ and depends on the difference among the film and substrate properties. It can be seen from Fig. 2 that SWs, as well as the MRW, have both vertical and longitudinal components. Guided waves polarized in the shear horizontal direction can also exist: they are called Love waves [36,37]. Also in the case of a slow film, above v_{thr} a HFPSW can exist, called LR because of its predominant longitudinal polarization (see Fig. 2).

In the case of multilayers the variety of modes increases; if all the layers are isotropic decoupling still occurs between modes polarized in the sagittal plane, still called Sezawa waves, and modes polarized in the shear horizontal direction, still called Love waves. In anisotropic media (crystals), either bare substrates or single layers or multilayers, velocities generally depend on the propagation direction. A distinction can be made between propagation along high symmetry directions and along any other direction.

If the sagittal plane is a plane of mirror reflection symmetry for the whole structure, decoupling still occurs between modes polarized in the sagittal plane and in the shear horizontal direction: most of the above description for the isotropic case remains valid. In the other directions instead all the three polarizations remain coupled, and waves generally have truly three directional displacements.

It can be noted that in acoustic microscopy and in laser acoustic methods, and in Brillouin scattering when the specimen surface is metallic, coupling with the acoustic

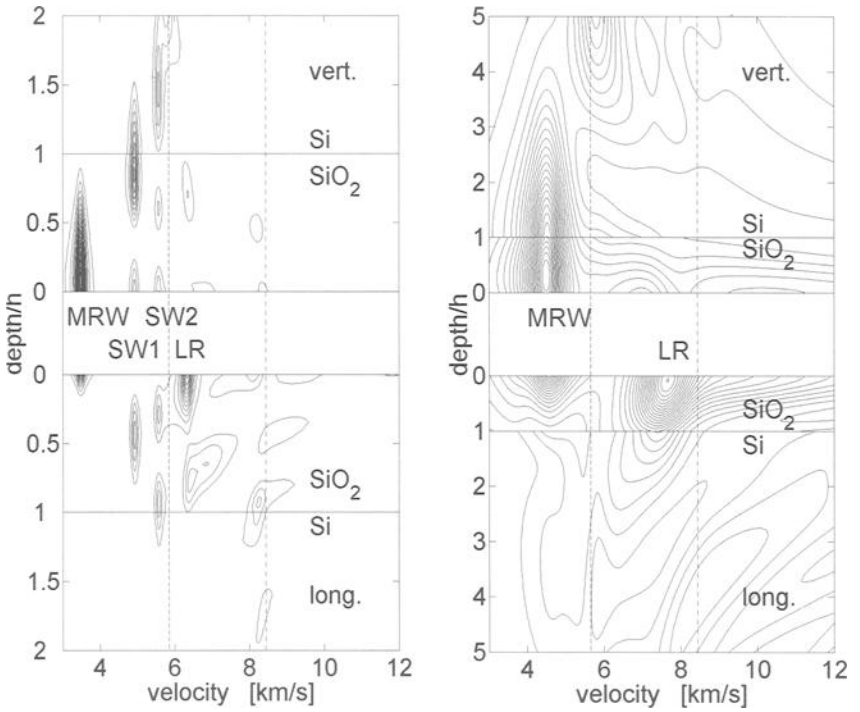

FIG. 2—*Power spectra, functions of velocity and depth, of the longitudinal and vertical displacement components of the SAWs of Fig. 1. Power spectra are represented by their contour lines. Each type of SAW gives a peak in either or both components: velocity and localization of displacement field are thus identified. Left: $q_{||}h = 4.71$; Right: : $q_{||}h = 0.84$. MRW: modified Rayleigh wave; SW1, SW2: Sezawa waves; LR: longitudinal resonance.*

waves occurs only by the ripple effect, the dynamic corrugation of the external surface due to the shear vertical displacement component. The RW, the MRW, and several SWs are thus observable, while all the shear horizontal waves and the waves which, at the external surface, have a mainly longitudinal polarization, such as the HFPSW and some of the SW, remain nonobservable. The latter group of waves can be observed only by Brillouin scattering from transparent or semi-transparent specimens [36,*38*].

Derivation of the Elastic Constants

This work focuses on a specific application: derivation of the elastic constants of a supported monolayer. Perfect adhesion of the film of thickness h is assumed; substrate and film are characterized by their respective mass density and tensor of the elastic constants, $\rho^{(s)}$, $C_{ij}^{(s)}$ and $\rho^{(f)}$, $C_{ij}^{(f)}$. SAW velocities can be computed [*5–10,13,18,21,39–41*] as functions of physical properties, obtaining the computed values $v_c(\rho^{(s)}, C_{ij}^{(s)}, \rho^{(f)}, C_{ij}^{(f)}; q_{||}h)$ (direct problem). These values can be fitted to the values $v_m(q_{||}h)$ measured by

any of the mentioned techniques, obtaining the values of the physical parameters. The amount of information contained in the measured velocities does not allow the derivation of many parameters: the properties of the substrate must be known. Furthermore, other methods like X-ray reflectivity and/or diffractometry, transmission electron microscopy, profilometry, are available to measure film thickness and mass density. Methods to directly measure the elastic constants are instead less available, the methods based on indentation also giving to this purpose rather indirect results. Fitting of the computed velocities to the measured ones can therefore be exploited to derive the film elastic properties, assuming that thickness and density are independently measured.

All the other parameters being known, the velocities for a set of values $q_{||}h^{(j)}$ remain functions of the film elastic properties alone: $v_c^{(j)}(C_{ij}^{(f)})$. If the measured velocities $v_m^{(j)}$ are available with their variances $\sigma_m^{(j)}$ the most probable values of the elastic constants are identified by the minimum of the generalized least squares (GLS) estimator [*31,42,43*]

$$GLS(C_{ij}^{(f)}) = \sum_j \left(\frac{v_c^{(j)}(C_{ij}^{(f)}) - v_m^{(j)}}{\sigma_m^{(j)}} \right)^2 . \qquad (1)$$

Once the most probable values $\overline{C_{ij}}$ are found (the superscript $^{(f)}$ is understood), the normalized *GLS* estimator $GLS(C_{ij})/GLS(\overline{C_{ij}})$ gives, via the F distribution (the Fisher function), the confidence regions at any given confidence level.

The reliability and robustness of these results have to be assessed [*44*], answering the following questions: which is the precision of the results? Can all the elastic constants be found with the same precision? Which precision is required from the various measurements (thickness, density, velocities) to make the derivation meaningfully possible? This work addresses these questions by a case study: an isotropic film on a crystalline silicon substrate, namely the (001) face of a silicon crystal on which velocity is measured for propagation along the [100] crystallographic direction. The MRW is analyzed in detail, because it is present, irrespective of the nature of the film; the information obtainable from the next branch of the dispersion relation, a SW or HFPSW according to the nature of the film, is then assessed.

The question about the precision of the obtained values $\overline{C_{ij}}$ has not a general answer, but has a heuristic answer: as noted above the same normalized GLS estimator identifies the confidence regions, if the variances $\sigma_m^{(j)}$ are correctly evaluated. Experience with different applications, and several simulations, indicates that the achievable precision depends on several factors. The choice of the elastic constant of concern and the quality of velocity measurements, i.e., the $\sigma_m^{(j)}$ values, are the most important ones, and are discussed in the following sections. It must however be remembered that the explored range of $q_{||}h$ also has an influence, since it is often not possible to explore a wide interval of $q_{||}$. If the explored range entirely lies at $q_{||}h < 1$ it is in a region in which the MRW penetrates deeply into the substrate (see Fig. 2, left): its velocity is mainly determined by the substrate and is less sensitive to the film properties. If on the other hand it entirely lies at $q_{||}h \gg 1$ it is in a region in which the MRW hardly reaches the substrate (see Fig. 2, right): the film essentially behaves as a semi-infinite medium and the MRW approaches the film RW. In this case the RW velocity precisely identifies a combination of elastic

constants, but only that combination. A quantitative background is thus given to a perhaps intuitive rule of thumb: when a film of thickness h is involved, the waves most affected by its presence are those having a wavelength comparable with h. This gives a criterion to select the most appropriate measurement technique for any given film thickness.

Sensitivity to the Various Elastic Constants

The various elastic constants are not identified with similar accuracies, due to the fact that the computed velocities are not sensitive to each elastic constant in the same way. In order to evaluate the sensitivity of computed velocities to the various constants, a sensitivity analysis study has been performed. As mentioned above the case of an isotropic film on a crystalline silicon substrate is considered. The results depend on the ratio of the properties of the film to those of the substrate, rather than on the values for each of them. Results are therefore expressed in terms of the ratios, such as $\rho^{(f)}/\rho^{(s)}$, and are thus applicable to any substrate/film combination, except for the fact that they are obtained with a substrate which has the specific cubic anisotropy of silicon. However most of the results provide very clear answers, and it cannot be expected that these answers be modified if the substrate is isotropic or has a cubic anisotropy ratio different from that of silicon. Only substrates with a strong anisotropy and a low symmetry could be expected to introduce significant modifications of the results. An earlier version of this study was performed specifically for surface Brillouin scattering [*45*].

Several parameters are available to characterize the elastic properties of the isotropic film: the elastic constants C_{11} and C_{44}, the Young's modulus E, the shear modulus G (in the isotropic case $G = C_{44}$), the bulk modulus B and the Poisson's ratio ν. In the isotropic case any two of these quantities can be taken as independent and determine all the others. In the anisotropic case the complete characterization requires more independent quantities, and all these parameters become direction dependent. The silicon substrate being cubic, it is fully characterized by a third constant like C_{12}; its E and ν have been computed for the considered propagation direction [100]: $E = 130.5$ GPa and $\nu = 0.278$ [*35*], the mass density being $\rho = 2330$ kg m^{-3}.

An analysis of the relationships among the various quantities for the isotropic case shows that E and G are more closely related and, loosely speaking, are more representative of the behavior under uniaxial states of stress. On the other hand C_{11}, B and ν are also more closely related and more representative of the behavior under triaxial states of stress (despite the way ν is defined). In order to assess the sensitivity to the various parameters it is appropriate to pick one parameter from each group. E and ν are selected, because they often are more directly of interest for the characterization of a material, and because of the simplicity in the definition of the domains of interest. The elastic constants must in fact satisfy thermodynamic stability limits due to the physical requirement that the elastic strain energy be definite positive. In terms of E and ν these requirements simply state that $-1 < \nu < 0.5$; since for practically all the known materials ν is non negative, the interval $0 < \nu < 0.5$ is considered.

The computed velocities v_c are thus considered as functions of $E^{(f)}$ and $\nu^{(f)}$ of the film material. In order to assess the sensitivity to the various elastic constants and to the independently measured quantities, the sensitivity study is performed assuming that the

substrate properties $\rho^{(s)}$, $E^{(s)}$ and $\nu^{(s)}$ are known without uncertainties, as well as the values of $q_{\parallel}$ (determined by the measurement geometry). The film mass density and film thickness instead, being the outcome of independent measurements, are assumed to be affected by uncertainties. The computed velocities are therefore considered as functions of four variables: $v_c = v_c(\rho^{(f)}, E^{(f)}, \nu^{(f)}, h)$ and the sensitivities to each of them are evaluated.

The analysis is performed by the method of Sobol [46,47], which identifies first order sensitivity indices and higher order indices, up to the total sensitivity indices TS(E), TS(ν), TS(ρ) and TS(h) which take into account all the possible interactions among the various parameters. These indices vary between 0 (null sensitivity) and 1 (maximum sensitivity), and it is worth noting that, due to the non linear dependence of the computed v_c on the input parameters and to the possible interactions, the sum of all the TS is not necessarily 1. The analysis is performed picking several regions in the four-dimensional space, chosen as follows: firstly, values of h are taken such that the product $q_{\parallel}h$ is of the order of unity, i.e., the order of magnitude the most appropriate for this kind of derivation. Intervals of $q_{\parallel}h$ are considered such that the ratio of the maximum to the minimum is 3 or less: this is typical amplitude of the interval scanned by surface Brillouin scattering. To the values of h uncertainties are associated as ±5% and ±15%. Five values of $\rho^{(f)}$ are considered: they scan the interval of $\rho^{(f)}/\rho^{(s)}$ from 0.35 to 7.6, which corresponds, for a silicon substrate, to the full meaningful range from 10^3 kg m^{-3} to 18×10^3 kg m^{-3}. Uncertainties are associated to the density values, which are representative of those achievable by X-ray reflectivity measurements [45].

For the elastic constants the whole physically meaningful region of the ($E^{(f)}$, $\nu^{(f)}$) plane is considered: ($0 < E^{(f)} < E_{diamond}$, $0 < \nu^{(f)} < 0.5$); with a silicon substrate this means $0 < E^{(f)}/E^{(s)} < 7.7$ and $0 < \nu^{(f)}/\nu^{(s)} < 1.65$. For each value of $\rho^{(f)}/\rho^{(s)}$ this region is divided in three parts, corresponding to the slow film case, the fast film case and a transition region arising from the uncertainty associated to the density. The three cases are considered separately because they correspond to different shapes of the dispersion relation (see above). For each region the sensitivity indices are computed at 128 points uniformly distributed within the region itself, in order to assess the possible variations of the indices with the physical parameters. The indices turn out to be remarkably stable: in each region nearly all the values computed at the 128 points lie within an interval of ±0.1 around their mean value. Furthermore, the fluctuations around the mean value are essentially random, and do not identify trends correlated with the values of the physical parameters. An example, chosen among those, which exhibit the wider fluctuations, is shown in Fig. 3. It is therefore appropriate to consider only the average values over each region, since they are fully representative of the results throughout the whole region.

A synopsis of the results from the various regions is presented in Fig. 4. The total index TS(E) turns out be always close to one, meaning that sensitivity is always high and the possibility of deriving its value is always good, while the total index TS(ν) is always close to zero, meaning that sensitivity is always low and that a good determination of ν is essentially impossible. Both the total indices TS(ρ) and TS(h) are also low, meaning that the sensitivity to both parameters is low and that a very high accuracy in their determination is not crucial. This was confirmed by the similarity of the results obtained by the two uncertainty levels for h mentioned above, and also by halving the uncertainty

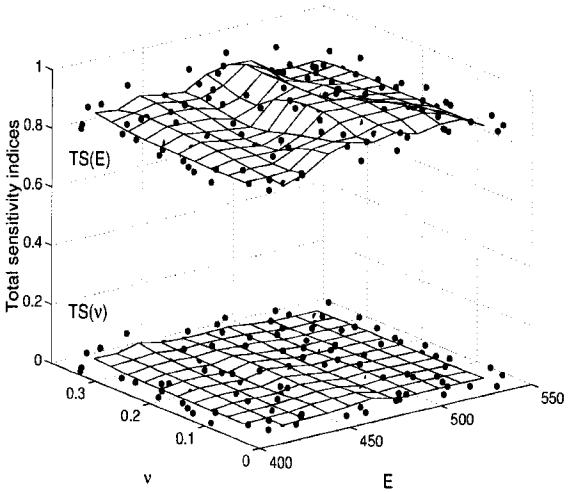

FIG. 3—*Total sensitivity indices TS(E) and TS(ν) evaluated at 128 points in an (E, ν) region, which corresponds in Fig. 4 to the Transition case with density ratio around 2.5. The surfaces are smoothed interpolations of the computed values, only a guide to the eye.*

level for ρ. In particular, the impossibility to obtain a precise value for ν is not due to the uncertainties of ρ and h, but is intrinsically due to the limited dependence of the computed velocities on ν itself. On the other hand, the low sensitivity to ρ and h means that E can always be determined to a reasonable precision, even when density and thickness are not known to a high precision, or when the film thickness is not perfectly uniform, as it easily happens in practice.

The outcome of the sensitivity analysis can be summarized as follows:

1. The dispersion relation of the modified Rayleigh wave (MRW) strongly depends on the film Young modulus E; the shear modulus G being strongly correlated to E, they both can be found. The dependence on ν, B and C_{11} is instead such that they cannot be determined. This conclusion holds true both for films acoustically slower and faster than the substrate.
2. The above conclusion does not depend on film properties, and holds for uncertainties in h and ρ up to at least several percent; better precisions for these parameters do not significantly improve the determination of the elastic constants;
3. The number of velocity measurements improve the determination of the elastic constants because the experimental errors are better averaged out, but the width of the explored interval of $q_{\|}h$ has only a minor influence;
4. If a further branch of the dispersion relation is present and can be measured, beside the MRW, the type of additional information depends on the type of structure. In the slow film case the next branch is a Sezawa wave. This type of wave is not more sensitive to ν and B, and its detection is beneficial only because it provides additional

velocity measurements. In the fast film case instead the only possible additional branch is a HFPSW, or Longitudinal Resonance; the velocity of this type of wave is more sensitive to v and B, and improves the possibility of deriving their values. As already noted this type of wave can be detected only by surface Brillouin scattering.

According to these findings E and G are the two constants which are more likely to be determined. The velocities are therefore computed as $v_c(\rho^{(f)}, E^{(f)}, G^{(f)}, h)$ and the *GLS* estimator (Eq 1) is accordingly defined, obtaining results in the (E,G) plane.

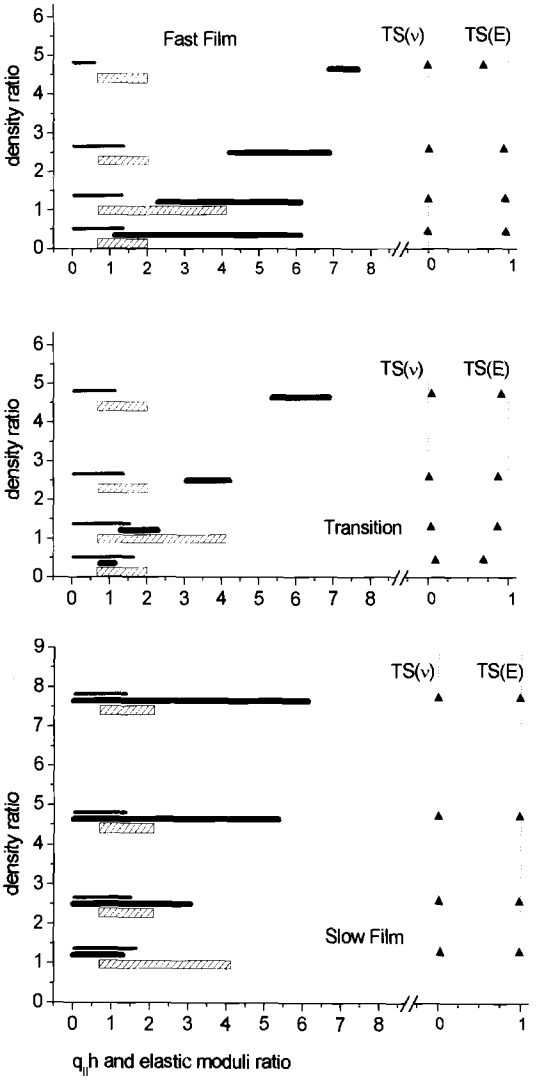

FIG. 4—*Total Sensitivity Indexes TS(v) and TS(E) for Poisson's ratio and Young's modulus evaluated for several Fast Film, Transition and Slow Film cases. For each density ratio interval the intervals of Young's modulus ratio (thick line) and Poisson's coefficient ratio (thin line) are shown. The considered intervals of $q_{||}h$ (dashed bar) are also shown.*

Effects of Velocity Measurement Precision

It has been shown that the derivation of the elastic constants is best performed in the (E,G) plane. It has been found that an extreme accuracy in the measurement of film thickness and mass density is obviously beneficial but is not crucial. The question remains to be answered on the accuracy required to the measured velocities $v_m^{(j)}$ (see Eq 1). This requirement has been explored by simulations. For a given (E,G) couple the velocities $v_c^{(j)}$ are computed; pseudo experimental velocities are obtained perturbing the $v_c^{(j)}$ values by values picked at random from normal distributions of predetermined variance; the (E,G) are then found exploiting these perturbed values as "measured" velocities $v_m^{(j)}$.

One of the simulations, fully representative of the results obtained by many simulations performed around various nominal layer properties, is shown in Figs. 5 and 6. This one involves a hypothetical heavy and stiff layer, having properties comparable to those of a very heavy ceramic layer, namely $\rho^{(f)} = 11 \times 10^3$ kg m^{-3}, $E^{(f)} = 450$ GPa and $G^{(f)} = 200$ GPa, i.e., $\rho^{(f)}/\rho^{(s)} = 4.72$, $E^{(f)}/E^{(s)} = 3.45$ and $\nu^{(f)}/\nu^{(s)} = 0.45$. The computed dispersion relation is shown in Fig. 5, together with two sets of pseudo experimental velocities obtained by samplings from normal distributions having variances of 0.5% (case (a), smaller perturbation) and 1.6% (case (b), larger perturbation), respectively. Derivation of the (E,G) couple by the first set of pseudo experimental data gives $E^{(f)} = 454$ GPa and $G^{(f)} = 196$ GPa with the confidence region of Fig. 6*a*); derivation by the second set gives $E^{(f)} = 460$ GPa and $G^{(f)} = 174$ GPa with the confidence region of Fig. 6*b*). The dispersion relations computed by these two couples of values are also shown in Fig. 5.

The following comments can be made. Firstly, results are always better represented by the two-dimensional confidence region, which only gives a precise evaluation of the uncertainty. Limits like e.g. $E^{(f)} = (454\ ^{+10}_{-20})$ GPa and $G^{(f)} = (196 \pm 20)$ GPa could be given, but they do not discriminate between confidence regions of rectangular or non rectangular shapes. Secondly, in case a) the confidence region encompasses a limited area, is closed well within the thermodynamic stability region $G > E/3$ and only marginally extends in the region $G > E/2$ corresponding to $\nu < 0$. To most purposes the determination of (E,G) of Fig. 6a) can be considered as a good determination. The case of Fig. 6*b*) gives instead an (E,G) couple which is more shifted from the original one and, more importantly, a confidence region that becomes very wide, would extend in the thermodynamic instability region $G < E/3$ and widely extends in the region $G > E/2$. E and G remain poorly determined, and more meaningful results can be obtained only considering additional physical knowledge, like e.g. considering only the part of the confidence region which satisfies the condition $E/3 < G < E/2$ [*42*].

The above example is fully representative of many other simulations. A threshold cannot be given, because the width of the confidence regions is a smoothly increasing function of the uncertainty of the measured velocities, but a guideline, valid in most cases, can be given in the following terms. If the inaccuracy of the measured velocities remains of the order of 0.5% a good determination of E and G is generally possible, while when the inaccuracy exceeds 1% the determination becomes poor or impossible. The results of the sensitivity analysis of the previous section are confirmed by the fact that

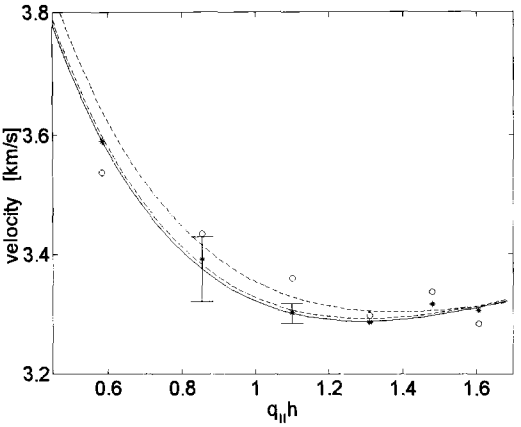

FIG. 5—*Computed dispersion relation of the MRW (continuous line) for a sample case (see text) and pseudo experimental dispersion relations obtained perturbing the computed values by a smaller (*, case (a)) and a larger (o, case (b)) amount. Dispersion relations computed in both cases by the values obtained by the best fit procedure (dashed lines).*

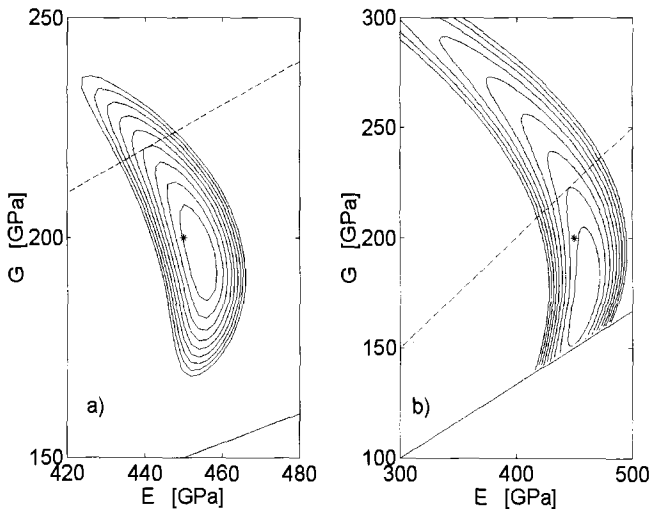

FIG. 6—*Isolevel curves at equispaced values of the GLS estimator (Eq 1) obtained from the pseudo experimental dispersion relations of Fig. 5, with the smaller (a) and the larger (b) perturbation. The outermost curve is the 90% confidence region. The thermodynamic stability limit G = E/3 corresponding to ν = 0.5 (continuos lines) and the line G = E/2 corresponding to ν = 0 (dashed lines) are shown.*

even when E and G are well determined the corresponding confidence region can encompass a wide interval of values of either ν or B, due to their gradients in the (E,G) plane.

Conclusions

The velocities of surface acoustic waves of layered structures can be measured by various experimental techniques and can be exploited to derive the elastic properties of supported films. The elastic constants can be derived if the film thickness and mass density are independently measured. Derivation is based on the computation of velocities predicted with given values of the physical parameters, and on fitting of the computed velocities to the measured ones. The data analysis procedure is assessed in detail, with reference to an isotropic layer on a crystalline silicon substrate, by simulations and a sensitivity analysis. The most appropriate wavelength interval is that for which $q_{\|}h$ is of the order of unity.

It is found that measuring the dispersion relation of the modified Rayleigh wave Young's modulus and shear modulus can be determined, while Poisson's ratio and bulk modulus remain essentially undetermined. The latter can be determined only in the fast film case and if the longitudinal resonance can be detected. It is also found that uncertainties of few percent in the measurements of thickness and density do not prevent the derivation of the above moduli. The velocity measurements must have an accuracy of the order of 0.5% to allow a meaningful derivation of the elastic moduli; inaccuracies above 1% generally prevent a good determination of the moduli. Surface Brillouin scattering achieves a sufficient accuracy if measurements are carefully conducted [48,49].

In the considered case study these conclusions are well established for wide ranges of film properties; they are expected to hold true also in cases with not too different symmetry, like an isotropic substrate. In principle the methodology can be extended to more complex structures, like anisotropic crystalline films or multilayered structures, like buried films. Extension implies a higher number of independent variables.

References

[1] Landau L. D. and Lifshitz E. M., *Theory of Elasticity*, Pergamon Press, Oxford, 1970.

[2] Cemal Eringen A. and Suhubi E. S., *Elastodynamics, Vol. 2*, Academic Press, New York, 1975.

[3] Every, A. G., "General Closed-Form Expressions for Acoustic Waves in Elastically Anisotropic Solids," *Physical Review B*, Vol. 22, 1980, pp. 1746–1760.

[4] Vacher, R. and Boyer, L., "Brillouin Scattering: A tool for the Measurement of Elastic and Photoelastic Constants," *Physical Review B,* Vol. 6, 1972, pp. 639–673.

[5] Farnell, G. W., "Properties of Elastic Surface Waves," *Physical Acoustics*, Vol. 6, W. P. Mason and R. N. Thurston, Eds., Academic Press, New York, 1970, pp. 109–166.

[6] Farnell, G. W. and Adler, E. L., "Elastic Wave Propagation in Thin Layers," *Physical Acoustics*, Vol. 9, W. P. Mason and R. N. Thurston, Eds., Academic Press, New York, 1972, pp. 35–127.

[7] Cottam, M. G. and Maradudin, A. A., "Surface Linear Response Functions," *Surface Excitations*, V. M. Agranovitch and R. Loudon, Eds., Elsevier Science

Publishers, Amsterdam, 1984, pp. 1–194.

[8] Kim, J. O., Achenbach, J. D., Mirkarimi, P. B., Shinn, M. and Barnett, S. A., "Elastic Constants of Single Crystal Transition-Metal Nitride Films Measured by Line-Focus Acoustic Microscopy," *Journal of Applied Physics,* Vol. 72, 1992, pp. 1805–1811.

[9] Garcia-Moliner, F. and Velasco, V. R., "Surface Green Function Matching," *Surface science,* Vol. 299/300, 1993, pp. 332–345.

[10] Perez-Alvarez R., Garcia-Moliner F., and Velasco V. R., "Simultaneous Surface Green Function Matching for N Interfaces," *Journal of Physics: Condensed Matter*, Vol. 7, 1995, pp. 2037–2049.

[11] Kim, J. O. and Achenbach, J. D., "Line Focus Acoustic Microscopy To Measure Anisotropic Acoustic Properties of Thin Films," *Thin Solid Films,* Vol. 214, pp. 25–34, 1992.

[12] Atalar, A., Koymen, H., Bozkurt, A., and Yaralioglu, G., "Lens Geometries For Quantitative Acoustic Microscopy," *Advances in Acoustic Microscopy*, A. Briggs Ed., Plenum Press, New York, 1995, pp.117–151.

[13] Sklar, Z., Mutti, P., Stoodley, N. C., and Briggs, G. A. D., "Measuring The Elastic Properties of Stressed Materials by Quantitative Acoustic Microscopy," *Advances in acoustic microscopy*, A. Briggs, Ed., Plenum Press, New York, 1995, pp.209–247.

[14] Neubrand, A. and Hess, P., "Laser Generation and Detection of Surface Acoustic Waves: Elastic Properties Of Surface Layers," *Journal of Applied Physics,* Vol. 71, 1992, pp. 227–238.

[15] Schneider, D., Schwarz, Th., Scheibe, H. J., and Panzner M., "Non Destructive Evaluation of Diamond and Diamond-Like Carbon Films by Laser Induced Surface Acoustic Waves," *Thin Solid Films,* Vol. 295, 1997, pp. 107–116.

[16] Schneider, D., Witke, Th., Schwarz, Th., Schöneich, B., and Schultrich, B., "Testing Ultra-Thin Films by Laser Acoustics," *Surface and Coatings Technology,* Vol. 126, 2000, pp. 136–141.

[17] Whitfield, M. D., Audic, B., Flannery, C. M., Kehoe, L. P., Crean, G. M., and Jackman, R. B., "Characterization of Acoustic Lamb Wave Propagation in Polycrystalline Diamond Films by Laser Ultrasonics," *Journal of Applied Physics,* Vol. 88, 2000, pp. 2984–2993.

[18] Nakahata, H., Hachigo, A., Higaki, K., Fujii, S., Shikata, S. and Fujimori, N., "Theoretical Study on Saw Characteristics of Layered Structures Including a Diamond Layer," *IEEE Transactions on Ultrasonics, Ferroelectrics and Frequency Control,* Vol. 42, 1995, pp. 362–375.

[19] Kim, J. Y., Chung, H. J., Kim, H. J., Cho, H. M., Yang, H. K., and Park, J. C., "Surface Acoustic Wave Propagation Properties of Nitrogenated Diamond-Like Carbon Films," *Journal of Vacuum Science and Technology,* Vol. A18, 2000, pp. 1993–1997.

[20] Sandercock, J. R., "Trends in Brillouin Scattering,", *Light Scattering in solids III*, M. Cardona and G. Güntherodt, Eds., Springer, Berlin, 1982, pp. 173–206.

[21] Stegeman, G. I and Nizzoli, F., "Surface Vibrations," *Surface Excitations*, V. M Agranovitch and R. Loudon, Eds..Elsevier Science Publishers, Amsterdam, 1984, pp. 195–378.

[22] Nizzoli, F. and Sandercock, J. R., "Surface Brillouin Scattering from Phonons," *Dynamical Properties of Solids*, G. K. Horton and A. A. Maradudin, Eds.,Vol. 6, Elsevier Science Publishers B.V., Amsterdam, 1990, pp. 281–335.

[23] Mutti, P., Bottani, C. E., Ghislotti, G., Beghi, M., Briggs, G. A. D., and Sandercock, J. R., "Surface Brillouin Scattering—Extending Surface Wave Measurements to 20 GHz," *Advances in Acoustic Microscopy*, A. Briggs, Ed., Plenum Press, New York, 1995, pp. 249–300.

[24] Grimsditch, M., "Brillouin Scattering," *Handbook of Elastic Properties of Solids,*

Liquids and Gases, Vol. 1, M. Levy, H. Bass, R. Stern, and V. Keppens, Eds., Academic Press/Harcourt Publishers Ltd., Sidcup, UK, 2000.

[25] Comins, J. D., "Surface Brillouin Scattering," *Handbook of elastic properties of Solids, Liquids and Gases, Vol. 1,* M. Levy, H. Bass, R. Stern and V. Keppens, Eds., Academic Press/Harcourt Publishers Ltd., Sidcup, UK, 2000.

[26] Lee, S., Hillebrands, B., Stegeman, G. I, Cheng, H., Potts, J. E. and Nizzoli, F., "Elastic Properties of Epitaxial ZnSe(001) Films on GaAs Measured by Brillouin Spectroscopy," *Journal of Applied Physics,* Vol. 63, 1988, pp. 1914–1916.

[27] Karanikas, J. M., Sooryakumar, R., and Phillips, J. M., "Dispersion of Elastic Waves in Supported CaF_2 Films," *Journal of Applied Physics*, Vol. 65, 1989, pp. 3407–3410.

[28] Carlotti, G., Fioretto, D., Palmieri, L., Socino, G., Verdini, L. and Verona, E., "Brillouin Scattering by Surface Acoustic Modes for Elastic Characterization of ZnO Films," *IEEE Transactions on Ultrasonics, Ferroelectrics, and Frequency Control*, Vol. 38,1991, pp. 56–60.

[29] Mirkarimi, P. B., Shinn, M., Barnett, S. A., Kumar, S., and Grimsditch, M., "Elastic Properties of TiN/(V_xNb_{1-x})N Superlattices Measured by Brillouin Scattering," *Journal of Applied Physics*, Vol. 71, 1992, pp. 4955–4958.

[30] Xia, H., Zhang, W., Qu, X. X., Zhang, J., Jiang, J. G., and Zhang, R., "Brillouin Scattering Determination of the Elastic Constants in Supported Ge Films," P*hysica Status Solidi (a),* Vol. 140, 1993, pp. 429–437.

[31] Makarov, S., Chilla, E., and Frölich, H. J., "Determination of Elastic Constants of Thin Films from Phase Velocity Dispersion of Different Surface Acoustic Wave Modes," *Journal of Applied Physics,* Vol. 78, 1995, pp. 5028–5034.

[32] Ferrari, A. C., Robertson, J., Beghi, M. G., Bottani, C. E., Ferulano, R., and Pastorelli, R., "Elastic Constants of Tetrahedral Amorphous Carbon Thin Films," *Applied Physics Letters,* Vol. 75, 1999, pp. 1893–1895.

[33] Nye, J. F., *Physical Properties of Crystals*, Oxford University Press, London, 1972.

[34] Zhang, X., Comins, J. D., Every, A. G., Stoddart, P. R., Pang, W., and Derry, T. E., "Surface Brillouin Scattering Study of the Surface Excitations in Amorphous Silicon Layers Produced by Ion Bombardment," *Physical Review B*, Vol. 58, 1998, pp. 13677–13685.

[35] McSkimin, H. J. and Andreatch, P., "Elastic Moduli of Silicon vs. Hydrostatic Pressure at 25.0 °C and –195.8°C," *Journal of Applied Physics,* Vol. 35, 1964, pp. 2161–2165.

[36] Ghislotti, G. and Bottani, C. E., "Brillouin Scattering from Shear Horizontal Surface Phonons in Silicon on Insulator Structures: Theory and Experiment," *Physical Review B*, Vol. 50, 1994, pp. 12131–12137.

[37] Bouden, M. and Datta, S. K., "Rayleigh and Love Waves in Cladded Anisotropic Medium," *Transactions of the ASME—Journal of Applied Mechanics*, Vol. 57, 1990, pp. 398–403.

[38] Chirita, M., Sooryakumar, R., Xia, H., Monteiro, O. R., and Brown, I. G., "Observation of Guided Longitudinal Acoustic Modes in Hard Supported Layers," *Physical Review B*, Vol. 60, 1999, pp. R5153–5156.

[39] Hardouin Duparc, O., Sanz-Velasco, E. and Velasco, V. R., "Elastic Surface Waves in Crystals with Overlayers: Cubic Symmetry," *Physical Review B*, Vol. 30, 1984, pp. 2042–2048.

[40] Byloos, C., Giovannini, L., and Nizzoli, F., "Theory of the Elasto-Optic Coupling for Surface Brillouin Scattering in a Supported Bilayer," *Physical Review B*, Vol. 51, 1995, pp. 9867–9874.

[41] Bria, D., El Boudouti, E. H., Nougaoui, A., Djafari-Rouhani, B. and Velasco, V. R., "Localized and Resonant Guided Elastic Waves in an Adsorbed Layer on a Semi-Infinite Superlattice," *Physical Review B*, Vol. 61, 2000, pp. 15858–15865.

[42] Beghi, M. G., Bottani, C. E., and Pastorelli, R., "High Accuracy Measurement of Elastic Constants of Thin Films by Surface Brillouin Scattering," *Mechanical Properties of Structural Films, ASTM STP 1413*, C. Muhlstein and S. B. Brown, Eds., American Society for Testing and Materials, West Conshohocken, PA, 2001.

[43] Pastorelli, R., Ferulano, R., Beghi, M. G., and Bottani, C. E., "About the Reliability of the Elastic Constants of Thin Supported Films Derived from Surface Brillouin Scattering Data," to be published.

[44] Nizzoli, F., Bhadra, R., de Lima, O. F., Brodsky, M. B., and Grimsditch, M., "Problems with the Determination of Elastic Constants from Higher Order Surface Waves: Results for Al on NaCl," *Physical Review B*, Vol. 37, 1988, pp. 1007–1010.

[45] Pastorelli, R., Tarantola, S., Beghi, M. G., Bottani, C. E., and Saltelli, A., "Design of Surface Brillouin Scattering Experiments by Sensitivity Analysis," *Surface Science*, Vol. 468, 2000, pp. 37–50.

[46] Saltelli, A., Tarantola, S., and Chan, K. P. S., "A Quantitative Model-Independent Method for Global Sensitivity Analysis of Model Output," *Technometrics*, Vol. 41, 1999, pp. 39–56.

[47] Chan, K., Tarantola, S., Saltelli, A., and Sobol, I. M., "Variance-Based Methods," *Sensitivity Analysis*, A. Saltelli, K. Chan, and E. M. Scott, Eds., John Wiley & Sons, Chichester, UK, Probability and Statistics Series, 2000.

[48] Stoddart, P. R., Crowhurst, J. C., Every, A. G. and Comins, J. D, "Measurement Precision in Surface Brillouin Scattering," *Journal of the Optical Society of America B,* Vol. 15, 1998, pp. 2481–2489.

[49] Beghi, M. G., Bottani, C. E., and Pastorelli, R., "Accuracy of Surface Acoustic Wave Velocity Measurements by Surface Brillouin Scattering," submitted for publication, 2000.

Nathan D. Masters,[1,2] *Maarten P. de Boer,*[1] *Brian D. Jensen,*[1,3] *Michael S. Baker,*[1] *and David Koester*[4]

Side-by-Side Comparison of Passive MEMS Strain Test Structures under Residual Compression

REFERENCE: Masters, N. D., de Boer, M. P., Jensen, B. D., Baker, M. S., and Koester, D., "**Side-by-Side Comparison of Passive MEMS Residual Strain Test Structures under Residual Compression,**" *Mechanical Properties of Structural Films, STP 1413,* S. B. Brown and C. L. Muhlstein, Eds., American Society for Testing and Materials, West Conshohocken, PA, Online, Available: www.astm.org/STP/1413/1413_23, 15 September 2001.

ABSTRACT: Knowledge and control of residual strain is critical for device design in MEMS, and therefore it is important to establish standards for residual strain measurement. In this study, pointer, microring, bent-beam, and fixed-fixed beam test structures are used to evaluate residual strain both theoretically and experimentally. An equation that enables easier evaluation of bent-beam structures is derived. Also, a finite difference model that incorporates the non-idealities of fixed-fixed beams and determines an optimum fit to the measured deflection curve is presented. The model allows accurate residual strain evaluation of each buckled fixed-fixed beam. Experimentally, pointer structures were found to be susceptible to adhesion. Microrings, intended for residual tension assessment, also could not be evaluated because the residual strain was compressive. Bent-beam and fixed-fixed beams could both be evaluated. The main criterion for test structure effectiveness was taken to be the repeatability of residual strain on structures in close proximity; each should exhibit the same value. Using optical microscopy, the residual strain of bent-beams was determined with $\pm$ 13 $\mu\varepsilon$ repeatability based on standard deviation of adjacent structures of similar design. Using optical interferometry, the residual strain of fixed-fixed beams was determined with $\pm$ 2 $\mu\varepsilon$ repeatability based on standard deviation for adjacent beams of different lengths. The strain values obtained from the two structures are in reasonably good agreement. Cantilevers were also evaluated to obtain film curvature values.

KEYWORDS: residual strain, MEMS test structures, bent-beams, microrings, pointers, fixed-fixed beams, cantilevers, optical metrology

Introduction

Polycrystalline silicon (polysilicon), used in integrated circuits and Microelectromechanical Systems (MEMS), is commonly deposited by chemical vapor deposition. Residual strain in polysilicon thin films is a result of the interactions of many factors that may be present during deposition, including thermal environments, dopants, impurities, and grain coalescence, orientation and growth, and surface as well as interfacial stress [1-6]. Because of the importance of residual strain in mechanical design and as a measure of fabrication control, many techniques and structures have been

[1] Sandia National Laboratories, PO Box 5800, Albuquerque, NM 87185, www.mdl.sandia.gov/Micromachine

[2] current address – Mechanical Eng. Dept., Brigham Young University, Provo, UT 84602.

[3] current address – Mech. Eng. Dept., University of Michigan, Ann Arbor, MI 48109-2125.

[4] Cronos Integrated Microsystems, 3026 Cornwallis Rd., Research Triangle Park, NC 27709.

suggested for residual strain measurements. However, it remains difficult to quantify strain to a known accuracy. Further, it is not known whether various laboratories will measure the same value even on the same structures. Usually, low residual strain is desired for device designs, leading to test structure designs that must be highly compliant to enable strain evaluation. Depending on the test structure design, this can lead to adhesion (i.e., stiction) or out-of-plane buckling that can render the test structures ineffective.

To address these issues, a round robin evaluation of test structures was organized and sponsored by the American Society of Testing and Materials (ASTM) Task Group E08.05.03. The intent of the study was to use passive structures that have been previously proposed and that could be easily analyzed. Pointers [7], bent-beams [8,9] microrings [10], and fixed-fixed beams [11-14] were chosen. Cantilevers [15,16] were also studied to obtain stress gradient information. In this paper, we report on the analysis of the test structures made by our group at Sandia National Laboratories. One other group has analyzed its results [17].

To decide how to measure and analyze the test structures, we made the following two considerations. First, nondestructive testing is important for round robin testing, and is also important in general to MEMS. Second, because residual strain can vary across a wafer, from wafer to wafer, and from lot to lot, it is important to quickly yet accurately assess residual strain values. Our analysis criteria are as follows:

1) The metrology is only by optical methods.
2) Only two-dimensional deflections and analyses are considered.

The first criterion allows for rapid and noncontacting measurements. While scanning electron microscopy (SEM) metrology enables higher resolution for in-plane measurements, we ruled it out as being too expensive and time consuming for routine metrology. Also, any concern that electrostatic charging may induce test structure deflection during the measurement is alleviated. Furthermore, for out-of-plane measurements, optical interferometry is more sensitive than SEM and is well calibrated. The second criterion is in keeping with most of the literature, and reflects our interest in keeping the analysis as simple as reasonably possible.

Given these criteria, our assessment of the test structures is based on addressing the following questions in the Discussion section:

1) How well are the critical deflections measured?
2) To what degree do the test structure deflections reflect the 2-D analysis?
3) How repeatable are the measurements on similar structures in close proximity?
4) What are the area requirements?
5) How long does it take to determine the strain value?

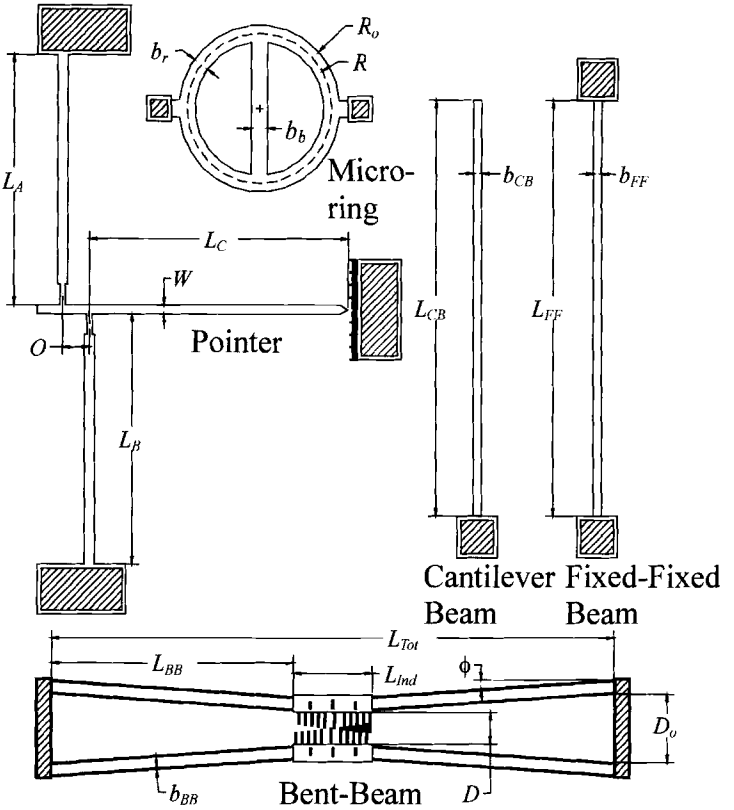

FIG. 1—*Test structures used for residual strain evaluation (top views).*

Test Structures and Analysis

The test structures we studied are shown schematically in Fig. 1. Critical geometric parameters for each device are indicated. We present the results of the two-dimensional mechanics analyses in this section. The equations are derived in Appendices A-D. For the pointers (Appendix A) and the microrings (Appendix C), literature references have been used. For the bent-beams (Appendix B), we introduce a new derivation that is simpler to use than previous literature references and applies for the strain range examined here. For idealized fixed-fixed beams (Appendix D), Euler buckling theory is used for first order modeling. This is appropriate because the test structures were under residual compression. Our approach for 2-D finite difference modeling incorporating the effects of boundary compliance in fixed-fixed beam structures is also outlined in this section. Cantilevers, also shown in Fig. 1, are used to measure curvature (allowing the stress gradient to be deduced), and are described in this section along with the fixed-fixed beams.

The analysis for several of the test structures (pointers, microrings, and rigidly supported fixed-fixed beams) can be carried out without knowledge of Young's modulus, E. However, the analyses for bent-beam sensors and the 2-D finite difference model for

the buckled fixed-fixed beams require E to be known. We will report the uniaxial residual strain ε_R of these devices assuming $E = 165$ GPa [18]. Uniaxial residual stress σ_R can be calculated from $\sigma_R = E\varepsilon_R$ (the loading condition of fixed-fixed beams is within 1% of plane stress conditions [19] - therefore no adjustment to E is made).

In Table 1, we compare the various structures from the point of view of test structure principle, area consumed, typical resolution and strain range, assumed limitations, layout dimensions and comments on the analyses. The test structures can be separated into two main families according to the primary measurement technique used to extract the residual strain value: in-plane (pointers and bent-beams) and out-of-plane (microrings and fixed-fixed beams). The area information in Table 1 is for all the structures on a given level of polysilicon, and the number of associated residual strain measurements is given as well. In making strain resolution comparisons, we assume a 0.5 μm (± 0.25 μm) deflection resolution for in-plane devices, and a 10 nm (± 5 nm) resolution for the out-of-plane measurements. These values stem from the limitations of the brightfield and interferometry optical techniques, respectively. The resolution values reflect the uncertainty in strain measurements due to metrology only. Because these structures are fabricated side-by-side, we obtain information on the relative accuracy of structures in a given family. For absolute accuracy, sensitivity to film thickness, line width, boundary conditions, and 3-D deflections would also have to be considered. Each test structure in Table 1 is discussed next.

Pointers

Pointers are in-plane test structures that make use of geometric layout to amplify small displacements induced by residual strain (compressive or tensile). The amplified output of the pointer indicator, y, is measured on a scale attached to the substrate [7]. The support beam lengths, L_A and L_B, are typically identical. Increasing the length of L_C or decreasing the separation distance O will enhance the amplification effect. Displacement readings at the pointer end are used to calculate the residual strain levels. The analysis in Ref 7, which is repeated in Appendix A, assumes an ideal geometric relationship between residual strain and the displacement of the indicator, augmented by a correction factor, C_F, derived from finite element models of the devices, resulting in Eq 1,

$$\varepsilon_R = \frac{Oy}{(L_A + L_B)(L_C + O/2)} \frac{1}{C_F}. \tag{1}$$

The area of pointers is relatively large at ~1 mm^2 per test structure. The resolution is 40 με, assuming an optical resolution of light microscopy of 0.5 μm (±0.25 μm), and dimensions of a studied device ($L_A = L_B = 490$ μm, $L_C = 575$ μm, $W = 20$ μm, $O = 20$ μm and $C_F = 0.425$). Three pointers were used here with O ranging from 20 μm to 60 μm. We determined the values of C_F for the geometries used here from finite-element analysis over a range of ± 3000 με. Pointers are capable of measuring compressive and tensile residual strain for negative (left) and positive (right) indicator values, respectively. In keeping with the 2-D analysis, the possibilities of buckling across the $L_A + L_B$ support arms, adhesion to the substrate and strain gradient along the pointer length (which may cause the tip to contact the substrate) are not considered.

TABLE 1—*Theoretical and practical residual strain test structure comparisons.*

	Pointers	Bent-beams	Microrings	F-F Beams
Principal of Structure	Geometric amplification	Geometric amplification	Conversion of tension to buckling	Buckling deflections converted into strain value
Area[5] (# of devices, # of measurements per poly level)	3.2 mm^2 (3,3)	1.35 mm^2 (6,6)	2.9 mm^2 (14,1)	1.0 mm^2 (5,5)
Resolution (με)	40 (O = 20 μm) 99 (O = 60 μm)	12.5 (L_{BB} = 300 μm, ϕ = 33.3 mrad) 5 (L_{BB} = 500 μm, ϕ = 20 mrad)	50	0.7 (L_{FF} = 596 μm, A=2 μm)
Range (με) (see text)	±3000	-312 to +235 (L_{BB} = 300 μm) -112 to +84 (L_{BB} = 500 μm)	+250 to +900	-15 to -6765
Assumed Limitations	±0.25 μm optical resolution 2-D modeling	±0.25 μm optical resolution 2-D modeling	Discrete measurement 2-D modeling	±5 nm interferometric resolution 2-D modeling
Layout Dimensions of Test Structures in the Class (see Fig. 1)	$L_A = L_B$ = 490 μm W = 20 μm O = 20 μm (C_F = 0.425), O = 40 μm (C_F = 0.530), O = 60 μm (C_F = 0.539), (with L_C = 585, 575, and 565 μm, respectively)	b_{bb} = 2 μm D = 38.5 μm L_{Ind} = 98 μm ϕ = 33.3, 66.7 and 135.4 mrad (L_{BB} = 300 μm) ϕ = 20.0, 20.0** and 79.5 mrad (L_{BB} = 500 μm)	b_r = 25 μm b_b = 10 μm R_0 varies from 97 to 900 μm	L_{FF} = 196 μm, 396 μm, 596 μm, 796 μm, and 996 μm b = 18 μm
Comments on Test Structure Modeling	Treats the device as a rigid body mechanism (ignoring elastic deformation). A correction is then made for bending. Out-of-plane deflections and boundary compliance are ignored. Applies to tension and compression.	Ignores out-of-plane deflections and boundary compliance. Applies to tension and compression.	Boundary compliance modeled but not measured. Tensile measurements only.	Reflects the 2-D flexures. Includes boundary compliance and strain gradients. Tensile residual strain can be measured using active techniques.

[5] Area measurements based on representative arrangement of devices on a given structural level: Pointers: Three pointers; Bent-beams: Six bent-beams (**for L_{BB} = 500 um, two bent-beams have ϕ = 20 mrad); Microrings: array of 14 rings with radii from 97 to 900 μm; Fixed-fixed beams: array of five fixed-fixed beams (connected to 100 × 100 μm^2 actuation pads).

Bent-Beams

Bent-beams also take advantage of geometric layout to amplify in-plane displacements induced by residual strain [8,9]. We develop in Appendix B a linear solution. The displacement, δ, of the indicators on freestanding structures is measured and the residual strain level is then computed from

$$\varepsilon_R = \delta \frac{\left[\frac{wt\,L_{BB}^3 \sin\phi}{\cos^4\phi} + \frac{12 I_{yy} L_{BB}}{\sin\phi} + \frac{6 I_{yy} L_{Ind}}{\sin\phi\cos\phi}\right]}{\left[(2L_{BB} + L_{Ind})\left(\frac{wt\,L_{BB}^3}{\cos^3\phi} - \frac{12 I_{yy} L_{BB}}{\cos\phi}\right)\right]}, \tag{2}$$

where L is the support beam span and L_{Ind} is the length of the indicator. For the double beam geometry in this study, $wt = 2(b_{BB}t)$ is the support cross sectional area and $I_{yy} = 2\left(t b_{BB}^3/12\right)$ is the in-plane moment of inertia. Also, ϕ is the support beam angle defined as $\phi = \arctan[(D_0 - D)/2L_{BB}]$, as indicated in Fig. 1. Our derivation for Eq 2 is distinct from those in Refs 8 and 9. It considers the residual strain in both the indicators and the supporting beams using Castigliano's theorem[6]. Equation 2 is accurate at low $|\varepsilon_R|$ values and is independent of E. Importantly, it is more quickly applied than the approaches in Refs 8 and 9. Also, the effect of L_{Ind}, not considered in Refs 8 and 9, is accounted for here. However, nonlinear effects, important at high $|\varepsilon_R|$ values as detailed in Ref 8, are not considered. In Fig. 2, we quantitatively compare the three cases for a specific geometry.

The area of bent-beams is small at ~0.23 mm^2 per structure. The resolution is 12.5 με assuming an optical resolution of light microscopy of 0.5 μm (±0.25 μm), and a layout representative of the studied devices (L_{BB} = 300 μm, ϕ = 33.3 mrad, $b_{bb} = t$ = 2 μm and L_{Ind} = 98 μm). The strain range is defined as shown in Fig. 2. At high residual strain values (ε_R < -313 με, ε_R > 235 με, based on 10% deviation in deflection from Ref 8), Eq 2 loses accuracy. However, this is beyond the acceptable strain level of many MEMS processes. It should be noted that for the layout dimensions considered in Fig. 2, the deflection range of the device is ±10 μm. If Eq 2 were used over this range, the accuracy would remain within 30%. Bent-beam incremental sensitivity over the entire range of the structure has been discussed in detail [8]. Five geometrical variations were used here, with ϕ = 33.3, 66.7 and 135.4 mrad (L_{BB} = 300 μm), and ϕ = 20.0, 20.0 and 79.5 mrad (L_{BB} = 500 μm). We note that two structures with ϕ = 20.0 mrad at L_{BB} = 500 μm were laid out.

---

[6] Castigliano's theorem is an energy method for determining the elastic deflection of a system. It requires that deflections be linear and elastic. As such the strain energy, U, stored in the system may be computed as the area under the load-deflection curve (which will be a triangle). The deflection of the system can then be found by differentiating the strain energy with respect to a load, P, acting in line with the deflection direction of interest $\Delta = \partial U/\partial P$ (in many cases this is accomplished by virtual loads). This method works for axial, bending, transverse shear, and torsional loading. See for example Ref 20.

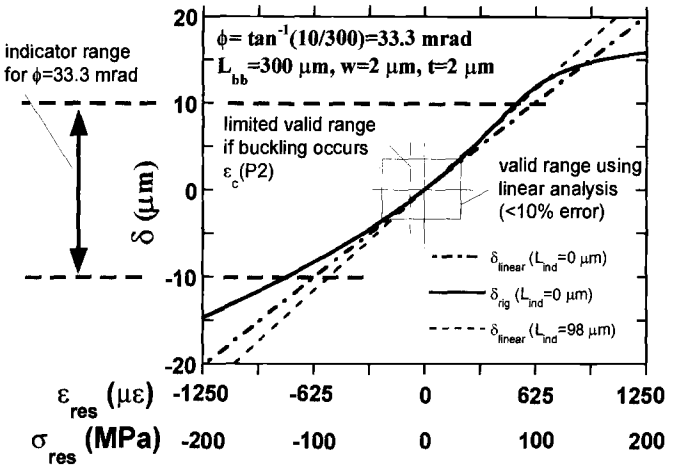

FIG. 2—*Comparison between rigorous analysis by Gianchandani (δ_{rig}) to linearized analysis from Appendix B (δ_{linear}) with L_{ind}=0 and L_{ind} = 98 μm.*

Bent-beams are capable of measuring compressive and tensile residual strain, indicating compression by a decrease in the distance between the indicators and tension by an increase. Resolution depends on layout geometry. If resolution at low stress values is desired, then L_{BB} must be large. However, this increases the proclivity of the structure to buckle out-of-plane. For example, if the thickness of the layer is less than the width b_{BB}, the effective strain range is reduced to –45 με, as indicated in Fig. 2 for the Poly2 layer, for which t = 1.46 μm (see experimental section). Figure 2 is discussed in more detail in Appendix B.

Microrings

Microrings are passive devices proposed by Guckel to measure tensile residual strain [10]. As shown in Fig. 1, a circular ring anchored at two diametrically opposite positions converts tensile residual strain into compressive strain in a crossbeam that is orthogonal to the ring anchors. Ranges (rather than precise measurements) of residual strain levels are determined by observing the transition from unbuckled to buckled crossbeams. The residual strain for the structures is

$$\varepsilon_R = \frac{\varepsilon_{cr}}{g(R)}, \tag{3}$$

where ε_{cr} is the critical strain needed to buckle the crossbeam and $g(R)$ is the conversion efficiency of tensile strain in the ring into compressive strain in the crossbeam. As briefly reviewed in Appendix C, Guckel et al.'s analytical model of the microring derives the effect of the ring to beam width ratio, b_r / b_b, and R on $g(R)$ using Castigliano's method [10]. Also, the effect of boundary rotation on ε_{cr} is determined. For thin films, the

normal mode of buckling is out-of-plane. If brightfield microscopy is used, detection of buckling requires focal plane adjustments. Interferometry is a more sensitive technique for detecting buckling. As suggested in Ref [7], a critically-buckled test structure is established when the crossbeam center deflection is ~0.6t, where t is the film thickness.

The area occupied to obtain a single measurement from microrings is large—2.9 mm^2. To determine the strain resolution and the range over which residual strain can be measured, Drieënhuizen et al. [7] showed that the number of buckling structures required is

$$N_{\min} = \frac{\log(\varepsilon_{\max} / \varepsilon_{\min})}{\log(1+r)} - 1, \tag{4}$$

where N_{min} is the minimum number of structures, ε_{max} and ε_{min} are the upper and lower limit of the desired range of study, and r is the resolution (in percent) of the measurement. Using this equation we can determine that 40 microrings would be required for a range of 10-500 με with a resolution of 10% of the range. In this study, 14 microrings of various sizes were distributed in each level of polysilicon, with a designed resolution of approximately 50 με over a range from 250 to 900 με tensile.

The microring is in reality a three-dimensional structure. It was demonstrated by 3-D finite element analysis that for small values of b_r, post-release microring shortening in the beam direction versus the constraining direction increases the critical strain for buckling [21]. Also, increasing the length of the connection supporting the ring decreases the critical strain [21]. Further, the strain gradient has been identified as affecting the flexures of the microring [22], meaning that the entire shape and not only the crossbeam flexures must be measured in order to correctly interpret the structure. We note that interferometric measurements integrated with 3-D modeling could be applied to reduce the required number of microrings. The technique would be similar to but more complicated than that used with cantilever and fixed-fixed beams covered in the next section.

Fixed-Fixed Beams

Fixed-fixed beams have been used as passive structures for compressive strain measurement by detecting buckling in an array of beams similar to the measurements of microrings [7,10,11,23]. However, the amplitude is sensitive to residual stress in the film, and this allows each buckled beam to be used for residual strain measurement. From Euler buckling theory as in Appendix D, residual strain for each buckled beam is determined from

$$\varepsilon_R = \frac{\pi^2}{L_{FF}^2}\left(\frac{A^2}{4} + \frac{t^2}{3}\right), \tag{5}$$

where A is the amplitude of the buckling deflection, L_{FF} is the beam length and t is the beam thickness. The shape will be sinusoidal according to

$$z(x) = \frac{A}{2}\left(1 + \cos\frac{2\pi x}{L_{FF}}\right), \quad -L_{FF}/2 \le x \le L_{FF}/2. \tag{6}$$

The area of fixed-fixed-beams is small at ~0.20 mm^2 per structure. Considering that A can be measured very well by interferometry, Eq 5 is very accurate for

$$L_{FF} > \approx 1.1\, L_{cr} = 1.1\, \pi t / \sqrt{3\varepsilon_R}\,, \tag{7}$$

where L_{cr} is the critical buckling length, as discussed in Appendix D. From Eq 6, the approximate strain resolution is

$$\Delta\varepsilon_R = 5.2 \frac{\Delta A \cdot A}{L_{FF}^2}, \tag{8}$$

where ΔA = 10 nm is the amplitude uncertainty. For example, with ΔA = 10 nm, L_{FF} = 596 μm, and A = 2 μm, a value of $\Delta\varepsilon_R$ = 0.7 με (± 0.35 με) is calculated. A lower limit to the strain range of 15 με can be estimated from Eq 5 using values of t = 2 μm, A = 0.05 μm (minimum detected amplitude) and L_{FF} = 996 μm. Likewise, an upper range of 6765 με can be approximated using values of t = 2 μm, A = 10 μm and L_{FF} = 196 μm (upper limit of small-slopes assumption in Appendix D). Five beams of lengths from 196 μm to 996 μm in 200 μm increments were used in the layout. Fixed-fixed beams may also be tested electrostatically, allowing extension to the case of residual tension [12-14,24].

The modeling in Appendix D does not take into account non-idealities such as boundary compliance, unloaded beam takeoff angle or strain gradient. To more accurately extract the residual strain, we can compare the full deflection curve (rather than just the amplitude) with a two-dimensional finite difference model (FDM). The FDM incorporates these non-idealities. We have applied it to the case of electrostatically actuated cantilevers [16] and fixed-fixed beams [13,14,24], and apply it in this paper to the case of passively buckled beams. Figure 3*a* schematically represents the FDM. The beam is discretized into elements having the material and cross section properties of the beam. Using the Bernoulli-Euler equation, deflections are calculated by performing the numeric integrals of successive loading, moment, and angular deflection profiles.

As shown in Fig. 1, cantilevers of dimensions similar to the fixed-fixed beams were also placed on the test chip. Unloaded cantilevers contain curvature information, and their deflection curve is closely approximated by

$$z(x) = \theta_o x + \kappa\, x^2 / 2\,, \tag{10}$$

where x is the position along the beam beginning at the support post. Our procedure to accurately determine unloaded beam takeoff angle θ_o and film curvature κ (due to strain gradient through the thickness of the film) from interferometric data has been described in Ref 16. Knowing κ from the cantilever beam, the internal moment due to strain gradient M_i is assigned according to

$$M_i = -E\, I\, \kappa\,. \tag{11}$$

Figure 3*b* shows the support post model used in the FDM. Loaded beam takeoff angle θ is different from θ_o in a cantilever due to the moment in the buckled beam at the support post. The contributions to θ are from θ_o, the moment due to buckling and M_i.

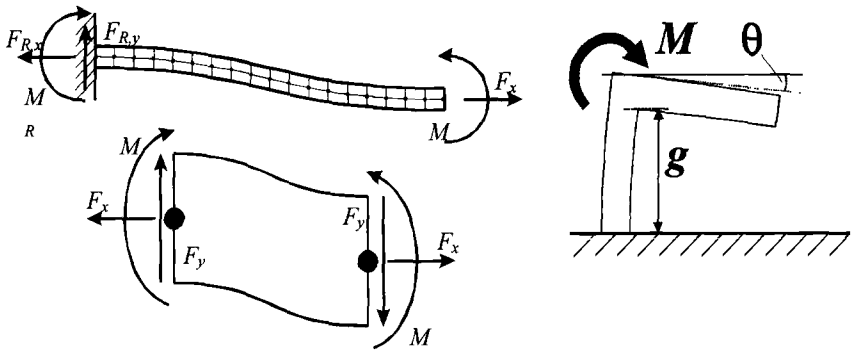

(a) Finite difference model diagram (b) Support post model

FIG. 3—*Finite difference model and support post model diagrams.*

The FDM for the case of passively buckled fixed-fixed beams was first compared and shown to agree with Eqs 5 and 6 for rigid boundaries. It also showed excellent agreement with analytical theory that describes the pre- ($|\varepsilon_R| < |\varepsilon_{cr}|$), transition ($|\varepsilon_R| \sim |\varepsilon_{cr}|$) and post buckling ($|\varepsilon_R| > |\varepsilon_{cr}|$) regimes for compliant boundaries [25], as shown in Fig. 4. Finally, as described in Ref 26, negative θ_o (cantilever takeoff angle is down) induces downward buckling, while negative strain gradient (cantilever curves down) induces upward buckling. The FDM also agrees with these predictions. These checks validate that the FDM appropriately handles the buckled beam mechanics.

When evaluating deflection curve data in our FDM implementation, θ and ε_R are simultaneously iterated upon in an optimization routine that minimizes the error between the modeled and measured deflection curve. Torsional compliance exerts a measurable effect on the deflection curve. Therefore, unlike Ref 25, this approach does not require finite element analysis of the boundaries conditions as input to the model, because the effect of the boundaries is taken into account by the optimization routine. The analysis here includes only the torsional compliance and not the axial compliance of the boundaries. However, for the beams analyzed in the experimental section, the effect of M on support post flexures is much larger than that of axial force P.

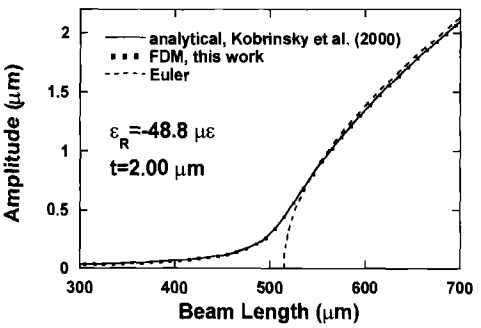

FIG. 4—*Using the same boundary conditions, FDM agrees with analytical model for buckling of fixed-fixed beams.*

Experimental

The test structures were processed as part of the Multi-User MEMS Processes (MUMPs™) MUMPS28 fabrication lot. Utilizing conventional surface micromachining technology, MUMPS provides three structural layers of polysilicon. Each of the test structures described above was fabricated side-by-side on a single test chip in the Poly1, Poly2, and Poly1/2 laminate structural layers. The nominal thicknesses of the layers are 2.0, 1.5, and 3.5 μm, respectively, and were measured at $t = 2.00$, 1.46, and 3.45 μm using profilometry [27]. The minimum allowable line width for structural layers is 2.0 μm. Typical etch profiles are 88-90°, and typical line width loss from the mask drawing is 0 to 0.2 μm.

The structures were released from the sacrificial oxide layers using an HF acid etch. To minimize stiction, supercritical carbon dioxide drying [28] was applied. After processing, the chips were placed on an adhesive, covered, and sent first to Sandia National Laboratories for analysis. The test structures were fabricated both over a Poly0 ground plane, and over nitride. We report the results of the former only, as they were less susceptible to adhesion (stiction) problems. Our group then sent parts to the next laboratory, which performed its testing, and the round robin continued sequentially. The evaluation period was from February to May, 1999, and a meeting was held in Seattle, Washington in May of 1999 to discuss results of the round robin.

All in-plane deflections were measured using high magnification bright field microscopy (100X objective, NA = 0.9). Magnification will depend on the focus used for each test structure. To minimize variation, the same operator focused and recorded all of the images. Optical micrographs were recorded on a CCD camera. With integrated circuit fabrication techniques, the pitch (linewidth and space) is well known. In-plane calibration was achieved by counting the pixels between Poly0 lines of 20 μm pitch. Transitions in intensity at line edges were used to determine the edge locations. For the 100X objective, a 60 μm length corresponded to 470 pixels, yielding a calibration factor of 0.128 μm/pixel.

Out-of-plane deflections were measured by interferometry (5X objective, NA = 0.09). As shown in Fig. 5, Michelson interferometry with green light of wavelength $\lambda = 546$ nm (obtained from an interference filter of 4 nm linewidth (HWFM) as characterized by spectrum photometry) was chosen because polysilicon is only weakly transmissive at this wavelength. This eliminates confusion with substrate reflections that arise in multi-wavelength interferometry techniques. Interferometry allows rapid acquisition of qualitative and quantitative out-of-plane deflection data (see Figs. 6–10). Interference patterns result from a difference in phase between the light reflected from the wafer and the reference surface. The resulting image is a superposition of the test structure and the interference pattern with fringes representing contour lines of the out-of-plane deflection. The direction of out-of-plane deflection (up or down) is determined by adjusting the focus and observing the direction of fringe movement. Images were captured on the CCD camera for further analysis. Linescans along the length of the structures are recorded. Each fringe in the interference pattern indicates a deflection of 1/2 wavelength, or 273 nm. Pixel by pixel out-of-plane deflections are extracted by interpolating linescan intensity data. The out-of-plane resolution of this technique is

better than 10 nm/pixel. In-plane pixel length calibration was achieved by measuring a structure of known length, with accuracy of about 1 pixel in 200.

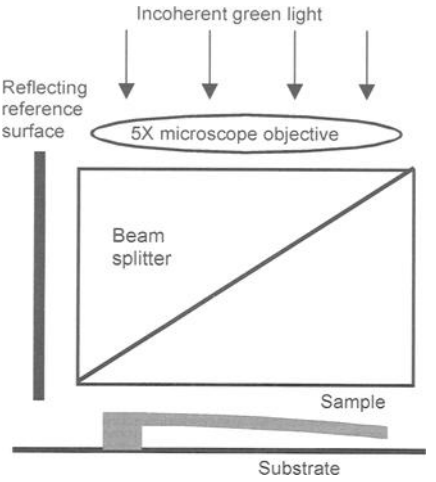

FIG. 5—*Schematic of interferometric microscope.*

TABLE 2—*Qualitative assessment from interferometry.*

Test structure	Poly1 Layer	Poly2 Layer	Poly1/2 Layer	Further Study?
Pointers	Adhered (Fig. 6)	Adhered	Adhered	No: adhered
Bent-beams	L_{BB} = 300 μm: free L_{BB} = 500 μm: free minimal out-of-plane deflections	L_{BB} = 300 μm: buckled up ~two fringes L_{BB} = 500 μm: two adhered, one buckled up ~three fringes (Fig. 7)	L_{BB} = 300 μm: free L_{BB} = 500 μm: free minimal out-of-plane deflections	*Yes*: evaluate effect of buckling for P2 structures
Micro-rings	No flexures apparent: compression (Fig. 8)	Flexures in crossbeams and rings due to stress gradient (Fig. 8)	Not attached to substrate. Not properly anchored	*No*: incompatible stress state
Canti-levers	L_{CB} = 196 μm: bending down L_{CB} = 396-996 μm: tip contacting (Fig. 9)	L_{CB} = 196 μm: bending down L_{CB} = 396 μm: tip contacting L_{CB} = 596-996 μm: long section adhered	L_{CB} = 196-596 and 996 μm: bending down L_{CB} = 796 μm: tip contacting (adhesion)	*Yes*: curvature measurement
Fixed-fixed Beams	L_{FF} = 196, 396 μm: flat L_{FF} = 596, 996 μm: buckled up L_{FF} = 796 μm adhered	L_{FF} = 196 μm: buckled up ~½ fringe (Fig. 10) L_{FF} = 396-996 μm: buckled up many fringes (Fig. 10)	196-796 μm: flat, 996 μm: buckled up ~1 fringe	*Yes*

For this single image/wavelength technique, quantitative analysis of interferograms (as applied here to the fixed-fixed and cantilever beams) requires that at least one half-fringe be available, that continuous structures be used to avoid phase problems, and that tilt adjustments of the reference surface setting the background fringes parallel to the structures be made. Although the interferometry yields high resolution z-deflection data, x and z-offsets must be determined. The interferometric data near the support post is noisy because of rapid changes in topography. Therefore, linescan data usually begins about 5 to 10 pixels away from the beam. By measuring the first pixel used relative to the support post and knowing the calibration factor, the x-offset can be adjusted within ±2 pixels. Because the interferometric data does not begin at the support post, the z-offset must also be determined. This is done by comparing the interferometric data to the model data, and assigning an optimum offset for a given model calculation at the first measured pixel.

Results

Qualitative Evaluation

Qualitative results are summarized in Table 2 and are discussed in this section. Interferometry was first used to evaluate any out-of-plane deflections that might affect the accuracy of the analyses. Pointer structures were plagued by adhesion to the substrate as seen in Fig. 6. The closely spaced fringes near the supports followed by a uniform section with very little contrast indicate that the devices are adhered to the substrate. All pointer structures were affected in a similar manner. A previous study has shown that valid measurements can be obtained from pointer structures adhered in their stress-relaxed position [29]. However, for the low residual strain values observed here, it is difficult to determine the relative contribution to deflections from adhesive forces versus residual strain forces. Therefore, the pointer structures were deemed unusable for further study.

Bent-beam structures fabricated in the Poly2 level are shown in Fig. 7. On the left side of the image where the $L_{BB} = 300$ μm long structures reside, a few fringes are visible on the support beams, indicative of small out-of-plane deflections. The deflections are away from the substrate (up). However, on the right side of Fig. 7 where the $L_{BB} = 500$ μm long bent-beams are located, more severe out-of-plane distortions are observed on the lower two bent-beams. These deflections are downwards. The structures were adhered to the substrate and therefore these two were not evaluated. The top bent-beam on the right hand side of Fig. 7 is not contacting the substrate, but is buckled up slightly. The bent-beams in the Poly1 and Poly1/2 levels were freely suspended and exhibited small out-of-plane deflections, and they were deemed appropriate for further analysis.

Figure 8 shows microrings in both Poly1 and Poly2. No out-of-plane flexures are observed for the Poly1 microrings, indicating that this layer is either in compression or low tension. Note that both the rings and the crossbeam exhibit roughly equal flexure for the Poly2 level. Both are bending down from a centerline defined by the clamps, which is a manifestation of the strain gradient-induced curvature of the films [22]. This is an excellent example of why it is necessary to consider not only residual strain but also strain gradient when evaluating the microrings. Without the complementary information

from the cantilevers and fixed-fixed beams below, we may have incorrectly inferred that the crossbeams were buckled and that the residual strain in the Poly2 level was tensile. In fact, a tensile state would only be indicated by significantly different out-of-plane flexures for the crossbeam compared to the ring. The Poly1/2 level microrings were not properly anchored to the substrate, and therefore could not be assessed.

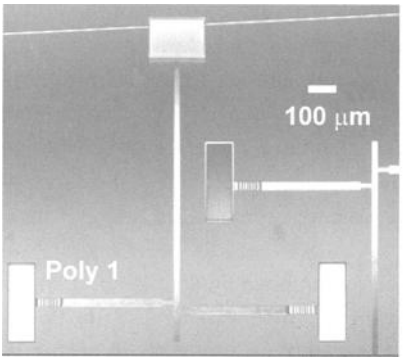

FIG. 6—*Interferogram of adhered pointers in Poly1.*

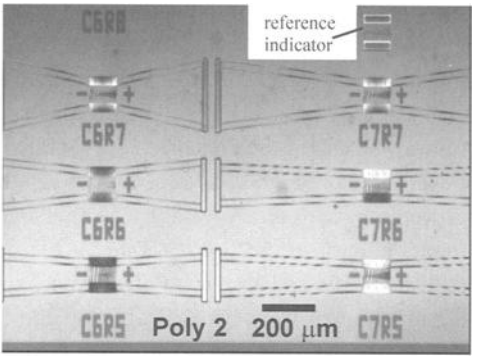

FIG. 7—*Inteferogram of Poly2 bent beams. L_{BB} = 300 μm show buckling (left), and L_{BB} = 500 μm are adhered (lower and middle right).*

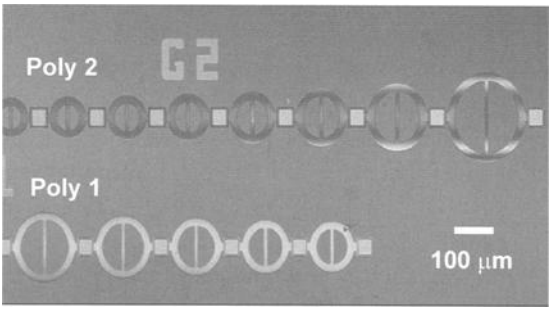

FIG. 8—*Interferogram of microrings. Poly2 exhibits a large stress gradient.*

An array of Poly1 cantilevers is shown in Fig. 9. From the shortest cantilever (196 μm), it is clear that the curvature is significant. This cantilever was determined to be bending down. Longer cantilevers were contacting the substrate at their tips because of the large curvature. For the longest cantilever (996 μm), the substrate imposes an upward force at the tip of the beam that causes its initial deflection beginning at the support post to be upwards. The Poly2 layer exhibited greater out-of-plane deflection than the Poly1 layer, with beams bending down again, and only the shortest cantilever was free. On the other hand, the Poly1/2 laminate exhibited small curvature, and even the 996 μm beam did not contact the substrate. For all layers, free cantilever beams bent down. The cantilever beams were deemed appropriate for obtaining curvature information. However, for the Poly1 and Poly2 layers, data could only be extracted from the shortest cantilever, while for the Poly1/2 layer only the longest cantilever exhibited enough fringe information for quantification.

Short (196 and 396 μm) Poly1 fixed-fixed beams exhibited no deflection. Longer (596 and 996 μm) were buckled out-of-plane (upwards). However, the 796 μm Poly1 fixed-fixed beam was adhered to the substrate. A set of Poly2 fixed-fixed beams is shown in Fig. 10, where it can be seen that increasing beam lengths exhibit more fringes. The deflections were upwards, implying the beams were compressively buckled. For the Poly1/2 laminate, all beams were free, but only the longest beam (996 μm) exhibited a slight upward out-of-plane flexure. Nonadhered, buckled fixed-fixed structures were deemed appropriate for quantitative analysis. From the observed buckling, all layers are in compression.

Quantitative Evaluation

The qualitative evaluation leads us to eliminate pointers and microrings from further evaluation, leaving one in-plane and one out-of-plane test structure for further study. Summaries of the quantitative analyses are found in Table 3 and in Fig. 11, and are discussed in this section.

Bent-beams—The separation between reference indicators fixed to the substrate

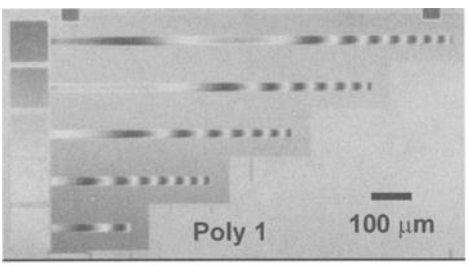

FIG. 9—*Interferogram of Poly1 cantilevers. Except for the shortest, all are contacting the substrate at their tips.*

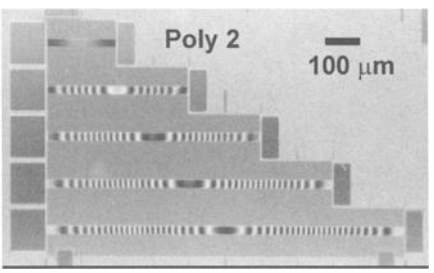

FIG. 10—*Interferogram of buckled Poly2 fixed-fixed beams.*

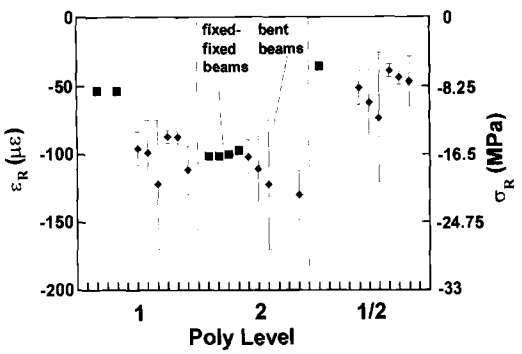

Sample calculation for bent-beams:
Poly 1 level

L_{BB}= 300 μm, L_{ind}= 98 μm,
ϕ=33.3 mrad,
$I_{yy}=2(wt^3/12)=2(2\cdot2^3/12)=2.666$ μm^4
$wt=2(b_{BB}t)=2(2\cdot2)=8$ μm^2
(2 supports),
δ =(285-300) pixels·0.127 μm/pixel
= -1.91 μm.

Inserting into Eq. (2) yields
ε_R = -95 με

For δ=-1.91 +/- 0.25 μm,
ε_R = -83, -108 με

FIG. 11 - *Scattergram of fixed-fixed (squares) and bent-beam (diamonds) results.*
Fixed-fixed beams: left to right lengths are 996, 796, 596 & 396 μm. Missing data indicates that beams were adhered or not buckled per Table 2 (error bars due to uncertainty in metrology are insignificant).
Bent-beams: left to right L_{BB}=300 μm, increasing ϕ, L_{BB}=500 μm increasing ϕ (error bars due to uncertainty in metrology included). Missing data (Poly2) indicates that bent beams were adhered.

(see Fig. 7) was first measured in pixels. Then, the separation between suspended indicators of the bent-beam structure was measured. The difference was multiplied by the calibration factor, and Eq 2 was used to calculate residual strain values. A sample calculation is adjacent to Fig. 11. In Fig. 11, we plot the values of residual strain for each poly level. The error bars indicate error for ±0.25 μm measurement resolution. For larger L_{BB} and smaller ϕ, the error bars are smaller. The average and standard deviation of residual strain for each poly level is shown in Table 3.

Cantilevers—In Fig. 12, best model fits to the cantilever deflections are shown, along with the deflection data from the interferometry. The Poly1/2 level is the flattest layer, and Poly2 is the layer with the greatest curvature. Agreement between model and data is better than 4 nm/pixel. Results for κ and θ_o are tabulated in Table 3. From contour plots in (κ, θ_o) space that evaluate the difference between the measured and model deflections [16], we can evaluate the confidence regime of the κ and θ_o values. To 95% confidence, the values of θ_o are accurate within ±50 μrad (implying that θ_o is different from 0), while the values of κ are accurate within ±2 m^{-1} for Poly1 and Poly2, and within ± 0.2 m^{-1} for Poly1/2. Note that the magnitude of θ_o correlates reasonably well with stress gradient ($E\kappa$), and as we shall see next, with ε_R. This is in agreement with observations in Ref 15.

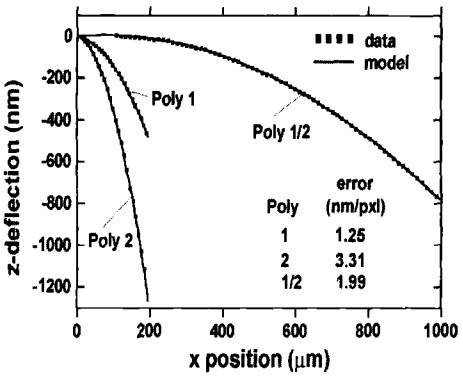

FIG. 12—*Measured and modeled deflections of cantilevers.*

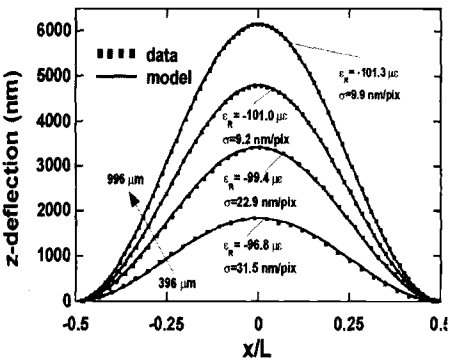

FIG. 13—*Poly2 deflections for 396, 596, 796, 996 μm long buckled fixed-fixed beams. σ is the error per pixel.*

Fixed-Fixed Beams—Using the finite difference model described in Section 2.4, and including the values of strain gradient determined for cantilevers, best fits to the measured deflection curves were found and associated ε_R values were calculated. Four different beam lengths are shown in Fig. 13 for the Poly2 fixed-fixed beams. The larger errors per pixel between modeled and measured data (10–30 nm/pixel) compared to the cantilevers are mainly due to a small offset in the measured heights of the two ends. This is likely not real, and can be reduced by making a linear correction to the data. Such a correction would affect the values of ε_R by less than 2%. For Poly1, the critical buckling length is $L_{cr} = \pi t / \sqrt{3|\varepsilon_R|} = 499$ μm ($|\varepsilon_R| = 52.9$ με and $t = 2.0$ μm). Therefore, the 996 and 596 μm Poly1 fixed-fixed beams were also in the post buckled state (the 796 μm Poly1 fixed-fixed beam was adhered to the substate), consistent with L_{cr}. For Poly2, $L_{cr} = 265$ μm ($|\varepsilon_R| = 100$ με, with $t = 1.46$ μm). Therefore, the fixed-fixed Poly2 beams of Figs. 10 and 13 are also in the post buckling regime (the 196 μm beam is in a pre-buckled state, $L_{FF} < L_{cr}$, and did not present enough fringe information for analysis). The Poly1/2 996 μm fixed-fixed beam was only weakly buckled. With $|\varepsilon_R| = 35.1$ με and $t = 3.45$ μm, L_{cr} is 1056 μm. This confirms that the boundary compliance is responsible for the apparent buckling of the longest Poly1/2 fixed-fixed beam, and that it is in the transition buckling regime.

TABLE 3—*Quantitative residual strain results (N- number of structures evaluated).*

	Bent-beams		Fixed-fixed beams		Cantilevers		
Layer	ε_R (st. dev.) με	N	ε_R (st. dev.) με	N	κ m^{-1}	θ_0 (μrad)	N
Poly1	-100 (13.9)	6	-52.9 (0.2)	2	-21.58	-344	1
Poly2	-118 (12.5)	4	-99.6 (2.1)	4	-60.59	-536	1
Poly1/2	-52 (12.8)	6	-35.1 (N/A)	1	-1.82	+139	1

TABLE 4—*Evaluation of assessment criteria*[a] *for test structures.*

[a]Assessment criteria for test structures:
1) How well are the critical deflections measured?
2) To what degree do the test structures reflect the 2-D analysis?
3) How repeatable are the measurements on similar structures in close proximity?
4) What are the area requirements?
5) How long does it take do determine the strain value?

[a] Crit.	**Fixed-fixed beams**
(1)	Out-of-plane deflection resolution is ±5 nm. Deflection measurements are made along the entire length of the structures, and the model is optimized to minimize the difference.
(2)	Deflections are essentially two-dimensional. The 2-D FDM captures the physical effects of strain gradient and boundary compliance. Agreement between the model and the data is excellent with typical error differences between the model and the data of 20 nm/pixel.
(3)	Beams in the same structural level but of different lengths yielded the same value of residual strain within 2 με standard deviation (Table 3).
(4)	The area required is 0.2 mm^2 per measurement (Table 1).
(5)	Taking and analyzing the interferograms requires about 15 minutes per beam. Setting up for the FDM code run requires about ten minutes. The code converges within about one minute.
	Bent-beams
(1)	In-plane resolution is ±0.25 μm. Only one deflection point on the structure is measured.
(2)	The design of these structures is forced to be more compliant so that strain resolution improves, but this makes them as susceptible to adhesion or to buckling. The flexures are clearly 3-dimensional for the Poly2 layer. However, the implications of this are minor, as addressed in the discussion.
(3)	Beams in the same structural level but of different sizes yielded the same value of residual strain within 14 με standard deviation (Table 3).
(4)	The area required is 0.23 mm^2 per measurement (Table 1).
(5)	Time to measure is about 15 minutes per structure. Analysis requires only a few minutes using Eq 2.
	Pointers
(1)	In-plane resolution of ±0.25 μm. Only one deflection point on the structure is measured.
(2)	Flexures did not satisfy the 2-D model due to adhesion to the substrate. Substrate interference can also be caused by buckling or out-of-plane bending from stress gradient.
(3)	Not able to assess repeatability due to substrate adhesion. At 40 με, the resolution for use in measuring residual strain is low.
(4)	The area requirements are large, 1.0 mm^2 per measurement (Table 1).
(5)	Time to measure is about 15 minutes per structure. Analysis requires only a few minutes using Eq 1.
	Microrings
(1)	Interferometry can be used to sensitively detect buckling. A critical structure must be defined, e.g., by $A = 0.6t$, because of the gradual transition to cross beam buckling for ring supports.
(2)	Out-of-plane deflections may be due to strain gradient rather than buckling. This can be detected in interferograms, but requires that the user make the distinction between stress gradient and stress, as discussed in Ref 22.
(3)	Cannot report repeatability data for these structures because compression rather than tension observed. Microrings do not have high resolution at 50 με.
(4)	The area requirements are large, 2.9 mm^2 (Table 1).
(5)	Evaluation time is just a few minutes.

Results for all the fixed-fixed beams are given in Table 3, and graphed against the bent-beams in Fig. 11. The standard deviation of these measurements is less than 2.1 με or less for adjacent structures in each of the Poly1 and Poly2 layers.

Discussion

Assessment of the Test Structures

The assessment criteria, questions (1)-(5) from the Introduction, are considered in Table 4, in order of the experimental effectiveness of the test structures. In addition, we make further comments on each test structure in this section.

Fixed-Fixed Beams—The fixed-fixed beams listed at the top of Table 4 yielded the highest resolution and most repeatable results. Further advantages of the fixed-fixed beam structures should be mentioned. First, if the post-buckled state is confirmed, the FDM code is not necessary. For the post-buckled beams, use of Eq 5 rather than the FDM model results in less than a 3% difference in the residual strain results. This indicates that the effect of boundary compliance on the residual strain measurements are small, as expected for post-buckled beams. The further into the post-buckled regime, the less the boundary compliance affects the buckled geometry and therefore the measured residual strain. The FDM is needed principally for evaluation of the transition- and prebuckled beams. Second, comparing the adhesion results, the fixed-fixed beam stiffness is comparable to that of the bent-beam sensors, and greater than the pointer structures. Third, because the structures are wide (18 μm), their area moment of inertia is relatively insensitive to process-induced nonidealities such as line width loss and nonvertical sidewalls. Also, because they are much wider than they are tall, there will be no buckling ambiguity (the buckling will be out-of-plane). Fourth, to obtain the intrinsic ε_R accuracy of fixed-fixed beams, it is essential to apply interferometry. It was originally proposed to use the transition from pre- to post-buckling with SEM or bright field microcopy to determine residual strain [11]. Using this criterion, repeatability of fixed-fixed beams for residual strain measurement was seen to be inferior to pointer structures [7]. More recently however, deflection curve measurements of post-buckled beams has also successfully been used by other authors to accurately determine residual stress [30,31]. For these reasons as well as those listed in Table 4, fixed-fixed beams measured by interferometry yielded the best residual strain measurement in this study.

It is also important to address the limitations of the fixed-fixed beams. First, the model assumed in the FDM for boundary conditions is oversimplified. Real boundaries are more complicated, as shown by finite element method simulations [24]. In particular, they exhibit a nonzero axial deflection, δ_0, that can significantly affect results, i.e., by $(2\delta_0/L_{FF})$. When possible, it is best to use long beams where boundary conditions are less important. Second, our experience indicates that the method of interferometry we used works best when there are at least several fringes present on the structure of interest. For very small deflections, errors in the deflection measurement become important. For example, the background fringes on the substrate are aligned parallel to the beam of interest. Small rotation error (~5°) in the background fringes can become important in inferring small out-of-plane deflections. These corrections are commonly made with

commercially available interferometers. Third, the fixed-fixed beams fortuitously buckled up rather than down, allowing even the longest beams with up to 6 mm amplitude to be analyzed. With a 2 μm support post height, the substrate would have interfered with the buckling had the beam deflections been downward, rendering the long beams unusable for residual strain evaluation. Our analysis indicates that the fixed-fixed beams should have buckled down because of the negative takeoff angles in the cantilevers. We believe that the buckling likely occurred before the release etch was completed. Then, before the oxide clears near the support posts, the downward curvature due to stress gradient would induce the fixed-fixed beams to buckle up. Fourth, cantilever curvature was used to refine the FDM result. The effect on ε_R was found to be minor (< 0.1% change). However, if films were more highly curved downwards, the correction would be more significant. Then, even shorter cantilevers would be necessary to avoid contact with the substrate to enable this correction. Also, for large curvatures, a concave or convex three-dimensional surface can be expected in cantilever and fixed-fixed beams, and therefore the deflections would become three-dimensional.

Bent-Beams—The most important conclusion from Table 4 is that based on the standard deviation value, the measurement repeatability of the bent-beams is about five times higher than for the fixed-fixed beams. Comparing the results for Poly2 and Poly1/2, the agreement between the bent-beam and fixed-fixed beam structures is reasonable. However, as seen in Fig. 11 for Poly1, the fixed-fixed beams indicate a smaller magnitude of compression than do the bent-beams. Although we have no satisfactory explanation, several factors can be considered in an attempt to rationalize this disagreement. First, the supports of the bent-beams can buckle out-of-plane, a feature not considered in the 2-D analysis of the bent-beams. This will act to relieve strain, but should decrease rather than increase in-plane deflections, resulting in a lower residual strain reading, which is opposite to the observation. For Poly2, the cross section moment of inertia for out-of-plane bending, I_{zz} ($b_{BB}t^3/12$), is about one half of the moment of inertia for in-plane bending, I_{yy} ($b_{BB}{}^3t/12$), and indeed about two fringes are seen in the interferograms of the L_{BB} = 500 μm structures, corresponding to an amplitude of 0.5 μm. The strain relieved is negligible as can be calculated from $\Delta\varepsilon = (A\pi/2L)^2 = 0.5$ με (from Eq D8, where $\Delta\varepsilon = \varepsilon_R$-$\varepsilon_c$). This explains how the agreement can be good between the two types of structures for the Poly2 level in spite of the buckling. Meanwhile for Poly1 and Poly1/2, minor out-of-plane buckling is expected and observed because I_{zz} is equal to or greater than I_{yy}. Second, the internal moment due to strain gradient is not assessed in the 2-D bent-beam analysis. However, based on the fixed-fixed beam results, this effect is minor. Third, line width may be incorrect by up to 0.2 μm due to overexposure and overetching. Evaluation shows that this will affect the strain readings by only 1 με or less. Fourth and most likely, some nonsystematic error such as improper focusing on the Poly1 structures may have caused the disagreement.

Pointer Structures—These structures are significantly larger than bent-beams because their intrinsic resolution is low. A folded-beam indicator structure with improved geometric amplification over pointer structures has recently been proposed [32] and optimized [33]. This structure requires an area about twice that of the bent-beam sensors, has similar sensitivity, is also evaluated by taking a measurement at a single point, and a simple equation applies. One concern is that the authors rely on sticking of

the structures to the substrate, but do not account for the extra strain that is induced when inferring stress.

Microrings—These are intended for measuring tensile residual strains and thus are not suited for the compressive states we found to be present here. Care must be taken not to mistake strain gradient for residual tensile stress.

Strain Properties of the Laminate

We investigated the idea that the laminate properties might be a simple composite of Poly1 and Poly2. Using residual strain and strain gradient measurements obtained from the cantilever and fixed-fixed beams and assuming a superposition model for noninteracting layers, values of $\kappa = -28.4\ m^{-1}$ and $\varepsilon_R = -72.9\ \mu\varepsilon$ were calculated. The measured values were considerably different: $\kappa = -1.82\ m^{-1}$ and $\varepsilon_R = -35.1\ \mu\varepsilon$ as seen in Figs. 14 *a* and *b*. To investigate this discrepancy, transmission electron microscopy (TEM) was applied to look for microstructural or nucleation differences of Poly2 on oxide versus on Poly1.

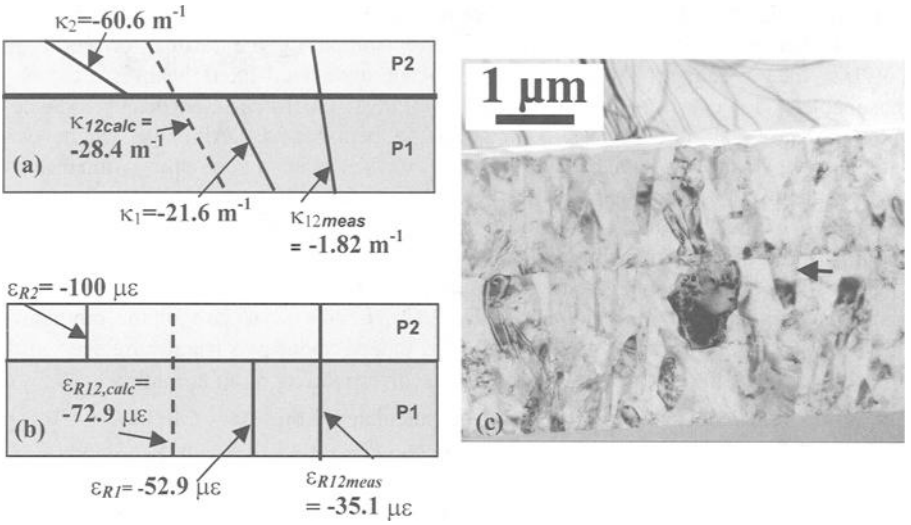

FIG. 14—*Using the properties of P1 and P2 individually, the P12 laminate propererties for (a) (steeper line implies lesser strain gradient) and (b) ε_R were predicted and measured (subscripts on ε and κ denote Poly layers). (c) TEM reveals a small degree of templating , as indicated by the arrow.*

A thin oxide at the Poly1/Poly2 interface indicates that the layers should not interact. However, there is a small degree of templating of Poly2 on Poly1, as can be seen in Fig. 14*c*, and this may be related to the large differences in the predicted versus measured laminate properties. Other features noted in both Poly1 and Poly2 layers include nucleation of grains at the interface, with growth processes resulting in some through-thickness grains of a given poly level. Also, some stacking faults and microtwins

are observed, similar to Ref 2.

Case of Tensile Residual Stress

We were only able to evaluate the performance of these test structures in compressive residual strain. It is desirable to have structures that measure both tension and compression so that a single set of devices and test procedures are used, and area requirements are minimized. We now consider which devices would have been the best had the residual strain been tensile.

Pointer structures would not suffer as much from adhesion. However, film curvature can still cause interference from the substrate. The theoretical resolution of pointers is low. In tension, microrings would work within the limitations described, i.e., resolution is dependent on the number of rings and space requirements are large. Both pointers and microrings are earlier MEMS developments (early 1990s and late 1980s, respectively) intended mainly to look at higher states of strain than observed in the present study. As MEMS matures, residual strains are decreasing to near zero, and more sensitive test structures and metrologies are required to accurately assess residual strain levels.

Bent-beams exhibit higher resolution than the pointer and microrings, and under tension would also be less likely to suffer from adhesion. Additionally, buckling would not occur, resulting in a situation that more closely matches the model conditions. However, resolution is lower than for the fixed-fixed beams. Use of active methods allows extension of the fixed-fixed beam test structures to the case of residual tension [12–14,24]. Furthermore, active methods allow additional validation of residual stress values of buckled beams. The deflections due to electrical loads at different voltages are compared to models that include the applied electrical load as a function of beam height, and are highly sensitive to residual strain. Once implemented, electrical actuation adds little in cost or time to the measurement process and can be used to obtain and average multiple data points from beams subject to either tensile or compressive residual strain. An integrated platform to accomplish interferometry of actuated devices at the wafer scale is under development [34].

Recommendations for the Next ASTM Round Robin

For the next ASTM residual strain round robin, we recommend investigating the bent-beam, folded beam [33], cantilever and fixed-fixed beam test structures in more detail. A significant drawback in the current study is that the number of test structures assessed is small (see Table 3). In the next study, only structures over Poly0 ground pads should be used, and some of the same exact geometries should be laid out side-by-side for improved repeatability quantification. Beams with more length variations should be employed to enable detailed study of the pre- and transition-buckling regimes. We also recommend that participants be equipped with interferometry so that the full deflection curves of beams can be compared. We have observed inconsistent deflection measurements when using a multi-wavelength interferometer (i.e., different results at different magnifications, and different results from profilometry). We believe this is due to the different transmission coefficient of light through silicon at different wavelengths. The effectiveness of a green interference filter in improving the reliability of the measurements on polysilicon structures should be further investigated.

Summary and Conclusions

The most important result of this study is summarized in Fig. 11, which shows that there is reasonable agreement between the bent-beam sensors and the beam structures. It also shows that especially good repeatability and small uncertainty is possible with post-buckled beam structures measured by optical interferometry. We now state the major conclusions:

(1) It is important to assess whether fabricated test structures satisfy the 2-D analyses that have been offered. Interferometry is a valuable tool in evaluating the 3-D flexures of the structures. We found that the flexures of fixed-fixed beam and bent-beam structures are essentially 2-D, while microrings can exhibit 3-D flexures because of strain gradient, which can cause the sign of residual strain to be incorrectly inferred. If test structures are adhered to the substrate, it is difficult to determine to what degree their flexures are due to adhesive versus residual strain forces, especially at the low residual strain levels typically achieved in MEMS. Any adhered structures were ruled out from further study because of adhesion to the substrate.

(2) Because of the high resolution afforded by interferometry, which can be used to obtain nanometer scale measurements across the length of structures, the standard deviation of ε_R values measured on geometrically different test structures on the same poly level is about 2 με for the fixed-fixed beam structures, The standard deviation was 13 με for the bent-beams, likely because of the lower resolution in-plane metrology.

(3) For the case of post-buckled beams, it was found that the non-idealities affect the residual strain measurement only to second order. A simple measurement of the amplitude of post-buckled beams, coupled with Eq (5), allows ε_R to be determined with high repeatability.

(4) The main importance of the cantilevers is as an aide in understanding the flexures of other structures (e.g., the buckling direction of fixed-fixed beams, the curvature of microrings).

(5) The strain measurements from the beam structures indicate that the strain state is different for polysilicon when grown on oxide versus polysilicon. The sensitive measurements enabled by the interferometry motivated us to find a microstructural difference in Poly2 on oxide versus on Poly1. With TEM, we were able to resolve some templating of Poly2 on Poly1, which may be responsible for this interactive effect.

(6) If the state of residual strain is tensile rather than compressive, the fixed-fixed beam test structures also will exhibit significant advantages over the other test structures. In that case, however, active techniques must be employed. Such techniques are under development [34]. Bent-beam structures are a reasonable alternative in the absence of active methods.

Acknowledgments

Sandia is a multiprogram laboratory operated by Sandia Corporation, a Lockheed Martin Company, for the United States Department of Energy under Contract DE-AC04-94AL85000. We would like to acknowledge Paul G. Kotula at Sandia National Laboratories for electron microscopy work.

References

[1] Kamins, T. I., "Design Properties of Polycrystalline Silicon," *Sensors and Actuators, A*, Vol. 21-23, 1990, p. 817.

[2] Krulevitch, P., Johnson, G. C., and Howe, R. T., "Stress and Microstructure in Phosphorus Doped Polycrystalline Silicon," *Materials Research Society Proceedings,* Vol. 202, 1992, pp. 79–84.

[3] Adamaczewska, J. and Budzynsky, T., "Stress in Chemically Vapour-Deposited Silicon Films," *Thin Solid Films*, Vol. 113, No. 4, 1984, p. 271.

[4] Maier-Schneider, D., Koepurueluelue, A., Ballhausen Holm, S. and Obermeier, E., "Elastic Properties and Microstructure of LPCVD Polysilicon Films," *Journal of Micromechanical Microengineering,* Vol. 6, 1996, p. 436.

[5] Fuertsch, M., Offenberg, M., Muenzel, H. and Morante, J. R., "Influence of Anneals in Oxygen Ambient on Stress of Thick Polysilicon Layers," *Sensors and Actuators A*, Vol. 76, 1999, p. 335.

[6] Floro, J. A., Hearne, S. J., Hunter, J. A., Kotula, P. G., Chason, E., Seel, S. C., and Thompson, C. V., "The Dynamic Competition Between Stress Generation and Relaxation Mechanisms During Coalescence of Volmer-Weber Thin Films," *Journal of Applied Physics,* Vol. 89, No. 9, 2001, p. 4886.

[7] van Drieënhuizen, B. P., Goosen, J. F. L., French, P. J., and Wolffenbuttel, R. F., "Comparison of Techniques for Measuring Both Compressive and Tensile Stress in Thin Films," *Sensors and Actuators A,* Vol. 37–38, 1993, p. 756.

[8] Gianchandani, Y. B. and Najafi, K., "Bent-Beam Strain Sensors," *Journal of Micromechanical Systems*, Vol. 5, No. 1, 1996, p. 42.

[9] Zavracky, P. M., Adams, G. G., and Aquilino, P. D., "Strain Analysis of Silicon-On-Insulator Films Produced By Zone Melting Recrystallization," *Journal of MEMS*, Vol. 4, No. 1, 1995, p. 42.

[10] Guckel, H., Burns, D., Rutigliano, C., Lovell, E., and Choi, B., "Diagnostic Microstructures for the Measurement of Intrinsic Strain in Thin Films," *Journal of Micromechanical Microengineering*, Vol. 2, 1992, p. 86.

[11] Guckel, H., Randzaao, T., and Burns, D. W., "A Simple Technique for the Determination of Mechanical Strain in Thin Films With Applications to Polysilicon," *Journal of Applied Physics*, Vol. 57, No. 5, 1985, p. 1671.

[12] Osterberg, P. M. and Senturia, S. D., "M-Test: A Test Chip for MEMS Material Property Measurement Using Electrostatically Actuated Test Structures," *Journal of MEMS*, Vol. 6, No. 2, 1997, p. 107.

[13] Jensen, B. D., de Boer, M. P. and Miller, S. L., "IMaP: Interferometry for Materials Property Evaluation in MEMS," *MSM '99*, San Juan, Puerto Rico, 1999, pp. 206–

209.

[14] Jensen, B. D., de Boer, M. P., and Bitsie, F., "Interferometric Measurement for Improved Understanding of Boundary Effects in Micromachined Beams," *Proceedings of the SPIE*, Vol. 3875, Santa Clara, CA, 1999, pp. 61–72.

[15] Fang, W. and Wickert, J. A., "Determining Mean and Gradient Residual Stresses in Thin Films Using Micromachined Cantilevers," *Journal of Micromechanical Microengineering*, Vol. 6, 1996, p. 301.

[16] Jensen, B. D., de Boer, M. P., Masters, N. D., Bitsie, F. and LaVan, D. A., "Interferometry of Actuated Cantilevers to Determine Material Properties and Test Structure Non-Idealities In Mems," *Journal of MEMS*, Vol. 10, No. 3, 2001, *in press.*

[17] Marshall, J. C., "Length and Strain Measurements Using An Optical Interferometer," NIST Internal NISTIR Report 6779, 2001.

[18] Sharpe, W. N., Yuan, B., and Edwards, R. L., "A New Technique for Measuring the Mechanical Properties of Thin-Films," *Journal of MEMS*, 1997, Vol. 6, No. 3, 1997, p. 193.

[19] Gupta, R. K., "Electrostatic Pull-In Test Structure Design For In-Situ Mechanical Property Measurement of MEMS," Ph. D. Thesis, Massachusetts Institute of Technology, 1997, 82 pages.

[20] Juvinall, R. C., *Stress, Strain and Strength*, First ed., New York, McGraw-Hill, 1967.

[21] Boutry, M., Bosseboeuf, A., Grandchamp, J. P., and Coffignal, G., "Finite-Element Method Analysis of Freestanding Microrings for Thin Film Tensile Strain Measurements," *Journal of Micromechanical Microengineering*, Vol. 7 , 1997, p. 280.

[22] Boutry, M., Bosseboeuf, A., and Coffignal, G., "Characterization of Residual Stress in Metallic Films on Silicon With Micromechanical Devices," *Proceedings of the SPIE*, Vol. 2879, 1996, pp. 126–134.

[23] Marshall, J. C., Read, D. T., and Gaitan, M., "Analysis of Fixed-Fixed Beam Structures," *Proceedings of the SPIE*, Vol. 2880, 1996, pp. 46–55.

[24] Baker, M. S., de Boer, M. P., Smith, N. F., and Sinclair, M. B., "Measurement of Residual Stress in MEMS to Sub Megapascal Accuracy," *Journal of MEMS*, submitted.

[25] Kobrinsky, M. J., Deutsch, E. R., and Senturia, S. D., "Effect of Support Compliance and Residual Stress on the Shape of Doubly Supported Surface Micromachined Beams," *Journal of Micromechanical Systems*, Vol. 9, No. 3, 2000, p. 361.

[26] Fang, W. L., Lee C. H., and Hu, H. H., "On The Buckling Behavior of Micromachined Beams," *Journal of Micromechanical Microengineering*, Vol. 9, No. 3, 1999, p. 236.

[27] http://www.memsrus.com/cronos/svcsdata28.html, .

[28] Mulhern, G. T., Soane, D. S., and Howe, R. T., "Supercritical Carbon Dioxide Drying of Microstructures," *Proceedings, 7th International Conference on Solid-State Sensors and Actuators, Transducers '93*, Vol. , Yokohama, Japan, 1993, pp. 296–299.

[29] Elbrecht, L., Storm, U., Catanescu, R., and Binder, J., "Comparison of Stress Measurement Techniques in Surface Micromachining," *Journal of Micromechanical Microengineering*, Vol. 7, 1997, p.151.

[30] Chan, E. K., Garikipati, K., and Dutton, R. W., "Comprehensive Static Characterization of Vertical Electrostatically Actuated Polysilicon Beams," *IEEE Design and Test of Computers,* Vol. 16, No. 4, 1999, p. 58.

[31] Nicu, L., Temple-Boyer, P., Bergaud, C., Scheid, E., and Martinez, A., "Energy Study of Buckled Micromachined Beams for Thin Film Stress Measurements Applied to SiO2," *Journal of Micromechanical Microengineering*, Vol. 9, 1999, p. 414.

[32] Lin, L., Pisano, A. P., and Howe, R. T., "A Micro Strain Gauge with Mechanical Amplifier," *Journal of MEMS,* Vol. 6, No. 4, 1997, p. 313.

[33] Ericson, F., Greek, S., Soederkvist, J., and Schweitz, J. A., "High Sensitivity Surface Micromachined Structures for Internal Stress and Stress Gradient Evaluation," *Journal of Micromechanical Microengineering*, Vol. 7, 1997, p. 30.

[34] de Boer, M. P., Smith, N. F., Masters, N. D., Sinclair, M. B., and Pryputniewicz, E. J., "Integrated Platform for Testing MEMS Mechanical Properties at the Wafer Scale by the IMaP Methodology," *Mechanical Properties of Structural Thin Films, STP 1413,* S. B. Brown and C. L. Muhlstein, Eds., American Society for Testing and Materials, West Conshohocken, PA, 2001.

[35] Gere, J. M., and Timoshenko, S. P., *Mechanics of Materials, 3rd ed.,* Boston: PWS, 1990.

[36] Chai, H., Babcock, C. D., and Knauss, W. G., "One Dimensional Modeling of Failure in Laminated Plates By Delamination Buckling,"*International Journal of Solid Structures*, Vol. 17, No. 11, 1981, p. 1069.

Appendix A – Pointers

The relationship of residual stress to displacement for pointers was derived by van Drieënhuizen et al. [7]. In the analysis, the device is treated as a rigid body mechanism. Ideal rotational points, or hinges, are assumed, allowing the deflection to be based purely on geometry. A correction factor is then applied to account for hinge compliance. The layout of pointers is shown in Fig. A1. After release from the substrate, the angles in Fig. A2 are calculated as follows:

$$\tan(\phi_1) = \frac{O}{-\varepsilon_R L_A + L_B + W}, \tag{A1}$$

$$\cos(\phi_2) = \frac{[(1+\varepsilon_R)^2 + 1] + (1+\varepsilon_R)^2 W^2 - (1+\varepsilon_R)^2 L_B^2 + (-\varepsilon_R L_B + L_B + W)^2}{2\{[(1+\varepsilon_R)^2 O^2 + (1+\varepsilon_R)^2 W^2][O^2 + (-\varepsilon_R L_A + L_B + W)^2]\}^2}, \tag{A2}$$

$$\tan(\phi_3) = \frac{W}{O}, \tag{A3}$$

$$\text{and } \alpha = \phi_1 + \phi_2 + \phi_3 - 90°, \tag{A4}$$

where L_A and L_B are the lengths of the support beams (for this study they are equal), W is the pointer width, O is the distance between the turning points and ε_R is the residual strain. The primes (L_A', L_B' etc.) in Fig. A2 indicate strain-relaxed lengths of members.

If $W << (L_A$ and $L_B)$ and if $\cos(\theta) \approx 1$ (true if $L_B >> O$), then the strain may be approximated by

$$\varepsilon_R = \frac{O\tan(\alpha)}{L_A + L_B}, \tag{A5}$$

$$\text{and } \tan(\alpha) = \frac{y}{L_C + O/2}, \tag{A6}$$

where y is the displacement of the indicator.

This allows a linear relationship between the displacement of the pointer, y, and the residual strain. Based on finite element modeling, a correction factor, C_F, is also included.

$$\varepsilon_R = \frac{Oy}{(L_A + L_B)(L_C + O/2)} \frac{1}{C_F}. \tag{A7}$$

Appendix B – Bent-beams

Bent-beams use geometry to amplify the small displacements due to residual stress. By using two opposing bent-beam structures the measured deflection is double the deflection of an individual bent-beam, increasing sensitivity. This analysis will use Castigliano's method [20], which assumes that all deflections remain linearly elastic, in-plane, and that material properties are homogeneous. These assumptions are valid because the deflections are small and polysilicon is elastically homogeneous at the length scale of the test structures. The analysis considers a single bent-beam ("One-Half" model) subject to an effective axial force, F, as shown in the top diagram of Fig. B1. The effective force, F, facilitates correlation between the residual strain and deflection of the indicator. At this stage the deflection due to the strain in the indicator is neglected (second diagram, Fig. B1), but will be added later.

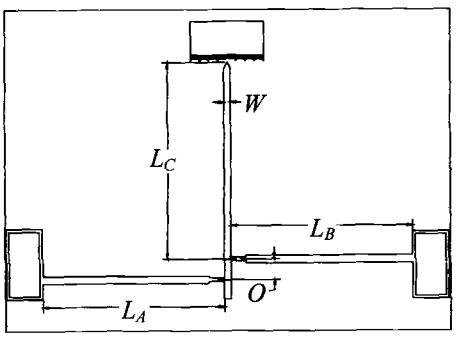

FIG. A1—*Pointer Structure*

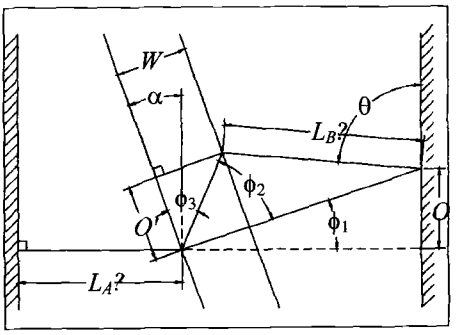

FIG. A2—*Geometry of Pointers*

By symmetry the bent-beam may be reduced to a fixed-guided member as shown in the third diagram (or "One-Quarter" model) of Fig. B1. The loading condition of a fixed-guided beam may be represented by point loads and an applied moment as shown in the final diagram of Fig. B1. The force Q is a virtual load used in Castigliano's method to evaluate the deflection of the beam in the direction of Q (which is the direction of the measured indicator displacement).

The top diagram of Fig. B2 shows how the model is further simplified (using the symmetry of a fixed-guided segment) to a simple cantilever beam (length = $L/2$) with point loads. The deflection of the complete bent-beam will be double that of this "One-Eighth" model. The middle diagram of Fig. B2 shows how the indicator may now be modeled by treating it as a segment having the same cross section as the support beams and susceptible only to axial deflections. This allows the axial strain of the modeled indicator to be equal to that of the support beams. Finally the coordinate axes are rotated to simplify the form of the derivation. The bottom diagram of Fig. B2 shows the model that will be used for the analysis.

L_b is the actual length of the support beam (as used in the "One-Eighth" model), equal to $L_{BB}/(2\cos\phi)$, where L_{BB} and $\phi = \arctan((D_0\text{-}D)/2L_{BB})$ are as indicated in Fig. 1. The functions for the moment and axial load along the beam and the axial load in the indicator are:

$$M_b(x) = (F\sin\phi + Q\cos\phi)x\,, \tag{B1}$$

$$P_b(x) = (F\cos\phi - Q\sin\phi)\,, \tag{B2}$$

$$\text{and } P_{Ind} = F\,. \tag{B3}$$

where $M_b(x)$ is the bending moment along the support beam. $P_b(x)$ is the transverse bending force and P_{Ind} is the axial force on the indicator.

The total elastic energy, U, of the deflected system of the one-eighth model is determined by the following integral (see Ref 20):

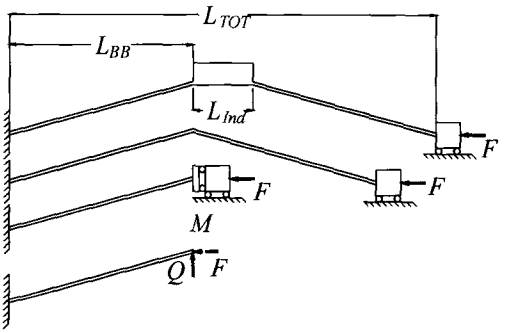

FIG. B1—*Bent beams One-Half and One-Quarter Models.*

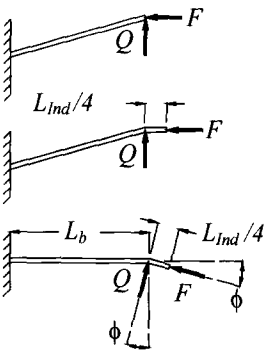

FIG. B2—*Simplified model for Castigliano's theorem evaluation.*

$$U = \int_0^{L_b} \frac{M_b^2}{2EI_{yy}} dx + \int_0^{L_b} \frac{P_b^2}{2EA} dx + \int_0^{(L_{Ind}/4)} \frac{P_{Ind}^2}{2EA} dx . \tag{B4}$$

where E is the modulus of elasticity, I_{yy} and A are the in-plane moment of inertia and area of the effective beam cross section (in the configuration used in this study the support beams are composed of two beams each, thus $I_{yy} = 2b^3t/12$ and $A = 2bt$). Transverse shear effects are negligible because support beams are long and slender.

By Castigliano's theorem, the deflections (in the directions of Q and F) are calculated by taking the derivative of the energy integral with respect to the forces Q and F:

$$\delta_Q = \frac{\partial U}{\partial Q} = \frac{(F\sin\phi + Q\cos\phi)L_b^3\cos\phi}{3EI_{yy}} - \frac{(F\cos\phi - Q\sin\phi)L_b\sin\phi}{EA} . \tag{B5}$$

$$\delta_F = \frac{\partial U}{\partial F} = \frac{(F\sin\phi + Q\cos\phi)L_b^3\sin\phi}{3EI_{yy}} + \frac{(F\cos\phi - Q\sin\phi)L_b\cos\phi}{EA} + \frac{FL_{Ind}}{4EA} . \tag{B6}$$

The virtual force, Q, is now set to zero and Eq B5 is solved for F in terms of δ_Q, the deflection in the direction of Q (the displacement of the indicator)

$$F = \frac{3EI_{yy}A\delta_Q}{\left[AL_b^3 - 3IL_b\right]\sin\phi\cos\phi} . \tag{B7}$$

This is substituted into Eq B6, yielding a function for δ_F, the deflection in the direction of F (the strain induced deflection), in terms of δ_Q, such that

$$\delta_F = \frac{\delta_Q}{\left[AL_b^3 - 3I_{yy}L_b\right]}\left[AL_b^3\tan\phi + 3IL_b\cot\phi + \frac{3I_{yy}L_{Ind}}{4\sin\phi\cos\phi}\right] . \tag{B8}$$

The strain of such a deflection is the total deflection (for the "Half model") divided by the total length of the device, as in the following equation,

$$\varepsilon_R = \frac{4\delta_F}{L_{TOT}} = \frac{4\delta_F}{2L_{BB} + L_{Ind}} . \tag{B9}$$

Substituting Eq B8 into Eq B9 and setting $L_b = L_{BB}/2\cos\phi$ and $\delta_Q = \delta/4$, we obtain

$$\varepsilon_{res} = \delta\frac{\left[\frac{AL_{BB}^3\sin\phi}{\cos^4\phi} + \frac{12I_{yy}L_{BB}}{\sin\phi} + \frac{6I_{yy}L_{Ind}}{\sin\phi\cos\phi}\right]}{\left[(2L_{BB} + L_{Ind})\left(\frac{AL_{BB}^3}{\cos^3\phi} - \frac{12I_{yy}L_{BB}}{\cos\phi}\right)\right]} . \tag{B10}$$

Eq B10 for the cases $L_{Ind} = 0$ and $L_{Ind} = 98$ μm is compared to Gianchandani's rigorous derivation in Fig. 2 in the main body (with other parameters as indicated). For residual stress near zero, the results between the rigorous and linearized derivation with $L_{Ind} = 0$ agree. The correction including $L_{Ind} = 98$ μm leads to a 15% increase in the slope,

meaning that for a given reading of δ, the value of residual stress will be 15% lower. A 2-D finite element model that included non-linear deflections was developed in ANSYS to confirm the linear bent-beam model presented here. The results of the linear model were found to be within 2% of those obtained from the FEA model for strains within the range encountered in this study.

It should be noted that Eq B10 is more quickly applied than the rigorous derivation. The derivations in refs. [8,9] include strain stiffening, which is not accounted for in the present analysis. This omission simplifies the derivation of Eq B10, but as such Eq B10 does not account for nonlinearities at higher stress levels. On the other hand, Gianchandani's derivation does not account for the effect of the indicator length on the apparent stress as his structures were designed with indicator of negligible length. The sensors used here are taken from the design of Zavracky [9] who used indicators of substantial length, and therefore their length should not be neglected.

In tension, the effect of axial elongation and stress stiffening on δ become greater than 10% at a strain value of +235 με (for the parameters used in Fig. 2). In compression, the axial elongation component is negligible compared to the bending contribution, and therefore the rigorous and linearized derivation with $L_{Ind} = 0$ μm agree within 10% to -312 με. Beyond this value, the nonlinear analysis becomes important because of loss of sensitivity inherent in the bending contribution. From this comparison we deduce that the linear model with $L_{Ind} = 98$ μm is valid over the range from –312 to 235 με (for $L_{BB} = 300$ and $(D_o\text{-}D)/2 = 10$). It should be noted that neither of these analyses takes buckling into account. If $I_{zz} > I_{yy}$, (as for Poly1 and Poly1/2 here), out-of-plane buckling is not expected. However, if $I_{zz} < I_{yy}$, buckling is complicated because out-of-plane buckling is favored by lower I_{zz}, but in-plane buckling is favored by ϕ. A simple way to evaluate out-of-plane buckling is by interferometry, as discussed in the main text.

In short, for the values of stress encountered here (from –50 to –130 με), Eq B10 with $L_{Ind} = 98$ μm gives the best values of residual stress. However, buckling is not accounted for, and may occur in Poly2 at values beyond $-(\pi t/L)^2/3 = -45$ με, the critical strain for out-of-plane bucking for this layer. Higher sensitivity is possible at low ϕ at the expense of a greater likelihood of buckling.

Appendix C – Microrings

The analysis of microrings, as presented by Guckel et al. [10], uses Castigliano's method to calculate the residual strain from the radius of the critical ring. The following is a brief overview of that derivation. In the first step, the conversion efficiency, $g(R)$, is found from the following formulae:

$$g(R) = -(2b_r f_2)/(2b_r f_1 + b_b f_1^2 - b_b f_2^2), \tag{C1}$$

$$f_1 = (\pi/4 - 2/\pi)(R/e) - 2e/\pi R + 4/\pi - \pi/4 + \pi k_f(1+\nu)/2, \tag{C2}$$

$$f_2 = (1/2 - 2/\pi)(R/e) - 2e/\pi R - 1/2 + 4/\pi - k_f(1+\nu). \tag{C3}$$

Definitions of the geometrical parameters b_r and b_b can be found in Fig. C1. The constant k_f is a form factor for transverse shear ($k_f = 1.2$ for rectangular cross sections, see

Appendix A.2. of Ref 10 for more explanation), ν is Poisson's Ratio (≈0.23 for polysilicon), R is the effective ring radius, and e is the eccentricity,

$$e = R - b_r / \ln(R_O/Ri). \tag{C4}$$

In the second step, the effect of boundary compliance due to ring torsion on the critical buckling strain ε_{cr} is calculated. The boundary stiffness (as defined by applied torque divided by rotation at the crossbeam to ring connection) for out-of-plane buckling (i.e., for crossbeams with $b_b > t$ where t is the film thickness) is

$$\alpha_o = \frac{4c_r E b_r t^3}{\pi R(6c_r + 1 + \nu)[1 - 4(1 + \nu - 6c_r)^2 / \pi^2 (1 + \nu + 6c_r)^2]}. \tag{C5}$$

where c_r is the torsional coefficient for the rectangular cross sections of the ring (the "o" subscript on α refers to out-of-plane). The torsional coefficent c_r is approximated to within 0.5% by

$$c_r \approx \frac{1}{3} - \frac{64}{\pi^5}\frac{t}{b_r}\tanh\left(\frac{\pi b_r}{2t}\right). \tag{C6}$$

For in-plane buckling ($b_b < t$) the boundary stiffness is

$$\alpha_i = \frac{\pi E t b_r^3}{3R(\pi^2 - 8)} \tag{C7}$$

(the "i" subscript on α now refers to in-plane).

Knowing α, the beam buckling criterion is found by solving the following transcendental equation for kR

$$kEI_b / \alpha + \tan(kR) = 0, \tag{C8}$$

where $k^2 = P_{cr} / EI_b$, $I_b = b_b t^3 / 12$ for out-of-plane buckling or $t b_b^3 / 12$ for in-plane buckling, and $P_{cr} = \varepsilon_{cr} E b_b t$. In the case of out-of-plane buckling, for example, if $b_r = 2 b_b$, $c_r = 1/3$ and $\nu = 0.23$, from Eqs C5 and C8,

$$\tan(kR) = -0.3098kR, \tag{C9}$$

resulting in $kR = -2.485$ and $\varepsilon_{cr} = t^2 (kR_{cr})^2 / 12R_{cr}^2 = 0.515(t / R_{cr})^2$, where R_{cr} is the radius of the first buckled ring. The tensile strain may now be calculated by dividing the critical buckling strain by the conversion efficiency resulting in

$$\varepsilon_R = \frac{\varepsilon_{cr}}{g(R_{cr})} = \frac{(kR)^2 (t / R_{cr})^2}{12 g(R_{cr})} = 0.515 \frac{(t / R_{cr})^2}{g(R_{cr})}. \tag{C10}$$

Appendix D – Fixed-fixed Beams

The governing equation for an elastically buckled beam supported by fixed clamps, assuming small slopes, is [35]

$$z''(x) + k^2 z(x) = M_o/(EI), \tag{D1}$$

where $k^2 = P/EI$, $I = b_{FF}t^3/12$, P is the axial load in the beam and M_o is the end moment supported by the clamps. The clamped boundary conditions are

$$z(-L_{FF}/2) = z'(-L_{FF}/2) = z(L_{FF}/2) = z'(L_{FF}/2) = 0. \tag{D2}$$

The general solution satisfying Eqs. (D1) and (D2) is

$$z(x) = \frac{A}{2}\left(1 + \cos\frac{2\pi n x}{L_{FF}}\right), \; n = 1,3,5,\ldots \; -L_{FF}/2 \le x \le L_{FF}/2. \tag{D3}$$

where A is the amplitude of the buckled beam. The only solution of practical interest, representing the smallest critical load, P_{cr}, is for $n = 1$. Then, $k = 2\pi/L_{FF}$ and $P_{cr} = EI(2\pi/L_{FF})^2$, giving a critical buckling strain ε_{cr} of

$$\varepsilon_{cr} = \frac{P_{cr}}{Eb_{FF}t} = \frac{\pi^2 t^2}{3L_{FF}^2}. \tag{D4}$$

The amplitude A can be related to the residual strain in the unbuckled beam in light of the following two considerations [36]. First, the length of the buckled beam can be determined from the arc length formula by using the small angle approximation (as justified by the assumption of small slopes),

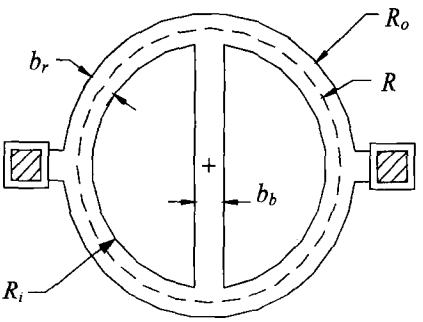

FIG. C1—*Microring diagram.*

$$l_{beam} = \int_{-L_{FF}/2}^{L_{FF}/2} \left[1 + \left(\frac{dz}{dx}\right)^2\right]^{1/2} dx \approx L_{FF}\left[1 + \left(\frac{A\pi}{2L_{FF}}\right)^2\right]. \tag{D5}$$

Second, for the assumption of small slopes, the stress in the buckled beam is equal to the buckling stress. Then, the residual strain released by buckling (i.e., the strain that contributes to a change in length of the beam) is

$$\delta\varepsilon = \varepsilon_R - \varepsilon_{cr}. \tag{D6}$$

where ε_R is the residual strain in the material. Therefore, the length of the buckled beam may also be expressed as

$$l_{beam} = L_{FF}(1 + \delta\varepsilon) = L_{FF}(1 + \varepsilon_R - \varepsilon_{cr}). \tag{D7}$$

From Eqs D5 and D7, and using Eq D4, we obtain

$$\varepsilon_R = \frac{A^2\pi^2}{4L_{FF}^2} + \frac{\pi^2 t^2}{3L_{FF}^2} = \frac{\pi^2}{12L_{FF}^2}\left(3A^2 + 4t^2\right). \tag{D8}$$

Both A and t can be accurately measured, and L_{FF} is well-known from the layout dimensions. Considering that the elastic supports built by surface micromachining methods are typically relatively stiff, Eq D8 gives excellent results for the measurement of ε_R using beams of lengths somewhat larger than the ideal critical Euler buckling length L_{cr}, i.e.,

$$L_{FF} >\approx 1.1\,L_{cr} = 1.1\left(\frac{\pi t}{\sqrt{3\varepsilon_{cr}}}\right), \tag{D9}$$

where we have rearranged Eq D4 to find L_{cr}. In Eq D9, we have used Fig. 4 in the main body to assign the 10% length correction compared to the ideally clamped boundary case. Note that the greater the value of L_{FF} with respect to L_{cr}, the smaller is M_o, and the lesser the effect of any boundary compliance on the deflection curve. Therefore, because the small slopes assumption remains valid, as L_{FF} grows large compared to L_{cr}, Eq D8 correspondingly improves in accuracy.

Tensile Testing of Structural Films

Ping Zhang,[1] *Hoo-Jeong Lee,*[2] *and John C. Bravman*[3]

Mechanical Tests of Free-Standing Aluminum Microbeams for MEMS Application

REFERENCE: Zhang, P., Lee, H. J., and Bravman, J. C., "**Mechanical Tests of Free-Standing Aluminum Microbeams for MEMS Application**," *Mechanical Properties of Structural Films, ASTM STP 1413*, C. Muhlstein and S. B. Brown, Eds., American Society for Testing and Materials, West Conshohocken, PA, Online, Available: http://www.astm.org/STP/1413/1413_18, 15 June 2001.

ABSTRACT: We studied mechanical properties and alloy effects of free-standing aluminum microbeams ($50 \times 500 \times 2$ μm) in a piezo-actuator-driven test apparatus with a load resolution of ±0.2 mN and a displacement resolution of ±10 nm. Pure Al and Al-2%Ti microbeams were fabricated using micromachining techniques. In tensile tests, we found the yield strength to be approximately 120 MPa for the pure Al beams, and approximately 75% higher for the alloyed beams. We examined the results with respect to those of bulk materials and thin films adhered to substrates. In stress relaxation tests, we observed a load drop of 56% over 10 min for the pure Al beams. We attributed this to grain boundary sliding and the nature of a free-standing thin film, i.e., the absence of a substrate. For the alloyed beams, the load drop was only 16%. We believed the difference was due to Al_3Ti precipitates formed at grain boundaries, which hindered dislocation movements. We used TEM to reveal the microstructural features of the microbeams.

KEYWORDS: micro electro mechanical systems (MEMS), micromachining, thin film, substrate, piezo-actuator, yield strength, alloy, stress relaxation, grain boundary.

Introduction

In micro electro mechanical systems (MEMS) devices, many of the active components exist in the form of a free-standing thin film. Such components are constantly in motion under various actuation or stimulation [1]. Understanding the mechanical properties of a free-standing thin film is therefore important for the design of MEMS devices, as well as for predicting their mechanical performances.

The mechanical behavior of a free-standing thin film is expected to be different from that of bulk material or a conventional thin film on substrate. In a free-standing thin film, the grain size is typically very small and the absence of a substrate leads to both its top and bottom surfaces being unconstrained. These microstructural characteristics may result in unique mechanical properties of a free-standing thin film. Although thin films on substrates have been extensively studied [2,3], knowledge on free-standing thin films was

[1]Ph.D. candidate, Stanford University, Dept. of Materials Science and Engineering, 416 Escondido Mall, Bldg. 550, Rm. 555C, Stanford, CA 94305-2205.

[2]Member of technical staff, Lucent Technologies, Inc., P.O. Box 13396, 2525 N. 12th St., Reading, PA 19612-3396.

[3]Professor, Stanford University, Department of Materials Science and Engineering, 416 Escondido Mall, Bldg. 550, Rm. 550I, Stanford, CA 94305-2205.

not available until the advent of micromachining techniques and is yet to be further explored [4]. The first part of our study examined the mechanical behavior of free-standing aluminum (Al) microbeams and compared the results with those reported for bulk Al and Al thin films on substrates.

Many MEMS structures employ alloyed, rather than pure, metals for the purpose of improved mechanical or electrical properties as required by certain device requirements. In the second part of our study, we investigated the mechanical properties of titanium (Ti) alloyed Al thin films. The alloyed free-standing microbeams contain 2% of Ti in atomic percentage. The Al-2%Ti beams were of the same dimension as the pure Al beams and were fabricated in a similar way. By comparing the mechanical test results on the alloyed samples with those of the pure Al samples, we were able to demonstrate the advantages of using Ti as an alloying material for MEMS devices.

The free-standing microbeams ($50 \times 500 \times 2$ μm) of pure Al and Al-2%Ti were fabricated using micromachining techniques at Stanford Nanofabrication Facility (SNF). For the mechanical tests, we used a dedicated micromechanical testing system. The heart of the system is a custom-designed piezo-actuator-driven test rig with a load resolution of ±0.2 mN and a displacement resolution of ±10 nm. We carried out microtensile tests as well as stress relaxation tests on both the pure Al and Al-2%Ti samples. Transmission electron microscopy (TEM) was used to reveal the microstructural features of the microbeam samples.

Sample Fabrication

The specimens were fabricated using micromachining techniques within a cleanroom facility. For both the pure Al and Al-2%Ti microbeams, the fabrication process made use of two masks. One mask is for the front side, which defines the beams; the backside mask defines the silicon windows to be etched away to release the beams. There are 34 dice per wafer, with each die (Fig. 1) measuring 8×21 mm. Each die contains one microbeam (Fig. 2), which measures 50 μm wide, 500 μm long (gage section), and 2 μm thick. For the ease of die removal upon completion of the process, a groove of about 500 μm wide is designed to surround each die. The groove is formed during the silicon backside etch, which leaves the die attached to the remainder of the wafer by only two small silicon support bridges at two corners of the die.

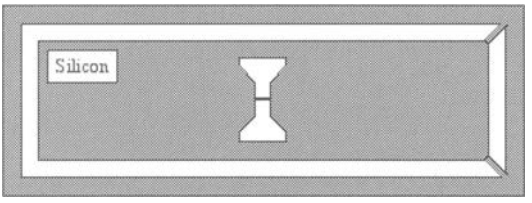

FIG. 1—*Die schematic of a microbeam specimen.*

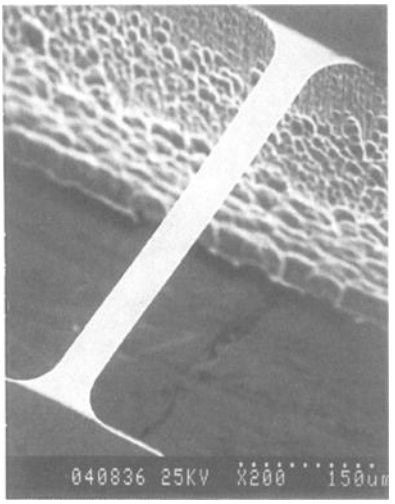

FIG. 2—*SEM micrograph of a free-standing Al microbeam specimen (prior to testing).*

To fabricate the pure Al microbeams, we used (100)-oriented 4-in. silicon wafers. First, 1 μm of silicon nitride was deposited by low pressure chemical vapor deposition (LPCVD) on both sides of the wafer. Using photo resist (PR) to protect the front-side nitride, the backside nitride was removed by a dry etch; the front-side nitride was used later as an etch-stop layer during the silicon bulk etch to release the microbeams from the backside. Next, 2 μm of pure Al was sputter deposited onto the front side of the wafer, and then patterned with the front-side mask to define the Al microbeams. Afterwards, a thick layer of PR was put down onto the backside of the wafer and patterned with the backside mask. This patterned PR acted as etch mask for the removal of silicon from the backside of the wafer through window regions defined by the backside mask. Silicon was then dry-etched through wafer thickness (about 500 μm) until the front-side LPCVD nitride was reached. Lastly, the nitride was removed by dry etch from the backside, and the Al microbeams were released.

For the fabrication of the Al-2%Ti microbeams, the procedure is identical except for the step of metal deposition. Instead of depositing pure Al, a 7-ply 0.5 μm-Al/10 nm-Ti multi-layer was deposited on the front side of the wafer followed by subsequent annealing at 550°C for 1 h in a nitrogen atmosphere. The multi-layer was formed by 3 layers of 10nm-Ti sandwiched alternately between 4 layers of 0.5 μm-Al, giving a total thickness of about 2 μm. This metal layer was then patterned and further processed. TEM studies on the cross section of the Al/Ti multi-layer (Fig. 3) before and after the annealing indicate that Ti had reacted with Al to form Al_3Ti precipitates along the Al grain boundaries during the heat treatment.

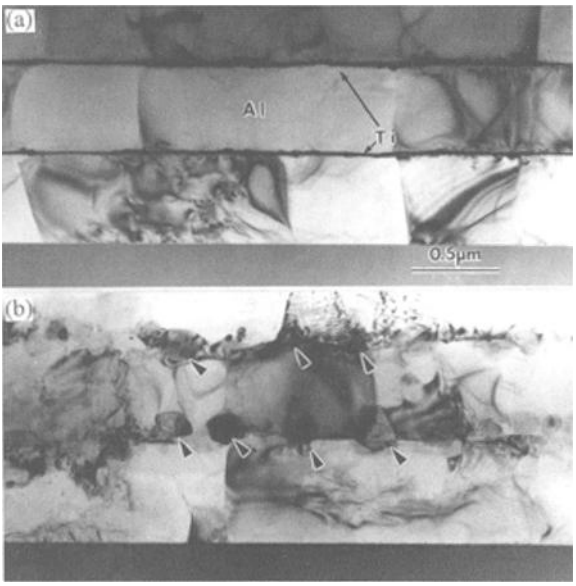

FIG. 3—*TEM cross-sectional view of (a) alternate layers of Ti and Al in the as-deposited Al/Ti multi-layer, (b) Al_3Ti precipitates formed at Al grain boundaries after annealing (arrows are pointed to the locations of Al_3Ti precipitates).*

Experimental Setup and Procedure

Micromechanical Testing System

The custom-designed micromechanical testing system (Fig. 4) comprises a piezoelectric actuator with position sensor, a load cell with temperature sensor, a height-adjustable alignment stage, and sample grips that are attached to the piezo-actuator and load cell. The control electronics include a waveform generator, an amplifier, a closed-loop piezo-controller, a signal conditioner, and an A/D board located in a control PC. Data acquisition is achieved by custom-developed LabVIEW© application. An optical microscope is mounted directly overlooking the top of the sample for the purpose of height alignment as well as test monitoring [5]. During testing, the system is kept in a thermally insulating box to eliminate possible effects that could be caused by temperature fluctuations, such as load cell drift or change in thermal expansion coefficients of the components of the system, which could lead to inaccurate measurement of stress or strain.

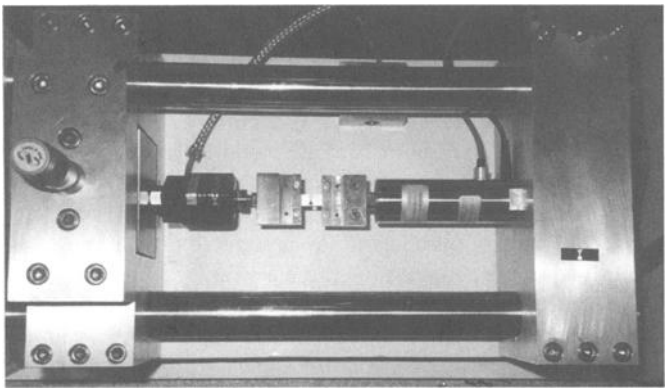

FIG. 4—*Top view of the main components of the custom-designed micromechanical testing system.*

The load cell has a maximum measurement range of 44.5 N and a load resolution of ±0.2 mN. The piezo-actuator has a maximum measurement range of 60 μm and a displacement resolution of ±10 nm. The load to stress conversion is given by

$$Stress = \frac{Load}{Area} = \frac{Load}{10^{-10} m^2} \tag{1}$$

where $Area = 50\mu m \times 2\mu m = 10^{-10} m^2$ is the cross-sectional area of the beam. The displacement to strain conversion is given by

$$Strain = \frac{GaugeDisplacement}{GaugeLength} \tag{2}$$

While we are only interested in the displacement of the gage section of the specimen, other parts of the system along the stress direction also contribute to the total measured displacement. Strain calibration is done by taking into account the stiffness of the load cell, root section of the specimen, and other compliant parts of the system in addition to the stiffness of the gage section of the specimen [5]. These additional stiffness values are, in fact, much greater than that of the gage section. To find the calibrated strain, we rewrite Eq 2 as

$$Strain = \frac{GaugeDisp}{TotalDisp} \cdot \frac{TotalDisp}{GaugeLength} = CorrectionFactor \cdot \frac{TotalDisp}{GaugeLength} \tag{3}$$

where *TotalDisp* is the total displacement measured in a tensile experiment, while *CorrectionFactor* is the ratio of actual gauge displacement over total displacement measured, which is calculated from the stiffness of all the compliant parts in the system, and differs for microbeams of different material and/or geometry. For a pure Al microbeam of 2 μm in thickness, its correction Factor is calculated to be approximately 0.76, meaning 76% of the measured displacement accounts for the actual gage section displacement. This correction factor is assumed to be the same for an Al-2%Ti microbeam due to the fact that the percentage of Ti is very small.

Experimental Procedure

Prior to testing, the electronics are energized and left to thermally equilibrate. The load cell is pre-calibrated [5]. The sample stage is adjusted under the optical microscope to eliminate any height difference between the two grips.

The test die is removed from the wafer by gently breaking the two silicon support bridges attached to the die corners and is then placed on the grips with the beam side facing downward. It is then clamped in place by four screws, two on each side, with care taken to ensure even clamping throughout the process (by monitoring the load response on the LabVIEW© screen). Upon securing the die onto the grips, the silicon supports on the two long sides of the die are cut with a hand-held rotary diamond saw. The Al microbeam is now free standing between the two grips, where one end is attached to the load cell and the other to the piezo. Finally, the system is enclosed in the thermally insulating box and allowed to reach thermal equilibrium before actual testing (the temperature is maintained ±0.5°C).

Tensile tests are performed by allowing the piezo control voltage to increase (i.e., to elongate the beam) monotonically, while the corresponding load (or stress) response of the beam and hence the stress versus strain relation is recorded by LabVIEW©. For a stress relaxation test, the beam is quickly loaded to a certain strain first and then held at this constant strain while the resulting load (or stress) change is recorded.

Results and Discussion

Tensile Test

From the stress vs. strain curve (Fig. 5) of the pure Al free-standing microbeams, we find Young's modulus from the initial slope of the elastic region. This slope is found to be about 60 GPa, close to the value of 62 GPa for bulk Al [6]. The yield strength at 0.2% strain for the pure Al free-standing microbeams is about 120 MPa. It is much higher than that of bulk Al, which is about 10 to 20 MPa [6]; yet somewhat lower than that of a conventional Al thin film on substrate, which has been reported to range from 200 MPa to 400 MPa depending on its thickness [7].

The significantly higher yield strength of our Al free-standing thin film as compared to bulk Al agrees with classical theory. It is known that the tensile strength of a material is proportional to the inverse square root of its grain size [8]. While bulk

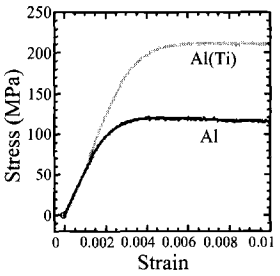

FIG. 5—*Stress vs. strain curves of pure Al and Al-2%Ti microbeams.*

materials commonly have grains in the millimeter range, thin films typically have grains in the range of microns or tens of microns, roughly equal to their film thickness. Our pure Al free-standing thin films have grains of about 2 μm (Fig. 6). The much smaller grain size results in much larger yield strength.

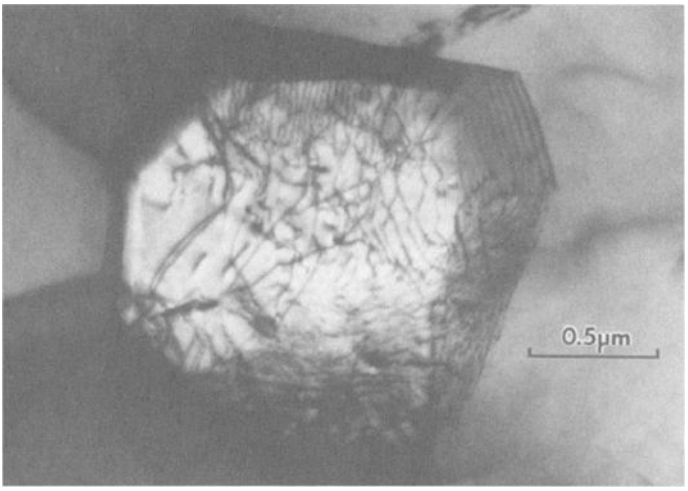

FIG. 6—*TEM bright filed image of a grain in a pure Al microbeam, showing dislocations after 0.4% strain.*

Conventional thin films on substrates typically have higher yield strengths than their bulk counterparts not only because of their small grain sizes, but also the presence of substrates. It has been shown that the stress required to move dislocations in a thin film adhered to substrate is greater than that for bulk material, due to the fact that misfit dislocations are pinned at the film-substrate interface, which makes the dislocation motion difficult [9]. The reason for the slightly lower yield strength of our Al free-standing thin film as compared to a conventional Al thin film on substrate, is, we believe, due simply to the absence of a substrate. For the case of a free-standing thin film, since both of its surfaces are free of constraint (because there is no film-substrate interface), dislocations can glide under lower applied loads than those in a conventional thin film adhered to substrate. Consequently, this will result in a lower yield strength for a free-standing thin film. This has been proved by our tensile test result.

From the stress vs. strain curve (Fig. 5) of the Al-2%Ti microbeams, we find a Young's modulus of about 60 GPa, similar to that of the pure Al microbeams. This is expected as the Ti concentration is reasonably low in these samples, and thus the modulus of the alloy is dominated by the modulus of the pure Al. The yield strength of the Al-2%Ti microbeams is found to be 210 MPa, about 75% higher than that of pure Al. This significant yield strength increase is due to Al_3Ti precipitates that have formed at grain boundaries. Al_3Ti has a much larger modulus than that of Al [10]. It is known that hard

precipitates (in this case, Al_3Ti) can block the motion of dislocations in a soft matrix (in this case, Al), and hence increase the amount of stress required to move these dislocations [11]. In effect, this will result in a higher yield strength in the Al-2%Ti microbeams than of those made from pure Al.

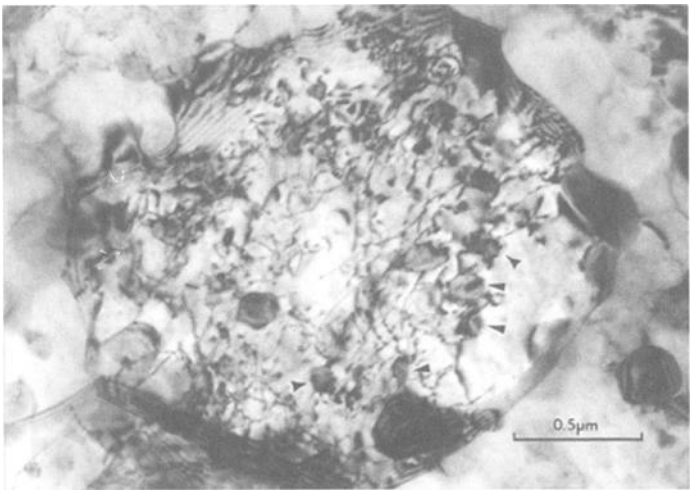

FIG. 7—*TEM bright field image of a grain in an Al-2%Ti microbeam, showing dislocations after 0.4% strain (arrows are pointed to the locations of Al_3Ti precipitates).*

Our TEM observation also showed a consistent result. The TEM samples were prepared from pure Al and Al-2%Ti beams after 0.4% strain of deformation. The bright field image of the pure Al sample (Fig. 6) under a two-beam condition ($\bar{g} = 111$) reveals many dislocations in the grain that are running rather straight. In the alloyed sample (Fig. 7), however, we see a different dislocation pattern, that is, dislocations in the alloyed beams appear to zigzag or swirl around Al_3Ti precipitates, indicating that their motion was indeed blocked by the presence of the precipitates.

We have therefore demonstrated that we can increase the yield strength of a pure Al free-standing thin film by alloying Al with Ti. In a particular MEMS device that requires high strength, this alloying method becomes of very practical importance. Especially when the electrical conductivity is important, such as in an RF circuit switch [1], and considering that the Ti alloy has a conductivity not much lower than that of pure Al [6], choosing Ti as an alloying material for building such MEMS structures offers advantages over pure Al.

Stress Relaxation Test

In stress relaxation tests, using a strain rate of 0.25 μm/s, we first quickly loaded the samples to a strain of 1.2×10^{-3}. Then, holding the strain constant at this value (piezo displacement held at a corresponding constant value), we recorded the load change over

time for both the pure Al and the Al-2%Ti microbeams (Fig. 8).

For the pure Al microbeams, over a relaxation time of about 9 min, the stress dropped from 50 MPa to 22 MPa, corresponding to a 56% relaxation from the initial stress. For the Al-2%Ti micro-beams, over the same period of relaxation time, the stress dropped from 50 MPa to 44 MPa, corresponding to a 16% relaxation.

As we study the relaxation behaviors in these microbeams, we suspect that there is certain amount of relaxation sustained in the testing apparatus other than the actual relaxation in the gage section of the beams. However, our earlier relaxation tests on some iridium microbeams (of the same lateral dimensions, yet 0.35 μm in thickness) revealed no relaxation (i.e., load drop) over periods of 40 to 60 min. Since iridium has very little relaxation in room temperature due to its high melting point, which implies that the additional system relaxation is almost negligible. Further experiments on measuring this system relaxation are in progress. At present stage, since we are not yet able to quantify the values of the system relaxation, we make the assumption that for the same constant strain and the same initial stress, the additional system relaxation is the same, and small, for the pure Al and the Al-2%Ti microbeams.

Stress relaxation has been widely investigated for bulk materials as well as thin films on substrates [12,13]. Those studies have found that grain boundary sliding is responsible for stress relaxation. It is noteworthy that the amount of stress relaxation from those studies was only a few percent [13], whereas we found more than 50% for our Al microbeams over the same time period. We have eliminated the possibility of test instrument errors and suggest that grain boundary sliding also accounts for relaxation in free-standing thin films. Qualitatively speaking, we would expect a free-standing thin film to have more grain boundary sliding taking place than a bulk material or a thin film on substrate, again because its top and bottom surfaces are unconstrained. Therefore, the amount of relaxation could be very large compared to bulk, which explains why the pure Al beams exhibit more than 50% of stress relaxation.

In the case of the Al-2%Ti microbeams, we see that the amount of relaxation is significantly less than that of the pure Al. This is probably due to the Al_3Ti precipitates formed at Al grain boundaries that hinder the grain boundary sliding, thereby decreasing the amount of relaxation compared to the pure Al.

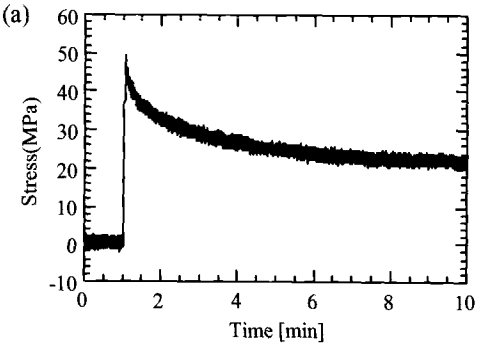

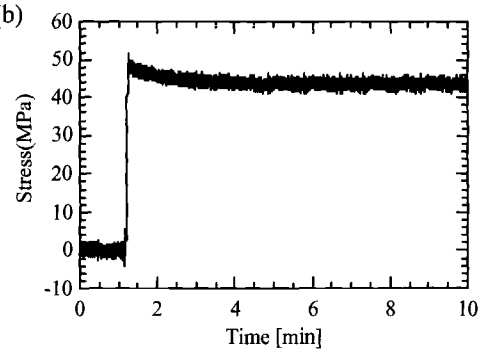

FIG. 8—*Stress relaxation of (a) pure Al micro beams, (b) Al-2%Ti microbeams.*

Since our stress relaxation tests were carried out in a stress range below 50 MPa, i.e., in the elastic regime, we can attribute the stress relaxation to anelasticity. We can, to first order, model the system as being a spring (E_∞) in parallel with a combination of a spring (E) and a dashpot (η) in series (Fig. 9). For a constant strain of ε_0, the relaxed stress is a function of time given by

$$\sigma(t) = \varepsilon_0 \left[E_\infty + E \cdot \exp\left(-\frac{t}{\tau} \right) \right] \tag{4}$$

where $\varepsilon_0 = \frac{\sigma_{initial}}{E_\infty + E} = \frac{\sigma_{final}}{E_\infty}$, and $\tau = \frac{\eta}{E}$. Since the elastic moduli for our pure Al and Al-2%Ti microbeams are nearly the same value, the difference in relaxation time, τ, is therefore directly related to η, the damping factor. As we can imagine, because of the Al_3Ti precipitates formed at Al grain boundaries, η is larger in value for the Al-2%Ti microbeams. Consequently, the relaxation time, τ, is longer for the Al-2%Ti microbeams, which again explains why the amount of relaxation in the same time period for the pure Al case is larger than for the Al-2%Ti case.

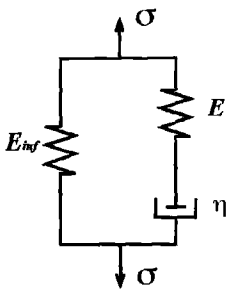

FIG. 9—*Simple anelastic model.*

Another argument we can use to validate our result is that anelasticity is said to increase with sample purity [14]. That is to say, pure Al should have more relaxation than alloyed Al. This again agrees with our result.

Conclusions

We studied the mechanical properties as well as alloying effects of pure Al and Al-2%Ti free-standing microbeams. From tensile tests, we found the yield strength for pure Al microbeams to be 120 MPa. The yield strength for Al-2%Ti was about 75% higher. From stress relaxation tests, we found the amount of relaxed stress is much larger for pure Al than for Al-2%Ti. It is therefore desirable to use certain alloyed materials for MEMS devices that require high strength and a small amount of stress relaxation.

References

[1] Yao, Z. J., Chen, S., Eshelman, S., Denniston, D. and Goldsmith, C., "Micromachined Low-Loss Mircowave Switches," *IEEE Journal of Micro Electro Mechanical Systems*, Vol. 8, No. 2, 1999, pp.129–134.

[2] Murakami, M., "Thermal Strain in Lead Thin Films," *Thin Solid Films*, Vol. 55, No. 1, 1978, pp. 101-111.

[3] Doerner, D. F. and Nix, W., "Stresses and Deformation Processes in Thin Films on Substrates," *CRC Critical Reviews in Solid State and Materials Sciences*, Vol. 14, No. 3, 1988, pp. 225–268.

[4] Read, D., "A New Method for Measuring the Strength and Ductility of Thin Films," *Journal of Materials Research*, Vol. 8, No. 7, 1993, pp. 1542–1549.

[5] Cornella, G., "Monotonic and Cyclic Testing of Thin Film Materials for MEMS Applications," Ph.D. dissertation, Stanford University, 1999.

[6] *Metals Handbook*, 8th ed., American Society for Metals.

[7] Doerner, M. F., Gardner, D. S. and Nix, W. D., "Plastic Properties of Thin Films on Substrates as Measured by Submicron Indentation Hardness and Substrate Curvature Techniques," *Journal of Materials Research*, Vol. 1, No. 6, 1986, pp. 845-851.

[8] Hall, E. O., "The Deformation and Aging of Mild Steel: III Discussion of Results," *Physical Society of London Proceedings*, 1951, Vol. 64, Part 9, No. 381B, 1991, pp. 747–753.

[9] Nix, W. D., "Mechanical Properties of Thin Films," *Metallurgical Transactions A, Physical Metallurgy and Materials Science*, 1989, Vol. 20A, No. 11, pp. 2217–2245.

[10] Nakamura, M. and Kimura, K., "Elastic Constants of $TiAl_3$ and $ZrAl_3$ Single Crystals," Journal of Materials Science, Vol. 26, No. 8, 1991, pp. 2208–2214.

[11] Courtney, T. H., *Mechanical Behavior of Materials*, 1990, McGraw-Hill, Inc.

[12] Nowick, A. S. and Berry, B. S., *Anelastic Relaxation in Crystalline Solids*, Academic Press, New York, 1972,

[13] Ke, T., "Experimental Evidence of the Viscous Behavior of Grain Boundaries in Metals," *Physical Review*, Vol. 71, No. 8, 1947, pp. 533–46.

[14] Prieler, M., Bohn, H. G., Schilling, W., and Trinkaus, H., "Grain Boundary Sliding in Thin Substrate-bonded Al Films," *Journal of Alloys and Compounds*, 1993, Vol. 211-212, pp. 424-427.

Toshiyuki Tsuchiya[1] *and Jiro Sakata*[1]

Tensile Testing of Thin Films Using Electrostatic Force Grip

REFERENCE: Tsuchiya, T. and Sakata, J., **"Tensile Testing of Thin Films Using Electrostatic Force Grip,"** *Mechanical Properties of Structural Films, STP No 1413*, C. L. Muhlstein and S. B. Brown, Eds., American Society for Testing and Materials, West Conshohocken, PA, Online, Available: www.astm.org/STP/1413/1413_01, 16 March 2001.

ABSTRACT: Thin film tensile testers using an electrostatic force grip system were developed to enable increased reliability in MEMS devices. This grip system uses electrostatic force to chuck a thin film specimen. The chucking force is easily controlled and the damage to the specimen during testing can be minimized. With these testers, silicon, silicon-dioxide, and silicon-nitride thin films fabricated with surface micromachining were tensile-tested in a vacuum and in air. The specimens were 2 to 10 μm wide, 30 to 300 μm long, and 0.7 to 2.0 μm thick. We compare the strength of these films and discuss the fracture properties of the films and the effect of the environment.

KEYWORDS: tensile test, tensile strength, fracture toughness, polysilicon, silicon dioxide, silicon nitride, electrostatic force grip

Introduction

The mechanical properties of several-micron-thick thin films are of concern to engineers who would like to use such films as structural materials in microsensors. The development of these microsensors has recently been moving from the research to the production stage, and knowledge of the mechanical reliability of these thin films is needed to ensure sensor reliability. The mechanical strength of thin films has previously been measured through a membrane fracture test by applying pressure (a bulge test [1,2]) and through a cantilever beam-bending test [3,4]. However, the measured strength values by these methods are affected by the specimen shape, because the fracture occurred at the edge of the membrane or the beam and the stress at the edge is significantly changed by the shape of the edge. To reveal the fracture mechanism of thin films and the relationship between the mechanical strength and thin film microstructure, such as grain size and surface roughness, the uniaxial tensile strength must be measured. However, tensile testing of thin films is difficult. Once a specimen is released from its substrate, it is too small to be easily manipulated and cannot be fixed to a tester by screwing it to the tester grips. Koskinen et al. used an adhesive to fix each specimen to the grips [5]. This allows easy attachment, but the fractured specimen is then difficult to release and the probe must be cleaned before the next test. It thus takes a long time to test many specimens.

We have proposed a grip system that uses electrostatic force and have developed a thin-film tensile tester [6]. Electrostatic force is weak compared with mechanically actuated force; although it is too weak for chucking bulk materials, it is strong enough to fix a thin film. A specimen can be easily fixed to and released from the tester grip by applying and cutting off the electrical power supply. Therefore, the large number of

[1] Advanced Device Lab, Toyota Central R&D Labs., Inc., Nagakute, Aichi 480-1192, Japan.

specimens needed for a statistical evaluation can be tested sequentially without excessively troublesome sample preparation.

Using this grip system, we have tested polysilicon [7,8] and SiO_2 films [9]. The polysilicon films were tensile tested in a vacuum. The effect of sample size on tensile strength was evaluated and the fracture origin was determined [7]. The strength of brittle materials is dominated by the size of the fracture-initiating flaw in the sample. The larger sample has a high probability of the existence of a larger flaw. Therefore, the larger sample shows lower strength than the smaller sample. Moreover, we can determine the location of the flaw analyzing which quantity (volume, surface area, length, and so on) of the sample affects its strength. In addition, the tensile strength and the fracture toughness of films fabricated under various process conditions were evaluated and the effects of annealing temperature and grain size were discussed [8]. Plasma CVD SiO_2 films were tensile tested both in air and in a vacuum. Static corrosion caused by corrosion arising from contact with water was observed [9].

In this paper, we compare the properties of LPCVD polysilicon, plasma CVD silicon-dioxide, and plasma CVD silicon-nitride films, focusing especially on durability against damage from the environment. In addition to our previous results, polysilicon films were tested in air, and silicon-nitride films were tested both in air and in a vacuum. Also, a specimen-fabrication process was developed. We begin by describing the electrostatic force grip and thin film tensile testers, then explain how the specimens, mainly silicon-nitride films, were prepared for testing. We show the tensile testing results for three materials in both environments and discuss the feasibility of using each film in MEMS applications in a vacuum or air environment.

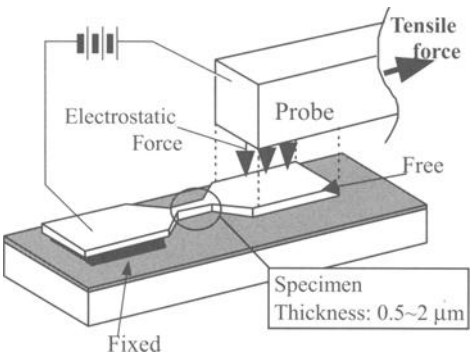

FIG. 1—*Electrostatic force grip.*

Electrostatic Force Grip

Working Principle

Figure 1 illustrates the concept of tensile testing using an electrostatic force grip. One end of a specimen is fixed to a silicon wafer as a substrate. The other end is free from the substrate and is fixed to a probe by electrostatic force. In the test, the specimen can be handled as fabricated on the substrate and can be fixed to the tester without

touching the thin film.

The electrostatic force between the probe and the specimen's free end is generated in two ways, depending on the testing material (Fig. 2). For a conductive film, the probe is made of a conductive material covered with an insulating film. By applying voltage between the probe and the specimen, an electrostatic force is generated. For an insulating film, the probe has two electrodes. An electrode is fabricated on the free end of the specimen. By applying voltage between the two electrodes on the probe, an electrostatic force is generated between the probe and the specimen.

In this system, the misalignment of the probe to the specimen causes the bending moment on the specimen. We have calculated the stress on the specimen using FEM. Assuming the vertical misalignment of the probe is 10 μm, the maximum stress that occurred at the end of the parallel part of the specimen is 102.6% of the nominal tensile stress. This is not so large, but we must care for its misalignment.

Chucking Force Calculation

We calculated, as follows, the electrostatic force needed to fix the specimen, assuming a polysilicon thin-film specimen whose tested part was 5 μm wide, 30 to 300 μm long, and 2 μm thick. The assumed probe was a silicon wafer covered with a silicon-nitride film (Si_3N_4). When a specimen is fixed to the probe, the electrostatic force acting perpendicularly to two parallel electrodes (F_V) is calculated as

$$F_V = \frac{\varepsilon_r \varepsilon_0}{2} \frac{S}{d^2} V^2, \tag{1}$$

where S is the area of the free end of the specimen, d and ε_r is the gap and dielectric constant between the probe and the free end, V is the applied voltage, and ε_0 is the permittivity constant (8.854×10^{-12} F/m). The gap d is equal to the thickness of the silicon nitride film that acts as an insulating film ($d = 0.2$ μm) and the dielectric constant ε_r is that of the silicon nitride film.

To fix the specimen to the probe in a way that prevents slipping while the tensile force is loaded, other forces parallel to the tensile stress are needed. Two forces can be used: the pure electrostatic force F_H, and the friction force F_F. The electrostatic force F_H acting parallel to two electrodes is

$$F_H = -\frac{\varepsilon_r \varepsilon_0}{2} \frac{w_g}{d} V^2 \tag{2}$$

where w_g is the width of the free end. The friction force F_F is

$$F_F = \mu F_V = -\mu \frac{\varepsilon_r \varepsilon_0}{2} \frac{S}{d^2} V^2, \tag{3}$$

where μ is the friction coefficient between the specimen and the probe. Though this coefficient is not well known, we assume μ as 0.3. The sum of the two forces has to exceed the fracture tensile force F_T,

$$F_F + F_H > F_T = \sigma_f wt, \tag{4}$$

where w is the width of the tested part of the specimen (2 to 5 μm). Since the tensile strength σ_f will be several GPa, the largest value of F_T is about 0.1 N. The applied voltage V is 100 V, considering the electrical breakdown strength of the insulating film (several

MV/cm). Assuming that the free end of the specimen is square ($S = w_g^2$), the area of this electrode needs to be more than 200 × 200 μm. In this case, the friction force F_F is dominant for fixing the specimen, and the electrostatic force F_H acting parallel to the specimen is about 1/1000 of F_F. The electrostatic force F_H is therefore much smaller than the fracture tensile force F_T. If no friction force were produced, the width of the specimen would have to be 60 mm. Such a large electrode is not practical.

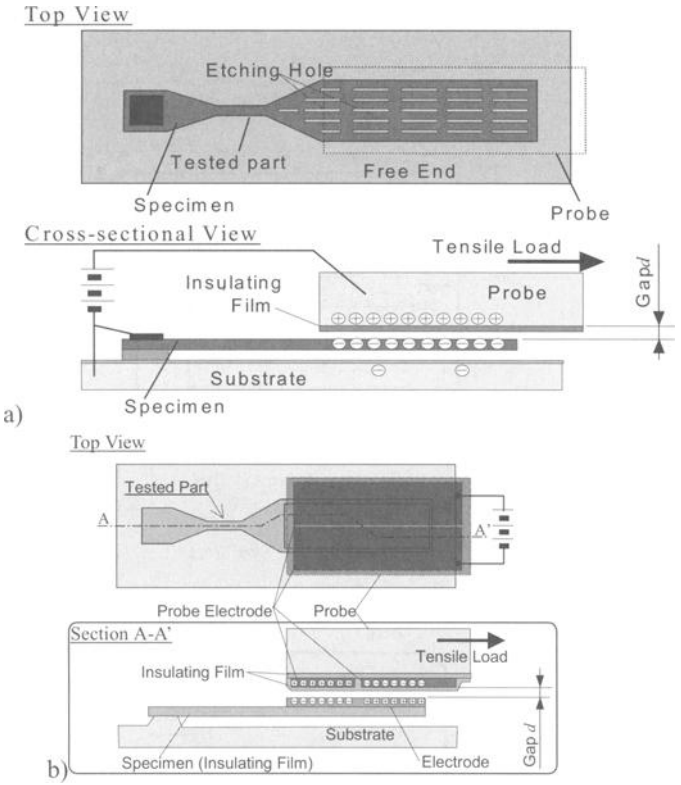

FIG. 2—*Electrostatic force grip for (a) a conductive film, and (b) an insulating film.*

In the case of the grip system for an insulating film, some parameters must be substituted, but the electrostatic force is still generated in the same way. The friction force F_F between one probe electrode and the electrode on the specimen is described by

$$F_F = \mu F_V = -\mu \frac{\varepsilon_r \varepsilon_0}{16} \frac{S}{d^2} V^2. \quad (5)$$

As a result, the friction force generated on two electrodes of the probe is a quarter

of that for conductive films. However, we can increase the friction force by increasing the voltage V, because the electric field applied to the insulating film becomes $V/2d$.

Thin-Film Tensile Tester

We have developed two tensile testers that use an electrostatic force grip in air and in a vacuum. Figure 3 shows schematic diagrams of the two testers. The tester in a vacuum was constructed in an SEM sample chamber through additional stages and mechanisms. All procedures of the tensile test were observed with the SEM. A stereoscopic microscope was used to observe the tensile test in air.

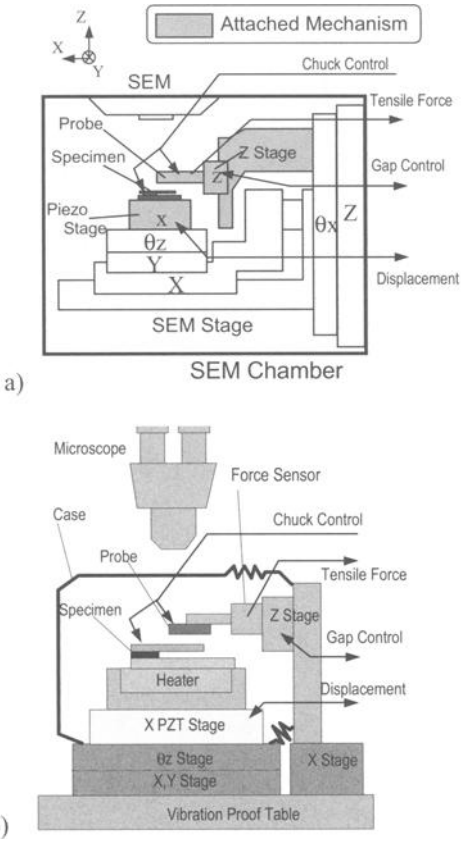

FIG. 3—*Schematic diagram of the thin-film tensile tester (a) in a vacuum, and (b) in air.*

These two testers worked in the same manner. The probe for chucking the specimen was fixed at the center of the microscope's visual field and moved along the optical axis to align the spacing between the specimen and probe. The sample stage that the specimen was put onto was driven in two ways. The stage driven by a micrometer could move along the two horizontal axes to align the specimen to the probe. The tester in

a vacuum used the SEM sample stage for this purpose. The tester in air used an XY translation stage. Tensile force was applied through the displacement of a stacked piezoelectric actuator on the stage. A loadcell connected to the probe measured the tensile force. The loadcells were specially made force sensors that used a semiconductor strain gage (in a vacuum) and a commercially available force transducer (Minebea UT-100GR) (in air).

Experiments

Specimen Fabrication

LPCVD polysilicon, plasma CVD SiO_2 (also referred to as NSG: nondoped silicate glass), and plasma CVD SiN (pCVD SiN) specimens were fabricated. We previously reported our results concerning the tensile properties of polysilicon films in a vacuum, focusing on the effects of the specimen size and the deposition and annealing conditions on tensile strength. Tensile testing of polysilicon in air is considered in this paper. The polysilicon films were deposited as amorphous films by LPCVD using Si_2H_6 gas at 520°C, 6 Pa, crystallized at 1000°C, and phosphorus doped using $POCl_3$ at 1000°C. The grain size of the polysilicon films was 0.3 μm. Details of the deposition conditions and the fabrication process have been reported [7].

The fabrication process of the NSG specimens has also been described elsewhere [9]. The NSG films were deposited by plasma CVD using TEOS (Tetra Ethyl Ortho Silicate) at 390°C, 1200 Pa. The RF power is 200 W.

Silicon-nitride films are often used as passivation films in semiconductor devices and as structural films in thermal-type infrared sensors and pressure sensors.

Figure 4 shows the fabrication process of the pCVD SiN specimens. A polysilicon film was deposited as a sacrificial layer, and then the SiN film was deposited by plasma CVD using SiH_4 and NH_3 gases at 400°C, 590 Pa. The RF power is 400 W. The SiN film is patterned to the specimen shape. The etching holes on the free end of the specimen were fabricated 20 μm apart to shorten the etching time. A titanium film that was deposited on the SiN film then patterned was used as the electrode on the free end. The sacrificial layer and silicon wafer were etched with a tetramethyl ammonium hydroxide (TMAH) solution to release the specimen.

Tensile Test

To measure the tensile strength and the fracture toughness, specimens with and without a notch were tested. The shape of the tested part of each specimen is shown in Fig. 5. The specimens without a notch for the tensile strength measurement had various lengths and widths. We calculated the tensile strength by dividing the measured fracture force by the cross-sectional area of the tested part. The specimens with a notch for the fracture toughness evaluation were 100 μm long and 5 or 10 μm wide. The notch was at the center of the tested part.

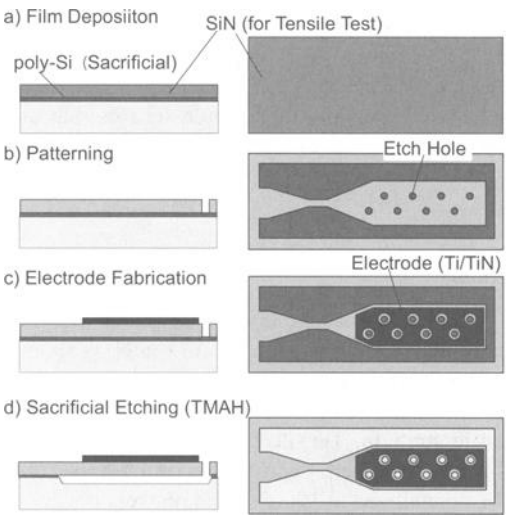

FIG. 4—*Fabrication process of silicon-nitride specimens.*

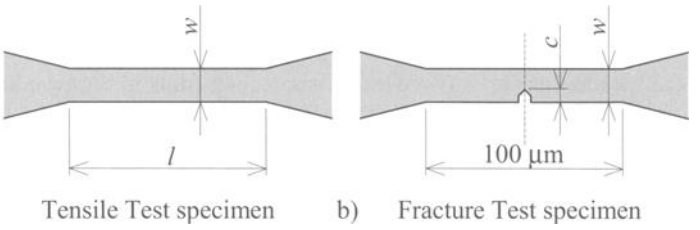

FIG. 5—*Specimen dimensions.*

The notched beam fracture toughness K_Q was calculated from the fracture stress of the notched specimen σ_f,

$$K_Q = \sigma_f f\sqrt{c} \tag{7}$$

where c is the notch length and f is a constant dependent on a/w:

$$f = 1.99 - 0.41(c/w) + 18.7(c/w)^2 - 38.48(c/w)^3 + 53.85(c/w)^4 . \tag{8}$$

The specimen sizes of the tested films are summarized in Table 1. The specimen widths w and the notch lengths c described in this paper are nominal values. The actual size is measured by SEM observation and is used for the strength and toughness calculation. These tensile tests were performed both in air and in a vacuum at room temperature. The relative humidity of testing environment in air is 40 to 50% (not controlled). The pressure in the SEM chamber cannot be measured, but it should be less than 10^{-3} Pa.

TABLE 1—*Specimen size of tested films.*

	poly-Si	NSG	SiN
Thickness, μm	2.0	0.65	0.70
Width, μm	2	5	2
Length, μm		30, 100, 300	

Results

Elastic properties of the tested films are calculated from the load-deflection curve of the square diaphragms [10]. The average values of the Young's modulus and the internal stress are listed in Table 2. The internal stress listed is released after the sacrificial etching.

TABLE 2—*Elastic properties of tested films.*

	poly-Si	NSG	SiN
Young's Modulus, GPa	167	70	150
Internal Stress, MPa	7.0	24	140

Polysilicon Films

The tensile strength of the polysilicon films was 2.5 to 2.8 GPa in air and 3.1 to 3.6 GPa in a vacuum (Table 3), and the fracture strain was as high as 2%. Figure 6 shows that the tensile strength in air was 70 to 80% of that in a vacuum. However, while the tensile strength in a vacuum was lower for the longer specimens, the tensile strength in air seemed to be unaffected by the specimen length.

The notched beam fracture toughness K_Q calculated from the fracture strength of the notched specimens was 3.2 to 3.5 MPa$\sqrt{m}$, as shown in Fig. 7. These values varied as the notch size changed, because the tip of the notch could not act as crack, which has an infinitesimal radius. The toughness K_Q in air was about 90% of that in a vacuum.

TABLE 3—*Tensile strength of polysilicon films.*

	Air			Vacuum		
Length, μm	30	100	300	30	100	300
Test number	2	4	4	7	7	7
Average, GPa	2.64	2.76	2.47	3.63	3.15	3.10
Std. dev., GPa	0.10	0.17	0.41	0.18	0.35	0.17
Max, GPa	2.71	3.00	2.86	3.94	3.67	3.37
Min, GPa	2.58	2.62	1.95	3.47	2.74	2.88

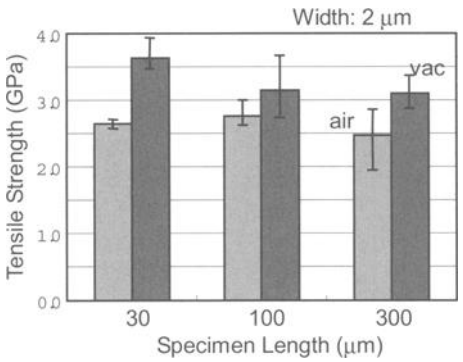

FIG. 6—*Effect of the environment on the tensile strength of polysilicon films for various specimen lengths. Error bars show the maximum and minimum measured tensile strength.*

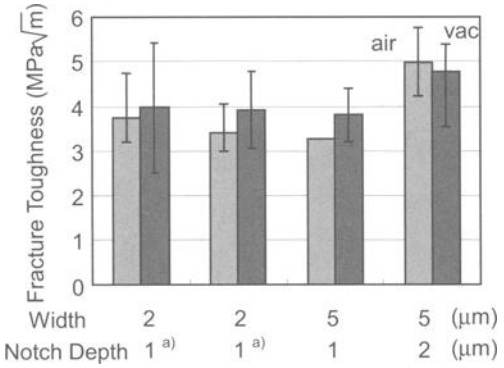

a) Notch openings differ.

FIG. 7—*Effect of environment on the notched beam fracture toughness K_Q of polysilicon films.*

Silicon-Dioxide Films

The tensile strength of the NSG films was 0.67 to 0.94 GPa in air and 1.58 to 1.84 GPa in a vacuum (Table 4). The fracture strain in a vacuum reached 2.5%. Figure 8 shows the effect of the environment on tensile strength against specimen length. The tensile strength in air was about 50% of that in a vacuum. The tensile strength was affected by the specimen length.

The notched beam fracture toughness K_Q was 0.6 to 1.0 MPa$\sqrt{m}$ in air, and 1.4 to 2.0 MPa$\sqrt{m}$ in a vacuum (Fig. 9). The toughness K_Q in air was also 50% of that in a vacuum.

TABLE 4—*Tensile strength of plasma CVD SiO_2 films.*

	Air			Vacuum		
Length, μm	30	100	300	30	100	300
Test number	3	4	2	9	9	6
Average, GPa	0.95	0.75	0.67	1.84	1.81	1.58
Std. dev., GPa	0.17	0.10	0.14	0.25	0.14	0.15
Max, GPa	1.12	0.86	0.77	2.16	2.01	1.71
Min, GPa	0.80	0.61	0.56	1.47	1.63	1.38

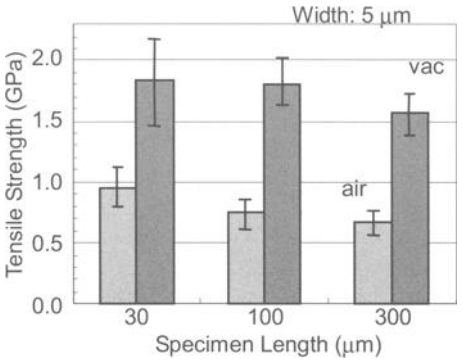

FIG. 8—*Effect of the environment on the tensile strength of plasma CVD SiO_2 films for various specimen lengths.*

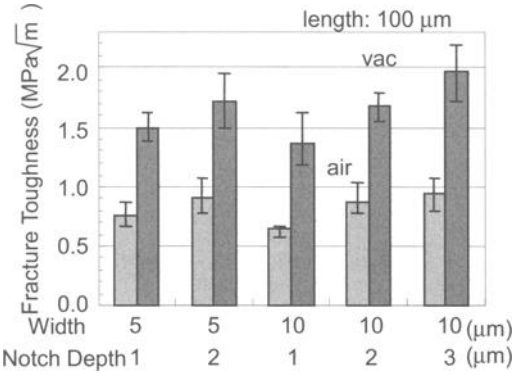

FIG. 9—*Effect of the environment on the notched beam fracture toughness K_Q of plasma CVD SiO_2 films.*

Silicon-Nitride Films

The tensile strength of plasma CVD SiN films was 4.2 to 4.6 GPa in air and 4.8 to 5.0 GPa in a vacuum (Table 5), and the fracture strain was more than 3%. Figure 10 shows the effect of the environment on the tensile strength against specimen length. The

tensile strength in air was 90% of that in a vacuum and decreased as the specimen length increased.

The notched beam fracture toughness K_Q was 2.3 to 3.2 MPa$\sqrt{m}$, as shown in Fig. 11. During the tests in a vacuum, specimens stuck to the substrate because of charges generated on the specimen during the SEM observation (the accelerating voltage = 2 kV). Due to this difficulty, only a small number of longer specimens and notched specimens could be tested. Thus, the notched beam fracture toughness K_Q could not be evaluated.

TABLE 5—*Tensile strength of pCVD SiN films.*

	Air			Vacuum		
Length, μm	30	100	300	30	100	300
Test number	14	24	13	13	11	2
Average, GPa	4.64	4.60	4.15	5.15	4.99	4.99
Std. dev., GPa	0.31	0.28	0.19	0.60	0.63	1.00
Max, GPa	5.35	5.27	4.51	6.14	5.88	5.70
Min, GPa	4.18	3.99	3.84	3.91	3.72	4.28

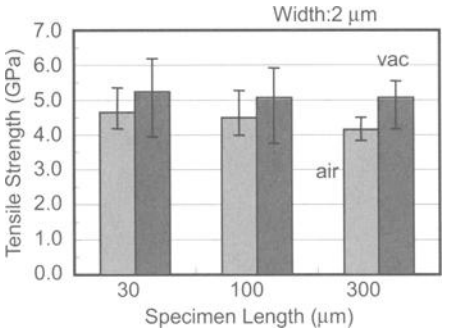

FIG. 10—*Effect of the environment on the tensile strength of pCVD SiN films for various specimen lengths.*

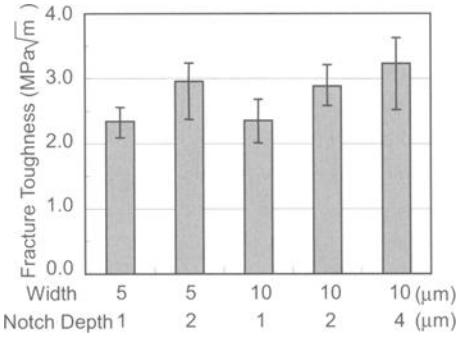

FIG. 11—*Effect of the environment on the notched beam fracture toughness K_Q of pCVD SiN films (in air).*

Discussion

Tensile Strength

All films that we tested showed brittle fracture. The stress was linearly increased until the fracture occurred. The tensile strength of most of the films was affected by the specimen length, which shows that fracture began at critical flaws in the specimens. The size effect on the tensile strength was clearly observed in the NSG and SiN films, because these films had glass or amorphous structures that were homogeneous in all directions. Fracture began at the largest crack on each of their surfaces. The cracks must have been created by the fabrication process, especially by the patterning of the specimens by reactive ion etching (RIE). The etched surfaces by RIE often have roughness due to chemical reaction during etching [11]. The patterned side surface was relatively rough, and would have had many potential fracture origins. However, the size effect was not clearly observed for the polysilicon film, especially in air. Heavily phosphorus-doped polysilicon often has phosphosilicate glass at its boundary structure [12]. This glass structure appears as etch pits on the specimen surface. We previously found these pits to be the fracture origin during tensile testing in a vacuum [7]. Corrosion of the glass structure at the boundary affects the fracture behavior of the polysilicon films.

Notched Beam Fracture Toughness

The notched beam fracture toughness K_Q of each film was relatively high compared to reported the plane-strain fracture toughness of bulk single crystal silicon (K_{IC} = 0.82 MPa/$\sqrt{m}$ for (111) plane-family orientation) [13]. As mentioned, the notches fabricated by photolithography and reactive ion etching had a finite tip radius. This radius differed among the tested materials because of differences in the materials' optical properties (e.g., refractive index, reflectance) and reaction with the etching gases; i.e., these notches would not have had the same radius even if the same mask design was used. Figure 12 shows the notch shapes of the tested materials. Because of the difference in notch shape, it was difficult to compare each value quantitatively.

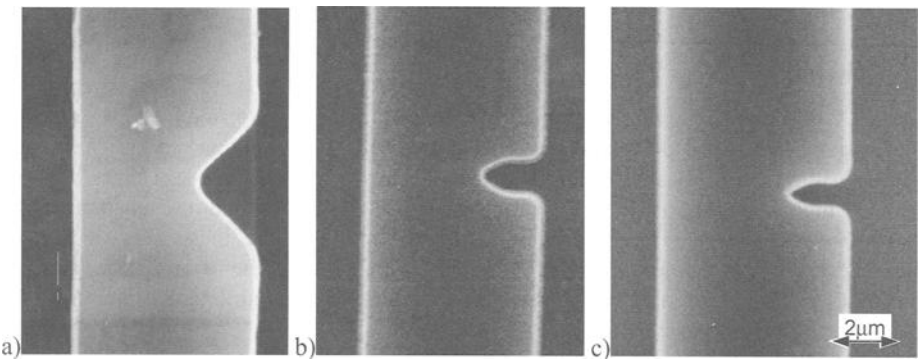

FIG. 12—*Notches in specimens used for the fracture test. The designed depth of all notches was 2 μm: (a) polysilicon, (b) NSG, and (c) SiN.*

Taking these differences in notch shape into consideration, the notched beam fracture toughness K_Q of the polysilicon film seems to be greater than that of the pCVD SiN film, while the tensile strength is less. The high fracture toughness shows that fractures occurred in the silicon grain at the notch tip. Sato et al. reported that single crystal silicon has a high fracture strain (more than 2%) [14]. The measured notched beam fracture toughness K_Q of the polysilicon film must show that of single crystal silicon.

Effect of the Environment

The tensile strength of the NSG film was the most affected by the testing environment. That of the polysilicon film was less affected, and that of the plasma CVD SiN film was almost completely unaffected. We have already discussed the environmental effect on the tensile strength of NSG films. The low tensile strength and notched beam fracture toughness of SiO_2 films in air was caused by crack propagation during the tensile test. This crack propagation was probably caused by water vapor in the air that absorbed at the crack tip and enhanced the crack propagation [15]. Therefore, use of an NSG structure in air is likely to lead to low mechanical reliability.

The decreased tensile strength of polysilicon films in air was probably caused by a grain boundary structure of phosphosilicate glass. This glass material also corrodes and shows static fatigue in a humid environment. Brown et al. reported that fatigue failure of the polysilicon structure appears to be related to the boundary silicate materials [16]. Therefore, care must be taken when a polysilicon film is to be used (e.g., polysilicon sensors are often packaged in a nitrogen environment). However, the grain of polysilicon that has a crystal structure must be stable in air, because the decrease in the notched beam fracture toughness K_Q of the polysilicon film in air, was smaller than the decrease in tensile strength and the same as that for a silicon-nitride film. Control of the grain boundary structure is thus important to improve reliability.

The silicon-nitride film showed high tensile strength, even in air. Thus, the stability of silicon-nitride films makes them suitable for use as insulating structures or passivation films in devices exposed to air.

Conclusion

We have successfully applied our thin-film tensile tester, which uses an electrostatic force grip, to evaluate the reliability of MEMS and silicon sensors. We tested LPCVD polysilicon, plasma CVD SiO_2, and plasma CVD SiN films. These films all showed high strength with fracture strains of about 2% in a vacuum, even though the fractures were brittle. The properties of the SiN films make these films good for applications in air, whereas the SiO_2 film suffers from static fatigue in air. The strength of polysilicon films is determined mainly by each film's boundary structure, which must be controlled to ensure device reliability.

Acknowledgments

We thank Ms. Atsuko (Inoue) Shibata for her experimental support. Part of this work has been conducted through the Standardization of Evaluation Methods of Material

Properties for Micromachines program under the Micromachine Center of the New Energy and Industrial Technology Development Organization, and is part of the Research and Development for International Standards to Support New Industries Program.

References

[1] Beams, J. W., *The Structure and Properties of Thin Films*, C. A. Neugebauer, J. D. Newkirk, and D. A. Vermilyea, Eds.,Wiley, New York, 1959, p. 183.

[2] Griffin, Jr., A. J., Brotzen, F. R., and Dunn, C. F., "Mechanical Properties and Microstructures of Al-1% Si Thin Film Metallizations," *Thin Solid Films*, Vol. 150, 1987, pp. 237–244.

[3] Johanson, S., Schweitz, J.-Å., Tenerz, L., and Tirén, J., "Fracture Testing of Silicon Microelements in Situ in a Scanning Electron Microscope," *Journal of Applied Physics*, Vol. 63, 1988, pp. 4799–4803.

[4] Weihs, T. P., Hong, S., Bravman, J. C., and Nix, W. D., "Mechanical Deflection of Cantilever Microbeams: A New Technique for Testing the Mechanical Properties of Thin Films," *Journal of Material Resources*, Vol. 3, 1988, pp. 931–942.

[5] Koskinen, J., Steinwall, J. E., Soave, R., and Johnson, H. H., "Microtensile Testing of Free-Standing Polysilicon Fibers of Various Grain Sizes," *Journal of Micromechanical Microengineering*, Vol. 3, 1993, pp. 13–17.

[6] Tsuchiya, T., Tabata, O., Sakata, J., and Taga, Y., "Tensile Testing of Polycrystalline Silicon Thin Films using Electrostatic Force Grip," *Transactions of the IEEJ Sensors and Micromachines Society*, Vol. 116-E, No. 10, December 1996, pp. 441–446.

[7] Tsuchiya, T., Tabata, O., Sakata, J., and Taga, Y., "Specimen Size Effect on Tensile Strength of Surface Micromachined Polycrystalline Silicon Thin Films," *Journal of Microelectromechanical Systems*, Vol. 7, No. 1, 1998, pp. 106–113.

[8] Tsuchiya, T., Tabata, O., Sakata, J., and Taga, Y., "Tensile Strength and Fracture Toughness of Surface Micromachined Polycrystalline Silicon Thin Films Prepared under Various Conditions," *MRS Symposium Proceedings*, Vol. 505, 1998, pp. 285–290.

[9] Tsuchiya, T., Inoue, A., and Sakata, J., "Tensile Testing of Insulating Thin Films; Humidity Effect on Tensile Strength of SiO2 Films," *Sensors and Actuators*, Vol. A82, 2000, pp. 286–290.

[10] Tabata, O., Kawahara, K., Sugiyama, S., and Igarashi, I., "Mechanical Property Measurement of Thin Films using Load-Deflection of Composite Rectangular Membranes," *Sensors and Actuators*, Vol. 20, 1989, pp. 135–141.

[11] Jansen, H., Gardeniers, H., de Boer, M., Elwenspoek, M., and Fluitman, J., "A Survey on the Reactive Ion Etching of Silicon in Microtechnology," *Journal of Micromechanical Microengineering*, Vol. 6, 1996, pp.14–28.

[12] Kamins, T., *Polycrystalline Silicon for Integrated Circuit Applications*, Kluwer Academic, Boston, 1988, p. 137.

[13] EMIS Datareviews Series No. 4, *Properties of Silicon*, INSPEC, London, 1988, p. 30.

[14] Sato, K.,Yoshioka, T., Ando, T., Shikida, M., and Kawabata, T., "Tensile Testing of Silicon Film Having Different Crystallographic Orientations Carried Out on a Silicon Chip," *Sensory Actuators,* Vol. A70, 1988, pp. 148–152.

[15] Kingery, W. D., Bowen, H. K., and Uhlmann, D. R., *Introduction to Ceramics*, 2nd ed., John Wiley & Sons, New York, 1976, pp. 800–806.

[16] Brown, S., Arsdell, W. V., and Muhlstein, C. L., "Materials Reliability in MEMS Devices," *Technical Digest of International Conference on Solid-State Sensors and Actuators*, Chicago, IL, 16-19 June 1997, pp. 591–593.

William N. Sharpe, Jr.,[1] *Kamili M. Jackson*,[2] *George Coles*,[3] *Matthew A. Eby*,[4] *and Richard L. Edwards*[5]

Tensile Tests of Various Thin Films

REFERENCE: Sharpe, W. N., Jr., Jackson, K. M., Coles, G., Eby, M. A., and Edwards, R. L. , **"Tensile Tests of Various Thin Films,"** *Mechanical Properties of Structural Films, ASTM STP 1413 (to be published)*, C. Muhlstein and S. B. Brown Eds., American Society for Testing And Materials, West Conshohocken, PA, Online, Available: www.astm.org/STP/1413/1413_19, 15 June 2001.

ABSTRACT: Test methods for two types of thin-film tensile specimens have been developed in earlier works, and these are reviewed as background for new applications. Two kinds of specimens are tested. The first is 600 μm wide and suspended across a support frame, and the second is 6 to 50 μm wide and fixed to the silicon substrate at one end. Test systems incorporating force, strain, and displacement measurement are used, and Young's modulus can be obtained by three methods, which yield equivalent results.

Tensile stress-strain curves of polysilicon have been recorded over the temperature range 30 to 250°C. The modulus decreases at a rate of 0.043 GPa/°C, and the strength increases slightly, although the scatter of the data is large in both cases. Polysilicon specimens produced by three vendors show essentially the same Young's modulus, but the fracture strengths vary by almost a factor of two.

The first tensile tests of silicon nitride film are reported. The specimens are 0.5 μm thick, 600 μm wide, and 4 mm long in the gage section. Young's modulus is measured as 255 ± 2.6 GPa, Poisson's ratio is 0.22 ± 0.02, and the fracture strength is 6.42 ± 1.11 GPa.

KEYWORDS: thin films, Young's modulus, Poisson's ratio, fracture strength, polysilicon, silicon nitride, temperature

Introduction

The rationale behind the tensile test as defined in ASTM standards E-8 for metals and C-1273 for ceramics is clear; the uniform state of stress is determined from the cross-sectional area and measurement of applied force with strain measured directly on the specimen. This approach eliminates the potential ambiguity of indirect or inverse methods, where properties are extracted from the force-deflection record of a modeled test structure containing sharp stress gradients. In most cases, tensile tests provide true material properties independent of specimen size and shape. However, tensile testing is not always possible or appropriate for the thin-film materials used in MEMS.

Thin films can be readily tested in tension provided the planar dimensions are large enough; in fact, ASTM E-345 for foils details the procedure. It is difficult to bring this down to the MEMS scale because the material is not normally produced over large areas, and one needs a specimen fabricated by the same processes as used for the microdevices themselves. This

[1]Decker Professor, Department of Mechanical Engineering, Johns Hopkins University.
[2]Graduate student, Department of Mechanical Engineering, Johns Hopkins University.
[3] Research assistant, Department of Mechanical Engineering, Johns Hopkins University.
[4] Undergraduate student, Department of Mechanical Engineering, Johns Hopkins University.
[5]Research engineer, Applied Physics Laboratory, Johns Hopkins University.

restriction has led to a variety of indirect methods using in-plane and out-of-plane bending as well as resonant structure techniques. A comprehensive review is not included here; an earlier review is from a 1996 reference [1]. A more recent example of in-plane bending is by Jones, Johnson, and Howe, who take video images of deflected beams [2]; an example of an out-of-plane measurement is presented by Serre et al., who use an AFM probe [3]. An on-chip out-of-plane bending test in which both ends of the beam are fixed has been introduced by Senturia and his students [4]. A good example of resonant structures is that of Brown and colleagues [5].

Tensile test techniques and procedures have been developed for MEMS materials where the gage sections are on the same size scale as microdevices, i.e., a few microns on a side. Such test methods can be used to determine "baseline" material properties, which can then be used to validate more convenient on-chip test structures. There are two arrangements currently used for tensile tests of thin-film MEMS materials: specimen in a supporting frame and specimen fixed to die at one end.

Read and Dally introduced the "specimen in a frame" concept in 1993 [6]. The tensile specimen is patterned onto the surface of a wafer, and then a window is etched through the back of the wafer to expose the gage section. The result is a specimen suspended across a rectangular frame that can be handled easily and placed into a test machine. The two larger ends of the frame are fastened to grips, and the two sides are cut to completely free the specimen. This is an extension of the earlier approach by Neugebauer [7] and has been adopted by others [8], [9], [10], [11], [12].

Tsuchiya introduced the concept of a tensile specimen fixed to the die at one end and gripped with an electrostatic probe at the other end [13]. This approach has been adopted at Johns Hopkins [14]. Knauss and Chasiotis have developed procedures for gluing the grip end to a force/displacement transducer [15] that enables the application of larger forces. A different approach is to fabricate the grip end in the shape of a ring and insert a pin into it to make the mechanical connection to the test system. Greek originated this with a custom-made setup [16], and LaVan uses the probe of a nanoindenter for the same purpose [17].

All of the above may appear impressive to the materials test engineer accustomed to common structural materials, but there is a continuing push toward smaller structural components—at the nanoscale. Yu et al. have successfully attached the ends of carbon nanotubes as small as 20 nanometers in diameter and a few microns long, to atomic force microscopy (AFM) probes. As the probes were moved apart inside a SEM, their deflections are measured and used to extract both the force in the tube and its overall elongation [18].

This paper describes the tensile test methods developed at Johns Hopkins as they are applied to various thin films—four polysilicons and silicon nitride. The two specimen designs (~ 600 μm wide and ~ 6 to 50 μm wide) along with a discussion of the difficulty in measuring dimensions are presented first and followed by brief descriptions of the test systems. After presenting representative stress-strain curves for the two kinds of specimens, a comparison of three different ways of obtaining Young's modulus is given. Then, new results on the effect of temperature on the modulus and strength of polysilicon are presented. This is followed by modulus and strength results for polysilicon specimens manufactured four different ways. The first tensile tests of silicon nitride in which both lateral and axial strain are measured are compared with earlier works. The paper closes with comments about the usefulness and validity of these test methods.

Specimens

The key to mechanical property testing is the specimen; producing and handling a tensile specimen on a suitable size scale is a challenge for MEMS materials. In most cases, one cannot pick up a specimen and mount it in a test machine. Thin-film specimens must remain attached to the silicon wafer die, which acts as both a carrier and a part of the gripping system. There are two general approaches for tensile specimens—one in which a portion of the die is etched away to free the gage section and one in which the fixed end of the specimen remains attached to the die.

Figure 1 illustrates the first approach. A polysilicon film, 3.5 μm thick, is deposited onto a 0.5 mm thick silicon wafer, which is then cut into dies that are 1 cm square. Both the film and the die are clearly visible in the figure. The film is patterned as a central tensile specimen with gentle radiuses into two large grip ends. A rectangular portion of the die is etched out from the backside of the die, but the rectangle does not extend the entire width of the die, which leaves two supporting side strips. The die with the specimen can be handled easily and placed into a test machine where the large ends are glued into grips. Then, the two side support strips are cut with a small diamond saw to leave a completely free tensile specimen. Details of the specimen preparation and test procedure are given in [9], and it should be noted that this approach derives from the work of Read and Dally [6]. This approach has the advantage of an easily handled specimen, but yields only one specimen per die. Further, the width is larger than typical minimum dimensions in a MEMS device.

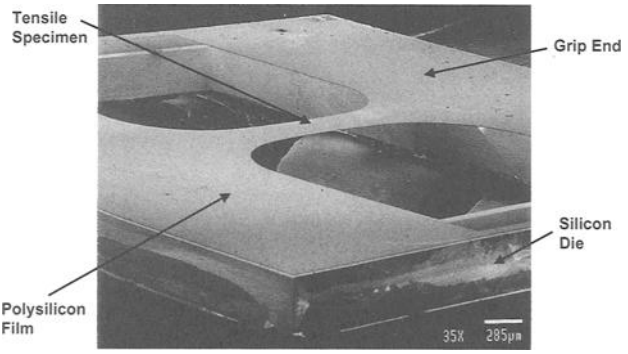

FIG. 1—*A polysilicon tensile specimen on a silicon carrier frame.The silicon die is one centimeter square, and the tensile specimen is 3.5 μm thick by 600 μm wide in the gage section.*

Smaller specimens that are fastened to the die at one end are illustrated in Fig. 2. The tensile specimen is fixed at the left end, where a gold pad is deposited for electrical contact. The large grip end is patterned with etch holes, as are the two transition regions designed to reduce stress concentrations at the grip ends. These specimens are fabricated by the MUMPs process of Cronos (as are the ones in Fig. 1), and dimples are incorporated under the grip end to prevent it

from sticking to the substrate. Each grip end is prevented from movement during the etching process and subsequent handling by four straps that are cut before testing.

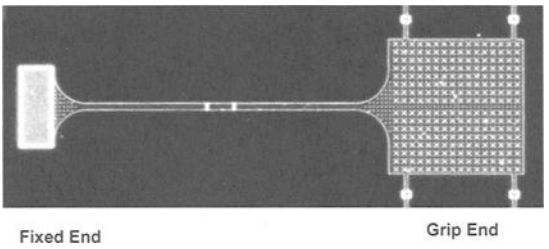

FIG. 2—*Tensile specimen fastened to substrate at one end. The gage section is 3.5 μm thick and 50 μm wide by 2000 μm long.*

Fourteen or more specimens can be patterned onto a 1 cm^2 die, and this is a very economical approach both in cost of specimens and in testing time. The free end of the specimen can be gripped with an electrostatic probe as introduced by Tsuchiya [13] and described in [14]. That works very nicely, but sometimes fails to provide adequate force to break wider and thicker specimens.

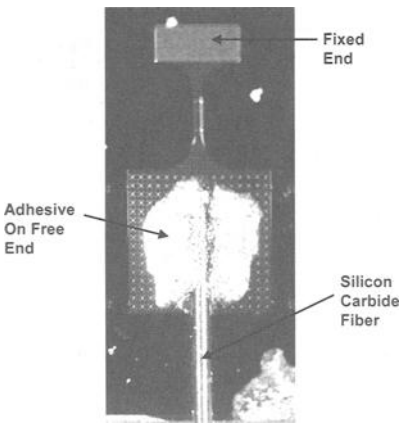

FIG. 3—*A polysilicon specimen with a silicon carbide fiber glued to the grip end. The diameter of the fiber is 150 μm.*

The authors have recently developed a new gripping technique that is more time-consuming, but stronger. Figure 3 shows a silicon carbide fiber glued to the grip end of a short tensile specimen of the type shown in Fig. 2. All but the most viscous adhesives will pass through the 5-μm square etch holes and glue the paddle to the substrate. A two-stage process has been developed. First, the fiber is glued to the grip with a small drop of a very viscous ultraviolet-curing adhesive (Norland 123) that is cured immediately after application. This provides enough adhesion to permit lifting of the paddle off the substrate with a micromanipulator. Then, a high-temperature and less viscous adhesive (Aremco Bond 805-B) is applied and cured either at room or elevated temperature. This final adhesive is the one visible in Fig. 3, and it is strong enough to break all specimens at temperatures up to 250°C.

Designing, handling, and gripping a tensile specimen is challenging enough, but it is not easy to determine its dimensions. The cross sections are not always the rectangular shape specified in the mask design, and the corners are invariably rounded due to the nature of the deposition processes. These rounded corners make precise determination of the edges difficult.

Xie and Hemker [19] polished the ends of polysilicon strips of various nominal widths to a taper using a special tripod to hold and tilt the samples. This enabled them to use transmission electron microscopy (TEM) to obtain images of the trapezoidal surface and determine the width at the top and bottom of the strip with high precision. The results, shown in Table 1, confirm that the bottom of a 3.5 μm thick polysilicon strip is wider than the top.

TABLE 1—*Measured widths of polysilicon samples—microns.*

Nominal Width	Bottom Width	Top Width	A_{nom}/A_{act}	Optical Width	A_{nom}/A_{act}
20	23.09	19.02	0.95	19.6	1.02
10	10.43	9.01	1.03	9.6	1.04
8	8.46	6.98	1.04	7.4	1.08
6	6.35	4.93	1.06	5.6	1.07
4	4.34	3.16	1.07	3.7	1.08
3	3.27	1.86	1.17	2.2	1.36
2	2.15	0.76	1.37	1.3	1.54

Another practical and useful approach to dimension measurement is simply optical microscopy. One approach is to take a photograph of the gage section of a specimen at 400X; a photo of a standard 1-mm ruling on a glass slide is also taken. That picture can then be scanned into an image-processing program where the edges can be located and the width determined using the image of the standard as a scale. The edges can be located to ± one pixel, which corresponds to 1/3 μm. Thus, the relative uncertainty of a 6-μm wide specimen is ±13%, while that of one 50-μm wide one is only ±1%. Optical measurements of the widths of strips from the same production run are also listed in Table 1. All of the specimens measured in Table 1 are from the MUMPs 25 run of Cronos.

A column is included for each kind of measurement to show the effect of using the actual measured area versus the nominal area. In all cases, the actual area is smaller than the designed area. However, the actual areas are within 5% of the nominal area in all but the narrowest specimens, and the two measurement procedures tend to agree with each other. From a practical viewpoint, the optical approach is more suitable.

Test Systems

It is preferable to measure strain directly on the specimen, as required by ASTM E-8, but that is not always possible. Techniques and procedures for direct strain measurement by laser interferometry (interferometric strain/displacement gage or ISDG) using thin and narrow gold markers placed in the gage section of tensile specimens have been developed over the years at Johns Hopkins—see [20] for example. The reflective markers define a gage length on the order of 200 μm, and the fringe patterns emanating from them move as the distance between the markers change when the specimen is elongated. Force application and strain measurement are controlled by a computer system, and the stress-strain curve is recorded in real time, each test taking a minute or so.

The systems for pulling the specimens and measuring the force applied are actually conventional; commercial components can be used. Figure 4 is a schematic of the setup for the wide specimens of Fig. 1. The specimens are glued into locally made grips connected to a 4.4 N load cell from Entran through a linear air bearing. This arrangement reduces friction in the connection to the piezoelectric actuator from Physik Instruments, which elongates the specimen. The laser and fringe detectors in the schematic are used for strain measurement as described below.

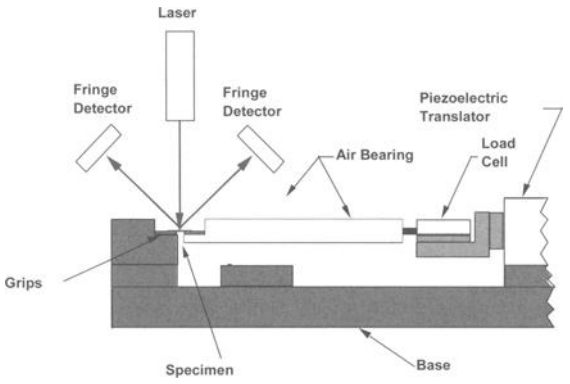

FIG. 4—*Schematic of test system for wide specimens.*

The arrangement for the narrow specimens of Fig. 2 differs, as Fig. 5 shows. It is important to align the specimen with respect to the electrostatic probe, and a five-axis Picomotor stage from New Focus, Inc. is used for this purpose. Alignment is done visually using a low-

power stereo microscope for the plan view and a telemicroscope for the side view. Force is measured with a 1 N load cell from Cooper Instruments; only the lower end of the range is used to maintain a high stiffness relative to the specimen. Specimens are elongated with a single-axis Picomotor, and the overall displacement of the system is measured with a capacitance probe from Capacitec. This system incorporates electrostatic gripping and enables the measurement of the stiffness of the specimen, from which Young's modulus can be extracted. Direct measurement of strain by laser interferometry can also be accomplished.

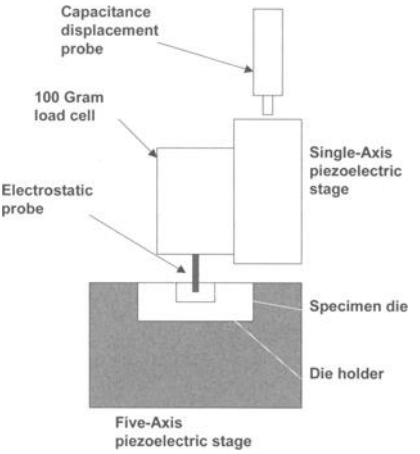

FIG. 5—*Schematic of test system for narrow specimens.*

A variation on the system of Fig. 5 uses the glued fiber gripping arrangement and permits measurements at high temperatures. This is shown in Fig. 6 where the force measurement and displacing mechanism are removed from the specimen, that is, heated by a small resistance furnace covered with a quartz window. The window allows optical access for direct strain measurement; heating of the fiber and glue precludes extraction of modulus from force-displacement measurements. A three-axis micrometer stage allows maneuvering of the fiber for alignment.

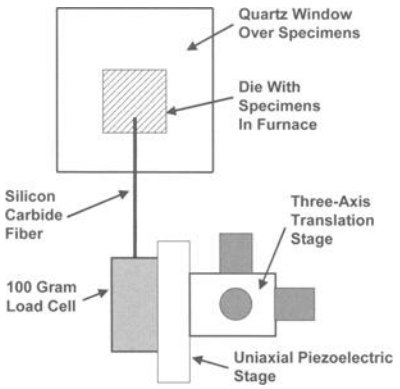

FIG. 6—*Schematic of test system for heated specimens.*

Typical values for a polysilicon specimen 3.5 μm by 50 μm in cross section and fracturing at 1 GPa are a force of 0.175 N and a strain of 0.00625 (using a modulus of 160 GPa). Thus, a 1000 μm long specimen experiences a total elongation of 6.25 μm. The resolution and relative uncertainties of the narrow specimen setup are discussed in [21]. Force can be measured to less than 1 mN, and the relative uncertainty at forces greater than 0.1 N is estimated to be ±1%. The relative uncertainty of the ISDG is estimated at ±5% with a resolution on the order of 10 μstrain. Displacements measured by the capacitance probe can be resolved to 10 nm, and the relative uncertainty of displacement of 1 μm or more is ±1%.

Young's modulus can be determined three different ways with these experimental arrangements. First, when the strain is measured directly, one simply takes the slope of the stress-strain plot. When the overall force-displacement is measured, one can compute the modulus if one knows the stiffness of the load cell and the grip ends of the specimen. If not, then the response of specimens of different lengths can be compared to eliminate those stiffnesses in the manner introduced by Greek et al. [16]. Reference [21] elaborates on these methods.

Polysilicon Results

Figure 7 presents a plot of stress versus strain measured in the axial and lateral directions. This result, similar to earlier ones [20], employs improved techniques and procedures gained through better alignment of the laser-based ISDG. There are 496 data points in each of the two stress-strain records.

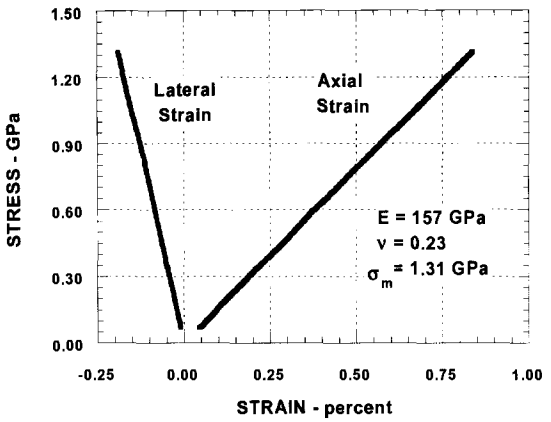

FIG. 7—*Stress-strain plot for a 600 μm wide polysilicon specimen from the MUMPs 25 run of Cronos.*

Stress-strain curves from narrow specimens measure only the axial strain and are more "noisy"; Figure 8 is an example. Note that the test begins at a non-zero stress because the specimen must be straightened before the ISDG measurements can be taken. The same is true for the wide specimen of Fig. 7, but the more robust, larger specimen is easier to get started. There are 167 data points in the plot.

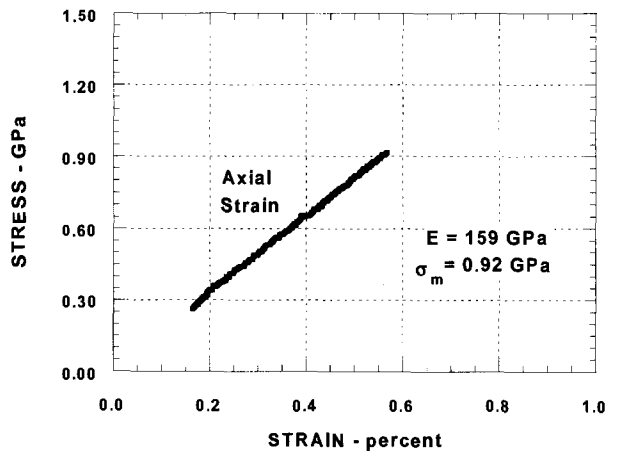

FIG. 8—*Stress-strain plot for a 50 μm wide polysilicon specimen from the MUMPs 30 run of Cronos.*

Note that the Young's modulus of the two specimens is nearly the same, but the strengths are different. Extensive testing of polysilicon has shown a tendency for the strength to increase as the surface area of the specimen decreases.

Young's modulus is more difficult to measure than strength because of the added requirement to determine strain. As mentioned above, there are three methods of arriving at the value—direct strain, stiffness, and differential stiffness—with details given in [21]. Figure 9 compares these three approaches for specimens of different widths, thicknesses, and lengths.

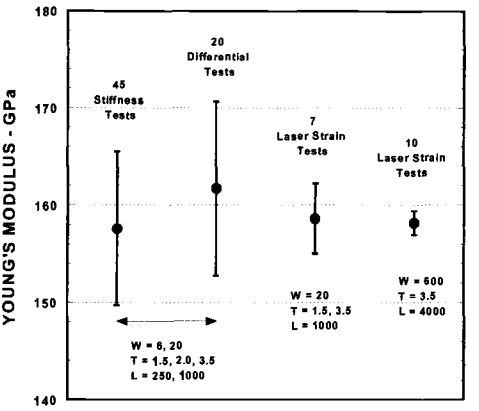

FIG. 9—*A comparison of Young's modulus measurements. W, T, and L refer to the specimens width, thickness, and length. The values plotted are the average ±1 standard deviation.*

Forty-five narrow specimens from MUMPs 25 were tested and the modulus determined from the force-displacement records. Of these, 20 pairs of results were compared differentially to extract the Young's modulus. The widest specimens were 20 μm wide, and it is difficult to obtain sufficiently bright fringe patterns from such small specimens for ISDG measurement; only 7 of the 45 tests included direct strain measurement. There were 10 wide specimens tested from the same MUMPs production run, and the modulus value, determined by direct strain measurement, is also plotted in Fig. 9.

The average Young's modulus determined by the three approaches for specimens over a wide range of sizes all hover around 160 GPa with no significant difference among them. This implies that each of the three approaches is valid. Direct strain measurement may be preferred, but it is more difficult and is limited to specimens that are 20 μm wide or larger. The average values in Fig. 9 include all of the tests; no variation with the width, thickness, or length was observed. It is indeed easier to test larger specimens as demonstrated by the much smaller scatter in the wide specimen results. One can therefore conclude that the larger scatter in the smaller specimen results arises from experimental variations and not differences in the material. Accounting for the uncertainties in dimension, force, and displacement measurement and the potential for misalignment at such small scales makes it easy to see why the scatter is so large.

MEMS are often subjected to higher temperatures; for example, in space or automotive applications, and it is important to know if there are dramatic changes in the stiffness and strength properties with increasing temperature. Figure 10 shows the effect on modulus and Fig. 11 the effect on strength for polysilicon specimens from MUMPs 30. All of the specimens were 3.5 μm thick and 50 μm wide, but the lengths were 250, 500, 1000, or 2000 μm. Strain was measured directly with the ISDG in each case; the unknown changes in the stiffness of the adhesive with temperature precluded the other two approaches to determining modulus.

Thirteen narrow specimens were tested with the complete stress-strain curve to failure recorded at temperature for each one. The specimens were heated in a small furnace using the test system shown schematically in Fig. 6, and temperature was recorded with a thermocouple placed on the die. All of the results were linear in stress versus strain and similar to the plot in Fig. 8; there was no evidence of any plasticity in the material response.

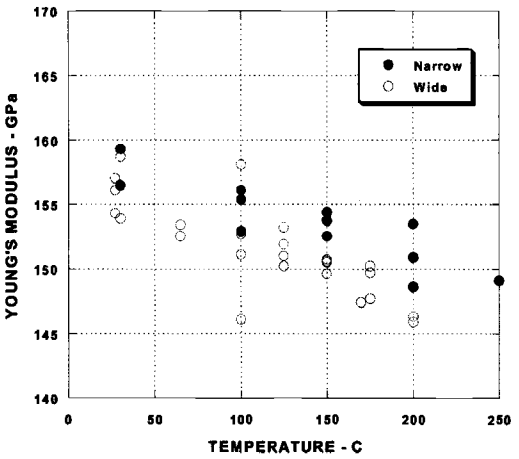

FIG. 10—*Young's modulus versus temperature for polysilicon from MUMPs 30 as measured on narrow and wide specimens.*

Two wide specimens were tested, taking modulus measurements at different temperatures on each one. These were heated resistively in open air and the temperature measured with an optical pyrometer. To get a modulus value, the specimen was heated to the test temperature and then a stress-strain test, limited to low stresses, was run. The trend is the same for both kinds of tests, and the scatter in the results illustrates the difficulty in high-temperature testing at this scale.

The strengths show a tendency to increase with temperature, which would be surprising for metals, but may not be for a brittle ceramic. The one wide specimen value shows the highest strength at 200°C, but the scatter in strength values is usually large. The fact that the modulus decreases only slightly and that the strength increases slightly over this temperature range gives confidence in the design of new MEMS.

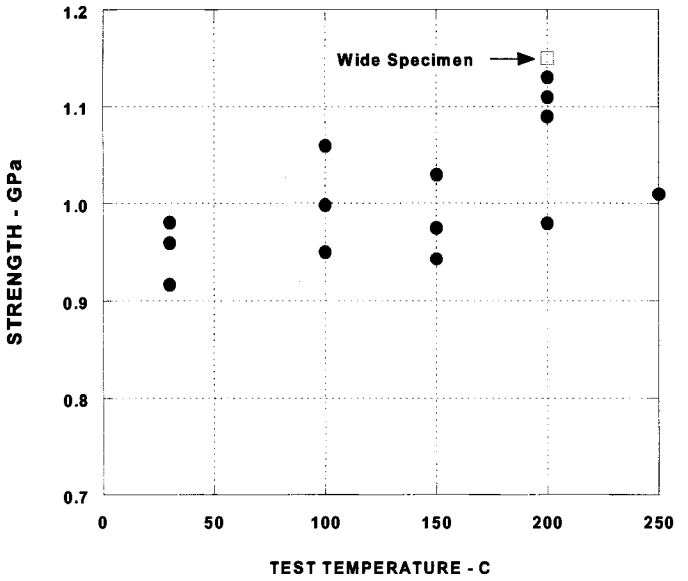

FIG. 11—*Strength versus temperature for polysilicon from MUMPs 30 as measured on 14 narrow specimens and 1 wide specimen.*

Polysilicon-based MEMS are produced at many installations, and the question of whether properties vary with manufacturing processes is an important one. Polysilicon tensile specimens from Cronos (MUMPs 25), Sandia, and Standard MEMS Inc. (SMI) were tested. SMI provided specimens from two different runs at different annealing temperatures. The modulus values, as determined by the stiffness approach, are presented in Fig. 12 where the data for Cronos is the same as in Fig. 9. The Cronos and Sandia results are essentially the same, but Student "t" tests show significant differences between the two SMI materials and between each of them and the Cronos/Sandia value.

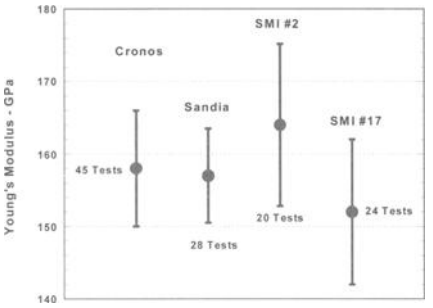

FIG. 12—*Young's modulus for four different polysilicons. The values plotted are the average ± one standard deviation.*

Fracture strength is a different story, as Fig. 13 shows. The Sandia material is considerably stronger than the other two; in fact, it is so strong that many specimens could not be broken using electrostatic gripping.

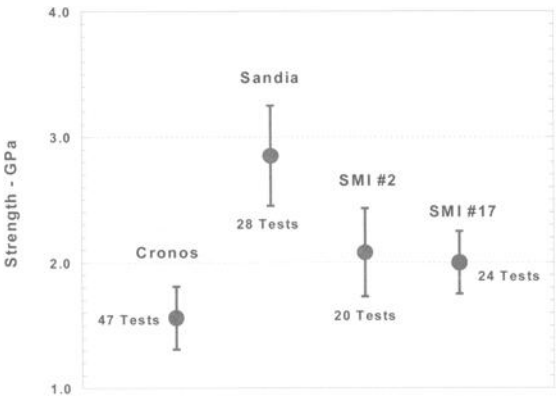

FIG. 13—*Fracture strength for four different polysilicons. The values plotted are the average ± one standard deviation.*

Silicon Nitride Results

The NASA Goddard Space Flight Center supplied silicon nitride films that had been deposited on silicon wafers by low-pressure chemical vapor deposition (LPCVD) at the Microelectronics Center of North Carolina (MCNC), now Cronos Integrated Microsystems. Specimen preparation began by patterning the 0.5 μm thick films in the shape of the wide tensile specimen of Fig. 1 using photolithography and reactive ion etching in a CF_4/O_2 plasma. A liftoff process was used to define two pairs of 10 μm wide gage markers at the center of the specimen by evaporating a 300 nanometer thick layer of Ti/Au. Using the method previously described [9], the silicon beneath the gage section was then removed by anisotropic wet chemical etching, leaving the specimen suspended between the two grip ends. Figure 14 is a photograph of such a specimen before mounting and testing.

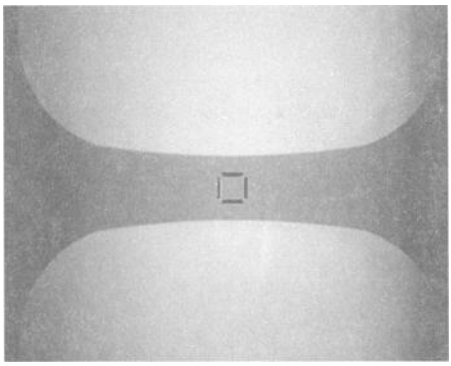

FIG. 14—*Photograph of the test section of a silicon nitride specimen showing the pattern of reflective lines for strain measurement. The specimen is 600 μm wide at its center.*

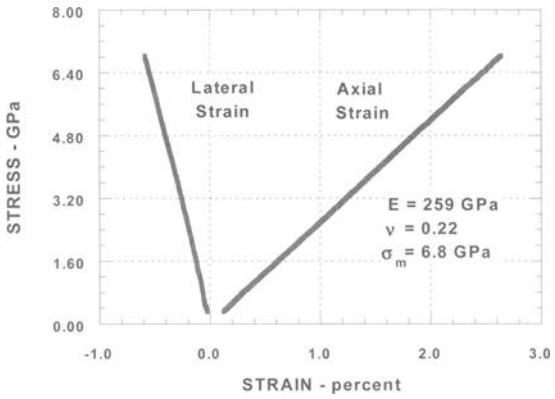

FIG. 15—*Stress-strain plot for silicon nitride.*

These specimens, though only 0.5 μm thick, are easily mounted and tested. The stress-strain record, shown in Fig. 15 is very similar to the one for polysilicon in Fig. 7, but the stresses are much larger. There are 666 data points for each plot of stress versus strain. It, too, is a linear, brittle ceramic material. These are, to our knowledge, the first stress versus biaxial strain results for silicon nitride, and for that reason the results from each test are listed in Table 2.

TABLE 2—*Measurements of mechanical properties of silicon nitride.*

Test No.	Young's Modulus, GPa	Poisson's Ratio	Fracture Strength, Gpa
SN1	255	0.19	6.13
SN3	209	0.23	8.38
SN4	254	0.25	5.00
SN5	258	0.23	6.37
SN6	253	0.24	7.21
SN7	251	0.22	5.05
SN8	259	0.22	6.84
SN9	258	0.24	
SN10	254	0.22	6.40
SN11	255		

Deleting the one low value (SN3) for modulus gives a value of 255 ± 2.6 GPa for the Young's modulus of silicon nitride. Poisson's ratio is 0.22 ± 0.018, and the fracture strength is 6.42 ± 1.11 GPa.

It is interesting to compare these values with those measured earlier by other researchers, and Table 3 summarizes earlier work. The reader will immediately notice the wide variation in values of Young's modulus and the lack of data for Poisson's ratio and fracture strength. One can expect the properties of silicon nitride to vary with deposition and annealing methods, and there is clearly a need for suitable test methods. The tensile approach presented here offers the potential for studying the effects of manufacturing processes.

TABLE 3—*Mechanical properties of silicon nitride thin films.*

Reference	Test Method	Young's Modulus, GPa	Poisson's Ratio	Fracture Strength, GPa
[22]	Bulge	222 ± 3	0.28**	
[23]	Resonant	192		
[24]	Bending of plate	128 ± 3.7 to 137 ± 2.3[a]		
[25]	Bulge	160 to 290	0.25[b]	
[26]	Bulge	86-125[a]		0.39-0.42
[27]	Ultrasonic	230-265		
[28]	Nanoindenter	101 - 251	0.27[b]	
[29]	Microbridge Bending	202.57 ± 15.80		
[30]	Bending	373		
[31]	Bulge	230, 330		
[32]	Bending	290		7.0 ± 0.9
This work	Tension	255 ± 2.6	0.22 ± 0.018	6.42 ± 1.11

[a]Calculated from researchers' plane strain or biaxial modulus assuming $\nu = 0.22$.
[b]Values assumed by researchers for modulus calculations.

Concluding Remarks

This paper summarizes tensile test techniques and procedures that have been developed at Johns Hopkins over the past five years and shows their extension and application to various new materials and to high temperature environments. The following are some general comments about these test methods.

These test methods are suitable for determining the "baseline" material properties of MEMS materials, but not for "on-chip" measurement or quality control. They are far too expensive in terms of the area required on a wafer and too time-consuming during specimen preparation and testing. The value of these larger specimens can be seen in Fig. 9 where the scatter in the modulus values for the wider ones is much smaller. These are large planar specimens manufactured by the same process as used for MEMS and give a good measure of the true material properties.

The wide specimens (one per 1 cm^2 die) are more robust, permit more precise measurements, and enable a direct measure of Poisson's ratio. However, they are more expensive and are more difficult to prepare than the narrow specimens, which are released without any

substrate etch. One does need to test more of the narrow specimens to build confidence in the average values because the uncertainties in the measurements are greater. Direct strain measurement is preferred, but not always possible. Figure 9 shows that Young's modulus can be determined from system force-displacement measurements, albeit with larger variations in the results.

Each new material requires the development of new specimen preparation procedures; this is more of an issue with the wide specimens. One must learn how to etch the substrate window without damaging the specimen and how to apply reflective lines if the manufacturing process does not include a suitable layer. It has been fairly easy to go from wide specimens of polysilicon to silicon nitride. Work is underway to learn to prepare wide specimens of silicon carbide.

Finally, the demonstration that tests can be conducted at high temperatures is important. This is a new effort, which can be extended to greater temperature ranges and further developed to permit testing in gaseous or even liquid environments. The questions that are being asked about the mechanical behavior of MEMS materials encompass a wide range, and these test methods can be useful in answering them.

Acknowledgments

Effort sponsored by the Defense Advanced Research Projects Agency (DARPA) and Air Force Research Laboratory, Air Force Materiel Command, USAF, under agreement number F30602-99-2-0553, is appreciated. The U.S. Government is authorized to reproduce and distribute reprints for Governmental purposes notwithstanding any copyright annotation thereon. Support for the high temperature tests came from AFOSR F49620-97-1-0277.

References

[1] Sharpe, W. N., Jr., Yuan, B., Vaidyanathan, R., and Edwards, R. L., "New Test Structures and Techniques for Measurement of Mechanical Properties of MEMS Materials," *Proceedings of SPIE*, Vol. 2880, 1996, pp. 78–91.

[2] Jones, P. T., Johnson, G. C., and Howe, R. T., "Fracture Strength of Polycrystalline Silicon," in *Microelectromechanical Structures for Materials Research Symposium,* San Francisco, CA, Materials Research Society, Warrendale, PA, 1998, pp. 197-202.

[3] Serre, C., Perez-Rodriguez, A., Romano-Rodriquez, A., Morante, J. R., Esteve, J. and Acero, M. C., "Test Microstructures for Measurement of SiC Thin Film Mechanical Properties," *Journal of Micromechanics and Microengineering*, Vol. 9, No. 2, 1999, pp. 190–193.

[4] Kobrinsky, E., Deutsch, Ed., and Senturia, S., "Influence of Support Compliance and Residual Stress on the Shape of Doubly-Supported Surface Micromachined Beams," *MEMS Microelectromechanical Systems*, ASME, Vol. 1, 1999, pp. 3–10.

[5] Van Arsdell, W. W. and Brown, S. B., "Subcritical Crack Growth in Silicon MEMS," *Journal of Microelectromechanical Systems*, Vol. 8, No. 3, 1999, pp. 319–327.

[6] Read, D. T. and Dally, J. W., "A New Method for Measuring the Constitutive Properties of Thin Films, *Journal of Materials Research*, Vol. 8, No. 7, 1992, pp. 1542–1549.

[7] Neugebauer, G., "Tensile Properties of Thin, Evaporated Gold Films, *Journal of Applied Physics*, Vol. 31, No. 6, 1960, pp. 1096–1101.

[8] Cunningham, S. J., Wan, S., and Read, D. T., "Tensile Testing of Epitaxial Silicon Films," in *Proceedings of the International Solid-State Sensors and Actuators*

Conference—TRANSDUCERS 95, Stockholm, Sweden, 1995, 96-99.

[9] Sharpe, W. N., Jr., Yuan, B., and Edwards, R. L., "A New Technique for Measuring the Mechanical Properties of Thin Films," *Journal of Microelectromechanical Systems*, Vol. 6, No. 3, 1997, pp. 193–199.

[10] Ogawa, H., Suzuki, K., Kaneko, S., Nakano, Y., Ishikawa, Y., and Kithara, T., "Measurements of Mechanical Properties of Microfabricated Thin Films, in *Proceedings IEEE, The Tenth Annual International Workshop on Micro Electro Mechanical Systems.* Nagoya, Japan, IEEE, New York, NY, 1997, pp. 430–435.

[11] Cornella, G., Vinci, R. P., Iyer, R. S., and Dauskardt, R. H., "Observations of Low-Cycle Fatigue of Al Thin Films for MEMS Applications," in *Microelectromechanical Structures for Materials Research. Symposium,* San Francisco, CA, Materials Research Society, 1998, pp. 81–86.

[12] Yi, C. J. and Kim, C. J., "Microscale Material Testing: Etchant Effect on the Tensile Strength," in *Transducers '99,* Sendai, Japan, 1999, pp. 518-521.

[13] Tsuchiya, T., Tabata, O., Sakata, J., and Taga Y., "Specimen Size Effect on Tensile Strength of Surface Micromachined Polycrystalline Silicon Thin Films," in *Proceedings IEEE, The Tenth Annual International Workshop on Micro Electro Mechanical Systems,* Nagoya, Japan, IEEE, New York, NY, 1997, pp. 529–534.

[14] Sharpe, W. N., Jr., Turner, K., and Edwards, R. L., *Polysilicon Tensile Testing with Electrostatic Gripping,* in *Microelectromechanical Structures for Materials Research. Symposium,* San Francisco, CA, Materials Research Society, 1998, pp. 191-196.

[15] Chasiotis, I. and Knauss, W. G., "Instrumentation Requirements in Mechanical testing of MEMS Materials, in *Microscale Systems: Mechanics and Measurements Symposium,* Orlando, FL, Society for Experimental Mechanics, Inc., 2000, pp. 56–61.

[16] Greek, S., Ericson, F., Johansson, S., and Schweitz, J., "In Situ Tensile Strength Measurement of Thick-Film And Thin- Film Micromachined Structures," in *Proceedings of the International Solid-State Sensors and Actuators Conference—TRANSDUCERS 95,* Stockholm, Sweden, 1995, pp. 56–59.

[17] LaVan, D. A., Bucheit, T. E., and Kotula, P. G., "Mechanical and Microstructural Characterization of Critical Features of MEMS Materials," in *Microscale Systems: Mechanics and Measurements Symposium,* Orlando, FL, Society for Experimental Mechanics, Inc., 2000, pp. 41–45.

[18] Yu, M.-F., Lourie, O., Dyer, M. J., Moloni, K., Kelly, T. F., and Ruoff, R. S. , "Strength and Breaking Mechanism of Multiwalled Carbon Nanotubes Under Tensile Load," *Science*, Vol. 287, No. 5453, 2000, pp. 637–40.

[19] Xie, Z. X. and Hemker, K. J., Private Communication, 1999.

[20] Sharpe, W. N., Jr., Bin, Y., and Vaidyanathan, R., "Measurements of Young's Modulus, Poisson's Ratio, and Tensile Strength of Polysilicon," in *Proceedings IEEE, The Tenth Annual International Workshop on Micro Electro Mechanical Systems,* Nagoya, Japan, IEEE, New York, NY, 1997, pp. 424–429.

[21] Sharpe, W. N., Jr., Turner, K. T, and Edwards, R. L., "Tensile Testing of Polysilicon." *Experimental Mechanics,* Vol. 39, No. 3, pp. 162–170.

[22] Vlassak, J. J. and Nix, W. D., "A New Bulge Test Technique for the Determination of Young's Modulus and Poisson's Ratio of Thin Films," *Journal of Materials Research*, Vol. 7, No. 12, pp. 3242–3249.

[23] Buchaillot, L., Farnault, E., Hoummady, M, and Fujita, H., "Silicon Nitride Thin Films

Young's Modulus Determination by an Optical Non Destructive Method," *Japanese Journal of Applied Physics*, Vol. 36, No. 6B, 1997, pp. L794–L797.

[24] Ziebart, V., Paul, O., Munch, U., Schwizer, J., and Baltes, H., "Mechanical Properties of Thin Films from the Load Deflection of Long Clamped Plates," *Journal of Microelectromechanical Systems*, Vol. 7, No. 3, 1998, pp. 320–328.

[25] Tabata, O., Kawahata, K., Sugiyama, S., and Igarashi, I., "Mechanical Property Measurements of Thin Films Using Load-Deflection of Composite Rectangular Membranes," *Sensors and Actuators*, Vol. 20, 1989, pp. 135–141.

[26] Cardinale, G. F. and Tustison, R. W., "Fracture Strength and Biaxial Modulus Measurement of Plasma Silicon Nitride Films," *Thin Solid Films*, Vol. 207, 1992, pp. 126–130.

[27] Schneider, D. and Tucker, M. D., "Non-Destructive Characterization and Evaluation of Thin Films by Laser-Induced Ultrasonic Waves," *Thin Solid Films*, Vol. 290-291, 1996, pp. 305–311.

[28] Taylor, J. A., "The Mechanical Properties and Microstructure of Plasma Enhanced Chemical Vapor Deposited Silicon Nitride Films," *Journal of Vacuum Science Technology*, Vol. 9, No. 4, 1991, pp. 2464–2468.

[29] Zhang, T. Y., Su, Y. J., Qian, C. F., Zhao, M. H., and Chen, L. Q., "Microbridge Testing of Silicon Nitride Thin Films Deposited on Silicon Wafers," *Acta Materialia*, Vol. 48, No. 11, 2000, pp. 2843–2857.

[30] Tai, Y. C. and Muller, R. S., "Measurement of Young's Modulus on Microfabricated Structures Using a Surface Profiler, in *IEEE Micro Electro Mechanical Systems*, 11-14 Feb. 1990, Napa Valley, CA, pp. 147–152.

[31] Hong, S., Weihs, T. P., Bravman, J. C. , and Nix, W. D., "Measuring Stiffnesses and Residual Stresses of Silicon Nitride Films," *Journal of Electronic Materials*, Vol. 19, No. 9, 1990, pp. 903–909.

[32] Kuhn, J. L., Fettig, R. K., Moseley, S. H., Kutyrev, A. S., and Orloff, J., "Fracture Tests of Etched Components Using a Focused Ion Beam Machine," *Proceedings of SPIE*, Santa Clara, CA, 2000, Vol. 4180, 2000, pp. 40–48.

Masahiko Demura,[1] *Kyosuke Kishida,*[1] *Osamu Umezawa,*[1] *Easo P. George,*[2] *and Toshiyuki Hirano*[1]

Ductile Thin Foils of Ni_3Al

REFERENCE: Demura, M., Kishida, K., Umezawa, O., George, E. P., and Hirano, T., "Ductile Thin Foils of Ni_3Al," *Mechanical Properties of Structural Films, STP 1413,* C. Muhlstein and S. B. Brown, Eds., American Society for Testing and Materials, West Conshohocken, PA, Online, Available: **www.astm.org/STP/1413/1413_04,** 16 March 2001.

ABSTRACT: Ni_3Al thin foils with 315 to 357 μm thickness were successfully fabricated by cold rolling. X-ray pole figures showed the formation of {110} rolling textures with various rolling directions in the foils cold rolled over 83% reduction. The deformation microstructure consists of fine slip traces and coarse and wavy shear bands. Banded deformation structure was observed in some foils. In the foils cold rolled to 83% reduction, the Vickers hardness number reached over 600 and the ultimate tensile strength over 1.7 GPa, irrespective of rolling texture and deformation microstructure. The cold rolled foils showed no tensile elongation, but it was possible to bend the foils. The foils recrystallized at temperatures over 1273 K had some tensile ductility (3.0 to 14.6%), though the polycrystalline Ni_3Al is known to be brittle due to severe grain boundary fracture. Electron backscatter diffraction measurements revealed that the large amount of total grain boundary area consists of low angle (LAB) and Σ3 coincidence lattice boundaries. This large fraction is probably a chief cause of the observed ductility.

KEYWORDS: intermetallic compounds, Ni_3Al, foil, cold rolling, texture, microstructure, mechanical properties, recrystallization, ductility

Introduction

Heat-resistant metallic foils have become important structural materials in microelectromechanical systems (MEMS) such as power-producing devices and chemical reactors [1]. Metallic foils have the advantage of high fracture toughness over ceramics, silicon carbides, alumina, et al. In semiconductor devices, Wagner and his co-workers [2-4] have recently fabricated silicon-based thin-film transistors on stainless steel foils with thickness ranging from 25 to 200 μm in order to provide flexibility and durability.

At present metallic foils below 100 μm in thickness are limited to ductile common metals, for example, aluminum, nickel, and stainless steel. Unfortunately, the high-temperature strength of these metals is low, and corrosion and oxidation resistances are not good enough. Compared to these common metals, intermetallic compounds have excellent physical and/or mechanical properties. In particular, Ni_3Al, whose crystal structure is of ordered fcc, $L1_2$, has attractive high-temperature properties such as anomalous strengthening with increasing temperature (see Fig. 1 [5,6]) and excellent resistance to oxidation and corrosion (see the review by Stoloff [7]). Table 1 lists the other physical properties at room temperature. Compared with stainless steel [6], Ni_3Al has higher thermal conductivity, lower coefficient of thermal expansion, and lower electrical resistivity, while the density and elastic constant are comparable. Because of

[1] National Research Institute for Metals, Sengen 1-2-1, Tsukuba, Ibaraki 305-0047, Japan.
[2] Oak Ridge National Laboratory, Oak Ridge, TN 37831-6093.

these excellent properties, Ni_3Al is considered to be a promising material for MEMS.

However, thin foils, particularly by cold rolling, have been unrealistic in brittle intermetallic compounds. In the case of Ni_3Al, the brittleness arises from intergranular fracture [9]. It is well known that the brittleness can be overcome by micro-alloying with boron additions [10,11], but with all this beneficial effect, the ductility is not sufficient to fabricate thin foils on an engineering scale by cold rolling [12]. Alternatively, we previously found that the directional solidification (DS) using a floating zone (FZ) method provides a significant ductility improvement for Ni_3Al without any alloying elements [13,14]. DS materials show high tensile elongation at room temperature in ambient air, more than 70%, even though they are of polycrystalline form with columnar-grained structure [15]. This ductility is larger than that of the boron-doped alloy, 53.8%, reported by Liu et al. [11]. The high ductility of the DS polycrystals was ascribed to the large fraction of low angle and low Σ-value coincidence site lattice boundaries in the columnar-grained structure [16]. Using this technique we recently have succeeded in growing single crystals of stoichiometric Ni_3Al [17,18], which has previously been considered to be difficult. As is well known, monocrystalline Ni_3Al has substantial ductility, more than 100% elongation [9]. Taking advantage of the high ductility of these DS materials, we have fabricated thin foils with thickness ranging from 53 to 300 μm by cold rolling [19].

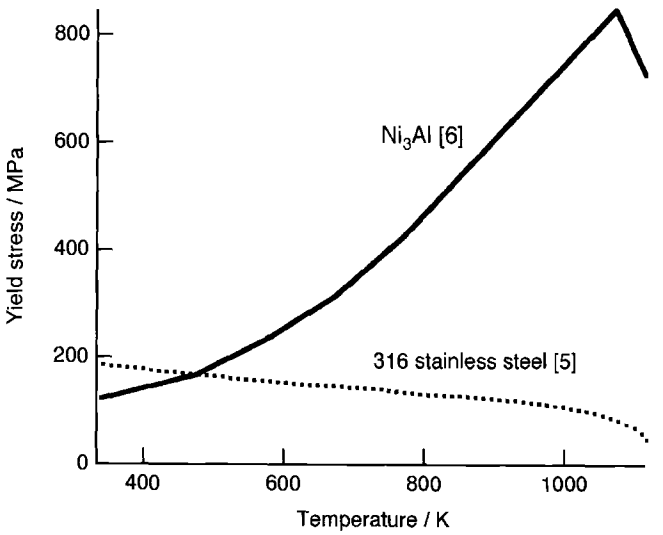

FIG. 1—*Temperature dependence of yield stress of Ni_3Al single crystal with<100> tensile direction, compared with those of 316 stainless steel.*

TABLE 1—*Density, elastic constant, thermal conductivity, coefficient of thermal expansion, and electrical resistively of Ni_3Al, compared with common metallic alloys such as 316 stainless steel, Al, and Ni at room temperature.*

Material	Density ($g\ cm^{-3}$)	Young's Modulus (GPa)	Thermal Conductivity ($W\ m^{-1}\ K^{-1}$)	Coefficient of Thermal Expansion ($10^{-6}\ K^{-1}$)	Electrical Resistivity ($\mu\ \Omega$ cm)
Ni_3Al	7.5	180	29	12.5	33
316 stainless steel	7.9	190	17	17	72
Al	2.7	70	238	24	2.7
Ni	8.9	200	88	13	6.9

The purpose of this paper is to present the deformation microstructure, rolling texture, and basic mechanical properties of the cold rolled foils. Another purpose is to examine the ductility of recrystallized foils in air at room temperature. This is because loss of ductility due to recrystallization is of great concern for structural applications. Cold-worked Ni_3Al recrystallizes at high temperatures and forms equiaxed grains which are similar to those in the cast and homogenized alloys. As is well known, these alloys are very brittle in the absence of boron [9,11]. They fracture at grain boundaries just after yielding mostly due to the presence of moisture in air [20,21]. Thus, we present here the recrystallized microstructures of the foils and the room-temperature tensile properties in air.

TABLE 2—*Analyzed Al contents and initial orientation (rolling plane and direction).*

Sample No.	Al Content (at%)	Initial Orientation	
		Rolling Plane	Rolling Direction
31-2	24.4	{0.2 0.1 1.0}	<1.0 0.0 0.2>
41-1	24.7	{3.9 1.0 5.2}	<4.0 9.0 4.8>
42-2	24.8	{2.0 1.0 4.3}	<1.1 2.0 1.0>
47-1	24.6	{3.0 0.1 4.9}	<0.0 1.0 0.0>

Experimental Procedures

Four rods, designated as Nos. 31-2, 41-1, 42-2, and 47-1 of boron-free binary stoichiometric Ni_3Al, were grown by the FZ method in an image furnace with double halogen lamps at a growth rate of 25 mm/h. The feed rod preparation and crystal growth procedure were previously described [13]. In order to obtain high single crystallinity, the crystal diameter was kept constant during the crystal growth by controlling the power of the lamps. On average the grown rods were 12 mm in diameter and 150 mm in length. Table 2 summarizes the Al contents of the four rods as determined by inductively coupled plasma spectroscopy. The Al contents are close to the stoichiometric composition (25 at% Al).

The grown rods were sectioned into sheets along the growth direction by electric discharge machining (EDM). Their surfaces were mechanically polished. The optical microstructures were examined by etching with marble reagent (2.5 g $CuSO_4$, 30 cm^3 HCl, and 25 cm^3 H_2O). Samples Nos. 31-2 and 47-1 were mostly single crystal but contained columnar grains with low angle boundaries in places. Samples Nos. 41-1 and 42-2 were single crystals. The initial rolling direction (or growth direction) and rolling plane of the sheets were determined by the Laue X-ray back reflection method as summarized in Table 2.

The sheets (about 1 or 2 mm in initial thickness, see Table 3) were cold-rolled to about 300 μm in thickness by using four-high mills with a work roll diameter of 110 mm (10% reduction per pass). Then, they were rolled further using cemented carbide rolls having a roll diameter of 75 mm (2% reduction per pass). Both the cold-rolling operations were performed without intermediate annealing or lubricant.

The rolling textures of the foils were measured by X-ray Schultz back reflection method. Optical microscopic examination, after polishing with Al_2O_3 paste and etching with the marble reagent, was conducted on the surface and the longitudinal section of the cold rolled foils. Basic mechanical properties of the cold rolled foils were examined by using samples Nos. 42-2 and 47-1. Vickers hardness was measured along the thickness direction on the longitudinal section. Tensile specimens with a gage length of 10 mm and a width of 5 mm were cut by EDM. Tensile tests were performed at room temperature in air at a strain-rate of 8×10^{-4} s^{-1}. The load data were collected at a frequency of 5 Hz with a computer.

The tensile properties of the recrystallized foils were studied using two foils of sample No. 31-2 with two different thicknesses: 73 μm—thick foil (92% reduction) and 315 μm—thick foil (67% reduction). These foils were recrystallized at 1273 K and 1573 K for 1.8 ks in a vacuum better than 1×10^{-4} Pa. The optical microstructures were examined by etching with Marble reagent. The average grain size was measured by line intercept method without correction. The orientation of the recrystallized grains was measured at 1 or 5 μm scanning steps by electron back scatter diffraction (EBSD) in a scanning electron microscope (SEM).

The grain boundary (GB) character, or Σ-value, was calculated based on Brandon's criterion [22]: if the deviation angle from an exact coincidence site lattice (CSL) relation is less than $15°/\Sigma^{1/2}$, the boundary is referred to as a CSL boundary with that Σ-value. The maximum Σ-value was set as 25 (i.e., those with higher Σ-values were

designated as random boundaries). The area fraction of each GB type was two-dimensionally evaluated by measuring GB length in the EBSD-SEM image, instead of number fraction.

Tensile specimens with gage length of 10 mm were cut from the recrystallized foils by electric discharge machining. The gage widths were 3 mm and 5 mm for 73 μm and 315 μm thick foils, respectively. Tensile tests were performed at room temperature in air at a strain-rate of 8×10^{-4} s^{-1} in the same way as those for cold rolled foils. The fracture surface was examined by SEM.

Results and Discussion

Cold Rolled Foils

It was possible to cold-roll the starting sheets to thin foil less than 100 μm in thickness without intermediate annealing. Figure 2 shows a 1 m long foil of sample No. 41-1 that is 91 μm thick and 10 mm wide. In this case the total reduction in thickness amounts to 96%. The surface is crack-free and smooth with little fluctuation in thickness (less than 1 μm) along the rolling direction. With a shiny metallic luster it looks like a mirror. It is worth noting that such high-quality thin foil was fabricated by cold rolling boron-free, binary Ni_3Al, which is considered a brittle intermetallic compound.

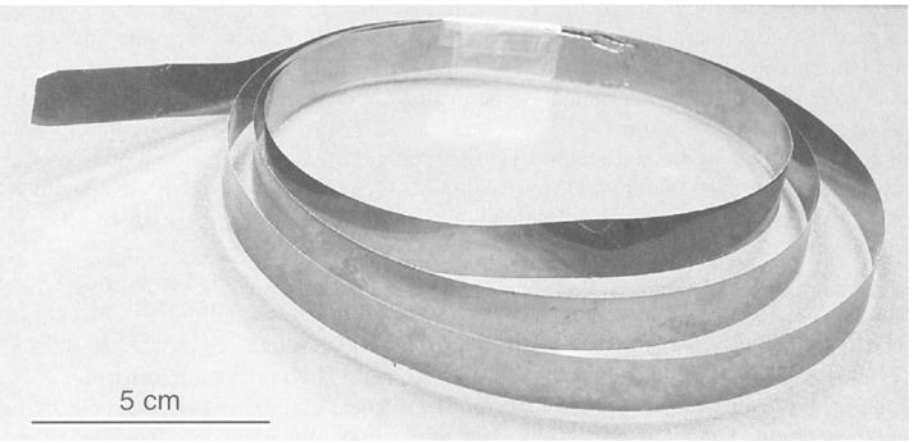

FIG. 2—*91 μm thick, 10 mm wide and about 1 m long foil of sample No. 41-1 cold-rolled to 96% reduction in thickness.*

TABLE 3— *Results of cold rolling: thickness of the sheet before and after cold rolling, reduction in thickness, and rolling texture.*

Sample No.	Thickness / μm		Reduction (%)	Rolling Texture
	Before Rolling	After Rolling		
31-2	959	315	67	...[a]
		73	92	{110}<113> + {110}<117>
		57	94	...[a]
41-1	2043	91	96	{110}<113>
42-2	1907	319	83	{110}<113>
47-1	1789	302	83	Diffused {110}<117>

[a]Not measured.

Similarly high rolling ductility was obtained in other samples, Nos. 31-2, 42-2, and 47-1, which had different initial orientations (Table 2). The results are summarized in Table 3. Samples Nos. 41-1 and 42-2 are single crystals, and hence the results may be somewhat expected because Ni_3Al is known to be ductile in a single crystal form [9]. In the case of binary, stoichiometric alloys, the problem is the difficulty in growing single crystal [18]. Samples Nos. 31-2 and 47-1 had some columnar grains, but this did not hinder cold rolling. As we previously reported [14], the columnar-grained polycrystals grown by the FZ method are ductile because most of the boundaries are low-angle and low Σ types [16].

Figure 3 shows two typical types of deformation microstructures observed in cold rolled foils. Slip traces appear on the surface and the longitudinal section after chemical etching. In the foil of Sample No. 42-2 (83.4% reduction), fine slip traces lie on the surface, being inclined about 60° to the rolling direction. Also, coarse and wavy lines, which are regarded as shear bands [23], are observed clearly on the longitudinal section, indicating inhomogeneous plastic deformation. These deformation microstructures, i.e., fine slip traces and wavy shear bands, are common in all the foils cold rolled over 83%. In the case of samples Nos. 47-1 (83.1% reduction) and 31-2 (92% reduction), however, the deformation structure is composed of repeated two bands with differently oriented slip lines. The width of the bands ranges from 20 to 100 μm parallel to the rolling direction [Fig. 3(b)].

Figure 4 shows the {220} pole figures of the foils cold rolled to 83% reduction: (a) sample No. 42-2 and (b) No. 47-1. In all the foils cold rolled over 83% reduction, the

{220} pole has the highest intensity peak at the normal direction (ND) and surrounding high intensity regions about 60 degrees away from the ND. This shows that the surface is almost parallel to {110} plane. This {110} texture is thought to be stable in Ni_3Al under compressive deformation normal to the rolling plane, as discussed elsewhere [19]. Regarding the rolling direction (RD), there is some difference among the samples, as seen in Table 3. Samples Nos. 41-1 and 42-2 possess a single {110}<113> texture. On the other hands, sample No. 31-2 consists of {110}<113> and {110}<117> textures. Sample No. 47-1 has a {110} texture, but the RD scatters around <117> direction, which indicates that the {110} texture consists of grains with slightly different RD. Probably the difference observed in the texture is due to the initial orientation of the sheet.

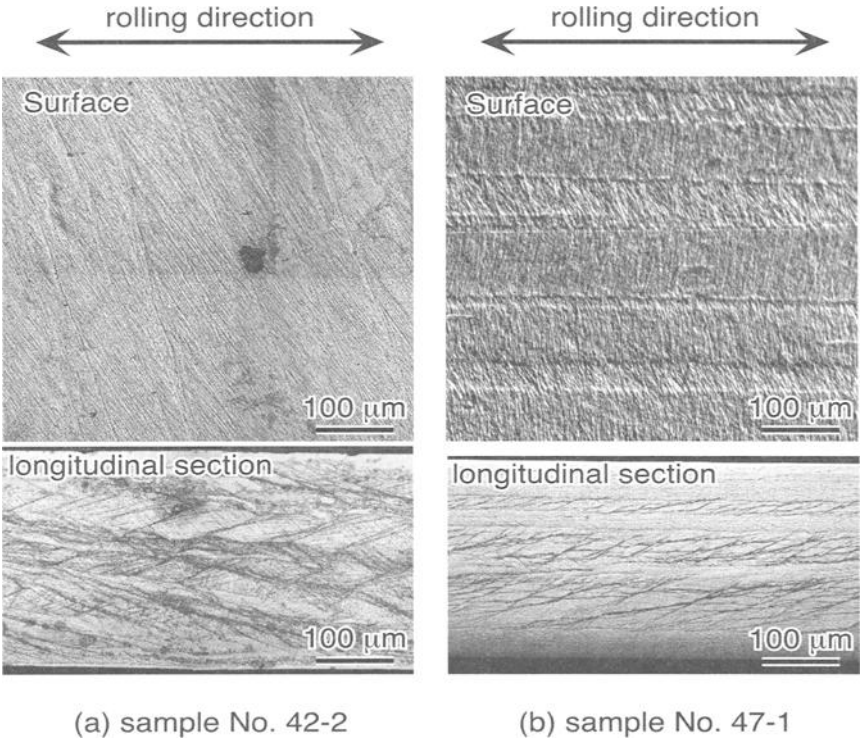

FIG. 3—*Optical microstructures observed on the etched surface and longitudinal section of cold rolled foils: (a) sample No. 42-2 and (b) No. 47-1.*

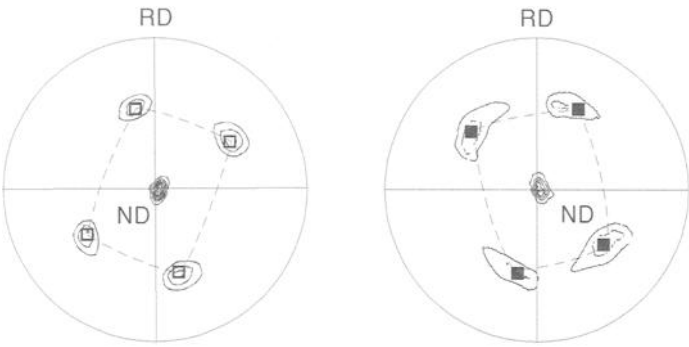

FIG. 4—*The {220} pole figures of the foils cold rolled to 83% reduction: (a) sample No. 42-2 and (b) No. 47-1. Open and solid squares represent {110}<113> and {110}<117> textures, respectively.*

Mechanical properties were examined by using the foils of samples Nos. 42-2 and 47-1, which were cold rolled to almost the same reduction, 83%. In both the foils, there was no appreciable change in the hardness number along the thickness direction. This indicates that macroscopically the foils are homogeneously cold-rolled. Average Vickers hardness numbers are 604 for sample No. 42-2 and 649 for No. 47-1, showing no significant difference. For reference, the Vickers hardness number of the starting sheet before cold rolling was about 260.

Figure 5 plots the engineering stress vs. engineering strain curves for samples Nos. 42-2 and 47-1. Since the foils are heavily cold rolled, they show extremely high tensile strengths: 1.7 GPa for sample No. 42-2 and 1.9 GPa for sample No. 47-1. Both the foils fractured with almost no plastic elongation. In spite of such brittle behavior, interestingly it is possible to bend as shown in Fig. 6, probably because of the thinness of the foils. There is almost no difference in the tensile properties and the Vickers hardness number between the two samples, though their deformation microstructures and textures are different.

Recrystallized Foils

It has been reported that the recrystallization of Ni_3Al starts between 900 and 1000 K, depending on the amount of rolling reduction [24]. Consistent with this, both 73 μm and 315 μm thick foils of sample No. 31-2 were fully recrystallized above 1273 K. Figure 7 is an optical micrograph of the 73 μm thick foil heat-treated at 1273 K for 1.8 ks. It shows a typical recrystallized microstructure that consists of equiaxed grains with homogeneous grain size. A similar grain morphology was observed in the foils heat-treated above 1273 K and also in the 315 μm thick foils. Table 4 lists the average grain sizes of 73 μm and 315 μm thick foils recrystallized at 1273 K and 1573 K. The grain size increases with increasing heat treatment temperature, as expected.

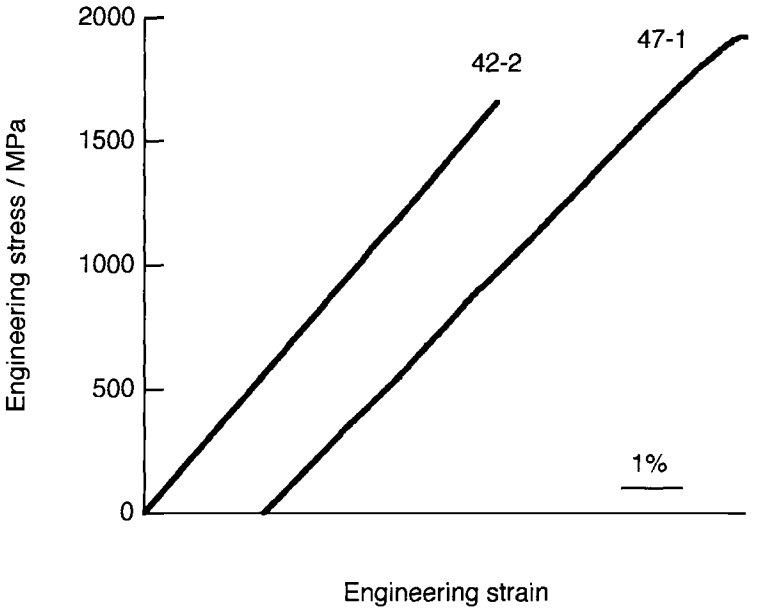

FIG. 5—*Engineering stress vs. engineering strain curves of the foils cold rolled to 83% reduction of samples Nos. 42-2 and 47-1.*

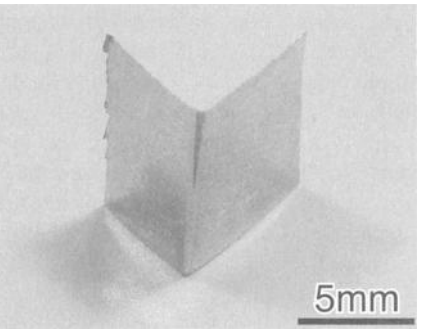

FIG. 6—*Photograph of 91 μm-thick foil cold rolled to 96% reduction of sample No. 41-1, showing bending.*

Table 4 summarizes the area fraction of each GB type in the 73 μm and 315 μm thick foils of sample No. 31-2 recrystallized at 1273 K and 1573 K. The recrystallized foils consist mostly of three types of boundaries, low angle (LAB), Σ3, and random boundaries (RB). Very small amounts of CSL boundaries between Σ5 and 25 exist in the foils recrystallized at 1273 K. Note that the foils have a large fraction of LAB and Σ

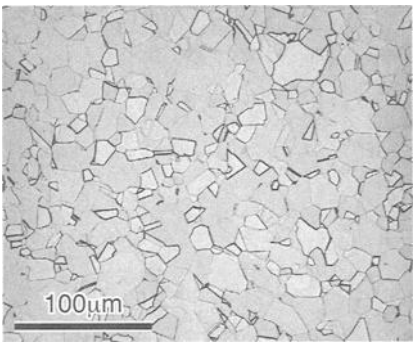

FIG. 7—*Microstructure of 73 μm-thick foil of sample No. 31-2 recrystallized at 1273 K for 1.8 ks.*

boundaries, which are considered to be crack-resistant [25,26]. There is a tendency that as the heat treatment temperature increases, the total fraction of LAB and Σ3 increases, and the fraction of RB, which is considered to be very susceptible to cracking, decreased.

Tensile properties, i.e., yield stress and elongation to fracture, of 73 μm and 315 μm thick foils of sample No. 31-2 recrystallized at 1273 K and 1573 K are summarized in

TABLE 4—*Average grain size, area fraction of grain boundary types, and tensile properties, yield stress (YS) and fracture elongation (FE) in the recrystallized foils of No. 31-2.*

Thickness (μm)	Heat Treatment Temperature (K)	Average Grain Size (μm)	Area Fraction (%)				Tensile Properties	
			LAB	Σ3	Σ5-25	RB	YS (MPa)	FE (%)
73	1273	11.9	11.7	31.0	3.1	54.2	250	3.0
73	1573	66.9	44.3	15.6	0.0	40.1	50	5.6
315	1273	14.5	3.2	37.8	0.8	58.2	294	3.4
315	1573	115	73.2	10.8	0.0	16.0	70	14.2

Table 4. Note that all the foils show some ductility after yielding. In particular, the foils recrystallized at 1573 K, which show 5.6% and 14% elongations for 73 μm and 315 μm thick foils, respectively. Though the ductility decreases with decreasing recrystallization temperature, the foils recrystallized at 1273 K still show 3% elongation. Thus, the ductility loss due to recrystallization is not a serious problem in our foils. These ductilities normally cannot be expected for boron-free polycrystalline Ni_3Al. The yield stress decreases with increasing recrystallization temperature, because of the increase in grain size.

Figure 8 shows the fracture surfaces of the recrystallized foils after the above tensile tests. Intergranular fracture is dominant in both the 73 μm and 315 μm thick foils recrystallized at 1273 K, while the fraction of transgranular fracture is rather high in the foils recrystallized at 1573 K. The change in fracture mode correlates well with both the ductility and the fraction of the LAB and Σ3 boundaries (Table 4). It is, therefore,

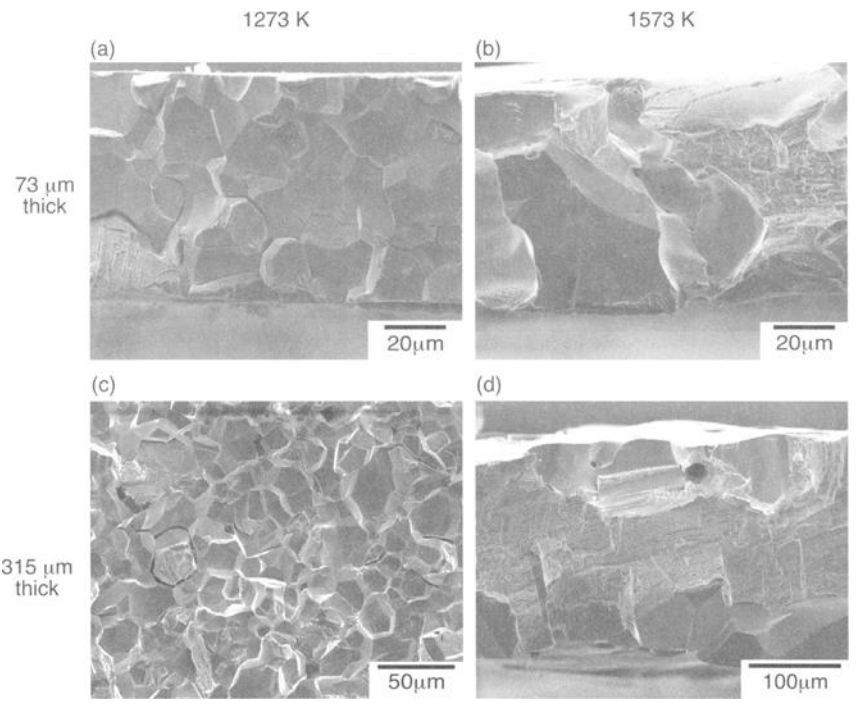

FIG. 8—*Fracture surfaces of the recrystallized foils of sample No. 31-2: (a) 73 μm-thick foil recrystallized at 1273 K, (b) 73 μm-thick at 1573 K, (c) 315 μm-thick at 1273 K, and (d) 315 μm-thick at 1573 K.*

concluded that with increasing heat treatment temperature, the fraction of the crack-resistant boundaries, LAB and Σ3, increases, resulting in high ductility by suppressing intergranular fracture.

Probably, the ductility of recrystallized foils is mainly due to the high area fraction of LAB and Σ3 boundaries. Hanada et al. [25] found no cracks along these boundaries in bent specimens of recrystallized, stoichiometric Ni_3Al, suggesting higher crack-resistance compared to other boundaries. This was confirmed by Lin and Pope [26] who examined the distribution of cracked boundaries as a function of Σ-value in bent specimens of melt-spun Ni_3(Al,0.2at%Ta) ribbons. In addition to these qualitative evaluations of grain boundary fracture strength, very recently we found that these LAB and Σ3 boundaries do not fracture in air by performing uniaxial tensile tests on bicrystal specimens, instead the bulk fractures [27]. This new finding shows that the fracture strength of these two types of boundaries is at least comparable to that of the bulk, which confirms that the presence of these two types of boundaries enhances the overall ductility of Ni_3Al.

Conclusions

Thin foils of stoichiometric Ni_3Al below 100 μm in thickness with crack free and smooth surfaces were fabricated by cold rolling without intermediate annealing. The basic mechanical properties of cold rolled—and heat treated—foils were examined and the following results were obtained:

1. Foils rolled over 80% reduction have strong {110} textures with various rolling directions depending on the initial orientations. The deformation microstructure of the rolled foils consists of fine slip lines and coarse and wavy shear band. Some of the foils, sample No. 31-2 and 47-1, shows banded structure. The Vickers hardness numbers of the foils cold rolled to 83% are extremely high: 604 and 649 for sample Nos. 42-2 and 47-1, respectively. These foils show high ultimate tensile strength of 1.7 GPa for sample No. 42-2 and 1.9 GPa for sample No. 47-1. The foils show no tensile ductility but they can be bent. There is no significant difference in the mechanical properties between the foils which have different rolling directions and deformation microstructure from each other.

2. The foils recrystallized at 1273 K and 1573 K for 1.8 ks had some ductility, 3 to 14.6%, in contrast to cast, polycrystalline Ni_3Al, which normally shows almost no elongation. The ductility was mainly related to the area fraction of low angle and Σ3 coincidence site lattice boundaries, which ranged from 41 to 84% depending on the heat treatment temperature. These boundaries are considered to be more crack-resistant than other boundaries, i.e. high Σ and random types.

Acknowledgment

This research was supported partially by the Division of Materials Science and Engineering at the Oak Ridge National Laboratory, managed by UT-Battelle, LLC, for the U.S. Department of Energy under contract DE-AC05-00OR22725.

References

[1] Spearing, S. M., "Materials Issues in Microelectromechanical Systems (MEMS)," *Acta Materialia*, Vol. 48, 2000, pp. 179–196.

[2] Theiss, S. D., Wu, C. C., Lu, M., Sturm, J. C., and Wagner, S., "Flexible, Lightweight Steel-Foil Substrates for a Si:H Thin-Film Transistor," *Material Research Society Symposium Proceedings*, Vol. 471, 1997, pp. 21–26.

[3] Suo, Z., Ma, E. Y., Gleskova, H., and Wagner, S., "Mechanics of Rollable and Foldable Film-on-Foil Electronics," *Applied Physics Letters*, Vol. 74, 1999, pp. 1177–1179.

[4] Ma, E. Y. and Wagner, S., "Amorphous Silicon Transistors on Ultrathin Steel Foil Substrates," *Applied Physics Letters*, Vol. 74, 1999, pp. 2661–2662.

[5] Brandes, E. A. and Brook, G. B., Eds., *Smithells Metals Reference Book*, 7th ed., 1992.

[6] Golberg, D., Demura, M., and Hirano, T., "Effect of Al-Rich Off-Stoichiometry on the Yield Stress of Binary Ni_3Al Single Crystals," *Acta Materialia*, Vol. 46, 1998, pp. 2695–2703.

[7] Stoloff, N. S., "Physical and Mechanical Metallurgy of Ni_3Al and Its Alloys," *International Materials Reviews*, Vol. 34, 1989, pp. 153–183.

[8] Epstein, A. H. and Senturia, S. D., "Macro Power from Micro Machinery," *Science*, Vol. 276, 19997, p. 1211.

[9] Aoki, K. and Izumi, O., "On the Ductility of the Intermetallic Compound Ni_3Al," *Transactions JIM* (the Japan Institute of Metals), Vol. 19, 1978, pp. 203–210.

[10] Aoki, K. and Izumi, O., "Improvement in Room Temperature Ductility of the $L1_2$ Type Intermetallic Compound Ni_3Al by Boron Addition," *Nihon Kinzoku Gakkai Shi*, Vol. 43, 1979, pp. 1190–1196.

[11] Liu, C. T., White, C. L., and Horton, J. A., "Effect of Boron on Grain-Boundaries in Ni_3Al," *Acta Metallurgica*, Vol. 33, 1985, pp. 213–229.

[12] Liu, C. T. and Sikka, V. K., "Nickel Aluminides for Structural Use," *Journal of Metals*, Vol. 38, 1986, pp. 19-21.

[13] Hirano, T., "Improvement of Room Temperature Ductility of Stoichiometric Ni_3Al by Unidirectional Solidification," *Acta Metallurgica et Materialia*, Vol. 38, 1990, pp. 2667–2671.

[14] Hirano, T., "Tensile Ductility of Stoichiometric Ni_3Al Grown by Unidirectional Solidification," *Scripta Metallurgica et Materialia*, Vol. 25, 1991, pp. 1747–1750.

[15] Hirano, T. and Kainuma, T., "Improvement of Room-Temperature Ductility of Stoichiometric Ni_3Al by Unidirectional Solidification," *ISIJ* (The Iron and Steel Institute of Japan) *International*, Vol. 31, 1991, pp. 1134–1138.

[16] Watanabe, T., Hirano, T., Ochiai, T., Oikawa, H., "Texture and Grain Boundary Character Distribution (GBCD) in b-Free Ductile Polycrystalline Ni_3Al," *Materials Science Forum*, Vol. 157-162, 1994, pp. 1103–1108.

[17] Demura, M. and Hirano T., "Stress Response by the Strain-Rate Change in a Binary Stoichiometric Ni_3Al Single Crystal," *Philosophical Magazine Letter*, Vol. 75, 1997, pp. 143–148.

[18] Golberg, D., Demura M., and Hirano, T., "Single Crystal Growth and

Characterization of Binary Stoichiometric and Al-rich Ni_3Al," *Journal of Crystal Growth*, Vol. 186, 1998, pp. 624–628.

[19] Demura M., Suga, Y., Umezawa, O., Kishida, K., George, E. P., and Hirano, T., "Fabrication of Ni_3Al Thin Foil by Cold Rolling," unpublished work, 2000.

[20] George E. P., Liu, C. T., and Pope, D. P., "Environmental Embrittlement: the Major Cause of Room-Temperature Brittleness in Polycrystalline Ni_3Al," *Scripta Metallurgica et Materialia*, Vol. 27, 1992, pp. 365–370.

[21] George E. P., Liu, C. T., and Pope, D. P., "Intrinsic Ductility and Environmental Embrittlement of Binary Ni_3Al," *Scripta Metallurgica et Materialia*, Vol. 28, 1993, pp. 857–862.

[22] Brandon, D. G., "The Structure of High-Angle Grain Boundaries," *Acta Metallurgica*, Vol. 14, 1966, pp. 1479–1484.

[23] Ball, J. and Gottstein, G., "Large Train Deformation of Ni_3Al + B: Part I. Microstructure and Texture Evolution During Rolling," *Intermetallics*, 1993, Vol. 1, pp. 171–185.

[24] Gottstein, G., Nagpal, P., and Kim, W., "Recrystallization and Texture in Boron-Doped Ni_3Al," *Materials Science and Engineering A*, Vol. 108, 1989, pp. 165–179.

[25] Hanada, S., Ogura, T., Watanabe, S., Izumi, O., and Masumoto, T., "Application of the Selected Area Channeling Pattern Method to the Study of Intergranular Fracture in Ni_3Al," *Acta Metallurgica*, Vol. 34, 1986, pp. 13–21.

[26] Lin, H. and Pope, D. P., "The Influence of Grain-Boundary Geometry on Intergranular Crack-Propagation in Ni_3Al," *Acta Metallurgica et Materialia*, Vol. 41, 1993, pp. 553–562.

[27] Su, J. Q., Demura, M., and Hirano, T., "Grain Boundary Fracture Strength in Ni_3Al Bicrystals," unpublished work, 2000.

Greg S. Long,[1] *David T. Read,*[2] *J. D. McColskey,*[2] *and Karen Crago*[3]

Microstructural and Mechanical Characterization of Electrodeposited Gold Films[4]

REFERENCE: Long, G. S., Read, D. T., McColskey, J. D., and Crago, K., **"Microstructural and Mechanical Characterization of Electrodeposited Gold Films,"** *Mechanical Properties of Structural Films, ASTM STP 1413,* C. L. Muhlstein and S. B. Brown, Eds., American Society for Testing and Materials, West Conshohocken, PA, Online, Available: www.astm.org/STP/1413/1413_9, 1 June 2001.

ABSTRACT: The effects of temperature and duration of thermal treatments on the microstructure and mechanical properties of electrodeposited gold films were evaluated. Specimens were synthesized by electrodeposition of gold on copper foil substrates followed by application of novel photolithographic and microetching techniques so as to produce a series of free-standing gold thin-films of dimensions 2.5 by 200 by 800 μm supported by copper foil frames. Seven different heat treatments, spanning temperatures from 25 to 300°C and up to 8 h in duration, were studied. In each case, thermal annealing of the samples was carried out in an inert atmosphere after the copper foil substrate beneath the tensile coupons had been removed by $CuCl_2$ etchants. X-ray diffraction was used to assess the microstructures. The crystalline texture of the films changed from predominantly <111> (perpendicular to the plane) to strongly <100>, and then back toward <111> with heat treatment. No evidence for grain growth was seen in the X-ray diffraction results. Tensile-strength analyses were performed using a piezo-actuated microtensile testing system. The properties of the heat-treated specimens varied significantly from those of the nontreated material. Tensile strength generally decreased with longer heat treatment. Cyclic fluctuations in the elongation-to-failure, strikingly similar to those in the ratio of <200> to <111> diffracted X-ray intensities, were observed as a function of increasing heat-treatment temperature.

KEYWORDS: ductility, electroformed, electroplated, heat treatment, strength, tensile, texture, x-ray, yield, ultimate

Introduction

This study reports the mechanical and microstructural characterization of a series of electrodeposited gold films with different heat treatments. Electrodeposited gold films are used in many different applications in electronic devices. The mechanical behavior of thin metal films used in electronic devices is important because poor mechanical performance can lead to reliability problems, and because large deviations from expected behavior can impact the function of other parts of the product. Tensile testing is a widely used method of characterizing the behavior of bulk metals; however, there is not yet an accepted ASTM standard for mechanical tensile testing of thin films. Many authors have reported techniques for tensile testing of thin films, as cited in [1-3]. The technique [3] used in the present study has the advantages that the specimen fabrication route is

[1]Department of Chemistry, Minnesota State University, Mankato, Mankato, MN.
[2]National Institute for Standards and Technology, Boulder, CO 80305.
[3]Engineered by Design Inc., Burnsville, MN.
[4]Contribution of the U. S. Department of Commerce; not subject to copyright in the U.S.A.

consistent with processes available and used in the manufacture of commercial devices and that the size scale of the specimen is consistent with that of the film as it is used in commercial products.

There are three significant problems with the tensile testing of thin films:

1. Determination of elongation to failure. It is impossible to adapt conventional techniques used for bulk specimens because the broken pieces of the specimen cannot be manually placed to allow measurement of the final length.
2. Verification of alignment of the specimen with the tensile axis. For bulk specimens, strain gages placed on the specimen can be used, but this cannot be done for microscale specimens.
3. Allowing for the effect of the high ratio of specimen width to specimen thickness. Values of 100 or more are not unusual.

All of these problems were encountered in the present set of tests.

Materials

Specimens were created by electrodeposition of gold on a support layer of copper foil. For tensile testing, a series of photolithographic and etching steps produced multiple specimens, each of which consisted of a free-standing tensile coupon of gold supported by a frame of copper foil, as shown in Figs. 1 and 2. All of the tensile specimens were electrodeposited using $NaAs_2O_3$ additive to the plating bath for grain refinement. The copper foil had been produced by a rolling operation and had indentations from the rollers. These indentations were transferred to the electrodeposited gold specimens, and are clearly visible in Fig. 2 as transverse indentations, lines, or scratches on the tensile coupon. Profilometry along the tensile axis indicated that the thickness varied by ±0.2 μm from the overall trend over spans of 10 μm or less. The longitudinal features on the specimens are related to the photolithography operation, and indicate that the specimen cross section is not exactly rectangular. The specimen thickness as measured by profilometry varied across its width, with a broad maximum in the center and tapers at the edges. Based on several measurements of different specimens, nominal cross-sectional dimensions of 2.5 by 200 μm were adopted. The significance of these dimensions is in the stress calculations. We estimate, based on the variability seen from specimen to specimen and from location to location within a specimen, that the area of any individual specimen might have deviated by as much as 5% from the nominal value.

Specimens with six different heat treatments, plus untreated specimens, were tested; the different heat treatments are listed (Table 1). These heat treatments consist of a temperature series, including 100, 200, and 300°C, all for 1 h, and a duration series, 1, 2, 4, and 8 h at 200°C.

Density was measured via X-ray fluorescence (XRF) prior to the X-ray diffraction (XRD) measurements, and the diffraction data confirm the results: all specimens had a density of 19.3 g/cm^3, consistent with bulk gold.

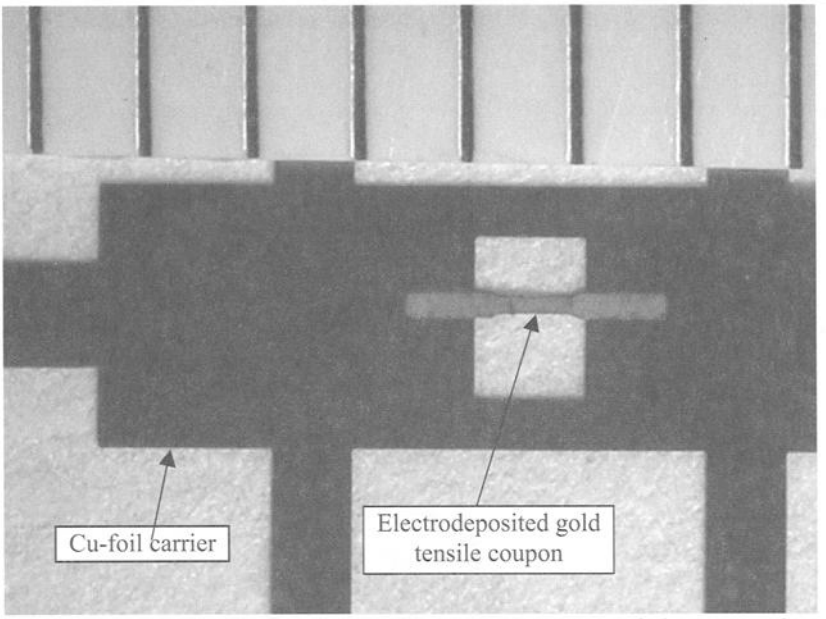

FIG. 1—*Electrodeposited gold tensile specimen on copper-foil carrier. The scale gradations are 1 mm. The specimen thickness is 2.5 μm.*

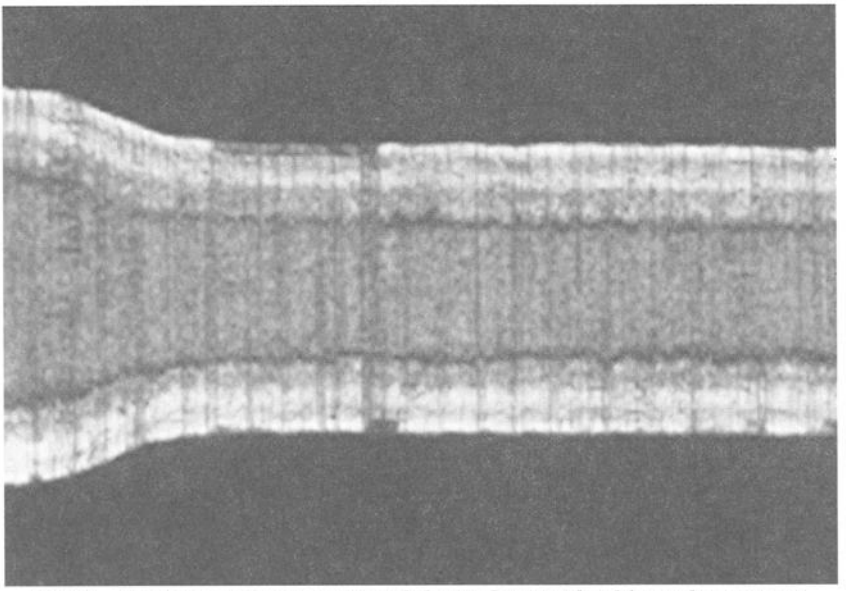

FIG. 2—*High-magnification view of electrodeposited gold tensile specimen, showing indentations transferred from the rolled substrate.*

Heat Treatment No.	Temp, °C	Time, h
0	20	0
1	100	1
2	200	1
3	300	1
4	200	2
5	200	4
6	200	8

Techniques

X-Ray Diffraction

The microstructures were characterized by X-ray diffraction measurements using a microdiffractometer that provided copper K-alpha radiation with a spot size of 50 by 50 μm. All of the spectra were K-alpha 2 stripped and corrected for background via a cubic-spline algorithm. Cell constants were calculated via indexing on a face-centered cubic (fcc) lattice to a goodness of fit of 98% or better. Measurements of peak position, width, and intensity were carried out for the <111>, <200>, <220>, <311>, and <222> peaks for specimens representative of all the heat treatments except heat treatment 6.

Tensile Testing

Tensile tests were carried out using a piezo-actuated test fixture described previously [3], Fig. 3. Test techniques as described previously for silicon-framed tensile specimens were used with two exceptions, the method used to section the frames just before testing, and the strain measurement technique. For silicon frames, sectioning with a dental drill or micro-cutting wheel has been successful [3,4]. For the copper-foil frames of the present study, the dental drill was unsatisfactory because it grabbed the foil, severely distorted the frame, and damaged the specimen. Instead, an electrical discharge technique was used. A static voltage of about 10 V was applied between the specimen frame and a tungsten electrode. The electrode was slowly brought into contact with the frame. As contact was made, a spark was created. The spark melted and removed part of the frame, on the order of 0.1 mm. This operation was repeated as necessary. In this manner, the frame could be sectioned without contacting or displacing the specimen. Force and grip displacement data were recorded as described previously [3]. The gage length strain was taken as the grip displacement divided by the gage length. As shown in the pictures of the specimen, Figs. 1 and 2, the specimen ends have a dogbone shape. The effective gage length was taken as the length of the straight section. Figure 4 displays a typical test record. The specimen number for this data set, HT_0_6, indicates heat treatment 0, which is no heat treatment, and specimen number 6 of that group. In this group, Specimens 1, 2, 3, and 5 were failed tests because the specimen was damaged during the sectioning of the frame. Tests of Specimens 4, 6, and 7 were successful. In subsequent groups, after the arc-cutting technique mentioned above was perfected, only an occasional test failed.

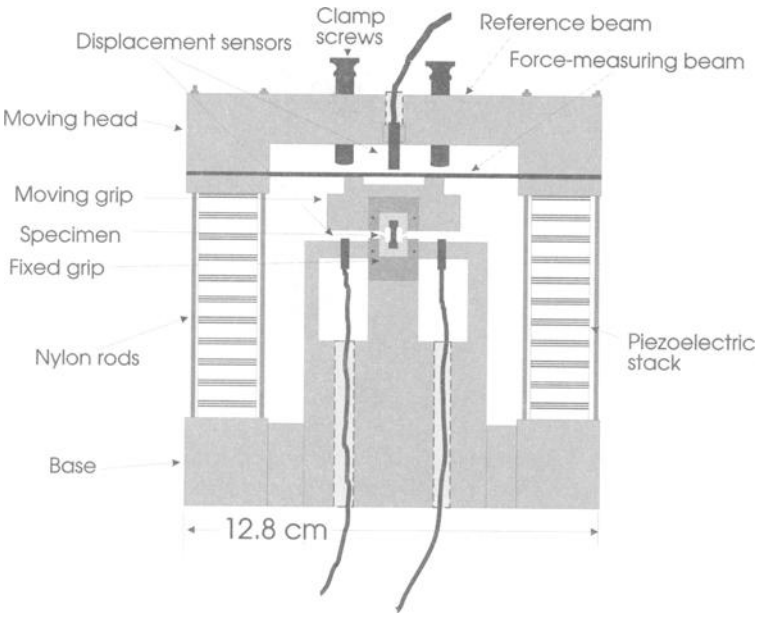

FIG. 3—*Piezo-actuated tensile tester.*

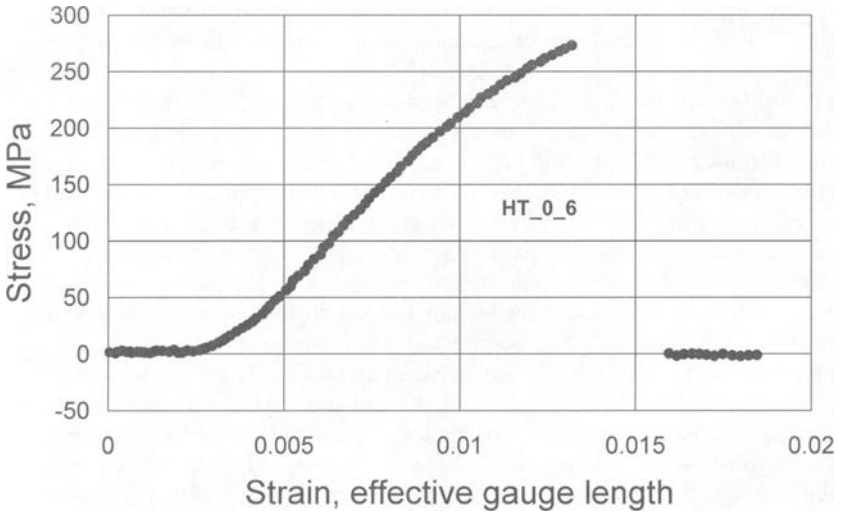

FIG. 4—*Plot of engineering stress vs gauge length strain for specimen HT_0_6, not heat-treated, the second specimen that was successfully tested.*

In addition to grip-to-grip displacement, local displacements were measured by digital image correlation (DIC). A series of images, typically about 100, were acquired by optical microscopy during the course of each tensile test. Images were acquired approximately every 5 s during the test. A typical image is shown in Fig. 5. Each image was labeled with information sufficient to associate it with a specific data record including the applied force and the grip displacement. The images were analyzed to produce strain values averaged along the gage section. Figure 6 shows the stresses plotted against strain as measured by DIC. The strain from DIC is a more accurate measurement of the actual strain because the gage length strain, as defined above, includes spurious displacement contributions from the parts of the specimen outside the gage length.

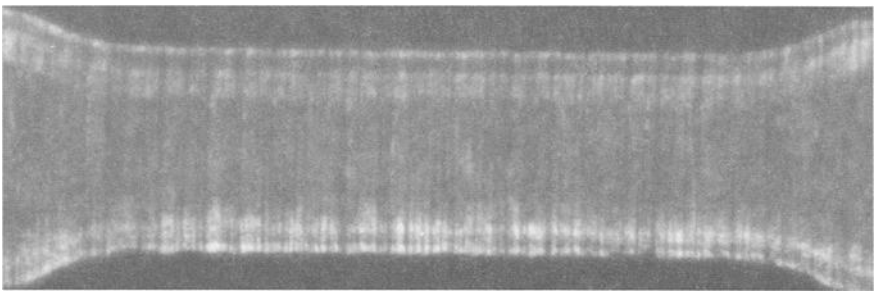

FIG. 5—*Image obtained during the test of specimen HT_0_6 and used for measurements of displacement by digital image correlation.*

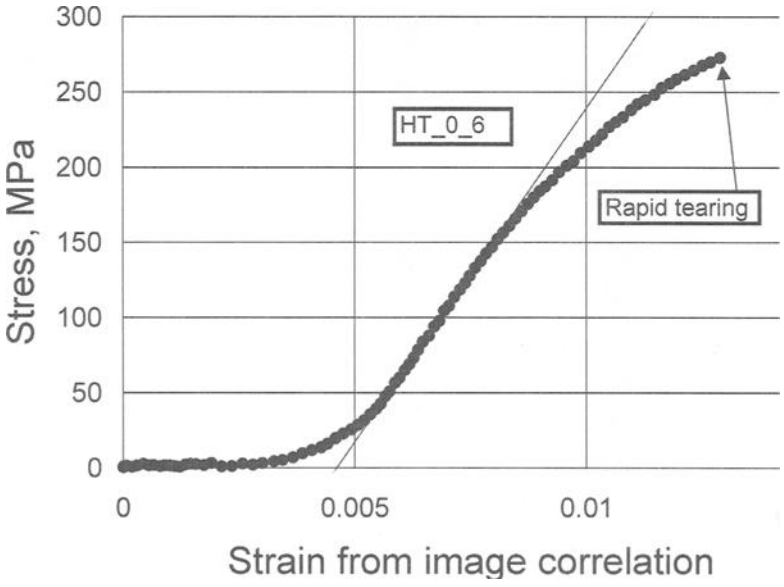

FIG. 6—*Stress strain plot for specimen HT_0_6, the second specimen tested successfully, not heat-treated.*

The appearance after failure is shown in Fig. 7. In this test the image previous to the one in Fig. 7 showed no tear, while Image 99 shows tearing completely across the specimen. Some of the heat-treated specimens showed slower tearing, where several images showing progressive tearing were obtained. In these cases, the start of tearing was taken as the image where the tear reached 20% of the specimen width. This determination was not always unambiguous, because often the tear seemed to follow a pre-existing indentation across the specimen. Care was taken to make consistent judgments across all the heat treatments. Adopting the strain from DIC as the critical value associated with this failure criterion allowed the tearing failure results to be based entirely on the images, with no dependence on the grip displacement.

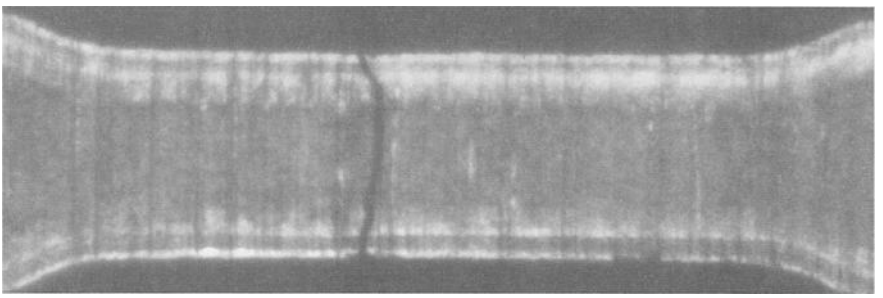

FIG. 7—*Specimen HT_0_6 after failure, image number 99.*

A more quantitative method of locating the failure point would be to use a stress criterion. Such a method was applied, with the failure criterion being the gage length strain where the stress had fallen to 50% of its maximum value. Using the gage length strain in this criterion removed it from any dependence on the images.

Results

X-Ray Diffraction

The X-ray diffraction results for peak position and peak width were constant for all the heat treatments, including as-received. All of the samples indexed nicely (99% confidence interval) on an fcc lattice with a lattice constant of 4.3 Å, inconsistent with the handbook value for bulk gold of 4.08 Å, and a density of 19.3 g/cm^3, which is consistent with the bulk value. Thus, all of the films were essentially the same material. Also, no significant differences (again at a 99% confidence level) were measured in the average peak width. Thus, the possibility of a significant change in grain size was not supported by the data.

In contrast to these findings, the relative intensities for diffraction peaks of different Miller indices changed significantly with heat treatment. Figures 8 and 9 show the behavior with heat treatment of the ratio of the peak intensities for the <200> and <111> peaks.

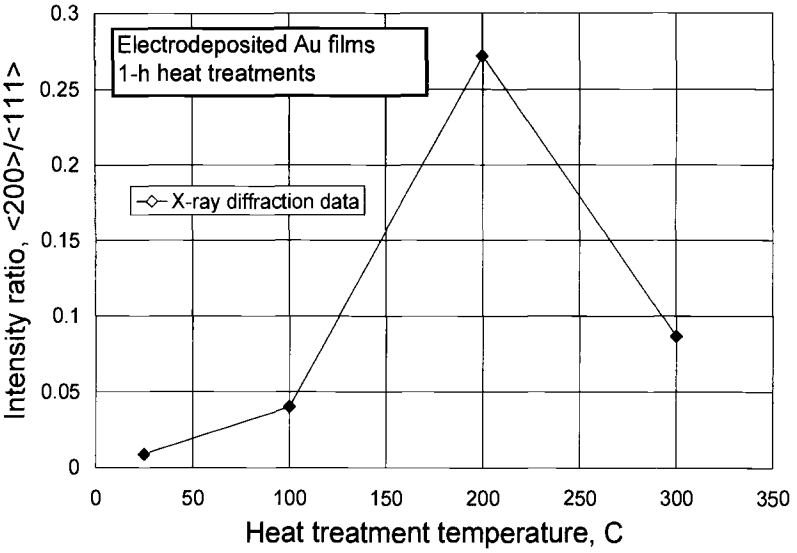

FIG. 8—*X-ray diffraction results for electrodeposited gold films heat treated for 1 h at 100, 200, and 300 °C.*

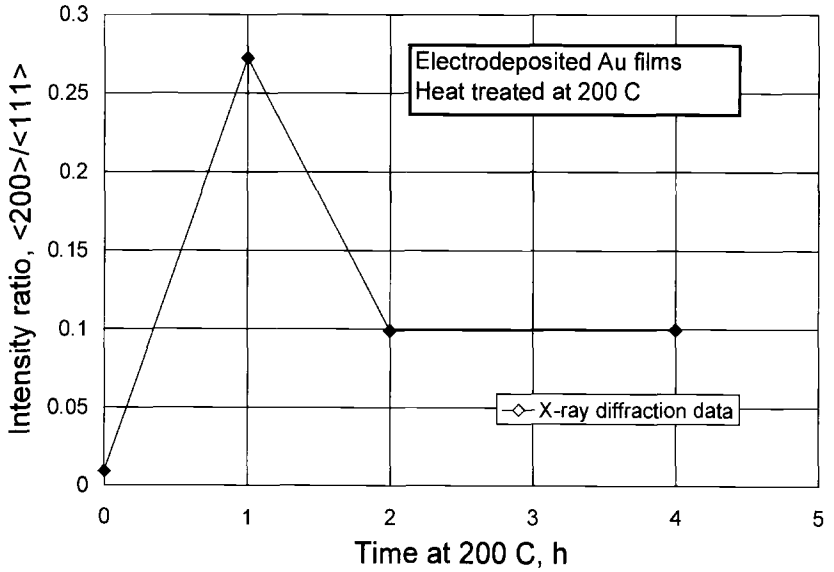

FIG. 9—*X-ray diffraction results for electrodeposited gold films heat treated at 200 C for 0, 1, 2, and 4 hours.*

Tensile Testing

The results of the tensile tests are listed in Table 2.

TABLE 2—*Results of the tensile tests for heat-treated electrodeposited gold films.*

Heat Treatment	Specimen	Yield strength, MPa	Ultimate strength, MPa	GL* strain to half max stress	DIC* strain to start of tearing
0					
	0_4	269	273	0.012	0.008
	0_6	258	259	0.011	0.009
	0_7	268	303	0.017	0.011
1					
	1_2	305	334	0.022	0.019
	1_4	253	253	0.010	0.007
	1_5	264	336	0.026	0.027
2					
	2_2	172	188	0.021	0.029
	2_3	151	173	0.019	0.027
	2_4	128	155	0.026	0.049
3					
	3_2	130	131	0.020	0.015
	3_3	132	136	0.026	0.034
	3_4	133	139	0.022	0.026
4					
	4_1	141	168	0.012	0.016
	4_3	158	162	0.016	NA
	4_4	175	178	0.015	0.023
5					
	5_1	144	157	0.014	0.018
	5_2	143	151	0.015	0.014
	5_3	227	227	0.011	0.011
6					
	6_1	127	132	0.017	0.022
	6_2	134	158	0.017	0.020
	6_4	133	144	0.021	0.026

*GL, gage length. DIC, digital image correlation.

Strength and strain to failure are plotted against heat-treatment time and temperature in Figs. 10-13. Figure 10 shows that heat treatments of 200 and 300°C reduced both the yield and the ultimate strength to about half of their initial values, while the 100°C treatment for 1 h produced no decrease.

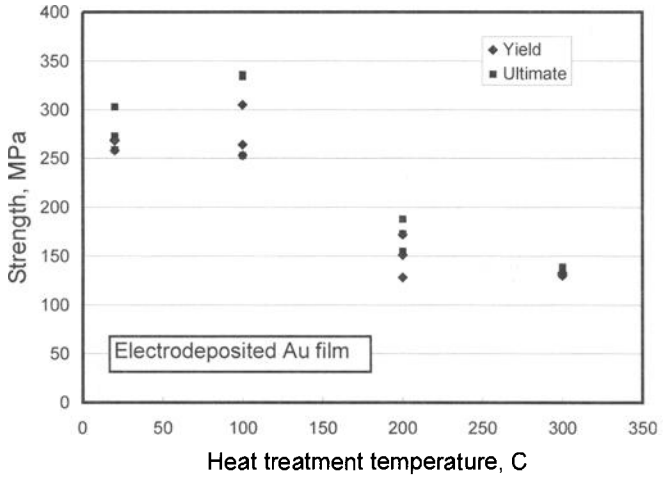

FIG. 10—*Yield and ultimate tensile strength plotted against heat treatment temperature for 1 h anneals.*

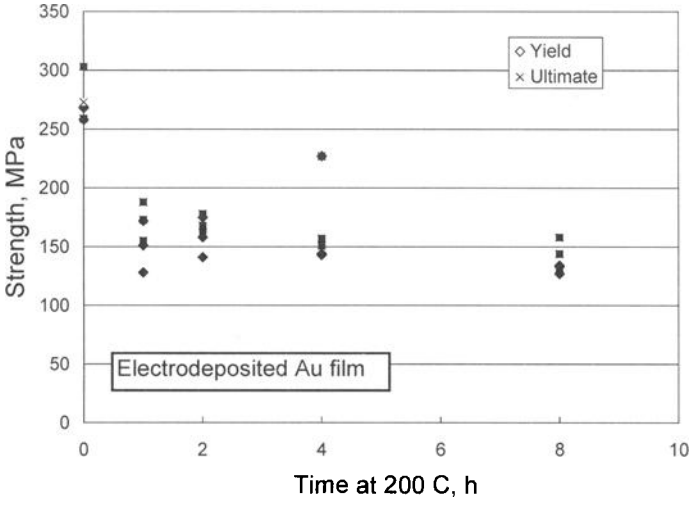

FIG. 11—*Yield and ultimate tensile strength plotted against duration of heat treatment at 200 °C.*

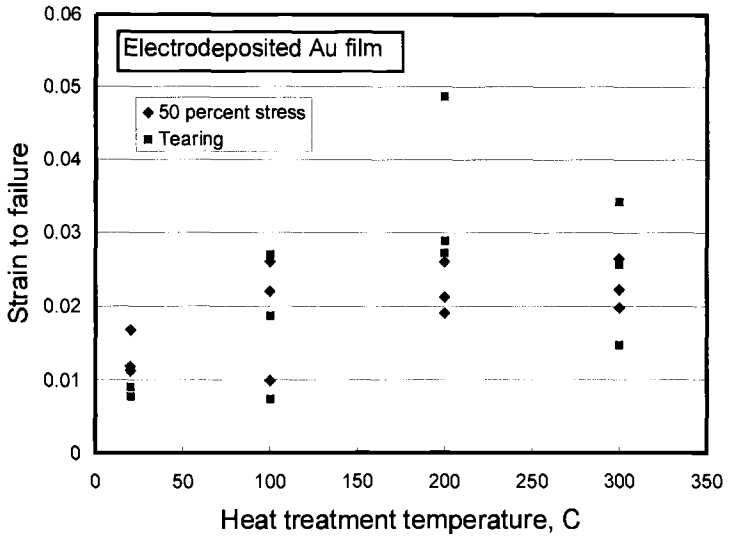

FIG. 12—*Strain to failure using two different criteria, a 50 percent stress drop and the initiation of tearing, plotted against heat-treatment temperature for 1 h anneals.*

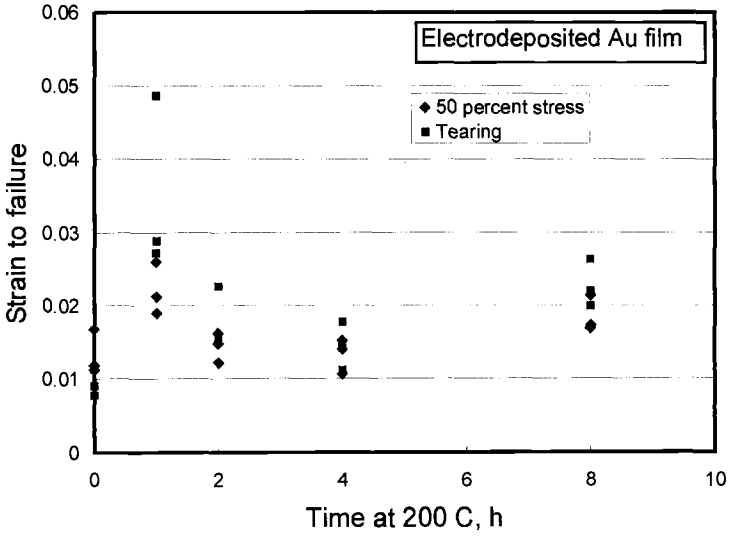

FIG. 13—*Strain to failure measure using two different criteria, a 50% stress drop and initiation of tearing, plotted against duration of the 200°C heat treatment.*

Figure 11 shows that for the 200°C heat treatment, practically all of the strength reduction occurred during the first hour of treatment.

Figure 12 shows the results for the effect of heat treatment temperature on strain to failure. Even a 100°C heat treatment appears to increase the strain to failure. The results are unambiguous for the 200°C treatment. The strain to failure after a 1 h heat treatment at 200°C is about 2.5 times its value for the untreated specimens. Strain to failure appears to decrease slightly as the heat-treatment temperature is raised from 200 to 300°C. Figure 13 shows that the strain to failure has a complex behavior as a function of heat treatment time at 200°C. The strain to failure increases initially, then decreases back to a value intermediate between the initial value and the value after the 1 h treatment, and then increases again.

Discussion

Handbook values for the ultimate strength of annealed polycrystalline bulk gold are given as 130 and 220 MPa for annealed and cold-worked material [5]. The respective elongations are given as 40 to 50 and 4% [5]. A review of the properties of electrodeposited gold [6] gave the tensile strength as 110 to 210 MPa and the elongations as 3 to 8% for specimens 25 μm thick, depending on the plating chemistry and current. The present results for as-deposited gold differ from these, having higher strength and lower elongation. However, no grain-refinement treatment was mentioned for the cited handbook results, and the present specimens are some ten times thinner. The high strengths seen here for as-deposited films are tentatively attributed to a small grain size in this material, which is typical for thin films. Three causes can be considered for the generally low elongation values seen here as compared to typical bulk values: (1) The transverse ridges and valleys in the specimens may introduce stress and strain concentrations; (2) The probability of a defect in the thin wide films tested here may be greater than in a bulk rod specimen; (3) The result may be characteristic of the geometry tested, indicating a sensitivity to biaxial stress. Resolution of this issue is beyond the scope of this work. Possibility (3) cannot be rejected out of hand, because recent results with electron-beam-evaporated aluminum films indicate that the same material that exhibits a 1 % elongation to failure for a specimen 200 μm wide by 1 μm thick can show 30 % elongation to failure when a specimen 10 μm wide by 1 μm thick is tested.

The stress-strain records, such as those in Figs. 4 and 6, typically showed a gradual increase in stress with imposed tension as the slack was removed from the specimen, followed by a linear region, followed by a region where the stress increased less than linearly with the strain. The slopes of the linear regions, calculated from the force and the displacement as measured by digital image correlation, were typically in the range of 30 to 40 GPa, compared to the bulk polycrystalline gold Young's modulus of 80 GPa [7]. The difference is attributed to the presence of deformation mechanisms in addition to lattice elastic strain, such as small-scale plasticity.

The deformation results are illustrated by Figs. 14 through 17. Figure 14 shows DIC results for two images bracketing the linear stress-strain region for specimen HT_0_6, Fig. 6. Figure 15 shows the displacement from the image at the end of the linear region to the last image before failure. Figure 16 shows the deformations from the end of the linear region to the beginning of significant tearing. Figure 17 shows image number 129 of specimen HT_2_3, which was taken as the beginning of significant tearing.

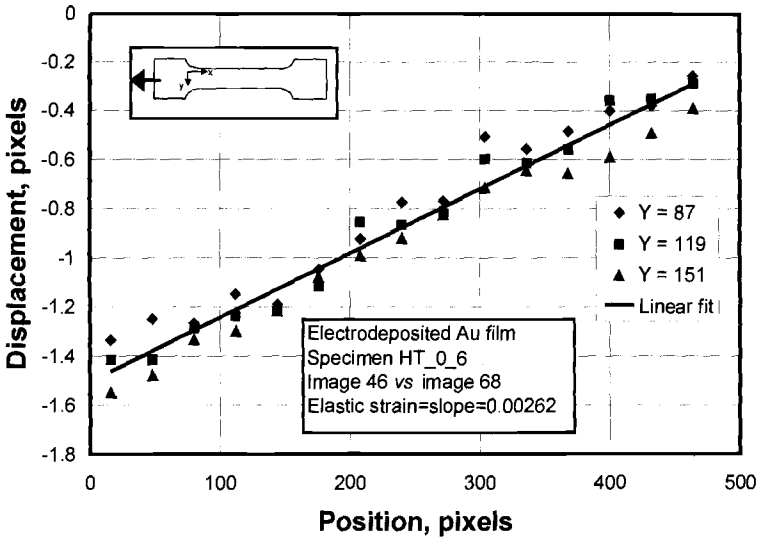

FIG. 14 —*Digital image correlation results for two images bracketing the linear stress-strain region for specimen HT_0_6. Y indicates transverse position. The slope of this line is the derivative of displacement with respect to position, which is the strain difference between these two images.*

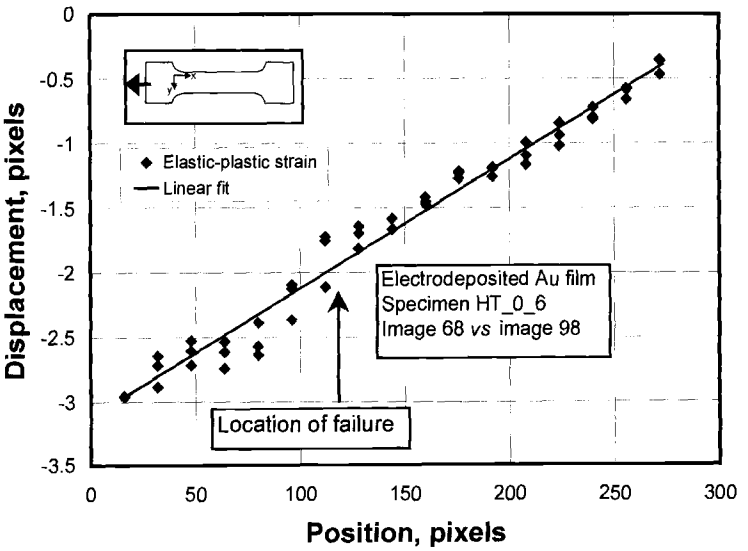

FIG. 15—*Digital image correlation results for two images bracketing the nonlinear stress-strain region for specimen HT_0_6. Image 99 shows complete failure. This result shows that little necking or strain localization occurred in this specimen before failure.*

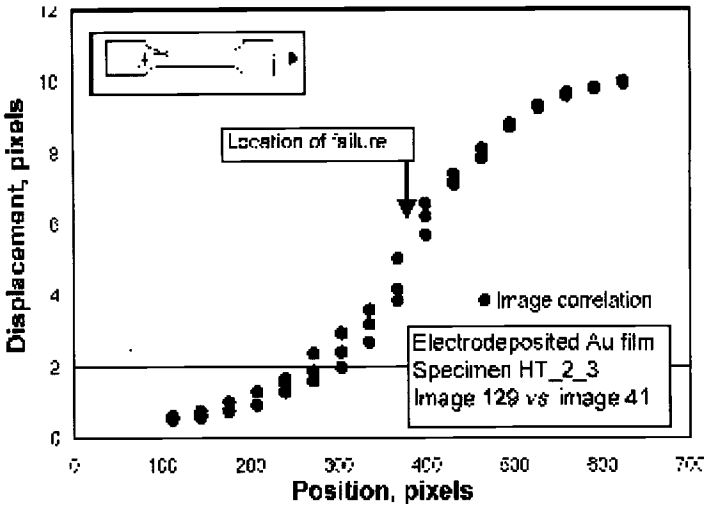

FIG. 16—*Strain localization occurred in this specimen before failure Digital image correlation results for two images bracketing the nonlinear stress-strain region for specimen HT_2_3.Image 129 is the image where tearing has initiated. This result shows that significant.*

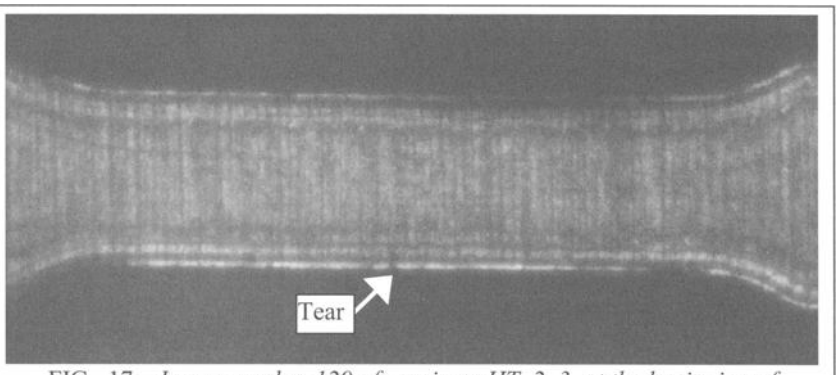

FIG. 17—*Image number 129 of specimen HT_2_3, at the beginning of tearing.*

A striking correlation is seen between the x-ray diffraction data for peak intensity ratios and the strain to failure as a function of heat-treatment duration. These data suggest that a <100> orientation of the film plane promotes a high strain-to-failure for in-plane tension, while a <111> orientation promotes a low strain-to-failure. This result is consistent with the slip planes and directions of fcc metals such as gold, in which the slip planes are the {111} planes, and the slip directions are the <110> directions [*8*]. Planes

oriented at 45° to the tensile axis have the highest Schmid factor, which relates resolved shear stress to axial stress. A low ratio of <200> to <111> peaks indicates that the plane of the film is a {111} plane. This orientation provides few {111} planes at 45° to the tensile axis, leading to higher axial stresses for a given resolved shear stress. On the other hand, a high ratio of <200> to <111> planes means that {100} planes are favored in the plane of the film. This orientation provides many opportunities for {111} planes to fall at orientations near 45° to the tensile axis, leading to higher resolved shear stresses at lower axial stresses.

Summary

Electrodeposited gold films, as tested with a thickness of 2.5 μm and a width of 200 μm, have high strength compared to handbook values for pure gold: three as-deposited specimens had an average ultimate strength of 278 MPa. But the electrodeposits had low elongation to failure, around 1% in the as-deposited specimens. On first loading, the stress-strain curves had a brief linear region after the slack in the specimen was removed, but the slope of this linear region was far below the handbook value of the Young's modulus. This behavior is attributed to the activity of inelastic deformation mechanisms. Heat treatment reduced the strength of the electrodeposited films, and increased their elongation to failure. The behavior of the strain to failure as a function of heat-treatment duration at 200°C was especially complex. As a means to increase the strain to failure, a 1-h treatment at 200°C would be preferable to longer times at this temperature.

A striking correlation was seen between the strain to failure and the ratio of X-ray diffraction intensities for the <200> versus <111> peaks as a function of heat-treatment temperature. This indicates that the changes in elongation to failure are a result of changes in the preferred orientation of the grains of the film. Films in which a high fraction of the grains had their <111> directions oriented perpendicular to the plane of the film had lower elongations to failure than films in which <100> directions were more numerous. The X-ray diffraction results provided no indication of significant changes of grain size with heat treatment.

The testing of free-standing, photolithographically produced gold electrodeposits on copper foil support frames in a piezo-actuated microtensile test rig proved feasible with the use of a manual spark-cutting technique to sever the frames immediately prior to testing. The use of a large number of digital images as part of the tensile test records was useful for calculating strains by digital image correlation, and for locating the beginning of significant tearing.

References

[1] Alexopoulos, P. S. and O'Sullivan, T. C., "Mechanical Properties of Thin Films," *Annual Reviews of Material Science,* Vol. 20, 1990, pp. 391–420.

[2] Hardwick, D. A., "The Mechanical Properties of Thin Films, A Review," *Thin Solid Films,* Vol. 154, 1987, pp. 109–124.

[3] Read, D. T., "Piezo-Actuated Microtensile Apparatus," *Journal of Testing and Evaluation,* JTEVA, Vol. 26, No. 3, May 1998, pp. 255–259.

[4] Sharpe, W. N., Jr., Yuan, B., Edwards, R. L., and Vaidyanathan, R., "Measurements of Young's Modulus, Poisson's Ratio, and Tensile Strength of Polysilicon," *Proceedings of the Tenth IEEE International Workshop on Microelectromechanical Systems*, Nagoya, Japan, 1997, pp. 424–429.

[5] Brandes, E. A., *Smithells Metals Reference Book, Sixth Edition*, Butterworths, London, 1983, p. 22–189.

[6] Safranek, W. H., *The Properties of Electrodeposited Metals and Alloys, A Handbook*, American Elsevier, New York, 1974, pp. 156–157.

[7] Simmons, G. and Wang, H., *Single crystal Elastic Constants and Calculated Aggregate Properties: A Handbook*, The M.I.T. Press, Cambridge, 1971, p. 189–190.

[8] Brown, F. C., *The Physics of Solids*, Benjamin, New York, 1967, p. 139.

George C. Johnson,[1] *Peter T. Jones,*[2] *Ming-Ting Wu,*[1] *and Tomonori Honda*[1]

Determining the Strength of Brittle Thin Films for MEMS

REFERENCE: Johnson, G. C., Jones, P. T., Wu, M. T. and Honda, T., "**Determining the Strength of Brittle Thin Films for MEMS,**" *Mechanical Properties of Structural Films, ASTM STP 1413*, C. Muhlstein and S. B. Brown, Eds., American Society for Testing and Materials, West Conshohocken, PA, Online, Available: www.astm.org/STP/1413/1413_22, 1 September 2001.

ABSTRACT: Design of micro-electro-mechanical systems (MEMS) requires characterization of the materials involved. However, because the structural dimensions found in MEMS are so small, measurement of even the most basic properties is challenging. This work focuses on techniques for determining the strength of MEMS materials. Several approaches are presented and compared. Results for the failure strength of a common brittle MEMS material are discussed. It is shown that a probabilistic approach must be used to understand the results, and that the apparent strength of this material depends considerably on the mode of deformation (tension vs. bending). The probabilistic approach suggests a dependence in strength on both specimen size and deformation mode. Issues such as load alignment and difficulty in determining specimen geometry are also considered.

KEYWORDS: fracture, thin films, brittle, Weibull statistics, MEMS, mechanical strength

Introduction

The need to understand the mechanical properties of materials used in MEMS has become clear over the past several years. As a result, a number of groups have examined this problem from a range of perspectives [1–9]. One important design parameter is, of course, the strength of the material. However, there has been little agreement as to what approach should be used. (See, for example, the MRS Proceedings on this topic [8] and the recent report by Ballarini [9].) Attempts to compare results from different approaches have been disappointing in that there is often a significant difference in the measured strength of the same material. One example of this [10] involves a "round robin" experiment in which four different research groups attempted to characterize the Young's modulus and fracture strength of the same polysilicon material from a structural layer produced by a MEMS foundry service, the Multi-User MEMS Processes (MUMPs). The results from the three groups that were able to measure the fracture strength were considerably different from one another, with specimens loaded in uniaxial tension tending to fail at a lower stress, on average, than specimens loaded in bending. The scatter of the data made by each group was also substantial, with the coefficient of variation on the order of 10% for most groups.

The ceramics community has also had to deal with the fact that the material of interest is brittle and that there is considerable scatter in observed fracture of nominally

[1] Professor, Graduate Student, and Undergraduate Student, respectively, Department of Mechanical Engineering, University of California, Berkeley, CA 94720-1740.

[2] DiCon Fiber Optics, Inc., 1331 Eighth Street, Berkeley, CA 94710.

identical devices. The approach taken there is to treat the problem statistically, focusing on identifying the failure distribution rather than just the mean strength with an associated standard deviation. It is well known that such a statistical approach can explain many of the observed differences in strength due to differences in size or loading [11,12].

In this paper, we draw heavily on the previous work on fracture testing of macroscopically-sized brittle materials to better characterize the fracture of structural thin films used in MEMS devices. The failure of a brittle material is a probabilistic event that depends upon the size of the specimen being tested as well as the loading conditions. A two-parameter Weibull model is used to analyze the results of a set of tests in which fracture strength was measured for a number of cantilever beams. It is shown that the model used captures the salient features of the data. Using the Weibull parameters obtained from the bending tests, the model predicts that identical beams loaded in uniaxial tension should exhibit an average strength that is about 40% lower than that for the cantilevers. General equations for relating specimen volume and inhomogeneous stress to expected mean strength are provided, along with an analysis of the effect of nonideal loading of uniaxial tension specimens. This work follows that of Greek, et al. [1] and Tsuchiya, et al. [3], who also advocate the use of Weibull statistics for describing the fracture behavior of polysilicon.

Weibull Statistics for Brittle Failure

Fracture in brittle materials is often governed by the presence of defects, the largest of which initiates failure. Small specimens are less likely than large specimens to contain a critically sized flaw that will cause failure at a given stress level. Therefore, one should expect the failure to depend upon the size of the part being tested. This understanding is a basic element of dealing with structural ceramics, but is less familiar to those accustomed to dealing with metals. This fundamental characteristic of brittle failure necessitates a probabilistic approach.

Failure Under Homogeneous Stress—Uniaxial Tension

The Weibull approach to describing failure is often referred to as a "weakest link" model, in which failure of any part of a structure results in failure of the entire structure. Let $P_f(\sigma)$ be the probability that an element (a link in a chain, for example) will have failed at a stress less than σ (i.e., $P_f(\sigma)$ is the cumulative probability for failure). The probability of survival of that element to this stress level is then $1-P_f$. If the structure (the chain) is made up of N identical elements (links) all subject to the same stress and having the same failure probability, then the probability P_s that the entire structure will survive is the product of the individual survivals,

$$P_s = 1 - P_{f,structure} = (1-P_f)^N . \tag{1}$$

Taking the natural log of both sides, and assuming that the probability of any individual element failing is small ($P_f << 1$ so that $\ln(1-P_f) \cong -P_f$), allows us to write

$$\ln(1-P_{f,structure}) = -NP_f . \tag{2}$$

The probability that the structure will fail at a stress less than σ is then

$$P_{f,structure}(\sigma) = 1 - \exp[-NP_f(\sigma)]. \tag{3}$$

For a continuous structure, rather than one made up of discrete elements, N is the ratio of the total volume V to the volume v of a reference element of the material, whose probability of failure is now denoted $P_{f;v}(\sigma)$. Thus,

$$P_{f;V}(\sigma) = 1 - \exp\left[-\frac{V}{v}P_{f;v}(\sigma)\right]. \tag{4}$$

Weibull [13] proposed a particular function to describe $P_{f;v}(\sigma)$ that has been found useful for many failure mechanisms. This function is

$$P_{f;v}(\sigma) = u(\sigma - \sigma_c)\left(\frac{\sigma - \sigma_c}{\sigma_0}\right)^m \tag{5}$$

where σ_c is called the "critical or threshold stress," below which failure does not occur; σ_0 is referred to as the "scale parameter," which has physical dimensions of stress, but which does not lend itself to easy identification in terms of experimental observations; m is called the "shape parameter" (or sometimes, the Weibull modulus); and $u(\alpha)$ is the unit step function whose value is zero if $\alpha < 0$ and is unity if $\alpha \geq 0$. The presence of the unit step function in Eq 5 accounts for the fact that failure is assumed to occur only when the stress is greater than the critical stress σ_c.

Much of the work involving the Weibull distribution assumes that $\sigma_c = 0$. We make this assumption as well, recognizing that it will be important to establish its validity on the basis of suitable experimental observations. The failure probability for a structure of volume V subject to uniform uniaxial stress is then

$$P_{f;V}(\sigma) = 1 - \exp\left[-\frac{V}{v}u(\sigma)\left(\frac{\sigma}{\sigma_0}\right)^m\right]. \tag{6}$$

It is common to reduce this expression to one linear in the shape parameter m by taking the natural logarithm of $(1 - P_{f;V})$ twice, to yield

$$\ln\left[\ln\left(\frac{1}{1 - P_{f;V}(\sigma)}\right)\right] = m\ln(\sigma) - \left(m\ln(\sigma_0) - \ln\left(\frac{V}{v}\right)\right). \tag{7}$$

If the Weibull approach is valid, a plot of the left-hand side of Eq 7 vs. $\ln(\sigma)$ should be a straight line with slope m.

As noted above, the scale parameter σ_0 is not readily identified from a set of experimental data. However, it can be eliminated in favor of the mean failure stress of the data by noting that the mean of this distribution, $\bar{\sigma}_{f;V}$, is given in terms of the

Weibull parameters as

$$\bar{\sigma}_{f;V} = \sigma_0 \Gamma\left(1+\frac{1}{m}\right)\left(\frac{v}{V}\right)^{1/m}, \tag{8}$$

where $\Gamma(\cdots)$ is the standard gamma function [14]. Using this, Eq 6 may be rewritten as

$$P_{f;V}(\sigma) = 1 - \exp\left[-u(\sigma)\left(\Gamma\left(1+\frac{1}{m}\right)\right)^m \left(\frac{\sigma}{\bar{\sigma}_{f;V}}\right)^m\right]. \tag{9}$$

Note that the volume ratio that appears in Eqs 4, 6, and 8 no longer appears explicitly in the expression for the failure probability. The volume effect is now contained in the mean failure stress, $\bar{\sigma}_{f;V}$. We see, then, that $\bar{\sigma}_{f;V}$ is not a true material constant, but instead depends upon both material constants (σ_0 and m) and the geometry of the specimens being tested. The above analysis suggests that if two sets of different sized specimens, with volumes V_1 and V_2, are tested in uniaxial tension, the ratio of the mean failure stresses should be

$$\frac{\bar{\sigma}_{f;V_1}}{\bar{\sigma}_{f;V_2}} = \left(\frac{V_2}{V_1}\right)^{1/m}. \tag{10}$$

The standard deviation of the distribution can also be determined, and when it is normalized with respect to the mean, depends only upon m. Let $s_{f,V}$ be the standard deviation associated with uniaxial loading of specimens of volume V. Then,

$$\frac{s_{f;V}^2}{\bar{\sigma}_{f;V}^2} = COV^2 = \frac{\Gamma\left(1+\frac{2}{m}\right)}{\Gamma^2\left(1+\frac{1}{m}\right)} - 1. \tag{11}$$

The coefficient of variation is seen to be independent of the volume of the specimens tested. Thus, if a set of data is taken, the mean and standard deviation of the data can be used to estimate the Weibull parameters σ_0 and m. The utility of these parameters, though, depends upon the extent to which the Weibull distribution actually describes the data. By way of example, a set of data drawn from a Weibull distribution with m = 12 would have a coefficient of variation of about 10%. A plot of the coefficient of variation vs. m is shown in Fig. 1.

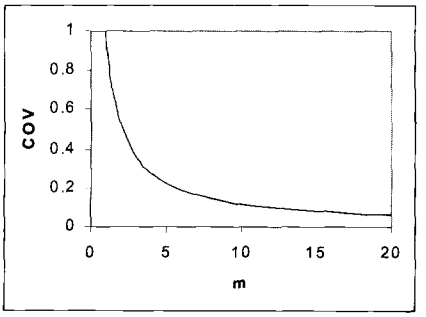

FIG. 1—*Coefficient of Variation vs. m for failure under Weibull distribution.*

Failure Under Inhomogeneous Stress—Bending

The work in the preceding section is valid only for specimens loaded in uniaxial tension, for which all material elements are subject to the same (uniform) stress σ. The basic structure of the above analysis is applicable for more general stress states as well. In this work, we focus on a relatively simple stress state – that generated during the bending of a beam. A variety of bending tests (three-point, cantilever and four-point bending) are used in testing of brittle materials. All have a stress state that is well approximated by a single nonzero component of the stress tensor that varies with position in the beam. The magnitude of the stress at any point in the body is proportional to the applied loading, but the stress itself is parameterized by the maximum stress that the loading causes within the body. Failure is then identified in terms of this maximum stress rather than in terms of the applied load.

Let $\sigma(\mathbf{r},\sigma_{\max})$ represent the (uniaxial) stress at position $\mathbf{r}$ under some loading condition that causes a maximum stress $\sigma_{\max}$ to occur at some location within the body. The failure of any individual element of the body is still governed by the probability $P_f(\sigma)$, but now the various elements making up the body have different stress levels, so the simple summation of failure probabilities must be replaced by an integral over the body. That is, Eq 3 must be rewritten as

$$P_{f,V}(\sigma_{\max}) = 1 - \exp\left[-\frac{1}{v}\int_V P_f(\sigma(\mathbf{r},\sigma_{\max}))dV\right]. \tag{12}$$

If $\sigma = \sigma_{\max}$ throughout the body (i.e., the stress is uniform, uniaxial tension), Eq 12 reduces to Eq 3.

Let us now consider the case of bending due to a point load F at the free end of a rectangular cantilever beam of length L, width b and depth h. Euler-Bernoulli beam theory provides the stress along the beam axis at any axial location x ($0 \le x \le L$) and depth z ($-h/2 \le z \le h/2$) as

$$\sigma(\mathbf{r},\sigma_{\max}) = \frac{2z(L-x)\sigma_{\max}}{Lh}, \quad \sigma_{\max} = \frac{6FL}{bh^2}. \tag{13}$$

Evaluating the integral in the exponent of Eq 12, with $P_f(\sigma)$ assumed to be of the form proposed by Weibull, allows us to write the probability of failure up to a loading with a maximum stress of $\sigma_{\max}$ as

$$P_{f;V;cantilever}(\sigma_{\max}) = 1 - \exp\left[-\frac{1}{2(1+m)^2}\frac{V}{v}\left(\frac{\sigma_{\max}}{\sigma_0}\right)^m\right]. \tag{14}$$

Comparing this expression with the equivalent expression for the failure probability under uniaxial tension, Eq 6 with $\sigma = \sigma_{\max}$, we see that they are the same except for the factor $2(1+m)^2$ in the denominator of the exponent in Eq 14. The significance of this factor lies in its effect on the mean failure stress. Specifically, the

mean stress to failure, $\overline{\sigma}_{\max_{f;V}}$, for this case is

$$\overline{\sigma}_{\max_{f;V;cantilever}} = [2(1+m)^2]^{1/m}\sigma_0\Gamma(1+\tfrac{1}{m})\left(\frac{v}{V}\right)^{1/m}. \tag{15}$$

The ratio of the means given in Eqs 8 and 15 for the uniaxial and cantilever loading cases again involves only the shape parameter m as

$$\frac{\overline{\sigma}_{\max_{f;V;uniaxial}}}{\overline{\sigma}_{\max_{f;V;cantilever}}} = [2(1+m)^2]^{-1/m}. \tag{16}$$

We therefore expect that the mean stress to failure for a set of cantilever beams of a brittle material to be significantly greater than the mean stress to failure for a set of uniaxial tension specimens of the same material and geometry. A plot showing the ratio of these mean stresses is given in Fig. 2.

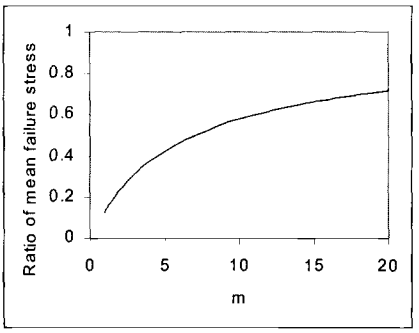

FIG. 2—*Ratio of mean stress to failure in uniaxial tension to cantilever bending vs. Weibull parameter m.*

The fact that the mean stress to failure for a set of tensile specimens should be lower than a similar set of bending specimens makes sense physically if one considers the stress states for these two loading conditions. If both beams are loaded to the same maximum stress σ_{max}, then the entire volume of the uniaxially loaded beam be at this stress, whereas the cantilever beam has only a single point at the outer fiber of the fixed end with stress σ_{max}. Since the chance of having a critically sized flaw capable of causing the material to fail at a given stress depends on the amount of material at that stress, there is a greater chance of the uniaxially loaded beam failing at σ_{max} than the cantilever beam.

Greek et al. [1], have presented a similar analysis for surface-dominated defects, and Tsuchiya et al. [3] have presented a volume-based analysis. In comparing this work to theirs, however, it is important to recognize that their "scale factors" are quite different than the scale factor σ_0 introduced above. The "normalizing factor" of Greek et al. [1] has physical dimensions of stress times area to the *1/m* power, while that of Tsuchiya, et al. [3] has physical dimensions of stress to the power m times volume. Clearly, these material "constants" differ from the scale factor σ_0, which is a measure of stress and contains no dependence on the shape parameter.

Misaligned Loading—Combined Tension and Bending

In many cases, it is difficult to obtain either perfect uniaxial tension or cantilever

bending. At the macroscopic scale, this is accommodated by using pinned grips or some other self-aligning mechanism. Such mechanisms do not exist at the microscale. Instead, loading is often applied to the top of a beam, either by attaching a structure to the upper surface of the film being tested or through electrostatic means. In either case, the loading is offset from the centerline of the beam, leading to some degree of bending.

We have analyzed the effect that such an offset has on the stress state in the beam and on the resulting mean failure strength. The problem addressed is shown in Fig. 3. The beam to be tested to failure has a gage length L and cross sectional area A. Loading is applied through a force F_0 at the end of a "loading beam." The loading beam is attached to the upper surface of the test beam near its free end and is constrained against out-of-plane motion at the point of the applied load. The nominal stress in the test beam is simply F_0 / A, but the actual stress depends upon position due to the offset of the load.

Simple beam theory cannot be used for this analysis since amount of offset increases as the loading increases, but not linearly. Numerical solutions for this problem were obtained using a commercial finite element code (ANSYS) for a range of applied loads. The material was taken to be polycrystalline silicon, with Young's modulus E = 167 GPa and Poisson's ratio $\nu = 0.25$. The test beam has length L = 100 μm, and square cross section of 2 μm × 2 μm. At each load step, the probability of failure of the test beam was computed for assumed values of the Weibull shape parameter m and scale factor σ_0. The mean failure stress was then obtained from this numerically generated cumulative distribution.

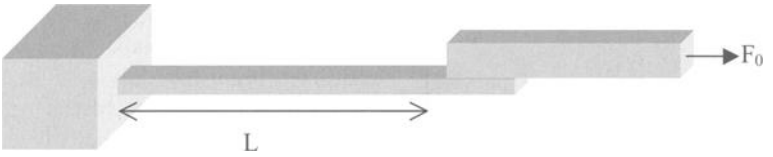

FIG. 3—*Schematic diagram of the geometry used in analyzing the effect of offset loading on the failure of a beam in uniaxial tension.*

Figure 4 shows a plot of the normalized mean failure strength as a function of scale factor σ_0 for several values of the shape parameter. The effect of the bending stress is largest, as a percentage of the nominal stress, at relatively low loads. As the loading increases, the stress state appears more nearly uniform. Therefore, if the material has a relatively low scale factor, the effect of the offset load is greater then if the material has a relatively large scale factor. The effect of the shape parameter is also seen in Fig. 4. As m increases, the region of high bending stress becomes increasingly important to the failure.

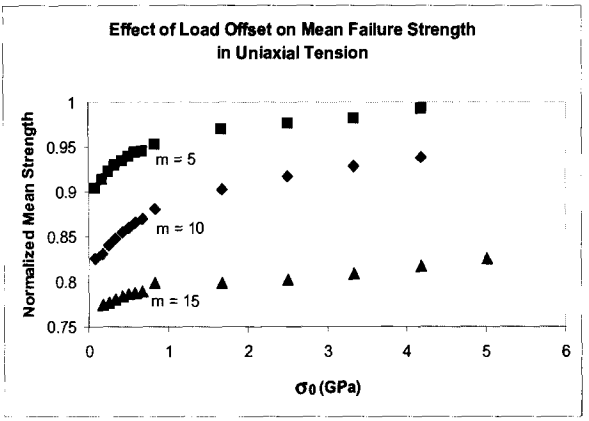

FIG. 4—*Ratio of mean failure stress with offset loading to ideal loading as a function of Weibull parameters.*

Fracture Test Structure

In order to perform a statistical evaluation of a set of fracture data, there must be a sufficient amount of data to make the results meaningful. The structures used in this work allow a large number of specimens to be tested to failure in a reasonable time. This is possible by testing the material in cantilever bending rather than the more traditional uniaxial tension. (For a comparison of the two techniques, see Refs. 1, 3, 8, and 10.) The structures used are quite small, only 320 μm by 500 μm, so that a large number of devices can be fabricated on a single die. The fabrication process can be performed using only one mask set, making this technique attractive for testing a wide range of thin film materials, not just those that might be found in traditional MEMS devices. The test structures are on the same length scale and are tested in a mode consistent with the deformation of many mechanical MEMS elements, thus providing information that is directly useful to designers. This device does not, however, allow a direct determination of the stress at failure. Rather, the strain at failure is determined, from which the associated stress may be obtained using Young's modulus.

The central element of the structure to measure the fracture strength of brittle MEMS materials is a shuttle tethered to the substrate by a folded flexure. Attached to the shuttle is an array of cantilever beams that are bent as the shuttle is displaced in-plane by an off-chip probe. As each beam breaks, the end displacement is determined from a video image of the structure. Because the beams are deformed in bending rather than in uniaxial tension, the magnitude of the motion is large and is readily detected using the optics available on the probe station used. Beam theory accounting for the geometric nonlinearity and the compliance of the beam support is then used to calculate the state of strain in the beam as a function of its tip deflection.

An SEM photograph of an undeformed structure is shown in Fig. 5. In this configuration, the probe tip will push the shuttle toward the bottom of the image. The six cantilever beams at first move rigidly with the shuttle, but after a short time contact the pads anchored near their free ends. A contact pad acts to fix the position of that point on the beam, causing the remainder of the beam to bend as the shuttle continues its motion. A scanned video image of the fracture test device during testing is shown in Fig. 6. Notice that in this image, the shortest two beams have already failed, and the longer beams are highly deformed.

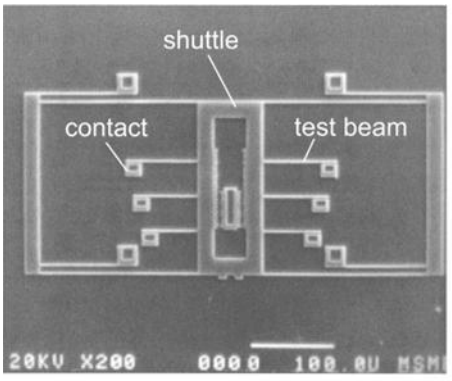

FIG. 5—*SEM micrograph of fracture strength test structure.*

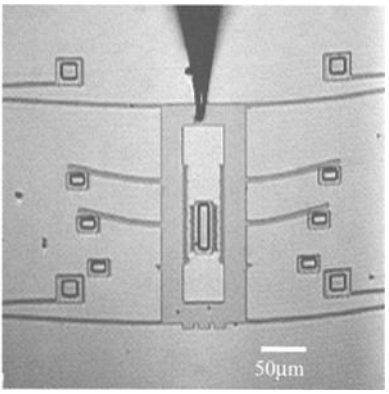

FIG. 6—*Scanned video image of fracture strength test structures during testing.*

The structures tested for this paper were fabricated in the Multi-User MEMS Processes (MUMPs). The fracture strength of the first polysilicon structural layer, nominally 2 μm thick, was tested. Consistent with a standard MUMPS run, films were deposited at 610°C, then sandwich doped with phosphorus during a 1 hour, 1050°C furnace anneal [15]. The beams tested were nominally 5 μm wide and 70, 80, and 90 μm long (distance from contact to the point where the beam attached to the shuttle).

The measured quantity for these tests is the displacement of the shuttle as each beam breaks. To facilitate the testing of the desired number of specimens, an automated system was created. A stepper motor advances the probe tip at a rate of 0.05 μm/s, while a video board captures an image every 4 seconds. The motion of the shuttle is assessed by comparing each image with an image taken before deformation. At maximum magnification, the system can resolve 0.18 μm/pixel, so the displacement resolution is limited by the rate at which images are captured. A displacement resolution of 0.2 μm corresponds to a worst-case strain resolution of 0.04%. Assuming a value for Young's modulus of E = 167 GPa, the stress resolution is then 67 MPa. A more detailed description of the automated data acquisition system is given by Jones [16].

After testing, the beam widths were measured on a calibrated SEM at a magnification of 2600X. The strain state was then determined from the displacement at fracture for each beam using the elastica solution of a bending beam [17]. The compliance of the shuttle supporting the beams was accounted for using the analysis of O'Donnell [18]. His result can be expressed as the ratio of the end deflection due to the support compliance $\delta_{support}$ to the deflection due to bending $\delta_{bending}$. Assuming that the beam is in a state of plane stress, this ratio has the simple form

$$\frac{\delta_{support}}{\delta_{bending}} = \frac{25}{6\pi}\frac{h}{L}, \tag{17}$$

where h is the depth of the beam in the plane of bending (nominally 5 μm, in this case) and L is the length of the beam. For these beams, this correction typically results in an 8% reduction in the estimated strain for a given displacement.

An example of the results of this testing is shown in Fig. 7, where three beam lengths are compared with one another in terms of mean failure strength and Weibull parameter. For each beam length, 38 valid measurements were obtained allowing a reasonable statistical comparison between the three lengths. These results indicate that the

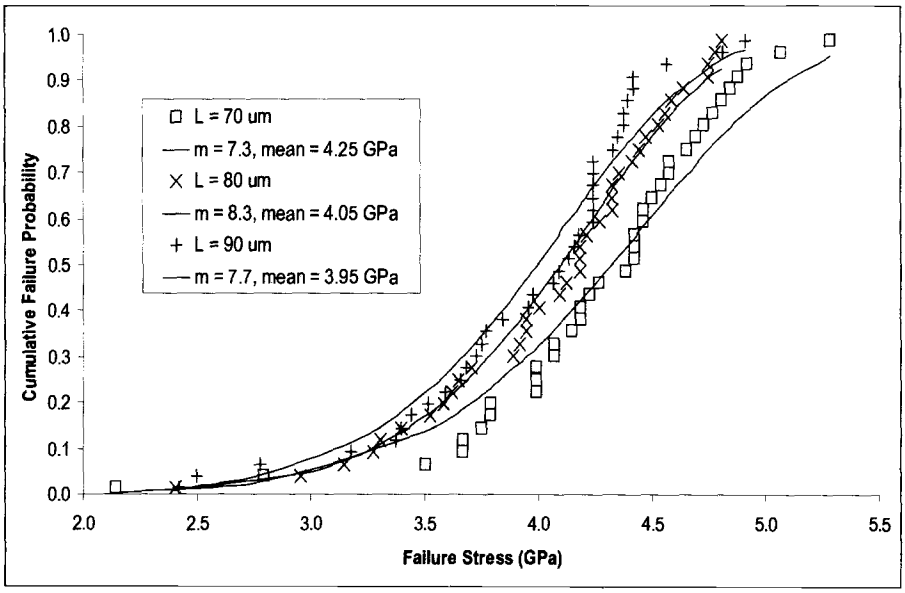

FIG. 7—*A comparison of the failure distributions for three lengths of beams loaded to failure in cantilever bending. All beams are nominally 5 μm wide and 2 μm thick.*

TABLE 1—*Comparison of the ratio of mean failure stresses for different length beams. Theoretical ratios are computed from Eq 10 using m = 8.*

Beam Lengths	Volume Ratio	Theoretical Ratio of Means	Experimental Ratio of Means
70:80	0.875	0.983	0.953
70:90	0.778	0.969	0.929
80:90	0.889	0.985	0.975

size effect predicted by the previous analysis may be evident for these structures. The volume ratio between two beams is essentially the ratio of the beam lengths. Taking m = 8 and using Eq 10 for the ratio between two means allows us to compare the experimentally determined ratios with the theoretical ratios as shown in Table 1. In each case, the experimental ratio is smaller than the theoretical ratio, indicating that the data contains a greater size effect than would be expected on the basis of the Weibull theory. However, it is important to note that the number of data points used for each beam length is still relatively small. The 95% confidence interval for the means reported is on the order of 0.2 GPA. The difference between the means for the 70 μm beams and the 90 μm beams appears to be statistically significant, but the same cannot be said about the differences between the mean for the 80 μm beams and the other beam lengths.

The data collected also suggests that the three parameter Weibull model may be more appropriate for this material than the two parameter model used for the analysis. A total of over 1200 structures from three separate dies were tested to failure, with a minimum failure stress of 2.0 GPa. Future work will focus on this issue.

Summary

Fracture testing of MEMS materials often focuses on determining a single value for the mechanical strength of the material rather than on determining the range within which this important parameter should be expected. This work emphasizes the importance of considering fracture strength of polycrystalline silicon in a probabilistic sense, and provides a detailed description of the use of the Weibull distribution in this regard. It is shown that the apparent strength of a structure tested in tension may be strongly affected by misalignment of the applied load. An alternative to uniaxial tension testing is presented and results for fracture strength in cantilever bending of MEMS beams are provided.

While progress has been made in understanding the fracture strength of MEMS materials, particularly polycrystalline silicon, much research remains. Differences between the apparent strengths in tension and bending shown in [10] have yet to be explained. Issues associated with load misalignment demand more attention as well.

References

[1] Greek, S., Ericson, F., Johansson, S., and Schweitz, J.-A., "In Situ Tensile Strength Measurement and Weibull Analysis of Thick Film and Thin Film Micromachined Polysilicon," *Thin Solid Films,* Vol. 292, 1997, pp. 247–254.

[2] Sato, K., Shikida, M., Yoshioka, T., Ando, T., and Kawabata, T., "Micro Tensile-Test of Silicon Film Having Different Crystallographic Orientations," *Transducers* 97, Vol. 1, 1997, pp. 595–598.

[3] Tsuchiya, T., Tabata, O., Sakata, J., Taga, and Y., "Specimen Size Effect on Tensile Strength of Surface-Micromachined Polycrystalline Silicon Thin Films," *Journal of Microelectromechanical Systems*, Vol. 7, 1998, pp. 106-113.

[4] Sharpe, Jr., W. N., Yuan, B., and Edwards, R. L., "A New Technique for Measuring the Mechanical Properties of Thin Films," *Journal of Microelectromechanical Systems*, Vol. 6, 1997, pp. 193–199.

[5] Jones, P. T., Johnson, G. C., and Howe, R.T., "Fracture Strength of Polycrystalline Silicon," *MRS Symposium Proceedings,* Vol. 518, 1998, pp.197–202.

[6] Saif, M. T. A. and MacDonald, N. C., "Microinstruments for Submicron Material Studies," *Journal of Material Resources*, Vol. 13, 1998, pp. 3353–3356.

[7] Schweitz, J.-A. and Ericson, F., "Evaluation of Mechanical Materials Properties By Means of Surface Micromachined Stuctures," *Sensors and Actuators,* Vol. 74, 1999, pp. 126–133.

[8] *Microelectromechanical Structures for Materials Research, MRS Symposium Proceedings,* Vol. 518, S. Brown, et al., Eds., Materials Research Society, 1998.

[9] Ballarini, R., "Contributive Research and Development Volume 130: The Role of Mechanics in Microelectromechanical Systems (MEMS) Technology," Air Force Research Laboratory Report No. AFRL-ML-WP-TR-1998-4209, Wright Patterson Air Force Base, 1998.

[10] Sharpe, W. N., Brown, S., Johnson, G. C., and Knauss, W., "Round-Robin Tests of Modulus and Strength of Polysilicon," *MRS Symposium Proceedings*, Vol. 518, 1998, pp.57–65.

[11] Stanley, P., Fessler, H., and Silva, A. D., "An Engineer's Approach in the Prediction of Failure Probability of Brittle Components," *Proceedings, British Ceramics Society*, Vol. 22, 1973, pp. 453–487.

[12] Kittle, P. and Diaz, G., "Weibull's Fracture Statistics, or Probabilistic Strength of Materials: State of the Art," *Res. Mechanica*, Vol. 24, 1988, pp. 99–204.

[13] Weibull, W., "A Statistical Distribution Function of Wide Applicability," *ASME Journal of Applied Mechanics*, Vol. 18, 1951, pp. 293–297.

[14] Abramowitz, M. and Stegun, I. A., *Handbook of Mathematical Functions,* New York: Dover, 1970.

[15] MCNC Electronic Technologies Div., 3021 Cornwallis Road, Research Triangle Park, NC.

[16] Jones, P. T., "The Fracture Strength of Brittle Films used for MEMS Devices," Dissertation, University of California at Berkeley, 1999.

[17] Frisch-Fay, R., *Flexible Bars,* Washington D.C.: Butterworth Inc., 1962.

[18] O'Donnell, W. J., "The Additional Deflection of a Cantilever Due to the Elasticity of the Support," *ASME Journal of Applied Mechanics*, Vol. 27, pp. 461–464, 1960.

Thermomechanical, Wear, and Radiation Damage of Structural Films

Kirk P. Seward,[1] *Philip B. Ramsey,*[1] *and Peter Krulevitch,*[1]

Thermomechanical Characterization of Nickel-Titanium-Copper Shape Memory Alloy Films

REFERENCE: Seward, K. P., Ramsey, P. B., and Krulevitch, P., **"Thermomechanical Characterization of Nickel-Titanium-Copper Shape Memory Alloy Films,"** *Mechanical Properties of Structural Films, STP 1413*, C. Muhlstein and S. Brown, Eds., American Society for Testing and Materials, West Conshohocken, PA, Online, Available: www.astm.org/STP/1413/1413_20, 1 September 2001.

ABSTRACT: In an effort to develop a more extensive model for the thermomechanical behavior of shape memory alloy (SMA) films, a novel characterization method has been developed. This automated test has been tailored to characterize films for use in micro-electromechanical system (MEMS) actuators. The shape memory effect in NiTiCu is seen in the solid-state phase transformation from an easily deformable low-temperature state to a "shape remembering" high-temperature state. The accurate determination of engineering properties for these films necessitates measurements of both stress and strain in microfabricated test structures over the full range of desired deformation. Our various experimental methods (uniaxial tensile tests, bimorph curvature tests, and diaphragm bulge tests) provide recoverable stress and strain data and the stress-strain relations for these films. Tests were performed over a range of temperatures by resistive heating or ambient heating. These measurements provide the results necessary for developing active SMA structural film design models.

KEYWORDS: shape memory, NiTiCu, nickel-titanium-copper, Nitinol, NiTi, TiNi, MEMS, microactuators

Introduction

The use of active materials actuation systems in micro-electromechanical systems (MEMS) is becoming more popular as solutions are sought for providing effective motion and force control on the microscale. Shape memory alloy films are an attractive solution in these systems because they provide the highest work output per unit volume of any microactuator alternatives (seen in Fig. 1) [1]. Concepts exist to use shape memory alloys (SMAs) in microvalves, pumps, and actuators [2-4], and several scientists [1,5-7] have characterized individual characteristics of SMAs. The tests and results described here move us one step closer to a comprehensive SMA characterization tool to allow effective and optimal design of MEMS that fully utilizes actuation properties.

Performing a comprehensive engineering analysis of this material has relied on the design of MEMS devices with incorporated SMA films. Microfabrication methods were used to generate test chips with the goals of avoiding alloy recrystallization and creating devices with similar geometry and scale to actual MEMS actuators that would operate via a shape memory effect. The testing method used here provides data based on the resistive heating of the films rather than ambient heating. Alloy characterization has been performed by other researchers to derive stress-strain relationships under isothermal

[1] Lawrence Livermore National Laboratory, PO Box 808, L-223, Livermore, CA 94550. Phone (925) 424-5218. Email: kirkpatrick@alum.mit.edu.

conditions or with temperature as a monitored variable [1,5-7]. Alternatively, this test utilizes resistive heating and thus constant current conditions are imposed on the films in a room temperature environment. Varying the strain and measuring the stress on the films under these conditions allows the plotting of characteristic curves and the derivation of constitutive relations for use in the design of new actuators.

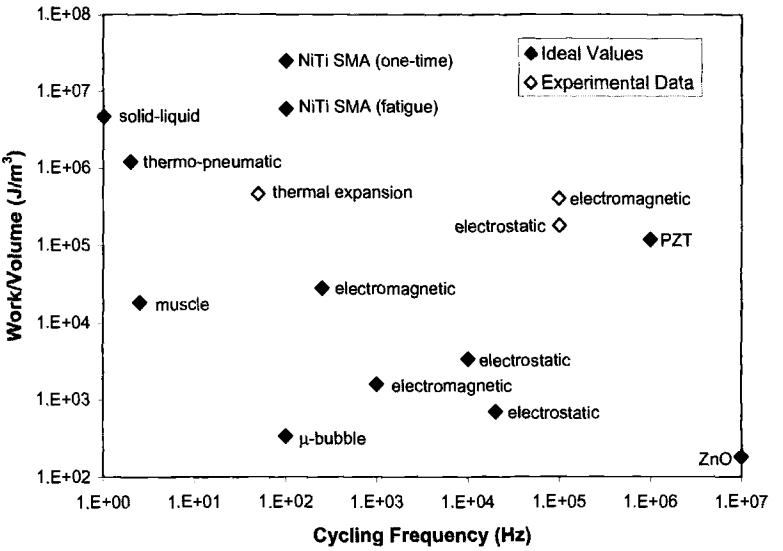

FIG. 1—*Work output per unit volume versus operating frequency for several standard microactuators.*

Because SMA films behave differently than bulk materials and vary in mechanical properties with distinct fabrication methods, a simple technique to provide all necessary mechanical data is beneficial. The automated test described here is non-destructive and provides a comprehensive range of thermomechanical and electromechanical information with simultaneous determination of stress-strain behavior and material resistivity of both phases, recoverable stress and strain against a load, actuation fatigue behavior, response and cycling times, and power requirements for actuation of fixed-fixed NiTiCu ribbons.

This paper begins by addressing the theory behind the shape memory effect. While a thorough knowledge of the phase transformations that allow shape memory are not entirely necessary to design actuators, an understanding of the materials science certainly aids in the design process. The fabrication of test structures used for these tests is described, with a list of processes that are not detrimental to shape memory film integrity. The testing methods are discussed along with the characteristic equations that allow formation of stress and strain relationships. Finally, results are presented based on our findings during uniaxial tensile tests, bimorph curvature tests, and diaphragm bulge tests.

Shape Memory Theory

Shape memory alloys are appropriately named because they "remember" their shape while undergoing a solid-to-solid phase transformation during heating. At room temperature, NiTiCu is in its low-temperature, martensite state. When it is heated beyond its transformation temperature, it undergoes the phase transformation to an austenite state. In the martensite phase, the material exhibits higher ductility than the austenite phase and is therefore easily deformed. When the material is heated it enters the austenite phase (known as reverse transformation). It regains its original shape as long as permanent plastic deformation did not occur in the martensite phase (around 4–10% strain for most SMAs [8]). Upon cooling to martensite again (martensite transformation), the SMA does not change macroscopic shape unless external loads are applied. In the two-way shape memory effect, both phases remember a unique shape [9-10], which can occur due to residual film stresses changing the shape of the material during the austenite to martensite transformation in the absence of external loading. Electrical resistance changes from the martensite phase to the austenite phase have been observed by other researchers [7,11-12] and were also studied in these experiments.

Shape memory transformations occur by solid-to-solid phase transitions from one crystal lattice structure to another, sometimes with an intermediate phase during heating or cooling. In NiTi, the austenite phase, or parent phase, has a tightly packed B2 structure, with the same symmetry as the body centered cubic lattice but with alternating atoms. The martensite phase is monoclinic or orthorhombic subject to alloy composition. NiTi martensite is monoclinic and NiTiCu martensite is orthorhombic. During the NiTi phase transformation upon cooling from austenite to martensite, the alloy passes through its intermediate R-phase, which has been described as both rhombohedral and orthorhombic by different scientists [13-15]. As the Cu content increases (substituting for nickel) from zero to 10% by weight, the alloy experiences phase transitions upon cooling of B2 $\rightarrow$ monoclinic, B2 $\rightarrow$ orthorhombic $\rightarrow$ monoclinic, and finally B2 $\rightarrow$ orthorhombic lattice structure [15]. The addition of Cu to NiTi acts to stabilize the dependence between transformation temperatures and alloy composition. It also leads to smaller hysteresis in the alloy's transformation temperatures [16].

Martensite Phase

The martensite phase has been described as ductile in its deformation. The reason behind this is the twinned structure encountered in martensite. For MEMS applications, the twinning dimensions are on the order of nanometers while the material dimensions are on the order of microns. This highly twinned structure is ductile because twin planes are able to slip with respect to one another. Since twins are moving with respect to each other, dislocations do not appear and there is no permanent, irrecoverable deformation. This leads to the method of interpreting the presence of twins in NiTi based shape memory alloys, as reported by Bhattacharya [17]:

1. The lattice on one side can be obtained by a simple shear of the lattice on the other.
2. The lattice on one side can also be obtained by a rotation of the lattice on the other.

These conditions are at the heart of twin variants. When lattices are sheared or rotated, they transform from one variant of the martensitic lattice structure into another.

Thus, variants change because of the twinned microstructure, which appears as macroscopic plastic deformation. The kinematic compatibility of the material states that the deformation of the material must be coherent, so macroscale martensitic material appears to have the same properties throughout, though it is made up of several variants of one lattice structure [17].

Martensitic material takes on the material property known as self-accommodation. This property allows for no macroscopic change in shape in the absence of external loads when the material transforms from austenite to martensite. During phase transformation, the new martensite variants align themselves to allow no macroscopic shape change in the material. Cooling the material below its transformation temperature can form the ductile martensite microstructure, but martensite can also be formed by physically increasing the transformation temperature. This behavior, known as stress-induced twinning, is governed by the Clausius-Clapeyron relationship, which states that as the stress and strain in the material increase, the martensite transformation temperature also increases. The balance between strain energy and heat energy therefore dictates whether the alloy is acting as a ductile martensite or a stiff austenite [18].

Austenite Phase

Since the formation of the crystalline shape memory structure requires annealing, all shape memory materials start out as austenite. Before annealing, the materials have amorphous microstructures without order or alignment of crystal lattices. Upon annealing, the highly symmetric B2 crystallization takes place, forming SMA austenite. When it cools, the alloy transforms to martensite for the first time and undergoes self-accommodation. When NiTiCu enters the austenite phase upon reverse transformation, twins are recovered during the transition to B2. As the multiple twin variants transform to the unique B2 variant, the material recovers its original shape. If strain was applied to the martensitic structure causing deformation, the transformation back to B2 includes a macroscopic shape change to its original, annealed shape.

Fabrication of Test Structures

Referring to Fig. 2, 4-in. diameter 380 μm thick {100} Si wafers (Step 1) with 6000 Å of thermally grown oxide (Step 2) served as substrates for the SMA film deposition. Nickel-titanium-copper films were DC magnetron sputter-deposited at 150 W from a 33 mm diameter alloyed NiTiCu target while heating the substrate (Step 3). Films were deposited in a high vacuum chamber under 5.4×10^{-8} to 1.9×10^{-7} Torr base pressure in 8 mTorr argon. Thermocouples mounted to the surface of the silicon substrate indicated a starting deposition temperature of 510°C and a final deposition temperature of 540°C. Deposition times of 2 h resulted in average film thickness across the wafer of 1.9 μm with variations of ±0.4 μm. Thickness variation resulted from a low target to substrate diameter ratio, with the thickest film depositing directly in line with the target and diminished film thickness from the center to the edge of the wafer. Film composition, measured by electron microprobe, was 39.5at%Ni, 52at%Ti, and 8.5at%Cu.

Patterning of the NiTiCu films was accomplished by photolithography of 1.8 μm thick AZ1518 resist (Step 4) and subsequent wet etching of the alloy in a 20:20:1 hydrochloric acid : nitric acid : hydrofluoric acid ($HCl:HNO_3:HF$) bath (Step 5). During

this etch, undercutting of the photoresist removed roughly 5 μm from the edges of the SMA patterns. The oxide layer in this step prevented any silicon from being etched by the combination of HNO_3 and HF.

Window structures were patterned onto the backside of the wafer with a 15 μm AZ4620 photoresist (Step 6) and the wafer was adhered to a handle wafer for deep reactive ion etch (DRIE) processing (Step 7). The exposed oxide was removed with 6:1 buffered HF (Step 8) and the silicon was etched in a ST Systems Advanced Silicon Etch tool (Step 9). Finally, the remaining oxide was reactive ion etched (Step 10) and the wafers were separated in an acetone bath and cleaved (Step 11). A photograph of the resulting test chips is seen in Fig. 3, in which a NiTiCu ribbon with two 2 mm gage sections is suspended by a silicon frame and electrical contact pads are patterned to allow resistive heating.

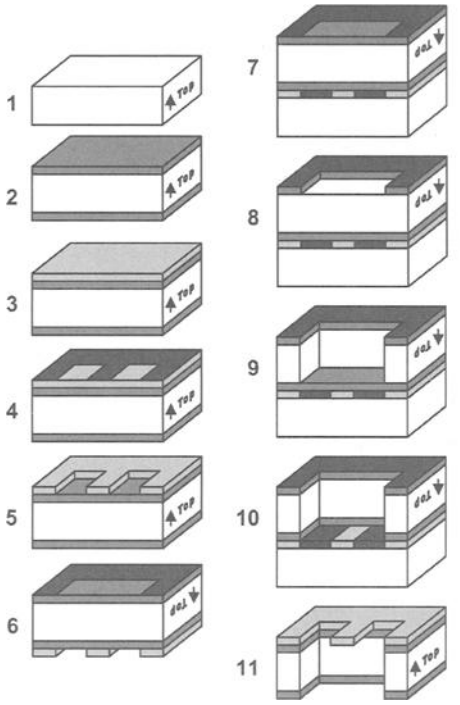

FIG. 2—*Fabrication process for test chips.*

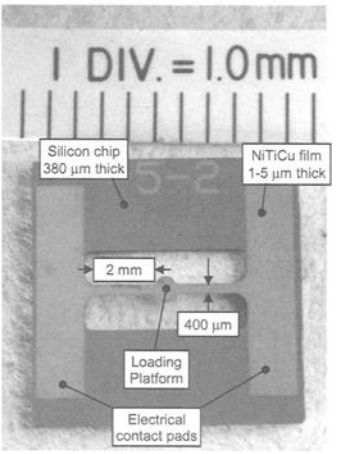

FIG. 3—*Suspended ribbon test chip layout.*

Experimental Method

Unlike traditional mini-tensile testing schemes in which strips of SMA film are totally or partially freed from the substrate and then strained [19], the tests described in this paper utilize out-of-plane stretching without detachment from the substrate.

Freestanding fixed-fixed NiTiCu ribbons were patterned on the same wafer as 1 cm square unpatterned (blank) chips used in curvature measurements and test chips with a blank pattern and a window etched beneath in the silicon, forming a NiTiCu membrane for use in pressurized diaphragm measurements.

NiTiCu Ribbon Tensile Test

In an effort to create a non-destructive method for characterizing these films, the out-of-plane test was developed. Rather than sputtering a film and detaching it from its substrate, a film was sputtered and the substrate was etched from under it, leaving a freed ribbon onto which loads and deflections were applied and measured as seen in Fig. 4. This test allows relatively large displacements to be measured and correlated back to small strains. Since film thickness was much less than ribbon width, out-of-plane loading produced negligible bending stresses and the ligaments were assumed to be in a state of uniaxial tension. Depressing the center of the ribbon with a spring-loaded transducer allowed the simultaneous measurement of the load on the ribbon and the consequent deflection of the center.

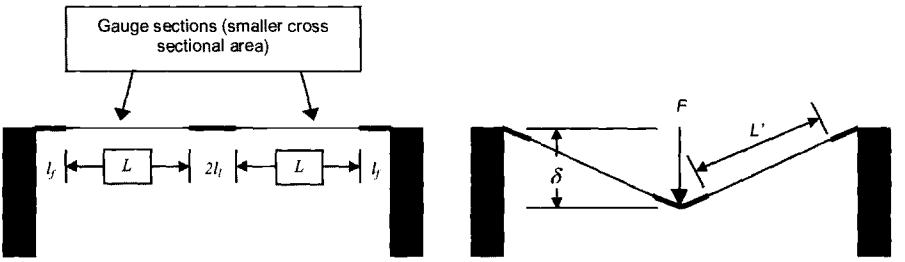

FIG. 4—*Loads and deflections were applied to the ribbons out-of-plane. The resulting force and deflection data yielded stress-strain relationships.*

The stresses in the gauge sections of the ribbon were calculated by resolving the downward force into each of the ribbon legs. In Eq 1, the true stress along the longitudinal axis of each ribbon leg σ_x is determined by the downward force F, the downward displacement δ, the ribbon length L_o (equal to $L + l_f + l_l$ from above), the original cross-sectional area of the ribbon gauge section $w_o t_o$, the material's Poisson's ratio ν, and the strain in the gage section, $\varepsilon_{g,x}$. Of course, without knowing Poisson's ratio for the material, the engineering stress is merely found by substituting $\nu = 0$.

$$\sigma_x = \frac{F\sqrt{\delta^2 + L_o^2}}{2\delta w_o t_o e^{-2\nu\varepsilon_x}} \tag{1}$$

A first-pass model was used to determine the proportion of strain in the gage sections and that in the fillets and loading platform. For this model, the assumption was made that since a similar strain (i.e., within the same order of magnitude) exists in the fillet, gage, and loading platform, a constant elastic modulus would prevail over all three sections. Since each leg of the ribbon is subject to uniaxial tension, the force through the length is also constant. This allows the assumption of inverse proportionality between

strain and cross-sectional area at any given ribbon section. Integrating over the fillet length l_f and the loading platform length l_l for our given geometry produced the relationships between the strain in all three sections: $\varepsilon_{fillet} = 0.651\varepsilon_{gage}$; $\varepsilon_{load} = 0.510\varepsilon_{gage}$. These constants of proportionality are denoted C_1 and C_2, respectively, for the sake of simplicity. Again using the geometry produced by deflection of the ribbon as seen in Fig. 4, the true strain ε_g is calculated for the gage section. In Eq 2, the new variable is the residual strain ε_o on the ribbon, which is subtracted from the measured strain in the equation to yield the actual strain in the ribbon.

$$l_f e^{C_1(\varepsilon_g-\varepsilon_o)} + l_l e^{C_w(\varepsilon_g-\varepsilon_o)} + L e^{(\varepsilon_g-\varepsilon_o)} = \sqrt{\delta^2 + L_o^2} \qquad (2)$$

From this equation, a lookup chart is created to compare the displacement δ to the gage section strain ε_g, which is necessary for the real-time automated tests performed on these ribbons.

To find the mechanical properties of SMA using the out-of-plane testing concept, the downward displacement and force were measured with a micro-miniature spring-loaded differential variable reluctance transducer (DVRT). The DVRT measured displacements with a resolution of 1 μm, precision of 1.5 μm and full stroke length of 6 mm by differentiating the reluctance output of a magnetic core moving through a coil. When filtered through a demodulator board, the DVRT outputs voltage proportional to its displacement. A calibration lookup table was created to compare this voltage and displacement using an automated linear stage to produce 5 μm incremental motions and measuring the DVRT output voltage. The force calibration of the spring in the DVRT was performed by again making 5 μm incremental motions and measuring the force produced on a load cell against the DVRT output voltage (i.e., the displacement). A lookup chart was made for both calibrations so that maximum accuracy could be obtained during the automated tests.

The force F for Eq 1 was determined by lookup of the DVRT output voltage, which indicated exactly what the spring compression was and thus the calibrated force. The displacement δ for Eq 1 and 2 were found by subtracting the lookup value of DVRT compression from the known displacement of the linear stage. Thus, if the stage was advanced 100 μm and the spring had been compressed 50 μm, the total displacement of the center of the ribbon (δ) would be 50 μm.

Bimorph Curvature Test

The test chips with unpatterned film covering a silicon square were subjected to heating and cooling while their radius of curvature ρ was measured to quickly confirm shape memory behavior and measure the residual stress in the unheated film. The biaxial film stress σ_f was calculated by the modified Stoney equation (Eq 3) [*20*] with a biaxial modulus $E_s/(1-\nu_s)$ equal to 180.5 GPa for {100} silicon [*21*], substrate thickness t_s of 380 μm, and film thickness t_f measured by stylus profilometry during the chip fabrication process. This equation provided the data for residual stress at room temperature and the recoverable stress in the film when it was heated to its austenite phase.

$$\sigma_f = \frac{1}{\rho}\frac{E_s t_s^2}{6(1-\nu_s)t_f} \tag{3}$$

Diaphragm Bulge Test

Alloy membranes were pressurized with load P from the backside of test chips with nitrogen. Membrane center deflection δ was measured in the center of the membrane using the DVRT without spring loading. In this case, the DVRT provided no counteracting force and could therefore act as a simple displacement sensor. The models used to determine the residual stress σ_o and biaxial Young's modulus $E/(1-\nu)$ of thin films subjected to this test have had various numerical constants [22-24], but all follow the same form of Eq 4, with film thickness t_f and square membrane half-length a.

$$P = C_1\frac{t_f\delta}{a^2}\sigma_o + C_2(\nu)\frac{t_f\delta^3}{a^4}\frac{E}{1-\nu} \tag{4}$$

In the model we use from Maier-Schneider et al. [22], C_1 has a loose dependence on ν and varies between 3.43 and 3.45 as ν varies from 0 to 0.5, while C_2 is given by Eq 5.

$$C_2 = 1.994(1-0.27\nu) \tag{5}$$

Although this model is more of an approximation at the high strains seen in the shape memory films (above 2%), it gives an idea of the relationship between the stress and the strain as characterized by other scientists and that seen with the uniaxial tension tests described here. When these equations are coupled with a more general equation to find the strain ε from the center deflection and the half-length as seen in Eq 6 [25], the stress-strain relationship is found by backing out the stress from the calculated Young's modulus and the strain.

$$\varepsilon = 0.462\frac{\delta^2}{a^2} \tag{6}$$

Results

Uniaxial Tensile Tests

Ribbons were loaded and unloaded with the DVRT spring and the forces and displacements were recorded to determine the stress and strain on the ribbons using Eqs 1 and 2. To create an engineering tool, families of stress-strain curves were plotted for various currents through the SMA ribbons. In Fig. 5, one of these families of curves is plotted for a single ribbon. Each curve is labeled with the initial current density through the gage section. The current was not decreased as strain was added to accommodate for the shrinking cross-sectional area. Therefore, as the tests were performed and the gage sections were strained the actual current density would rise slightly. This is not shown in the plots in Fig. 5.

The lowest three current densities (12.3, 24.6, and 46.3 A/mm^2) did not heat the ribbon significantly, for the stress-strain behavior was that of martensitic material, with

large deformations taking place to accommodate the stress placed on the ribbon. The highest three current densities (121.3, 145.7, and 169.7 A/mm^2) heated the ribbon enough to cause full reverse transformation and did not allow stress-induced twinning in the material. The intermediate two current densities (97.0 and 73.2 A/mm^2) caused an austenite reverse transformation in the absence of external loads, but progressive loading caused large deformations by stress inducing twins.

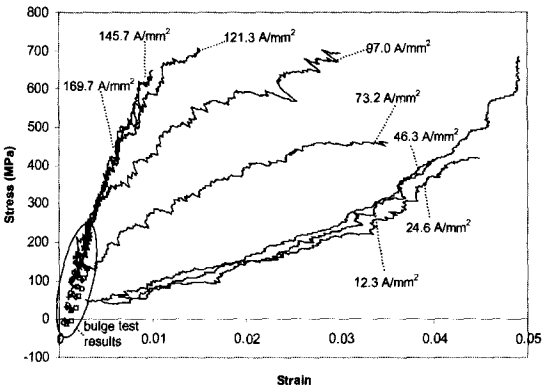

FIG. 5—*Family of stress-strain curves generated for a ribbon during loading at various current densities. The small stress-strain data in the lower left that appear as individual data points were obtained by bulge testing.*

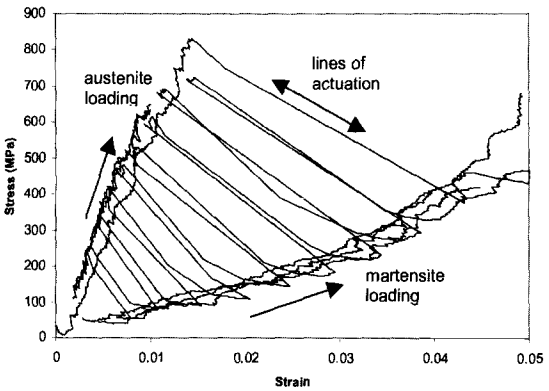

FIG. 6—*Lines of actuation illustrate the recoverable stress and strain achievable by full actuation from martensite to austenite.*

The results shown in Fig. 6 display the behavior of the alloy to a varying current density during loading and unloading of the ribbon in uniaxial tension. In this case, the lower current density, which keeps the alloy fully martensitic, is 0 A/mm^2 and the higher current density, which causes the reverse transformation, is 145.7 A/mm^2. It was later

noticed that the same actuation lines could be produced using the lower current density of 121.3 A/mm^2, because full reverse transformation was still seen. The lines of actuation that connect the martensite and the austenite curves are particular to the loading conditions and therefore are predetermined by the loading geometry and the spring constant of the transducer. It is through actuation lines like this that the stress-strain results can be applied to actuator design and the necessary actuation current density is found.

A microactuator usually employs a biasing force against the SMA recoverable stress to generate bistable motion. In actuator design, the alloy is strained at ambient temperature to a certain point on the martensite curve to create a deformation. The equations dictated by the actuator geometry and biasing force determine how much stress and strain the alloy will respond with when heated. In Fig. 6, both a recoverable stress (vertical motion between martensite and austenite plots) and a recoverable strain (horizontal motion between plots) are seen upon actuation. In a design with a constant force on a freed ribbon of NiTiCu, the actuation line would be purely horizontal as the stress remains constant to produce a only a recoverable strain. Vice-versa, if the displacement is held constant, a pure recoverable stress would be produced and the actuation line would be vertical. Knowing the envelope within which the actuator will operate allows the actuator design to be optimized to produce the maximum force and displacement for optimum work output.

The work output per unit volume is simply found by the product of the recoverable stress and the recoverable strain. The longest actuation line in Fig. 6 gives the maximum work output in this test case, in which the ribbon actuates from a stress of 375 MPa and a strain of 0.043 to a stress of 820 MPa and a strain of 0.014. The product of the recoverable stress (445 MPa) and the recoverable strain (0.029) lead to a work output per unit volume of 1.29×10^7 J/m^3. This value is sensible because it lies between those displayed in Fig. 1 for NiTi SMA for a one-time and a fatigue operational regime.

Bimorph Curvature Tests

Curvature results for seven chips from the same substrate are shown in Fig. 7. The residual stress in the martensite phase, equivalent to the martensitic yield stress [1], was 95 MPa averaged over all test chips.

A benefit of the curvature test is that transition temperatures for this loading condition can also be discovered. The austenite start temperature, or the point where the reverse transformation begins, is 50°C and the austenite finish temperature is 61°C. The martensite start temperature is encountered upon cooling to 58°C and the martensite finish temperature is 37°C. Note that since this film is part of a bimorph structure rather than a freestanding ribbon, the loading conditions differ and the stress state is likely causing stress-induced twins to form. Twinning results in higher transformation temperatures than those encountered in the freed films as stated by the Clausius-Clapeyron relationship. The relative transformation temperatures and hysteresis width are still useful in design of actuators, for they indicate the suitable ambient temperature in which actuation can occur. For instance, the transformation temperatures indicated here would allow room temperature (23°C) and probably body temperature (37°C) applications, but would not be very useful in automotive applications or hot

environments. For these other applications, different alloys with higher transformation temperatures must be considered and characterized.

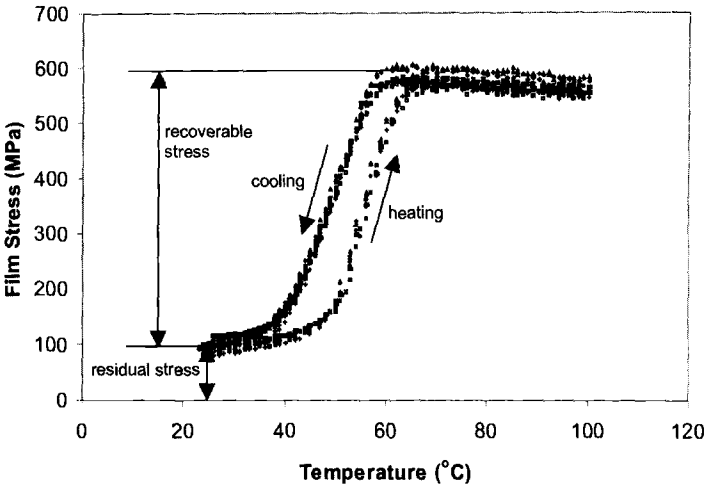

FIG. 7—*Curvature results on seven chips randomly distributed across the processed wafer show uniformity of shape memory effect. Residual stress is determined to be 95 MPa and recoverable stress is ~500 MPa.*

Diaphragm Bulge Tests

Data were taken as the 5 × 5 mm NiTiCu diaphragms were pressurized from the backside at various gage pressures from 0 to 85 kPa and various current densities from 0 to 25 A/mm^2. The results are seen as individual data points in the bottom left corner (the small stress-strain regime) of Fig. 5. The diaphragms ruptured above 85 kPa, which related to a strain below 0.005 and a stress below 200 MPa. Because only small stresses and strains could be applied to these membranes before catastrophic failure, they were only used to find the low end of the stress-strain curves. These small values were out of the detectable range of the DVRT spring during ribbon deflections due to small amounts of friction in the linear transducer. Using the residual stress value found by the bimorph curvature tests of 95 MPa and solving Eq 4 with a Poisson's ratio of zero, the engineering stress versus strain were found and the biaxial Young's modulus was ascertained at 80 GPa by averaging the results for each current density.

Conclusions

With the comprehensive testing instrument described here, the design of SMA microactuators is greatly simplified. Accurate material property measurements enable design by the simple determination of the characteristic equations for the device in question and correlation of those equations with the stress-strain curves found by testing ligaments with the same composition and fabrication methods. With the stress-strain curves from these tests, analytic solutions to the design problems associated with SMA films are ascertained.

The benefits of this instrument do not stop at qualifying films of certain composition to aid in the design of microdevices. It can also be used to qualify the devices after they are fabricated by directly measuring the forces and displacements they achieve while they are loaded. An instrument like this can be used in-line for device qualification to allow for quality control during a MEMS manufacturing process by checking one or several devices per wafer for forces, deflections, power requirements, and calibration errors all at the same time and in just a few seconds.

Acknowledgments

This work was performed under the auspices of the U.S. Department of Energy by Lawrence Livermore National Laboratory under Contract W-7405-Eng-48.

References

[1] Krulevitch, P., Lee, A. P., Ramsey, P. B., Trevino, J. C., Hamilton, J., and Northrup, M. A., "Thin Film Shape Memory Alloy Microactuators," *Journal of Microelectromechanical Systems*, Vol. 5, No. 4, December 1996, pp. 270–282.

[2] Miyazaki, S. and Kohl, M., "Recent Development in TiNi-based Shape Memory Alloys," *SPIE Conference on Smart Materials Technologies*, San Diego, CA, March 1998, *SPIE*,Vol. 3324, pp. 2–13.

[3] Benard, W. L., Kahn, H., Heuer, A. H., and Huff, M. A., "Thin-Film Shape-Memory Alloy Actuated Micropumps," *Journal of Microelectromechanical Systems*, Vol. 7, No. 2, June 1998, pp. 245–251.

[4] Kahn, H., Huff, M. A., and Heuer, A. H., "The TiNi Shape-Memory Alloy and Its Applications for MEMS," *Journal of Micromechanics and Microengineering*, Vol. 8, 1998, pp. 213–221.

[5] Miyazaki, S. and Ishida, A., "Shape Memory Characteristics of Sputter-Deposited Ti-Ni Thin Films," *Materials Transactions, JIM*, Vol. 35, No. 1, 1994, pp. 14–19.

[6] Ishida, A., Takei, A., and Miyazaki, S., "Shape Memory Thin Film of Ti-Ni formed by sputtering," *Thin Solid Films*, Vol. 228, 1993, pp. 210–214.

[7] Johnson, A. D., "Vacuum-Deposited TiNi Shape Memory Film: Characterization and Applications in Microdevices," *Journal of Micromechanics and Microengineering*, Vol. 1, 1991, pp. 34–41.

[8] Kennedy, J. B. (translator), *Shape Memory Alloys*, H. Funakubo, Ed., Gordon and Breach, New York, 1984.

[9] Perkins, J. and Hodgson, D., "The Two-Way Shape Memory Effect," in *Engineering Aspects of Shape Memory Alloys*, T. W. Duerig, K. N. Melton, D. Stockel, and C. M. Wayman, Eds., Butterworth-Heinemann, London, UK, 1990, pp. 195–206.

[10] Sato, M., Ishida, A., and Miyazaki, S., "Two-Way Shape Memory Effect of Sputter-Deposited Thin Films of Ti 51.3 at.% Ni," *Thin Solid Films*, Vol. 315, 1998, pp. 305–309.

[11] Ling, H. C. and Kaplow, R., "Stress-Induced Shape Changes and Shape Memory in the R and Martensite Transformations in Equiatomic NiTi," *Metallurgical Transactions A*, Vol. 12A, December 1981, pp. 2101–2111.

[12] Ling, H. C. and Kaplow, R., "Phase Transitions and Shape Memory in NiTi," *Metallurgical Transactions A*, Vol. 11A, January 1980, pp. 77–83.

[13] Tietze, H., Müllner, M., Selgert, P., and Assmus, W., "The Intermediate Phase of the Shape-Memory Alloy NiTi," *Journal of Physics F: Metallurgical Physics*, Vol. 15, 1985, pp. 263–271.

[14] Goubaa, K., Masse, M., and Bouquet, G., "Detection of the R-Phase in Ni-Ti Shape Memory Alloys," *Journal de Physique IV*, Vol. 1, Col. C4, November

1981, pp. 361–366.
[15] Bricknell, R. H., Melton, K. N., and Mercier, O., "The Structure of NiTiCu Shape Memory Alloys," *Metallurgical Transactions A*, Vol. 10A, June 1979, pp. 693–697.
[16] Krulevitch, P., Ramsey, P. B., Makowiecki, D. M., Lee, A. P., Northrup, M. A., and Johnson, G. C., "Mixed-Sputter Deposition of Ni-Ti-Cu Shape Memory Films," *Thin Solid Films*, Vol. 274, 1986, pp. 101–105.
[17] Bhattacharya, K., "Theory of Martensitic Microstructure and The Shape-Memory Effect," *Shape Memory Alloys: From Microstructure to Macroscopic Properties*, G. Airoldi, I. Müller, and S. Miyazaki, Eds., Trans Tech Publications, 1997.
[18] Wayman, C. M. and Duerig, T. W., "An Introduction to Martensite and Shape Memory," *Engineering Aspects of Shape Memory Alloys*, T. W. Duerig, K. N. Melton, D. Stockel, and C. M. Wayman, Eds., Butterworth-Heinemann, Boston, 1990.
[19] Miyazaki, S., Nomura, K., Ishida, A., and Kajiwara, S., "Recent Developments in Sputter-Deposited Ti-Ni-Base Shape Memory Alloy Thin Films," *Journal de Physique IV*, Vol. 7, Col. C5, 1997, pp. 275–280.
[20] Hoffman, R. W. in *Physics of Thin Films*, Vol. 3, G. Hass and T. E. Thun, Eds., Academic, New York, 1996.
[21] Brantley, W. A., *Journal of Applied Physics*, Vol. 44, 1973, p. 543.
[22] Maier-Schneider, D., Maibach, J., and Obermeier, E., "A New Analytical Solution for the Load-Deflection of Square Membranes," *Journal of Microelectro-Mechanical Systems*, Vol. 4, No. 4, December 1995, pp. 238–241.
[23] Wolf, R. H. and Heuer, A. H., "TiNi (Shape Memory) Films on Silicon for MEMS Applications," *Journal of Microelectromechanical Systems*, Vol. 4, No. 4, December 1995, pp. 206–212.
[24] Small, M. K. and Nix, W. D., "Analysis of the Accuracy of the Bulge Test in Determining the Mechanical Properties of Thin Films," *Journal of Materials Research*, Vol. 7, No. 6, June 1992, pp. 1553–1563.
[25] Timoshenko, S., *Theory of Plates and Shells*, McGraw-Hill, New York, 1959, pp. 250–307.

Martin L. Dunn,[1] *Yanhang Zhang,*[2] *and Victor M. Bright* [3]

Deformation and Stability of Gold/Polysilicon Layered MEMS Plate Structures Subjected to Thermal Loading

REFERENCE: Dunn, M. L., Zhang, Y., and Bright, V. M., "**Deformation and Stability of Gold/Polysilicon Layered MEMS Plate Structures Subjected to Thermal Loading,**" *Mechanical Properties of Structural Films, ASTM STP 1413,* C. Muhlstein and S. B. Brown, Eds., American Society for Testing and Materials, West Conshohocken, PA, Online, Available: www.astm.org/STP/1413/1413_07, 1 May 2001.

ABSTRACT: We study the deformation and stability of a series of gold/polysilicon MEMS plate structures fabricated by the MUMPS surface micromachining process and subjected to uniform temperature changes. We measured, using an interferometric microscope, full-field deformed shapes of a series of circular gold (0.5 μm thick)/polysilicon (1.5 μm thick) plate structures of diameters ranging from D = 150 to 300 μm. From these measurements we determined the pointwise and average curvature of the deformed plates. Although the curvature generally varies with position, the deformation response of the plates can be broadly characterized in terms of the average curvature as a function of temperature change. In terms of this, three regimes were observed: i) linear thermoelastic response independent of plate size, ii) geometrically nonlinear thermoelastic response that depends on plate size, and iii) bifurcations in the curvature-temperature response that also depend on plate size. We modeled the deformation response both analytically and with the finite element method. Good qualitative and quantitative agreement was obtained between predictions and measurements in all three deformation regimes, although the details of bifurcation are less accurately predicted than the linear and nonlinear response. This is attributed to their strong sensitivity to slight imperfections. Good agreement was also obtained between measurements and predictions of the spatial nonuniformity of the curvature across the plate.

KEYWORDS: MEMS plate structures, multilayers, geometric nonlinearity, bifurcation

Introduction

Multilayer material systems abound in microelectromechanical systems (MEMS) applications, serving both active and passive structural roles. In many of these, dimensional control is a critical issue. An inherent characteristic of multilayer material structures is that misfit strains between the layers (for example, due to intrinsic processing stresses or thermal expansion mismatch between the materials upon a temperature change) lead to stresses in the layers and deformation of the structure. In the microelectronics industry curvature measurements are routinely used to determine stresses in films deposited on a substrate. Their attractiveness is based on the fact that wafer curvature can be easily and accurately measured, and through use of the Stoney [1] formula (based on small-deformation considerations), the measured curvature can be

[1] Associate professor, Department of Mechanical Engineering, University of Colorado at Boulder.
[2] Graduate student, Department of Mechanical Engineering, University of Colorado at Boulder.
[3] Associate professor, Department of Mechanical Engineering, University of Colorado at Boulder.

directly related to the film stress (which is typically biaxial and spatially uniform) without knowledge of the source of the stress or even the thermoelastic properties of the film. Much of the understanding regarding deformation of multilayers that has come from microelectronics applications is applicable to MEMS applications, but significant differences exist and must be well understood to optimize the design of reliable MEMS. For example, in MEMS applications, layer thicknesses are small (on the order of μm) relative to in-plane dimensions and often comparable. This can lead to much larger deflections, relative to the thickness of structures, than are observed in microelectronics applications. A representative example for microelectronics applications is a 0.5 μm gold film on a 500 μm thick 100 mm diameter silicon substrate subjected to a 100°C temperature change. In this case, the maximum deflection is about 2% of the thickness. For MEMS applications, a reasonable example is a 0.5 μm gold film on a 1.5 μm thick 400 μm diameter polysilicon plate. For this case, when subjected to a 100°C temperature change, the maximum deflection is about six times the thickness. This can make it necessary to include geometric nonlinearity in order to accurately model deformation. Furthermore, the geometric nonlinearity can lead to bifurcations in the deformation behavior. These can be detrimental when dimensional stability is a requirement, or can be beneficial for actuator applications. Since the layers are of comparable thicknesses, stresses can vary appreciably through the thickness of the layers; the average stress in the layer may not be suitable to characterize film stresses as it is in many microelectronics applications. Furthermore, the connection between stress and curvature is more complex than that given by the Stoney formula. Tradeoffs between stress and curvature exist; for a given metal film thickness on a polysilicon layer, decreasing the polysilicon thickness can reduce the stress in the metal, but at the expense of increasing the curvature. The significance of this is obvious as many MEMS applications have strict deformation requirements, perhaps more severe than stress requirements. The curvature, and thus stresses, can vary significantly over the in-plane dimensions of the structure. The average curvature may thus be insufficient to adequately describe the deformation state of the structure. Spatially nonuniform curvature and stresses makes the use of common average wafer curvature measurements to determine film stress, via the Stoney formula, questionable; interpretation of such measurements must be made with care. Finally, the patterning geometry of metal films on polysilicon (or other materials) may be arbitrary, as opposed to relatively simple blanketed or thin line patterns. This can result in complex spatially nonuniform deformation states.

In this work we study, via measurements and analysis, the deformation behavior of a series of circular gold/polysilicon MEMS plate structures fabricated by the MUMPS surface micromachining process and subjected to uniform temperature changes. The observed deformation of the plate structures includes linearity and geometric nonlinearity, along with bifurcations in the equilibrium deformed shapes. Our interpretation of the experimental results and our analysis relies significantly on an excellent body of previous work in the thermomechanical behavior of structural composites [2-5] and thin film/substrate systems [6-14]. Indeed, many of the phenomena discussed in our work have been discussed in these papers and the interested reader is referred therein for more detailed expositions.

Samples and Measurements

We designed a series of circular gold/polysilicon plate microstructures and fabricated them using the commercially available Multi-User MEMS Process (MUMPs) [15]. Specifically, the samples were fabricated using the MUMPS 36 surface micromachining process. In the series of microstructures, the polysilicon layer was fully covered by the gold layer. We varied the diameter D to include D = 150, 200, 250, and 300 μm, keeping the thickness of the gold and polysilicon fixed at nominal values of 0.5 and 1.5 μm, respectively, as produced by the MUMPS process. The idea behind the design of the microstructures was to yield a circular gold/polysilicon bilayer structure that rests as freely as possible. To this end, the plates were supported on the substrate by a 16 μm diameter polysilicon post. A scanning electron micrograph of a typical plate structure is shown in Fig. 1.

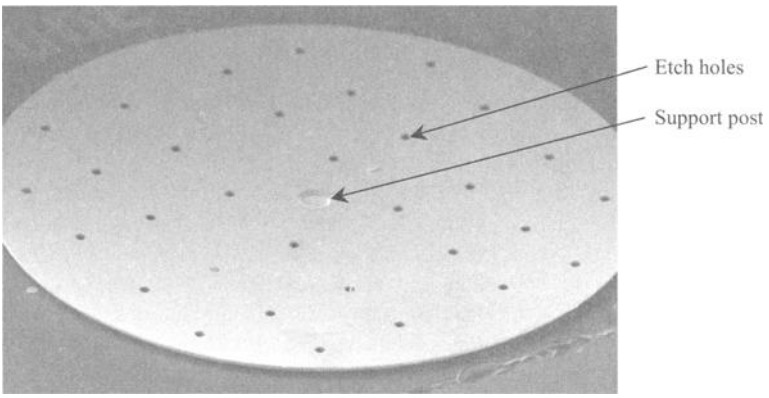

FIG. 1—*Scanning electron micrograph of a 300 μm diameter circular gold/polysilicon plate structure.*

We measured the deformation of the plate structures as a function of temperature change using an interferometric microscope and a custom-built thermal chamber that is covered by a quartz window to allow optical access. Full-field measurements of the out-of-plane displacement of the structure were made with the scanning white light interferometric microscope as the temperature was changed. The resolution of the out-of-plane displacement measurement, $w(x,y)$, is on the order of nanometers [16]; the resolution of the temperature chamber is about 1°C. The specific test protocol consists of heating the sample to approximately 100°C where it is flat. The sample is held at this temperature for a time sufficient to ensure it has reached thermal equilibrium and a stable flat shape (about 3.5 min). The sample is then slowly cooled to room temperature. The temperature is held constant for about 3.5 min roughly every 5°C so that thermal equilibrium is reached. Full-field out-of-plane displacements $w(x,y)$ of the surface of the plate are then measured. During the cooling process we measured $w(x,y)$ over a circular

region of 150 μm diameter centered at the center of each plate using a 2.5x objective (at room temperature we measured *w(x,y)* over the entire plate surface using a 10x objective). From the measured *w(x,y)*, we calculate the curvatures $\kappa_x(x,y) \approx -\partial^2 w(x,y)/\partial x^2$ and $\kappa_y(x,y) \approx -\partial^2 w(x,y)/\partial y^2$. These are computed by fitting *w(x,y)* with a 6th-order polynomial in x and y directions (which was sufficient to accurately describe the displacement profile in all cases) and then differentiating this function. We are confident that temperature gradients in the temperature chamber are insignificant based on measurements of curvature developed in similar-size single-material polysilicon plate microstructures: they are about three orders of magnitude less than those developed in the gold/polysilicon plate microstructures.

Analysis

As mentioned in the Introduction, numerous efforts have been forwarded to model the response of multilayer plate structures subjected to thermomechanical loading. Each of these authors has used/developed an analytical model to describe the deformation phenomena (linear, nonlinear, and bifurcation) and we use this same type of model for some of the comparisons that follow. The basic idea of the model is to assume an admissible displacement field *w(x,y)* in terms of unknown parameters (d_i) that are suitably chosen to be consistent with observed deformation modes. Values of the parameters d_i are then determined via a Ritz procedure so as to minimize the total potential energy of the system. Details of the procedures are given in References 2 to 14. Such analyses are sufficient to qualitatively, and in many cases quantitatively, explain the behavior discussed in the Introduction. In fact, quite simple closed-form expressions result for special cases that provide illuminating descriptions of observed phenomena [13,14]. A disadvantage of the analytical approaches is that for simplicity a displacement field that is consistent with a constant curvature deformation mode is usually chosen. As will be seen in our measurements and predictions, this is accurate in certain deformation regimes, but not in all. Additionally, these formulations are strictly valid for only simple plate shapes; this may be adequate for the structures considered here, but it is not for more complex in-plane shapes, of either or both layers, that arise in MEMS applications (see Ref 17 for an example). While the assumed displacement field used in the Ritz procedure could be modified to incorporate the dependence of curvature on position, perhaps the simplest approach to tackle these more general problems is to use the finite element method to solve the geometrically nonlinear equations over an arbitrary spatial domain. This is also the most viable approach for complicated geometries. We used this approach with the ABAQUS finite element code and used composite shell elements to approximate the thin-plate kinematics of the Kirchoff theory, including the von Karman geometric nonlinearity. Both materials are modeled as linear elastic with isotropic material properties. Input parameters to the finite element calculations are E_p = 163 GPa, ν_p = 0.22 (in line with measurements of Sharpe et al. [18,19]), E_g = 78 GPa, ν_g = 0.42 [*20*]. The thermal expansion coefficients of the materials were assumed to vary linearly with temperature and values at 100(23)°C used are $\alpha_p = 3.1(2.6) \times 10^{-6}$/°C, and $\alpha_g = 14.6\ (14.2) \times 10^{-6}$/°C [*20*]. Here and throughout the subscripts *p* and *g* denote polysilicon and gold,

respectively. Typical finite element meshes for the circular plate structures contained elements of with a characteristic dimension of about 12.5 μm, a size that was chosen after a convergence study with mesh size. Calculations were carried out to model the effect of the support post, and it was found to be insignificant on the resulting displacements, curvatures, and stresses except in a region very near the post. In order to break the perfect geometric and material symmetry of the geometry, we used an orthotropic thermal expansion coefficient for the gold. Specifically, we defined the in-plane thermal expansion coefficients to be $\alpha_x = \alpha_g$ and $\alpha_y = \alpha_g + \delta\alpha$, where $\delta\alpha$ was taken to be 0.01% of α_g.* With this slight perturbation, the prebifurcation response was indistinguishable from that with the isotropic thermal expansion. Without doing this, the analysis will only capture the linear and geometrically nonlinear portion of the deformation response; the bifurcation can not be captured. As discussed by Freund [14], details of the bifurcation, e.g., its sharpness, are strongly influenced by small changes in the imperfection. We discuss this later in light of both our measurements and predictions. Calculations were carried out for the loading situation of an applied uniform temperature change consistent with that experienced in the measurements.

Results and Discussion

In Fig. 2 we plot the average curvature in the x- and y-directions as a function of the temperature change during cooling. In these plots, the average curvatures are determined from the measured and computed $w(x,y)$ by averaging $\kappa_x = -\partial^2 w(x,0)/\partial x^2$ and $\kappa_y = -\partial^2 w(0,y)/\partial y^2$ along the paths $y = 0$ and $x = 0$, respectively, over a length of 150 μm. The x- and y- directions are taken to be aligned with the principal curvatures after bifurcation. Before bifurcation, the response is axially symmetric and so the x- and y-directions are arbitrary and indistinguishable. The use of the average curvature as a measure of the plate deformation is obviously quite appropriate if the curvature is (or is close to) spatially uniform. This aspect will be taken up to some degree later. Both Figs. 2*a* (measured) and 2*b* (predicted) show that in general three regimes of deformation exist: i) linear thermoelastic response independent of plate size, ii) geometrically nonlinear thermoelastic response that depends on plate size, and iii) bifurcations in the curvature-temperature response that also depend on plate size. By bifurcations we mean that as the temperature changes, the plate develops a nearly axially-symmetric curvature with $\kappa_x = \kappa_y$ which at first increases linearly with the temperature change, and then nonlinearly. At some critical temperature change, the deformation mode changes from axially-symmetric to a mode closer to cylindrical bending where $\kappa_x \neq \kappa_y$; as the temperature change

*Since gold and silicon are cubic, crystallographic texture would not be expected to result in orthotropy in thermal expansion, a second-rank tensorial quantity. Processing imperfections that lead to voids, defects, etc., could potentially lead to slight anisotropy. However, it is probably not possible to measure thermal expansion and elastic properties on thin film samples to this accuracy presently, so definitive confirmation of this supposition is lacking. We note, though, that the stresses developed upon a uniform temperature change depend on the thermal expansion *and* elastic moduli. The latter, being fourth-rank tensors, would exhibit orthotropy in the presence of general crystallographic texture.

increases beyond this value, the difference between κ_x and κ_y increases. In the first two regimes the measured deformations are axially symmetric, while in the third they are strongly nonsymmetric. Following Freund [14], we introduce the nondimensional curvature K and temperature change (mismatch strain) S:

$$K = \frac{\kappa D^2}{16 t_p} \qquad S = \frac{3\Delta\alpha\Delta T D^2 t_g M_g}{8 t_p^3 M_p}$$

In these expressions, t_i is the layer thickness, $M_i = E_i/(1-\nu_i)$ for both the polysilicon and gold ($i = p,g$), and $\Delta\alpha = \alpha_p - \alpha_g$. The data of Fig. 2, before bifurcation, are plotted in terms of these nondimensionalized variables in Fig. 3. The four curves collapse to a single curve and the plate size effect is described by the nondimensionalization. In agreement with Freund's results, the geometric nonlinear effects initiate at a normalized temperature change (mismatch strain) of about $S = 0.3$.

Figures 2*a* and 2*b* show good agreement between the measurements and predictions in all three deformation regimes. The major discrepancy is the sharpness of the bifurcation for the D = 300 μm plate; it is quite sharp in the predictions but much more gradual in the measurements. To understand this, we remind that the source of the bifurcation is an *imperfection* of some sort that breaks the ideal symmetry. In the calculations that imperfection was simulated via the slight anisotropy of the thermal expansion coefficient. Although not shown, we found that increasing $\delta\alpha$ from 0.01% of α_g to 1.0% of α_g resulted in a much more gradual bifurcation that initiated about 15°C higher than that shown in Fig. 2*b*. In fact, the results much more closely matched the measurements. These results, along with similar ones reported by Freund [13,14], show that the details of the bifurcation are strongly influenced by slight perturbations of the imperfection. This sensitivity will probably preclude a sharp bifurcation in practice. Indeed, the $\delta\alpha$ used here to simulate the imperfection is not an unreasonable measure of the anisotropy that can develop as a result of processing variations. It is, though, probably not easy to measure the thermal expansion anisotropy this accurately with available means. Furthermore, other imperfections such as slight variations in the circular geometry, the etch holes, and anisotropy and/or heterogeneity in other material properties also can play a role in the exact bifurcation details. As a result, the prediction of the bifurcation details is prohibitively difficult because of the strong sensitivity to the imperfection.

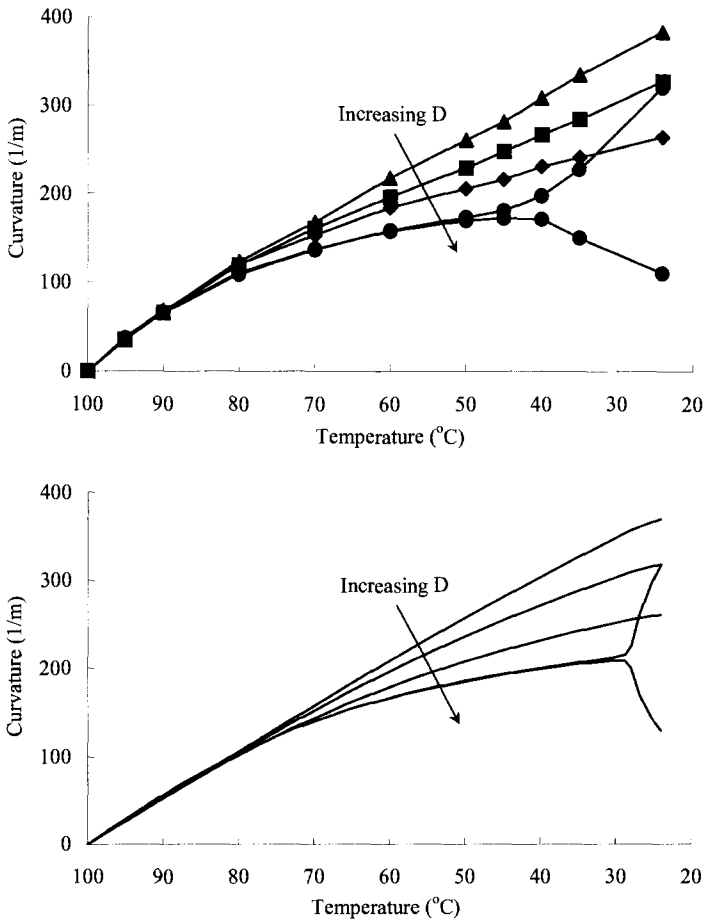

FIG. 2—*Average measured (top) and predicted (bottom) curvature as a function of temperature upon cooling from 100°C to room temperature. The curves from top to bottom are for the D = 150, 200, 250, and 300 μm structures, respectively. The measurements (filled symbols) are connected by lines to aid viewing.*

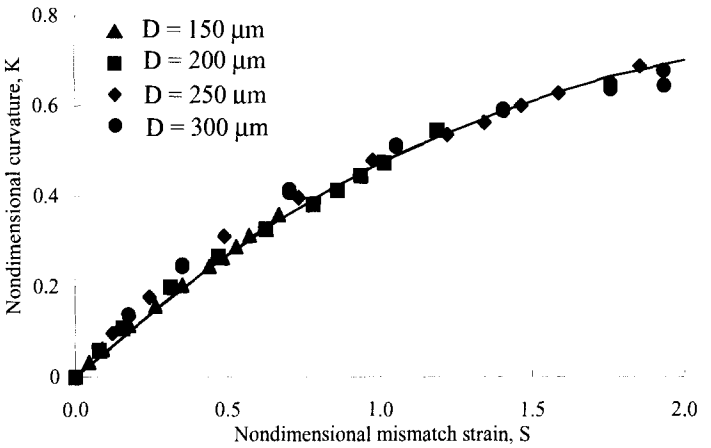

FIG. 3— *Nondimensional average curvature as a function of temperature change for the linear and nonlinear regimes. Measurements (symbols) and the prediction (solid line) are the same data as in Fig. 2.*

In Fig. 4 we further compare the measurements and predictions quantitatively. Measured and predicted contour plots of the displacement $w(x,y)$ at room temperature are shown for all four plate sizes. These results show clearly that due to the thermal expansion mismatch between the polysilicon and gold the $D = 150$ μm sample deforms in a spherically symmetric manner as the contours of constant transverse displacement $w(x,y)$ are nearly circles. This is also the case as the size increases to $D = 200$ μm and $D = 250$ μm. At $D = 300$ μm, though, the transverse displacement contours have become more like ellipses, indicating that the deformation is no longer spherically symmetric. Both the measured and predicted $w(x,y)$ contours show this same behavior and agree quite well. From these results it is apparent that the deformation upon cooling depends on the size of the plate. As the in-plane dimension of the plate increases with the thickness held constant, the deformation mode changes from one of spherical symmetry to one more like cylindrical symmetry. This size dependence is described by the normalization introduced earlier.

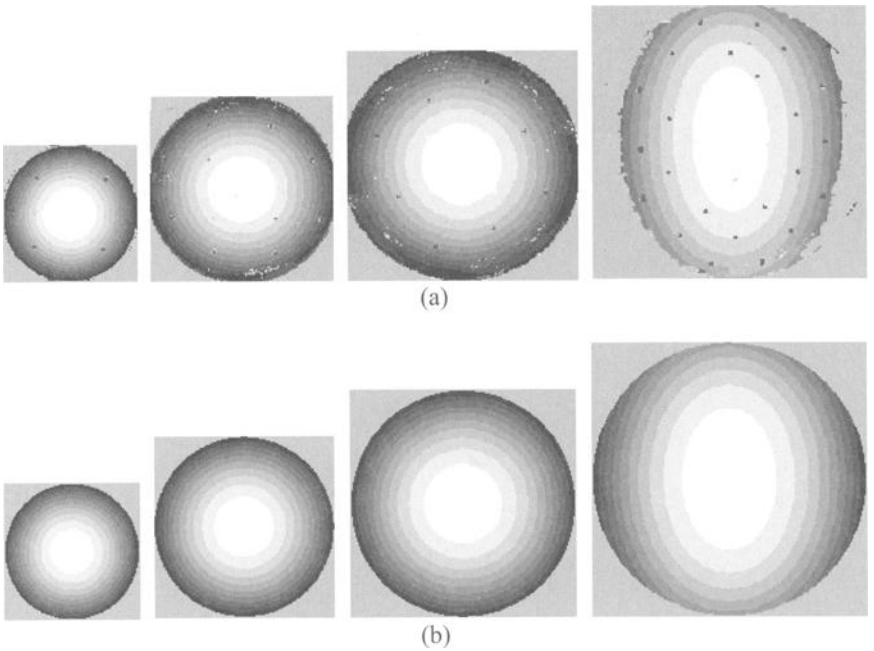

FIG. 4—*Contour plots of the (a) measured, and (b) predicted transverse displacements w(x,y) across the plate at room temperature for the four gold/polysilicon circular plates: D = 150, 200, 250, and 250 μm from left to right. Each contour band represents a displacement of 0.11, 0.18, 0.24, and 0.41 μm for the D = 150, 200, 250, and 300 μm plates, respectively.*

In the analytical treatments discussed previously it is assumed that the curvature is spatially uniform. The power of the finite element calculations is that this requirement is relaxed and the spatial variation of the curvature can be studied theoretically. Additionally, our full-field measurement capability allows us to study this experimentally as well. We take up this line of inquiry briefly in Fig. 5 where predicted and measured curvatures $\kappa_x(x,y)$ and $\kappa_y(x,y)$ are plotted as a function of temperature change for four points along the x-axis ($y = 0$) for the $D = 300$ μm plate: $x/R = 0.20$, 0.33, 0.50, and 0.67 where R is the plate radius. In the linear regime, the curves are indistinguishable, implying that the curvature is essentially uniform across the plate. In the nonlinear regime, though, the curvature varies appreciably with position, increasing by about a factor of two from the center to the periphery of the plate. As with the average curvature, good agreement also exists between measurements and predictions here, with the most significant discrepancy being the details of the bifurcation as discussed previously. The spatial variation of the curvature casts serious doubt on the suitableness of an analysis based on constant curvature.

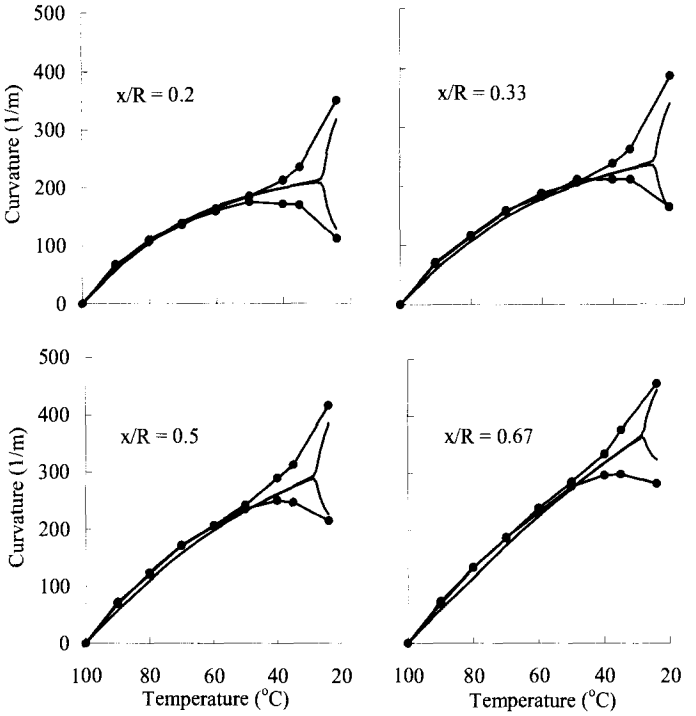

FIG. 5—*Pointwise curvature as function of temperature change for the D = 300 μm structure at four locations, x/R. Solid lines are predictions and the filled circles are measurements that are connected by lines to aid viewing.*

Conclusions

We studied the deformation response of polysilicon/gold circular plate microstructures subjected to uniform temperature changes. Consistent with previous observations, we observed three regimes of deformation in terms of the average curvature-temperature response: linear thermoelastic response, geometric nonlinear response, and bifurcations in the deformation behavior. In all three regimes we found good agreement between measurements and predicted curvatures, the latter based on both an analytical calculation assuming a constant curvature deformation mode, and finite element calculations that removed this restriction. The most significant discrepancies between the measurements and predictions occurred in the details of the bifurcations, but we showed that these are unlikely to be accurately modeled without detailed information regarding the imperfection that initially triggers the bifurcation. When geometric nonlinearity occurs, the average curvature depends on the in-plane dimensions of the plate, and the curvature can vary significantly over these dimensions. We obtained good agreement between measurements and predictions for this nonuniform curvature.

Acknowledgments

This effort is sponsored by the Defense Advanced Research Projects Agency (DARPA) and the Air Force Research Laboratory, Air Force Materiel Command, USAF, under agreement number F30602-98-1-0219. Useful comments of the referees are greatly appreciated, especially the comments suggesting clarification of the anisotropy in thermal expansion as a driver for the bifurcation.

References

[1] Stoney, G. G., "The Tension of Metallic Films Deposited by Electrolysis," *Proceedings of the Royal Society of London,* Vol. A82, 1909, pp. 172–175.

[2] Hyer, M. W., "Some Observations on the Cured Shape of Thin Unsymmetric Laminates," *Journal of Composite Materials,* Vol. 15, 1981, pp. 175–194.

[3] Hyer, M. W., "Calculation of the Room-Temperature Shapes of Unsymmetric Laminates," *Journal of Composite Materials,* Vol. 15, 1981, pp. 296–310.

[4] Hyer, M. W., "The Room-Temperature Shape of Four-Layer Unsymmetric Cross-Ply Laminates," *Journal of Composite Materials,* Vol. 16, 1982, pp. 318–340.

[5] Dano, M. L. and Hyer, M. W., "Thermally-Induced Deformation Behavior of Unsymmetric Laminates," *International Journal of Solids Structures*, Vol. 17, 1998, pp. 2101–2120.

[6] Masters, C. B. and Salamon, N. J., "Geometrically Nonlinear Stress-Deflection Relations for Thin Film/Substrate Systems," *International Journal of Engineering Science,* Vol. 31, 1993, pp. 915–925.

[7] Masters, C. B. and Salamon, N. J., "Geometrically Nonlinear Stress-Deflection Relations for Thin Film/Substrate Systems With a Finite Element Comparison," *Journal of Applied Mechanics*, Vol. 61, 1994, pp. 872–878.

[8] Salamon, N. J. and Masters, C. B., "Bifurcation in Isotropic Thin Film/Substrate Plates," *International Journal of Solids Structures,* Vol. 32, 1995, pp. 473–481.

[9] Finot, M. and Suresh, S.,"Small and Large Deformation of Thick and Thin Film Multilayers: Effects of Layer Geometry, Plasticity and Compositional Gradients," *Journal of Mechanical and Physical Solids,* Vol. 44, 1996, pp. 683–721.

[10] Finot, M., Blech, I. A., Suresh, S., and Fujimoto, H., "Large Deformation and Geometric Instability of Substrates with Thin Film Deposits," *Journal of Applied Physics*, Vol. 81, 1997, pp. 3457–3464.

[11] Freund, L. B., "The Stress Distribution and Curvature of a General Compositionally Graded Semiconductor Layer," *Journal of Crystal Growth,* Vol. 132, 1993, pp. 341–344.

[12] Freund, L. B., "Some Elementary Connections Between Curvature and Mismatch Strain in Compositionally Graded Thin Films," *J. Mech. Phys. Solids,* Vol. 44, 1996, pp. 723–736.

[13] Freund, L. B., "The Mechanics of a Free-Standing Strained Film/Compliant Substrate System," *Thin Films: Stresses and Mechanical Properties VI* (Mater. Res. Soc. Proc. 436, Pittsburgh, PA), W. W. Gerberich, H. Gao, J. E. Sundgren, and S. P. Baker, Eds., 1997, pp. 393–404.

[14] Freund, L. B., "Substrate Curvature due to Thin Film Mismatch Strain in the Nonlinear Deformation Range," *Journal of the Mechanics and Physics of Solids*, Vol. 48, 2000, pp. 1159–1174.

[15] Koester, D. A., Mahadevan, R., Hardy, B., and Markus, K. W., *MUMPs™ Design Rules*, Cronos Integrated Microsystems, a JDS Uniphase Company, 2001, http://www.memsrus.com/cronos/svcsrules.html.

[16] De Groot, P. and Deck, L., "Surface Profiling by Analysis of White-Light Interferograms in the Special Frequency Domain," *Journal of Modern Optics*,

Vol. 42, 1995, pp. 389–401.

[*17*] Dunn, M. L., Zhang, Y., Roy, J. M., Labossiere, P. E. W., and Bright, V. M., "Nonlinear Deformation of Multilayer MEMS Structures," *Proceedings of the MEMS Symposium,* ASME International Mechanical Engineering Congress and Exposition, Nashville, TN, 14-19 Nov. 1999.

[*18*] Sharpe, W. N., Yuan, B., and Edwards, R. L., "A New Technique for Measuring the Mechanical Properties of Thin Films," *Journal of Microelectromechanical Systems*, Vol. 6, 1997, pp. 193–199.

[*19*] Sharpe W. N., Turner, K. T., and Edwards R. L., "Tensile Testing of Polysilicon," *Experimental Mechanics*, Vol. 39, 1999, pp. 162–170.

[*20*] King, J. A., *Materials Handbook for Hybrid Microelectronics,* Teledyne Microelectronics, Los Angeles, CA, 1988.

R. L. Newton[1] *and J. L. Davidson*[2]

The Effects of Radiation on the Mechanical Properties of Polysilicon and Polydiamond Thin Films

REFERENCE: Newton, R. L. and Davidson, J. L., "The Effects of Radiation on the Mechanical Properties of Polysilicon and Polydiamond Thin Films," *Mechanical Properties of Structural Films, ASTM STP 1413*, C. Muhlstein and S. B. Brown, Eds., American Society for Testing and Materials, West Conshohocken, PA, Online, Available: **www.astm.org/STP/1413/1413_05**, 10 April 2001.

ABSTRACT: Due to its many excellent properties, diamond is being explored as a material for MicroElectroMechanical Systems (MEMS). However, as is true in the case of silicon, a large amount of basic material characterization issues still warrant investigation. This paper presents preliminary results from charged particle irradiation of Chemical Vapor Deposited (CVD) polycrystalline diamond films. The films were simultaneously dosed to a level of 9.4×10^{13} particles/cm^2 using 700 keV protons and 1 MeV electrons. The samples were then subject to cross-sectional nanoindention analysis and Raman spectroscopy. Polycrystalline silicon was also investigated for comparison purposes. The diamond was unaffected by the irradiation. However, the silicon did indicate a slight decrease in Young's modulus.

KEYWORDS: CVD diamond, polycrystalline silicon, radiation effects, nanoindention, Raman Spectroscopy, MEMS, hardness, Young's Modulus, cross-sectional

Introduction

Despite over two decades of research and development, MicroSructural Technologies (MST) and MicroElectroMechanical Systems (MEMS) have to date experienced only moderate commercial success. U.S. sales were approximately 6 billion in 1999, yet sales are expected to be somewhere between 14 and 23 billion by the year 2004 [1]. This forecast projects significant growth. However, many materials-related issues must be better understood in order to produce robust, high-durability MST/MEMS products for widespread scientific and commercial uses. Further research must be performed in the areas of tribology, mechanics, and surface analysis.

Due to the smallness of size, volume, and advanced technical performance, the Air Force, National Aeronautics and Space Administration (NASA), and foreign space agencies such as the European Space Agency (ESA) are very interested in MEMS/MST technology. Microsatellite research and development has been underway for some time.

In addition to the above-mentioned materials-related issues needing investigation, MST/MEMS systems that operate in low- or near-earth orbits will also face a radiation environment. This will be primarily composed of protons and electrons. In lower orbits, protons will be the more prevalent species, and at higher orbits, electrons will dominate the radiation environment [2]. It is well known that radiation degrades electronic device

[1]Materials Engineer, ED 36A, NASA Marshall Space Flight Center, Huntsville, AL 35812.

[2]Professor, Department of Electrical and Computer Engineering, Vanderbilt University, Nashville, TN 37235.

performance and can render them inoperable. However, it is lesser known what effects radiation has on the mechanical properties of micron-sized quantities of material when used for structural purposes, especially when no high-temperature annealing regime will be available to remove crystal defects caused by the exposure.

In recent years, a new MST/MEMS "building block" material has emerged—that of polycrystalline diamond [3,4]. Given the superior properties of diamond as compared to polycrystalline silicon, this material is a good candidate for high-temperature and extreme environment MEMS applications. Diamond MEMS (DMEMS) components and devices are already being fabricated and reported in the literature [3,5]. Studies indicate that polycrystalline diamond is also a very "radiation hard" material [6]. Thus, this material may prove to be a superior candidate for MEMS applications in radiation environments. However, to date, few investigations have looked at proton and/or electron radiation.

In order to straightforward compare the effects of the combination of proton and electron irradation upon the mechanical properties of polycrystalline diamond, a cross-sectional "dose-versus-mechanical property" investigation was performed on irradiated specimens that had no post-radiation annealing. This article presents initial results of the hardness and Young's modulus of irradiated polycrystalline diamond thin films at a dose of 9.4×10^{13} particles/cm^2. For comparison, polycrystalline silicon was also investigated. Mechanical property characterization was performed using nanoindentation techniques. The films were also characterized using Scanning Electron Microscopy (SEM) and micro-Raman spectroscopy.

Experiment

Polycrystalline diamond (polyDi) of approximately 12 μm in thickness was prepared on a 50.8 mm single crystal silicon substrate by using microwave-plasma-assisted chemical vapor deposition (MPACVD) at a temperature of 800°C and a pressure of 110 Torr. The hydrogen flow rate was 479 sccm, and methane flow rate was 18 sccm with a microwave power of 5 kW. The total time of film deposition was 20 h. The schematic presented in Fig. 1 illustrates a cross-sectional view of the as-deposited wafer.

Polycrystalline silicon was procured from Cermat Technologies, Murray Hill, N.J. An approximately 22 μm film of polycrystalline silicon (polySi) was deposited on top of a 1000Å of silicon dioxide, which was itself grown on a single crystal silicon wafer. The polySi was deposited by low-pressure chemical vapor deposition (LPCVD) at a temperature of 615°C and a pressure of 400 mTorr using dilute silane (in nitrogen) as a precursor. A cross-sectional schematic of this wafer is also shown in Fig. 1.

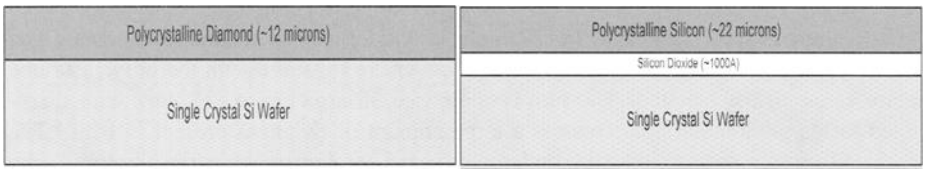

FIG. 1—*Cross-sectional schematic of the polycrystalline diamond and polycrystalline silicon used in the investigation.*

The depth of proton implantation into the specimens was calculated using the computer code TRIM [7]. This program calculates the energy loss of energetic ions in matter using a binary collision approximation (BCA) Monte Carlo simulation program. Table 1 presents the range (*Rp*) and straggle (ΔRp) profile for 700 keV protons implanted into these materials. The propagation code TIGER [8] was chosen to model the effects of electron irradiation on the samples. According to the calculations, electrons within the energy range under investigation (1 MeV) are not stopped in these films. These values were chosen due to facility limitations yet these energy levels are within expected ranges in near earth orbits.

TABLE 1—*Theoretical range (Rp), straggle (ΔRp), lattice displacement energy (E_d), and vacancies per ion for 700 keV protons deposited in the specimens.*

Specimen Identification	Range (*Rp*) microns	Straggle (ΔRp) microns	Dis. Energy (E_d), eV	Vacancies per Ion
Polydiamond	4.61	0.11	45	6.2
Polysilicon	9.31	0.31	15	32.5

The wafers were sectioned into approximately half-inch squares and vacuum baked overnight at 60°C to remove any residual surface contaminates. The samples were simultaneously dosed to a level of 9.4×10^{13} particles/cm^2 with 700 keV protons using a NEC model 2SH Pelletron and 1 MeV electrons using an NEC 7.5SH Pelletron. The beam flux was ~1 nA/cm^2. Irradiation was carried out at room temperature. After irradiation, the samples were cleaved to expose a cross-sectional surface. They were then cold mounted in epoxy and polished to 0.5 μm following standard metallurgical procedures. Scanning Electron Microscopy (SEM) analysis (prior to mounting) was performed using an ElectroScan Environmental SEM. Nanoindention testing was performed using a Nanoinstruments Nanoindentor II®. A Berkovich tip made of diamond was used for all indentations. Micro-Raman Spectroscopy was performed using an argon laser operating at 514.5 nm. A X100 Olympus lens focused the backscattered light into a DILOR spectrometer. In this configuration, the sampling volume is approximately 1 μm in diameter and 2 μm in height.

Results and Discussion

Figure 2 shows the SEM micrographs of the top surface of the as-deposited and irradiated polyDi films. The grains uniformly cover the substrate with the polycrystalline nature being clearly evident. The film is composed of large grains (>3 μm), with sharp-edged facets predominating. There is a large amount of twinning present as well. The irradiated sample appears to have undergone some amount of grain tip blunting. The surface of the individual grains, while still retaining most of their sharp edges, have been rounded to a small degree and appear to have a much rougher surface than the as-deposited material.

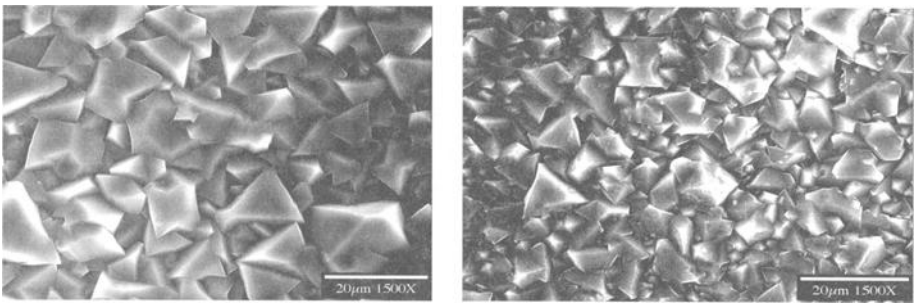

FIG. 2—*SEM image of the top surface of the as-deposited (left) and irradiated (right) polycrystalline diamond film.*

SEM images of the as-deposited and irradiated polySi are presented in Fig. 3. The polycrystalline nature of this film is apparent although the individual grains, and their boundaries are much less pronounced than in the diamond specimen. The grains are large (>6 μm) with no particular orientation or facet evident. No change in the surface structure of the irradiated sample was observed.

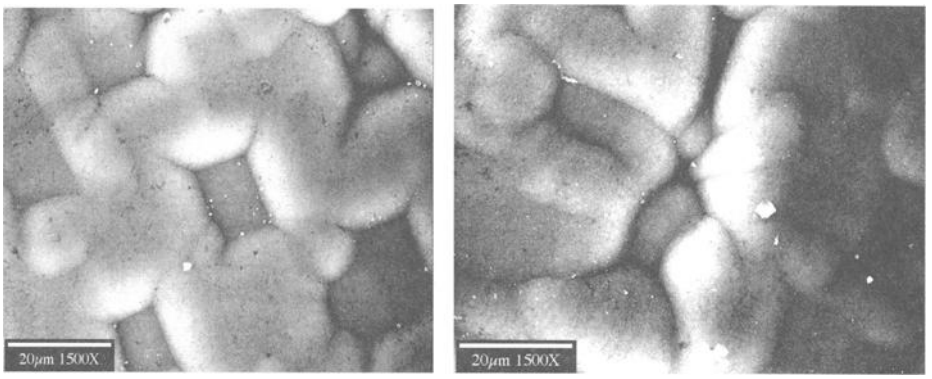

FIG. 3—*SEM images of the top surface of the as-deposited (left) and irradiated (right) polycrystalline silicon films.*

Figure 4 shows the SEM micrographs of an edge-on analysis of the polyDi films. From this perspective, the cross section of the as-deposited (left) and irradiated (right) diamond films can be observed. Near the substrate, the grains are small and somewhat random in orientation, but, as film deposition continues, the grains become longer and more columnar in nature. The interface between substrate and film appears to be free of voids or film to substrate delamination. The irradiated sample shows no sign of degradation either near the surface or at the calculated depth of maximum proton deposition (4 μm).

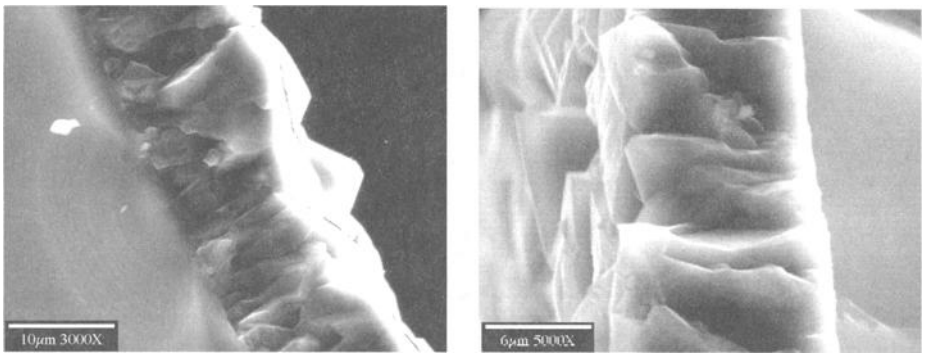

FIG. 4—*Edge-on SEM images. No radiation damage is evident from the SEM images of the polycrystalline diamond films; non-irradiated (left), irradiated (right).*

While there was no visible evidence present in the SEM cross-sectional images of radiation damage in the polyDi, a post-radiation artifact was observed in the polySi. In the right image of Fig. 5, there is evidence of a boundary about 8 μm from the top surface. This region corresponds to the depth calculated by the TRIM program as to being the maximum depth as to where the protons would be deposited.

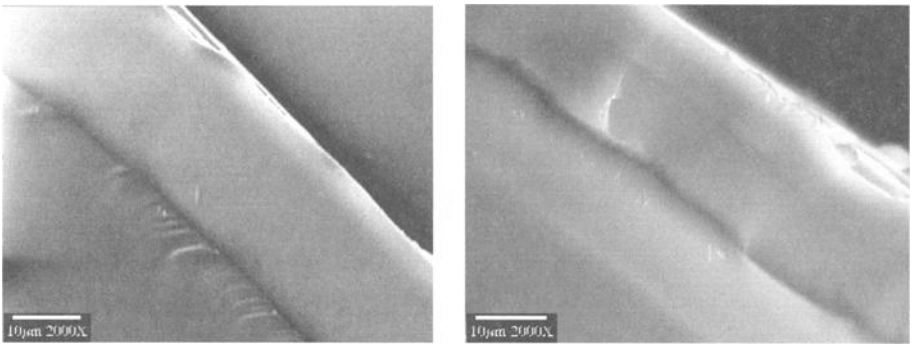

FIG. 5—*Edge-on SEM images of the before (left) and after (right) irradiation of the polycrystalline silicon is presented in this figure. There does appear to be some sort of boundary or difference in the irradiated sample about 8 μm from the top surface.*

The epoxy-mounted and polished samples were indented in an edge-on, cross-sectional fashion versus the normal top-down approach. This method was chosen so as to observe any depth-dependent effects of the radiation. This testing configuration also eliminates any substrate effects from influencing the material response of the film. The indentations were performed, starting near the top edge of the film, and ending near the film substrate interface. Each indention had a tip approach segment followed by a loading segment. The indenter was then held under load so as to compensate for any

error due to material creep. The indenter was partially unloaded 20% while still in contact with the specimen so as to measure thermal drift. The indenter was then fully unloaded. Contact stiffness was measured throughout the load segment. The maximum indention load for the polyDi was 16 mN for both samples. The maximum indentation depth was 105 nm for the blank and 92 nm for the irradiated sample. The sample exhibited complete elastic load and unloading with representative load/unload curves for both the non-irradiated and irradiated samples being shown in Fig. 6. These data were taken from measurements around 3 μm from the top surface. An analysis of the unloading curve for the as-deposited polyDi did indicate a power law dependence of the form $y = ax^m$, with m being approximately equal to 1.97. The value of m for the unloading curve from the irradiated sample was equal to 1.67. Hardness and Young's Modulus were calculated using the method derived by Sneddon [9,10]. The experimentally measured hardness and Young's Modulus values reported (Table 2) for the non-irradiated sample is some 10 to 15% higher than expected. This is also the case in the irradiated sample as well. While ion implantation of hydrogen could have displaced the nitrogen in the film and resulted in perhaps some increase in mechanical property, this is likely not the case since no depth-dependent hardness and/or Young's modulus variation was detected in the irradiated specimens, regardless of depth. Rather, these values are likely due to error introduced into the indenter area function via tip blunting and surface non-uniformity. Tip rounding and deformation are known to exist when the modulus of the indenter and the specimen are similar. This is the subject of much current work, but it appears that finite element modeling is needed to obtain accurate values [11].

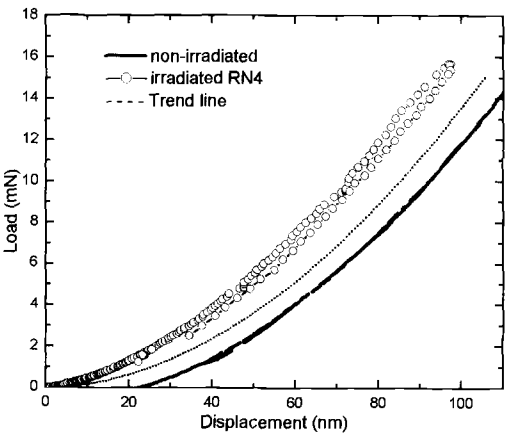

FIG. 6—*Representative cross-sectional load versus indenter displacement for the polycrystalline diamond sample at highest peak load. The non-irradiated curve has been horizontally offset for comparison purposes and to reveal the trend line.*

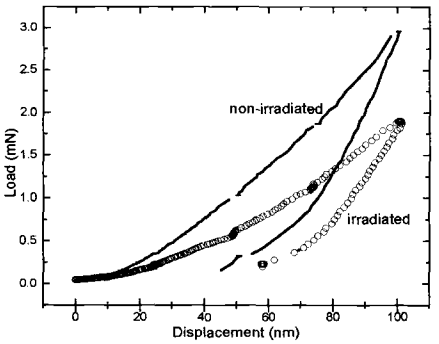

FIG. 7—*Representative cross-sectional load versus unloading data for polycrystalline silicon. Comparison of the non-irradiated versus the irradiated sample indicates a decrease in Young's Modulus in the irradiated sample.*

Representative polySi load versus displacement curves are shown in Fig. 7. A large amount of plastic deformation in the non-irradiated sample is evident due to the fact that the indented surface does not return to its pre-indented depth. Not only is plasticity observed, but the discontinuity in the curves also indicates film cracking as well. Conversely, a measure of the elastic response of material is to examine the percent elastic recovery. This value is obtained by the ratio of the final deposition depth, h_f, to the maximum indenter depth, h_m. A lower value indicates a greater elastic response of the sample. The non-irradiated sample has a percent elastic recovery of 45% versus 58% for the irradiated specimen. Also note that the load needed to drive the indenter to the maximum depth is much greater in the polyDi than in the polySi. This is expected due to the much higher yield strength of polyDi.

TABLE 2—*Measured values of the hardness and Young's Modulus for the polycrystalline diamond and silicon.*

Specimen Identification	Hardness (GPa)	Young's Modulus (GPa)
Polycrystalline Diamond as-prepared/irradiated	89.9/90.1	1155/1207
Polycrystalline Diamond Reference [12]	67	1000
Polycrystalline Silicon as-prepared/irradiated	10.5/10.7	174/154
Polcrystalline Silicon Reference [13]	11.0	160

Micro-Raman Spectroscopy is an excellent tool for the study of carbon-based

materials. This is in large part due to the fact that the Raman intensity of graphite is approximately 50 times higher than that of diamond. In this research project, the Raman analysis serves two functions. One is to non-invasively analyze (in a cross-sectional fashion) the samples for any radiation-induced changes in the material. However, the other and equally important reason for utilizing Raman sampling is to monitor any changes in the specimens due to sample preparation. This is required because, as already mentioned, prior to nanoindention analysis the samples must be mounted and polished to a 0.5 μm surface smoothness. Raman spectroscopy was employed to observe whether this mounting and polishing activity did alter the near surface microstructure of both the polyDi and polySi specimens.

In both Figs. 8 and 9, a Lorentzian function was fitted to each of the Raman spectra in order to determine the peak frequency. The full width at half maximum (FWHM) was also calculated from the Lorentzian analysis. Figure 8 compares the irradiated and non-irradiated polycrystalline diamond samples. The single first-order Raman line at approximately 1332.09 cm^{-1} is clearly evident, and no other peaks are present. Within experimental error, the non-irradiated and irradiated samples appear to be identical. This indicates that the carbon did not undergo a measurable change as a result of the irradiation. Also, these two spectra are virtually identical to spectra collected from an unmounted/unpolished/non-irradiated sample as well (not shown). The data from the not shown sample (i.e., peak frequency, 1329.9 cm^{-1}, and FWHM of 5.23 cm^{-1}) lend supporting evidence to indicate that there was no microstructural or surface alteration from sample mounting and polishing. These Raman values compare very well with low stress state natural and synthetic diamond, both mono and polycrystalline [14].

The polySi data is given in Fig. 9. Since this sample was essentially silicon deposited on silicon, the substrate was used as a reference material. The peak at 520.04 cm^{-1} is indicative of silicon. However, as the overlaid spectra indicate, the silicon peak disappears in the polished/unirradiated and polished/irradiated specimens. It is not clear why this occurred since no extreme or unusual processing was performed on the samples.

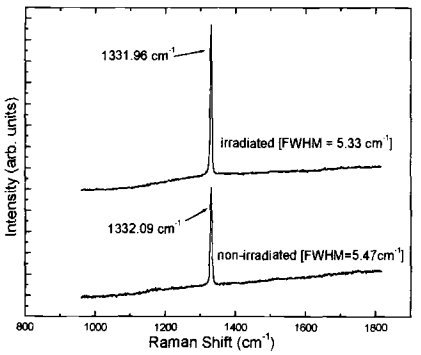

FIG. 8—*Cross-sectional micro-Raman data for the polycrystalline diamond samples. The spectra have been shifted vertically for comparison purposes. These spectra were collected near the top edge of the cross sections. No difference within statistical variation is indicated.*

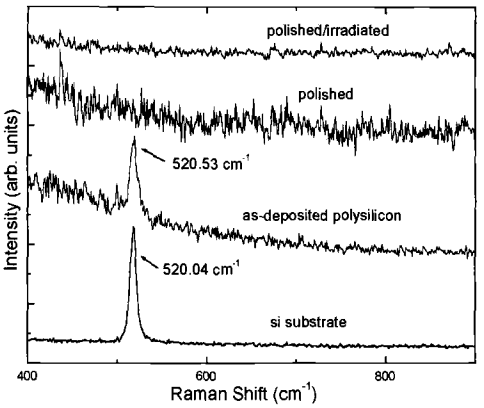

FIG. 9—*Cross-sectional micro-Raman spectra of the polycrystalline silicon samples. The spectra have been translated vertically for comparison purposes. While the as-deposited film gave a Raman peak characteristic of silicon, the polished samples did not.*

Conclusion

The preliminary results of the hardness and Young's modulus of proton and electron irradiated polycrystalline diamond have been presented. Polycrystalline silicon was also tested for comparison purposes. At the irradiation level under consideration (700 keV protons and 1 MeV electrons) and dosage (9.4×10^{13} particles/cm^2), it was determined via nanoindentation techniques that the mechanical properties of the diamond material were unaffected. The effects of radiation were also studied non-invasively via micro-Raman spectroscopy. These results also indicated that no damage was caused by the radiation. Future work will be performed using much higher radiation dosages ($>10^{17}$) of protons. Additionally, the effects due to tip blunting must also be corrected. Recent work indicates that finite element analysis will allow one to determine the true Young's modulus and hardness of diamond-like coatings.

The polycrystalline silicon used in this investigation did indicate a decrease in Young's modulus after irradiation. However, the Raman data indicated an alteration of the near surface microstructure. Future work will investigate this phenomenon.

While further work is warranted, irradiation with both protons and electrons did not alter the mechanical properties of irradiated but non-annealed polycrystalline diamond used in this investigation. These results further support the idea that diamond-based MEMS devices, or diamond coated MEMS structures, may provide a much higher degree of mechanical property stability for applications in high radiation environments such as that encountered in space, nuclear power generation, and medical applications as compared to polycrystalline silicon.

Acknowledgment

This work is supported by NASA Marshall Space Flight Center under project IR&D 36-09. Laura Reister of Oak Ridge National Labs collected the nanoindention measurements. Oak Ridge National Laboratory is sponsored by the Assistant Secretary for Energy Efficiency and Renewable Energy, Office of Transportation Technologies, as part of the High Temperature Materials Laboratory User Program, Oak Ridge National Laboratory, managed by UT-Battelle, LLC, for the U.S. Department of Energy under contract number DE-AC05-000R22725. Also, thanks to Dr. Vora and Dr. Catledge from the University of Alabama in Birmingham for assistance with the Raman Spectroscopy.

References

[1] Venture Development Corporation, "MicroStructures Technology (MST) and MEMS: An Applications and Market Evaluation," Online, URL: http://www.vdc-corp.com/ products/br00-12.html (cited July 24, 2000).

[2] Daly, E. J., Hilgers, A., Drolshagen, G., and Evans, H. D. R., "Space Environment Analysis: Experience and Trendsm" (online), URL: http://www.estec.esa.nl/CONFANNOUN/96a09/Abstracts/abstract45 (cited August 18, 2000).

[3] Davidson, J. L., et. al., "Diamond as an Active Sensor Material," *Diamond and Related Materials*, Vol. 8, 2000, pp. 1741–1747.

[4] Kohn, E., Gluche, P., and Adamschik, M., "Diamond MEMS—A New Emerging Technology," *Diamond and Related Materials*, Vol. 8, 1999, pp. 934–940.

[5] Cagin, T., et al., « Simulation and Experiments on Friction and Wear of Diamond : A Material for MEMS and NEMS Application," *Nanotechnology*, Vol. 10, 1999, pp. 278-284.

[6] Gonan, P., Prawer, S., Jamieson, D. N., and Nugent, K. W., "Radiation Hardness of Polycrystalline Diamond," *Diamond and Related Materials*, Vol. 6, 1997, pp. 314–319.

[7] Ziegler, J. F., Biersack, J. P., and Littmark, U., *The Stopping Range of Ions in Solids*, Pergamon Press, New York, 1978.

[8] Alstatt, R. L., "Brief Description of Modeling Results for Electron and Proton Beams Incident on Thin Materials," NASA-Marshall Space Flight Center internal report, February, 2000.

[9] Sneddon, I. N., International Journal of Engineering Science, Vol. 3, No. 47, 1965.

[10] Harding, J. W. and Sneddon, I. N., *Proceedings of the Cambridge Philosophical Society*, Vol. 41, No. 12, 1945.

[11] Hay, J. C., Bolshakov, A., and Pharr, G. M., "A Critical Examination of the Fundamental Relations used in the Analysis of Nanoindention Data," *Journal of Materials Research*, Vol. 14, No. 6, 1999, pp. 2296–2305.

[12] Kant, A., et al., "Microstructural Effects on the Hardness, Elastic Modulus and Fracture Toughness of CVD Diamond," *Materials Research Society Symposium Proceedings*, Vol. 505, 1998, pp. 611–616.

[13] Bhushan, B. and Koinkar, V. N., "Mirotribological Studies of Doped Single-Crystal Silicon and Polysilicon Films for MEMS Devices," *Sensors and Actuators*, Vol. 57, 1996, pp. 91–102.

[14] Knight, D. S. and White, W. B., "Characterization of Diamond Films by Raman Spectroscopy," *Journal of Materials Research*, Vol. 4. No. 2, 1989, pp. 385–393.

Author Index

Subject Index